Spatially-resolved trace element records in cultured and fossil foraminifera: Cenozoic ocean chemistry, palaeoseasonality and tropical temperature reconstruction

David Evans

Supervised by

Wolfgang Müller

A thesis submitted for the degree of

Doctor of Philosophy

January 2015

Department of Earth Sciences

Royal Holloway University of London

Egham, UK

Declaration of authorship

I, David Evans hereby declare that this thesis and the work presented in it is entirely my own, except where indicated by the heading **Author contributions** at the start of some chapters. Where I have consulted the work of others, this is always clearly stated.

Signed:

Date:

Acknowledgements

I have been helped and supported by too many generous friends and scientists to name everyone individually here; I hope that my gratitude has been and continues to be obvious.

In particular, I am greatly indebted to my supervisor, and friend, Wolfgang Müller, whose encouragement, kindness and expert guidance have been fundamental to the success of this project. I could not have wished for a better supervisor, and I look forward to a long and fruitful ongoing collaboration. I am also extremely grateful for the support of Jonathan Erez, from whom I have learnt an enormous amount. My time spent culturing foraminifera in Israel was undoubtedly the highlight of this project and I am especially thankful for the help and advice in developing my career beyond my doctoral studies.

I acknowledge NERC for funding my PhD studentship, and I am grateful to the Royal Holloway University of London travel bursary scheme. This latter funding enabled me to spend a further two months working in Israel, for which I am very grateful.

I would like to thank both of my parents for their love and guidance throughout my life; you are the most wonderful, kind people and I will always be thankful for everything you have done for me. My childhood curiosity for finding out how things work, which you encouraged, is certainly the reason I have pursued a scientific career, and for this I will always be especially grateful. Everything I have achieved is as a result of the best possible start in life that I have had, and I hope – as ever – that you are proud of my achievements, which are also your achievements.

Abstract

The incorporation of trace elements into biogenic carbonates, particularly foraminifera, forms a substantial portion of our knowledge of Cenozoic ocean temperatures. However, analogously to isotopic systems, trace element partioning into carbonates is also dependent on the composition of the solution from which biomineralisation takes place. Seawater chemistry, in particular the concentration of the alkali earth metals, is known to have undergone significant secular variation during the Phanerozoic. In order to form the basis of more accurate ocean temperature and seawater chemistry reconstructions throughout the Cenozoic, detailed laboratory calibrations of the relationship between temperature, seawater chemistry and test chemistry for two very different foraminifera were conducted. The long-lived large benthic foraminifer *Operculina ammonoides* was targeted for its potential as a seasonal proxy archive, whilst an improved understanding of these relationships in the widely utilised planktic foraminifer *Globigerinoides ruber* have the potential to improve Plio-Pleistocene palaeoceanic reconstructions. These data constrain the complexity of the controls on trace element incorporation into foraminifera. In particular, seawater-test Mg/Ca were found to vary nonlinearly, demonstrating that such coupled calibrations are a prerequisite for quantitative palaeoceanic reconstruction before the Pleistocene, when seawater chemistry cannot be assumed to be the same as at present. Based on highly spatially-resolved laser-ablation trace element depth profiles, tracks and 2D mapping, these calibrations are applied to the abundant Eocene nummulitids, which are shown to have excellent potential as an archive of seawater chemistry and palaeoseasonality. These data indicate a 1.5-2$\times$ increase in surface ocean temperature seasonality compared to present, and provide new constraints on secular seawater chemistry variation. The observed seasonality increase in a greenhouse world is interpreted to be related to the frequency and/or intensity of tropical storms. Finally, applying these *G. ruber* calibrations to the offset between Mg/Ca and biomarker-derived palaeotemperatures for published Plio-Pleistocene datasets spanning the last 5 million years enables Pliocene seawater Mg/Ca to be more accurately constrained. This seawater chemistry reconstruction indicates that the ocean calcium concentration was 20-25% higher in the Pliocene, with the direct implication that deep ocean temperatures and ice volume may have been previously underestimated.

Contents

List of acronyms

[X]	Denotes concentration of X
AES	Atomic emission spectroscopy
ASW	Artificial seawater
BGS	British Geological Survey
CCD	Carbonate compensation depth
D_x	The distribution coefficeint of x, equal here to $[x_{calcite}]/[x_{sw}]$
DIC	Dissolved inorganic carbon
DSDP	Deep sea drilling program
EMPA	Electron micro probe analysis
EOT	Eocene-Oligocene transition
ESL	Eustatic sea level
ESW	Eilat seawater
GCM	General circulation model
GDGT	Glycerol dialkyl glycerol tetraethers
LA-ICPMS	Laser-ablation inductively-coupled-plasma-mass-spectrometry
LBF	Large benthic foraminifera
LGM	Last glacial maximum
LOESS	Locally weighted scatterplot smoothing
MAT	Mean annual temperature
NERC	Natural Environment Research Council (UK)
NIST	National Institute of Standards and Technology (US)
NLR	Nearest living relative
ODP	Ocean Drilling Program
PETM	Paleocene-Eocene Thermal Maximum
PWP	Pliocene Warm Period
REE	Rare earth element
RSD	Relative standard deviation
RSL	Relative sea level
SE	Standard error
SEM	Scanning electron microscopy
SIMS	Secondary ion mass spectrometry
SRM	Standard reference material
SST	Sea surface temperature
TEX_{86}	Tetraether index of 86 carbon atoms (SST proxy)

Introduction

1.1 Rationale

Anthropogenic CO_2 is currently being released at a rate of 9.5 Pg C year^{-1} (petagrams = gigatons), with a total of 515 Pg C released directly to the atmosphere since the industrial revolution [e.g. *Keeling*, 1960; *IPCC*, 2013]. Our current understanding of the carbon cycle from the geological record indicates that a sustained carbon release of this magnitude is unprecedented since at least the Palaeocene-Eocene Thermal Maximum 56 million years (Ma) ago [e.g. *Bowen et al.*, 2014]. Present day atmospheric CO_2 is 400 ppm, at least 120 ppm higher than any point in the last 800 ka [*Lüthi et al.*, 2008], and is likely higher than at any point during the last 2.8 Ma [*Fedorov et al.*, 2013; *Seki et al.*, 2010]. The greenhouse effect is evident in the Recent instrumental record [e.g. *Hegerl et al.*, 2006], and there is abundant geochemical and palaeontological evidence that geological periods characterised by higher than present-day CO_2 (such as the Paleogene, 66-23 Ma) were indeed substantially warmer. For example, early-mid Eocene Antarctica is thought to have been ice-free [*Lear et al.*, 2000] and populated by temperate fauna and flora [*Greenwood and Wing*, 1995], despite being at a similar latitude to present-day. Extensive evidence exists that even a moderate increase in greenhouse gas concentration, for example during the Pliocene Warm Period (PWP, 3.26-3.03 Ma, mean $pCO_2 = \sim$400 ppm), exerts a substantial control on global temperature, atmospheric circulation, precipitation patterns and the acidity of the ocean [*LaRiviere et al.*, 2012; *Brierley et al.*, 2009; *Seki et al.*, 2010]. As a result, a substantial amount of effort has been focused on creating and interpreting increasingly complex General Circulation Models (GCMs) in order to predict and mitigate against the effects of climate change. However, such models are typically tuned to the instrumental record, and may not accurately capture all aspects of greenhouse warming [*Dowsett et al.*, 2012]. Therefore, quantitative proxy-based reconstructions of past climates are desirable for two principal reasons. Firstly, such data have the potential to inform the community of possible model bias, which may be linked to missing or poorly understood physical mechanisms, or unrepresentative parameterisation of complex oceanic and/or atmospheric phenomenon [*Randall et al.*, 2003]. Secondly, coeval reconstructions of pCO_2, sea level and temperature enable Earth system sensitivity (the pCO_2-global mean temperature slope) or the relationship between sea level and other parameters to be constrained [*Pagani et al.*, 2009; *Foster and Rohling*, 2013]. Although it is important to remember that there are fundamental differences between the present day and intensively studied time intervals such as the PETM and PWP [*Haywood et al.*, 2011], improved reconstructions of

critical Earth system parameters are of clear and direct societal relevance.

For a number of intervals, model and proxy data are broadly in good agreement [e.g. *Lunt et al.*, 2012; *Haywood et al.*, 2013] although important discrepancies exist. Amongst the most controversial of these are the differences between model and proxy data-derived latitudinal and zonal temperature gradients during past warm periods. The former is intimately linked to the ability of models to produce reduced latitudinal temperature gradients whilst maintaining tropical sea surface temperatures (SST) within the range indicated by the proxy data [*Huber and Sloan*, 2001], see figure 1.1. For example, proxy reconstructions of the Eocene subtropics indicate SST only a few °C higher than present-day [*Keating-Bitonti et al.*, 2011; *Pearson et al.*, 2007], whilst some GCMs indicate the tropics may have been 8-10°C warmer [*Heinemann et al.*, 2009; *Hollis et al.*, 2012]. However, for intervals deeper in geological time it should be borne in mind that reconstructions of Eocene tropical ocean temperatures are sparse, and that the oxygen isotope (δ^{18}O) data of some studies [e.g. *Pearson et al.*, 2007, 2001] should be considered to be transient summer maxima, and not directly comparable to the mean annual model representations. Zonal temperature gradients have received much attention; in particular, the magnitude and inter-annual variability of the E-W Pacific SST gradient is of particular relevance given the large impact the El Niño Southern Oscillation exerts on the temperature and aridity of the western Americas [*Piechota and Dracup*, 1996]. Pliocene to Recent proxy data indicate that this gradient may have been absent before the Pleistocene [*Wara et al.*, 2005], although more recent TEX_{86}-derived reconstructions [*Zhang et al.*, 2014], whilst in broad agreement, suggest that the mean gradient may not have been as low as previously

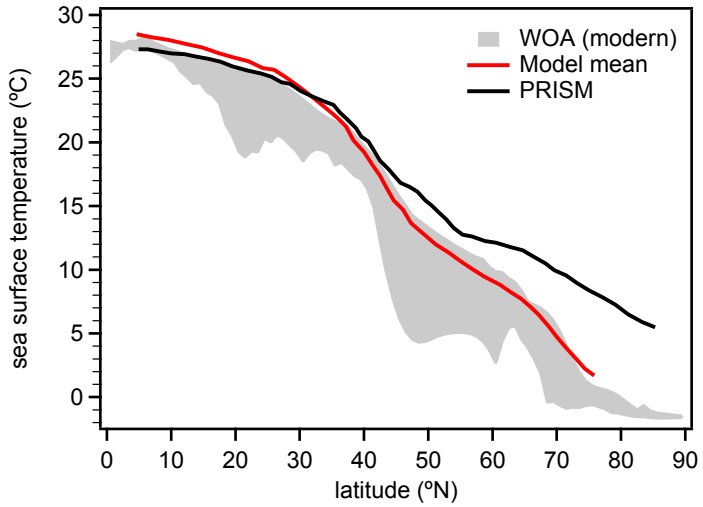

Figure 1.1: North Atlantic sea surface temperature model-data comaprison, redrawn from *Dowsett et al.* [2012]. Whilst the data are in overall agreement, the models reconstruct steeper latitudinal gradients. Modern SST data from *Locarnini et al.* [2010].

thought. In contrast, many models are characterised by an equatorial Pacific gradient similar to present-day [*Fedorov et al.*, 2013; *Haywood et al.*, 2013], although tropical cyclones or cloud albedo have been suggested as potential mechanisms by which this discrepancy may be resolved [*Fedorov et al.*, 2010; *Burls and Fedorov*, 2014].

At least some of these issues may be related to seasonality. Seasonal proxy bias and the time-averaged nature of some proxy datasets have been justifiably invoked in order to explain data-model offsets [e.g. *Lunt et al.*, 2012; *Haywood et al.*, 2013; *Prescott et al.*, 2014]. This issue is confounded by the sparse nature of accurate seasonality reconstructions at any point in the geological past, particularly in the Paleogene [*Hollis et al.*, 2012]. Many published values are derived from micro-sampled mollusc δ^{18}O [*Ivany et al.*, 2000; *Tripati and Zachos*, 2002], incorporating information regarding changes in both seasonal temperature and freshwater flux to shallow marine sites, which are challenging to disentangle (but see *Keating-Bitonti et al.* [2011]). Seasonal temperature reconstruction has also been attempted using the distribution of multiple individual planktic foraminifera δ^{18}O, yielding mixed results [*Wit et al.*, 2010]. The relatively low number of palaeo-tropical SST means that improved spatial coverage of proxy data with improved accuracy is a priority. Combining such data with seasonal reconstructions for the surface ocean not only offers the possibility of better constraining a relative unknown in the geological record, but would enable potential bias on other proxies to be systematically investigated, facilitating improved data-model comparison.

1.2 Trace element palaeothermometry: The state of the art

Past changes in sea surface temperature were historically known only from the oxygen isotope ratio of carbonate shells (δ^{18}O) [*Emiliani*, 1954, 1966; *Shackleton and Opdyke*, 1973; *Erez and Luz*, 1983], which gained wide popularity as a technique because of the abundance of foraminifera in ocean sediment cores. Since its conception, this proxy was known to depend on the oxygen isotopic composition of the fluid from which biomineralisation takes place, which seriously hampers the accuracy of δ^{18}O palaeothermometry in the past. This is a particular problem after the first major Antarctic glaciation over the Eocene-Oligocene transition [*Zachos et al.*, 2008], following which geologically rapid changes in Antarctic ice volume mean that it is challenging to accurately assess the likely seawater composition for the time of interest.

More recently, the exponential relationship between foraminiferal Mg/Ca and temperature [*Nürnberg et al.*, 1996] has been suggested as a promising alternative [*Klein et al.*, 1996], requiring no knowledge of the isotopic composition of the ocean. Furthermore, Mg/Ca coupled with

$\delta^{18}O$ temperature equations facilitates a method of simultaneously calculating $\delta^{18}O_{sw}$, which may relate to salinity once corrected for changes in global ice volume [*Shackleton and Opdyke*, 1973].

The ratio of Mg to Ca in the ocean is known to have undergone large secular variation [*Stanley and Hardie*, 1998; *Dickson*, 2004; *Horita et al.*, 2002], which is unsurprising given the relatively short $\sim$1 Ma oceanic residence time of Ca [*Li*, 1982]. Most studies utilising calcite Mg/Ca as a temperature proxy acknowledge that, analogously to isotopic systems, seawater Mg/Ca also exerts a control on Mg incorporation [e.g. *Lear et al.*, 2002; *Dutton et al.*, 2005; *Creech et al.*, 2010]. Specifically, with one notable exception [*Medina-Elizalde et al.*, 2008], all previous work assumes that seawater-test Mg/Ca vary linearly and pass through the origin. There is evidence that this is not the case for inorganic calcite [*Mucci and Morse*, 1983; *De Choudens-Sánchez and González*, 2009] as well as the majority of marine calcifiers for which this relationship has been examined [*Ries*, 2004]. Together, these studies indicate that variation of the Mg distribution coefficient (D_{Mg} = $[Mg/Ca_{test}]/[Mg/Ca_{sw}]$) with Mg/Ca_{sw} is best described by a power relationship. Two studies have examined the seawater-test Mg/Ca relationship in laboratory cultured foraminifera. *Segev and Erez* [2006] studied two species of the high-Mg large benthic foraminifera *Amphistegina*, and data for the planktic species *Globigerinoides sacculifer* are given by *Delaney et al.* [1985]. Whilst pioneering, this latter study requires revision as several factors co-varied in these cultures. Consequently there is no detailed study of the control exerted by Mg/Ca_{sw} on Mg/Ca_{test} for a planktic species. A detailed understanding of the relationship between Mg/Ca_{sw} and Mg/Ca_{test} is clearly required. Furthermore, two other widely held assumptions regarding the incorporation of Mg into foraminiferal calcite remain. Firstly, the sensitivity of the Mg/Ca thermometer, i.e. the increase in Mg/Ca associated with a 1°C rise in temperature, is unknown at non-modern Mg/Ca_{sw}. All published work implicitly assumes that this sensitivity does not change, an assumption which underpins the basis of the use of Mg/Ca for relative temperature reconstruction during times when Mg/Ca_{sw} is not well known [e.g. *Zachos et al.*, 2003]. Secondly, it is always assumed that it is the seawater Mg/Ca ratio that exerts a control on Mg/Ca_{test}, and not seawater [Mg] or [Ca]. *Segev and Erez* [2006] demonstrate that this is the case for *Amphistegina*, although it remains untested for a low-Mg calcite species such as those commonly utilised for SST reconstruction.

Aside from complications regarding the lack of detailed calibration of the relationship between Mg/Ca_{test}, seawater chemistry and temperature, foraminifera Mg/Ca also suffers from other secondary controls. The most widely known of these are the so-called vital effects; poorly constrained biological processes by which test chemistry (especially Mg/Ca) is mediated. The most obvious

of these is exemplified by the sensitivity of the Mg/Ca thermometer; inorganic calcite is characterised by a 3%$^{\circ}C^{-1}$ increase in Mg/Ca, whilst most planktic foraminifera have a sensitivity $\sim 3\times$ greater [*Bentov and Erez*, 2006]. Further complications include the control exerted by salinity [*Arbuszewski et al.*, 2010] and pH or carbonate ion concentration [*Russell et al.*, 2004]. Finally, fossil foraminifera Mg/Ca is susceptible to bias from both dissoution [*Dekens et al.*, 2002; *Regenberg et al.*, 2014] and Mg-rich diagenetic overgrowths such as kutnahorite [*Pena et al.*, 2005], precluding the use of poorly-preserved specimens for palaeothermometry and requiring all material to undergo rigorous preservational assessment. These factors may significantly complicate the application of this palaeothermometer, particularly deeper in geological time when there are few or no extant species on which to base measurements. Despite these issues, foraminifera Mg/Ca has been shown to produce more reliable estimates of SST change compared to other proxies for at least one location during the last glacial maximum [*Tripati et al.*, 2014], and more detailed investigation in order to improve the reliability of this proxy during climate-relevant time intervals (in particular the Pliocene and Paleogene) is therefore justified and required.

To this end, this thesis presents data from laboratory cultures of the relationship between Mg/Ca_{test}, Mg/Ca_{sw} and temperature for the widely utilised planktic foraminifera *Globigerinoides ruber* and the shallow-dwelling large benthic species *Operculina ammonoides*. These calibrations are designed not only to improve the accuracy of past ocean temperature reconstruction, but also to provide new methods of seawater chemistry reconstruction, and in the case of *O. ammonoides*, to examine the potential of long-lived foraminifera for palaeoseasonality reconstruction independent of mollusc $\delta^{18}O$.

1.3 Secular variation in seawater Mg/Ca and Sr/Ca

Seawater Mg/Ca is known to have varied over geological time [*Sandberg*, 1983], with a broad rise over the Cenozoic, as a result of a combination of changes in: the Mg/Ca ratio and flux of freshwater runoff, the rate of seafloor spreading, dolomitization rates, and the amount of Mg and Ca burial [see *Broecker and Yu*, 2011, for a recent review]. The latter principally occurs through the deposition of calcifying organisms which precipitate shells or tests that are characterised by a range of Mg/Ca ratios, although the majority of the major calcifiers produce low-Mg calcite. The modern ocean is characterised by [Mg] = 53 mM and [Ca] = 10.2 mM (Mg/Ca = 5.2 mol mol^{-1}).

Seafloor spreading rates have likely not changed substantially over the Cenozoic [*Seton et al.*, 2009], which means that this process can be ruled out as a possible control on Paleogene-Recent

Mg/Ca_{sw}. In contrast, dolomitization rates may have changed following the onset of major ice build-up on Antarctica, as sea level fell and the area of the shallow seas in which this process may take place decreased. Dolomitization replaces one mole of buried Ca with one mole of Mg from solution, and an increase in seawater Mg/Ca over the Cenozoic is therefore consistent with a decrease in dolomitization rates. Freshwater Mg/Ca depends on the lithologies weathered by a given catchment area, but is generally characterised by Mg/Ca closer to 1 and [Mg] and [Ca] $\leq$1 mM [e.g. *De Villiers et al.*, 2005]. An increase in $CaCO_3$ burial to the point where Ca removal outstripped supply from dolomitization and weathering would also increase Mg/Ca_{sw}.

Reconstructions of broad shifts in seawater Mg/Ca, derived by a number of methods, are in reasonable agreement over both the Cenozoic and Phanerozoic [*Dickson*, 2004; *Wilkinson and Algeo*, 1989; *Lowenstein et al.*, 2001; *Coggon et al.*, 2010]. These indicate that Mg/Ca_{sw} has undergone quasi-periodic fluctuation between 1-2 mol mol^{-1} and $\sim$5 mol mol^{-1} with a period of approximately 250 Ma (figure 1.2). However, further data are clearly required; whilst most studies agree on the broad trends on 50-100 Ma timescales, the magnitude of the disagreement between models and different proxy-derived reconstructions mean that useful data for correcting foraminifera Mg/Ca measurements are currently not available. The $\sim$1 Ma residence time of Ca means that Mg/Ca_{sw} ratios cannot be assumed further than 0.5-1 Ma from a reliable proxy datapoint. Furthermore, accurate reconstruction of the oceanic concentration of the alkali earth metals may inform us of the secular dynamics of the processes controlling these concentrations [*Wilkinson and Algeo*, 1989]. Recent proxy data indicate that a significant rise in Mg/Ca_{sw} may have occurred since the Oligocene [*Rausch et al.*, 2013], with one study suggesting that a large change has occurred since the Pliocene [*Fantle and DePaolo*, 2006]. There has been considerable recent debate regarding the plausibility of a change of this magnitude over a relatively short interval of geological time [*Broecker and Yu*, 2011; *Coggon et al.*, 2011]. Whilst at least some of this debate results from a misunderstanding of the accuracy of previous foraminifera-derived proxy Mg/Ca_{sw} reconstructions [*Broecker and Yu*, 2011; *Broecker*, 2013; *Lear et al.*, 2002], further constraints on the exact magnitude and timing of this rise would greatly benefit our understanding of weathering rates, dolomitisation, carbonate burial and sea floor spreading, as these processes exert a control on seawater [Mg] and [Ca].

Strontium arrives to seawater principally through weathering and is removed through calcite and aragonite precipitation, and has a residence time of $\sim$4 Ma [*Li*, 1982]. In contrast to Mg/Ca, seawater Sr/Ca reconstructions are in poor agreement. Those from ridge flank vein carbonates [*Coggon et al.*, 2010] indicate a large rise in Sr/Ca_{sw} over the Cenozoic, whilst benthic foraminifera

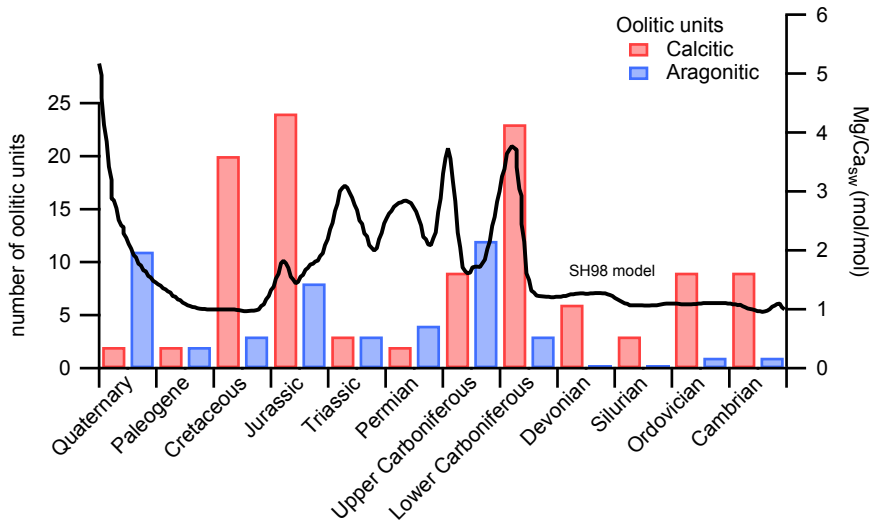

Figure 1.2: The secular variation of seawater Mg/Ca during the Phanerozoic, as indicated by the dominant phase of oolite mineralogy [*Sandberg*, 1983] and the model of *Stanley and Hardie* [1998], showing the oscillation between calcite (low Mg/Ca) and aragonite (high Mg/Ca) seas. The precise y-axis location of the switch between the dominant $CaCO_3$ polymorph also depends on seawater [SO_4^{2-}] [*Bots et al.*, 2011].

and mollusc-derived data suggest little change or a slight decrease [*Lear et al.*, 2003; *Sosdian et al.*, 2012]. It may be that it is difficult to correct for trace element changes during carbonate vein alteration using the methods employed by *Coggon et al.* [2010].

1.4 Foraminifera biology and ecology

Foraminifera are a diverse group of unicellular marine protists, distributed globally and found in most environments from the surface plankton to the deep ocean benthos [e.g. *Fraile et al.*, 2008]. Many species biomineralise a shell composed of calcite which may either be hyaline, wherein the test has a glassy appearance because the calcite crystals are aligned, or porcelaneous, which appears opaque as a result of the randomly orientated calcite needles [*Haynes*, 1981]. This section briefly outlines what is known about the foraminifera utilised in this study, including previous geochemical investigation.

1.4.1 *Operculina ammonoides*

The large benthic foraminifera (LBF) *O. ammonoides* (family: Nummulitidae) have a peak abundance-depth distribution of 20-40 m [*Renema et al.*, 2001; *Renema*, 2006], equivalent to that of planktic foraminifera considered to be surface dwelling. The nummulitids have diatom symbionts and are

oligotrophic specialists [*Hallock*, 1985], thus restricting them to the upper euphotic zone. Many species of LBF, including the nummulitids, are sexually dimorphic. Reproduction may be either sexual or asexual, producing microspheric and megalospheric generations respectively, where micro and megalo refers to the diameter of the initial chamber [see *Beavington-Penney and Racey*, 2004, and references therein]. The microspheric generation is multinucleate and generally has a smaller test diameter, the macrospheric form is uninucleate with a larger diameter [*Dettmering et al.*, 1998]. The nummulitids are defined by the presence of the marginal chord (figure 1.3), the thickened test margin which has an integral role in inter-chamber transport, reproduction and feeding [*Röttger et al.*, 1984]. Little direct data is available on the longevity of the nummulitids, and LBF in general. Spatially-resolved δ^{18}O and δ^{13}C data of modern *Marginopora vertebralis* and *Cyclorbiculina compressa* show periodic variation, interpreted as relating to seasonal changes in water temperature [*Wefer and Berger*, 1980], which thus imply growth over more than one year [see also *Briguglio and Hohenegger*, 2014].

Relatively little geochemical study has been conducted on LBF for the purposes of palaeoceanic reconstruction, presumably because exceptionally-preserved shallow marine sections are relatively rare. *Purton and Brasier* [1999] demonstrated that δ^{18}O in Eocene *Nummulites laevigatus* may be used as an indicator of palaeoseasonality, as also demonstrated in Recent specimens [*Wefer and Berger*, 1980; *Luz and Reiss*, 1983]. The incorporation of the alkali earth elements have been studied in cultured LBF, particularly *Amphistegina*, on which much of the work from the laboratory of Jonathan Erez (The Hebrew University of Jerusalem) is based [see e.g. *Erez*, 2003, and

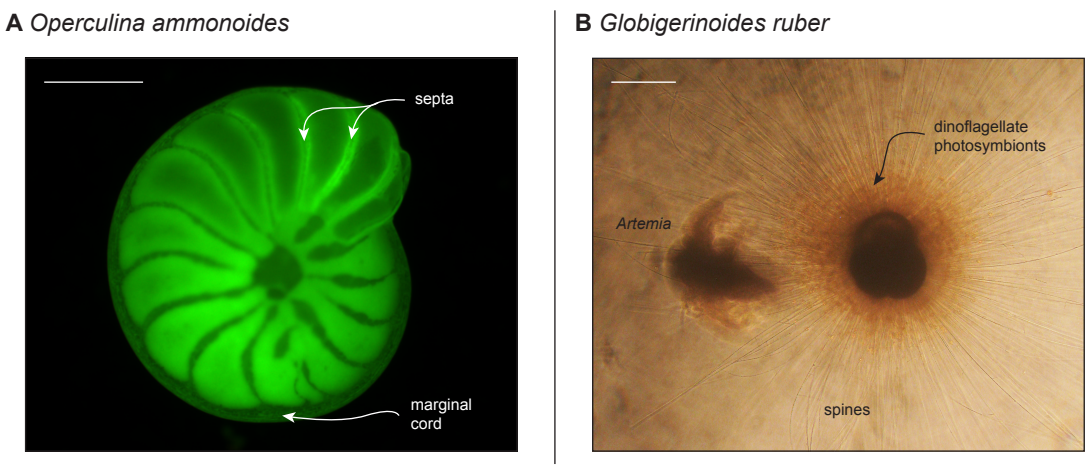

Figure 1.3: Microscope photographs of the foraminifera utilised in this study. (A) Fluorescent confocal image of the large benthic foraminifera *O. ammonoides* labelled with calcein. Scale bar 500 μm. (B) Transmitted light microscope image of *G. ruber* during feeding on a $\sim$1 day-old brine shrimp. Scale bar 100 μm.

references therein]. Whilst such experiments have yielded invaluable information regarding the biomineralisation process, relatively little systematic study of how the incorporation of trace elements relates to environmental parameters has been carried out. *Toyofuku et al.* [2000] and *Raja et al.* [2005, 2007] investigated the response of Mg/Ca to temperature and salinity in several extant hyaline and porcelaneous species, demonstrating the viability of Mg/Ca palaeothermometry in LBF. However, there are no previous studies which use trace elements in large shallow-dwelling foraminifera for palaeoceanic reconstruction in the fossil record.

1.4.2 *Globigerinoides ruber*

The spinose foraminifera *G. ruber* is found in oligotrophic (sub)tropical oceans. It is carnivorous and has dinoflagellate photosymbionts [*Bé and Hutson*, 1977], see figure 1.3, inhabiting the upper mixed layer at depths of $<$50 m [*Anand et al.*, 2003], producing a hyaline calcite test. Reproduction follows a bi-lunar cycle [*Bijma et al.*, 1990]. A layer of gametogenic calcite is added as reproduction takes place. The observation that there is no δ^{18}O relationship with size fraction [*Elderfield et al.*, 2002] indicates that this species does not significantly migrate through the water column. Therefore, it is unlikely that data may be biased by measuring specimens from a certain size fraction in this respect.

The geochemistry of *G. ruber* has been extensively studied due to the abundance of this species in ocean sediment cores throughout the Plio-Pleistocene, and the relationship between Mg/Ca and temperature is well-known in modern seawater. The majority of calibrations agree that the response of Mg incorporation is best described by an exponential relationship with an exponential coefficient of 0.09, based on a calibration of the form Mg/Ca = $B\exp^{AT}$ [e.g. *Anand et al.*, 2003]. As for other species, salinity and pH/[CO_3^{2-}] is known to exert a control on Mg/Ca [*Kisakürek et al.*, 2008]. Along with site-specific secular variation in preservation due to dissolution, these are likely to be the biggest complicating factors in temperature and $\delta^{18}O_{sw}$ reconstruction using *G. ruber* Mg/Ca.

1.5 Laser-ablation inductively coupled plasma mass spectrometry

1.5.1 The requirement for spatially resolved analysis

Traditionally, both fossil and modern foraminifera trace element data are derived from solution ICP-MS/AES analyses of multiple ($>$10) dissolved individual tests. This is advantageous in that

individual-specific variation is averaged over [cf. *Sadekov et al.*, 2008], however non-spatially resolved analysis does not enable inter- and intra-chamber heterogeneity to be assessed. This internal variability in trace element incorporation relates on a single chamber scale to biological processes [*Allison et al.*, 2011; *Eggins et al.*, 2004], and on an inter-chamber scale to vertical migration through the water column during the life of an individual [*Ravelo and Fairbanks*, 1992]. Inter-specimen variability may relate to seasonal changes in temperature [*Wit et al.*, 2010], which have been used to reconstruct palaeoseasonality variation in the recent geological record [*Goudeau et al.*, 2014]. Furthermore, solution analysis of multiple dissolved fossil specimens that are variably diagenetically compromised may be biased as a result. Spatially-resolved LA-ICPMS analysis enables simultaneous monitoring of both proxies and elements indicative of diagenesis, such as Al or Mn. This enables data from poorly-preserved specimens to be excluded. Moreover, useful data may be obtained from specimens that are partially well-preserved, for example the inner and outer walls of the test, which typically suffer from recrystallisation to a greater extent, may be discounted before the calculation of mean chamber values [e.g. *Creech et al.*, 2010].

Solution analysis continues to offer some benefits, namely that crushed foraminifera are easier to clean, and that it may be difficult to compare spatially resolved data when different sampling techniques are used [*Dawber and Tripati*, 2012]. Laser-ablation and SIMS measurements are derived from a small fraction of the foraminifera, whereas solution work obviously produces an average whole-test value. If chamber wall thickness-weighted averages of all chambers are not calculated, laser-ablation data will be biased to the thickest chambers analysed, for example. Despite these issues, careful microanalytical work demonstrably produces useful palaeoceanic data [e.g. *Reichart et al.*, 2003; *Sadekov et al.*, 2009; *Creech et al.*, 2010], and the benefits of spatially-resolved data outweigh these disadvantages in the majority of cases.

1.5.2 Analytical technique fundamentals

LA-ICPMS is the fastest and cheapest analytical technique capable of determining low-ppb concentration trace elements at a spatial resolution of $<$100 μm when tracking (line scanning) across the surface of a sample and sub-μm vertical resolution when depth profiling. Many comprehensive overviews of the technique have been published [e.g. *Russo et al.*, 2002; *Koch and Günther*, 2011]. Briefly, a ns-long high energy-density pulsed laser beam (GW m^{-2}) is focused onto the sample surface, usually within a He atmosphere, causing particles, atoms and ions to become entrained into the sample gas stream, whereupon they are transported to the ICPMS for (ideally) complete atom-

isation, ionisation and analysis. The laser source is usually an excited dimer (excimer) such as ArF (as in the 193 nm LA-ICPMS setup at Royal Holloway University of London [*Müller et al.*, 2009]) or a frequency-quadrupoled or quintupoled 1024 nm Neodymium-doped Yttrium-Aluminium Garnet (Nd:YAG), producing 266 nm and 213 nm laser beams, respectively. There is extensive evidence that laser-induced fractionation, i.e. the depth-dependent offset between measured and actual element/internal standard (X/I_{STD}) ratios is less problematic for 193 nm systems in comparison to 213/266 nm lasers for a variety of sample matricies [e.g. *Hathorne et al.*, 2008]. This is principally due to the lower and more consistent particle-size distribution of 193 nm lasers [*Guillong and Günther*, 2002]. A limiting factor for achievable spatial resolution is the gas washout time of the laser ablation cell. Large cells are desirable in order that multiple samples and standards can be accommodated simultaneously, yet larger cell volumes mean greater spatial heterogeneity of intra-cell gas mixing and longer washout times. This issue has been resolved with the advent of two-volume ablation cells [*Eggins et al.*, 1998; *Eggins and Shelley*, 2002], wherein laser-sample interaction takes place inside a small inner cell (1-2 cm^3).

Improvements in LA-ICPMS data quality have focused on the addition of a diatomic gas downstream of the ablation cell [*Durrant*, 1994]. This is usually N_2, which is thought to improve sensitivity by raising plasma temperature, or H_2 which reduces the background on masses for which a plasma/LA gas is significant (such as the ^{31}P interference by $^{15}N^{16}O$) by shifting the gas interference by one mass unit (e.g. to $^{15}N^{16}O^{1}H$). This is broadly less readily achieved for sample analytes, and the sensitivity reduction when using H_2 compared to N_2 may be outweighed by the ability to measure m/z = 31 (P), 32 (S) or 55 (Mn) with far lower limits of detection. More recently, a reduction in laser pulse duration has been shown to further reduce fractionation [*Pisonero and Günther*, 2008; *Jochum et al.*, 2014], as a result of reduced thermal effects of laser-sample interaction [*Fernández et al.*, 2007]. Further improvement in LA-ICPMS data quality since the late 1990s are mainly a result of the development of increasingly more sensitive ICPMS systems with collision/reaction cells for isolating analytes from larger or more readily reactable interference molecules.

The most significant source of inaccuracy in LA-ICPMS analysis of carbonates is that no carbonate standard exists that meets all of the requirements for laser-ablation, namely (1) μm-scale homogeneity, and (2) well characterised for all analytes of interest by a range of techniques. As a result, laser-ablation carbonate data are almost ubiquitously standardised to synthetic glasses, of which NIST612 and 610 ($NaO\text{-}SiO_2\text{-}CaO\text{-}Al_2O_3$ glasses doped with $\sim$400 and 40 ppm trace elements respectively [*Eggins and Shelley*, 2002]) are the most commonly utilised because they are rea-

sonably homogeneous [*Ibid*] and were produced in substantial quantity. This presents the problem of mismatched matrix-derived inaccuracies which are difficult to assess. Such inaccuracies are undoubtedly significant in cases where percent-level accuracy are required (e.g. Mg for palaeothermometry, [see *Hathorne et al.*, 2008]) or where large matrix-specific fractionation factors are likely, such as for the volatile elements Zn, Rb and Pb [*Jochum et al.*, 2014]. Available data, derived primarily through analysis of the USGS pressed-powder carbonate standard MACS-3 [*Jochum et al.*, 2012], indicate that accuracy is better than 10% for most proxy elements of interest. However, accuracy corrections are not routinely applied because the relative contributions of matrix-dependent fractionation, standard heterogeneity and inaccuracies in the information values to reported-measured concentration offsets is often unclear. Therefore, whilst laser-ablation data are comparable to each other (especially between systems with the same laser wavelength), offsets of $\sim$10% are possible when comparing to data derived from other techniques [*Jochum et al.*, 2011].

1.6 Thesis overview

Methodology

Chapter 2 examines, in detail, the long term quality of 193 nm ArF laser-ablation ICPMS trace element data.

Chapter 3 develops 2D laser-ablation trace element mapping, with specific reference to complex discontinuous samples such as chambered large benthic foraminifera.

Chapters 5-7 contain details (often in the supplementary material) pertaining to the development of laser-ablation methodology specifically for the sample types utilised in those publications.

Mg/Ca palaeothermometry theory

Chapter 4 examines the fundamental assumptions that are frequently made when applying this proxy, especially before the Pleistocene (2.6 Ma) when seawater chemistry may have been substantially different from present-day.

Results and discussion

Chapter 5 demonstrates the potential of the nummulitid large benthic foraminifera for palaeoceanic reconstruction, focusing on seawater chemistry and thermal seasonality.

Chapter 6 presents laboratory calibrations of seawater-test chemistry and test chemistry-temperature relationships for the nummulitid *Operculina ammonoides*. The implications for detailed palaeoceanic reconstruction and the biomineralisation of this group

of foraminifera are discussed.

Chapter 7 presents equivalent laboratory calibrations for the widely utilised planktic foraminifera *Globigerinoides ruber*, and examines the implications of these calibrations for Pliocene ocean temperature and sea level reconstructions.

Critical evaluation

Chapter 8 presents data not published or forming part of the earlier chapters, and provides an overview discussion

Chapter 9: Conclusions

1.6.1 Principal hypotheses

- Foraminifera are characterised by a nonlinear seawater-test Mg/Ca relationship.
- Trace elements in LBF are viable palaeoceanic archives.
- Paleogene seawater Mg/Ca was lower than many previous studies have argued.
- Tropical ocean seasonality in a high-CO_2 world is similar to present-day.
- Tropical ocean temperatures are positively correlated with pCO_2 on long timescales, but to a lesser extent than climate models indicate. The slope of this relationship decreases with increasing pCO_2.
- Pliocene seawater Mg/Ca was significantly lower than at present.

Chapter 2

Evans, D. & Müller, W. Automated extraction of a five year 193 nm ArF laser-ablation trace element dataset: Long-term errors, trends, data optimisation and cell homogeneity based on ten commonly analysed glass and carbonate standards. Planned submission to *Geostandards and Geoanalytical Research*.

This manuscript is in preparation. Together with chapter 3 it forms the methodology part of this thesis. Note that application-specific methodology can also be found in the methodology sections of chapters 5-7. See appendix A for an extended version of figure 4.

Automated extraction of a five year 193 nm ArF laser-ablation trace element dataset: Long-term errors, trends, data optimisation and cell homogeneity based on ten commonly analysed glass and carbonate standards

David Evans* & Wolfgang Müller

Department of Earth Sciences, Royal Holloway University of London, TW20 0EX, UK

* david.evans.2007@rhul.ac.uk

Abstract

The capability of laser-ablation inductively-coupled-plasma mass spectrometry (LA-ICPMS) for producing quantitative data of a multi-element suite for many different sample matrices has resulted in a large increase in the popularity of this technique for a wide range of applications. Sample data are usually normalised to an external standard, in order to correct for element/element fractionation during ablation, sample transport or ionisation and analysis in the ICPMS. Whilst this is demonstrably capable of producing precise and accurate data for a wide range of elements, little is known about the long-term quality of such data. For example, a small amount of standard analyses conducted over a brief period are likely to overestimate reproducibility, as this does not account for long-term variation in (e.g.) ICPMS tuning optimisation. Furthermore, it is known that some ubiquitously used standards, such as the synthetic NIST glasses, suffer from reported value uncertainties, yet no long-term dataset with analyses conducted over a range of ablation and tuning conditions exists. This means there has been little rigorously examination of the extent to which offsets observed in LA-ICPMS data are the combined result of real error in these values compared to the ablation parameter-specific fractionations that may bias data. Finally, few sufficiently large datasets exist with which to test the homogeneity of ablation cells. In order to overcome these issues, we present a Matlab program capable of automatically extracting all the standard data produced by a system over a specified time period. Crucially, no user-input is required to analyse the LA log files and ICPMS data files, which means that very large amounts of data can be evaluated quickly. Based on a dataset generated in this way, using the last 5 years of analyses produced by our

LA-ICPMS system (RESOlution M-50 coupled to an Agilent 7500ce), we present ~5000 individual analyses of 10 of the most commonly utilised standards (NIST, MPI-DING, STDP, MACS). This dataset possibly constitutes the largest LA standard analysis database, allowing us to (1) examine the relative effects of standard-specific accuracy offsets compared to possible error in previously reported values. For this purpose we give a mass-specific breakdown of 20 of the most commonly analysed elements, including a discussion of long-term data quality, temporal trends and standard homogeneity. (2) Give a broad discussion of how analyte data quality may be improved using specific ablation conditions and/or diatomic gas type. (3) Assess spatial homogeneity in measured element/Ca ratios in our two-volume cell. We find no significant long-term trends, demonstrating that appropriately standardised data are comparable over long time periods. However, precision is likely to have been underestimated. As expected, LA parameters exert a substantial effect on data quality, enabling us to give specific recommendations. Finally, these data show that the two-volume ablation cell of our system is characterised no discernible heterogeneity in measured trace element ratios.

1. Introduction

Laser-ablation inductively coupled plasma mass spectrometry (LA-ICPMS) is the fastest and cheapest quantitative tool capable of measuring ppm-ppb concentration trace elements at (sub)µm spatial resolution in a wide variety of geological, environmental, biological and material science substrates [Jackson et al. 2004; Heinrich et al. 2003; Russo et al. 2002; Srinivasan 2015; Becker 2002]. The growing popularity of LA-ICPMS is a result of the capability of this technique for fast, quantifiable analysis of a multi-element suite at %-level accuracy and precision. Accurate quantification is possible at a lateral and vertical spatial resolution of up to 5 µm and <0.5 µm respectively [Eggins et al. 2003; Lazartigues et al. 2014], ideal for applications for which µm-scale resolution is required, for example when targeting individual mineral grains or characterising compositional variability in growth-banded carbonates. The principle alternative technology is secondary ion mass spectrometry (SIMS), the only comparable quantitative analytical technique in terms of spatial resolution and

detection limits. SIMS offers greater spatial resolution [e.g. Vigier & Rollion-Bard 2007], and allows isotopic measurement of the light non-metals [Eiler et al. 1997; Rollion-Bard et al. 2007] which is not possible using gas-sourced plasma mass spectrometers. Electron microprobe analysis (EPMA) also offers superior spatial resolution and is capable of analysing almost any element (boron and above), but detection limits are typically 3-4 order of magnitude higher compared to LA-ICPMS. LA sampling coupled to a multicollector plasma mass spectrometer (LA-MC-ICPMS) offers similar data quality to SIMS for light isotope ratios such as $^{11}B/^{10}B$ [Blamart et al. 2007; Kaczmarek et al. 2014; Fietzke et al. 2010], whereas single collector quadrupole instruments are capable of resolving only permille-scale isotopic variation [Moens et al. 2001]. NanoSIMS instruments extend the capability of SIMS for highly spatially-resolved analysis beyond that which is possible by laser-ablation (down to 50 nm) and offer low-mid-precision isotopic data at a spatial resolution higher than that achievable by LA-multicollector-ICPMS [Hoppe et al. 2013]. Whilst there are clearly applications for which other techniques are more suitable, there are many significant advantages to LA compared to SIMS: (1) Little or no sample preparation is required and analysis takes place at atmospheric pressure. Whilst line-scans benefit from a polished sample surface, depth profiling can be carried out on samples with an irregular morphology such as foraminifera [Reichart 2003; Hathorne 2003; Evans et al. 2014]. In contrast, SIMS requires a flat sample surface and samples must be coated for most geological applications, and analysis takes place in a vacuum. (2) Sample throughput is much higher with LA-ICPMS (~1 analysis/1-2 minutes) and consequently the technique is cheaper. Furthermore, the far lower capital cost of LA-ICPMS systems means there are more available. (3) The pulse/analogue switching electron multiplying detectors of quadrupole ICPMS instruments offer a linear response over a dynamic range of 9 orders of magnitude, which means that spatial heterogeneity in concentration from ppb to % may be accurately determined. (4) LA-ICPMS offers simultaneous detection of most of the periodic table, although a compromise is usually struck between total ICPMS sweep time and the number of monitored masses. In contrast, NanoSIMS offers simultaneous detection of up to seven masses. These features make laser-ablation a flexible and versatile method

ideally suited to the determination of major and trace elements in geological materials, especially where a multi-element analysis spanning much of the periodic table is required.

Despite the increasing popularity of laser-ablation, little is known about the long-term quality of the large volumes of data that are produced. Quoted uncertainties are frequently derived from short periods of analysis and are therefore likely to underestimate error (particularly precision), especially when comparing temporally-separated data. Whilst it is common to quote long-term reproducibility for single element isotope analysis in (radiogenic) isotope geochemistry [Thirlwall 1991], the same is not true for LA-ICPMS because of the versatility of sample types and range of potential analytes. The use of external standards means that matrix-matched data may be accurate, provided the external standard is well characterised, yet it is not certain if such corrections are applicable to samples which typically have a different (and possibly variable) matrix. Temporally-variable accuracy corrections may introduce or exacerbate sample errors where these are matrix-dependent. Ubiquitously used standards such as the doped NIST glasses are characterised by spatial heterogeneity [Eggins & Shelley 2002], whilst others may be poorly characterised for some elements. Furthermore, there has been little systematic study of the effect of ablation parameters, including spot size, repetition rate and gas type on long-term data quality. Because other factors may influence the reliability of data collected over short time periods (e.g. ICPMS tuning and sensitivity), a long-term view is required in order to accurately gauge how such parameters may be optimised for certain elements and sample types. Furthermore, there has been a recent trend towards ablation cells with increasing volume in order to improve routine-analysis throughput between sample exchanges [Fricker et al. 2011]. Whilst these large cells typically contain a low-volume, partially-isolated space within which ablation takes place [Eggins & Shelley 2002; Müller et al. 2009], thus minimising spatial variability in transport gas flow dynamics, there is little data regarding the extent to which ablation cells are homogeneous in terms of elemental fractionation. In order to address these concerns, and to provide a comprehensive long-term overview of both matrix and non-matrix matched standardisation using a 193 nm excimer (ArF) laser-ablation system, we

present a Matlab program capable of mining all the data from a system over any specified period. Crucially, it runs automatically without user input which means that, depending on computing power, years of data acquisition can be reduced in a period of a few hours.

We apply this program to all of the data produced by our laser-ablation laboratory at Royal Holloway University of London [Müller et al. 2009] since January 2010, thus presenting a significant dataset of 5000 standard analyses of routinely utilised NIST, silicate (MPI-DING) and phosphate (STDP) glasses as well as a pressed-powder carbonate (MACS-3) [Eggins & Shelley 2002; Jochum et al. 2011; Jochum et al. 2006; Klemme et al. 2008]. Whilst a wide range of materials were analysed over this period, our laboratory is particularly focuses on the determination of trace elements in carbonates and phosphates. Consequently our dataset is biased towards elements and standards that are commonly associated with such analyses, although a significant amount of time has been dedicated to other applications, for example tephra [Tomlinson et al. 2010] and ice cores [Müller et al. 2011; Della Lunga et al. 2014]. Many of the analyses carried out over this period were line-scans (tracks) across relatively large growth-banded carbonate samples. Thus there are fewer analyses than may be expected, as sample analysis lengths are frequently on the order of several tens of minutes to hours. However, this does mean that – to our knowledge – we present the first extensive dataset of laser-ablation line-scan data of standards. Whilst some analysis of this type of data has been reported [Jochum et al. 2014], virtually all previous studies examining LA data quality focus on (vertical) spot analysis. Furthermore, we present a significant new dataset of the STDP phosphate glasses, for which little inter-laboratory comparative data are available compared to many other standards (only 1-2 previous datasets are available on the GeoReM database). Finally, as well as a detailed investigation of long-term data quality and the implications of observed offsets for LA or ICPMS-induced fractionation compared to potential error in the reported value of these standards, this dataset uniquely enables us to examine the effect of ablation parameter, including additional diatomic gas type, on long-term accuracy and precision. Thus the conclusions that we draw from this

are not biased by session-specific tuning or sensitivity. Because stage coordinates are available from the LA log files, we also discuss the homogeneity of the Laurin-Technic two volume ablation cell.

2. Experimental

2.1 LA-ICPMS

The LA-ICPMS system is described in detail in [Müller et al. 2009]. Briefly, it features a RESOlution M50 prototype laser-ablation system (193 nm ArF) connected to an Agilent 7500ce/cs ICPMS. ICPMS tuning conditions vary widely according to application, for example tephra analyses require sensitivity optimisation across the mass range [Tomlinson et al. 2010] whereas analysis of biogenic carbonates are typically characterised by optimised low-mass sensitivity in order to improve Li-B/Ca counting statistics in small, fragile samples [Evans et al. 2013]. The principal change to the system since it was described is the installation of an H_2 gas line, which means either N_2 or H_2 can now be selected as the additional diatomic gas added downstream of the ablation cell. The gas type is not written into the Geostar log file and therefore this information is not directly available, however the optimal tuning conditions differ between these diatomic gases which means the gas type for each analysis can be identified using the flow rate of this mass flow controller; N_2 flow rates are routinely 6 ml min^{-1} whereas H_2 is optimised around 8.5 ml min^{1}. Scan speed, repetition rate and spot size varied between 0-50 µm s^{-1}, 2-20 Hz and 15-96 µm respectively across the entire five year period. A small subset of data using the rotatable rectangular spot with variable dimensions for growth-banded samples is also present. Fluence was typically 3-5 J cm^{-2}. He flow rate was set to 850 ml min^{-1} irrespective of other variables without exception. Whilst Geostar records almost all of the critical ablation condition parameters required to assess this dataset, the presence of absence of the 'squid' signal smoothing device and the ICPMS dwell times of the analysed masses are not available. Therefore, it is not possible to assess the benefits of in-line signal smoothing or sweep time-repetition rate optimisation using the dataset that we present here, although the squid is used the majority of the time.

156 **2.2 Matlab program**

157 The Matlab program that was developed is designed to analyse all Agilent and Geostar csv files
158 created by the LA-ICPMS system at RHUL since the 1st January 2010, (~10^4 of each). A key advantage
159 of this software over data reduction programs already available for laser-ablation trace element
160 analysis [Paton et al. 2011; Rittner & Müller 2011; Guillong et al. 2008] is that it was designed to
161 require no user input in order to mine large quantities of LA data spanning a long period of time
162 (although it is not intended as a replacement for these programs), as the large amount of files
163 involved means that it was impractical to individually assess each manually. Previously available
164 software is not designed to achieve this for two principal reasons: (1) it is difficult to define criteria in
165 the data alone which unambiguously identify a specific standard rather than samples, and (2) the
166 laser-ablation and ICPMS hardware are often controlled by different programs running on separate
167 computers which are typically isolated from the internet (and intranet), and therefore have an
168 associated non-constant offset in machine time. This is particularly an issue for LA-ICPMS data where
169 an analysis may be initiated manually by the user on both systems, with a resultant analysis-specific
170 recorded time offset between the output generated by the laser-ablation and ICPMS software.
171 Whilst it may be prohibitively time consuming to produce a program that is capable of dealing with
172 any data, we simplify this problem in several ways in order to produce a program that is capable of
173 differentiating samples and standards, with subsequent data manipulation, in a sufficient proportion
174 of cases to be useful. Before detailing these simplifications we briefly outline the characteristics of
175 the data produced by our system. Users typically program a set of analyses using the laser-ablation
176 software (Geostar) which produces a csv log file containing information regarding timing (start and
177 end of each analysis), coordinates within the ablation cell, laser repetition rate, spot size, scan speed
178 (zero in the case of spot analysis/depth profiling) and the flow rate through the mass flow
179 controllers – that of helium through the ablation cell and an additional diatomic gas added
180 downstream [Müller et al. 2009]. After selecting all or part of the sequence for analysis, ICPMS data
181 acquisition is initiated manually by the user. Whilst the laser-ablation system may be interrupted

during this process, for example if re-analysis of a sample is required, in virtually all cases each Agilent csv file contains all standards and samples that the user intends to form part of the same run. Thus, the program assumes that each Agilent csv also contains every standard analysis that the user wishes to use to manipulate the sample data (the calibration standards(s), typically NIST61x) and the secondary standards, treated as unknowns, used to assess data quality. A small modification to the program would remove this constraint and thus allow data to be read from laboratories that routinely place every single analysis in a different ICPMS file, and could alternatively decide which secondary-primary standard pairs should be considered together based on a stated maximum time separation between them. In our laboratory, ICPMS data are almost always exported as a counts/second (cps) time series for each analysed m/z; at present the program cannot read data exported as raw counts because it relies on intensity ratios to identify NIST glasses. Before data processing, all sequences were split into sub-sequences wherein every analysis was carried out under identical ablation conditions (spot size, repetition rate, scan speed). User-free data reduction is achieved in five basic steps:

(1) The program reads in all Agilent csv data files from a specific day and then finds all Geostar csv log files that fall within the time (within tolerances) given by the first and last line of the data file.

(2) The start and end of each analysis within the data file is located using the times derived from the Geostar logs. Before this can be done, the computer time offset between the start of the analysis on the laser-ablation and ICPMS computers must be calculated, which is non-constant as the computers are not synchronised and because each set of analyses are initiated manually by the user on each computer; the start time recorded in the data and log csv file can never be the same even if machine time was identical for this reason. Attempts to achieve this by (e.g.) assuming that gas blank analysis between samples is characterised by a total ion beam intensity below a certain threshold (such as Iolite's 'detect from beam intensity' option) are not accurate in many cases, for example when a track is placed across a discontinuous sample filled with clean resin [Evans & Müller

2013] or when depth profiling breaks through the base of the sample to the resin below. In order to overcome this, our program assumes that the machine time offset between the start of the first analysis in the log files created by the two computers is no greater than ±1000 ICPMS sweep times. For each of these 2001 assumptions all gas blank data are removed (the portions not between the start and end times of each analysis given in the Geostar log files), and the sum of the total ion beam of the remaining data is calculated. The actual sequence-specific offset is then given by the time difference that results in the greatest sum of the total ion beam for the remaining segments, as this will be the offset that results in the best match between the analysis times given by the Geostar logs and the data peaks in the Agilent data file (figure 1). Whilst the accuracy of this technique is limited to ±0.5 ICPMS sweep times, this is usually <0.5 s and always <1 s, which is sufficient resolution given that the initial and final portions of each analysis are cut as these represent times of signal intensity increase and decrease respectively.

(3) NIST glasses are identified based on *raw* Sr/Ca and U/Sr intensity ratios (NIST612: $2>^{88}Sr/^{43}Ca>0.55$; $2>^{238}U/^{88}Sr>0.4$. NIST610: $8>^{88}Sr/^{43}Ca>4$;; $6>^{238}U/^{88}Sr>0.8$). Ratios derived from Ca, Sr and U were chosen because at least one isotope of all three of these elements was analysed in >82% of cases and these elements show low-negligible ICP mass load effects [Kroslakova & Günther 2007], which means that raw intensity ratios based on these elements are likely to show relatively little ablation-condition dependent variation [see also Jochum et al. 2012]. Furthermore, Sr and U are known to show little fractionation relative to Ca during laser-ablation depth-profiling [Fryer et al. 1995; Jochum et al. 2014]. Whilst more complex algorithms could use a variety of ratios to increase the percentage of files analysable in this way, we targeted 80% as an acceptable point at which sufficient standard analyses were being retrieved whilst minimising the time taken to produce this code. Figure 2 shows the range of raw (background corrected only) $^{88}Sr/^{43}Ca$ and $^{238}U/^{88}Sr$ intensity ratios for all commonly analysed standards. Despite a wide range of ICPMS tuning conditions, ablation conditions and gas flow parameters, these show relatively narrow spread. Crucially, all standards occupy Sr/Ca-U/Sr space which is distinct from most other standards as well as virtually all

234 samples analysed on our system (which are broadly characterised by Sr/Ca ratios intermediate
235 between NIST610 and NIST612 at the U/Sr ratio of the NIST glasses). The STDP-3 phosphate glasses
236 [Klemme et al. 2008] are an exception; STDP3-150 overlaps NIST612 and STDP5/1500 overlap
237 NIST610 (figure 2). In order to overcome this, NIST-STDP analyses were differentiated using two
238 mechanisms. If more than one NIST analysis was identified within a specific sequence then the U
239 signal intensity was used to check whether all analyses were of the same material (the STDP glasses
240 have significantly higher Sr and U concentrations than NIST610/2). If the intensities were different by
241 >5× then the analysis with a lower U intensity was identified as the NIST glass. If both analyses had
242 similar U intensities, or there was only one analysis, then the user analysis labels from the laser-
243 ablation software were used to identify the standard(s). Whilst user analysis labels were avoided as
244 far as possible because of potential errors, the design of the code beyond this point (see below)
245 means that if a standard is misidentified, or a sample is identified as a standard, it is not practically
246 possible for data reduced to that analysis to form part of the dataset that we present here. Finally,
247 some volcanic glasses have similar Sr/Ca and U/Sr ratios to NIST610/2. This problem was overcome
248 using U/Th ratios (Th is routinely analysed in volcanic glass in our laboratory), which are always ~1 in
249 the NIST glasses but not in tephra. Very long analyses (>1000 ICPMS sweep times) were also
250 assumed to represent samples. The code that we present here may not be directly relevant to other
251 laboratories, if for example other materials are routinely analysed which are characterised by similar
252 Sr/Ca-U/Sr ratios to the NIST glasses, or if Ca, Sr and U are not routinely analysed. Given the need to
253 avoid user labels which potentially contain errors, especially when there are frequent external users,
254 element/element ratios provide a robust alternative which may easily be tailored to suit the needs
255 of a specific laboratory, for example by choosing alternative ratios that are reasonably infrequently
256 encountered in samples, or by defining additional criteria for samples which are similarly
257 characterised compared to NIST61x with respect to these chosen ratios. The code is designed so that
258 such sub-criteria may be easily inserted, and we again stress that standard misidentification does not

propagate through to the final dataset but instead results in data for the entire analysis session being excluded.

(4) Once the location of all NIST glasses has been ascertained, data reduction is performed following standard procedures [Longerich et al. 1996; Heinrich et al. 2003] using Ca as an internal standard. Drift correction was not applied where more than one NIST glass was used to standardise the other analyses within a sequence because unknowns are never routinely separated from NIST analyses by more than ~1 hour. Drift over this time frame is rarely significant in our system and we do not apply a correction because it is likely to add noise to the reduced data, for example taking the mean intensity values from two NIST analyses provides a better indication of the intensity-concentration relationship at that time, whilst a drift correction would add scatter to the data given that scatter in the NIST analyses is likely to result from other causes (e.g. NIST heterogeneity or drift that is present and directionally variable on a timescale shorter than the time separating the bracketing NIST analyses). For track analyses, i.e. those with non-constant stage coordinates during analysis, all equivalent NIST analyses were combined and mean values used for data reduction. For spot analyses down-hole (element/Ca) fractionation was assumed to be linear. Intensity-depth regressions are calculated for each analysed m/z, and these noise-free regressions are then used to provide laser pulse (depth) specific intensity-concentration values for standardisation. Outliers are removed from all background and signal analyses (3SD).

(5) Non-NIST standards are identified by initially assuming that all analyses could be any secondary standard. The measured X/Ca ratios are then ratioed to the literature values for each of the 10 secondary standards that we routinely analyse. Analyses are correlated to specific standards when the mean offset between the measured and reported values is no more than 30% for all m/z, with no more than 20% of the analysed masses differing by >30% from the reported values. These conditions are never met if non-NIST analyses are accidentally identified as NIST glasses because although such analyses have similar Sr/Ca and U/Sr intensity ratios, this is never the case for all the other element/Ca ratios analysed within a particular sequence. As an additional check, user analysis

285 labels were also monitored in order to evaluate how many standard analyses were never identified.
286 Assuming that these labels are mostly not erroneous and really do represent missed standards, the
287 program is 95.4% effective. In order to ensure that unidentified standards were not excluded from
288 the final dataset, these analyses were included but were of sufficiently small number (~200) to be
289 manually checked to ensure that the dataset only contained standards. We semi-manually
290 incorporated these missed standards because they are likely to represent the worst data, as analyses
291 were not recognised as standards only if the measured values deviated from the reported values by
292 >30% on average. Excluding these would artificially improve the quality of the dataset. Our program
293 does not enable constraints to be placed on the relationship between data quality and variables that
294 are not recorded by the LA system, such as ICPMS tuning parameters, although it should be noted
295 that this is also the case for virtually all previous work.

296 **3. Results and discussion**

297 **3.1 Dataset statistics**

298 In total, 4938 standard analyses were identified from the period 01/01/2010 to 27/10/2014 of which
299 4775 were identified without resorting to user analysis labels. A breakdown of this total between the
300 12 most commonly analysed standards in our laboratory is shown in table 1, including the ratio of
301 spot to track analysis and the ratio of analyses conducted using N_2 and H_2 as the additional diatomic
302 gas. The NIST glasses are by far the most commonly analysed standard because both NIST610/2 are
303 used as bracketing standards for almost every sequence of analyses that are performed. The STDP-3
304 phosphate glasses [Klemme et al. 2008] are almost entirely represented by track analyses, as these
305 standards are almost always used to assess data quality for bioapatite. The MPI-DING glasses ATHO-
306 G and StHs are predominantly represented by spot analyses associated with tephra data [Tomlinson
307 et al. 2010], whereas MACS-3 and the remaining MPI-DING standards are often analysed with
308 carbonates which may be either tracks for larger, growth-banded material [Warter et al. 2014;
309 Evans et al. 2013; Stoll et al. 2012] or spots for small fragile specimens such as planktic and deep
310 benthic foraminifera.

Within the NIST612-standardised dataset, a total of 83 m/z were monitored at some point within the ~5 year period, with 46 m/z measured over 100 times and 36 m/z measured over 1000 times, from ^{7}Li to ^{238}U (figure 3). The alkali earth metals and U were by far the most commonly measured m/z (>3100 standards include these masses), followed by ^{89}Y (2945) and ^{140}Ce (2630). ^{55}Mn, ^{208}Pb and ^{25}Mg were measured over 2000 times. We focus the results and discussion of our dataset on a subset of the 37 masses shown in figure 3, for which a sufficient number of analyses are available with which to make an assessment of long term data quality over a range of ablation conditions. Within this set of 37 analytes, 19 are distributed approximately equally between the standards whilst the remaining 18 were frequently associated with the analysis of volcanic glasses for which the MPI-DING glasses ATHO-G and StHs were primarily used as secondary standards. Because these m/z (^{29}Si, ^{45}Sc, ^{47}Ti, ^{60}Ni, ^{90}Zr, ^{93}Nb and the REE with the exception of La, Ce and Nd) are not routinely analysed other than in relation to tephra, we omit these from our discussion because Tomlinson *et al*. [2010] discuss the quality of these data in detail.

3.2 Accuracy and precision

Where this dataset is discussed in relation to the GeoReM database (http://georem.mpch-mainz.gwdg.de/), version 17 of this database was used. Accuracy and precision for all standards for which more than 20 analyses were available for a given set of ablation conditions are shown for NIST612 standardised analyses in table 2 and NIST610 standardised analyses in table 3. Similar spot sizes were pooled; data are shown for both spot and track analyses in bins containing 20-25 µm, 44-57 µm and 74-96 µm diameter spots. These bins represent 23.9, 54.5 and 8.0% of all analyses respectively; most available data are shown in tables 2 and 3, with the only significant omission being analyses that utilised a 34 µm spot (6.4%). Whilst these data average analyses derived from a range of repetition rates and/or scan speeds, these were broadly invariant through time. Specifically, almost all spot analyses were performed at either 2 or 5 Hz whilst the majority of the track data were acquired at 15-20 Hz and a scan speed of 1 mm min^{-1} (59.4%), with 19.2% acquired at 2 mm min^{-1}. Therefore, whilst spot and track accuracy and precision are not comparable in terms of

ablation conditions, spot and track data of different standards were obtained using broadly equivalent ablation parameters. The MPI-DING glasses ATHO-G and StHs [Jochum et al. 2006] contained insufficient analyses within a given set of ablation conditions for us to report data quality, although broad trends may still be recognisable. Accuracy data are shown relative to the reported values (accuracy = measured/reported and precision = 2SD measured/reported). Detailed examples of this dataset including all individual analyses are displayed with respect to time in figure 4, for three selected analytes, in order to give an example of how long-term accuracy, precision and temporal trends may be assessed. Each m/z for which there are sufficient data will now be described in the context of previously published analyses in turn. We make the fundamental assumption that Ca is well characterised and homogeneously distributed in all of these standards, which is likely to be the case given that it is a major constituent of all of them.

^{7}Li: As expected given the similar matrix, standardising NIST612 to NIST610 and vice versa produces, on average, excellent LA-ICPMS Li data. Taking the mean of all data, track and spot accuracy is better than 2% and 1% respectively and there is no significant offset between the two techniques (n = >250 and ~180). Long-term precision is better than 3% for spots and 4% for tracks, which is less than the combined reported precision for the two standards from Jochum *et al*. [2011]. GOR128 and GOR132, the only MPI glasses for which a significant amount of data are available, are consistently offset to accuracies of 6-12% and 17-19% respectively when calibrating to NIST612; NIST610 standardisation produces values ~2% worse (tables 2 and 3). This is consistent with the original MPI-DING dataset [Jochum et al. 2006], wherein LA-derived values are offset from the reported overall mean by 17% and 8% for GOR128 and GOR132 respectively and are positively offset compared to both solution ICPMS and other microanalytical techniques. Averaged over all ablation parameters, spot analyses results in accuracies ~4% worse for GOR128 and ~8% worse for GOR132. For standards with low-ppm Li concentrations such as these, the accuracy offset might conceivably be an artefact of spot analyses more frequently being carried out using H_2 rather than N_2 as the additional diatomic gas, as N^{2+} interferes with ^{7}Li. However, averaging all ablation conditions

363 together, GOR132 (which shows the largest spot-track accuracy offset) analysed with H_2 has an
364 accuracy of 15.3%, compared to 14.3% with N_2, therefore this cannot explain the difference that we
365 observe. Similarly, surface contamination of standards with lower Li concentrations cannot explain
366 why spots are further offset from the reported value than tracks. The MACS-3 pressed powder
367 carbonate does not show this difference. Within a given set of ablation conditions, long-term
368 precision is always better than 3% (tables 2 and 3), except for GOR128 with the smallest spot sizes
369 for which sufficient data were available (4.1%). MACS-3 is more heterogeneous than the glasses,
370 although not substantially so (precision is 4.3-5.3%). Accuracy of this carbonate compared to the
371 information value of 62.2 ppm is 4.5% and ~11% for tracks with spot sizes between 40-57 and 20-25
372 µm respectively, irrespective of the NIST glass used for standardisation. This is within error of
373 Jochum *et al*. [2014], who report 58-61 ppm for both 200 nm fs and 213 nm Nd:YAG LA systems.
374 There are insufficient data from the STDP glasses to discuss Li data quality. In summary: NIST-
375 komatiite standardisation exhibits excellent long term precision (<4%), even for small (20-25 µm)
376 spot sizes within a given set of ablation conditions. Averaged over all analyses over five years,
377 accuracy is 6-7% for spot and 12-14% for track analyses. We recommend that an error of this
378 magnitude is appropriate when comparing data from different systems acquired under different
379 conditions, when Li is present at low-mid ppm concentration in the sample. Consistent, significant
380 positive accuracy for the MPI glasses in both this and published datasets may indicate that LA
381 overestimates Li concentration in these standards compared to SIMS and solution ICPMS and
382 therefore that an accuracy correction may be appropriate when calibrating volcanic glasses to NIST
383 standards. MACS-3 may be sufficiently homogeneous (precision 11-15%) for most purposes. There is
384 insufficient data here to recommend a carbonate Li accuracy correction when standardising using
385 NIST glasses.
386 **^{11}B:** Boron data quality shows significant trends through time, directly related to boron
387 background intensity and signal/background ratios. A significant drop in typical B background
388 intensity from ~6000 cps in early 2011 to ~250 cps by mid-2013 (figure 5) was associated with the

389 replacement of the major tubing components within the laser-ablation system, including the squid
390 gas smoothing device, with Nylon-6. This tubing material was originally installed in order to improve
391 sulphur data quality, as Nylon-6 is produced without the use of sulphur in the manufacturing
392 process, whilst this is not the case for Nylon-11 or Nylon-12. However, we find that another
393 significant advantage of this material is that it also results in improved B data, either as a result of a
394 lower propensity for boron memory due to particles sticking to the transport tubes, or lower boron
395 degassing directly from the Nylon. The timing of this change is associated with an improvement in
396 NIST612 B accuracy and precision from 19.1±22.9% prior to June 2011 to 4.8±9.7% after May 2012,
397 and demonstrates how tubing may have a significant effect on data quality. Taking into account only
398 data collected after mid-2012, NIST610-standardised accuracy±precision is 12.8±6.1%, 3.6±6.8% and
399 4.1±4.5% for GOR132, GOR128 and NIST612 respectively, for spot analyses averaged over all
400 ablation conditions, within error of the equivalent track data. Given that NIST612 & GOR128
401 standardised to NIST610 produce accurate and precise long-term data despite significant observed B
402 heterogeneity in the NIST glasses [Eggins & Shelley 2002], this indicates that the reported B value for
403 GOR132 may be too low. There are insufficient data from alternative techniques in the GeoReM
404 database to test whether this is the result of laser-induced fractionation, although the mean of all LA
405 values is offset from the reported by 8.6% (following removal of one outlier), similar to the long-
406 term accuracy of our system for this standard. MACS-3 is significantly heterogeneous (2RSD of all
407 analyses is 42.0%; n = 111), which is similar to that calculated from all data in the GeoReM database
408 (48.8%, or 33.2% minus one outlier). Based on the mean of all analyses on our system after mid-
409 2012, we measured a MACS-3 B concentration of 9.1±3.8 ppm standardised to NIST610, broadly
410 higher but within the range of previously reported LA values [Chen et al. 2011; Jochum et al. 2012].
411 Hathorne *et al*. [2008] also report LA B/Ca data higher than solution ICPMS for the JCp-1 coral
412 powder. Absolute carbonate B concentrations calibrated using glasses should therefore be treated
413 with caution, particularly if a 213 nm system is used. In summary: B data may be both accurate and
414 precise, provided careful attention is paid to factors such as variable gas blanks from sample tubing.

Nylon-6 is recommended for all applications for which high quality B data are desirable. Long-term accuracy and precision of 4% and 5-7% is possible for closely-matched standards; an accuracy correction is unwarranted based on our dataset. There is no improvement in data quality if ablation parameters are constrained to spots or tracks with a narrow range of spot sizes. We observe no significant offset between track and spot analyses of the same material. MACS-3 exhibits significant heterogeneity (±42%) to the point where this carbonate standard is not likely to be useful for calibration or assessing B data quality.

^{23}Na: NIST610 standardised NIST612 Na data are both highly accurate (<1%) and precise (<2.5%), even averaged over all ablation conditions and analysis type (spot/track). The MPI glasses GOR132, GOR128 and KL2-G are all characterised by a significant accuracy offset between spot and track analyses, irrespective of spot size (tables 2 and 3). On average, spots are offset to values 7-10% greater than reported whilst tracks are offset to -7% to -10%. It is not possible to distinguish between the potential effects of analysis type and repetition rate in our dataset, as almost all track data acquisition is carried out at much higher repetition rates. However, we observe no such offset for MACS-3 which is characterised by similar spot and track accuracy and precision. The offset we observe for the MPI glasses is consistent irrespective of which diatomic gas is used. Jenner & O'Neill [2012] also observe a similar positive accuracy offset (6.4%) for laser-ablation depth profiling (standardised using the USGS basaltic glass BCR-2G) compared to EPMA analysis. Together, these observations imply that Na fractionation is not constant for glasses with significantly different matrices and/or is dependent on repetition rate. Therefore, we suggest that this commonly observed offset is more likely to be a result of differential Na fractionation during LA depth profiling than a problem with EPMA data of the MPI glasses or BCR-2G [Melson et al. 2002], especially given that our track data at high repetition rates is characterised by a consistent negative accuracy. The fact that these offsets are not observed for MACS-3 may imply that this is not an issue for NIST-standardised carbonates. Based on these data, long-term Na accuracy and precision are <5% and 10-13% averaged over all ablation conditions.

Mg: Long-term Mg precision is excellent, particularly given that both NIST glasses exhibit significant Mg heterogeneity (7.5% and 6.7% for NIST612/610 respectively [Jochum et al. 2011]). For specific ablation parameters (tables 2 and 3), NIST610-standardised precision is 4-8% for spot and track analyses, broadly better than expected based on reported heterogeneity in the calibration standard alone. Averaged over all ablation conditions, 5-year Mg accuracy for ^{25}Mg is remarkable; <4% for spot analysis of NIST612 and MPI glasses for which data are available, and <3% for track analyses of the phosphate glasses STDP3-150/1500 (figure 4). The fact that NIST-standardised GOR128 and GOR132 accuracy from the same analysis sequence are highly correlated [Evans et al. 2014, supplementary material] demonstrates that even more precise Mg data are possible if the NIST glasses are not used as the external calibration standard. The 2 Hz depth-profiling MPI analyses of Evans *et al*. [2014] show that closely-matched standardisation (e.g. GOR132 to GOR128) can result in Mg data with a precision of <2%. For this reason, we recommend GOR132/128 as a preferred alternative to NIST610/612 when accurate Mg data are required (e.g. the analysis of carbonates for palaeoclimatic data), although it would not be appropriate to standardise samples with sub-% Mg to komatiite glasses. NIST-standardised accuracy is consistently poor for all standards (figure 4). The MPI glasses GOR132/128 and KL2-G, MACS-3 and STDP3-150/1500 are all offset to values ~7-10% lower than reported using NIST610 for calibration, which is inconsistent with the NIST610-standardised NIST612 accuracy in this dataset (-12% to -17%). Together, this implies that both NIST610 and NIST612 Mg values require revision, in particular because the consistent offset between six other standards with very different matrices demonstrates that this discrepancy does not have its origin in matrix-matching. Taking the average of all ^{24}Mg and ^{25}Mg data standardised using NIST610 (excluding NIST612) gives a mean NIST610-standardised Mg offset of 0.9249 (i.e. mean accuracy = -7.5%), therefore based on our data NIST610 Mg is 467±0.9 ppm (2SE, n = 933). Using a similar approach (except without ^{24}Mg, see below), NIST612 Mg is 62.4±0.19 ppm (2SE, n = 2245). Note that these errors relate to the accuracy of the mean value of multiple wafers and are not an indication of heterogeneity. Our NIST610 value is indistinguishable from that widely used

before Jochum *et al*. [2011] updated these values (i.e. that of Pearce *et al*. [1997], 465 ppm). Whilst the compiled values of Jochum *et al*. [2011] undoubtedly resulted in overall improved NIST data, both the analyses we report here, as well as the mean of all LA-ICPMS data in the GeoReM database suggest that the value given by Pearce *et al*. [1997] is more accurate. The offset between LA-ICPMS and other techniques for NIST610 is not observed for GOR128, for which EPMA and LA are in excellent agreement. Using our recommended NIST values, accuracy is better than 5% for most ablation conditions.

^{24}Mg and ^{25}Mg show a significant offset when standardised using NIST612, ^{25}Mg data are consistently offset to values ~5% higher. This is most easily explained by the $^{48}Ca^{2+}$ interference on ^{24}Mg, as shown previously [Jochum et al. 2012], given that we observe no such difference for NIST610-standardised data (with the exception of NIST612 data which are characterised by accuracies 3% lower on ^{24}Mg, as expected). Assuming that this offset is explicable by some combination of mass bias and $^{48}Ca^{2+}$, mean doubly charged Ca production under typical ablation conditions on our system can be calculated to be ≤1.6% (1.6% if no significant mass bias). We see no evidence for Mg heterogeneity resulting from the possible presence of micro-olivines in our GOR128/132 chips [Jochum & Enzweiler 2014]. MACS-3 precision is 12-16% which makes this standard more heterogeneous than any of the glasses we routinely analyse for Mg. Using our Mg value for NIST610 (or that of Pearce *et al*. [1997]), mean MACS-3 accuracy is 0.8% and 2.5% for spot and track analyses respectively. Therefore, we do not observe the same accuracy issue when standardising carbonates to glasses as reported by Hathorne *et al*. [2008]; our dataset indicates that accurate carbonate data are possible using the NIST glasses for calibration. Whilst Hathorne *et al*. [2008] utilised the NIST612 Mg concentration of Pearce *et al*. [1997], this cannot explain the observed offset between NIST and COCAL carbonate-standardised data. In summary: Mg analysis by LA is both precise and accurate. Long-term 2% precision is possible when using well characterised homogeneous standards such as the MPI glasses. Accurate data are possible, although both this and previous LA studies imply that currently preferred NIST Mg values require revision [e.g. Gagnon et al.

493 2008]. Until the cause of this discrepancy is identified, we recommend that the NIST612 should not
494 be used for external calibration of Mg, and that the NIST610 value of this study or Pearce *et al*.
495 [1997] should be used over that of Jochum *et al*. [2011]. For samples with >1% Mg, standardisation
496 using the MPI glasses is likely to result in less standard-induced data scatter. GOR128 is the most
497 homogeneous standard based on our dataset. MACS-3 may be sufficiently homogeneous for some
498 applications (where >±10% precision is acceptable), although this is not the case for trace element-
499 based palaeothermometry wherein MACS-3 standardisation is likely to result in errors in the order of
500 several °C. ^{24}Mg should be avoided for carbonate analysis with <100 ppm Mg, as previously shown
501 [Jochum et al. 2012].
502 **^{27}Al:** Standardisation of Al in phosphate and volcanic glasses (at %-concentration) to
503 NIST610/2 is both accurate (broadly better than 3-4%) and precise (sub-3%, some ablation
504 conditions characterised by long term accuracy of ~1%, tables 2 and 3). There is no significant
505 benefit of preferentially using either NIST610/612 for standardisation. We find MACS-3 to be
506 considerably more heterogeneous (precision 32-38%) than previously reported by Chen *et al*. [2011]
507 (<10%), although it is agreement with studies that use an internal standard rather than bulk
508 component normalisation [Lazartigues et al. 2014; Jochum et al. 2012]. Given that both latter studies
509 and this work utilises Ca as an internal standard, this discrepancy may simply result from the
510 relatively small amount of analyses performed by Chen *et al*. [2011]. The majority of studies show
511 that MACS-3 is characterised by Al heterogeneity on a scale that means it is unlikely to be useful for
512 standardisation or as an indicator of accuracy.
513 **^{31}P:** Phosphorus analysis by LA-ICPMS is challenging because of the interference of $^{15}N^{16}O$ on
514 m/z = 31. Our data demonstrates the importance of using H_2 instead of N_2 as an additional diatomic
515 gas for the purposes of precise P determination. Averaged over all standards and ablation conditions
516 for which diatomic gas-type data are available, we observe an improvement in precision from 109%
517 using N_2 to 12% with H_2. NIST612-standardised P data for NIST610, GOR132/128 and KL2 have

accuracies of <10%, demonstrating that reasonably accurate and precise P data at ~100 ppm is possible. Jenner & O'Neill [2012] report P data of similar quality using H_2.

^{55}Mn: At concentrations above 10 ppm, Mn is one of the easiest elements to measure by laser ablation. Long-term accuracy and precision for all glasses is generally better than 5% and 3% respectively (tables 2 and 3). Optimising laser parameters may enable precision of ~1% (e.g. NIST612-standardised KL2-G track analysis using a 44 µm spot). The MPI glasses are consistently offset to values 1-4% above reported, however this is more likely to be matrix-induced than a systematic error in these values, given that this offset is independent of which NIST glass is used for calibration and that standardising the NIST glasses to each other gives an accuracy of 0.4-1.0%. It would be highly coincidental for both NIST (or all MPI) Mn values to be inaccurate by the same amount. A small accuracy correction when calibrating volcanic glass data to NIST610/612 may therefore be justified. Similarly, the -5 to -6% accuracy we observe for MACS-3 (identical to that of Jochum *et al*. [2012] using a 193 nm laser coupled to an ICPMS in low mass resolution mode) may be matrix-related, given that Chen *et al*. [2011] observe no offset between MACS-3 Mn data acquired by LA and solution ICPMS. Because m/z 55 suffers from a large gas blank correction as a result of $^{40}Ar^{15}N$, it is more challenging to accurately quantify Mn concentrations in samples at low/sub ppm concentration. Using H_2 as an additional diatomic gas reduces the m/z = 55 gas blank by almost two orders of magnitude (18×) from 4×10^5-3×10^6 to $<1\times10^4$ on average. This improvement is a necessity for Mn determination when low repetition rates or small spot sizes are desirable [Evans et al. 2014; Evans & Müller 2013]. For example, the detection limit for slow depth-profiling (44 µm, 2 Hz) is improved from 87 to 6 ppm on average, comparable to that of Chen *et al*. [2011] derived from a LA system with no diatomic gas but at a higher repetition rate (8 Hz).

^{57}Fe: Fe determination by standardisation to NIST612 is not possible because of the interference of $^{40}Ca^{16}O^{1}H$. NIST610-standardisation of the MPI glasses produces data in the broad region of reported values (i.e. within ±50%), but with significant offsets that means accurate or precise Fe concentrations are not feasible on our system using NIST for calibration. Previous studies

have reported accurate Fe data and good LA-EPMA agreement when calibrating to high-concentration reference materials such as BCR-2G, or by using a multi-standard calibration line [Liu et al. 2008; Arevalo Jr et al. 2011; Jenner & O'Neill 2012]. Accurate and precise LA-derived Fe data are possible at high concentrations.

^{66}Zn: Track data are severely compromised by Zn contamination, the most likely cause of which is zinc stearate powder from disposable gloves [Friel et al. 1996; Evans & Müller 2013]. Whilst samples are routinely pre-ablated, it may be that not all users pre-ablate standards in the same way, which means that there is some remnant surface contamination. NIST610-standardised track data are offset to accuracies between 1-1.5, whilst NIST612-standardised data is reasonably accurate but very imprecise (randomly varying greater/less contamination than the calibration standard) because it has a more similar [Zn] to MACS-3 and the MPI glasses. This precludes further discussion of data obtained by LA tracks. However, depth profiling obviously does not suffer from surface contamination which allows some assessment of Zn data quality on our system. Standardising the NIST glasses to each other produces data that is both accurate (<4%) and precise (<6%). NIST-standardised GOR132/128 data are also excellent (precision <6% and accuracy ~10%). On average, GOR132 and GOR128 data are offset to values -5% and +5% from reported, respectively. This may be a result of differential NIST-MPI fractionation factors at smaller spot sizes [Jochum et al. 2012; Kroslakova & Günther 2007] and the magnitude of the offset that we observe is not large enough to warrant recommendation of an accuracy correction. The limited data available for MACS-3 indicate an accuracy comparable to the MPI glasses, albeit with a higher precision (20%) in common with most other elements in this standard.

^{85}Rb: Long-term Rb accuracy is better than 3% for all sets of ablation conditions (tables 2 and 3), with the exception of small spots and track data of the MPI and STDP glasses (7-14%). Spot size-dependent variation in fractionation indices, a known feature of our system and for LA in general for the volatile elements [e.g. Tomlinson et al. 2010], is the most likely explanation. Rb accuracy in these standards is principally dependent on concentration. The higher concentration MPI glasses ATHO-G

and StHs have accuracies of 13% and 7% respectively, whilst GOR128 (406 ppt) is substantially worse (tables 2 and 3). The STDP3-150/5 phosphate glasses are consistently offset (accuracy = -10%), however there is little data with which to place this in context. The compiled value of Klemme *et al*. [2008] is the average of solution and LA ICPMS data which do not show this same relative difference (i.e. the LA data is not lower but vice versa). The offset that we observe may be a result of the higher repetition rate of these laser track data compared to the 5 Hz spot analysis of the original study. The low Rb concentration of MACS-3 (along with likely heterogeneity) means that it is difficult to assess accurately by LA-ICPMS, however as a preliminary working value, the mean of all spot and track analyses from two different MACS-3 pellets is 58±8 ppb (n = 64, 2SE, range of individual analyses = 40-200 ppb). This is within error of that reported by Jochum *et al*. [2014] using a 200 nm fs LA system (70±8 ppb).

^{88}Sr: NIST612-standardised accuracy for both NIST610 and all the regularly analysed MPI glasses in our lab are generally characterised by accuracies of <1% and precision of <4% (table 2). Standardisation using NIST610 produces data of equivalent quality. Spot analyses of ATHO-G and StHs are equally accurate but considerably less precise (11% and 5% respectively), indicating that these standards are less homogeneous than both NIST610/612 and the more basic MPI glasses. These precisions are higher than those associated with most data in the GeoReM database, although the SIMS data of Jochum *et al*. [2006] indicates µm-scale heterogeneity of a similar magnitude. Aside from those derived from this study, all of the analyses in this database are LA-derived and have an overall 2RSD of 18%, indicating that inter-grain heterogeneity may be even greater than suggested by our data. Whilst there are insufficient analyses to break STDP phosphate glass data quality down by ablation parameter, mean long-term accuracies are 2-4%. This represents a significant offset given that these standards are homogeneous (precision 1.9-4.5%). The inconsistent offset (STDP3-1500 has a negative accuracy whilst the others are positive) indicates that this is unlikely to be a result of NIST-phosphate fractionation that requires an accuracy correction. There is little data with which to test this, although the 4.3% offset we observe for STDP3-5 (i.e. a Sr concentration of 1496

596 ppm) is in much better agreement with the 200 nm fs-LA data of Jocum *et al*. [2014] than the
597 recommended value [Klemme et al. 2008]. Further data from more laboratories is required to verify
598 this, however our analyses indicate that these offsets should not be applied as an accuracy
599 correction to samples. Rather, the recommended values may require minor revision in the future.
600 MACS-3 is considerably more heterogeneous than the other standards (precision = 8-13%) and
601 consistently offset to an accuracy of -5%. This is in poor agreement with previous 193 nm LA studies
602 using both normalisation of bulk components and internal standardisation strategies [Chen et al.
603 2011; Tabersky et al. 2013; Jochum et al. 2012], which broadly agree with the information value of
604 6760 ppm. The 200 nm fs-LA data of Jochum *et al*. [2014] further support these existing datasets,
605 which may suffer to a lesser extent from bias resulting from the use of a calibration standard with a
606 different matrix. The reason for this offset is not clear and cannot be an artefact of our data
607 processing given that we demonstrate excellent Sr data for other standards. It may be that the
608 relatively low fluence that we frequently use (3-5 J cm^{-2}) compared to other studies reporting MACS-
609 3 Sr data is an important factor, as has been shown for Cu [Jackson & Günther 2003]. Irrespective,
610 the high MACS precision prevents us from recommending an accuracy correction when analysing Sr
611 in carbonates. In summary: Accurate and precise Sr data are possible, even with non-matrix matched
612 standardisation. However, a new carbonate standard is required for applications where precision of
613 <15% is desirable. Minor adjustments to the Sr concentrations of the STDP phosphate glasses may
614 be appropriate, although further data are required to confirm the small accuracy offsets we observe.
615 **^{89}Y:** Y accuracy is generally better than 2-3% for track analyses and ~4% for spots. The fact
616 that all NIST612-standardised Y accuracies are negative (except the STDP phosphates), irrespective
617 of matrix, indicates that the NIST612 Y value may be too low by 2.9%. This is well within the range of
618 previously reported and compiled values, which are 38.5±3.9 ppm and 38.3±2.5 ppm for solution
619 and LA-ICPMS respectively based on data in the GeoReM database. However, our NIST612 Y value is
620 derived from at least 10 NIST slithers calibrated to seven other well-characterised standards,
621 whereas a large portion of the LA Y data for this standard in the GeoReM database is based on

calibration to NIST610. The accuracy of the other standards is better than we can reasonably assess given possibly errors of this magnitude (~3%) in the preferred value of the NIST glasses. Ablation parameter-specific precision is better than 5% for all standards with the exception of MACS-3 (6-16% depending principally on spot size). There is a hint of a long-term trend in the accuracy of our Y data for the MPI glasses GOR132/128, discussed in section 4.1. Diatomic gas type exerts no discernible control on accuracy for most standards, which is unsurprising for standards with Sr/Y ratios of ~1. However, MACS-3 (Sr/Y = 302) accuracy is offset by 8.0% when H_2 instead of N_2 is used as the diatomic gas (n = 138 and 62 respectively, figure 6). Given that these data represent the average of a range of spot sizes, mostly at 15 Hz repetition rate, it is unlikely that other factors could lead to this bias. An 8% increase in MACS-3 Y is equivalent to 1.8 ppm, which equates to an average $^{88}Sr^{1}H^{+}$production rate of 0.027% for carbonate ablation using H_2. This may be a significant Y bias for carbonates or phosphates (e.g. the shells of marine organisms or tooth enamel) which often have Sr concentrations >1000 ppm. Given that Y/Ca (and other REE/Ca) ratios have been used as an indicator of diagenesis in such material [Müller et al. 2009], this is something that should be taken into account when adding H_2 to the carrier gas stream.

^{138}Ba: Ba data quality in standards with >10 ppm is both accurate and precise. NIST, STDP and the MPI glasses with relatively high [Ba] have long-term accuracies of <6%, and <2% is possible for certain ablation conditions. Precision is routinely <5%. The consistent negative offset of NIST612-standardised data may indicate that NIST612 [Ba] should be ~2% higher, or at least that the ID-TIMS data published in Jochum *et al*. [2005] (1% higher than the compiled value) should be adopted. The only other notable offset within these standards is for the phosphate glass STDP3-5, for which all data are offset to positive values (accuracy = 6%). This is in broad agreement with the 200 nm fs-LA data of Jochum *et al*. [2014] which are also offset from the recommended value of Klemme *et al*. [2008] (by +3%). Together these analyses suggest that the LA data used to define this recommended value may be inaccurate, as the original solution data are in good agreement with this study and that of Jochum *et al*. [2014]. In contrast to the higher concentration standards, GOR132/128 accuracy are

significantly dependent on analysis type (spot/track). This offset is more pronounced for GOR132 (0.82 ppm Ba; 15% difference) than GOR128 (1.1 ppm; 7%), where track analyses are characterised by worse accuracies and higher measured values than spots (figure 4). The reason for this offset may either be surface contamination, to which ablation tracks are obviously more susceptible than spots, or a problem with the extrapolation of the NIST concentration-Ba/Ca intensity ratio to glasses with much lower [Ba]. The high repetition rate (15-20 Hz) of the majority of the track data may exacerbate possibly different fractionations between the standards. This feature makes these data difficult to interpret. Assuming the lower repetition rate spot data are more likely to be reliable (the small size of these glass chips makes long line scans impractical), Ba accuracy and precision at 1 ppm are ~7% and 8-10% respectively.

The REE: Spot analysis of the REE in many of the MPI glasses on our system is discussed in detail by Tomlinson *et al*. [2010]. Track data of KL2-G and GOR132/128 indicate data quality equivalent to spot analyses, with principal differences due to the low concentration of the REE in GOR132/128. Nonetheless, GOR132 ^{139}La data are both accurate and precise (2% and 32% respectively), given the 84 ppb concentration. We observe a track-spot offset of 5% in the low concentration MPI glasses for ^{140}Ce (and possibly for ^{146}Nd, although there are few track analyses for this m/z), but otherwise sub-5% accuracy and precision is easily possible. Both GOR132/128 are consistently offset to -10% accuracies for ^{146}Nd, although this is within the range of the LA data of Jochum *et al*. [2006] and subsequent studies [e.g. Jenner & O'Neill 2012]. This offset may be most easily explained by inter-grain heterogeneity, given that our MPI data are derived from one set of these standards. The STDP glasses are characterised by excellent homogeneity for ^{140}Ce (precision 2-4% when standardised using NIST610), although our data do indicate that the STDP3-1500 Ce information value is too high by 8%. Similarly, our data indicate that the STDP3-150 Nd information value should be decreased to 0.17 ppm (the original analysis is reported to 1SF [Klemme et al. 2008]). We find all of these phosphate glasses to be considerably more homogeneous for Nd than original reported, STDP3-150/1500 are characterised by 2RSD Nd of 14% and 9% respectively (n = 30

in both cases). Finally, the lanthanides are one part of the periodic table to which the MACS-3 carbonates may have particular application. NIST-standardised MACS-3 data are both accurate (all data <10% and most <5%) and reasonably precise in comparison to most other elements in this pressed powder. La, Ce and Nd have 2RSD of ~10% which is probably sufficient for most applications. These data demonstrate that accurate carbonate REE data are possible when standardising using the NIST glasses. Tanaka *et al*. [2007] report data of similar quality (when ablation takes place in a He atmosphere), with the exception of La, for which our analyses are far more accurate (~-2% in this study cf. -6 to -11%). Whilst this may extol the benefits of using a 193 nm laser, a similar offset between 213 nm and 193 nm LA data was not observed by Jochum *et al*. [2012] when analysing MACS-3.

^{208}Pb: The volatility of Pb is a well-known issue for LA [Jackson 2001], with larger fractionation factors unsurprisingly further from unity on average for spot analyses [Jochum et al. 2014] because of the crater depth-dependent particle size distribution [Jackson & Günther 2003]. Nonetheless, at >10 ppm (GOR132, StHs and the STDP glasses) reasonably precise (<10%) Pb data are easily possible with a 193 nm ArF laser. Precision may be further improved by using an external standard with greater Pb homogeneity than the NIST glasses [see Eggins & Shelley 2002]. We do not attempt to assess the accuracy of the MPI glasses, as the offsets we observe are likely smaller than what may be expected from differential NIST-MPI fractionation factors (GOR132 and StHs accuracy is <5%). In contrast, our data suggest the Pb information values of both STDP3-150/1500 requires downwards revision, which have overall mean accuracies of -8% and -13% respectively. The agreement of our data for STDP3-5 with the recommended value indicates that these offsets may not be matrix-induced. In the case of STDP3-150, our measured value (139 ppm) is in excellent agreement with the original solution ICPMS data (145 ppm) [Klemme et al. 2008]. Spot analyses of MACS-3 indicate heterogeneity of 8% (collected from the first 1.5 years only) whilst track data are considerably worse.

699 **^{232}Th:** ATHO-G and StHs Th data are discussed in Tomlinson *et al*. [2010]. Approximately 50
700 analyses of KL2-G indicate that accurate and precise (<2% and <10% respectively) are possible even
701 at 1 ppm. However, our GOR128 data show that at low-ppb concentrations precision is ~400% even
702 though these analyses were above LOD. MACS-3 precision is 13%, although our data indicate that
703 the Th concentration in this standard requires revision; the mean value based on our dataset is 46
704 ppm. This is in agreement with the 213 nm data of Jochum *et al*. [2014], whereas the 200 nm fs LA
705 data of that study, along with most other data in the GeoReM database [Tabersky et al. 2013; Chen
706 et al. 2011; Jochum et al. 2012] agrees with the information value. This may be related to the
707 relatively high repetition rates and low fluence of our analyses.
708 **^{238}U:** The higher concentration MPI standards (1-2 ppm, ATHO-G and StHs) have a long-term
709 precision of 14-15% (figure 4). Reasonable (~20%) precision is still possible for GOR132 (48 ppb),
710 however at lower concentrations (GOR128 = 12 ppb) only analytical conditions associated with
711 relatively high ion beam intensities (high repetition rate, large diameter beam) produce useful data
712 (track and spot precision are 40% and 80% respectively). MPI glass accuracy is excellent given the
713 low concentrations, the long term average is <5% except for GOR132/128 (<10%). The higher
714 concentration STDP glasses are all characterised by precisions of 4-7%. Our measured values for
715 STDP3-150 is in excellent agreement with the reported/information, whereas our STDP3-150/5 data
716 have accuracies of -2% to -4% and +5-9% depending on which NIST glass is used for standardisation.
717 This is broadly in agreement with the data of Jochum *et al*. [2014], which is offset by +2.3%
718 compared to the information value. Ablation parameter-specific MACS-3 data are characterised by
719 long-term precision of ~30% which is reasonable given the 1.5 ppm U concentration of this
720 carbonate (figure 4).
721 **4. Further discussion**
722 **4.1 Long-term trends**
723 We observe few significant long term trends in the dataset, demonstrating that appropriately
724 standardised, blank-corrected 193 nm laser ablation measurements do not suffer from long term

biases. The only exceptions to this are our B data, which show a marked improvement in accuracy related to the installation of Nylon-6 tubing (discussed in section 3.2), and possibly ^{89}Y (figure 7). This latter trend is evident in both GOR132/128, irrespective of which NIST glass is used for standardisation (i.e. the trend would not be evident if one GOR were standardised to the other, or in the NIST-standardised NIST data). There are insufficient data covering this period for the other glass standards to assess whether this is a broader feature of Y data quality over this time. This would either imply that the cause is a shift in the matrix-dependent Y/Ca fractionation over this time, or that the trend is an artefact of the change in dominant analysis style from line-scans using N_2 as the diatomic gas to a mixture of lines and spots with H_2. The $^{88}Sr^1H^+$ production rate that we calculate in section 3.2 cannot account for this offset, given that both the NIST and GOR glasses have low Sr/Y ratios (~1-2). Therefore, it is not clear why such a difference should be associated with the additional diatomic gas type. The change in transport tubing (figure 6) roughly coincides with this shift, which may provide an explanation. It is possible that tubing-induced element/element fractionation may have a minor effect on data quality of even the less volatile elements, given that this fractionation could be matrix-dependent (as a result of LA yield or analyte concentration).

4.2 Diatomic gas type

Whilst geberal instances of data quality significantly influenced by diatomic gas type were given in section 3.2, the dataset also allows broader trends to be recognised. Of these, the most obvious is the difference in long term accuracy and precision when using H_2 rather than N_2 for spot analyses, shown in figure 8. Whilst there are more subtle differences in accuracy, with notable examples such as ^{31}P and ^{57}Fe discussed earlier, there is a significant difference in long-term precision (i.e. 2SD of all analyses for a particular standard). NIST610 and GOR132 shown as examples in figure 8, standardised using NIST612. In both cases the masses associated with significant improvements are those with a major N_2-derived gas interference (m/z = 29, 31, 55), or volatile elements (GOR132 Pb) which indicates that the use of H_2 may reduce volatile-element fractionation downstream of the ablation cell, for at least some standards (in all cases the ablation process took place in a pure He

atmosphere). However, figure 8 indicates that such processes affecting volatile elements do not behave predictably, given that there is no statistically significant difference in ^{66}Zn or ^{85}Rb precision. In order to maximise the amount of data available, all data for a specific analysis type (spot/track) and diatomic gas type were used. Although this means that the data are potentially biased by different spot sizes or repetition rates being commonly associated with certain analytical conditions, these were reasonably invariant between spots and tracks (see above).

Because diatomic gas type can only influence transport and ionisation processes in the plasma, it is difficult to explain why an overall similar phenomena is not observed for track data. This may perhaps be related to the more limited fractionation processes occurring at the ablation site for this style of analysis, i.e. that post-ablation fractionation is related to element/element ratios and is therefore more constant when these ratios are more stable in the sample gas stream. The benefit of H_2 for track data is limited to masses with a gas interference (27, 29, 55 for NIST610), whilst the worse precision for track analyses observed for some m/z may simply be related to the broadly lower sensitivity and therefore lower signal/background ratios when using H_2, especially for low concentration trace elements. The use of H_2 clearly does not always offer this benefit, although the improvement in data quality for some elements may outweigh the associated negative aspects, such as the precision of NIST610 ^{25}Mg data. Some features are difficult to explain, such as the greatly improved ^{140}Ce data with H_2.

4.3 Spatial variability/Cell homogeneity

Because stage coordinates are available for each analysis, potential spatial variation in data quality, fractionation factors or sensitivity can be investigated. The location of all of the analyses described in this study are shown in figure 9. In order to maximise the amount of data available for the assessment of possible heterogeneity in element/element fractionation, all analyses were normalised to the mean measured value for that standard (i.e. accuracy was forced to equal 1). This ensures that the unavoidable preferential placement of some standards due to sample holder

776 constraints into certain positions (e.g. NIST612, figure 9), does not produce apparent spatial
777 variation as a result of error in the reported value of these standards.
778 Figure 10 shows three different ways of representing spatial variability in measured
779 element/Ca ratios, normalised in this way. Mg/Ca offsets are shown as a function of analysis position
780 using the locations given in figure 9. This provides a visual indication that there is no significant bias
781 in Mg data depending on the location of the standard, for example close to the corners of the
782 ablation cell where He gas flow might be expected to be impacted by the proximity of the cell wall.
783 The obvious outliers in figure 10A are likely to be a result of occasional more extreme ablation
784 conditions, such as very small spot sizes or high repetition rates. Even this subset shows no obvious
785 spatial trend. Figure 10B shows normalised U/Ca ratios as a function of distance from the cell centre,
786 again showing a slope within error of zero (all pooled U/Ca data are characterised by a centre-edge
787 gradient of 0.11% mm^{-1}). Examining gradients produced in this way, for all 38 m/z considered in this
788 study, moreover demonstrates that no significant trend exists in any of the data and therefore that
789 the two volume cell of our system can be considered homogeneous. This should of course be viewed
790 in the context of the long-term precision of these analyses, clearly data derived from a number of
791 standards over a long time period are not capable of resolving sub-% differences in accuracy when
792 analytical parameters and/or limitations induce overall precision around an order of magnitude
793 higher than this. Nonetheless, the largest gradients apparent in our data are in the order of 0.5%
794 mm^{-1}. Furthermore, gradients this high are only observed for some m/z between 50-60 which are
795 either associated with a gas interference (55, 57) or are volatile (^{66}Zn).
796 **5. Conclusions**
797 The LA-ICPMS trace element data mining program that we present highlights the need to consider
798 large datasets in order to representatively report accuracy and precision. However, whilst we show
799 that precision may be larger than typically reported based on a limited number of analyses
800 conducted under a specific set of ablation conditions, this long term (5 year) dataset of 5000
801 standard analyses also highlights that excellent trace element data is available with sub-5% precision

and accuracy easily possible for some analytes. Our mass-specific breakdown of data quality in 10 commonly analysed standards, including the NIST glasses, highlights where care must be taken in order to produce good data (for example boron), and enables us to assess the relative effects of LA-ICPMS-induced fractionation and error in the reported value of some elements in certain standards (for example NIST magnesium). With one or two exceptions, we observe no temporal trends in accuracy and precision for any analyte in any of the standards we routinely ablate, demonstrating that data acquired over long time periods are comparable, provided that long-term accuracy and precision are appropriately characterised. However, we do observe significant differences in both accuracy and precision depending on ablation conditions, particularly relating to the addition of either H_2 or N_2 as the additional diatomic gas. Finally, because our dataset is spatially resolved, i.e. stage coordinates are available for each analysis, we are able to assess long-term ablation cell homogeneity for the first time. We find no significant gradient in any element/Ca ratio, providing good evidence that the two-volume Laurin Technic cell of our system does not suffer from spatially varying fractionation at a level likely to significantly bias trace element data. The Matlab program may be especially useful for inter-laboratory comparison, as similar datasets from other LA-ICPMS systems could be produced in a short period of time. Because the data we present are derived from commonly analysed standards, pursuing this line of enquiry would give a comprehensive overview of the comparability of trace element data between LA-ICPMS systems.

6. References

Arevalo Jr, R., McDonough, W.F. & Piccoli, P.M., 2011. In Situ Determination of First-Row Transition Metal, Ga and Ge Abundances in Geological Materials via Medium-Resolution LA-ICP-MS. *Geostandards and Geoanalytical Research*, 35(2), pp.253–273.

Becker, J.S., 2002. Applications of inductively coupled plasma mass spectrometry and laser ablation inductively coupled plasma mass spectrometry in materials science. *Spectrochimica Acta Part B*, 57, pp.1805–1820.

Blamart, D. et al., 2007. Correlation of boron isotopic composition with ultrastructure in the deep-sea coral Lophelia pertusa : Implications for biomineralization and paleo-pH. *Geochemistry, Geophysics, Geosystems*, 8(12), Q12001.

Chen, L. et al., 2011. Accurate determinations of fifty-four major and trace elements in carbonate by LA-ICP-MS using normalization strategy of bulk components as 100%. *Chemical Geology*, 284(3-4), pp.283–295.

Eggins, S., De Deckker, P. & Marshall, J., 2003. Mg/Ca variation in planktonic foraminifera tests: implications for reconstructing palaeo-seawater temperature and habitat migration. *Earth and Planetary Science Letters*, 212(3-4), pp.291–306.

Eggins, S.M. & Shelley, J.M.G., 2002. Compositional Heterogeneity in NIST SRM 610-617 Glasses. *Geostandards and Geoanalytical Research*, 26, pp.1–18.

Eiler, J.M., Graham, C. & Valley, J.W., 1997. SIMS analysis of oxygen isotopes: matrix effects in complex minerals and glasses. *Chemical Geology*, 138(3-4), pp.221–244.

Evans, D. et al., 2013. Eocene seasonality and seawater alkaline earth reconstruction using shallow-dwelling large benthic foraminifera. *Earth and Planetary Science Letters*, 381, pp.104–115.

Evans, D. et al., 2014. Mg/Ca-temperature and seawater-test chemistry relationships in the shallow-dwelling large benthic foraminifera Operculina ammonoides. *Geochimica et Cosmochimica Acta*. 148, pp.325-342.

Evans, D. & Müller, W., 2013. LA-ICPMS elemental imaging of complex discontinuous carbonates: An example using large benthic foraminifera. *Journal of Analytical Atomic Spectrometry*, 28(7), p.1039.

Fietzke, J. et al., 2010. Boron isotope ratio determination in carbonates via LA-MC-ICP-MS using soda-lime glass standards as reference material. *Journal of Analytical Atomic Spectrometry*, 25(12), p.1953.

Fricker, M.B. et al., 2011. High spatial resolution trace element analysis by LA-ICP-MS using a novel ablation cell for multiple or large samples. *International Journal of Mass Spectrometry*, 307(1-3), pp.39–45.

Friel, J.K. et al., 1996. Laboratory Gloves as a Source of Trace Element Contamination. *Biological trace element research*, 54(3), pp.135-142.

Fryer, B.J., Jackson, S.E. & Longerich, H.P., 1995. The design, operation and role of the laser-ablation microprobe coupled with an inductively coupled plasma-mass spectrometer (LAM-ICP-MS) in the earth science. *The Canadian Mineralogist*, 33, pp.303–312.

Gagnon, J.E. et al., 2008. Quantitative analysis of silicate certified reference materials by LA-ICPMS with and without an internal standard. *Journal of Analytical Atomic Spectrometry*, 23(11), p.1529.

Guillong, M. et al., 2008. SILLS: A Matlab-based program for the reduction of laser ablation ICP-MS data of homogeneous materials and inclusions. *Mineralogical Association of Canada Short Course 40*, pp.328–333.

Hathorne, E.C., 2003. Determination of intratest variability of trace elements in foraminifera by laser ablation inductively coupled plasma-mass spectrometry. *Geochemistry Geophysics Geosystems*, 4(12), 8408.

Hathorne, E.C. et al., 2008. Physical and chemical characteristics of particles produced by laser ablation of biogenic calcium carbonate. *Journal of Analytical Atomic Spectrometry*, 23(2), p.240.

Heinrich, C. a. et al., 2003. Quantitative multi-element analysis of minerals, fluid and melt inclusions by laser-ablation inductively-coupled-plasma mass-spectrometry. *Geochimica et Cosmochimica Acta*, 67(18), pp.3473–3497.

Hoppe, P., Cohen, S. & Meibom, A., 2013. NanoSIMS: Technical Aspects and Applications in Cosmochemistry and Biological Geochemistry. *Geostandards and Geoanalytical Research*, 37(2), pp.111–154.

Jackson, S.E. et al., 2004. The application of laser ablation-inductively coupled plasma-mass spectrometry to in situ U–Pb zircon geochronology. *Chemical Geology*, 211(1-2), pp.47–69.

Jackson, S.E., 2001. The application of Nd:YAG lasers in LA-ICPMS. In *Laser ablation-ICP-MS in the Earth sciences – Principles and applications. Mineralogical Association of Canada Short Course Series 29*. pp. 29–46.

Jackson, S.E. & Günther, D., 2003. The nature and sources of laser induced isotopic fractionation in laser ablation-multicollector-inductively coupled plasma-mass spectrometry. *Journal of Analytical Atomic Spectrometry*, 18(3), pp.205–212.

884 Jenner, F.E. & O'Neill, H.S.C., 2012. Major and trace analysis of basaltic glasses by laser-ablation ICP-
885 MS. *Geochemistry Geophysics Geosystems*, 13(3), pp.1–17.
886 Jochum, K.P. et al., 2012. Accurate trace element analysis of speleothems and biogenic calcium
887 carbonates by LA-ICP-MS. *Chemical Geology*, 318-319, pp.31–44.
888 Jochum, K.P. et al., 2005. Chemical Characterisation of the USGS Reference Glasses GSA-1G, GSC-1G,
889 GSD-1G, GSE-1G, BCR-2G, BHVO-2G and BIR-1G Using EPMA , ID-TIMS , ID-ICP-MS and LA-ICP-
890 MS., 29, pp.285–302.
891 Jochum, K.P. et al., 2011. Determination of Reference Values for NIST SRM 610-617 Glasses
892 Following ISO Guidelines. *Geostandards and Geoanalytical Research*.
893 Jochum, K.P. et al., 2006. MPI-DING reference glasses for in situ microanalysis: New reference values
894 for element concentrations and isotope ratios. *Geochemistry Geophysics Geosystems*, 7(2).
895 Jochum, K.P. et al., 2014. Non-Matrix-Matched Calibration for the Multi-Element Analysis of
896 Geological and Environmental Samples Using 200 nm Femtosecond LA-ICP-MS: A Comparison
897 with Nanosecond Lasers. *Geostandards and Geoanalytical Research*, 38(3), pp.265–292.
898 Jochum, K.P. & Enzweiler, J., 2014. *Reference Materials in Geochemical and Environmental Research.*
899 *In: Holland, H.D. and Turekian, K.K (Eds.) Treatise on Geochemsitry,* 2nd ed., vol. 15, pp.43-70.
900 Kaczmarek, K. et al., 2014. Simultaneous determination of $\delta^{11}B$ and B/Ca ratio in marine biogenic
901 carbonates at nanogram level. *Chemical Geology*, 392, pp.32–42.
902 Klemme, S. et al., 2008. Synthesis and preliminary characterisation of new silicate, phosphate and
903 titanite reference glasses. *Geostandards and Geoanalytical Research*, pp.39–54.
904 Kroslakova, I. & Günther, D., 2007. Elemental fractionation in laser ablation-inductively coupled
905 plasma-mass spectrometry: evidence for mass load induced matrix effects in the ICP during
906 ablation of a silicate glass. *Journal of Analytical Atomic Spectrometry*, 22(1), p.51.
907 Lazartigues, A. V., Sirois, P. & Savard, D., 2014. LA-ICP-MS Analysis of Small Samples: Carbonate
908 Reference Materials and Larval Fish Otoliths. *Geostandards and Geoanalytical Research*, 38,
909 pp.225-240.
910 Liu, Y. et al., 2008. In situ analysis of major and trace elements of anhydrous minerals by LA-ICP-MS
911 without applying an internal standard. *Chemical Geology*, 257(1-2), pp.34–43
912 Longerich, H.P., Jackson, S.E. & Gunther, D., 1996. Laser ablation inductively coupled plasme mass
913 spectrometric transient signal data acquisition and analyte concentration calculation. *Journal of*
914 *Analytical Atomic Spectrometry*, 11, p.899.
915 Della Lunga, D. et al., 2014. Location of cation impurities in NGRIP deep ice revealed by cryo-cell UV-
916 laser-ablation ICPMS. *Journal of Glaciology*, 60(223), pp.970–988.
917 Melson, W.G., O'Hearn, T. & Jarosewich, E., 2002. A data brief on the Smithsonian Abyssal Volcanic
918 Glass Data File. *Geochemistry, Geophysics, Geosystems*, 3(4), pp.1–11.
919 Moens, L.J. et al., 2001. Elimination of isobaric interferences in ICP-MS, using ion?molecule reaction
920 chemistry: Rb/Sr age determination of magmatic rocks, a case study. *Journal of Analytical*
921 *Atomic Spectrometry*, 16(9), pp.991–994.
922 Müller, W. et al., 2009. Initial performance metrics of a new custom-designed ArF excimer LA-ICPMS
923 system coupled to a two-volume laser-ablation cell. *Journal of Analytical Atomic Spectrometry*,
924 24(2), p.209.
925 Müller, W., Shelley, J.M.G. & Rasmussen, S.O., 2011. Direct chemical analysis of frozen ice cores by
926 UV-laser ablation ICPMS. *Journal of Analytical Atomic Spectrometry*, 26(12), p.2391.
927 Paton, C. et al., 2011. Iolite: Freeware for the visualisation and processing of mass spectrometric
928 data. *Journal of Analytical Atomic Spectrometry*, 26(12), p.2508.
929 Pearce, N.J.G. et al., 1997. A Compilation of New and Published Major and Trace Element Data for
930 NIST SRM 610 and NIST SRM 612 Glass Reference Materials. *Geostandards and Geoanalytical*
931 *Research*, 21(1), pp.115–144.
932 Reichart, G., 2003. Single foraminiferal test chemistry records the marine environment. *Geology*,
933 31(4), pp.355–358.

934 Rittner, M. & Müller, W., 2011. 2D mapping of LAICPMS trace element distributions using R.
935 *Computers & Geosciences*. 42, pp.152-161.
936 Rollion-bard, C., Vigier, N. & Spezzaferri, S., 2007. In situ measurements of calcium isotopes by ion
937 microprobe in carbonates and application to foraminifera. *Chemical Geology*, 244, pp.679–690.
938 Russo, R.E. et al., 2002. Laser ablation in analytical chemistry — a review. *Talanta*, 57, pp.425–451.
939 Srinivasan, R., 2015. Ablation of and Polymers Ultraviolet Biological Lasers Tissue by Mechanism of
940 Absorption of Light. *Science*, 234(4776), pp.559–565.
941 Stoll, H.M., Müller, W. & Prieto, M., 2012. I-STAL, a model for interpretation of Mg/Ca, Sr/Ca and
942 Ba/Ca variations in speleothems and its forward and inverse application on seasonal to
943 millennial scales. *Geochemistry, Geophysics, Geosystems*, 13(9), Q09004.
944 Tabersky, D. et al., 2013. Aerosol entrainment and a large-capacity gas exchange device (Q-GED) for
945 laser ablation inductively coupled plasma mass spectrometry in atmospheric pressure air.
946 *Journal of Analytical Atomic Spectrometry*, 28(6), p.831.
947 Tanaka, K., Takahashi, Y. & Shimizu, H., 2007. Determination of rare earth element in carbonate
948 using laser-ablation inductively-coupled plasma mass spectrometry: an examination of the
949 influence of the matrix on laser-ablation inductively-coupled plasma mass spectrometry
950 analysis. *Analytica chimica acta*, 583(2), pp.303–9.
951 Thirlwall, M.F., 1991. Long-term reproducibility of multicollector Sr and Nd isotope ratio analysis.
952 *Chemical Geology*, 94(2), pp.85–104.
953 Tomlinson, E.L. et al., 2010. Microanalysis of tephra by LA-ICP-MS — Strategies, advantages and
954 limitations assessed using the Thorsmörk ignimbrite (Southern Iceland). *Chemical Geology*,
955 279(3-4), pp.73–89.
956 Vigier, N. et al, C., 2007. In situ measurements of Li isotopes in foraminifera. *Geochemistry*
957 *Geophysics Geosystems*, 8, Q01003.
958 Warter, V. et al., 2014. Late Miocene seasonal to subdecadal climate variability in the indo-west
959 Pacific (East Kalimantan, Indonesis) preserved in giant clams. *Palaios*, 29.

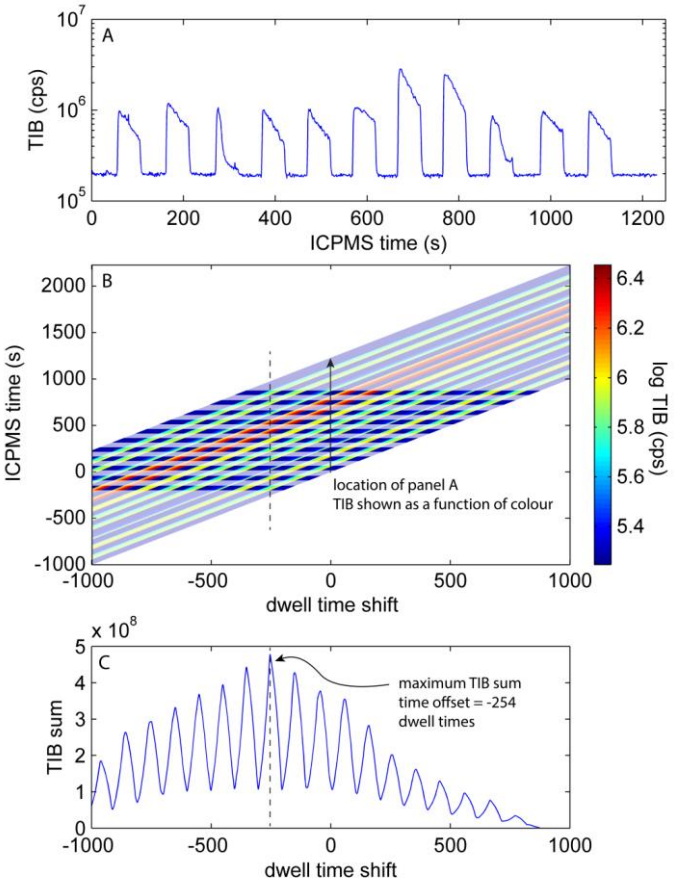

960

961 **Figure 1.** Automatic calculation of the time offset between laser-ablation and ICPMS
962 computers. (A) An example ICPMS file, showing summed ion beam against time. (B) The TIB
963 is shifted incrementally in steps of one ICPMS dwell time, assuming that the time offset
964 between the computers lies within ±1000 dwell times. Lightly shaded areas are deleted
965 portions of the matrix according to the start and end times of each analysis given by the
966 laser log file. (C) Summing the TIB for each dwell time shift gives the time offset as this is
967 maximised only when the deleted portions of data match the location of the background
968 segments of the TIB.

969

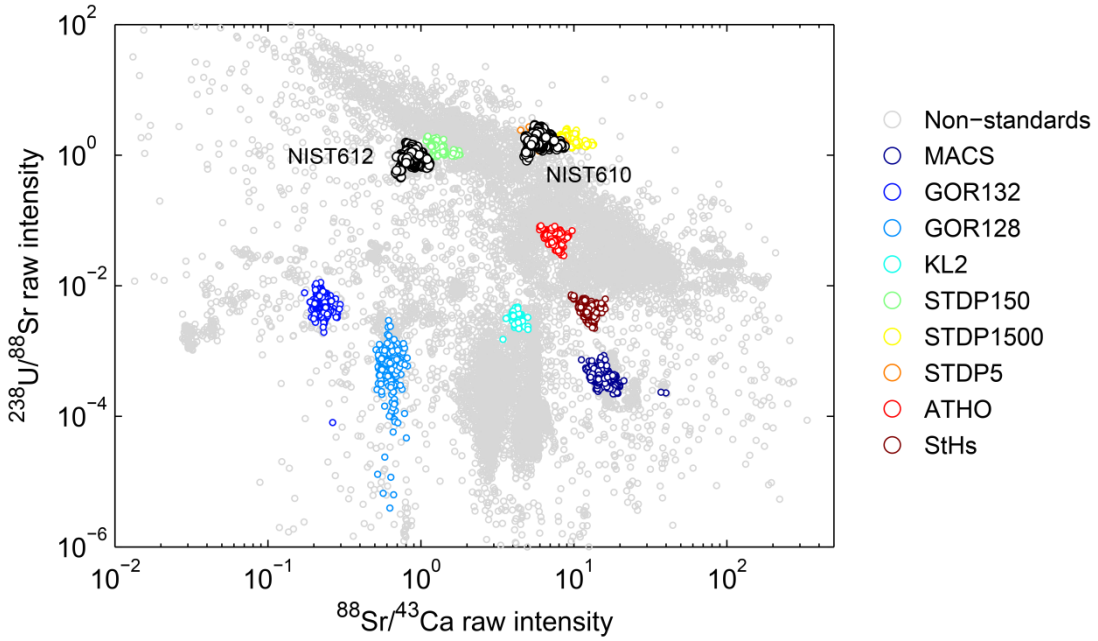

970

971 **Figure 2.** All raw Sr/Ca and U/Sr ratios for the most commonly analysed standards in our
972 laboratory over the last five years. All other standards and the majority of non-standards are
973 distinct from the NIST glasses in Sr/Ca-U/Sr space, with the exception of the phosphate
974 glasses STDP3-150 and STP3-5/1500 which overlap with NIST610 and NIST612 respectively
975 (see text for details of the resolution to this problem and resolution of minor overlap with
976 some sample types). These ratios therefore provide a robust means of identifying NIST
977 analyses without user confirmation.

978

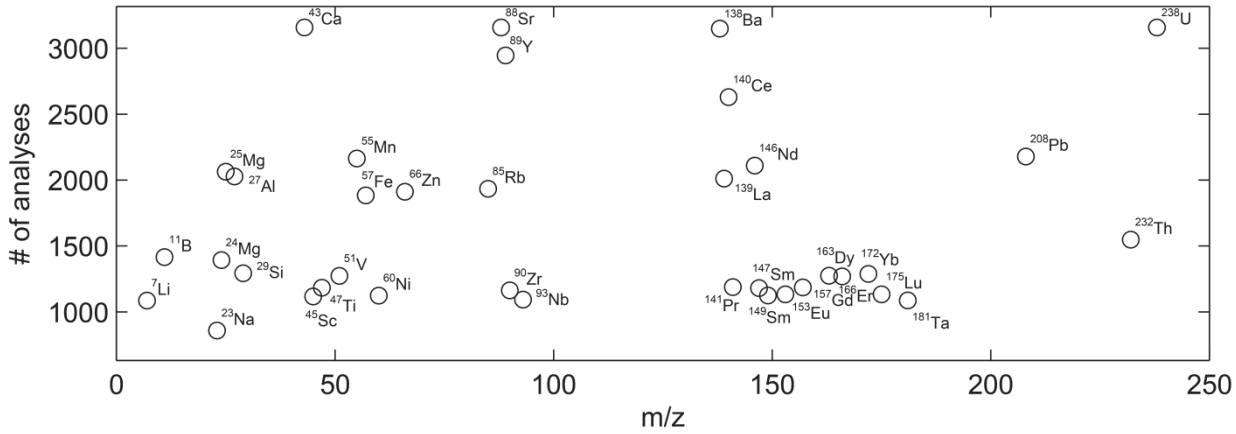

Figure 3. The number of times each m/z was analysed within the NIST612-standardised dataset, summed across all secondary standards. Only the 37 m/z with >800 analyses are shown.

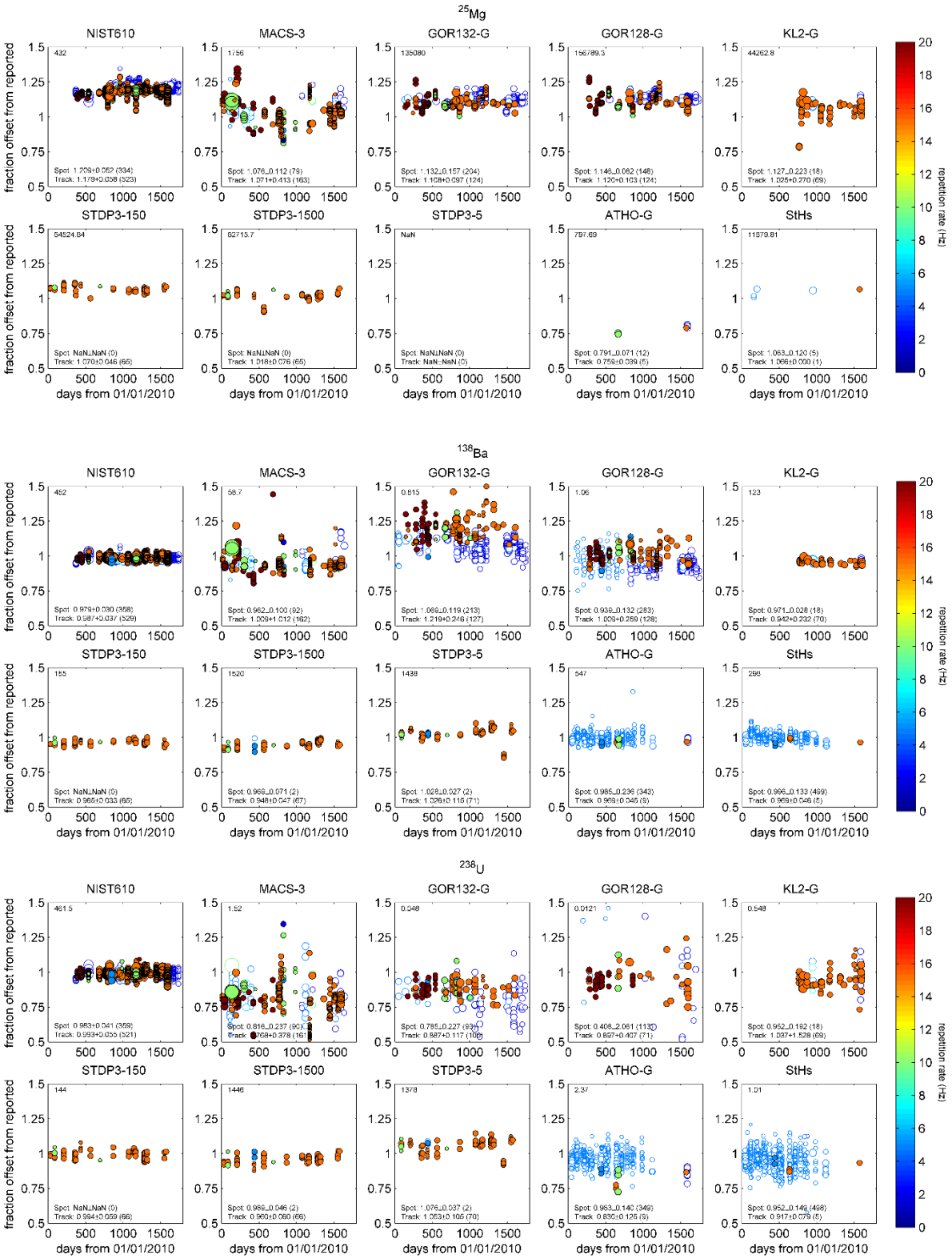

Figure 4. All NIST612-standardised data for three selected m/z (25, 138, 238). Open and closed symbols represent spot and track analysis respectively. Marker size is shown as a function of spot size and colour is shown as a function of repetition rate. Fraction offset (= accuracy) is given as the ratio of the measured X/Ca ratio to that reported (values >1 imply measured>reported), standardised using the NIST concentration values of [Jochum et al. 2011]. Analyte concentration in

each standard is shown in the top left, average accuracy±precision (n) is shown in the bottom left. See the supporting material for similar graphs for all isotopes with >800 analyses.

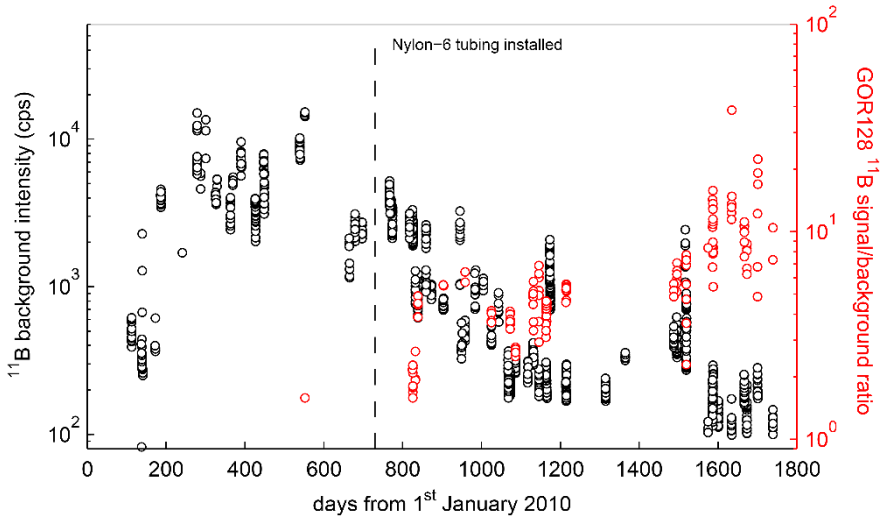

995

996 **Figure 5.** The effect of installing Nylon-6 tubing on the ^{11}B background intensity. Following an initial
997 sharp rise during 2010, attempts were made to reduce the B background by replacing the tubing,
998 torch and thorough cleaning of the ablation cell, resulting in a modest reduction. On replacement of
999 the entire tubing (including the squid gas signal smoothing device) with Nylon-6, the gas blank on
1000 m/z = 11 reduced by more than an order of magnitude over a period of ~1 year. The GOR128
1001 signal/background ratio when slow depth profiling (2 Hz, 44 µm) increased by an order of magnitude
1002 as a result.

1003

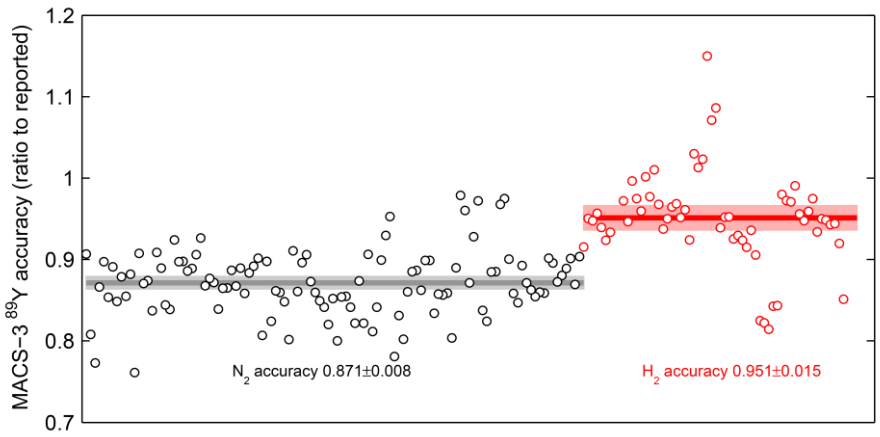

1004

1005 **Figure 6.** ^{89}Y accuracy in the pressed powder carbonate standard MACS-3, using both N_2 and H_2 as an
1006 additional diatomic gas. The use of H_2 when analysing this standard results in a positive accuracy
1007 shift of 8±0.02%, which is most easily explained by the formation of $^{88}Sr^{1}H^{+}$ (MACS-3 Sr/Y = 302).

1008

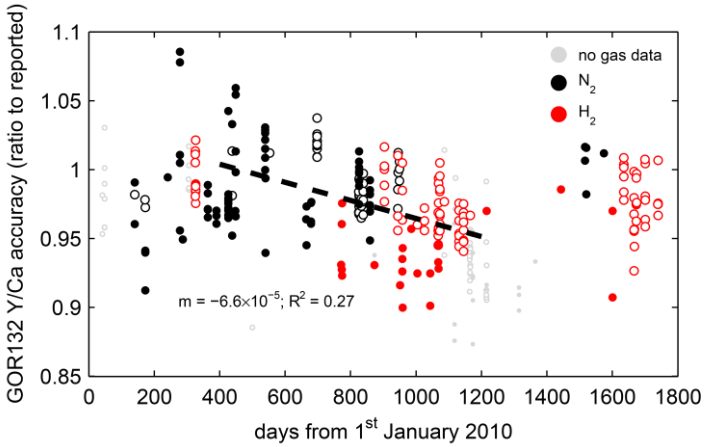

1009

1010 **Figure 7.** Long-term trend in GOR132 ^{89}Y accuracy, standardised using NIST612. Open and closed
1011 symbols show spot and track analyses respectively. Gas type is determined by flow rate from the
1012 mass flow controller, possible because our system is almost always tuned to use 6.5 ml min^{-1} N_2 but
1013 8 ml min^{-1} H_2. Because it was not always possible to read the mass flow controller rates from the
1014 Geostar log file, diatomic gas type for some analyses is unknown. A ~0.05 accuracy shift is observed
1015 between February 2011 and April 2013.

1016

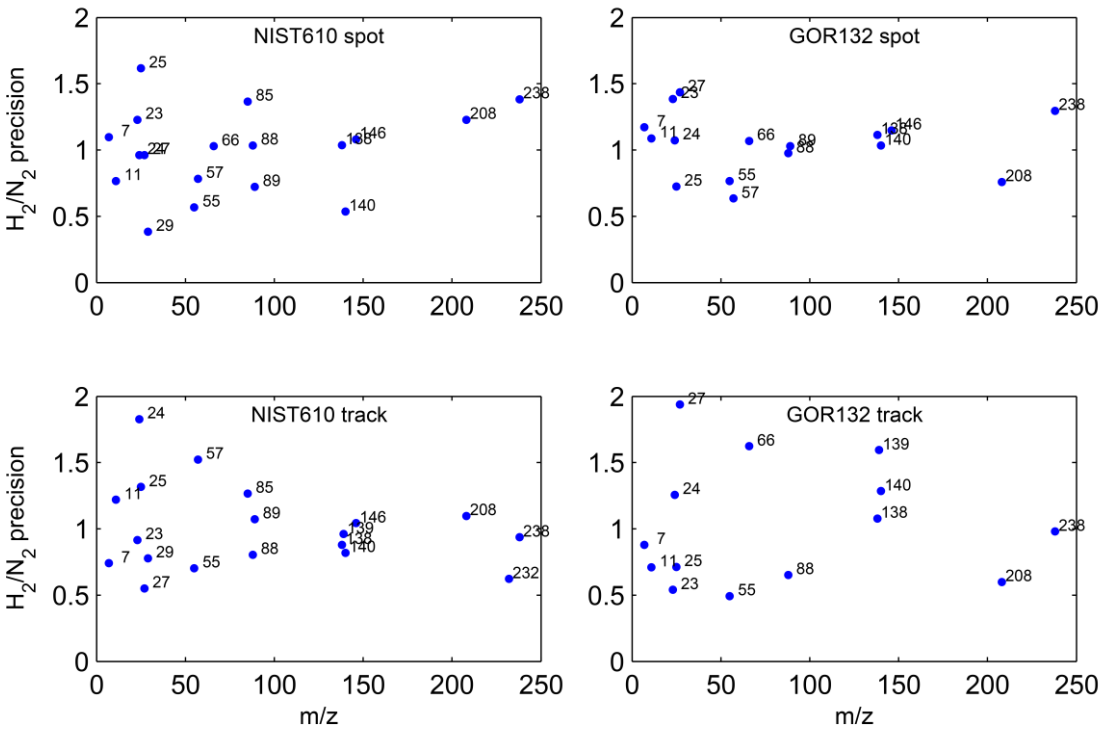

1017

1018 **Figure 8.** The effect of diatomic gas type on precision for NIST610 and GOR132 standardised using
1019 NIST612. Precision is defined as 2SD of all analyses. Both spot (depth profiling) and track data are
1020 shown. For both standard matrices, using H_2 as the additional diatomic gas instead of N_2 results in
1021 significantly improved long-term precision for some masses. Only masses for which more than 10
1022 datapoints for both diatomic gas types were available are shown.

1023

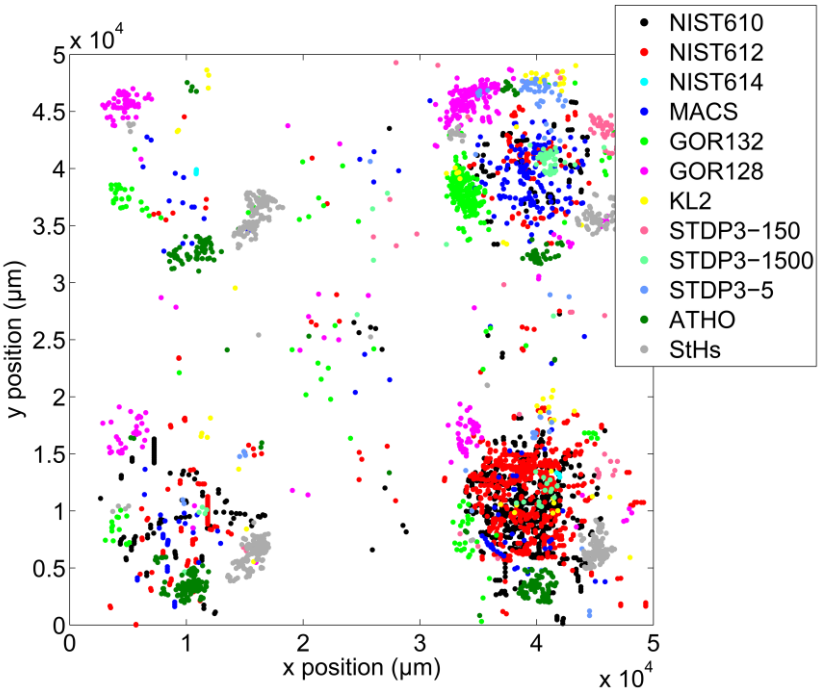

1024

1025 **Figure 9.** The location within the ablation cell of all the standard analyses presented here. These are
1026 biased towards the right-hand side of the LA cell as the slide sample holder only allows standards to
1027 be placed on this side.

1028

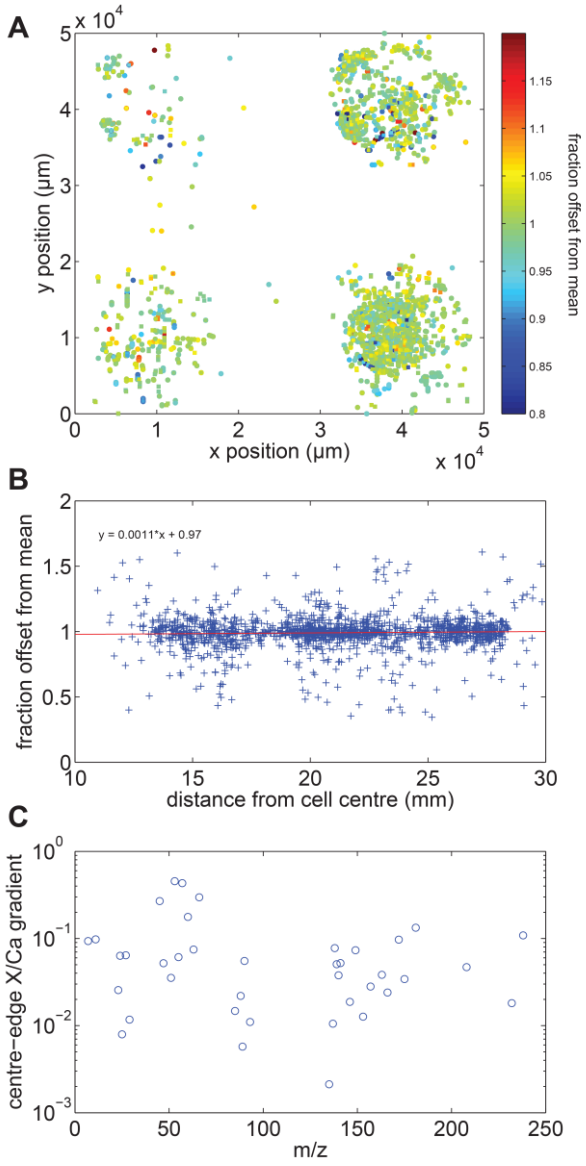

Figure 10. Examples of long-term ablation cell heterogeneity. All data are shown, normalised to the mean measured value for each standard in order to remove the accuracy offset associated with reported value error or analytical conditions. (A) Mg/Ca offsets as a function of analysis position, shown as a function of colour. Circles indicate spot analyses whilst squares show the start location of tracks. (B) U/Ca offset shown as a function of distance from the cell centre. (C) Centre-edge gradients for all m/z with >1000 total analyses, derived as for U/Ca in panel B. The gradient is shown in %/mm, i.e. accuracy shift with distance.

	NIST610 standardised			NIST612 standardised		
	n	S/T	H_2/N_2	n	S/T	H_2/N_2
NIST610				898	0.39	0.20
NIST612	846	0.40	0.23			
NIST614	22	0.00	0.00	25	0.12	0.00
MACS-3	150	0.17	0.04	260	0.36	0.04
GOR132-G	275	0.61	0.08	346	0.62	0.07
GOR128-G	270	0.59	0.06	418	0.69	0.05
KL2-G	76	0.22	0.03	89	0.20	0.03
ATHO-G	16	0.81	0.00	365	0.98	0.00
StHs	13	0.75	0.00	532	0.99	0.00
STDP3-150	35	0.00	0.00	68	0.00	0.00
STDP3-1500	39	0.05	0.00	70	0.03	0.00
STDP3-5	39	0.05	0.00	75	0.03	0.00

Table 1. The number of analyses of each standard treated as an unknown, using both NIST610 and NIST612 as a primary standard. Analysis type spot/track (S/T) ratios show that almost all STDP3-x analyses were tracks, whereas most ATHO-G and StHS analyses were spots. The additional diatomic gas ratios do not necessarily reflect usage on our system because data from this mass flow controller is sometimes missing from the Geostar log files.

spots		accuracy																				precision																	
		m/z																				m/z																	
spot size	standard	7	11	23	24	25	27	55	57	66	85	88	89	138	139	140	146	208	232	238		7	11	23	24	25	27	55	57	66	85	88	89	138	139	140	146	208	232	238
74-96	NIST610	1.028	1.055	1.032	1.241	1.318	1.016	1.104	-	1.021	-	1.002	0.973	1.008	-	-	1.002	-	-	0.999		0.008	0.024	0.010	0.023	0.016	0.011	0.052	-	0.023	-	0.009	0.015	0.011	-	-	0.013	-	-	0.018
	MACS-3	-	-	-	-	-	-	-	-	-	-	-	-	-	-	-	-	-	-	-		-	-	-	-	-	-	-	-	-	-	-	-	-	-	-	-	-	-
	GOR132-G	-	-	-	1.113	1.211	-	1.083	-	-	-	0.931	0.957	1.055	-	0.762	0.753	-	-	0.821		-	-	-	0.089	0.161	-	0.050	-	-	-	0.018	0.018	0.044	-	0.073	0.061	-	-	0.078
	GOR128-G	-	-	-	-	-	-	-	-	-	-	-	-	-	-	-	-	-	-	-		-	-	-	-	-	-	-	-	-	-	-	-	-	-	-	-	-	-
44-57	NIST610	0.986	0.957	0.989	1.167	1.209	0.987	1.006	0.412	0.988	0.976	0.983	0.976	0.979	0.982	0.982	0.992	0.977	0.971	0.982		0.014	0.046	0.010	0.024	0.024	0.009	0.017	0.094	0.028	0.020	0.012	0.016	0.013	0.012	0.015	0.015	0.018	0.014	0.019
	MACS-3	-	-	-	-	1.078	0.949	0.943	0.356	-	-	0.930	0.873	0.965	0.939	0.918	0.906	1.014	-	0.812		-	-	-	-	0.048	0.062	0.030	0.144	-	-	0.049	0.032	0.048	0.029	0.028	0.034	0.041	-	0.102
	GOR132-G	1.172	1.091	1.070	1.086	1.131	1.031	1.022	0.350	0.947	-	0.975	0.966	1.059	-	1.009	0.870	1.030	-	0.767		0.034	0.041	0.036	0.027	0.032	0.013	0.028	0.113	0.033	-	0.015	0.025	0.052	-	0.056	0.080	0.029	-	0.120
	GOR128-G	1.104	0.993	1.089	1.095	1.141	1.031	1.039	0.365	1.047	-	0.998	0.969	0.936	-	0.860	0.851	-	-	0.420		0.026	0.036	0.035	0.027	0.026	0.013	0.030	0.118	0.037	-	0.015	0.021	0.041	-	0.064	0.059	-	-	0.381
20-25	GOR128-G	-	-	-	-	-	-	-	0.338	-	0.928	1.002	0.987	0.939	0.822	0.864	0.811	0.818	-	0.295		-	-	-	-	-	-	-	0.111	-	0.287	0.026	0.028	0.093	0.222	0.106	0.162	0.252	2.301	1.504
tracks																																							
74-96	NIST610	-	-	-	-	1.175	0.980	1.007	0.393	-	0.983	0.987	0.985	0.990	0.991	0.992	-	0.987	0.989	0.986		-	-	-	-	0.030	0.009	0.020	0.071	-	0.019	0.010	0.021	0.018	0.016	0.019	-	0.029	0.021	0.035
	MACS-3	-	-	-	-	1.088	0.935	0.998	-	-	-	0.943	-	0.982	-	0.942	-	1.142	-	0.762		-	-	-	-	0.129	0.162	0.062	-	-	-	0.057	-	0.091	-	0.093	-	0.144	-	0.329
44-57	NIST610	0.995	0.854	0.989	1.145	1.187	0.986	1.013	0.411	0.872	0.983	0.995	0.990	0.989	0.992	0.999	0.986	0.982	1.016	1.000		0.019	0.098	0.008	0.046	0.021	0.011	0.014	0.106	0.117	0.016	0.016	0.017	0.019	0.013	0.020	0.017	0.025	0.037	0.021
	MACS-3	1.043	-	-	0.963	1.013	1.026	0.952	-	1.017	-	0.912	0.909	0.932	0.974	0.961	0.923	1.132	-	0.840		0.053	-	-	0.076	0.076	0.165	0.028	-	0.199	-	0.042	0.056	0.040	0.045	0.059	0.049	0.155	-	0.124
	GOR132-G	-	1.115	0.904	1.035	1.099	1.039	1.012	-	1.033	0.884	0.990	0.975	1.215	0.981	1.094	-	1.022	-	0.887		-	0.116	0.047	0.040	0.051	0.026	0.031	-	0.362	0.058	0.020	0.045	0.136	0.059	0.048	-	0.061	-	0.058
	GOR128-G	-	0.990	0.932	1.047	1.103	1.035	1.029	-	1.116	-	1.008	0.976	1.032	0.920	0.916	-	2.276	-	0.917		-	0.093	0.059	0.049	0.055	0.028	0.045	-	0.282	-	0.027	0.039	0.080	0.051	0.041	-	1.396	-	0.226
	KL2-G	-	-	-	1.046	1.032	1.024	1.018	-	0.897	0.862	0.989	0.911	0.949	0.961	0.975	-	1.147	-	0.934		-	-	-	0.022	0.107	0.013	0.015	-	0.095	0.029	0.015	0.025	0.012	0.015	0.024	-	0.221	-	0.055
	STDP3-150	0.942	-	-	-	1.066	1.011	-	-	-	0.899	1.037	1.051	0.963	-	0.982	0.833	0.916	-	0.988		0.036	-	-	-	0.022	0.014	-	-	-	0.039	0.010	0.022	0.017	-	0.014	0.068	0.041	-	0.027
	STDP3-1500	-	-	-	-	1.013	0.975	-	-	-	-	0.971	1.003	0.950	-	0.915	0.958	0.873	-	0.963		-	-	-	-	0.041	0.014	-	-	-	-	0.021	0.023	0.024	-	0.022	0.056	0.035	-	0.025
	STDP3-5	1.054	-	-	-	-	-	-	-	-	0.950	1.025	0.999	1.041	-	0.982	-	1.051	-	1.068		0.033	-	-	-	-	-	-	-	-	0.028	0.022	0.021	0.030	-	0.028	-	0.042	-	0.036
20-25	NIST610	0.980	0.933	-	1.131	1.178	0.987	1.001	-	0.876		0.983	0.989	0.980	0.987	0.982	-	-	-	0.982		0.016	0.046	-	0.025	0.021	0.018	0.012	-	0.128	-	0.011	0.019	0.013	0.012	0.011	-	-	-	0.026
	MACS-3	1.101	-	-	1.120	1.155	0.760	0.982	-	1.130	-	1.021	0.866	0.962	0.950	0.892	-	-	-	0.610		0.052	-	-	0.079	0.077	0.194	0.040	-	0.076	-	0.064	0.075	0.051	0.059	0.062	-	-	-	0.129
	GOR132-G	-	1.120	-	1.050	1.106	1.042	1.059	-	1.177	-	0.983	0.945	1.218	-	1.072	-	-	-	-		-	0.064	-	0.038	0.030	0.016	0.112	-	0.307	-	0.024	0.040	0.108	-	0.051	-	-	-	-
	GOR128-G	1.081	-	-	1.083	1.133	1.056	1.038	-	1.057	-	1.003	0.939	0.996	0.864	0.901	-	-	-	-		0.041	-	-	0.044	0.031	0.022	0.019	-	0.132	-	0.011	0.024	0.125	0.094	0.030	-	-	-	-

Table 2. Ablation parameter and standard-specific accuracy and precision, based on primary standardisation to NIST612. ^{43}Ca was used as an internal standard in all cases. Data are only shown where more than 20 analyses were available for a given standard and specific set of analytical conditions.

spots		accuracy																					precision																				
		m/z																					m/z																				
spot size	standard	7	11	23	24	25	27	55	57	66	85	88	89	138	139	140	146	208	232	238	7	11	23	24	25	27	55	57	66	85	88	89	138	139	140	146	208	232	238
74-96	NIST612	-	-	1.004	-	0.828	1.012	-	-	1.013	-	1.021	1.026	1.028	-	-	1.023	-	-	1.019	-	-	0.010	-	0.012	0.012	-	-	0.026	-	0.010	0.016	0.010	-	-	0.014	-	-	0.018
	GOR128	-	-	-	-	0.946	1.070	1.022	-	-	-	-	-	-	-	-	-	-	-	-	-	-	-	-	0.017	0.022	0.018	-	-	-	-	-	-	-	-	-	-	-	-	-
44-57	NIST612	1.015	1.050	1.012	0.859	0.830	1.015	0.996	-	1.016	1.032	1.019	1.027	1.023	1.019	1.021	1.010	1.026	1.031	1.020	0.015	0.054	0.010	0.018	0.018	0.009	0.011	-	0.028	0.016	0.013	0.017	0.012	0.014	0.014	0.016	0.019	0.013	0.021
	GOR132	1.189	1.137	1.081	0.931	0.936	1.045	1.019	0.866	0.956	-	0.991	0.985	1.081	-	1.018	0.879	1.049	-	0.781	0.033	0.066	0.036	0.018	0.022	0.013	0.019	0.074	0.027	-	0.017	0.029	0.055	-	0.054	0.077	0.022	-	0.121
	GOR128	1.122	1.037	1.100	0.937	0.945	1.046	1.034	0.876	1.061	-	1.016	0.991	0.955	-	0.872	0.860	-	-	0.429	0.024	0.053	0.039	0.019	0.018	0.012	0.020	0.082	0.030	-	0.016	0.024	0.043	-	0.070	0.062	-	-	0.391
tracks																																									
74-96	NIST612	-	-	-	-	0.854	1.020	0.994	2.652	-	1.017	1.014	1.016	1.011	1.010	1.009	-	1.016	1.011	1.016	-	-	-	-	0.023	0.009	0.020	0.375	-	0.020	0.011	0.020	0.018	0.015	0.019	-	0.028	0.024	0.039
44-57	NIST612	1.005	1.187	1.010	0.876	0.844	1.015	0.987	2.524	1.175	1.018	1.006	1.010	1.013	1.008	1.003	1.016	1.020	0.987	1.002	0.018	0.156	0.007	0.037	0.015	0.011	0.012	0.677	0.188	0.015	0.015	0.016	0.015	0.012	0.017	0.015	0.025	0.038	0.022
	MACS-3	1.045	-	-	0.842	0.854	1.037	0.944	-	1.184	-	0.919	0.925	0.943	-	0.963	-	1.165	-	0.832	0.043	-	-	0.051	0.056	0.132	0.022	-	0.110	-	0.037	0.045	0.032	-	0.048	-	0.131	-	0.106
	GOR132-G	-	1.232	0.928	0.910	0.935	1.062	1.005	-	1.263	0.903	1.002	0.983	1.252	0.994	1.099	-	1.048	-	0.891	-	0.172	0.050	0.029	0.039	0.032	0.038	-	0.432	0.054	0.027	0.049	0.163	0.070	0.050	-	0.084	-	0.059
	GOR128-G	-	1.107	-	0.916	0.940	1.060	1.016	-	1.350	-	1.018	0.983	1.054	0.930	0.919	-	1.987	-	0.920	-	0.133	-	0.028	0.035	0.034	0.036	-	0.323	-	0.024	0.044	0.095	0.058	0.033	-	0.964	-	0.264
	KL2-G	-	-	-	0.886	0.887	1.035	1.008	-	1.052	0.876	0.991	0.914	0.958	0.968	0.981	-	1.157	-	0.942	-	-	-	0.021	0.069	0.011	0.016	-	0.053	0.031	0.011	0.035	0.015	0.020	0.026	-	0.234	-	0.058
	STDP3-150	-	-	-	-	0.891	1.024	-	-	-	0.928	1.048	1.072	0.977	-	0.987	0.855	0.951	-	0.995	-	-	-	-	0.012	0.015	-	-	-	0.040	0.016	0.017	0.023	-	0.020	0.068	0.049	-	0.038
	STDP3-1500	-	-	-	-	0.856	0.991	-	-	-	-	0.984	1.026	0.970	-	0.927	0.956	0.903	-	0.971	-	-	-	-	0.006	0.009	-	-	-	-	0.011	0.017	0.015	-	0.012	0.047	0.028	-	0.024
	STDP3-5	-	-	-	-	-	-	-	-	-	0.975	1.041	1.022	1.062	-	0.996	-	1.093	-	1.086	-	-	-	-	-	-	-	-	-	0.022	0.011	0.010	0.013	-	0.012	-	0.027	-	0.026
20-25	NIST612	1.022	1.080	-	0.887	0.848	1.013	0.999	-	1.192	-	1.017	1.012	1.021	1.013	1.018	-	-	-	1.017	0.019	0.054	-	0.019	0.018	0.019	0.014	-	0.341	-	0.011	0.020	0.013	0.012	0.011	-	-	-	0.026
	MACS-3	1.116	-	-	0.972	0.975	0.739	0.975	-	1.190	-	1.041	0.861	0.974	0.961	0.895	-	-	-	0.606	0.047	-	-	0.067	0.066	0.191	0.032	-	0.066	-	0.066	0.079	0.026	0.061	0.056	-	-	-	0.120
	GOR132-G	-	-	-	0.931	0.944	1.058	1.020	-	1.430	-	1.009	0.948	1.258	-	-	-	-	-	-	-	-	-	0.020	0.022	0.012	0.023	-	0.277	-	0.016	0.047	0.116	-	-	-	-	-	-
	GOR128-G	1.116	-	-	0.957	0.970	1.062	1.047	-	1.227	-	1.023	0.943	1.022	0.876	0.921	-	-	-	-	0.030	-	-	0.025	0.021	0.015	0.018	-	0.165	-	0.013	0.033	0.132	0.099	0.032	-	-	-	-

Table 3. Ablation parameter and standard-specific accuracy and precision, based on primary standardisation to NIST610. See table 2 caption.

Chapter 3

Citation: Evans, D. & Müller, W. [2013]. LA-ICPMS elemental imaging of complex discontinuous carbonates: An example using large benthic foraminifera. *Journal of Analytical Atomic Spectroscopy* **28**:1039. doi: 10.1039/c3ja50053e.

Includes 5-page electronic supplementary information.

Author contributions: DE designed the research in discussion with WM, performed the analyses, wrote the Matlab data reduction software, interpreted the data and wrote the manuscript. WM designed the analytical procedure with DE and edited the manuscript.

Corrigendum: The second-to-last line of the first paragraph of section 2 (page 1040) incorrectly uses 'ultrasonicated' as a verb. This should read: Samples were cleaned in methanol and deionised H_2O with ultrasonic agitation.

JAAS

Journal of Analytical Atomic Spectrometry

www.rsc.org/jaas

Volume 28 | Number 7 | July 2013 | Pages 961–1132

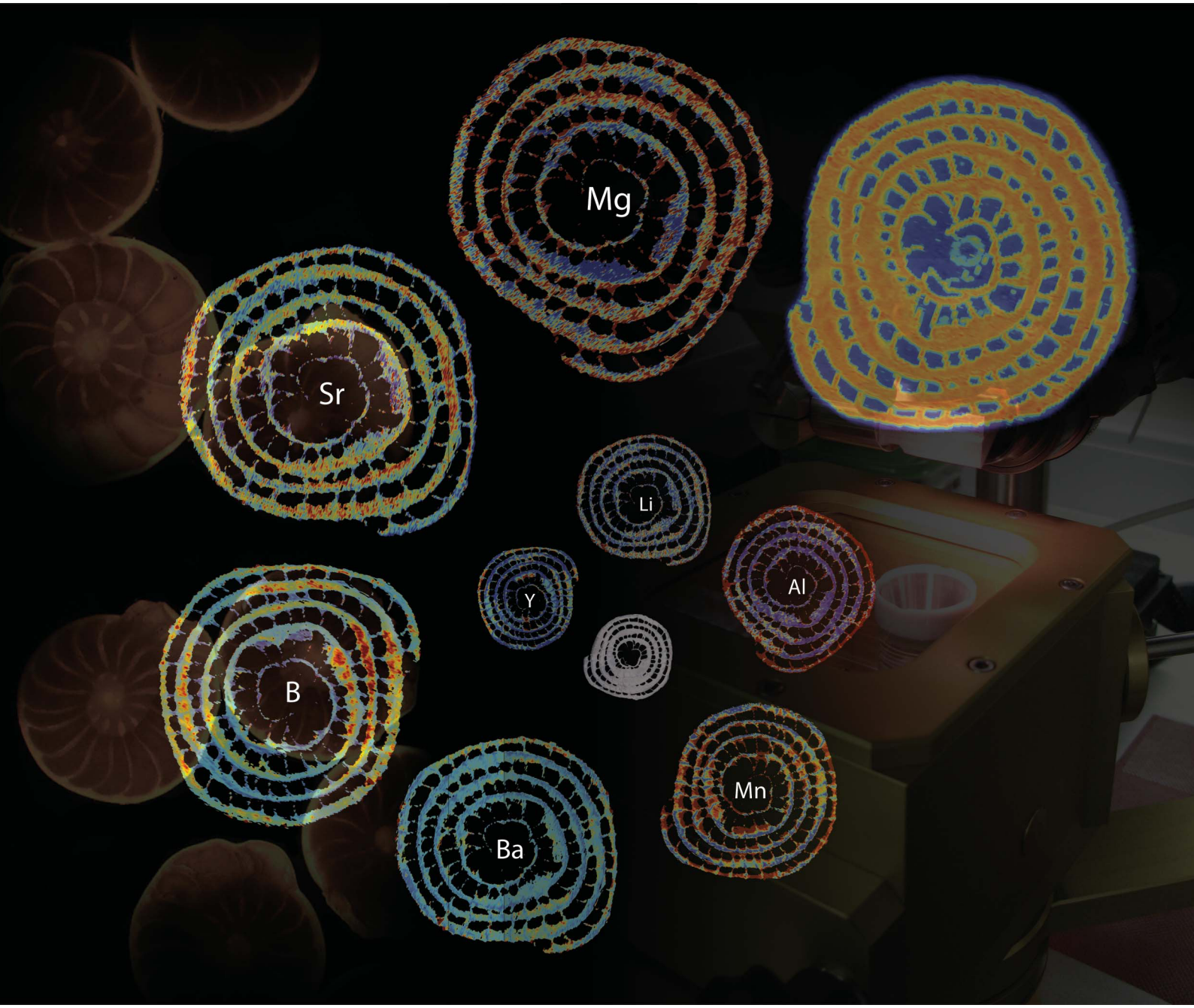

ISSN 0267-9477

RSC Publishing

TECHNICAL NOTE

David Evans and Wolfgang Müller

LA-ICPMS elemental imaging of complex discontinuous carbonates: An example using large benthic foraminifera

JAAS

RSC Publishing

TECHNICAL NOTE

LA-ICPMS elemental imaging of complex discontinuous carbonates: An example using large benthic foraminifera†

Cite this: *J. Anal. At. Spectrom.*, 2013, **28**, 1039

David Evans* and Wolfgang Müller

Trace element concentrations in biogenic and inorganic carbonates are a valuable source of palaeoenvironmental information. Because laser-ablation spot or 1D track analyses do not fully capture the complex (bio)mineralisation processes, 2D maps are required to arrive at a better understanding of the controls on minor/trace element incorporation. Foraminifera (marine protists) have a complex internal geometry and yield discontinuous sections characterised by calcite–resin–calcite transitions over distances as small as 10 μm. Order of magnitude differences in the total ion beam intensity over such transitions enables effective data exclusion. Inline signal smoothing devices, despite slightly increasing washout time and thus reducing spatial resolution, prevent excessive artificial noise in analyses, of particular concern when utilising small laser spot sizes (<30 μm) in order to maximise spatial resolution. We find surface Al/Ca and Zn/Ca ratios elevated by two and 5–10 times respectively, highlighting the need for pre-acquisition ablation cleaning. Through these analytical considerations we show how the quality of images acquired from discontinuous samples can be maximised, enabling – in this case – seasonality reconstruction in the fossil record from large benthic foraminifera.

Received 15th February 2013
Accepted 18th April 2013

DOI: 10.1039/c3ja50053e

www.rsc.org/jaas

1 Introduction

Laser-ablation imaging is a key tool for high-resolution *in situ* elemental and isotopic analysis of materials which exhibit at least two-dimensional heterogeneity. LA-derived 2D elemental images are frequently used within the biological sciences, to identify spatial uptake of trace metals to tissues (*e.g.* Becker *et al.*[1]), but are only relatively recently gaining popularity in the earth sciences[2] despite the abundance of potential applications.[3–6] Some attention has been focused on imaging biologically and inorganically precipitated carbonates,[2,7–10] predominantly because certain trace element and isotopic systems within these materials are valuable palaeoclimatic and palaeoenvironmental proxies.[11] However, much of this work is based on electron microprobe mapping, which – whilst potentially offering higher spatial resolution – is slower, has far higher limits of detection and may suffer from data quantification difficulties.[7,12]

Foraminifera are unicellular marine protists which biologically precipitate a calcite test. These organisms are widely utilised as a source of palaeoenvironmental proxy information because the incorporation of many trace elements (as well as trace and major element isotopic systems) has been demonstrated to relate to environmental parameters in a systematic manner (*e.g.* Nürnberg *et al.*[13]). These include, but are not limited to,[11] Mg and $\delta^{18}O$ (temperature), B and U (CO_3^{2-}) as well as a number of non-conservative/productivity-limiting trace elements which correlate with regional seawater concentrations and therefore enable environmental reconstruction of the sample site. Planktic foraminifera generally live for days or weeks and grow up to a few hundred μm in diameter, therefore individually providing a snapshot of conditions during the lifetime of that organism. However, given the critical role of seasonality in the climate system,[14] it is clearly a priority to find palaeoenvironmental archives that enable seasonal changes in important climate parameters to be reconstructed.

In order to provide a new method of seasonality reconstruction, we have produced trace element maps of large benthic foraminifera (LBF). LBF are an informal group that are shallow-dwelling and symbiont-bearing, which mineralise over a period of months or years, growing up to several cm in diameter.[15] They are abundant in geological epochs which are important in further constraining the extent to which atmospheric CO_2 controls global temperature (such as the Eocene; 56–34 million years ago). We compare fossil and recent samples from the family Nummulitidae in order to assess the potential of these organisms for the reconstruction of seasonal variations in trace element incorporation in the fossil record. These foraminifera add chambers sequentially and therefore provide a

Department of Earth Sciences, Royal Holloway University of London, Egham, TW20 0EX, UK. E-mail: david.evans.2007@rhul.ac.uk

† Electronic supplementary information (ESI) available: Details of the Matlab data reduction program, data exclusion rationale and comparative maps of the MACS-3 carbonate standard. See DOI: 10.1039/c3ja50053e

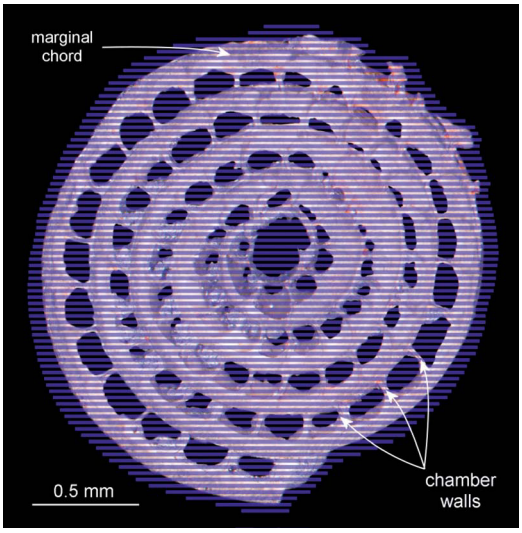

Fig. 1 An Eocene large benthic foraminifera (*N. djokdjokartae*) sectioned for analysis. Elemental images were created by analysing a series of paths spaced at 1.6 × track width (overlain in blue). Features referred to in the text are labelled. Spaces between the chamber walls and marginal chord are filled with resin as a consequence of the sample preparation procedure.

method of temporal proxy reconstruction throughout the mineralisation period.[16] Unlike carbonates previously mapped using LA-ICPMS,[2,10,17] these samples have a complex internal geometry after the necessary embedding and sectioning for analysis (Fig. 1), characterised by relatively thin calcite chamber walls of irregular shape surrounded by epoxy or Crystalbond resin. Because there is great potential for similarly complex sample geometries within many areas of the earth, physical and archaeological sciences, we show how ablation conditions and data reduction procedures can be optimised for resin–sample mixes and highlight considerations that are applicable to any sample or imaged area which has a substantially variable matrix.

2 Materials and methods

Fossil *Nummulites djokdjokartae* and live *Operculina ammonoides* (the nearest living relative of Eocene Nummulites) were collected from the Djokdjokartae Beds of Central Java and the northernmost Gulf of Eilat (Red Sea) respectively. Foraminifera were embedded in resin (smaller recent samples in Epofix (Struers) epoxy resin; fossil samples in Crystalbond (Agar Scientific), a thermo-softening, acetone–soluble resin) and then ground down to expose the marginal chord, the thickened margin of the shell. Samples were polished using 3 μm diamond suspension and ultrasonicated in methanol and deionised H_2O.

All analyses were carried out using the LA-ICPMS set-up at Royal Holloway,[18] featuring the prototype RESOlution M-50 laser-ablation system connected to an Agilent 7500ce ICPMS. Analytical parameters are the same as those given previously[18] with the exception of the additional diatomic gas added downstream of the ablation cell, which was changed to 8.5 ml min^{-1} H_2 in order to reduce the background on $m/z = 55$. Monitored masses were ^{11}B, ^{24}Mg, ^{25}Mg, ^{27}Al, ^{43}Ca, ^{55}Mn, ^{66}Zn and ^{238}U. Spot size, laser repetition rate and scan speed were 20–25 μm, 10–15 Hz and 16.6–25 μm s^{-1} respectively. Acquisition time under these conditions is ~50 min mm^{-2}, excluding pre-ablation and standard analysis. In order to avoid analysing the minimal ablation blanket of the previous track (a low fluence of ~3 J cm^{-2} was used), spacing was set at ≥60% track width. Smaller samples were analysed twice in order to double *y*-axis spatial resolution (tracks were always horizontal), with the second set of tracks offset by half of the centre to centre track distance and subsequent combination of the datasets. As in all cases, the shifted tracks were pre-ablated to avoid analysing condensate from the previous set.† Comparative maps of the pressed-powder carbonate standard MACS-3† demonstrate that there are no resolvable artefacts associated with analysing either the slightly irregular sample surface or the minimal ablation blanket that result from overlap with the first pre-ablation and acquisition run respectively. In order to investigate the effect of signal smoothing, maps were created both with and without the 'squid' smoothing manifold,[18] which results in greater signal stability but doubles cell washout time (99% washout time is 1–2 s without the 'squid' tubing). The impact of pre-ablation cleaning was investigated by analysing part of one specimen both with and without a pre-data acquisition cleaning run.

Image pixel dimensions are defined by the centre-to-centre track spacing (*y*-axis) and scan speed multiplied by ICPMS sweep time plus spot size (*x*-axis). For small samples (<1 mm diameter) which were analysed twice with offset tracks as described above, $x \times y$ pixel dimensions were 27 × 22.5 μm. For larger samples, resolution was decreased to 35 × 40 μm in order to lower the total acquisition time, by using a faster scan speed and larger spot size. The *x*-axis spatial resolution is unavoidably lower than this because cell washout is not instantaneous. With the squid connected, order-of-magnitude washout time is ~1.5 s and therefore each pixel potentially represents material derived from 40 and 62.5 μm of carbonate for smaller and larger samples respectively.

Blank-corrected raw intensity ratios were converted to molar ratios by external standardisation to NIST612/610 and the MPI-DING komatiite glass GOR132.[19] Recently revised NIST concentration values were used.[20] The calibration standard for each m/z was chosen by comparing GOR132 and GOR128 accuracy derived from both NIST610 and NIST612; the NIST glass which gave the lowest accuracy was picked as this implies a more representative reported value for that NIST glass, where the difference between the NIST610 and NIST612 accuracy was consistent for both NIST61X-GOR128/132 combinations. Accuracy for all isotopes was better or equivalent using NIST612 with the exception of Mg/Ca which was calibrated to GOR132 because both NIST glasses are characterised by relatively large Mg heterogeneity (~7% *cf.* 0.9% (ref. 19 and 20)). Accuracy was better than 5% in all cases with the exception of Zn/Ca and U/Ca (15% and 22% respectively). Mg/Ca accuracy was 1% when comparing GOR132 to GOR128 and 7% when comparing GOR132 to NIST610, essentially identical to the quoted 1 SD

heterogeneities for these glasses. The pressed-powder carbonate standard MACS-3 was not used as a calibration standard because it is significantly more heterogeneous than standard glasses and only preliminary values are available. It has previously been shown that there are minimal matrix effects when standardising carbonates using glasses ablated with a 193 nm laser,[21] with the exception of Li and Mg. Unpublished data from the system described here show that MACS-3 accuracy standardised to GOR132 is ~10%, with a precision of 13%. It is not possible to assess whether this relatively worse accuracy is the result of matrix effects or an inaccurate MACS-3 Mg information value. Therefore, whilst it is possible that Mg/Ca accuracy in carbonates when sampled by laser ablation is greater than generally reported, it is unlikely that any potential error is larger than ~10%.

Data-reduction followed standard procedures[22] and was performed using an in-house Matlab program which automatically selects standard, sample and background intervals from the Agilent csv data file using the laser log file produced by Geostar, the Resonetics laser-control software.† Outliers are defined as being values >3 and >2 SD from the mean for background and analyses respectively. We use this program over those previously available (*e.g.* Paul *et al.*[23]) because it (1) allows different elements to be standardised using different glasses without the need to rerun the program and (2) crucially, it enables the easy exclusion of data based on the total ion beam intensity (see below). The images shown here were created by distributing X/Ca ratios into a 2D matrix, re-sampled to 8 times the original x and y dimensions with linear interpolation in order to avoid pixelation.

Ablation paths across small-scale calcite–resin transitions produce complex signals requiring data exclusion (resin areas are not of analytical interest). This was performed on the basis of the total ion beam intensity which is several orders of magnitude smaller when ablating resin compared to calcite.† The cut-off point was optimised for each individual sample. This is an effective technique for samples mounted in Crystalbond which has a low viscosity when heated, but results in errors for samples mounted in epoxy which did not always fill every chamber. In the latter case, further exclusion was performed by matching the LA-derived image to that produced using a binocular microscope, which is especially important for the centre of the foraminifera.

3 Results and discussion

Comparative X/Ca images of both recent and Eocene large benthic foraminifera are shown in Fig. 2. The recent *O. ammonoides* specimen demonstrates the potential for these organisms, coupled with laser-ablation imaging, as archives of seasonal trace element incorporation. Given an average growth rate of 2–3 chambers per week, this specimen mineralised from late summer to spring (sampled in May), consistent with the Mg/Ca profile which shows a clear decrease from high values in the centre (the earliest formed chambers) towards the outside of the test (Mg/Ca increases with temperature in all foraminifera species studied[11]). This decrease is broadly anti-correlated with B/Ca which is likely to be the combined result of seasonal changes in CO_3^{2-} and temperature, which exerts a secondary control on B/Ca in planktic foraminifera.[24] Al/Ca and Mn/Ca (commonly used to assess preservation of fossil samples) are shown to demonstrate typical values in material that cannot be affected by post-burial diagenesis. The fossil *N. djokdjokartae* images (Fig. 2) demonstrate how these alteration indicators can be used to evaluate the reliability of trace elements which are interesting in terms of palaeonvironment reconstruction. Areas of very high B/Ca are broadly associated with higher Mn/Ca, implying that this may not be a primary signal. Mg/Ca does not show the same pattern and these data therefore appear more reliable; the relatively high Mg concentration of these foraminifera means that this ratio is more resilient to alternation from later (non-biogenic) secondary calcite mineralisation. Although the magnitude of long-period Mg/Ca variability is smaller in the fossil material there are subtle changes on the order of 5–10 mmol mol^{-1} which may be interpreted as seasonal palaeotemperature change.

This application demonstrates the benefit of images over spot analyses or track rastering. The fine scale distribution of some trace elements is clearly complex in biogenic carbonates; alternative analytical approaches could be easily biased by the precise positioning of tracks or spots. The use of clean resins enables analysis of parts of the foraminifera that are smaller than the laser spot size, provided analyte counts on the resin are indistinguishable from the gas blank and X/Ca ratios remain constant during washout. Elements present at very high concentrations in the sample may be measured in this way irrespective of the resin contribution as this becomes insignificant (*e.g.* ^{24}Mg counts are 500–1000 and 2000–5000 cps for blank and resin respectively, but typically greater than 10^6 cps in these foraminifera).

3.1 Signal smoothing

Uniformly fast cell washout is essential for highly spatially resolved analysis.[2,18] Although washout times are 2× longer with the signal smoothing device (referred to as the squid[18]), simple mass-balance calculations show that the error in the reconstructed X/Ca profile (*i.e.* the difference between the observed and actual sample variability along the track) is on the order of a few percent for concentration changes of up to 1% μm^{-1}, typical of proxy trace elements in foraminifera. Significant signal dampening would result from the twofold increase in washout time with the squid if the sample contained heterogeneity as great as concentration doubling per ICPMS sweep time, under these circumstances in-line signal smoothing devices should not be used. This is because with the squid connected the ICPMS sweep time is always shorter than the cell washout time, therefore significant sample heterogeneity on a scale smaller than a distance equal to the scan speed multiplied by the cell washout time is not accurately resolvable. Reducing the scan speed would alleviate this problem at the expense of minimising ablation track depth and acquisition time. There is no evidence for changes of this magnitude in these foraminifera, as far as is possible to tell given that each ICPMS sweep time

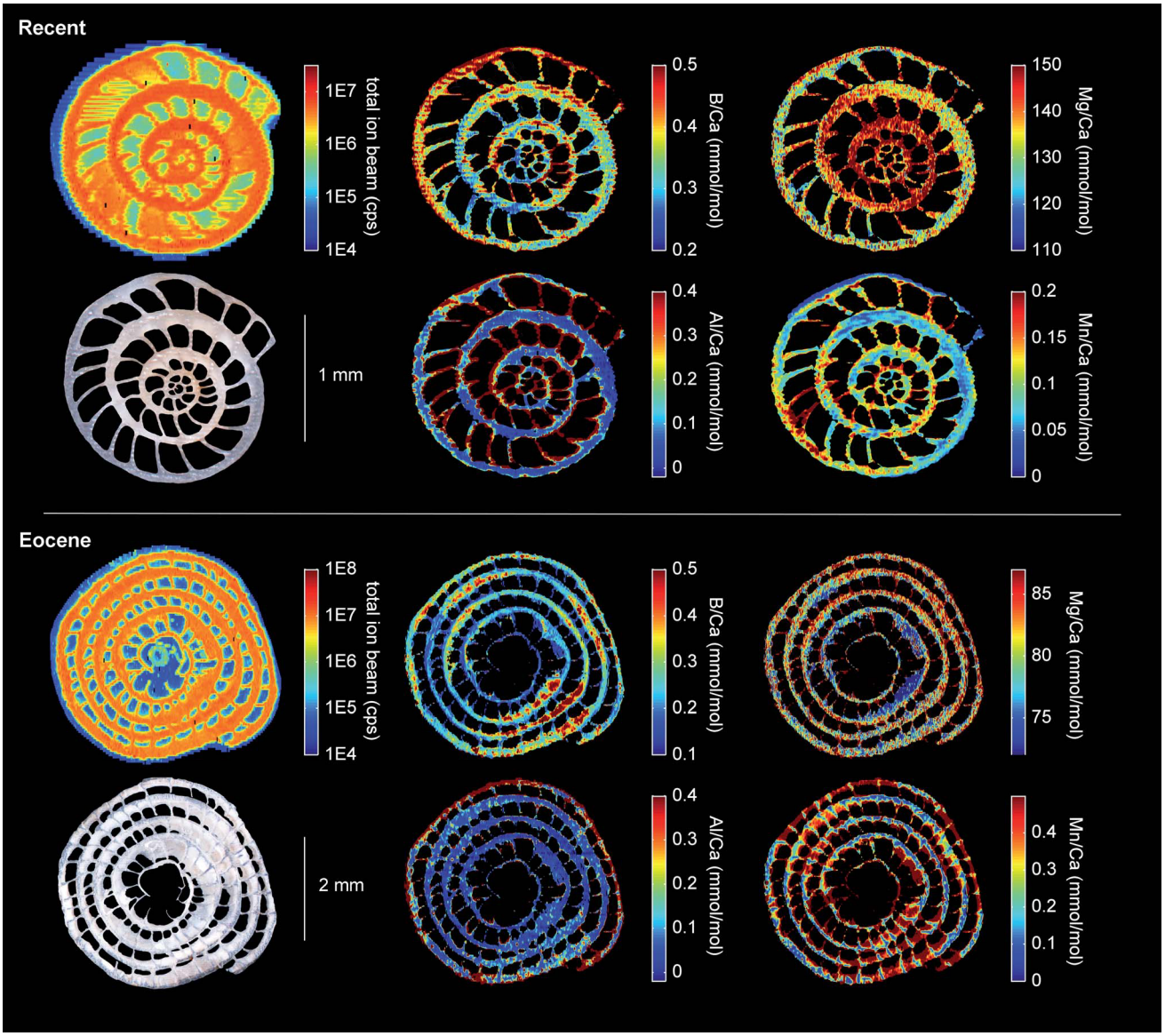

Fig. 2 Comparative trace element maps of a recent *O. ammonoides* (upper panel) and Eocene *N. djokdjokartae* (lower panel). Resin areas and those below the focal plane of the laser are primarily excluded from the final images using the total ion beam intensity. The *O. ammonoides* image demonstrates seasonal B/Ca and Mg/Ca incorporation (see text for details), whilst that of a fossil *N. djokdjokartae* highlights the necessity of diagenesis Al/Ca and Mn/Ca maps when interpreting proxy data – note the similarity between the spatial distribution of B/Ca and Mn/Ca.

represents an average of 27–35 μm of adjacent carbonate. Fig. 3 shows in detail the differences between a single track from the middle of an image acquired both with and without the squid. A running SD of the respective Mg/Ca data clearly shows substantially more variability when the squid is not used. A histogram of mean RSD for each individual analysis segment, defined as the calcite part of a resin–calcite–resin sequence (an individual path within the overall image acquisition contains several segments as the laser tracks across the various chamber walls of the foraminifera), shows this quantitatively (Fig. 3C). The mean and mode Mg/Ca RSD from the complete image sequence are 19 and 4% higher respectively when the squid is not used. This phenomena is not the result of potential fine-scale heterogeneity in the sample masked by the use of the squid, as standard glass RSDs are also typically ~20% higher without signal smoothing when using this spot size.

It has previously been noted[2] that achieving the fastest possible cell washout time is of great importance when producing elemental images; ablation cells with a complete washout time in the order of tens of seconds are clearly not suitable for producing good-quality elemental images. However, we demonstrate that the benefits offered by enhanced signal stability are worth the minor sacrifice in resolution provided (1) 99% washout time is no more than 2–3 s and (2) the sample to be mapped does not contain order of magnitude concentration changes over distances equivalent to the product of this washout time and the laser scan speed. A larger laser spot size would help in minimising this problem, although this is not

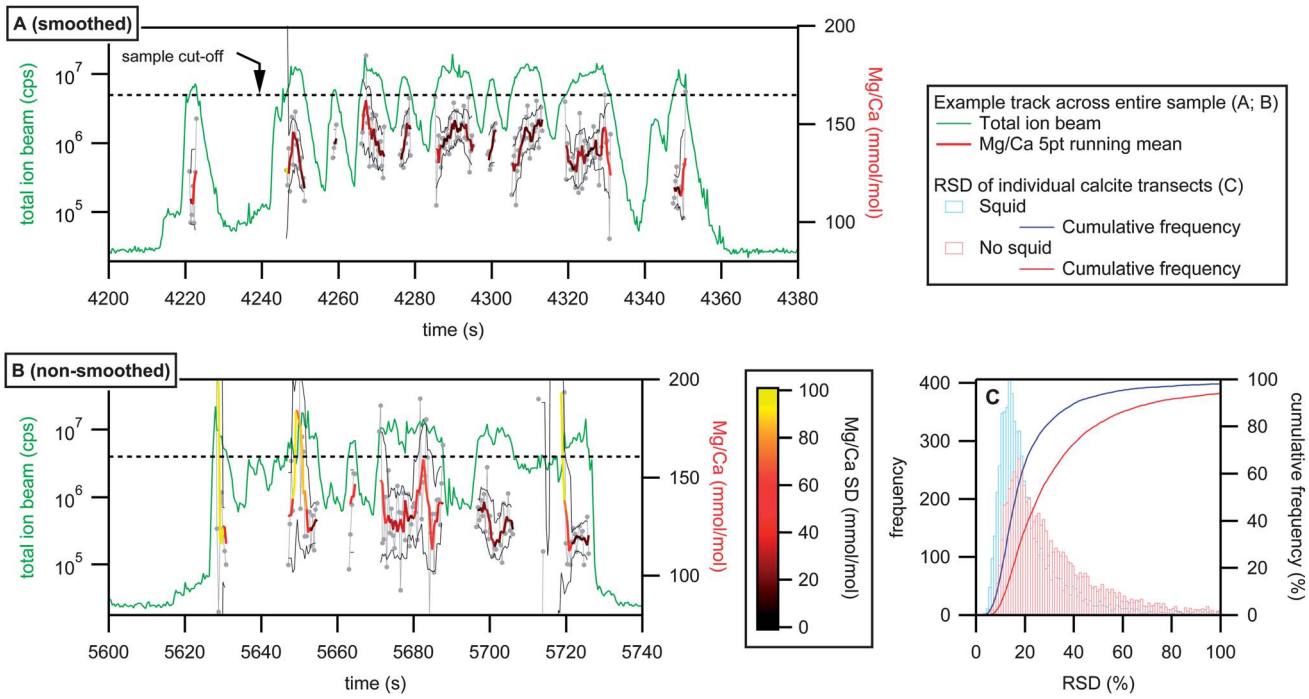

Fig. 3 A typical profile across the width of a sample (A) with and (B) without pre-analysis signal smoothing (Mg/Ca ratios shown as an example). Sample areas are distinguished from resin by a total ion beam cut-off point (dashed lines). Mg/Ca measurements (grey circles and line) and smoothed Mg/Ca profiles (thick coloured line) ±1 SD (thin black lines) are shown to highlight the much higher (artificial) variability without signal smoothing (B). Colour is shown as a function of a 5-point running Mg/Ca SD. (C) Smoothed and non-smoothed Mg/Ca RSD frequency distributions for all discrete calcite segments encountered whilst collecting data for the entire map (for example there are 10 individual segments in (A) and six in (B)). Smoothed analyses clearly result in substantially less noisy data.

suitable for discontinuous samples such as these where it is important to maximise resolution.

3.2 Pre-ablation cleaning

Part of an Eocene *N. djokdjokartae* specimen analysed before and after pre-ablation surface cleaning is shown in Fig. 4. Pre-ablation cleaning is important as a step to remove both potential surface contamination and the deposited aerosol from the previous ablation track. Here, we ensure that the parallel ablation tracks were sufficiently widely spaced (1.6 × track width) to avoid any deposition of condensate on subsequent tracks. Comparative images show that this surface removal results in significantly lower Zn/Ca and Al/Ca ratios (3–4 times and a factor of two lower respectively). Given the potential importance of Zn/Ca in foraminifera as a seawater [Zn] or CO_3^{2-} proxy[25] and the use of Al/Ca as a residual clay mineral indicator,[26] this extra surface cleaning step is an obvious requirement if these data are of importance. Both the mean and spatial relationships of all other ratios are virtually unaffected

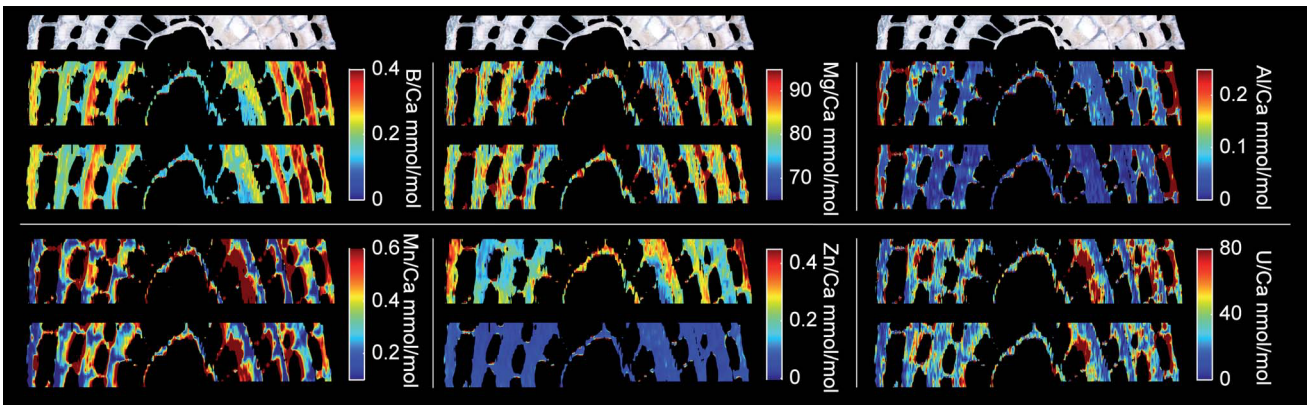

Fig. 4 The effect of pre-ablation cleaning on measured X/Ca ratios in a fossil large benthic foraminifera. For each displayed ratio the upper image was analysed with no pre-ablation whereas tracks in the lower image were pre-ablated. Most images are virtually identical, with the exception of Zn/Ca and Al/Ca which are markedly lower when pre-ablation is carried out. Note 1.9 × vertical exaggeration, image height is 0.5 mm.

by pre-ablation cleaning. Both Mn/Ca and U/Ca images have equivalent ranges and distributions despite being present at substantially lower levels than Al-Zn/Ca, suggesting a Zn-rich contaminant introduced after ultrasonication (potentially from latex gloves[27]). Because there is no detectable B, Mg and U contamination, these plots provide a repeatability test. Given the relatively high analysis RSD when using small spot sizes (Fig. 3) the similarity between these images is remarkable; the majority of the fine structure is identical, showcasing laser-ablation as a powerful tool capable of replicable images of complex geometries on a ~20 μm scale.

4 Conclusions

We show how analytical parameters can be optimised for the analysis of carbonates with complex internal geometries. Using the total ion beam intensity as a method of distinguishing sample from resin or areas that are not in the focal plane of the laser is an effective way of excluding data from discontinuous samples. The technical considerations highlighted here demonstrate that samples with complex and discontinuous geometries can be imaged, yielding good quality, repeatable data with *x* and *y*-axis image pixel dimensions of better than 30 and 25 μm respectively. Whilst a laser-ablation cell design with a uniformly fast washout time is a basic requirement in the production of high-resolution elemental images, the use of a gas signal-smoothing device results in considerably more stable signals and less artificial noise in the data; an increase in the 99% cell washout time of 1–2 s is an acceptable compromise. Pre-ablation is shown to be a necessity in the accurate analysis of certain trace elements, particularly Al and Zn which may be liable to contamination even after careful sample preparation and cleaning. We demonstrate this using both recent and fossil large benthic foraminifera, which show good potential as archives of seasonally varying ambient conditions.

Acknowledgements

DE acknowledges a NERC postgraduate studentship at RHUL. We are grateful to Willem Renema and Shai Oron for providing the Eocene and recent samples respectively. We thank L. Danyushevsky and two anonymous reviewers for constructive comments which improved this contribution.

References

1 J. Becker, M. Zoriy, C. Pickhardt, N. Palomero-Gallagher and K. Zilles, *Anal. Chem.*, 2005, **77**, 3208–3216.
2 J. Woodhead, J. Hellstrom, J. Hergt, A. Greig and R. Maas, *Geostand. Geoanal. Res.*, 2007, **31**, 331–343.
3 T. Ulrich, B. Kamber, P. Jugo and D. Tinkham, *Can. Mineral.*, 2009, **47**, 1001–1012.
4 P. Treble, J. Chappell and J. Shelley, *Geochim. Cosmochim. Acta*, 2005, **69**, 4855–4863.
5 A. E. Koenig, R. R. Rogers and C. N. Trueman, *Geology*, 2009, **37**, 511–514.
6 R. R. Large, L. Danyushevsky, C. Hollit, V. Maslennikov, S. Meffre, S. Gilbert, S. Bull, R. Scott, P. Emsbo, H. Thomas and J. Foster, *Econ. Geol.*, 2009, **104**, 635–668.
7 L. Pena, I. Cacho, E. Calvo, C. Pelejero, S. Eggins and A. Sadekov, *Geochem., Geophys., Geosyst.*, 2008, **9**, Q07012.
8 A. Sadekov, S. Eggins and P. De Deckker, *Geochem., Geophys., Geosyst.*, 2005, **6**, Q12P06.
9 J. Fehrenbacher and P. Martin, *IOP Conference Series: Earth and Environmental Science*, 2010, vol. 9, p. 012018.
10 R. Ortega, R. Maire, G. Devès and Y. Quinif, *Earth Planet. Sci. Lett.*, 2005, **237**, 911–923.
11 M. Katz, B. Cramer, A. Franzese, B. Hönisch, K. Miller, Y. Rosenthal and J. Wright, *J. Foraminiferal Res.*, 2010, **40**, 165–192.
12 S. Eggins, A. Sadekov and P. De Deckker, *Earth Planet. Sci. Lett.*, 2004, **225**, 411–419.
13 D. Nürnberg, J. Bijma and C. Hemleben, *Geochim. Cosmochim. Acta*, 1996, **60**, 803–814.
14 G. Denton, R. Alley, G. Comer and W. Broecker, *Quat. Sci. Rev.*, 2005, **24**, 1159–1182.
15 S. Beavington-Penney and A. Racey, *Earth-Sci. Rev.*, 2004, **67**, 219–265.
16 L. Purton and M. Brasier, *Geology*, 1999, **27**, 711–714.
17 M. Rittner and W. Müller, *Comput. Geosci.*, 2012, **42**, 152–161.
18 W. Müller, M. Shelley, P. Miller and S. Broude, *J. Anal. At. Spectrom.*, 2009, **24**, 209–214.
19 K. Jochum, B. Stoll, K. Herwig, M. Willbold, A. Hofmann, M. Amini, S. Aarburg, W. Abouchami, E. Hellebrand, B. Mocek, *et al.*, *Geochem., Geophys., Geosyst.*, 2006, **7**, Q02008.
20 K. Jochum, U. Weis, B. Stoll, D. Kuzmin, Q. Yang, I. Raczek, D. Jacob, A. Stracke, K. Birbaum, D. Frick, *et al.*, *Geostand. Geoanal. Res.*, 2011, **35**(4), 397–429.
21 E. Hathorne, R. James, P. Savage and O. Alard, *J. Anal. At. Spectrom.*, 2008, **23**, 240–243.
22 H. Longerich, S. Jackson and D. Günther, *J. Anal. At. Spectrom.*, 1996, **11**, 899–904.
23 B. Paul, C. Paton, A. Norris, J. Woodhead, J. Hellstrom, J. Hergt and A. Greig, *J. Anal. At. Spectrom.*, 2012, **27**, 700–706.
24 J. Yu, H. Elderfield and B. Hönisch, *Paleoceanography*, 2007, **22**, PA2202.
25 T. Marchitto, J. Lynch-Stieglitz and S. Hemming, *Earth Planet. Sci. Lett.*, 2005, **231**, 317–336.
26 S. Barker, M. Greaves and H. Elderfield, *Geochem., Geophys., Geosyst.*, 2003, **4**, 8407.
27 J. Friel, C. Mercer, W. Andrews, B. Simmons and S. Jackson, *Biol. Trace Elem. Res.*, 1996, **54**, 135–142.

1 Data reduction

A full description of the principles of the Matlab code used to produce the images is given below.

1. Read in all csv files
   (a) Read laser log files (which always contain the word *log* in the file name) in as text
   (b) Read Agilent data files (which never contain the word *log* in the file name) as matrices
   (c) Read the date and time from the first data line of the Agilent csv files
2. Find analyses using the laser-log files
   (a) Read the date and time from the first data line of the Geostar log file
   (b) Compare the start time of all csv files and match them into log file-data file pairs
3. Produce an analysis sequence
   (a) Identify standards based on analyses labelled in Geostar as containing all or part of their name (e.g. '610', 'NIST612' etc.)
   (b) Samples are identified using a sample identifier (requires user input)
4. Split data into standards, samples and background
   (a) Read stage coordinates from the Geostar log files
   (b) Find the start time of each path from the Geostar log files
   (c) Convert all dates to serial date number
   (d) Define the LA-ICPMS computer time difference
      i. The first analysis is defined as being the first point in the ICPMS data file which is greater than 1.5× the mean of the first background segment, provided this is also the case for the subsequent 20 data points (in order to avoid errors due to outliers)
      ii. The difference between the time stamp of this data point and the time given in the Geostar log defines the time offset between the two computers
      iii. Correct all data points for this offset
   (e) Each analysis track is separated into an individual matrix based on the start and end times of the Geostar log files
5. Data manipulation
   (a) Background segments are identified as being all lines of data more than 5 seconds away from analyses start and end points
   (b) Outliers are removed from each background segment (±3 SD from the mean)
   (c) Background intensities are subtracted from each analysis, based on the mean of the two adjacent background segments; in this way background drift is accounted for
   (d) Sample intensities are summed for each ICPMS sweep to calculate the total ion beam intensity
   (e) element/Ca ratios are calculated for all analyses

(f) Outliers are removed from the standards (±2 SD from the mean)

(g) Mean standard X/Ca ratios are calculated

(h) Every datapoint is assigned coordinates based on the Geostar log file

(i) Where images were collected twice to improve resolution, the datasets are combined

(j) Analysed isotopes are read from the header of the Agilent csv and molar ratios for each element are calculated for each standard used

(k) User input is required to define which available standard should be used to standardise each analysed isotope

(l) Raw sample element/Ca ratios are standardised using the relationship defined by *Longerich et al.* [1996]:

$$\frac{i^{STD}_{measured}}{c^{STD}_{reported}} = \frac{i^{SAMP}_{measured}}{c^{SAMP}_{actual}}$$

Where i denotes the background-corrected raw intensity ratio and c denotes the X/Ca molar ratio

(m) All sample data is output to an $m \times n$ matrix where m is the total number of data points and n is the number of isotopes analysed, plus the total ion beam and stage coordinates

(n) Standards not used for sample standardisation are treated as samples and output in the same way

6. Image production

(a) The length of the image in the x-axis direction is defined based on the maximum and minimum Geostar x-coordinates

(b) x-axis coordinates are replaced with integers in order to produce consistent values between rows

(c) The dataset is re-distributed into an $m \times n \times p$ matrix where m is the number of laser tracks, n is approximately equal to the number of data points in the longest track (analysis time/dwell time) and p is the number of isotopes analysed plus the total ion beam

(d) A user-defined cut-off point removes all data associated with a total ion beam intensity less than a specified value (e.g. 5×10^6 cps)

(e) The matrix is re-sampled to double the original dimensions; each new component is filled with the mean of all components with which it shares an edge or corner

(f) The above step is repeated three times in order to create an image eight times the raw pixel dimensions, large enough for pixels to be smaller than visible (typically around 16 megapixel)

2 Rationale for data exclusion

Although the resins used were clean (all analysed isotopes were below the limit of detection with the exception of ^{11}B, m/z=24 (^{24}Mg, ?$^{12}C_2$) and ^{66}Zn), chambers not filled with resin were analysable. Furthermore, subtracting the mean background intensity from all analyses inevitably leaves 50% of gas-blank data points and therefore ∼25% (0.5×0.5) of gas-blank data points may be given an X/Ca ratio (Figure 1a), assuming independence of X and Ca.

An image with no total ion beam data exclusion is shown in Figure 1b. Whilst the shape of the foraminifera is evident, it is confusing and contains much data which are of no interest.

Because it is not possible to standardise data from chambers that were not filled with resin (because the calcite in these locations is far below the focal point of the laser) and because data points that only relate to resin contain no useful information, we exclude these areas of the analysis using the total ion beam intensity.

3 Comparative standard maps

In order to demonstrate that (1) condensate from the previous ablation track (minimised by using a low fluence of $\sim$3 J cm^{-2}) does not affect data acquired from the adjacent track, and (2) that overlapping previous tracks (where samples were analysed twice to improve resolution) does not affect the data, the same techniques were applied to the pressed powder carbonate standard MACS-3 (figure 2).

The standard was analysed in the same way as a small foraminifera, i.e. the image was acquired twice with the second set of tracks offset by half the track spacing in order to double y-axis resolution. The evolution of the sample/standard surface topography is shown in the upper left corner of figure 2. Crater depth is not exaggerated and is based on the assumption that each laser pulse removes a $\sim$0.1 μm-thick layer of material from the surface. A third set of images (right side of figure 2) were produced by subtracting the first and second maps, shown as a percentage of the USGS information values for this standard. The fact that these images all average within 3% of 0 simultaneously demonstrates that (1) standardisation of carbonates using NIST and GOR glasses produces accurate data, (2) there is no significant offset as a result of the irregular sample surface following the acquisition of the first image (figure 2) and (3) the ablation blanket of the adjacent track does not contribute significantly to subsequent analyses. The random distribution of non-zero values in these images strongly implies that this noise is the result of heterogeneity in the standard, which has raw intensity RSDs $\sim$5% higher than NIST610 at an equivalent spot size, and the relatively small spot size itself (20 μm). Furthermore, note that these images are not repeat analyses of the same tracks. Although we subtract the two acquisitions in figure 2 (in order to demonstrate no significant offset from zero) they are derived from different (adjacent) material which is likely to explain much of the fine-scale difference.

4 References

Longerich, H., S. Jackson, and D. Günther (1996), Laser ablation inductively coupled plasma mass spectrometric transient signal data acquisition and analyte concentration calculation, *Journal of Analytical Atomic Spectrometry*, *11*(9), 899–904.

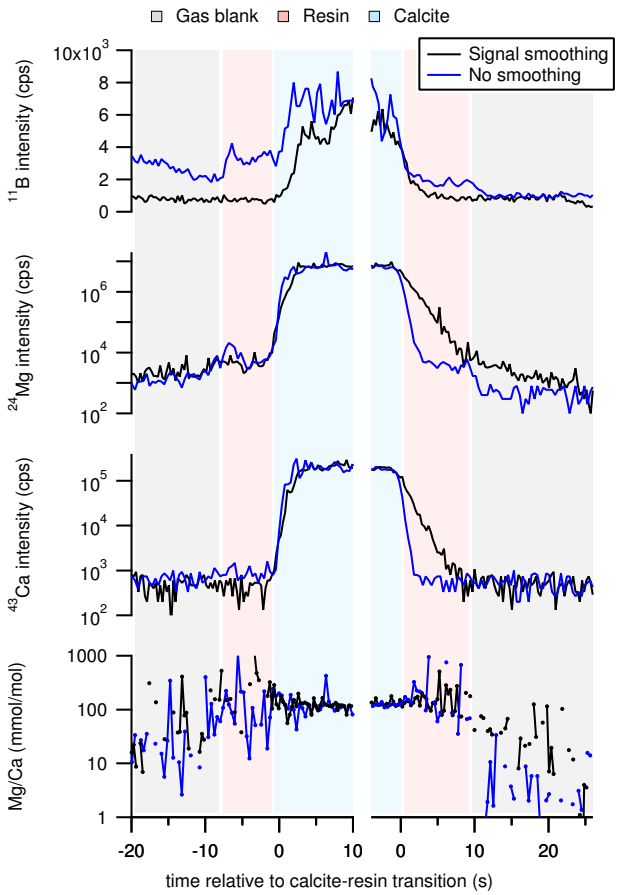

(a) Gas-blank, resin and sample analyses showing wash-in/out times for data collected with and without the squid signal smoothing device. Note that it is possible to produce Mg/Ca ratios for the gas-blank and resin, despite Mg and Ca intensity lower than the LOD, as a consequence of mean background subtraction removing only 50% of the gas-blank values.

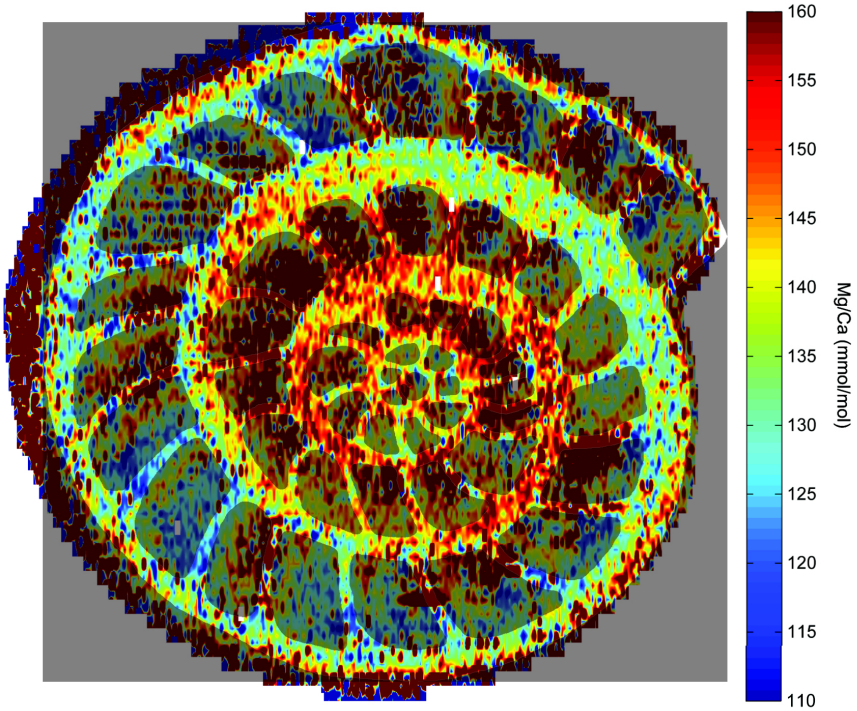

(b) An image with no data exclusion based on the total ion beam intensity, Mg/Ca shown as an example. The shaded area shows the approximate position of the excluded data.

Figure 1: Rationale for data-exclusion based on the total ion beam intensity. Element/Ca ratios exist for resin and gas blank producing distracting and meaningless data.

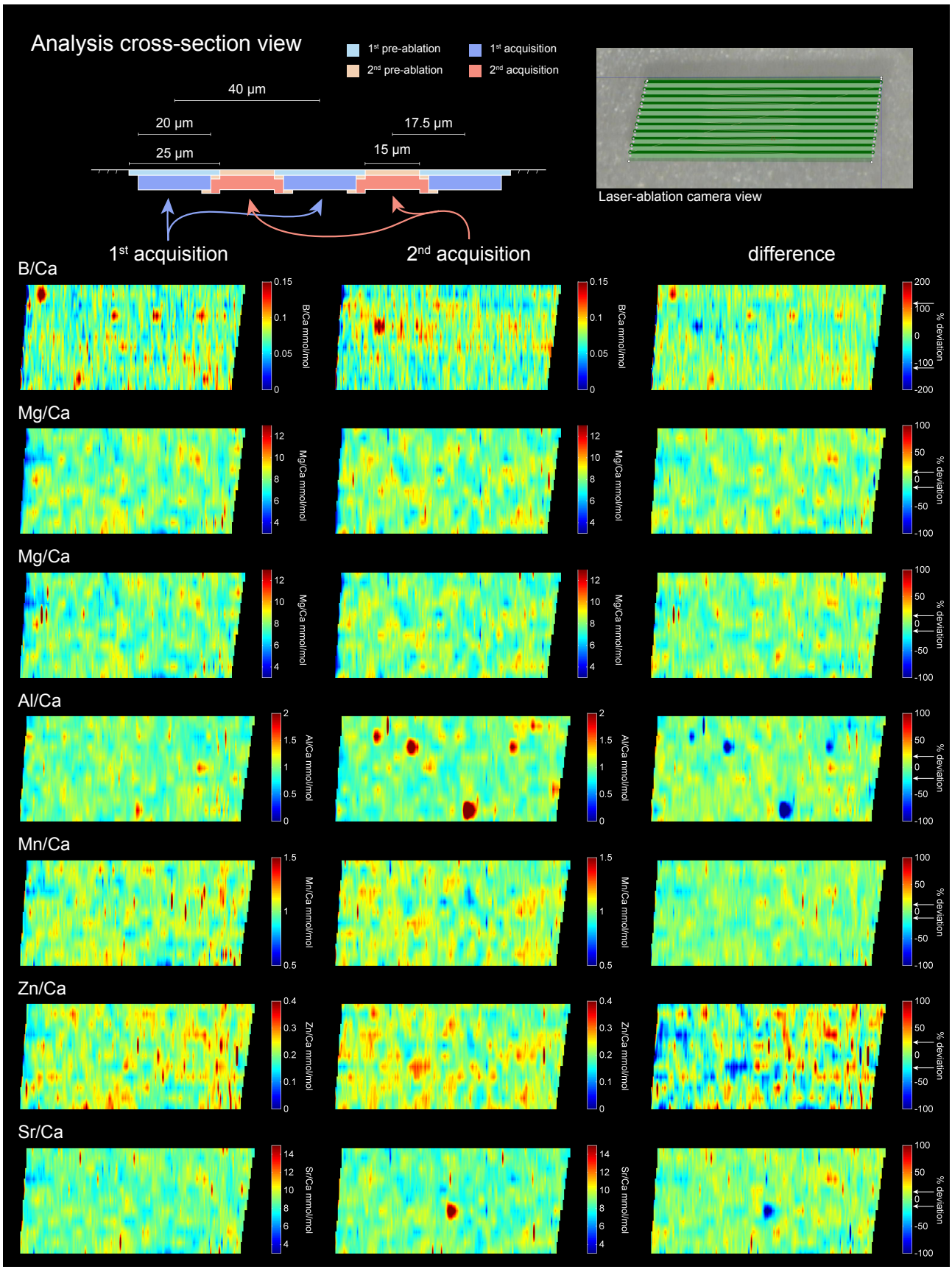

Figure 2: Trace element maps of the carbonate standard MACS-3. The maps were collected twice to mimick the analytical imaging procedure for small samples (left and center panels; see text). A cross-section view through five ablation tracks is shown to illustrate topographic changes during analysis. The set of images on the right shows the difference between these two acquisitions, expressed as a percentage of the MACS-3 information value. Arrows on these scale bars show the position of ±1SD. There is no discernable difference between the images related to the ablation procedure. Mg data derived from both ^{24}Mg (above) and ^{25}Mg (below) are shown.

Chapter 4

Citation: Evans, D. & Müller, W. [2012]. Deep time foraminifera Mg/Ca paleothermometry: Nonlinear correction for secular change in seawater Mg/Ca. *Paleoceanography* **27**(PA4205). doi:10.1029/2012PA002315.

Author contributions: DE designed the research in discussion with WM, performed the data analysis and wrote the manuscript. WM edited the manuscript.

Overlap with previously examined research

Part of this paper appear in an earlier form in the unpublished MSc thesis of *Evans* [2011].

- Section 2.1 of this paper appears in a similar form in section 2.3 of *Evans* [2011]. However, this thesis erroneously describes the control on test Mg/Ca as applied as a correction for secular seawater Mg/Ca change as being the Mg/Ca distribution coefficient, which was corrected in the paper.
- An earlier version of figure 5 occurs in *Evans* [2011] (figure 2.7)
- The conclusion that Paleogene seawater Mg/Ca was lower than previously thought is also a conclusion (based on similar grounds) of *Evans* [2011].

The remainder of the paper is not previously presented elsewhere. The detailed implications for Mg/Ca palaeotehermometry and the specific constraint of Paleogene Mg/Ca_{sw} using coupled deep-benthic foraminifera Mg/Ca-$\delta^{18}O$ represent new work.

Corrigendum: The second line of section 2.2 should read 'referred to in Figure 1'.

Deep time foraminifera Mg/Ca paleothermometry: Nonlinear correction for secular change in seawater Mg/Ca

David Evans[1] and Wolfgang Müller[1]

Received 7 March 2012; revised 20 September 2012; accepted 21 September 2012; published 10 November 2012.

[1] The Mg/Ca ratio of foraminifera tests is increasingly being utilized as a paleotemperature proxy. Deep time (pre-Pleistocene) Mg/Ca paleothermometry is complicated by the fact that the Mg/Ca ratio of seawater (Mg/Ca_{sw}) has undergone considerable secular variation over the Cenozoic. Previous studies have corrected for this by assuming an invariant Mg distribution coefficient (D_{Mg}) with Mg/Ca_{sw}. More recent laboratory culturing has shown that this is not the case, demonstrating that a power relationship best describes the variation in test Mg/Ca (Mg/Ca_{test}) with Mg/Ca_{sw}. Therefore, previous corrections are likely to have led to inaccurate temperature reconstructions. Here, we show how the systematics of such a correction should be applied and demonstrate why this provides good evidence that the Mg/Ca ratio of Paleogene seawater was lower than previously implied by foraminiferal constraints, in agreement with the majority of the proxy Mg/Ca_{sw} evidence. We also demonstrate how it is indirectly possible to constrain the value of H, the power component of a Mg/Ca_{test}–Mg/Ca_{sw} calibration, potentially enabling the appropriate correction of results derived from species where this relationship has not been calibrated. However, this technique should not be treated as a substitute for culturing. The previous erroneous assumptions regarding both (1) the relationship between Mg/Ca_{test} and Mg/Ca_{sw} and (2) the Mg/Ca ratio of seawater at a given time in the past may counteract each other to differing extents. As a result, previous absolute pre-Pleistocene paleotemperature estimates derived from Mg/Ca ratios in foraminifera should be treated with caution, although relative temperature changes over short (<1 Ma timescales) are likely to be reliable.

Citation: Evans, D., and W. Müller (2012), Deep time foraminifera Mg/Ca paleothermometry: Nonlinear correction for secular change in seawater Mg/Ca, *Paleoceanography*, *27*, PA4205, doi:10.1029/2012PA002315.

1. Introduction

[2] The Mg/Ca ratio of foraminifera tests is increasingly being utilized as a paleotemperature proxy. Since the first detailed laboratory culture studies demonstrated a systematic relationship between Mg/Ca and temperature [*Nürnberg et al.*, 1996], the potential of this technique for paleoclimate reconstruction has been reflected by its growing popularity. Although most work has so far focused on the Quaternary, examining oceanic temperature changes over glacial-interglacial cycles, the most relevant periods of Earth's history with respect to the oceanic response to anthropogenic greenhouse gas emissions are thought to lie deeper in geological time. Because $\delta^{18}O$-derived temperatures suffer from uncertainties due to assumptions made regarding the past $\delta^{18}O$ of seawater [e.g., *Norris et al.*, 2002; *Tripati and Zachos*, 2002], it was initially thought that the Mg/Ca ratio of foraminifera tests may be a more promising paleothermometer [*Klein et al.*, 1996]. However, more recent work has identified several potential complications in the Mg/Ca paleothermometer, including salinity [e.g., *Arbuszewski et al.*, 2010] and test size [*Elderfield et al.*, 2002]. It also appears that the Mg/Ca ratio of at least some benthic foraminifera are largely controlled by the carbonate ion saturation state (ΔCO_3^{2-}) at temperatures below ~5°C [e.g., *Yu and Elderfield*, 2008], potentially rendering the bottom water temperature proxy unreliable in some species during cooler intervals. There is currently limited evidence for the effect of ΔCO_3^{2-} on test Mg/Ca (Mg/Ca_{test}) at higher temperatures.

[3] A significant advantage of the Mg/Ca-paleothermometer over $\delta^{18}O$-derived results is that trace element data may be obtained by plasma-based analytical techniques which, particularly when sampling by laser ablation, are faster and offer intraspecimen spatial resolution [*Evans et al.*, 2011; *Eggins et al.*, 2003]. For these reasons, the Mg/Ca paleothermometer represents the best possibility of simultaneously extracting detailed temperature information while also rigorously assessing sample preservation. Continued

[1]Department of Earth Sciences, Royal Holloway University of London, Egham, UK.

Corresponding author: D. Evans, Department of Earth Sciences, Royal Holloway University of London, Egham TW20 0EX, UK. (david.evans.2007@rhul.ac.uk)

0883-8305/12/2012PA002315

refinement of this proxy is therefore of great importance to our knowledge of paleo-ocean temperatures.

[4] When comparing data over timescales greater than several million years, the most significant source of inaccuracy inherent in this technique is that the Mg/Ca ratio of seawater (hereafter Mg/Ca_{sw}) has not remained constant. Mg/Ca_{sw} may be modified by changes in the rate of dolomite/carbonate precipitation and oceanic crust formation, as well as the Mg/Ca ratio and flux of riverine input (Mg and Ca have ocean residence times of ~14 Ma and ~1 Ma, respectively). All or some of these parameters have varied over geological time, resulting in a broad increase in Mg/Ca_{sw} over the Cenozoic [e.g., *Sandberg*, 1983; *Coggon et al.*, 2010]. The majority of studies utilizing foraminiferal Mg/Ca as a pre-Pleistocene paleotemperature proxy [e.g., *Billups and Schrag*, 2003; *Creech et al.*, 2010; *Dutton et al.*, 2005; *Lear et al.*, 2000, 2002; *Tripati and Elderfield*, 2004; *Tripati et al.*, 2003] have applied or considered a correction for secular Mg/Ca_{sw} variation. However, it is increasingly becoming apparent that the method employed by previous foraminifera-based reconstructions is inaccurate, demonstrated in detail below. This is because the basic assumption made by these studies is that the Mg distribution coefficient ($D_{Mg} = [Mg/Ca_{test}]/[Mg/Ca_{sw}]$) remains constant irrespective of varying Mg/Ca_{sw}. Recent work has shown that this assumption is incorrect [*Raitzsch et al.*, 2010; *Segev and Erez*, 2006], demonstrating that a power law describes the relationship between D_{Mg} and Mg/Ca_{sw} more appropriately [*Hasiuk and Lohmann*, 2010]. The implications of this are that (1) previous Paleogene temperature reconstructions are likely to be inaccurate to varying degrees dependent on the specific assumptions made and (2) the discrimination against certain Mg/Ca_{sw} model and proxy data in the literature for the correction of Mg/Ca-derived temperatures is a consequence of assuming D_{Mg} to be invariant. Therefore, suggested foraminiferal constraints on the Mg/Ca ratio of early mid-Cenozoic oceans require reconsideration. We stress that these comments are not intended as criticism of previous work, which were largely published before this aspect of Mg/Ca paleothermometry was under investigation. As a result of recent culturing experiments, leading to a significant advance in our understanding of this topic, this issue can now be properly addressed in all future studies attempting accurate temperature reconstruction via this technique.

[5] Based on a synthesis of existing data from both foraminifera culturing studies and applied foraminifera temperature reconstructions, we demonstrate that previous assumptions regarding the relationship between D_{Mg} and Mg/Ca_{sw} have produced inaccurate results. We then show how such corrections should be applied in future. While all previously published Mg/Ca-derived temperatures are potentially unreliable because of previous erroneous assumptions, *relative* reconstructed temperature variations over timescales shorter than ~1 Ma are not necessarily subject to change following this new method. This is because the maximum potential rate of Mg/Ca_{sw} variability is dominantly controlled by the shortest elemental residence time. Furthermore, previous assumptions (a relatively high paleo-Mg/Ca_{sw} *and* an invariant D_{Mg} with Mg/Ca_{sw}) may cancel out, and it is therefore possible that some estimated paleotemperatures will undergo limited change when adjusted properly. We demonstrate that reliable paleo-oceanic temperature information can only be obtained when an accurate correction for temporal change in the Mg/Ca_{sw} ratio have been applied.

2. Results and Discussion

2.1. Theory

[6] The majority of foraminifera Mg/Ca-temperature calibrations are presented in the form $Mg/Ca = Be^{AT}$, where B and A are constants to be defined for a species, genera or group of foraminifera (referred to as the preexponent and exponent component of the calibration, respectively), and T is temperature. The majority of studies that apply such calibrations to fossil material to reconstruct paleo-ocean temperatures have recognized that Mg/Ca_{sw} exerts a control on Mg/Ca_{test} and therefore a correction is required, even though until the study of *Segev and Erez* [2006] only preliminary information was available regarding the relationship between test and seawater Mg/Ca in foraminifera [*Delaney et al.*, 1985]. Virtually all studies so far have assumed that the relationship between Mg/Ca_{sw} and Mg/Ca_{test} is linear, equivalent to a horizontal straight line on a D_{Mg}–Mg/Ca_{sw} plot. Expressed as an equation, this requires D_{Mg} to be constant irrespective of Mg/Ca_{sw}:

$$D_{Mg}^{t=0} = D_{Mg}^{t=t} = \frac{Mg/Ca_{test}^{t=0}}{Mg/Ca_{sw}^{t=0}} = \frac{Mg/Ca_{test}^{t=t}}{Mg/Ca_{sw}^{t=t}} \quad (1)$$

where $t = 0$ is the present and $t = t$ is some point in the past. It then follows that for a fossil sample

$$Mg/Ca_{test}^{t=t} = \frac{Mg/Ca_{sw}^{t=t}}{Mg/Ca_{sw}^{t=0}} \times Mg/Ca_{test}^{t=0} \quad (2)$$

[7] Therefore, because the fossil foraminifera Mg/Ca ratio is a function of both temperature and the Mg/Ca ratio of seawater at some point in the past, equation (2) can be combined with the preexponent component of a temperature calibration derived from recent foraminifera to give

$$Mg/Ca_{test}^{t=t} = \frac{Mg/Ca_{sw}^{t=t}}{Mg/Ca_{sw}^{t=0}} \times B\exp^{AT} \quad (3)$$

This is the method that has been used by virtually all deep time foraminifera Mg/Ca paleotemperature reconstructions so far to correct for the secular variation in Mg/Ca_{sw} over the Cenozoic (see introduction for references).

[8] More recent work attempting to quantify the relationship between Mg/Ca_{sw} and Mg/Ca_{test} has demonstrated that equation (1) is not applicable to virtually all marine organisms studied so far. *Hasiuk and Lohmann* [2010] provide a synthesis of data from abiogenic calcite, echinoids, crabs, shrimps and coccoliths (amongst others) and show that D_{Mg} is not invariant with Mg/Ca_{sw}; in almost all cases the least squares regression results from a power function curve fit. There are currently only three studies that have investigated this relationship in foraminifera, that of *Delaney et al.* [1985], who cultured the planktic foraminifera *Globigerinoides sacculifer*, *Segev and Erez* [2006], who cultured two symbiont-bearing benthic species; *Amphistegina lobifera* and *A. lessonii*,

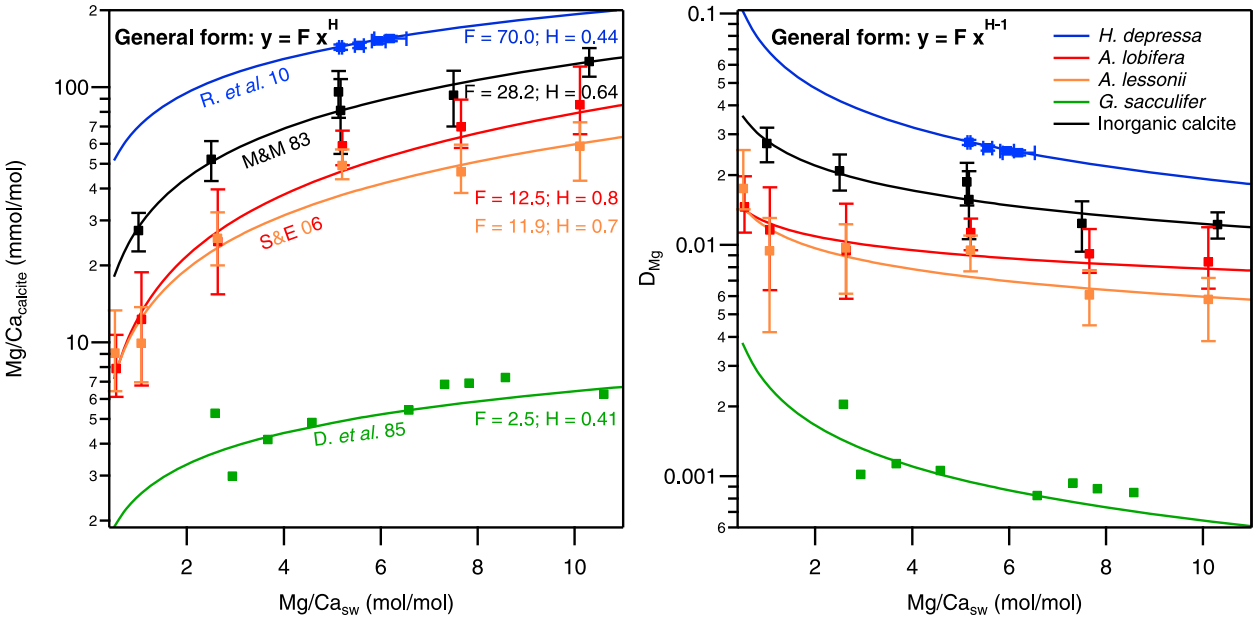

Figure 1. Currently available calibrations of (left) foraminifera Mg/Ca_{test} and (right) D_{Mg} plotted against Mg/Ca_{sw} (see text for details). Data from *Delaney et al.* [1985], *Segev and Erez* [2006], *Raitzsch et al.* [2010] (foraminifera) and *Mucci and Morse* [1983] (inorganic calcite). Note that for all current calibrations the constant $H \neq 1$ (no calibration is a horizontal straight line on a D_{Mg}–Mg/Ca_{sw} plot). Calibration best fit lines are plotted for all Mg/Ca_{sw}, irrespective of the range of values covered by the original study. Scatter in the data of *Delaney et al.* [1985] is likely the result of several covarying controlling factors in the experiments.

and most recently *Raitzsch et al.* [2010], who cultured *Heterostegina depressa*. All of these studies demonstrate that a power best fit between Mg/Ca_{test} and Mg/Ca_{sw} gives the least squares regression (Figure 1), with the implication that this is also the case for the relationship between D_{Mg} and Mg/Ca_{sw}. Therefore, in the general form, the relationship can be described as

$$Mg/Ca_{test} = F \times Mg/Ca_{sw}{}^{H} \quad (4)$$

where F and H are constants to be calibrated for a specific group or species. H is hereafter referred to as the power component of such a calibration. Equation (4) can be alternatively expressed in terms of the Mg distribution coefficient (cf. equation (1)):

$$D_{Mg} = F \times Mg/Ca_{sw}{}^{(H-1)} \quad (5)$$

[9] *Segev and Erez* [2006] not only calibrated this relationship in two benthic foraminifera species but also examined the effect of absolute Mg and Ca concentrations on test Mg/Ca. This study demonstrated that Mg/Ca_{test} is dependent only on the Mg/Ca_{sw} ratio; foraminifera grown in seawaters with the same ratio but different Mg and Ca concentrations produced equivalent test Mg/Ca ratios. This experiment therefore appears to preclude the absolute concentrations of ions in seawater as a further source of Mg/Ca-temperature reconstruction inaccuracy.

[10] Based on these culture studies, a more appropriate correction that should be applied to future pre-Pleistocene Mg/Ca-derived temperature reconstructions is to combine equation (4) with an exponential temperature calibration to give

$$Mg/Ca_{test} = \frac{F \times Mg/Ca_{sw}^{t=t^H}}{F \times Mg/Ca_{sw}^{t=0^H}} \times B \exp^{AT} \quad (6)$$

This can then be simplified [after *Ries*, 2004; *Hasiuk and Lohmann*, 2010] to the form

$$Mg/Ca_{test} = E \times Mg/Ca_{sw}^{t=t^H} \exp^{AT} \quad (7)$$

where

$$E = \frac{F}{F \times Mg/Ca_{sw}^{t=0^H}} \times B = \frac{B}{Mg/Ca_{sw}^{t=0^H}} \quad (8)$$

An obvious implication of this is that the nonpower component of the Mg/Ca_{test}–Mg/Ca_{sw} calibration (the constant F) cancels out and is therefore irrelevant when correcting for secular variation in Mg/Ca_{sw}. Thus the magnitude of such a correction depends entirely upon the age of the samples and on the value of the constant H (the power component of a Mg/Ca_{test}–Mg/Ca_{sw} calibration).

2.2. Implication

[11] Figure 2 shows the Mg/Ca_{test}–Mg/Ca_{sw} calibration data for the four species previously referred to Figure 1 along with two hypothetical data sets with $H = 0$ and $H = 1$, with the constant F removed. As previously discussed, almost all Mg/Ca-based paleotemperature studies have assumed D_{Mg} to be invariant with Mg/Ca_{sw}, i.e., $H = 1$. The consequence

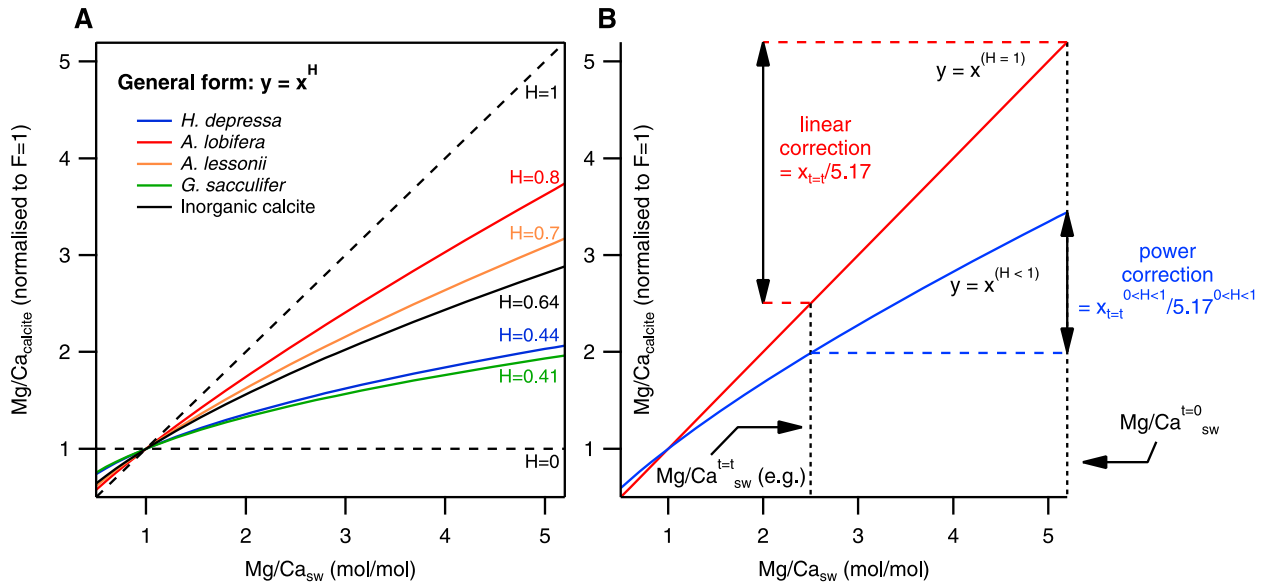

Figure 2. (a) All current calibrations of Mg/Ca_{test} variation with Mg/Ca_{sw} (i.e., those shown in Figure 1), with the nonpower component of the calibration removed. This enables easy visual and conceptual understanding of the effect of the constant H on the correction applied to fossil Mg/Ca data, (b) shown schematically. Because the constant F cancels out when applying a correction for secular variation in Mg/Ca_{sw} (see text), the magnitude of the difference in the y value of these curves between a paleo-Mg/Ca_{sw} and the present-day value of 5.17 mol mol^{-1} defines the correction to be applied to the preexponent constant of a temperature calibration. The correction applied by almost all deep time foraminifera-based Mg/Ca studies so far is defined by the line $H = 1$, which assumes no change in D_{Mg} with Mg/Ca_{sw}. The term "correction" on Figure 2b refers to the fraction reduction in the preexponent component of a Mg/Ca-temperature calibration given by $y_{t=t}/y_{t=0}$. From this it is clear that previous studies have overcompensated for Cenozoic variation in Mg/Ca_{sw}, as all calibrations so far have defined $H < 1$. An H value of 0 would imply no correction need be applied. Data are derived from the same sources as Figure 1. Only values lower than present-day Mg/Ca_{sw} are shown as there is no evidence for higher values during the Cenozoic.

of this is that any correction applied to Mg/Ca data in this way is more extreme than necessary, because the magnitude of difference between $Mg/Ca_{sw}^{t=0^H}$ and $Mg/Ca_{sw}^{t=t^H}$ increases as H increases (Figure 2). Therefore the correction applied to the preexponent component (the constant B) of a temperature calibration will necessarily be larger if H is assumed to be 1 compared to $H < 1$, which is the case in all Mg/Ca_{test}–Mg/Ca_{sw} calibrations so far. There is one published foraminifera-based study which has not made the same assumption (that $H = 1$), namely *Medina-Elizalde et al.* [2008], who for the first time applied a nonlinear correction to their Mg/Ca results based on the Mg/Ca_{sw} curve of *Fantle and DePaolo* [2006] and the $Mg/Ca_{calcite}$–Mg/Ca_{sw} calibration for inorganic calcite given by *Mucci and Morse* [1983]. While this study represents a significant advance because it is the first to recognize that a linear correction is not appropriate when adjusting results for paleo-Mg/Ca_{sw}, Figure 2 shows that the power component of such a calibration is highly group or species specific. Therefore, utilizing the inorganic calcite calibration when correcting foraminifera-derived results is also likely to result in inaccuracies.

[12] Figure 3 compares the effect of using a power correction ($H < 1$) and a linear correction ($H = 1$) on the preexponent component (the constant B) of a Mg/Ca-temperature calibration. Here, the correction applied is expressed as the fraction reduction (Fr) of this component (i.e., $B \times Fr$ is the modification that would be applied to a Mg/Ca-temperature calibration), while the error in the linear correction (Figure 3b) previously applied is expressed as the absolute difference between the dashed line $H = 1$ and the species specific calibrations shown above it in Figure 3a:

$$\Delta Fr = \frac{Mg/Ca_{sw}^{t=t^{H\neq1}}}{5.17^{H\neq1}} - \frac{Mg/Ca_{sw}^{t=t^{1}}}{5.17^{1}} \quad (9)$$

where ΔFr denotes the fraction difference in the correction applied between a linear and power law Mg/Ca_{test}–Mg/Ca_{sw} calibration to the preexponent component of a Mg/Ca-temperature calibration.

[13] For a given Mg/Ca_{sw} value the linear correction greatly overestimates the necessary adjustment, or alternatively, a linear calibration requires a higher Mg/Ca_{sw} value in order for an equivalent correction to be applied (Figure 3a), and therefore an equivalent paleotemperature estimate to be derived. The lower the H value of the Mg/Ca_{test}–Mg/Ca_{sw} calibration for a given species, the greater the error in the method previously utilized by most studies. This is of particular concern as the single (albeit preliminary) data set

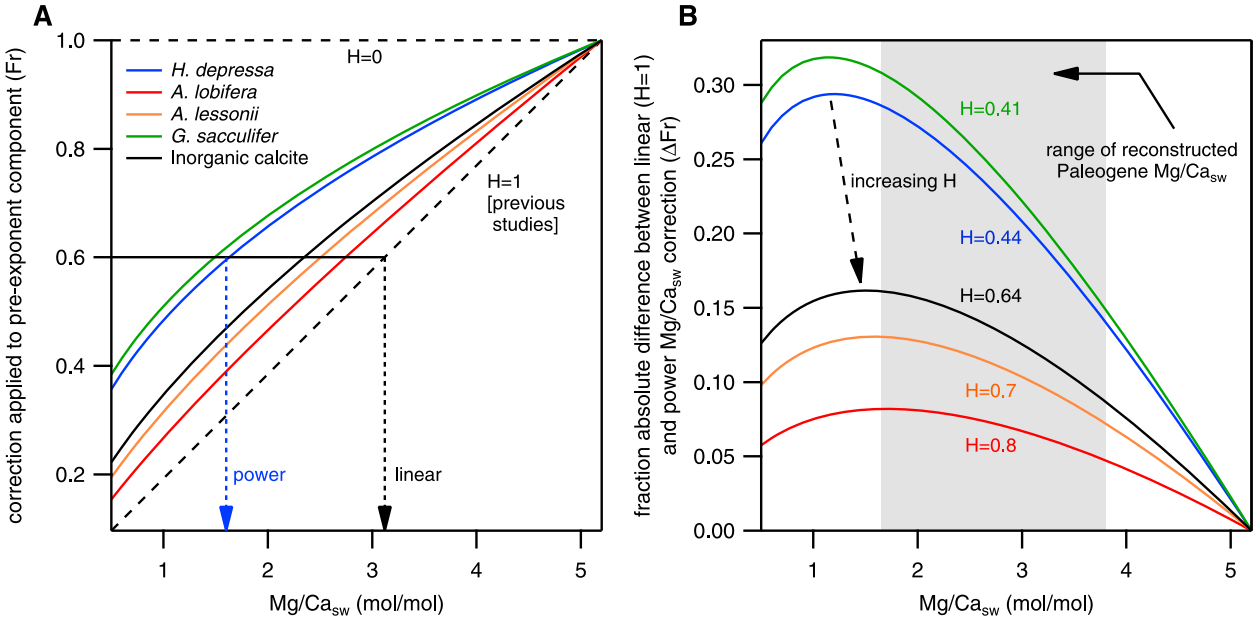

Figure 3. (a) The difference in applying a linear and power correction to the preexponent component of a Mg/Ca-temperature calibration. The line $H = 1$ defines the correction that almost all previous studies have applied. This line lies below those experimentally derived, which implies that previous results have been overcorrected, i.e., that the preexponent component of a Mg/Ca-temperature calibration has been reduced by too much. Alternatively, it demonstrates that when a linear correction is applied a higher Mg/Ca_{sw} value is necessary to arrive at the same paleotemperature estimate (example value selected for illustrative purposes only). (b) The magnitude of the difference between the correction previously applied ($H = 1$) and the correction that should be applied based on the Mg/Ca_{test}–Mg/Ca_{sw} calibrations currently available (expressed as the absolute difference in the fraction reduction of the preexponent component (the constant B) between a linear and power correction). A lower H value results in a greater error when applying a linear correction.

available for a planktic foraminifera (*G. sacculifer* [*Delaney et al.*, 1985]) suggests a relatively low value of H (0.41). If this is common to many, or most, planktic foraminifera species then previous absolute temperature estimates derived from these are likely to be particularly unreliable. For comparison, Figure 3b also shows the total range in reconstructed Paleogene Mg/Ca_{sw} reconstructions, including all model and proxy data. This shows that previous corrections to the constant B may be a factor of up to 40% too great (e.g., at $Mg/Ca_{sw} = 2$, $Fr_{H=1} = 0.39$ whereas $Fr_{H=0.4} = 0.68$).

[14] The difference between assuming a linear Mg/Ca_{test}–Mg/Ca_{sw} relationship and the method outlined here will be illustrated using the Mg/Ca-temperature calibration of *Dekens et al.* [2002], along with a range of assumptions regarding the value of the constant H for this species. *Dekens et al.* [2002] determined the constants B and A to be 0.38 and 0.09 for the planktic species *Globigerinoides ruber* (white), respectively. Figure 4 explores the effect of hypothetically changing the value of H, while also varying Mg/Ca_{sw} to cover the total range of values reconstructed for the Paleogene.

[15] Increasing H shifts the calibration downward, while increasing Mg/Ca_{sw} shifts the calibration relatively upward. Therefore, an incorrect assumption regarding the value of H in species where this parameter remains unknown (i.e., assuming $H = 1$) could be largely counteracted by assuming a Mg/Ca_{sw} value that is too high. Because $H < 1$ in all Mg/Ca_{test}–Mg/Ca_{sw} calibrations so far, it seems likely that constraints placed on Mg/Ca_{sw} by results derived from foraminifera, particularly in the Paleogene, tend toward values that are high, because such values are required to produce sensible temperature estimates. This is because assuming $H = 1$ shifts the original calibration so far downward that a high Mg/Ca_{sw} value is needed to counteract this. Compare, for example, on Figure 4 the solid blue line (assuming $H = 0.5$, $Mg/Ca_{sw} = 2.5$ mol mol^{-1}) with the red dashed line (assuming $H = 1$, $Mg/Ca_{sw} = 3.5$ mol mol^{-1}, i.e., the correction applied by previous studies). These two different sets of combined Mg/Ca_{sw} and H values produce corrected calibration lines to be applied to fossil measurements that are almost identical, because the higher H value of the red dashed line is almost exactly counteracted by the lower Mg/Ca_{sw} value of the solid blue line. Thus, apparently sensible paleotemperature reconstructions were derived from these two (counteracting) incorrect assumptions.

[16] One major assumption of this correction technique, even if the power relationship between Mg/Ca_{test} and Mg/Ca_{sw} is taken into account, is that the exponential component of a Mg/Ca-temperature calibration remains constant, irrespective of Mg/Ca_{sw} (i.e., that the constant A does not change whatever value of H or Mg/Ca_{sw} is used). For this reason, relative temperature changes (over periods <1 Ma) derived in this way are not at all affected by any conjecture regarding either Mg/Ca_{sw} or any inaccuracies in the determination of the value of H for a specific species or group

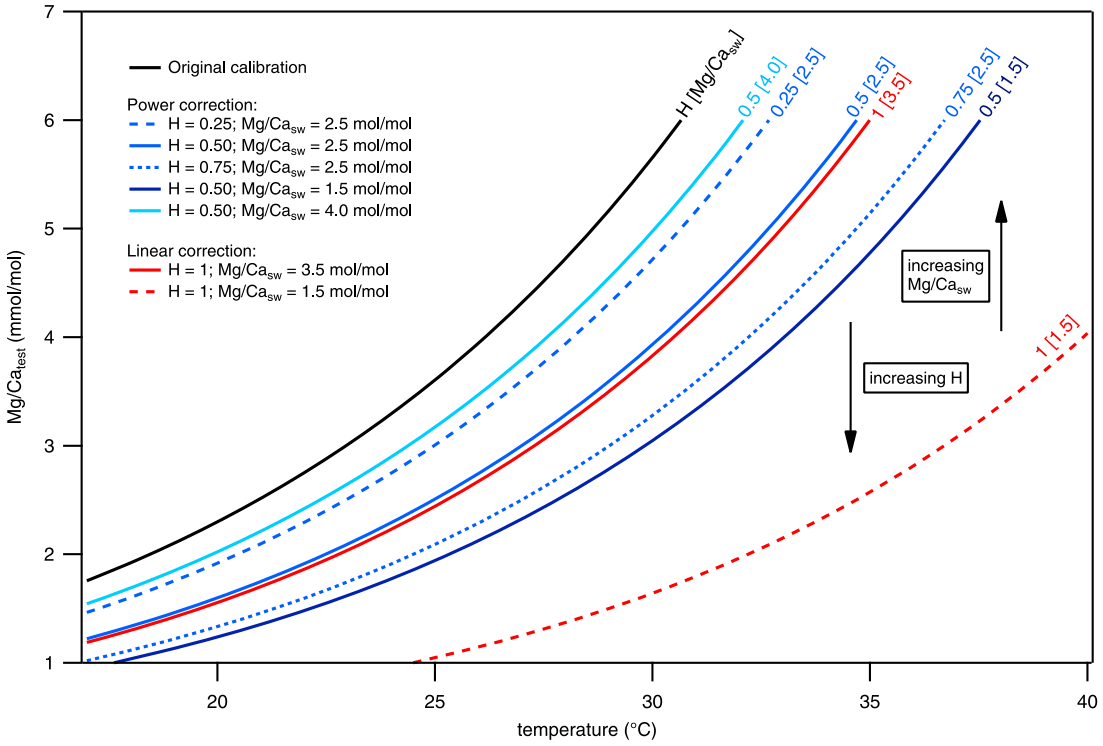

Figure 4. The calibration of *Dekens et al.* [2002] used as an example to illustrate the effects on a foraminifera Mg/Ca-temperature curve of hypothetically varying the *H* value of this species for a number of assumptions regarding Mg/Ca$_{sw}$. Solid blue lines demonstrate the effect of varying Mg/Ca$_{sw}$ (darker blues represent lower values). Dashed lines show the effect of increasing *H*. A larger value of the constant *H* shifts the calibration downward (to lower Mg/Ca$_{test}$ values) for a given temperature and Mg/Ca$_{sw}$, while increasing Mg/Ca$_{sw}$ shifts the calibration upward for a given temperature and *H* value. Because the two variables act to move the original calibration in opposite directions, incorrect assumptions regarding both of these parameters may lead to apparently sensible (but potentially erroneous) temperature estimates. The solid red line demonstrates this point, assuming $H = 1$ produces essentially the same modified calibration line as $H = 0.5$ but requires a higher Mg/Ca$_{sw}$ value. The dashed red line demonstrates why it was previously thought that low Mg/Ca$_{sw}$ values could be precluded based on foraminiferal Mg/Ca; combined with the assumption that $H = 1$, this produced paleotemperature estimates unrealistically high.

of organisms. The validity of this assumption remains to be proven and would require comparative Mg/Ca$_{test}$–Mg/Ca$_{sw}$ calibrations to be carried out over a number of temperatures.

2.3. Application: Paleogene Seawater Mg/Ca

2.3.1. Proxy and Model Data

[17] For the reasons outlined above it is now clear that both a Mg/Ca-temperature calibration and a Mg/Ca$_{test}$–Mg/Ca$_{sw}$ calibration are required in order for the Mg/Ca paleotemperature proxy to produce accurate results. However, a further requirement is a well-constrained Mg/Ca$_{sw}$ value for the age of the fossil samples under study. Several proxy and model reconstructions for Cenozoic Mg/Ca$_{sw}$ are available and while most of these agree on the broad trend of Mg/Ca$_{sw}$ variation over the Phanerozoic, there is disagreement in the detail of these estimates within the Cenozoic, where accurate data at million year resolution is required. Paleogene proxy reconstructions are available using fluid inclusions in halite [*Horita et al.*, 2002; *Lowenstein et al.*, 2001], from the analysis of ridge flank vein carbonates [*Coggon et al.*, 2010] and by comparing the Mg/Ca ratio of fossil and modern echinoderms [*Dickson*, 2004] (Figure 5). All of these techniques are associated with (in some cases large) uncertainties but are generally in good agreement with each other, suggesting early mid-Cenozoic values of 1.5–2 mol mol^{-1} followed by a rise over the last ~20 Ma to the present-day value of 5.2 mol mol^{-1}. In the Paleogene, these proxy data are in agreement with the models of *Stanley and Hardie* [1998], *Demicco et al.* [2005] and *Berner* [2004] (Figure 5) but contrast the overall much higher Cenozoic Mg/Ca$_{sw}$ values suggested by the model of *Wilkinson and Algeo* [1989]. If an error of ±0.5 mol mol^{-1} is added to the model of *Stanley and Hardie* [1998] then almost all of the proxy data fall within this range suggesting that it is much more likely to be representative of Cenozoic Mg/Ca$_{sw}$ than the models suggesting relatively higher Paleogene Mg/Ca$_{sw}$ values (>3 mol mol^{-1}).

2.3.2. Constraints on Paleogene Mg/Ca$_{sw}$: Coupled δ^{18}O-Mg/Ca Data

[18] Some previous studies [e.g., *Broecker and Yu*, 2011; *Creech et al.*, 2010; *Lear et al.*, 2000, 2002] have argued that higher Cenozoic Mg/Ca$_{sw}$ values are more realistic, specifically in some cases that the model of *Wilkinson and Algeo* [1989] is more likely to be correct than all other

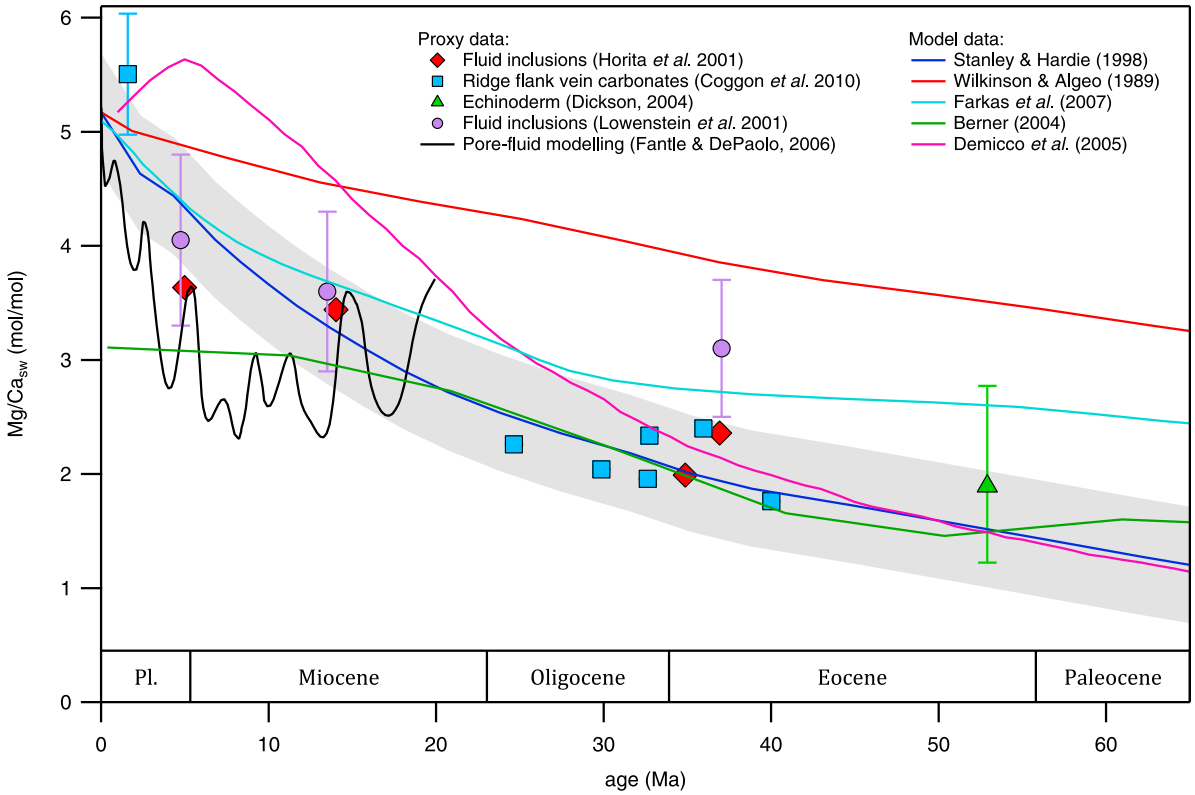

Figure 5. Cenozoic Mg/Ca_{sw} reconstructions based on both proxy [*Fantle and DePaolo*, 2006; *Horita et al.*, 2002; *Coggon et al.*, 2010; *Dickson*, 2004; *Lowenstein et al.*, 2001] and model [*Stanley and Hardie*, 1998; *Demicco et al.*, 2005; *Wilkinson and Algeo*, 1989; *Berner*, 2004; *Farkas et al.*, 2007] data. The majority of the proxy data agree well with *Stanley and Hardie* [1998] if an error of 0.5 mol mol^{-1} is applied to this model (gray band). The proxy evidence also agree with the models of *Demicco et al.* [2005] and *Berner* [2004] in the Paleogene. None of the proxy data are in agreement with the model of *Wilkinson and Algeo* [1989]. Error bars are shown where they are reported in the original study and are larger than symbols.

model and proxy data arguing for lower values, particularly in the Paleogene. As discussed above, this conclusion results from an incorrect assumption regarding the value of H in a Mg/Ca_{test}–Mg/Ca_{sw} calibration.

[19] In principle, coupled $\delta^{18}O$-Mg/Ca measurements from foraminifera allow both temperature and $\delta^{18}O_{sw}^{t=t}$ to be evaluated: an approach taken by many previous studies to calculate changes in global ice volume over both the Cenozoic and the Quaternary [*Elderfield and Ganssen*, 2000; *Lear et al.*, 2000; *Billups and Schrag*, 2002, 2003]. It is now apparent that there are in fact six variables to be constrained: $\delta^{18}O_{sw}^{t=t}$, $Mg/Ca_{sw}^{t=t}$, temperature and the value of the constant H, as well as $\delta^{18}O_{test}$ and Mg/Ca_{test} which can be analyzed in well-preserved samples. In an ice-free world, the assumption that deep water $\delta^{18}O$ was −1.2 or −0.9% (*Lear et al.* [2002] and *Cramer et al.* [2011], respectively), allows either $Mg/Ca_{sw}^{t=t}$ or H to be calculated if the other is known. Because H is known for only a few species of foraminifera, while almost all of the proxy and model Mg/Ca_{sw} evidence for the Paleogene suggests low (<2.5 mol mol^{-1}) values (Figure 5), we show how the value of H can be calculated for a species where a calibration is not yet available, thereby fully reconciling Cenozoic Mg/Ca_{sw} values lower than that of *Wilkinson and Algeo* [1989] with $\delta^{18}O$-derived temperatures from foraminifera.

[20] *Oridorsalis umbonatus* is an extant benthic foraminifera which is also present throughout the Cenozoic, enabling direct comparison of recent and fossil material without the need for species-specific corrections. There are several Mg/Ca-temperature calibrations available for this species, which are not all in agreement. It is also unclear whether a linear or exponential fit more appropriately describes the data. *Lear et al.* [2000] used an exponential calibration, whereas the data of *Lear et al.* [2010] and *Bryan and Marchitto* [2008] suggest a linear fit is more appropriate. In particular, calibrations focusing on low temperatures show that a linear fit is equally or more suitable. A linear or exponential best fit appear to represent the data of *Rathmann et al.* [2004] equally well.

[21] *Lear et al.* [2002] suggest that early Paleogene Mg/Ca_{sw} values are likely to be in the region suggested by *Wilkinson and Algeo* [1989], around 3.6 mol mol^{-1}. This is because when H is assumed to be 1, lower Mg/Ca_{sw} values shift the calibration to much higher temperatures for a given Mg/Ca_{test} value (or rather Mg/Ca_{test} values are shifted downward for a given temperature) and therefore produce

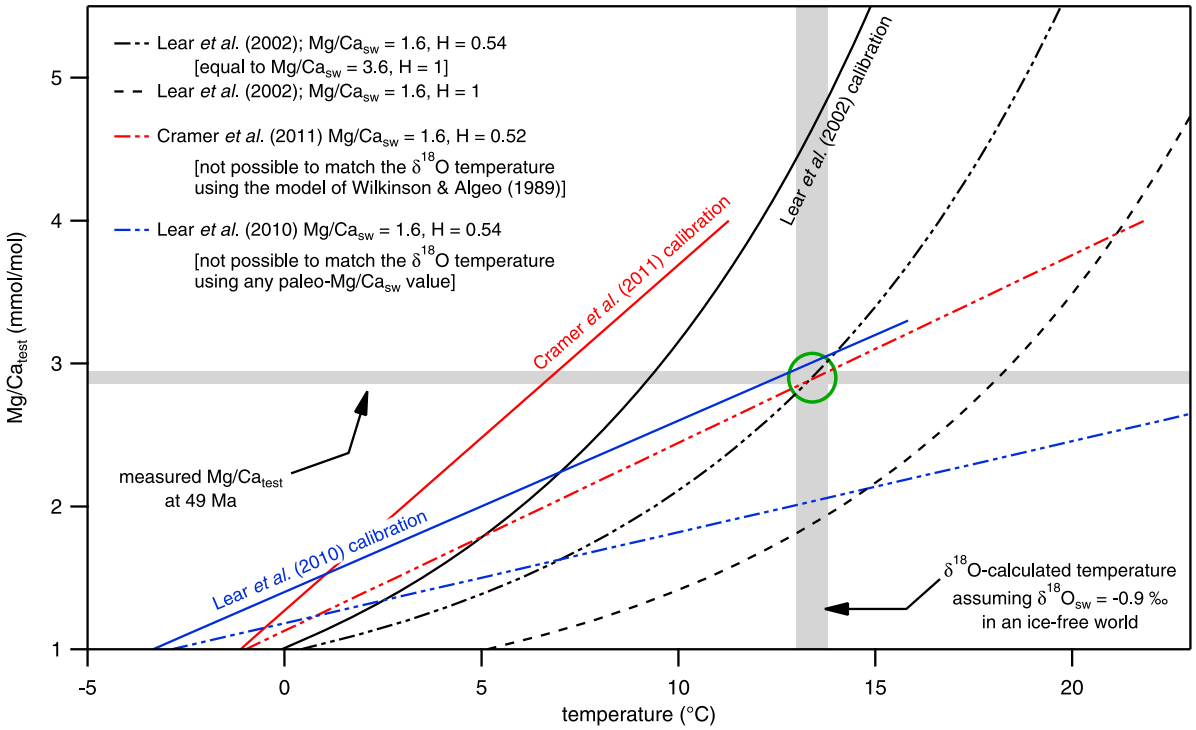

Figure 6. Reconciling the low proxy and model estimates of Paleogene Mg/Ca$_{sw}$ with data from foraminifera. Three calibrations that have been applied to fossil *O. umbonatus* are shown, that of *Lear et al.* [2002, 2010] and the data of *Rathmann et al.* [2004] with the linear fit applied by *Cramer et al.* [2011]. Because δ^{18}O in an ice-free world can be calculated and *O. umbonatus* Mg/Ca can be measured at a time when the world was ice free (49 Ma), this information can be used to calculate the value of H in this species, by solving equation (7). Doing so results in a range in H from 0.52 to 0.54 depending on which calibration is used (*Lear et al.* [2002] and *Cramer et al.* [2011], respectively), assuming a Paleogene Mg/Ca$_{sw}$ value of 1.6 mol mol^{-1} [*Stanley and Hardie*, 1998]. In the case of the calibration of *Lear et al.* [2002], exactly the same result can be produced by using the far higher Mg/Ca$_{sw}$ value of *Wilkinson and Algeo* [1989] at this time with the assumption that $H = 1$. We therefore show how two previously held incorrect assumptions (namely, that Paleogene Mg/Ca$_{sw}$ was <3 mol mol^{-1} and that the value of $H = 1$) can result in a sensible Mg/Ca-temperature estimate, leading to erroneous foraminiferal constraints on Mg/Ca$_{sw}$. It is not possible to recreate the δ^{18}O-derived temperature using the calibration of *Cramer et al.* [2011] coupled to the Mg/Ca$_{sw}$ of *Wilkinson and Algeo* [1989], adding support to this argument. The calibration of *Lear et al.* [2010], with a significantly lower slope, would appear to suggest $H \approx 0$.

reconstructed paleotemperature estimates in very poor agreement with comparative δ^{18}O-derived results.

[22] At 49 Ma the Earth is assumed to be ice free, which, along with the aforementioned assumption of ocean bottom water δ^{18}O on an ice-free planet and depending on which δ^{18}O-temperature calibration is used, has led to a range in reported temperatures for this time of 12.4–13.4°C [*Lear et al.*, 2002; *Cramer et al.*, 2011]. An uncertainty in the value of δ^{18}O$_{sw}$ of 0.1% results in a temperature error of ~0.4°C. By using the measured δ^{18}O and Mg/Ca ratio of *O. umbonatus* at 49 Ma (2.9 mmol mol^{-1}), the constant H can be calculated by combining both these data and respective temperature calibrations; at one specific value the Mg/Ca temperature will match precisely the δ^{18}O-derived temperature. Because the model of *Stanley and Hardie* [1998] is within error of the majority of the Mg/Ca$_{sw}$ data currently available (Figure 5), and an independent temperature estimate is available from δ^{18}O measurement, the value of H for this species can be calculated. Specifically, we derive H by iteratively solving equation (6) so that $T = 13.4$°C when Mg/Ca$_{sw}$ = 1.6 mol mol^{-1} (the value given by *Stanley and Hardie* [1998] at 49 Ma). This gives a value of H for this foraminifera species of 0.52 or 0.54 based on the Mg/Ca-temperature data of *Rathmann et al.* [2004] and *Lear et al.* [2002], respectively (Figure 6). This value of H is for δ^{18}O$_{sw}$ = − 0.9%, a value of −1.2% would result in H = 0.44 or 0.48, respectively. Following *Cramer et al.* [2011] a correction has been applied to those lines in Figure 6 relating to paleo-Mg/Ca$_{sw}$ values for changes in the calcite compensation depth (CCD), using a CCD depth at 49 Ma of 3.25 km [*Van Andel*, 1975]. Such a correction is necessary as a relatively higher CCD lowers ΔCO_3^{2-} for a given depth.

[23] In the absence of any calibration study this result should be treated as preliminary, particularly as Mg/Ca$_{sw}$ is not very well constrained throughout much of the Cenozoic. In section 2.3.1 we noted that with one exception all of the Mg/Ca$_{sw}$ proxy evidence lies within ±0.5 mol mol^{-1} of

the model of *Stanley and Hardie* [1998]. However, propagating this error through to our calculation of H results in an uncertainty of $\sim\pm0.14$, therefore until early mid-Paleogene Mg/Ca_{sw} is better constrained, this methodology can be used as a guide only. Furthermore, an uncertainty in $\delta^{18}O_{sw}^{t=49}$ of $\pm0.1\%$ results in an error in H of approximately ±0.04.

[24] Despite considerable uncertainties in the calculation of H, we demonstrate how it is possible to reconcile low Mg/Ca_{sw} values with $\delta^{18}O$-derived temperatures from foraminifera. Given that for all species studied so far $H < 1$, the possibility of high (>2.5 mol mol^{-1}) Paleogene Mg/Ca_{sw} values are precluded. Previously, constraints have been placed on Paleogene Mg/Ca_{sw} by assuming $H = 1$. This resulted in the exclusion of estimates from the lower range of Mg/Ca_{sw} values, as a Paleogene ratio of 3.6 mol mol^{-1} was required to match the $\delta^{18}O$ with the Mg/Ca-derived temperatures, despite the available proxy evidence suggesting that such higher values were unlikely. The reasons for this result are discussed above, however it should again be noted that this aspect of Mg/Ca paleothermometry was only understood after the publication of the majority of studies that assume $H = 1$. Because virtually all of the paleo-Mg/Ca_{sw} direct proxy evidence lies reasonably close to the model of *Stanley and Hardie* [1998] and $H < 1$ for all foraminifera species studied so far, it is not possible that the model of *Wilkinson and Algeo* [1989] is representative of the magnitude of increase in Cenozoic Mg/Ca_{sw}.

[25] Recently, *Cramer et al.* [2011] calculated a Cenozoic Mg/Ca_{sw} record by combining the Cenozoic benthic foraminifera Mg/Ca and $\delta^{18}O$ records with a sea level record (used as a proxy for ice volume). We outline in this contribution the inaccuracy in previous Mg/Ca_{sw} corrections and the associated assumptions and constraints placed on Paleogene Mg/Ca_{sw}. The recent reconstruction of *Cramer et al.* [2011] is therefore not assessed in detail here, as such a discussion is outside the intended remit of this paper. Briefly, however, the *Cramer et al.* [2011] Mg/Ca_{sw} reconstruction is not included in Figure 5 because it is not entirely independently derived. The record was produced by matching the Cenozoic Mg/Ca and $\delta^{18}O$ temperature curves by varying Mg/Ca_{sw} at each time interval and therefore requires some assumption of the value of H or Mg/Ca_{sw} at one or several tie points. Given that H is not known from culturing for any deep benthic foraminifera species, the assumption is of Mg/Ca_{sw} and it is therefore not independent of the reconstructions shown in Figure 5. This is important because the relatively high Mg/Ca_{sw} values that *Cramer et al.* [2011] reconstruct (broadly >3 mol mol^{-1}) are a result of their assumption regarding Mg/Ca_{sw} at some point in the past. Assuming a lower Mg/Ca_{sw} value at this time would shift the entire reconstruction downward and it therefore does not provide independent evidence that lower Mg/Ca_{sw} estimates are incorrect.

[26] Although the discussion has so far focused on the Paleogene, because seawater Mg/Ca ratios were significantly different before ~20 Ma in comparison to the present day, it is also important to appropriately adjust Mg/Ca data from fossil material younger than this. The model of *Fantle and DePaolo* [2006] (Figure 5), based directly on high-resolution proxy evidence, suggests that the Mg/Ca ratio of seawater may have undergone fluctuation on submillion year timescales significant enough to greatly increase the inaccuracy in Mg/Ca-derived temperatures. If Mg/Ca_{sw} has indeed undergone far more short-term fluctuation than previously accounted for, then any study based on samples older than 0.5 Ma reporting absolute temperatures should take the correction outlined here into account [see *Medina-Elizalde et al.*, 2008]. Furthermore, any high-resolution study spanning more than 0.5–1 Ma should consider the effect of potential changes in Mg/Ca_{sw}. While the majority of the Mg/Ca_{sw} proxy data agree well with the model of *Stanley and Hardie* [1998], further high-resolution model and proxy reconstructions of secular variation in Cenozoic Mg/Ca_{sw} are clearly a priority.

3. Conclusion

[27] We demonstrate here that previous assumptions regarding the correction of Mg/Ca analyses of fossil foraminifera for secular change in Mg/Ca_{sw} are incorrect. Studies have hitherto assumed that the Mg distribution coefficient is invariant with Mg/Ca_{sw}, which is equivalent to $H = 1$ on a Mg/Ca_{test}–Mg/Ca_{sw} calibration in the form $Mg/Ca_{test} = F \times Mg/Ca_{sw}^{H}$. Recent calibration studies that have quantified this relationship have shown that this is not the case. The implication is that previous studies have overcorrected their Mg/Ca-derived results, leading to the conclusion that the Mg/Ca ratio of (in particular) Paleogene seawater was much higher than suggested by proxy or model evidence. We detail how future corrections should be applied, highlighting the need for further culturing studies that calibrate this relationship (specifically the value of H) in species that are more routinely used for paleotemperature reconstruction. However, given that temperature information is independently available from $\delta^{18}O_{test}$ analyses, the value of H for a given species can also be calculated because Mg/Ca_{test} can be measured and Mg/Ca_{sw} is known from proxy evidence. Caution should be exercised when indirectly assessing H in this manner because there are uncertainties associated with both the oxygen isotopic composition of paleoseawater and the exact value of Mg/Ca_{sw} for any given time. By applying this technique to the benthic species *O. umbonatus* we calculate a range of H based on certain clear assumptions, which are compatible with previous culture experiments demonstrating that $H < 1$ for all foraminifera species studied so far. Using the same species, we demonstrate that Paleogene $Mg/Ca_{sw} > 2.5$ mol mol^{-1} are not possible, in line with almost all independent proxy evidence.

[28] For this approach to be valid, a reasonable assumption of $\delta^{18}O_{sw}$ is required. It is more difficult to reasonably assess a likely $\delta^{18}O_{sw}$ value for ocean surface waters, particularly away from the tropics, as evaporation and freshwater input broadly increase and decrease $\delta^{18}O_{sw}$, respectively. An indirect assessment of the value of the constant H in planktic foraminifera species using this technique is therefore likely to be inherently less accurate, but may still provide some constraint. The use of well-preserved samples from or before the early Paleogene (>48 Ma), when the world is considered to have been ice free [*Lear et al.*, 2000; *Zachos et al.*, 2008], may lessen the error in whatever assumption regarding $\delta^{18}O_{sw}$ is made.

[29] There are two potential approaches to solving this problem via culturing. The first is based on the assumption made here, that the exponential component of a temperature calibration (A) is not dependent on Mg/Ca_{sw}, in which case only a temperature calibration and a Mg/Ca_{test}–Mg/Ca_{sw} calibration are required. However, this hypothesis requires confirmation, which could be implemented by calibrating the Mg/Ca_{test}–Mg/Ca_{sw} relationship at several different temperatures. The second approach is to choose a relevant value of Mg/Ca_{sw} and to calibrate the Mg/Ca_{test}-temperature relationship at this value. While this approach is advantageous in that it makes no assumption regarding the behavior of the exponent component of the calibration, it is disadvantageous because it is inflexible and therefore time consuming, as a large number of such calibrations would be necessary in order to be useful for correcting long-term data sets that cover a wide range of Mg/Ca_{sw} values. It also would not allow data to be updated if new information of the Mg/Ca_{sw} ratio at a particular time became available.

[30] **Acknowledgments.** D.B.J.E. acknowledges a NERC postgraduate research studentship at Royal Holloway University of London. We thank two anonymous reviewers, whose constructive comments have greatly improved this paper.

References

Arbuszewski, J., P. Demenocal, A. Kaplan, and E. Farmer (2010), On the fidelity of shell-derived $\delta^{18}O_{seawater}$ estimates, *Earth Planet. Sci. Lett.*, *300*, 185–196.

Berner, R. (2004), A model for calcium, magnesium and sulfate in seawater over Phanerozoic time, *Am. J. Sci.*, *304*(5), 438–453.

Billups, K., and D. P. Schrag (2002), Paleotemperatures and ice volume of the past 27 Myr revisited with paired Mg/Ca and $^{18}O/^{16}O$ measurements on benthic foraminifera, *Paleoceanography*, *17*(1), 1003, doi:10.1029/2000PA000567.

Billups, K., and D. P. Schrag (2003), Application of benthic foraminiferal Mg/Ca ratios to questions of Cenozoic climate change, *Earth Planet. Sci. Lett.*, *209*, 181–195.

Broecker, W., and J. Yu (2011), What do we know about the evolution of Mg to Ca ratios in seawater?, *Paleoceanography*, *26*, PA3203, doi:10.1029/2011PA002120.

Bryan, S., and T. Marchitto (2008), Mg/Ca–temperature proxy in benthic foraminifera: New calibrations from the Florida Straits and a hypothesis regarding Mg/Li, *Paleoceanography*, *23*, PA2220, doi:10.1029/2007PA001553.

Coggon, R., D. Teagle, C. Smith-Duque, J. Alt, and M. Cooper (2010), Reconstructing past seawater Mg/Ca and Sr/Ca from mid-ocean ridge flank calcium carbonate veins, *Science*, *327*, 1114–1117.

Cramer, B., K. Miller, P. Barrett, and J. Wright (2011), Late Cretaceous–Neogene trends in deep ocean temperature and continental ice volume: Reconciling records of benthic foraminiferal geochemistry ($\delta^{18}O$ and Mg/Ca) with sea level history, *J. Geophys. Res.*, *116*, C12023, doi:10.1029/2011JC007255.

Creech, J., J. Baker, C. Hollis, H. Morgans, and E. Smith (2010), Eocene sea temperatures for the mid-latitude southwest Pacific from Mg/Ca ratios in planktonic and benthic foraminifera, *Earth Planet. Sci. Lett.*, *299*, 483–495.

Dekens, P., D. Lea, D. Pak, and H. Spero (2002), Core top calibration of Mg/Ca in tropical foraminifera: Refining paleotemperature estimation, *Geochem. Geophys. Geosyst.*, *3*(4), 1022, doi:10.1029/2001GC000200.

Delaney, M., A. W. H. Bé, and E. A. Boyle (1985), Li, Sr, Mg, and Na in foraminiferal calcite shells from laboratory culture, sediment traps, and sediment cores, *Geochim. Cosmochim.a Acta*, *49*(6), 1327–1341.

Demicco, R. V., T. K. Lowenstein, L. A. Hardie, and R. J. Spencer (2005), Model of seawater composition for the Phanerozoic, *Geology*, *33*(11), 877–880, doi:10.1130/G21945.1.

Dickson, J. (2004), Echinoderm skeletal preservation: calcite-aragonite seas and the Mg/Ca ratio of Phanerozoic oceans, *J. Sediment. Res.*, *74*(3), 355–365.

Dutton, A., K. Lohmann, and R. Leckie (2005), Insights from the Paleogene tropical Pacific: Foraminiferal stable isotope and elemental results from Site 1209, Shatsky Rise, *Paleoceanography*, *20*, PA3004, doi:10.1029/2004PA001098.

Eggins, S., P. De Deckker, and J. Marshall (2003), Mg/Ca variation in planktonic foraminifera tests: Implications for reconstructing palaeo-seawater temperature and habitat migration, *Earth Planet. Sci. Lett.*, *212*(3-4), 291–306.

Elderfield, H., and G. Ganssen (2000), Past temperature and $\delta^{18}O$ of surface ocean waters inferred from foraminiferal Mg/Ca ratios, *Nature*, *405*, 442–445.

Elderfield, H., M. Vautravers, and M. Cooper (2002), The relationship between shell size and Mg/Ca, Sr/Ca, $\delta^{18}O$, and $\delta^{13}C$ of species of planktonic foraminifera, *Geochem. Geophys. Geosyst.*, *3*(8), 1052, doi:10.1029/2001GC000194.

Evans, D. B. J., W. Müller, J. A. Todd, and W. Renema (2011), An Eocene analogue for the future oceanic response to increased CO_2—Existence of a tropical thermostat?, *Mineral. Mag.*, *75*, 821.

Fantle, M., and D. DePaolo (2006), Sr isotopes and pore fluid chemistry in carbonate sediment of the Ontong Java Plateau: Calcite recrystallization rates and evidence for a rapid rise in seawater Mg over the last 10 million years, *Geochim. Cosmochim. Acta*, *70*(15), 3883–3904.

Farkas, J., F. Böhm, K. Wallmann, J. Blenkinsop, A. Eisenhauer, R. Van Geldern, A. Munnecke, S. Voigt, and J. Veizer (2007), Calcium isotope record of Phanerozoic oceans: Implications for chemical evolution of seawater and its causative mechanisms, *Geochim. Cosmochim. Acta*, *71*(21), 5117–5134.

Hasiuk, F., and K. Lohmann (2010), Application of calcite Mg partitioning functions to the reconstruction of paleocean Mg/Ca, *Geochim. Cosmochim. Acta*, *74*(23), 6751–6763.

Horita, J., H. Zimmermann, and H. Holland (2002), Chemical evolution of seawater during the Phanerozoic: Implications from the record of marine evaporites, *Geochim. Cosmochim. Acta*, *66*(21), 3733–3756.

Klein, R., K. Lohmann, and C. Thayer (1996), Bivalve skeletons record sea-surface temperature and $\delta^{18}O$ via Mg/Ca and $^{18}O/^{16}O$ ratios, *Geology*, *24*(5), 415–418.

Lear, C. H., H. Elderfield, and P. A. Wilson (2000), Cenozoic deep-sea temperatures and global ice volumes from Mg/Ca in benthic foraminiferal calcite, *Science*, *287*, 269–272.

Lear, C. H., Y. Rosenthal, and N. Slowey (2002), Benthic foraminiferal Mg/Ca-paleothermometry: A revised core-top calibration, *Geochim. Cosmochim. Acta*, *66*(19), 3375–3387.

Lear, C. H., E. M. Mawbey, and Y. Rosenthal (2010), Cenozoic benthic foraminiferal Mg/Ca and Li/Ca records: Toward unlocking temperatures and saturation states, *Paleoceanography*, *25*, PA4215, doi:10.1029/2009PA001880.

Lowenstein, T., M. Timofeeff, S. Brennan, L. Hardie, and R. Demicco (2001), Oscillations in Phanerozoic seawater chemistry: Evidence from fluid inclusions, *Science*, *294*, 1086–1088.

Medina-Elizalde, M., D. Lea, and M. Fantle (2008), Implications of seawater Mg/Ca variability for Plio-Pleistocene tropical climate reconstruction, *Earth Planet. Sci. Lett.*, *269*(3–4), 585–595.

Mucci, A., and J. Morse (1983), The incorporation of Mg^{2+} and Sr^{2+} into calcite overgrowths: influences of growth rate and solution composition, *Geochim. Cosmochim. Acta*, *47*(2), 217–233.

Norris, R. D., K. L. Bice, E. A. Magno, and P. A. Wilson (2002), Jiggling the tropical thermostat in the Cretaceous hothouse, *Geology*, *30*(4), 299–302.

Nürnberg, D., J. Bijma, and C. Hemleben (1996), Assessing the reliability of magnesium in foraminiferal calcite as a proxy for water mass temperatures, *Geochim. Cosmochim. Acta*, *60*(5), 803–814.

Raitzsch, M., A. Dueñas-Bohórquez, G. Reichart, L. de Nooijer, and T. Bickert (2010), Incorporation of Mg and Sr in calcite of cultured benthic foraminifera: impact of calcium concentration and associated calcite saturation state, *Biogeosciences*, *7*(3), 869–881.

Rathmann, S., S. Hess, H. Kuhnert, and S. Mulitza (2004), Mg/Ca ratios of the benthic foraminifera *Oridorsalis umbonatus* obtained by laser ablation from core top sediments: Relationship to bottom water temperature, *Geochem. Geophys. Geosyst.*, *5*, Q12013, doi:10.1029/2004GC000808.

Ries, J. (2004), Effect of ambient Mg/Ca ratio on Mg fractionation in calcareous marine invertebrates: A record of the oceanic Mg/Ca ratio over the Phanerozoic, *Geology*, *32*(11), 981–984.

Sandberg, P. (1983), An oscillating trend in Phanerozoic non-skeletal carbonate mineralogy, *Nature*, *305*, 19–22.

Segev, E., and J. Erez (2006), Effect of Mg/Ca ratio in seawater on shell composition in shallow benthic foraminifera, *Geochem. Geophys. Geosyst.*, *7*, Q02P09, doi:10.1029/2005GC000969.

Stanley, S., and L. Hardie (1998), Secular oscillations in the carbonate mineralogy of reef-building and sediment-producing organisms driven by tectonically forced shifts in seawater chemistry, *Palaeogeogr. Palaeoclimatol. Palaeoecol.*, *144*(1–2), 3–19.

Tripati, A., and H. Elderfield (2004), Abrupt hydrographic changes in the equatorial Pacific and subtropical Atlantic from foraminiferal Mg/Ca

indicate greenhouse origin for the thermal maximum at the Paleocene-Eocene boundary, *Geochem. Geophys. Geosyst.*, *5*, Q02006, doi:10.1029/2003GC000631.

Tripati, A., and J. Zachos (2002), Late Eocene tropical sea surface temperatures: A perspective from Panama, *Paleoceanography*, *17*(3), 1032, doi:10.1029/2000PA000605.

Tripati, A. K., M. L. Delaney, J. C. Zachos, L. D. Anderson, D. C. Kelly, and H. Elderfield (2003), Tropical sea-surface temperature reconstruction for the early paleogene using Mg/Ca ratios of planktonic foraminifera, *Paleoceanography*, *18*(4), 1101, doi:10.1029/2003PA000937.

Van Andel, T. (1975), Mesozoic/Cenozoic calcite compensation depth and the global distribution of calcareous sediments, *Earth Planet. Sci. Lett.*, *26*(2), 187–194.

Wilkinson, B., and T. Algeo (1989), Sedimentary carbonate record of calcium-magnesium cycling, *Am. J. Sci.*, *289*(10), 1158–1194.

Yu, J., and H. Elderfield (2008), Mg/Ca in the benthic foraminifera *Cibicidoides wuellerstorfi* and *Cibicidoides mundulus*: Temperature versus carbonate ion saturation, *Earth Planet. Sci. Lett.*, *276*(1–2), 129–139.

Zachos, J., G. Dickens, and R. Zeebe (2008), An early Cenozoic perspective on greenhouse warming and carbon-cycle dynamics, *Nature*, *451*, 279–283.

Chapter 5

Citation: Evans, D., Müller, W., Oron, S. & Renema, W. [2013]. Eocene seasonality and seawater alkaline earth reconstruction using shallow-dwelling large benthic foraminifera. *Earth and Planetary Science Letters* **381**:104. doi: 10.1016/j.epsl.2013.08.035.

Includes 17 pages of supplementary material.

Author contributions: DE designed the research in discussion with WM, carried out the analytical work, interpreted the data and wrote the manuscript. WM developed the analytical methodology with DE, aided in the interpretation of the data and edited the manuscript. SO provided live foraminifera from the Gulf of Eilat. WR provided all other Recent and all fossil material and edited the manuscript.

Overlap with previously examined research

Part of this paper appears in an earlier form in the unpublished MSc thesis of *Evans* [2011].

- Figure 2 is a modified version of figure 3.1 from *Evans* [2011].
- Data of Recent foraminifera samples from the Great Barrier Reef and Sulawesi appear in *Evans* [2011] (this represents approximately 25% of the *Operculina* analyses that appear in this paper).
- The majority of the fossil *Nummulites* trace element data were also used in *Evans* [2011].

The interpretation of the data is substantially different from *Evans* [2011], particularly regarding the seasonality estimate and the discussion of the causes of this. Sufficiently more recent samples have been added that the Mg/Ca-temperature calibration can be considered new work. The 2D trace element images of these foraminifera, the interpretation of all data other than Mg/Ca, and the seawater chemistry reconstructions do not form part of *Evans* [2011].

Corrigenda:

- Across lines 11-12 of the left hand column on page 109, the term significant is used to describe the intra-test changes in Mg/Ca in Eocene *N. djokdjokartae*. This term is meant in

its general qualitative sense (i.e. having meaning, being indicative or suggestive of something), and is not meant to imply that these changes have been statistically tested.

- Figure 4 on page 108 shows a Mg/Ca-temperature regression for *Operculina* based on the mean Mg/Ca measurements of all specimens analysed from each sample site. For reference, figure 5.1 is an equivalent plot showing each individual analysis. Performing the Mg/Ca-temperature regression in this way results in the linear relationship $\mathrm{Mg/Ca} = 2.75 \pm 0.63\mathrm{T} + 74.3 \pm 16.9$ (errors are 99% confidence intervals). Note that the slope is (1) significantly different from 0 ($p<0.01$) despite the scatter in the data, and (2) within error of that shown in figure 4 of this paper based on the mean of all data from each location; the regression produced in this way is characterised by m = 2.83 at 25 C.

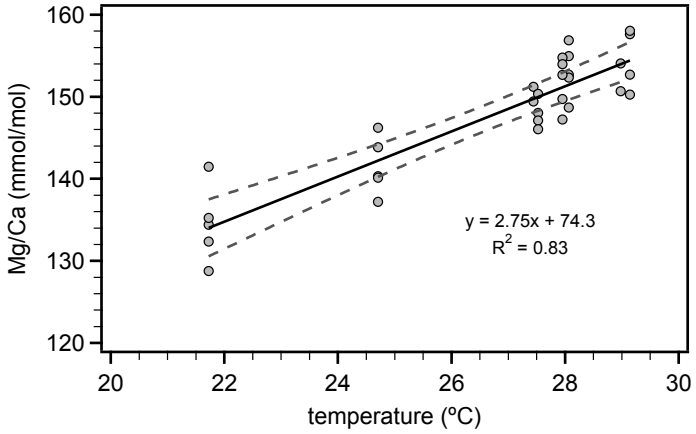

Figure 5.1

Earth and Planetary Science Letters 381 (2013) 104–115

Contents lists available at ScienceDirect

Earth and Planetary Science Letters

www.elsevier.com/locate/epsl

Eocene seasonality and seawater alkaline earth reconstruction using shallow-dwelling large benthic foraminifera

David Evans [a,*], Wolfgang Müller [a], Shai Oron [b,c], Willem Renema [d]

[a] Department of Earth Sciences, Royal Holloway University of London, Egham, TW20 0EX, UK
[b] Department of Geological and Environmental Sciences, Ben-Gurion University of the Negev, Beer-Sheva, Israel
[c] The Interuniversity Institute for Marine Sciences (IUI), Eilat, Israel
[d] Naturalis Biodiversity Center, Leiden, The Netherlands

ARTICLE INFO

Article history:
Received 10 January 2013
Received in revised form 31 July 2013
Accepted 15 August 2013
Available online xxxx
Editor: G. Henderson

Keywords:
large benthic foraminifera
LA-ICPMS
Mg/Ca
Eocene
seasonality
Nummulites
Operculina
deep-time

ABSTRACT

Intra-test variability in Mg/Ca and other (trace) elements within large benthic foraminifera (LBF) of the family Nummulitidae have been investigated using laser-ablation inductively-coupled plasma mass spectrometry (LA-ICPMS). These foraminifera have a longevity and size facilitating seasonal proxy retrieval and a depth distribution similar to 'surface-dwelling' planktic foraminifera. Coupled with their abundance in climatically important periods such as the Paleogene, this means that this family of foraminifera are an important but under-utilised source of palaeoclimatic information. We have calibrated the relationship between Mg/Ca and temperature in modern *Operculina ammonoides* and observe a $\sim 2\%$ increase in Mg/Ca $^{\circ}C^{-1}$. *O. ammonoides* is the nearest living relative of the abundant Eocene genus *Nummulites*, enabling us to reconstruct mid-Eocene tropical sea surface temperature seasonality by applying our calibration to fossil *Nummulites djokdjokartae* from Java. Our results indicate a 5–6 °C annual temperature range, implying greater than modern seasonality in the mid-Eocene (Bartonian). This is consistent with seasonal surface ocean cooling facilitated by enhanced Eocene tropical cyclone-induced upper ocean mixing, as suggested by recent modelling results. Analyses of fossil *N. djokdjokartae* and *Operculina* sp. from the same stratigraphic interval demonstrate that environmental controls on proxy distribution coefficients are the same for these two genera, within error. Using previously published test–seawater alkaline earth metal distribution coefficients derived from an LBF of the same family (Raitzsch et al., 2010) and inorganic calcite, with appropriate correction systematics for secular Mg/Ca_{sw} variation (Evans and Müller, 2012), we use our fossil data to produce a more accurate foraminifera-based Mg/Ca_{sw} reconstruction and an estimate of seawater Sr/Ca. We demonstrate that mid-Eocene Mg/Ca_{sw} was $\lesssim 2$ mol mol^{-1}, which is in contrast to the model most commonly used to correct deep-time Mg/Ca data from foraminifera, but in agreement with most other Paleogene proxy and model data. This indicates that Mg/Ca_{sw} has undergone a substantial (3–4×) rise over the last ~ 40 Ma.

1. Introduction

The trace element chemistry of foraminifera tests is increasingly being used as a palaeoceanic reconstruction tool. Many potential proxies linking test chemistry to palaeoenvironmental information have been developed (see e.g. Katz et al., 2010), which are most commonly applied in the fossil record to either planktic or deep benthic foraminifera (where deep is used here to distinguish these foraminifera from the shallow-dwelling large benthic species under consideration in this study) (e.g. Tripati et al., 2011; Bohaty et al., 2012; Lear et al., 2000). The abundance of foraminifera in sediment cores, along with the widespread distribution of some species (Fraile et al., 2008) has resulted in this group of organisms becoming one of the key sources of palaeoceanic proxy information available (Pearson, 2012).

A disadvantage with the use of planktic foraminifera for palaeoceanic reconstruction is that they are relatively short lived, mineralising over days or weeks (Anderson and Faber, 1984), thus providing a short temporal record of changes in (e.g.) sea surface temperature (SST) (but see Wit et al., 2010). This may be further complicated by migration through the water column during the lifespan of some foraminifera (Eggins et al., 2003) or seasonal bias in biomineralisation (e.g. Jonkers et al., 2010). Seasonality is increasingly being recognised as a key component of climate change (Hollis et al., 2012; Denton et al., 2005; Crowley et al., 1986), although there are a limited amount of studies that have attempted to reconstruct seasonality from periods such as the Paleogene, potentially one of the most important time intervals with respect to similarity to predicted future pCO_2 (Zachos et al., 2008). Much of

* Corresponding author.
E-mail address: david.evans.2007@rhul.ac.uk (D. Evans).

0012-821X/$ – see front matter
http://dx.doi.org/10.1016/j.epsl.2013.08.035

what is currently known is derived from $\delta^{18}O$ measurements in bivalves (e.g. Ivany et al., 2004; Andreasson and Schmitz, 2000; Dutton et al., 2002; Kobashi et al., 2004), which – whilst being an almost unique source of Paleogene ocean seasonality reconstruction – may suffer from biases resulting from freshwater-modified seawater $\delta^{18}O$ in near-coastal environments. Clumped isotope data may offer a solution to this problem (Keating-Bitonti et al., 2011), particularly with improved precision of such measurements.

Reconstructing seawater Mg/Ca (Mg/Ca_{sw}) is of great importance as fossil Mg/Ca data must be corrected for secular changes in this ratio when applying Mg/Ca–temperature calibrations derived from samples grown in or collected from modern seawater. The Cenozoic evolution of Mg/Ca_{sw} has been the subject of considerable debate (e.g. Coggon et al., 2011; Broecker and Yu, 2011; Lear et al., 2002), some of which is the result of uncertainties regarding the appropriate methodology for the correction of foraminiferal Mg/Ca data (summarised in Evans and Müller, 2012). It is clear that in order for the Mg/Ca palaeothermometer to produce accurate pre-Pleistocene palaeotemperatures, further reconstructions of palaeo-Mg/Ca_{sw} are required.

In order to (1) provide a method of seasonality reconstruction other than mollusc $\delta^{18}O$ and (2) produce an accurate foraminifera-derived Mg/Ca_{sw} reconstruction, we have investigated trace element heterogeneity in the tests of large benthic foraminifera (LBF). We utilise laser-ablation inductively-coupled-plasma mass spectrometry (LA-ICPMS) as a highly spatially-resolved technique capable of identifying µm-scale heterogeneity whilst simultaneously assessing sample preservation. LBF are an informal group that typically exceed 3 mm^3 in volume (Ross, 1974) and have photosymbiotic algae (Hallock, 1984), inhabiting the photic zone. We present data from LBF of the family Nummulitidae, with focus on the Eocene genus *Nummulites*, as well as its nearest living relative *Operculina*, which was also present in the Eocene. Our data are primarily derived from *Nummulites* because they are more abundant than *Operculina* and form far larger tests, implying growth over a longer time period, therefore *Nummulites* have greater potential as tools for seasonal palaeoenvironment reconstruction. By comparing Recent *O. ammonoides* and *O. complanata* from seven modern locations to fossil samples of both *Operculina* sp. and *N. djokdjokartae* from the Eocene Nanggulan Formation of Central Java, we demonstrate how these foraminifera can be used as a palaeoceanic reconstruction tool. The size, abundance and (sub)tropical distribution of LBF such as the nummulitids make them a hitherto under-utilised source of proxy information from a climatically critical region of the oceans – the low latitudes – of which our knowledge of palaeocean temperatures is currently limited.

1.1. Ecology and biology of the nummulitids

The main morphological features of the nummulitids (order: Rotaliida) referred to in the text are shown in Fig. 1. The nummulitids are defined by the presence of a marginal cord (Fig. 1), the thickened margin of the shell exposed in an equatorial section (Loeblich and Tappan, 1987). This serves as a method of communication and transport between chambers, as well as playing an important role during sexual reproduction (Röttger et al., 1984). These foraminifera initially construct their chambers with walls consisting of two layers of calcite formed on either side of a primary organic membrane (Reiss, 1958). The test is hyaline, giving well-preserved calcite a glassy appearance.

LBF have a complex reproductive cycle resulting in morphologically distinct generations. Those with a large proloculus and a small number of chambers are known as the macrospheric generation, or A-forms. These reproduce sexually to form a microspheric generation (B-form) with a small proloculus and a large number of chambers (Dettmering et al., 1998; Kuile and Erez, 1991). This generation undergoes multiple fission, producing A-forms. Through this reproductive cycle at least two morphologically distinct generations of the same species are produced.

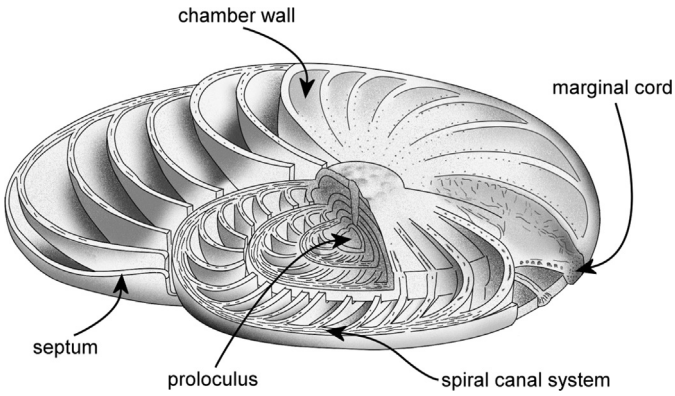

Fig. 1. Cutaway diagram of *O. ammonoides* with features referred to in the text labelled. Re-drawn from Carpenter et al. (1862). Although there are morphological differences between Recent *O. ammonoides* and Eocene *N. djokdjokartae*, all features labelled are present in both genera.

O. ammonoides are epifaunal, prefer sandy substrates and have a peak abundance range of 10–35 m water depth (Renema, 2008, 2006; Renema and Troelstra, 2001) but may live as deep as 130 m in the northernmost Red Sea (Reiss and Hottinger, 1984). This depth range may be related to the less turbid waters of the Gulf of Eilat; the nummulitids are sensitive to high light intensity and live at shallower depths if suspended sediment reduces the extent of the photic zone (Reiss and Hottinger, 1984). *O. complanata* prefers lower light intensities and occurs slightly deeper than *O. ammonoides* (Renema, 2003). Although temperature at the peak abundance depth of *O. ammonoides* may be 1–2 °C below SST, planktic foraminifera such as *Globigerinoides ruber* that are routinely considered to be surface dwelling inhabit a similar range (Anand et al., 2003). Hence, results derived from these LBF can be considered comparable to surface-dwelling planktic foraminifera, with respect to the extent to which these results relate to surface ocean conditions. *O. ammonoides* are limited to areas with minimum SST > 18 °C and are currently found in the Indian and west Pacific Oceans (Langer and Hottinger, 2000).

1.2. Previous LBF proxy development and application

Given the abundance of LBF in geologically and palaeoclimatologically important periods such as the Paleogene it is surprising that there has been relatively little work investigating their use as palaeoenvironmental archives. Wefer and Berger (1980) investigated intra-test stable isotope variability in the Recent LBF *Marginopora vertebralis* and *Cyclorbiculina compressa*. $\delta^{18}O$ microsampled from these foraminifera showed seasonal variation matching instrumental records in both species, demonstrating that these organisms record seasonality along their test growth axis. Recent *O. ammonoides* from the Red Sea precipitate calcite slightly lighter than expected for inorganic calcite (Fermont et al., 1983), although using the *Cibicidoides* $\delta^{18}O$–temperature calibration of Lynch-Stieglitz et al. (1999) and the local $\delta^{18}O_{sw}$ value (1.9‰) yields mean reconstructed temperature virtually identical to measured sea surface temperature (SST). Brasier and Green (1993) and Purton and Brasier (1999) were the first to apply mean $\delta^{18}O$ and stable isotope heterogeneity data from fossil LBF to reconstruct palaeoseasonality and temperature respectively. This work, based on well-preserved Eocene *Nummulites* revealed what the authors interpreted to be seasonal cycles, demonstrating the potential of these organisms for palaeoseasonality reconstruction.

Table 1
Sample site details. MAT is the mean annual sample site temperature with half of the seasonal range in temperature given as an error, with the exception of the Gulf of Eilat for which the November–April mean was used (specimens were collected in early May and have a test size implying growth over ~6 months). The number of specimens analysed from each sample site is also given.

Location	Sample prefix	*n*	Co-ordinates	Water depth (m)	MAT (°C)	Mean Mg/Ca (mmol mol^{-1})	Notes
Recent							
Great Barrier Reef	SS07613	5	19.73°S, 150.22°E	74	24.7 ± 0.8	141.5 ± 7.0	
Spermonde Shelf,	BTE27	5	5.053°S, 119.332°E	27	28.0 ± 0.8	153.1 ± 6.2	See Renema and Troelstra (2001)
SW Sulawesi	KKE30	5	5.106°S, 119.290°E	30	28.0 ± 0.4	151.7 ± 6.3	
Celebes Sea,	BBx25C	2	2.057°N, 118.441°E	53	27.4 ± 0.4	150.3 ± 2.5	See Renema (2006)
NE Kalimantan	BBx49A	4	1.388°N, 118.819°E	48	27.5 ± 0.5	147.9 ± 3.7	
Kepulauan Seribu,	SER	6	5.51–6.00°S,	14–24	29.0 ± 0.5;	155.4 ± 7.9;	See Renema (2008)
Jakarta			106.56–106.83°E		28.9 ± 0.5	153.5 ± 7.3	
Gulf of Eilat, Red Sea	Eil12	8	29.543°N, 34.972°E	10–15	21.9 ± 0.8	136.7 ± 9.3	
Eocene							
Nanggulan, Central Java	KW	26	–	–	–	–	See Lelono (2000)

Even less is known about trace element variation in LBF. Using electron microprobe analysis, Raja et al. (2005) produced the first (and only previous) Mg/Ca–temperature calibration for an LBF species, namely *Marginopora kudakajimaensis*. A Mg/Ca increase of ~3% °C^{-1} was observed, validating the Mg/Ca palaeothermometer in LBF. Raja et al. (2007) demonstrated the need for spatially-resolved analytical techniques when studying LBF; whole test Mg/Ca showed no relationship with temperature.

These studies demonstrate the potential of LBF as palaeoceanic archives and provide a basis for more detailed investigations into intra-test geochemical variability in the nummulitids, with the particular goal of assessing the use of such material in palaeoclimate reconstruction. With this aim we present highly spatially-resolved LA-ICPMS-derived element/Ca maps and profiles of both Eocene and Recent *Nummulites* and *Operculina*.

2. Materials and methods

Recent *O. ammonoides* were hand sampled live from reefs from five locations in Indonesia, the Great Barrier Reef (GBR) and the Gulf of Eilat (see Table 1 for details). In order to assess possible geochemical differences between different nummulitids, *O. complanata* was also collected from one of the sample sites (sample BBx49A from offshore northeast Kalimantan). Temperature data for the purposes of calibration were taken from the nearest available location in the World Ocean Atlas 2009 (Locarnini et al., 2010), with the exception of those from the Gulf of Eilat for which daily SST monitoring was available from the Interuniversity Institute for Marine Sciences in Eilat (http://www.iui-eilat.ac.il). The depth that matched the sampling depth most closely was used. With the exception of the Gulf of Eilat, sample site seasonality is small (maximum 1.6 °C) and therefore the mean annual temperature for each location was used to assess trace element–temperature relationships. For the Gulf of Eilat, the November–April mean was used (see Section 3.2.3).

Eocene *N. djokdjokartae* and *Operculina* sp. were collected from four stratigraphic levels within the Nanggulan Formation, Central Java. The Nanggulan Formation is a sequence of overall deepening upwards marine mudstones, sandstones and conglomeratic sandstones. At the top of the sampled interval the presence of abundant large *Discocyclina* indicates that this stratigraphic level correlates with the middle Bartonian Ta–Tb boundary (see Renema, 2007). Based on this, the samples are considered to be early Bartonian (38–40 Ma). During the mid-Eocene, the palaeolatitude of Central Java was 6°S (Hall, 2002). *N. djokdjokartae* were recovered from sandy beds from all four intervals, *Operculina* from only the lowest of these levels.

N. djokdjokartae were sectioned along the equatorial plane, mounted in epoxy resin and polished to expose the marginal cord. *Operculina* specimens were smaller and were embedded into epoxy without prior sectioning. All samples were cleaned prior to laser-ablation analysis (see the supplementary material for details). The LA-ICPMS system at RHUL features the RESOlution M-50 prototype laser-ablation system (193 nm ArF) coupled to an Agilent 7500ce ICPMS (Müller et al., 2009). Methodology and LA-ICPMS parameters different from those described in Müller et al. (2009) are given in Table S1. Monitored masses were ^{11}B, ^{24}Mg, ^{25}Mg, ^{27}Al, ^{43}Ca, ^{55}Mn, ^{66}Zn, ^{88}Sr, ^{89}Y, ^{138}Ba, ^{139}La, ^{140}Ce and ^{238}U. Eocene marginal cord profiles and mean marginal cord measurements of the Recent samples were obtained by profiling along the exposed marginal cord using a 44 µm laser spot (effective resolution was 120 µm because the 99% cell washout time is ~1.5 s). In order to investigate intra-test trace element variability in greater detail, element maps were created for three Recent *O. ammonoides* from the Gulf of Eilat. The methodology for the production of LA-ICPMS elemental images of these foraminifera is detailed in Evans and Müller (2013).

Eocene seasonal temperature change was reconstructed using the magnitude of long-period Mg/Ca variability along the marginal cord profiles. Because there is considerable fine-scale Mg/Ca heterogeneity in both Eocene and Recent material, the magnitude of Mg/Ca variability was measured from a 20-point running mean, equivalent to an average of 430 µm of marginal cord calcite at a laser scan speed of 50 µm s^{-1} and an ICPMS total dwell time of 0.43 s.

3. Results

3.1. Visual preservation

The tests of Eocene *N. djokdjokartae* appear glassy under optical microscopy. Comparative SEM images of Recent and Eocene material show that the fossil material is not recrystallised, has no secondary calcite overgrowths and that the pores are not infilled (Fig. 2). Features such as the spiral canal system (Figs. 1, 2) are clearly visible in the fossil material, demonstrating that significant recrystallisation of the tests cannot have taken place.

3.2. Geochemistry

Analytical data are available in Tables S3 and S4. Representative comparative Recent *O. ammonoides* and Eocene *N. djokdjokartae* example LA-ICPMS profiles are shown in Fig. 3. Measured element/Ca ratios not plotted are typically homogeneous within the marginal cord, where they are not modified by µm-scale diagenetic alteration.

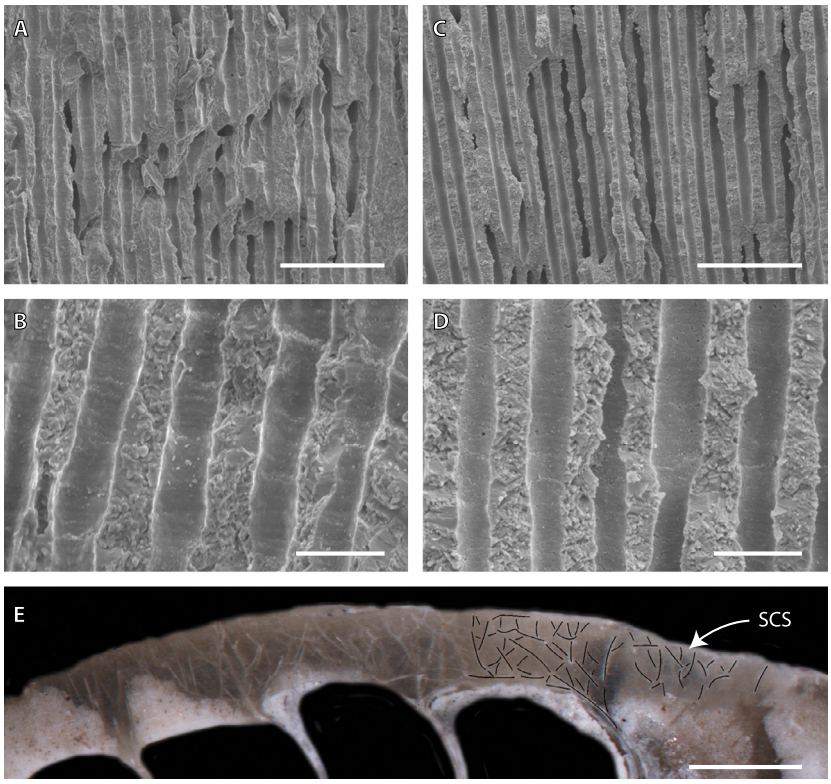

Fig. 2. Comparative SEM images of broken chamber walls of Recent *O. ammonoides* (A, B) and *N. djokdjokartae* (C, D). There is no evidence of secondary calcite overgrowths or recrystallisation of the fossil material. (E) Optical image of part of the marginal chord of an Eocene *N. djokdjokartae* specimen, with the spiral canal system (SCS) clearly visible (overlain with black lines on the right of the image). This demonstrates that significant recrystallisation cannot have taken place. Scale bars 20 μm (A, C), 5 μm (B, D), 500 μm (E).

3.2.1. Geochemical preservation

Certain element/Ca ratios were analysed specifically in order to identify poorly preserved samples, or less well-preserved areas of the tests of visually exceptionally-preserved samples. Al/Ca was used to assess the presence of clay minerals, Mn/Ca, Y/Ca and two rare earth element/Ca (REE/Ca) ratios – La/Ca and Ce/Ca – were used to identify areas affected by secondary calcite mineralisation; secondary calcite is generally expected to have higher Mn/Ca and REE/Ca ratios than the primary foraminiferal calcite (Scherer and Seitz, 1980; Pena et al., 2005). Mean Mn/Ca ratios in the fossil material are 220 μmol mol^{-1}, compared to 4–100 μmol mol^{-1} in Recent *O. ammonoides*, depending on sample site (Fig. S3). Y/Ca and REE/Ca ratios are also 5–10× higher in the fossil material. Al/Ca ratios are comparable in Recent and fossil material, suggesting no clay-mineral contamination.

Occasional portions of approximately half the Recent and Eocene profiles have elevated Al/Ca and Mn/Ca (e.g. Fig. 3, top). These areas (Al–Mn/Ca >1 mmol mol^{-1}) were excluded for the purposes of mean specimen X/Ca calculation and error propagation. Exclusion of small amounts of data in this way does not affect our results which are based on numerous specimens.

3.2.2. Nummulitid Mg/Ca–temperature relationship

Our data demonstrate that, like other foraminifera, Mg/Ca responds systematically to temperature in *O. ammonoides* (Fig. 4). Sample site temperature ranges between 22 °C during winter/spring in the northernmost Gulf of Eilat to 29 °C north of Jakarta Bay.

The resulting Mg/Ca–temperature relationship with 95% confidence intervals is ($n = 32$):

$$\ln(\mathrm{Mg/Ca}) = 0.0198 \pm 0.0012T + 4.47 \pm 0.03 \quad (1)$$

or in linear form:

$$\mathrm{Mg/Ca} = 2.86 \pm 0.44T + 71.4 \pm 11.8 \quad (2)$$

This calibration is based on the mean of all analyses for each of the seven sample sites (see the supplementary information), each analysis itself representing the mean of all data collected from a laser-ablation track following the entirety of the marginal cord of an individual specimen. There are eight data points in Fig. 4 because samples were collected from more than one depth from Kepulauan Seribu, Jakarta. Mg/Ca error bars are ±2SD of the mean of all analyses from each sample site. These error bars are relatively larger than those typical of measurements produced by the bulk analysis (typically ICP-AES) of multiple individuals, because the analysis of whole dissolved tests masks natural sample variability. We report 2SD errors in order to show the degree of individual sample variability but highlight that the error in the slope of our calibration is smaller as it assumes that the mean of each sample set is well known. It is necessary to analyse at least five individual foraminifera using the technique outlined here in order to obtain a representative mean. There is no difference between a linear and exponential approximation of the Mg/Ca data in terms of goodness of fit ($R^2 = 0.977$ and 0.980 respectively), both regressions have gradients amounting to a ∼1.9% increase in Mg/Ca °C^{-1}.

3.2.3. Recent material intra-test and inter-site variability

Of the sampled locations, the Gulf of Eilat has the largest seasonal temperature variation and therefore these samples are expected to show the greatest potential for seasonally varying trace element concentrations. Corresponding element/Ca maps (Fig. 5) show intra-test Mg/Ca variation of ∼25 mmol mol^{-1}. There is no co-variation between the distribution of this Mg/Ca variation and heterogeneity in any other element/Ca ratio (with the exception of Ba/Ca), negating differential cleaning as the product of the observed Mg/Ca variability. These samples were collected in early May and have higher Mg/Ca ratios in the centre, decreasing towards the outer whorls. In the Gulf of Eilat, maximum

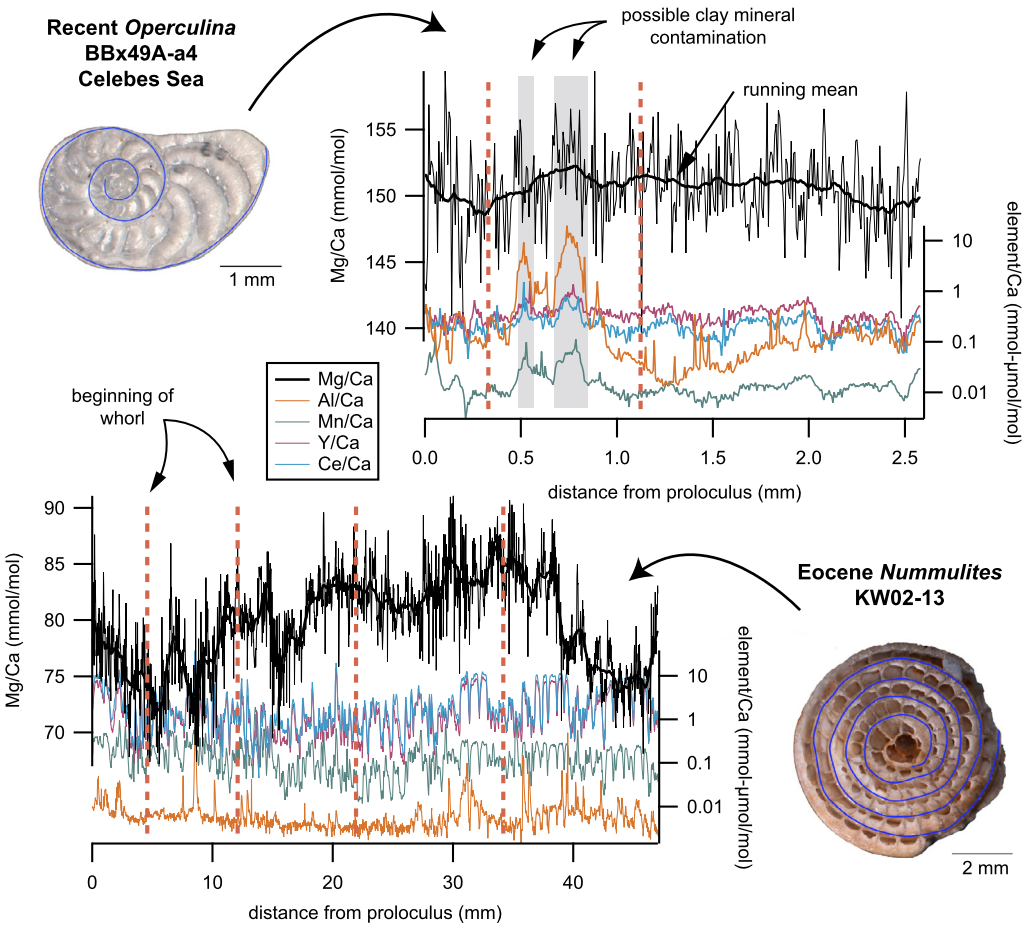

Fig. 3. Representative Mg/Ca (linear scale) and trace element profiles (log scale) of Recent *O. ammonoides* (top) and Eocene *N. djokdjokartae* (bottom). Specimens sectioned for analysis are shown alongside, with ablation paths overlain in blue. Eocene *N. djokdjokartae* show significant long term changes in Mg/Ca (solid black lines) interpreted as being the result of seasonal temperature variation. Trace element ratios used to identify artefacts from the preparation procedure (Al/Ca) or areas affected by diagenesis (Mn–Y–Ce/Ca) are shown.

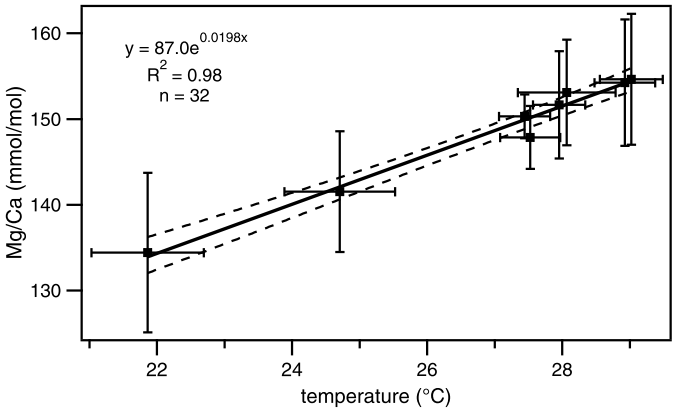

Fig. 4. Mg/Ca–temperature field calibration for *O. ammonoides*. Mg/Ca data are the mean ±2SD of all analyses from each sample location. These errors provide an estimate of uncertainty if only one single specimen were to be analysed. Temperature errors are 2SD of all mean monthly data from the World Ocean Atlas.

summer temperature (~27 °C) occurs during late August, decreasing steadily until the end of the year where temperature remains within 1 °C of 21 °C until May. Assuming a mean growth rate of one chamber per 3–4 days, these specimens lived for up to six months and therefore exhibit intra-test Mg/Ca variability that matches the observed temperature variation remarkably well, providing evidence that seasonal temperature change is recorded via the Mg/Ca ratio of modern LBF tests.

Excluding the Gulf of Eilat, maximum sample site seasonality is 1.6 °C on the Spermonde Shelf (WOA 2009, Locarnini et al., 2010); seasonal Mg/Ca shifts are not expected to be resolvable within these samples. Mg/Ca fluctuation is observed (Fig. 3), although on a scale too fine for temperature to be a viable control of this heterogeneity. The mean Mg/Ca RSD of a single specimen is 5.6%, similar to that reported elsewhere for LBF (Raitzsch et al., 2010). Given the magnitude of this variability, statistically significant long-period Mg/Ca shifts of <5 mmol mol^{-1} are not identifiable and therefore it is not possible to accurately reconstruct seasonal temperature changes of less than 3 °C. With the exception of trace element ratios used to identify diagenesis or contamination, there is little coherent variation within the tests from all locations in any of the other 'proxy' element/Ca ratios. An exception to this is Ba/Ca, which is elevated in samples from the Gulf of Eilat compared to the other Recent sample sites, and appears to be anti-correlated with Mg/Ca (Fig. 5).

3.2.4. Eocene intra- and inter-test variability

Fine-scale trace element heterogeneity, assessed by single specimen standard deviations, are similar in Eocene and Recent material. *N. djokdjokartae* fine-scale Mg/Ca heterogeneity is within the range observed in Recent *O. ammonoides* precluding this being a diagenetic feature. A plot of the mean of all proxy element/Ca measurements from coexisting Eocene *N. djokdjokartae* and *Operculina* sp. shows no significant deviation from a 1:1 line for B, Mg, Zn and Sr (Fig. S4), suggesting that the distribution coefficients for

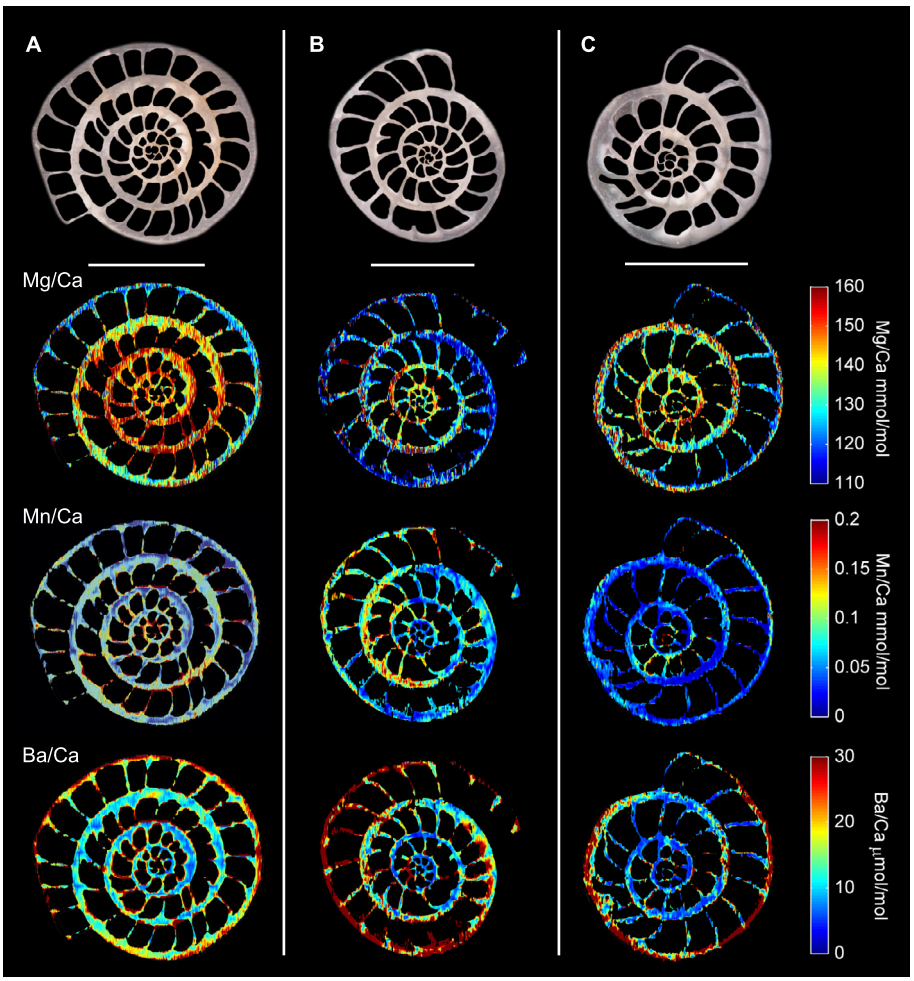

Fig. 5. LA-ICPMS maps for three modern *O. ammonoides* specimens from the Gulf of Eilat (top). All specimens show consistent and coherent Mg/Ca variability, implying first chamber growth beginning during a warmer period with subsequent chambers mineralised as temperature decreased, consistent with the date of collection (see text for details). Ba/Ca is anti-correlated with Mg/Ca, possibly as a result of winter upwelling. Scale bars 1 mm.

the trace elements under discussion here are the same or similar in both foraminifera.

Eocene samples have substantially lower Mg/Ca than Recent LBF. *N. djokdjokartae* and *Operculina* sp. have mean ±2SD Mg/Ca ratios of 86.4 ± 13.2 ($n = 20$) and 82.3 ± 4.8 ($n = 6$) respectively. Given the excellent preservation of these samples, the lower ratios are most parsimoniously explained as being a function of lower Eocene seawater Mg/Ca (Mg/Ca_{sw}), which exerts a control on foraminifera Mg/Ca at least as great as temperature (Evans and Müller, 2012; Segev and Erez, 2006), see Section 4.2. Eocene *N. djokdjokartae* specimens are characterised by the presence of significant long-period changes in Mg/Ca, manifest as 10 mmol mol^{-1} shifts in marginal cord laser-ablation profiles and present in the majority of the specimens analysed. Typical profiles are shown in Fig. 6. The period of these approximately sinusoidal curves is consistent between specimens and is the same for both A- and B-forms.

N. djokdjokartae are not perfectly flat in the equatorial plane; the shape of these foraminifera is more appropriately described as a parabolic hyperboloid. Consequently it is very difficult to produce an equatorial section that exposes only the marginal cord. The example Eocene profile of Fig. 3 shows rapid fluctuations in Mn–Y–Ce/Ca (and to a lesser extent Al/Ca) by an order of magnitude, particularly between 30–40 mm. Such areas are those where the marginal cord is not exposed, the rapid changes represent the difference between the non-porous septal calcite and the perforate chamber wall, which have higher and lower Mn/Ca and Y–Ce/Ca ratios respectively. This is not observed in Mg, B or Sr, which demonstrates that our mean marginal cord measurements are not biased by this unavoidable sample preparation problem. However, it is possible that switching between the marginal cord, septa and chamber wall may explain some of the minor irregularities in the Mg/Ca profiles, as these three parts of the test are likely to have calcified at slightly different times and therefore at potentially different temperatures.

Sr/Ca and Ba/Ca are similar between Eocene *N. djokdjokartae* and Recent *O. ammonoides*. Comparative means of all analyses are 2.39 ± 0.39 and 2.44 ± 0.27 mmol mol^{-1} respectively for Sr/Ca and 2.90 ± 0.37 and 3.06 ± 1.1 for Ba/Ca.

4. Discussion

The 1.9% increase in Mg/Ca per degree temperature change found here is comparable to the 3.1% observed by Raja et al. (2005) for the LBF *Marginopora kudakajimaensis* insofar as both species are characterised by a far smaller gradient than planktic species (typically ∼10%). The exponential component of this calibration is almost identical to that for inorganic calcite (Mucci, 1987; Burton and Walter, 1991) and the slope is similar to the Mg/Ca–temperature calibration of Burton and Walter (1991) at modern (late 20th century) pCO_2 (1.7% °C^{-1}). Whilst both linear and exponential regressions are equally applicable over the

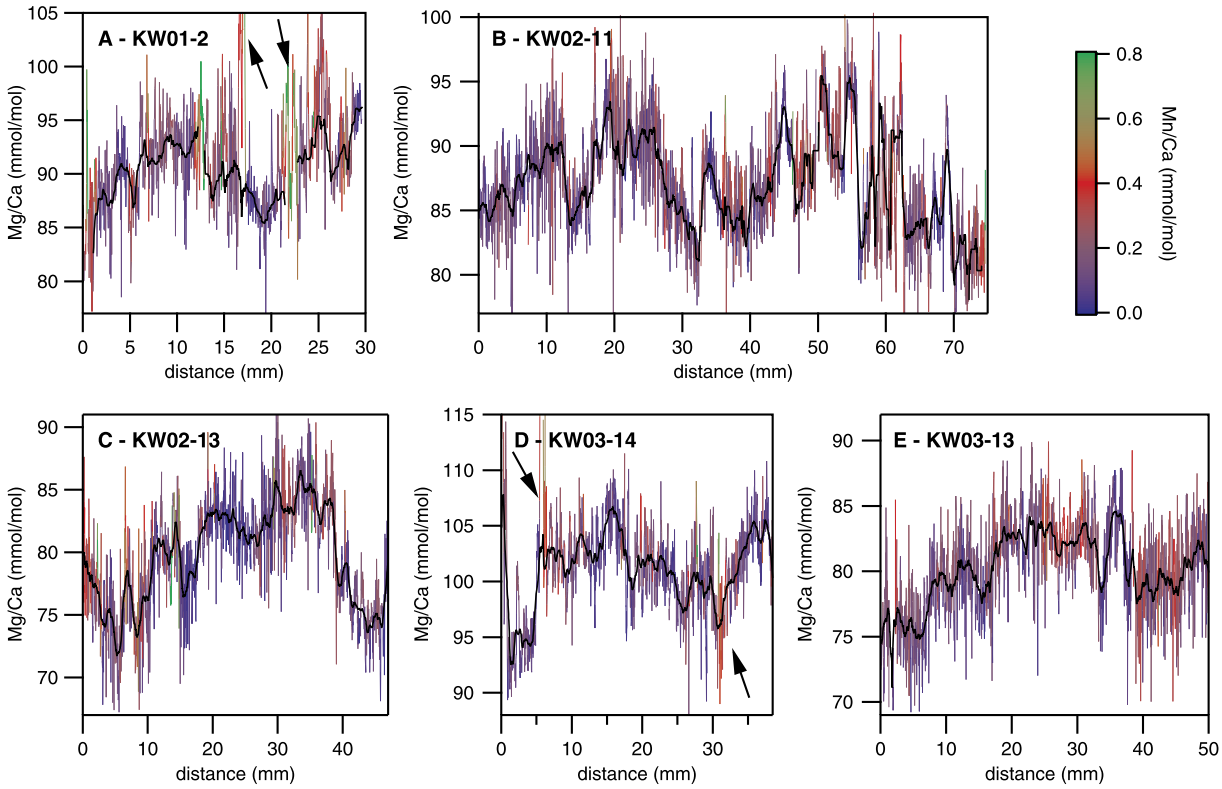

Fig. 6. Representative Eocene *N. djokdjokartae* Mg/Ca marginal cord profiles showing significant quasi-periodic shifts. Thick black lines are 40-point running means. Unsmoothed data colour is shown as a function of Mn/Ca, demonstrating that anomalous or noisy portions of the Mg/Ca profiles are explicable by minor diagenesis, highlighted with arrows.

sampled temperature range, we base our further discussions on the exponential best-fit only because it is not possible to calculate palaeoseasonality using a linear calibration without prior knowledge of Mg/Ca_{sw}. This is because, unlike an exponential relationship between temperature and Mg/Ca, the difference between two Mg/Ca-derived temperature reconstructions (i.e. those derived from maximum and minimum Mg/Ca_{test}) is not constant as Mg/Ca_{sw} varies (see the supplementary material).

The relationship between Mg/Ca and temperature reported here is biased towards sample sites with mean annual SST in the range 27–29 °C. However, four geographically distinct sample sites (BTE27, KKE30, BBx25C, BBx49A – see Table 1) exhibit a temperature range of just 0.6 °C but are otherwise hydrographically different (e.g. in terms of seasonal salinity variation). Therefore these samples provide a good test of Mg/Ca repeatability when environmental factors other than temperature are not the same. The mean of all measurements of samples from these locations exhibit a Mg/Ca range of 3.5%, of which one third is explicable as a result of temperature, leaving a residual variation of just 2.3%, which is similar to the achievable precision of these measurements (1.6%). This consistency of results implies that our data accurately represent the shape of the Mg/Ca–temperature curve and demonstrates that the addition of further temperature points is unlikely to significantly alter the shape of the curve over the studied temperature range, because the mean of all measurements from these four samples are essentially identical even though they are from waters with different physical (and possibly chemical) properties. Furthermore, because the nummulitids have a lower temperature tolerance of ~ 18 °C, and are therefore applicable as environmental indicators to the palaeo low-mid latitudes, the temperature range covered here provides a basis for palaeoenvironment reconstruction in the (sub)tropics.

4.1. Eocene seasonality

Palaeoseasonality can be estimated using the fraction difference between the minimum and maximum Mg/Ca ratios in the Eocene *N. djokdjokartae*, coupled with the gradient of Eq. (1). The Mg/Ca curves are consistent in that virtually all show amplitudes of ~ 10 mmol mol^{-1}, which is equivalent to a seasonality of 5–6 °C. Present day seasonality on the southeast Java coast is 4 °C due to August to October upwelling associated with a temperature drop to 26.5 °C from a summer maximum of 30.5 °C when the Indonesian throughflow dominates SST (Hendiarti et al., 2004). Reconstructed Eocene palaeoseasonality is greater than any open ocean tropical seasonality at the present day and 50% greater than upwelling-induced seasonal temperature change on the modern Java coast, either implying enhanced middle-Eocene temperature seasonality or a greater degree of seasonal upwelling at this location. The lower Ba/Ca of the Eocene samples compared to Recent *O. ammonoides* from the Gulf of Eilat may imply that enhanced upwelling cannot explain the greater than modern seasonality reconstruction, given that elevated seawater Ba/Ca is associated with upwelling (e.g. Lea et al., 1989) and seawater Ba/Ca is recorded in foraminiferal calcite (Hönisch et al., 2011), which is also suggested by our laser-ablation Ba/Ca maps (Fig. 5).

The amplitude of reconstructed seasonality from these Mg/Ca profiles is (to an extent) dependent upon the degree of smoothing applied (Fig. S6). We use a 40-point running mean (Fig. 6) as this was found to remove outliers and artificial variation from the fine-scale Mg/Ca variability present in both Recent and Eocene nummulitids (±5 mmol mol^{-1}), without dampening temperature-controlled Mg/Ca variation.

Seasonal temperature variation decreases with water depth, therefore it is possible that our reconstruction is an under-estimate of seasonality if the habitat of *N. djokdjokartae* is towards the lower extreme of that of Recent *O. ammonoides*. In the modern Gulf of

Eilat, seasonal temperature range decreases approximately linearly at the rate of 1 °C 40 m^{-1} over the top 100 m of the water-column. However, the relatively coarse grain size of the sampled stratigraphic horizons (see the supplementary information) suggests high palaeo-turbidity, implying (by analogy to their nearest living relative) a shallow peak abundance depth for these fossil samples and therefore a representative estimate of the surface annual amplitude of temperature variation.

Some of the profiles in Fig. 6 show (occasional) sharp jumps in Mg/Ca (e.g. profile B at ~35 mm; profile D at ~7 mm) that may suggest discontinuous growth in some specimens. Whilst this potentially accounts for the deviation of some of these profiles from a sinusoidal Mg/Ca curve, it seems improbable that seasonality reconstructions are biased by growth cessation as there is no coherent pattern in the position of these features; they do not all occur at Mg/Ca minima. Instead, it is more likely that these shifts are the combined result of minor µm-scale diagenesis (e.g. profile A at ~23 mm) and the precise positioning of the laser-ablation tracks. The trace element images of Recent *O. ammonoides* (Fig. 5) also show occasional sharp changes in Mg/Ca, despite overall coherence in Mg incorporation.

The elevated Mn–REE/Ca ratios of the fossil material is unlikely to bias our seasonality reconstruction or any of the fossil proxy trace element data. There is no correlation between any of the diagenesis indicators and proxy trace element ratios with the exception of U/Ca–Y/Ca (Fig. S3), both within and between specimens. Furthermore, there is no correlation between any of the diagenesis indicators and proxy trace element ratios and all ratios measured for purposes other than to assess diagenesis are within the range of those in Recent *O. ammonoides*, with the exception of Zn/Ca. If all of the excess Mn in the fossil samples is attributed to kutnahorite ($Ca(Mn,Mg,Fe)(CO_3)_2$, an identified secondary carbonate contaminant phase in foraminifera, see Pena et al., 2005), then simple mass-balance calculations would indicate that the resulting worst case Mg/Ca bias would be 0.9%, which is non-resolvable given that analytical accuracy is ~2%.

A further feature of these profiles is that there is a relatively large range in mean test Mg/Ca. For example, profiles A and B (Fig. 6) have mean Mg/Ca ≈ 90 mmol mol^{-1} whereas C and E have mean Mg/Ca ≈ 80 mmol mol^{-1}. Similar natural variation is observed within the Recent *O. ammonoides* populations (e.g. samples from the Gulf of Eilat have a range in mean marginal cord Mg/Ca values of 129–142 mmol mol^{-1}), therefore this feature of the fossil data is not unexpected and analysis of several individuals ($\geqslant 5$) is necessary in order to produce a representative mean (see also Sadekov et al., 2008). However, the magnitude of long period intra-test Mg/Ca variability is consistent between all samples.

Our seasonality estimate is similar to previous Eocene reconstructions from both the Gulf of Guinea (Andreasson and Schmitz, 1998) and Panama (Tripati and Zachos, 2002), to our knowledge the only other estimates of early-mid Cenozoic tropical palaeoseasonality. Andreasson and Schmitz (1998) invoked upwelling as the reason for large $\delta^{18}O$ shifts in molluscan aragonite, whereas the $^{87}Sr/^{86}Sr$ data of Tripati and Zachos (2002) (also micro-sampled mollusc-derived) suggest some bias by freshwater input. It is important to understand the extent to which our seasonality estimate is controlled by other factors, given that there is no current estimate of Eocene palaeoseasonality unequivocally from an area unaffected by coastal processes. The concentration of Mg and Ca in seawater is substantially higher than average global river water; consequently it is not possible to modify seawater Mg/Ca by mixing with freshwater within the salinity tolerance of foraminifera (mixing 60% freshwater with 40% seawater results in a < 5% decrease in solution Mg/Ca but a ~20‰ salinity reduction, depending on exact freshwater composition). This is in contrast to seawater $\delta^{18}O$ which can be easily modified in coastal proximal environments. Therefore, our estimate does not suffer from this potential bias. Whilst it has been shown that high salinity environments can modify foraminifera Mg/Ca (e.g. Arbuszewski et al., 2010; Hoogakker et al., 2009), there is no palaeogeographic evidence that this should be the case for our fossil samples which lived in an open shallow sea to the south of a landmass comprising present day west Borneo, northwest Java and Sumatra (Hall, 2009).

Our seasonality reconstruction implies that at least one surface ocean location was characterised by higher magnitude seasonal temperature changes during the mid-Eocene compared to the present. Whilst recent clumped isotope measurements of palaeosols and molluscs suggest that Eocene continental interiors were not as equable as previously thought (Snell et al., 2013), there is limited proxy evidence that would imply a greater than present day surface ocean seasonality. Interpretation of our data is dependent upon the cause of the greater reconstructed seasonality; more vigorous Eocene upwelling on the southernmost Sunda Shelf would require a different mechanism to increased seasonality related to (for example) seasonal shifts in the position of ocean currents. We therefore discuss our results both with and without increased upwelling as the fundamental cause of the greater than present reconstructed annual temperature shift.

Whilst our Eocene Ba/Ca analyses do not provide evidence for upwelling at this fossil site, it is possible that it is not evident in our data. Analysis of coeval bivalves could provide a method of testing this, as Ba/Ca in some bivalve shells has been shown to be a sensitive indicator of chlorophyll concentration which may in turn relate to seasonal upwelling (Elliot et al., 2009). Reduced Eocene equator to pole SST temperature gradients may have resulted in broadly weaker Hadley Cell circulation and lower zonal wind speed (Sloan and Rea, 1995; Vecchi and Soden, 2007), which may result in a decrease in the vigour and frequency of tropical upwelling. However, there is strong proxy and model evidence for a link between increased atmospheric CO_2 and the intensity of tropical cyclones (e.g. Schmitz and Pujalte, 2007; Oouchi et al., 2006) which also has the effect of reducing SST through thermocline mixing (Price, 1981; Sriver and Huber, 2007). Furthermore, slow-moving hurricanes may directly cause coastal upwelling (Shi and Wang, 2007). Both of these closely related mechanisms can explain our greater than present day seasonality estimate, particularly because the depth over which modelled hurricane-forced upper ocean mixing occurs significantly increases at higher atmospheric CO_2 (Korty et al., 2008), which in turn leads to greater surface ocean cooling during any given event. If this was the case for southeast Asia during the mid-Eocene, these relatively sudden events may also explain the deviation of our Mg/Ca profiles from smooth curves.

Alternative explanations for increased Eocene seasonality that do not invoke upwelling may come from seasonal shifts in ocean currents. There is recent model evidence for anticyclonic gyres in the Eocene Indian Ocean during the northern hemisphere winter, which would result in seaward directed ocean mass transport on the southern Asian shelf (Huber and Goldner, 2012; Winguth et al., 2010). This was not observed during the northern hemisphere summer and may provide a mechanism for greater Eocene seasonal temperature change in this region if this current carried cooler water, or itself induced upwelling in the region. Finally, a smaller mid-Eocene obliquity compared to the present day would result in greater seasonally variable incoming shortwave radiation (Heinemann et al., 2009), however this cannot account for seasonal temperature shifts of the magnitude which we reconstruct.

Deep-time surface ocean seasonality reconstructions are of insufficient spatial coverage to place accurate constraints on Eocene climate dynamics. However, given that there is evidence for increased seasonality during periods of global cooling (e.g. Ivany

et al., 2000), it seems more likely that the explanation for our reconstructed seasonality lies in dynamic events such as cyclone-induced thermocline mixing rather than resulting from an implied link between higher temperature (and/or pCO_2), and tropical ocean seasonality. Whilst our Eocene Ba/Ca data do not prove that upwelling was an important process at this time, mixing of the upper ~200 m of the water column (as implied by Winguth et al., 2010) may not necessarily result in greatly increased surface seawater Ba/Ca.

4.2. Implications for palaeoseawater Mg/Ca and Sr/Ca

Previous studies attempting to reconstruct Mg/Ca_{sw} using foraminifera have produced results that are in poor agreement with virtually all other proxy evidence and model-derived results (Coggon et al., 2011). This is a consequence of assuming a linear relationship between test and seawater Mg/Ca; laboratory culture calibrations have demonstrated that Mg/Ca_{test} variation with Mg/Ca_{sw} is best described by a power regression (summarised in Evans and Müller, 2012). An appropriate equation to use when reconstructing palaeo-Mg/Ca_{sw} is:

$$Mg/Ca_{sw}^{t=t} = \sqrt[H]{\frac{Mg/Ca_{test}^{t=t} \times Mg/Ca_{sw}^{t=0\,H}}{B\exp^{AT}}} \quad (3)$$

where $t=0$ is the present day and $t=t$ is some point in the past. H is the power component of a seawater-test Mg/Ca calibration (Ries, 2004; Hasiuk and Lohmann, 2010; Evans and Müller, 2012) and B and A are constants to be defined for a specific species or group of species.

In order to reconstruct seawater Mg/Ca from fossil data, the power relationship between test and seawater Mg/Ca (H) must be known. We provide a reconstruction based on (1) the inorganic calibration of Mucci and Morse (1983) and (2) the relationship between test and seawater Mg/Ca which has been calibrated in *Heterostegina depressa*, a closely related nummulitid (Raitzsch et al., 2010). Because our fossil *N. djokdjokartae* and *Operculina* sp. have, within error, identical proxy X/Ca ratios the Mg/Ca–temperature and test–seawater Mg–Sr/Ca relationships of the two genera must be similar, as it would be highly coincidental if the hypothetically different Mg/Ca–temperature responses of the two species crossed at the palaeotemperature of the fossil sample site. The application of calibrations based on Recent *O. ammonoides* to measurements of fossil *N. djokdjokartae* is therefore justified. The value of H that Raitzsch et al. (2010) derive for *H. depressa* may be more applicable, given that we demonstrate above that trace element distribution coefficients are the same within error for all nummulitids analysed, however this calibration was carried out over a narrow range of Mg/Ca_{sw} values and is not well constrained between 1–3 mol mol^{-1}. The inorganic value of H may be appropriate when reconstructing Mg/Ca_{sw} utilising these samples because of the similarity between our Mg/Ca–temperature calibration and those of inorganic calcite. Whichever value of H is used, we use an appropriate correction technique with defined test–seawater chemistry relationships and our data therefore yield a more reliable estimate of alkaline earth palaeoseawater chemistry based on foraminifera.

In order to reconstruct Mg/Ca_{sw} using Eq. (3) some constraint of palaeotemperature is required (or vice versa). In order to demonstrate the extent to which foraminifera-derived Mg/Ca_{sw} has previously been over-estimated, we plot a range of potential values based on a temperature range of 25–35 °C, equivalent to assuming the palaeotemperature of the sample site is similar to or greater than present day tropical ocean temperatures, with an upper bound defined by the addition of a realistic error to the maximum reconstructed Eocene $\delta^{18}O$-derived temperature (Pearson et al., 2007). Reconstructed Mg/Ca_{sw} (Fig. 7) ranges

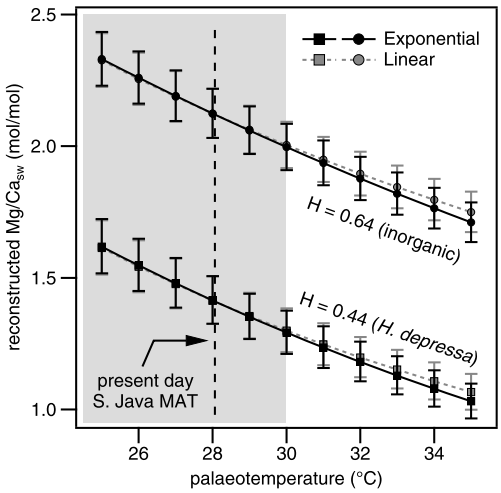

Fig. 7. Mg/Ca_{sw} reconstruction based on the calibrated relationship between Mg/Ca and temperature given in this study and the Mg/Ca_{sw}–Mg/Ca_{test} calibrations of Raitzsch et al. (2010) and Mucci and Morse (1983), for a range of palaeotemperature assumptions for Java at 39 Ma. The present range of modern tropical mean annual sea surface temperature (MASST) (shaded region) and the current MASST off the south Java coast are shown for comparison. The exponential and linear series relate to the format of the Mg/Ca–temperature regression.

from 1.0–1.8 mol mol^{-1} based on the value of H for *H. depressa* (Raitzsch et al., 2010) or 1.6–2.2 mol mol^{-1} based on that of inorganic calcite (Mucci and Morse, 1983). This range includes uncertainty in the mean *N. djokdjokartae* Mg/Ca_{test} value over the entire temperature range. We thereby demonstrate that Mg/Ca_{sw} at ~39 Ma was below or close to 2 mol mol^{-1}, in good agreement with the majority of model and proxy evidence suggesting relatively low Paleogene values (e.g. Stanley and Hardie, 1998; Coggon et al., 2010). This contrasts previous foraminifera-based constraints of palaeo-Mg/Ca_{sw} (Broecker and Yu, 2011; Lear et al., 2002), which are inaccurate because they are based on the assumption that Mg/Ca_{test} varies linearly with Mg/Ca_{sw} (Evans and Müller, 2012). Based on this, it seems probable that Mg/Ca_{sw} has undergone a 2.5–4× increase over the last 40 Ma, although the question regarding the mechanisms for such a relatively large change remains.

Reconstruction of Sr/Ca_{sw} is in some respects less complicated than Mg/Ca_{sw} because the Sr distribution coefficient (D_{Sr}) does not vary with Sr/Ca_{sw} (Raitzsch et al., 2010). However, a $Mg/Ca_{calcite}$ control on $Sr/Ca_{calcite}$ has been demonstrated by Mucci and Morse (1983), which must be taken into account when reconstructing Sr/Ca_{sw} using LBF as these foraminifera exhibit a large range in test Mg/Ca. Mucci and Morse (1983) find a linear relationship between Sr/Ca and Mg/Ca (at constant solution [Sr]), amounting to a 0.010 mmol mol^{-1} increase in Sr/Ca per 1 mmol mol^{-1} increase in Mg/Ca. We apply this correction to our fossil data (characterised by Mg/Ca_{test} ~60 mmol mol^{-1} lower than our Recent samples), which amounts to an upwards shift of our measured Eocene Sr/Ca ratios by 0.67 mmol mol^{-1}. This method assumes that the inorganic calcite calibration of Mucci and Morse (1983) is applicable to the nummulitids, which may be reasonable given similar Mg incorporation in nummulitid and inorganic calcite.

The D_{Sr} of *O. ammonoides* is 0.26 derived from our data, which is in close agreement with that of *H. depressa*, (D_{Sr} = 0.28, Raitzsch et al., 2010). Using our value for D_{Sr} results in reconstructed Sr/Ca_{sw} at 39 Ma of 10.4 and 10.9 mmol mol^{-1} derived from Eocene *N. djokdjokartae* and *O. ammonoides* respectively, compared to a modern day ratio of 8.5 mmol mol^{-1}. This estimate would be 1.5 mmol mol^{-1} lower if no correction is applied for the difference between Eocene and Recent Mg/Ca_{test}.

There is significant disagreement between previous Sr/Ca_{sw} reconstructions. Data from ridge-flank vein carbonates suggests Cenozoic values as low as ~ 2 mmol mol^{-1} (Coggon et al., 2010) whereas analyses of deep benthic foraminifera broadly suggest a slight (1–2 mmol mol^{-1}) increase over the last 50 Ma (Lear et al., 2003). Tripati et al. (2009) and Sosdian et al. (2012) reconstructed Sr/Ca_{sw} in the range 11–18 mmol mol^{-1} and 10–14 mmol mol^{-1} for the period 38–64 and 0–40 Ma respectively, based on gastropod aragonite. An in-depth discussion of the reasons for the differences between these studies is beyond the scope of this contribution (see Sosdian et al., 2012 for a recent synthesis). However our reconstruction is in broad agreement with the studies of Sosdian et al. (2012), Lear et al. (2003) and Tripati et al. (2009) for samples of an equivalent age. Support for a middle Eocene value in this range (7.2–7.9 mmol mol^{-1} for 47–51 Ma) is also provided by Balter et al. (2011), who analysed the Sr/Ca ratio of shark and ray tooth enamel. Coupled with the data presented here, these independent Sr/Ca_{sw} reconstructions based on a variety of organisms converge on a mid-Eocene value within $\sim \pm 20\%$ of present day.

5. Conclusion

Large benthic foraminifera are an important and widespread component of shallow marine ecosystems. The abundance of large genera in climatically important periods such as the early-mid Paleogene means that this group of foraminifera have excellent potential for palaeoceanic reconstruction. Mean Mg/Ca measurements of sectioned Recent foraminifera of the genus *Operculina* demonstrate a systematic relationship with temperature. Laser-ablation-derived element/Ca maps show that intra-test variation in Mg/Ca responds as expected to seasonal sample site temperature variation, demonstrating that this group of organisms can be used as an alternative to molluscs for palaeoseasonality reconstruction. We apply this technique to fossil *N. djokdjokartae* from a mid-Eocene succession in Java and show that this site was characterised by 5–6 °C seasonal temperature shifts, > 2 °C higher than the equivalent present day location. The fossil sample site contains coeval *Operculina* sp., enabling us to demonstrate that different nummulitids have equivalent alkaline earth/Ca ratios, validating the application of *O. ammonoides*-derived calibrations to Paleogene *Nummulites*.

Furthermore, because a calibration between seawater Mg/Ca and test Mg/Ca has already been carried out for a foraminifer from the same family (Raitzsch et al., 2010), coupled with an improved understanding of foraminiferal Mg/Ca systematics (Evans and Müller, 2012) our fossil Mg/Ca data enable us to produce a more accurate estimate of palaeoseawater Mg/Ca using foraminifera. We demonstrate that Mg/Ca_{sw} at ~ 39 Ma was close to or below 2 mol mol^{-1}, in agreement with most other proxy and model estimates for the Paleogene but in contrast to the relatively high values implied by the model of Wilkinson and Algeo (1989). This is important because this model has most commonly been applied to fossil samples when correcting for secular change in Mg/Ca_{sw}. The reconciliation of foraminiferal Mg/Ca with other lines of Mg/Ca_{sw} proxy evidence should mark a shift in the debate regarding the chemical evolution of the oceans and the use of proxy Mg/Ca_{sw} data in the production of more accurate Mg/Ca-derived pre-Pleistocene palaeotemperatures.

Acknowledgements

D.E. acknowledges a NERC postgraduate studentship at Royal Holloway University of London. We are grateful to Jonathan Erez and Yair Rosenthal for insightful discussions, and Alex Ball (NHM London) for help with SEM imaging. We are indebted to three anonymous reviewers for providing detailed comments which have significantly improved this contribution.

Appendix A. Supplementary material

Supplementary material related to this article can be found online at http://dx.doi.org/10.1016/j.epsl.2013.08.035.

References

Anand, P., Elderfield, H., Conte, M., 2003. Calibration of Mg/Ca thermometry in planktonic foraminifera from a sediment trap time series. Paleoceanography 18, 28–31.

Anderson, O., Faber, W., 1984. An estimation of calcium carbonate deposition rate in a planktonic foraminifer *Globigerinoides sacculifer* using ^{45}Ca as a tracer: A recommended procedure for improved accuracy. J. Foraminiferal Res. 14, 303–308.

Andreasson, F., Schmitz, B., 1998. Tropical Atlantic seasonal dynamics in the early middle Eocene from stable oxygen and carbon isotope profiles of mollusk shells. Paleoceanography 13, 183–192.

Andreasson, F.P., Schmitz, B., 2000. Temperature seasonality in the early middle Eocene North Atlantic region: Evidence from stable isotope profiles of marine gastropod shells. Geol. Soc. Am. Bull. 112, 628–640.

Arbuszewski, J., Demenocal, P., Kaplan, A., Farmer, E., 2010. On the fidelity of shell-derived $\delta^{18}O_{seawater}$ estimates. Earth Planet. Sci. Lett. 300, 185–196.

Balter, V., Lécuyer, C., Barrat, J., 2011. Reconstructing seawater Sr/Ca during the last 70 My using fossil fish tooth enamel. Palaeogeogr. Palaeoclimatol. Palaeoecol. 310, 133–138.

Bohaty, S.M., Zachos, J.C., Delaney, M.L., 2012. Foraminiferal Mg/Ca evidence for Southern Ocean cooling across the Eocene–Oligocene transition. Earth Planet. Sci. Lett. 317, 251–261.

Brasier, M., Green, O., 1993. Winners and losers: Stable isotopes and microhabitats of living Archaiadae and Eocene *Nummulites* (larger foraminifera). Marine Micropaleontology 20, 267–276.

Broecker, W., Yu, J., 2011. What do we know about the evolution of Mg to Ca ratios in seawater? Paleoceanography 26, PA3203.

Burton, E.A., Walter, L.M., 1991. The effects of pCO_2 and temperature on magnesium incorporation in calcite in seawater and $MgCl_2$–$CaCl_2$ solutions. Geochim. Cosmochim. Acta 55, 777–785.

Carpenter, W., Parker, W., Jones, T., 1862. Introduction to the Study of the Foraminifera. Piccadilly, London. Published for the Ray society by R. Hardwicke.

Coggon, R., Teagle, D., Smith-Duque, C., Alt, J., Cooper, M., 2010. Reconstructing past seawater Mg/Ca and Sr/Ca from mid-ocean ridge flank calcium carbonate veins. Science 327, 1114–1117.

Coggon, R., Teagle, D., Jones, T., 2011. Comment on "What do we know about the evolution of Mg to Ca ratios in seawater?" by Wally Broecker and Jimin Yu. Paleoceanography 26, PA3224.

Crowley, T., Short, D., North, G., Mengel, J., 1986. Role of seasonality in the evolution of climate during the last 100 million years. Science 231, 579–584.

Denton, G., Alley, R., Comer, G., Broecker, W., 2005. The role of seasonality in abrupt climate change. Quat. Sci. Rev. 24, 1159–1182.

Dettmering, C., Hohenegger, J., Schmaljohann, R., 1998. The trimorphic life cycle in foraminifera: Observations from cultures allow new evaluation. Eur. J. Protistol. 34, 363–367.

Dutton, A., Lohmann, K., Zinsmeister, W., 2002. Stable isotope and minor element proxies for Eocene climate of Seymour Island, Antarctica. Paleoceanography 17.

Eggins, S., De Deckker, P., Marshall, J., 2003. Mg/Ca variation in planktonic foraminifera tests: Implications for reconstructing palaeo-seawater temperature and habitat migration. Earth Planet. Sci. Lett. 212, 291–306.

Elliot, M., Welsh, K., Chilcott, C., McCulloch, M., Chappell, J., Ayling, B., 2009. Profiles of trace elements and stable isotopes derived from giant long-lived *Tridacna gigas* bivalves: Potential applications in paleoclimate studies. Palaeogeogr. Palaeoclimatol. Palaeoecol. 280, 132–142.

Evans, D., Müller, W., 2012. Deep time foraminifera Mg/Ca paleothermometry: Nonlinear correction for secular change in seawater Mg/Ca. Paleoceanography 27, PA4205.

Evans, D., Müller, W., 2013. LA-ICPMS elemental imaging of complex discontinuous carbonates: An example using large benthic foraminifera. J. Anal. At. Spectrom. 28, 1039–1044.

Fermont, W., Kreulen, R., Van der Zwaan, G., 1983. Morphology and stable isotopes as indicators of productivity and feeding patterns in recent *Operculina ammonoides* (Gronovius). J. Foraminiferal Res. 13, 122–128.

Fraile, I., Schulz, M., Mulitza, S., Kucera, M., 2008. Predicting the global distribution of planktonic foraminifera using a dynamic ecosystem model. Biogeosciences 5, 891–911.

Hall, R., 2002. Cenozoic geological and plate tectonic evolution of SE Asia and the SW Pacific: Computer-based reconstructions, model and animations. J. Asian Earth Sci. 20, 353–431.

Hall, R., 2009. Southeast Asia's changing palaeogeography. Blumea 54, 148–161.
Hallock, P., 1984. Distribution of selected species of living algal symbiont-bearing foraminifera on two Pacific coral reefs. J. Foraminiferal Res. 14, 250–261.
Hasiuk, F., Lohmann, K., 2010. Application of calcite Mg partitioning functions to the reconstruction of paleocean Mg/Ca. Geochim. Cosmochim. Acta 74, 6751–6763.
Heinemann, M., Jungclaus, J., Marotzke, J., 2009. Warm Paleocene/Eocene climate as simulated in ECHAM5/MPI-OM. Clim. Past 5, 785–802.
Hendiarti, N., Siegel, H., Ohde, T., 2004. Investigation of different coastal processes in Indonesian waters using SeaWiFS data. Deep-Sea Res., Part 2, Top. Stud. Oceanogr. 51, 85–97.
Hollis, C.J., Taylor, K.W., Handley, L., Pancost, R.D., Huber, M., Creech, J.B., Hines, B.R., Crouch, E.M., Morgans, H.E., Crampton, J., Gibbs, S., Pearson, P., Zachos, J., 2012. Early Paleogene temperature history of the Southwest Pacific Ocean: Reconciling proxies and models. Earth Planet. Sci. Lett. 349, 53–66.
Hönisch, B., Allen, K., Russell, A., Eggins, S., Bijma, J., Spero, H., Lea, D., Yu, J., 2011. Planktic foraminifers as recorders of seawater Ba/Ca. Marine Micropaleontology 79, 52–57.
Hoogakker, B., Klinkhammer, G., Elderfield, H., Rohling, E., Hayward, C., 2009. Mg/Ca paleothermometry in high salinity environments. Earth Planet. Sci. Lett. 284, 583–589.
Huber, M., Goldner, A., 2012. Eocene monsoons. J. Asian Earth Sci. 44, 3–23.
Ivany, L.C., Patterson, W.P., Lohmann, K.C., 2000. Cooler winters as a possible cause of mass extinctions at the Eocene/Oligocene boundary. Nature 407, 887–890.
Ivany, L., Wilkinson, B., Lohmann, K., Johnson, E., McElroy, B., Cohen, G., 2004. Intra-annual isotopic variation in *Venericardia* bivalves: Implications for early Eocene temperature, seasonality, and salinity on the US Gulf Coast. J. Sediment. Res. 74, 7–19.
Jonkers, L., Brummer, G.J.A., Peeters, F.J., van Aken, H.M., De Jong, M.F., 2010. Seasonal stratification, shell flux, and oxygen isotope dynamics of left-coiling *N. pachyderma* and *T. quinqueloba* in the western subpolar North Atlantic. Paleoceanography 25.
Katz, M., Cramer, B., Franzese, A., Hönisch, B., Miller, K., Rosenthal, Y., Wright, J., 2010. Traditional and emerging geochemical proxies in foraminifera. J. Foraminiferal Res. 40, 165–192.
Keating-Bitonti, C.R., Ivany, L.C., Affek, H.P., Douglas, P., Samson, S.D., 2011. Warm, not super-hot, temperatures in the early Eocene subtropics. Geology 39, 771–774.
Kobashi, T., Grossman, E., Dockery, D., Ivany, L., 2004. Water mass stability reconstructions from greenhouse (Eocene) to icehouse (Oligocene) for the northern Gulf Coast continental shelf (USA). Paleoceanography 19. PA1022.
Korty, R.L., Emanuel, K.A., Scott, J.R., 2008. Tropical cyclone-induced upper-ocean mixing and climate: Application to equable climates. J. Climate 21, 638–654.
Kuile, B., Erez, J., 1991. Mechanisms for calcification and carbon cycling in algal symbiont-bearing foraminifera. In: Biology of Foraminifera. Academic Press, London, pp. 73–89.
Langer, M., Hottinger, L., 2000. Biogeography of selected "larger" foraminifera. Micropaleontology 46, 105–126.
Lea, D.W., Shen, G.T., Boyle, E.A., 1989. Coralline barium records temporal variability in equatorial Pacific upwelling. Nature 340, 373–376.
Lear, C.H., Elderfield, H., Wilson, P.A., 2000. Cenozoic deep-sea temperatures and global ice volumes from Mg/Ca in benthic foraminiferal calcite. Science 287, 269–272.
Lear, C.H., Rosenthal, Y., Slowey, N., 2002. Benthic foraminiferal Mg/Ca-paleothermometry: A revised core-top calibration. Geochim. Cosmochim. Acta 66, 3375–3387.
Lear, C., Elderfield, H., Wilson, P., 2003. A Cenozoic seawater Sr/Ca record from benthic foraminiferal calcite and its application in determining global weathering fluxes. Earth Planet. Sci. Lett. 208, 69–84.
Lelono, E.B., 2000. Palynological study of the Eocene Nanggulan Formation Central Java, Indonesia. PhD thesis. 453 pp.
Locarnini, R., Mishonov, A., Antonov, J., Boyer, T., Garcia, H., 2010. World Ocean Atlas 2009, vol. 1: Temperature. NOAA Atlas NESDIS. U.S. Government Printing Office, Washington DC.
Loeblich, A., Tappan, H., 1987. Foraminifera Genera and Their Classification. Van Nostrand/Reinhold Co., New York.
Lynch-Stieglitz, J., Curry, W.B., Slowey, N., 1999. A geostrophic transport estimate for the Florida Current from the oxygen isotope composition of benthic foraminifera. Paleoceanography 14, 360–373.
Mucci, A., 1987. Influence of temperature on the composition of magnesian calcite overgrowths precipitated from seawater. Geochim. Cosmochim. Acta 51, 1977–1984.
Mucci, A., Morse, J., 1983. The incorporation of Mg^{2+} and Sr^{2+} into calcite overgrowths: Influences of growth rate and solution composition. Geochim. Cosmochim. Acta 47, 217–233.
Müller, W., Shelley, M., Miller, P., Broude, S., 2009. Initial performance metrics of a new custom-designed ArF excimer LA-ICPMS system coupled to a two-volume laser-ablation cell. J. Anal. At. Spectrom. 24, 209–214.
Oouchi, K., Yoshimura, J., Yoshimura, H., Mizuta, R., Kusunoki, S., Noda, A., 2006. Tropical cyclone climatology in a global-warming climate as simulated in a 20 km-mesh global atmospheric model: Frequency and wind intensity analyses. J. Meteorol. Soc. Jpn. 84, 259–276.
Pearson, P., 2012. Oxygen isotopes in foraminifera: Overview and historical review. Paleontol. Soc. Pap. 18, 1–38.
Pearson, P., Van Dongen, B., Nicholas, C., Pancost, R., Schouten, S., Singano, J., Wade, B., 2007. Stable warm tropical climate through the Eocene Epoch. Geology 35, 211–214.
Pena, L.D., Calvo, E., Cacho, I., Eggins, S., Pelejero, C., 2005. Identification and removal of Mn–Mg-rich contaminant phases on foraminiferal tests: Implications for Mg/Ca past temperature reconstructions. Geochem. Geophys. Geosyst. 6.
Price, J.F., 1981. Upper ocean response to a hurricane. J. Phys. Oceanogr. 11, 153–175.
Purton, L., Brasier, M., 1999. Giant protist *Nummulites* and its Eocene environment: Life span and habitat insights from $\delta^{18}O$ and $\delta^{13}C$ data from *Nummulites* and *Venericardia*, Hampshire basin, UK. Geology 27, 711–714.
Raitzsch, M., Dueñas-Bohórquez, A., Reichart, G.J., de Nooijer, L., Bickert, T., 2010. Incorporation of Mg and Sr in calcite of cultured benthic foraminifera: Impact of calcium concentration and associated calcite saturation state. Biogeosciences 7, 869–881.
Raja, R., Saraswati, P., Rogers, K., Iwao, K., 2005. Magnesium and strontium compositions of recent symbiont-bearing benthic foraminifera. Marine Micropaleontology 58, 31–44.
Raja, R., Saraswati, P., Iwao, K., 2007. A field-based study on variation in Mg/Ca and Sr/Ca in larger benthic foraminifera. Geochem. Geophys. Geosyst. 8.
Reiss, Z., 1958. Classification of lamellar foraminifera. Micropaleontology 4, 51–70.
Reiss, Z., Hottinger, L., 1984. The Gulf of Aqaba. Ecol. Stud., vol. 50. Springer-Verlag, Berlin.
Renema, W., 2003. Larger foraminifera on reefs around Bali (Indonesia). Zoöl. Verh. 345, 337–366.
Renema, W., 2006. Habitat variables determining the occurrence of large benthic foraminifera in the Berau area (East Kalimantan, Indonesia). Coral Reefs 25, 351–359.
Renema, W., 2007. Fauna development of larger benthic foraminifera in the Cenozoic of Southeast Asia. In: Biogeography, Time and Place: Distributions, Barriers and Islands. Springer, Berlin.
Renema, W., 2008. Habitat selective factors influencing the distribution of larger benthic foraminiferal assemblages over the Kepulauan Seribu. Marine Micropaleontology 68, 286–298.
Renema, W., Troelstra, S., 2001. Larger foraminifera distribution on a mesotrophic carbonate shelf in SW Sulawesi (Indonesia). Palaeogeogr. Palaeoclimatol. Palaeoecol. 175, 125–146.
Ries, J., 2004. Effect of ambient Mg/Ca ratio on Mg fractionation in calcareous marine invertebrates: A record of the oceanic Mg/Ca ratio over the Phanerozoic. Geology 32, 981–984.
Ross, C., 1974. Evolutionary and ecological significance of large calcareous Foraminiferida (Protozoa), Great Barrier Reef. In: Proceedings of the Second International Coral Reef Symposium, pp. 327–334.
Röttger, R., Spindler, M., Schmaljohann, R., Richwien, M., Fladung, M., 1984. Functions of the canal system in the rotaliid foraminifer, *Heterostegina depressa*. Nature 309, 789–791.
Sadekov, A., Eggins, S., De Deckker, P., Kroon, D., 2008. Uncertainties in seawater thermometry deriving from intratest and intertest Mg/Ca variability in *Globigerinoides ruber*. Paleoceanography 23.
Scherer, M., Seitz, H., 1980. Rare-earth element distribution in Holocene and Pleistocene corals and their redistribution during diagenesis. Chem. Geol. 28, 279–289.
Schmitz, B., Pujalte, V., 2007. Abrupt increase in seasonal extreme precipitation at the Paleocene–Eocene boundary. Geology 35, 215–218.
Segev, E., Erez, J., 2006. Effect of Mg/Ca ratio in seawater on shell composition in shallow benthic foraminifera. Geochem. Geophys. Geosyst. 7.
Shi, W., Wang, M., 2007. Observations of a Hurricane Katrina-induced phytoplankton bloom in the Gulf of Mexico. Geophys. Res. Lett. 34.
Sloan, L.C., Rea, D., 1995. Atmospheric carbon dioxide and early Eocene climate: A general circulation modeling sensitivity study. Palaeogeogr. Palaeoclimatol. Palaeoecol. 119, 275–292.
Snell, K.E., Thrasher, B.L., Eiler, J.M., Koch, P.L., Sloan, L.C., Tabor, N.J., 2013. Hot summers in the Bighorn Basin during the early Paleogene. Geology 41, 55–58.
Sosdian, S.M., Lear, C.H., Tao, K., Grossman, E.L., O'Dea, A., Rosenthal, Y., 2012. Cenozoic seawater Sr/Ca evolution. Geochem. Geophys. Geosyst. 13. Q10014.
Sriver, R.L., Huber, M., 2007. Observational evidence for an ocean heat pump induced by tropical cyclones. Nature 447, 577–580.
Stanley, S., Hardie, L., 1998. Secular oscillations in the carbonate mineralogy of reef-building and sediment-producing organisms driven by tectonically forced shifts in seawater chemistry. Palaeogeogr. Palaeoclimatol. Palaeoecol. 144, 3–19.
Tripati, A., Zachos, J., 2002. Late Eocene tropical sea surface temperatures: A perspective from Panama. Paleoceanography 17.

Tripati, A., Allmon, W., Sampson, D., 2009. Possible evidence for a large decrease in seawater strontium/calcium ratios and strontium concentrations during the Cenozoic. Earth Planet. Sci. Lett. 282, 122–130.
Tripati, A.K., Roberts, C.D., Eagle, R.A., Li, G., 2011. A 20 million year record of planktic foraminiferal B/Ca ratios: Systematics and uncertainties in pCO_2 reconstructions. Geochim. Cosmochim. Acta 75, 2582–2610.
Vecchi, G.A., Soden, B.J., 2007. Global warming and the weakening of the tropical circulation. J. Climate 20, 4316–4340.
Wefer, G., Berger, W., 1980. Stable isotopes in benthic foraminifera: Seasonal variation in large tropical species. Science 209, 803–805.
Wilkinson, B., Algeo, T., 1989. Sedimentary carbonate record of calcium–magnesium cycling. Am. J. Sci. 289, 1158–1194.
Winguth, A., Shellito, C., Shields, C., Winguth, C., 2010. Climate response at the Paleocene–Eocene Thermal Maximum to greenhouse gas forcing – A model study with CCSM3. J. Climate 23, 2562–2584.
Wit, J., Reichart, G.J., Jung, S., Kroon, D., 2010. Approaches to unravel seasonality in sea surface temperatures using paired single-specimen foraminiferal $\delta^{18}O$ and Mg/Ca analyses. Paleoceanography 25. PA4220.
Zachos, J., Dickens, G., Zeebe, R., 2008. An early Cenozoic perspective on greenhouse warming and carbon-cycle dynamics. Nature 451, 279–283.

1 Sample localities

A location map showing both Recent and fossil sample localities is shown in figure S1.

All four fossil samples from the Kali Watupuru river section, Nanggulan were sampled from between the 39 Ma and 37 Ma sequence boundaries of *Lelono* [2000]. *Nummulites*

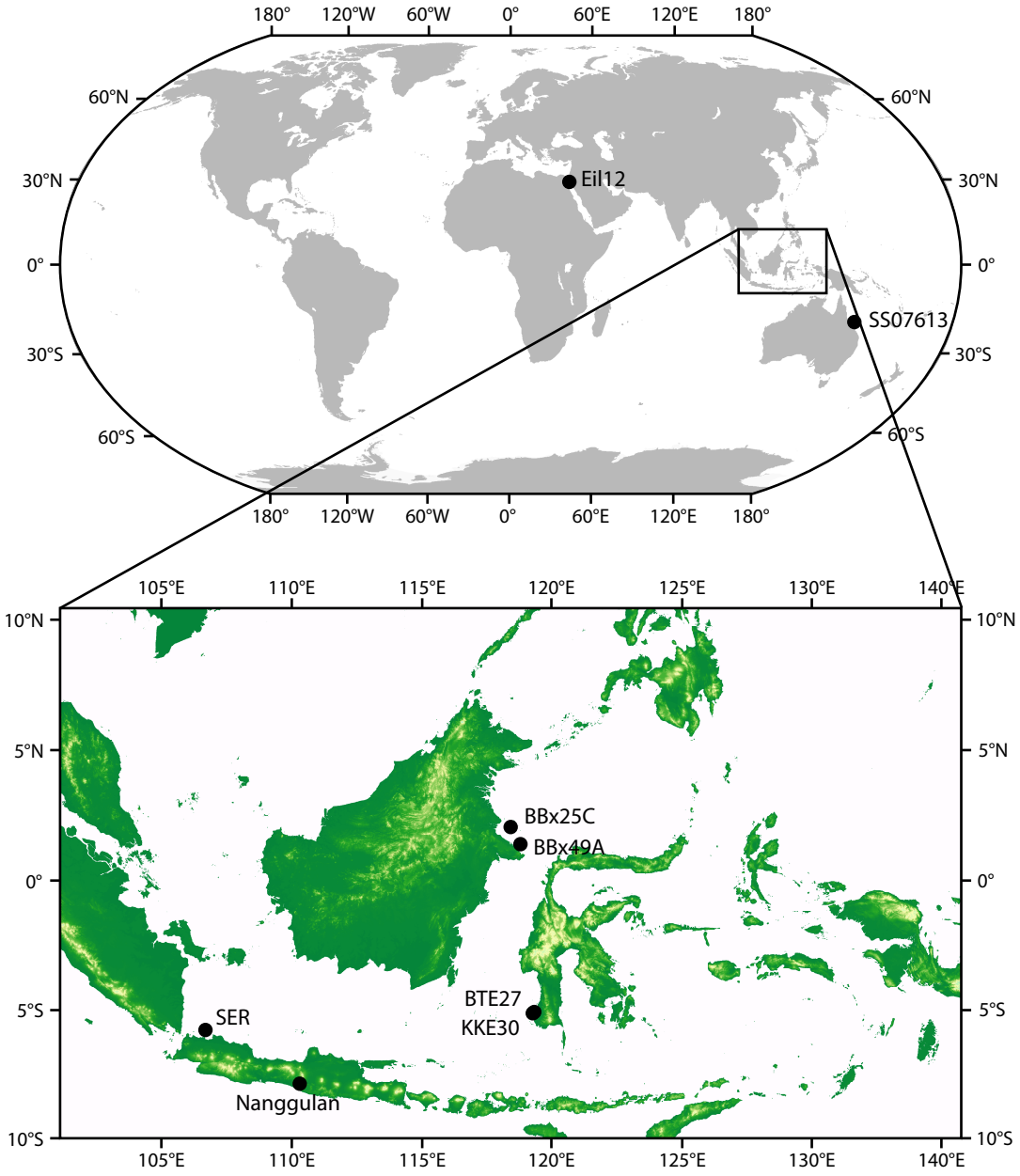

Figure S1: Recent sample sites and the location of the sampled Nanggulan Beds. Sample identifiers refer to those given in tables S3 and S4, and table 1 of the main text.

are present at discrete intervals within the section, typically in well sorted, coarse grained sandstones implying relatively shallow intervals within the sucession. The sedimentology and fauna suggest deepening upwards from around 10-20 m water depth at the lowermost marine bed to 50-60 m water depth for the beds stratigraphically above the Djokdjokartae Beds, from which all samples were collected.

2 Sample preparation

N. djokdjokartae were sectioned along the equatorial plane with a 150 μm-thick diamond impregnated saw. Deionised water was used as a coolant/lubricant. Samples were then embedded in resin (Struers EpoFix) and ground down to expose the marginal chord using wet sand paper (*Operculina* were mounted directly in resin without prior sectioning). The resin blocks were polished using diamond suspension to avoid contamination from Al-based polishing agents. In order to assess any potential effect of the preparation process on the data, some Eocene samples were mounted directly into the ablation cell. Prior to analysis, all samples (mounted and unmounted) were ultrasonicated in methanol twice and deionised water three times, for 20 minutes each. Acetone was not used as it was found to degrade the epoxy resin.

3 Analytical technique

3.1 SEM imaging

All SEM images were taken using a Philips XL30 at the Natural History Museum, London using the secondary electron detector. Accelerating voltage was 5 kV and working distance $\sim$10 mm.

3.2 Laser-ablation

LA-ICPMS parameters for the analyses reported here are shown in table S1 where they are significantly different from those given by *Müller et al.* [2009]. The RESOlution M-50 laser-ablation system is particularly well-suited to highly spatially-resolved analysis because it features a two-volume Laurin Technic (Canberra) cell, resulting in uniform signal response across the ablation cell, superior signal stability (standard glass RSD $<$2%) and facilitating 99% washout of ablated material (the time taken for the raw signal intensity to decrease by two orders of magnitude) within $\sim$1.5 s. Fast signal washout times enable superior spatial resolution and avoid peak dampening.

For typical ablation parameters used to produce marginal-chord raster profiles (spot size 44 μm; scan speed 3 mm min^{-1}) the effective spatial resolution (with 99 % washout of the previously analysed material) is 120 μm. Before data acquisition the surface of the sample was further cleaned by pre-ablating the sample surface using a larger spot size, fast scan speed and higher repetition rate.

Table S1: Typical laser-ablation and ICPMS parameters, where they differ significantly from *Müller et al.* [2009]. Typical values are shown, trace element maps were created using a smaller spot size, lower repetition rate and slower scan speed (see text for details). PAC denotes pre-ablation cleaning.

Laser-ablation system (RESOlution M-50 prototype)	
N_2 gas flow	6 ml min^{-1}
Laser repetition rate	25 Hz (acquisition), 40 Hz (PAC)
Laser spot size	44 μm (acquisition), 75 μm (PAC)
Scan speed	3 mm min^{-1} (acquisition), 6 mm min^{-1} (PAC)
ICPMS (Agilent 7500ce)	
Carrier gas flow	$\sim$0.45 l min^{-1} (optimised daily)
Isotopes analysed	^{11}B, ^{24}Mg, ^{25}Mg, ^{27}Al, ^{43}Ca, ^{55}Mn, ^{66}Zn, ^{88}Sr, ^{89}Y, ^{138}Ba, ^{139}La, ^{140}Ce, ^{238}U
Total sweep time	0.4282 s

Trace element maps were made by covering the specimens in evenly spaced, horizontal profiles. In order to maximise y-axis resolution a smaller laser spot size was used (20 μm), along with a slower scan speed and lower repetition rate (1 mm min^{-1} and 10 Hz respectively). Track spacing, the distance between the centre of adjacent tracks, was either 40 or 32 μm. This was checked to ensure that subsequent tracks were not affected by the ablation blanket of those already analysed. The methodology used to create these maps is described in detail in *Evans and Müller* [2013].

Prior to the calculation of element/Ca ratios, mean background intensities for each m/z were subtracted from all standard and sample data. Outliers were removed from all data, defined as being anything >4 SD from the mean for background data and >3 SD from the mean for standard and sample data. Conversion of raw intensities into concentration data then followed standard published procedures [*Heinrich et al.*, 2003; *Longerich et al.*, 1996]. Sample data were calibrated using either NIST610 or NIST612, with the exception of Mg which was calibrated to GOR132. This is because the GOR132 standard matches the foraminifera Mg concentration much more closely, and is considerably less heterogeneous than either of the NIST glasses for this element. Accuracy was assessed over a two year period using the MPI-DING komatiite glasses GOR132 and GOR128 [*Jochum et al.*, 2006]. With the exception of Zn/Ca, accuracy was below 10% in all cases, and was often substantially lower than 5%. Accuracy data are shown in table S2. Two NIST glasses were used (with an order of magnitude difference in trace element concentration) as it was found that considerably better accuracies could be achieved for certain elements using certain NIST glasses. For example, GOR128 B/Ca accuracy was found to be 8.8% when calibrated to NIST612, but 12.2% when calibrated with NIST610 (table S2), presumably as a result of greater B/Ca heterogeneity in NIST610. The pressed carbonate standard MACS-3 was also analysed, however accuracies are not reported relative to this material

Table S2: LA-ICPMS accuracy and precision. Accuracy is defined as the mean percent deviation from the MPI-DING komatiite GOR synthetic glass reported values given by *Jochum et al.* [2006]. This was calculated by comparing two MPI-DING glasses, GOR128 and GOR132, to both NIST612 and NIST610, uncertainties are 2 SD of this value. The combination of standards that resulted in the best accuracy (in bold) was used for error propagation, alternate combinations with poorer accuracies were taken to imply greater element-specific heterogeneity within one or both of those standards. Data shown are those for laser tracks with spot sizes >44 μm only. Precision is given as the mean magnitude percentage deviation of four triplicate *N. djokdjokartae* analyses from the first measured value. Certified values for the MPI-DING standards used are also given (B-Sr in mmol/mol, Y-U in μmol/mol).

Accuracy	NIST610			NIST612			**Precision**	Certified values	
(%) →	GOR128	GOR132	MACS-3	GOR128	GOR132	MACS-3	↓ (%)	GOR132	GOR128
B/Ca	12.2±22.5	30.2±32.8		**8.8**±13.7	15.5±18.0		16.0	1.06	1.95
Mg/Ca	**2.2**±3.4	2.5±3.7	15.0±10.2	6.2±6.6	5.6±6.1	8.7±11.8	1.6	3688	5797
Al/Ca	5.2±5.1	5.3±6.1	14.4±27.3	**3.2**±3.8	3.4±4.0	13.2±24.9	87.3	1432	1747
Mn/Ca	**2.3**±4.1	2.4±3.8	8.5±8.2	3.0±5.6	2.6±5.2	5.8±7.0	5.8	14.4	22.3
Zn/Ca	41.0±59.7	29.5±107.7	10.1±15.3	22.4±46.4	**18.2**±42.8	10.9±17.5	74.3	0.78	1.03
Sr/Ca	2.3±3.6	1.6±3.8	12.4±5.1	**1.2**±2.5	1.6±2.3	10.5±9.1	2.3	0.12	0.31
Y/Ca	2.4±3.2	**2.0**±5.2	9.4±13.1	2.7±2.7	2.5±4.2	12.3±10.0	11.9	96.3	119.3
Ba/Ca	5.1±8.2	23.4±36.2	8.3±8.2	**4.2**±6.6	20.7±16.6	9.0±6.6	9.1	3.94	6.94
La/Ca	5.4±6.9	**3.0**±6.9	4.7±8.7	5.6±6.3	3.3±7.1	7.3±5.3	14.2	0.40	0.64
Ce/Ca	**7.9**±5.6	9.7±7.1	8.2±9.3	8.6±6.6	9.5 ±6.7	6.9±7.8	15.2	1.86	2.89
U/Ca	9.7±14.5	10.2±9.3	17.3±24.4	**9.5**±14.8	10.7±10.2	16.7±17.9	11.1	0.13	0.05

because (1) it was found to be considerably more heterogeneous on a μm-scale, and (2) because only preliminary concentration data are available, and no B data is published. In

all cases NIST concentration values were taken from *Jochum et al.* [2011], with the exception of NIST610 Mg, for which the value used was that previously given as 'preferred' on the GeoReM website (http://georem.mpch-mainz.gwdg.de/), 432 ppm. This is because our data show that this value produces significantly more accurate data, ^{24}Mg accuracy on GOR132 is 9.0% and 2.7%; on GOR128 8.3% and 2.2%; on MACS-3 20.9% and 14.8% for the value of *Jochum et al.* [2011] and 432 ppm respectively. In all cases the previous value gives 6% better accuracy.

Precision was assessed by the triplicate analysis of four Eocene *N. djokdjokartae* samples, see table S2. Precision is very poor for Al/Ca and Zn/Ca data because marginal chord profiles of these element/Ca ratios are highly heterogeneous. The errors associated with these measurements are consequently large.

4 Supplementary observations

Whilst we cite a peak abundance range of 10-35 m for *O. ammonoides*, this species has been found at depths of up to 130 m in the Gulf of Eilat [*Reiss and Hottinger*, 1984]. Water temperatures at this depth may (seasonally) be up to 2° C cooler than sea surface temperature. Samples for this study were collected at a depth of up to 74 m (Great Barrier Reef). Data from the 2009 World Ocean Atlas [*Locarnini et al.*, 2010] show that at this depth the mean annual temperature is 1.4° C below the surface mean annual temperature and it is possible that our fossil data are also biased to lower temperatures by the same amount. This potential bias equally applies to planktic foraminifera considered to be surface-dwelling.

No geochemical differences were observed between samples mounted in resin and those mounted directly into the laser-ablation chamber.

4.1 Recent *O. ammonoides* X/Ca correlations

Within the Recent *O. ammonoides* specimens, there is no correlation between Mg/Ca and any other X/Ca ratio, with the exception of intratest Ba/Ca in samples from the Gulf of Eilat and mean marginal cord REE/Ca for all samples, which are negatively and positively correlated with Mg/Ca respectively. This precludes temperature as a dominant control for most element/Ca ratios given that we demonstrate above that LBF Mg/Ca is temperature dependent. Furthermore, because the samples from southeast Asia have different trace element ratios and grew in three distinct locations at similar temperatures, these data demonstrate that trace element/Ca ratios in LBF can be used to identify chemically distinct areas of the modern ocean.

There are significant location-specific differences in the mean marginal cord trace element profiles. Specimens from the GBR have Al-Mn-Zn/Ca ratios an order of magnitude lower than those from the Spermonde Shelf or the Celebes Sea (figure S2). All of these three locations have distinctive B/Ca, Sr/Ca, Ba/Ca and REE/Ca ratios. Furthermore,

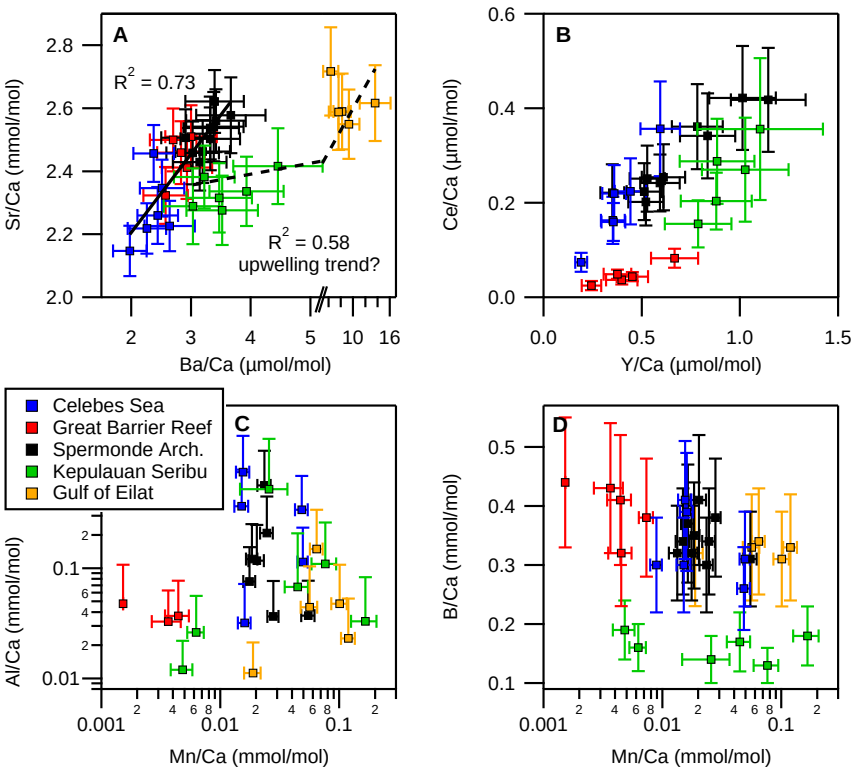

Figure S2: Recent *O. ammonoides* trace element correlations. Sr/Ca-Ba/Ca and Ce/Ca-Y/Ca show strong positive correlation, Ce-Y appears to be site specific whereas Sr-Ba may not be (the solid regression line R^2 value shown relates to a best fit line placed through samples from the Celebes Sea, GBR and Spermonde Archipelago only). Note the break in the x-axis. Al/Ca-Mn/Ca is shown to highlight the large natural variation in these 'diagenesis' trace element ratios. Each datapoint represents the mean of all data from one individual specimen.

Sr/Ca-Ba/Ca (figure S2A) and Y-La-Ce/Ca (figure S2B) show a clear linear relationship (Sr-Ba/Ca $R^2 = 0.73$), implying a common control. Samples from Kepulauan Seribu, Jakarta Bay are offset to higher Ba/Ca for a given Sr/Ca as are those from the Gulf of Eilat (mean Ba/Ca = 9.0 μmol mol^{-1}). Specimens from these two locations also have significantly higher Zn/Ca ratios (24-25 μmol mol^{-1}, compared to 1-9 μmol mol^{-1}). This implies that the local seawater chemistry of these regions is fundamentally different, potentially as a result of upwelling at the time of sample collection, or the proximity of these sample sites to highly populated areas. The anticorrelated intratest Mg-Ba/Ca data of samples from the Gulf of Eilat (figure 5, main text) strongly support the hypothesis that winter upwelling in the Gulf is the cause of the overall much higher Ba/Ca values of these samples.

There is a large range in test B/Ca between sample sites although individual measurements from a single site show good repeatability. B/Ca does not correlate with Mn/Ca (figure S2D), precluding early-stage diagenesis or sample contamination as a control of these ratios. In the absence of detailed records of sample site pH and ΔCO_3^{2-} it is not

possible to relate our B/Ca measurements to ocean carbonate chemistry. The relationship between B/Ca and U/Ca in samples from the five Recent locations is also difficult to assess given a lack of detailed site-specific carbonate chemistry data. There is no relationship between either B-U/Ca and Al-Mn/Ca suggesting that there is no bias resulting from incomplete sample cleaning or alteration.

B/Ca is ∼30% lower in the Eocene material, consistent with a more acidic than present ocean given that (1) test B/Ca decreases as $[CO_3^{2-}]$ decreases (provided pH also decreases) in at least some planktic foraminifera [e.g. *Allen et al.*, 2012] and (2) that existing pH proxy evidence suggests a more acidic ocean than at the present day [e.g. *Pearson and Palmer*, 2000]. Mean±2SD *N. djokdjokartae* B/Ca is 0.24±0.06 mmol mol^{-1}, indistinguishable from the fossil *Operculina* sp. which have mean B/Ca of 0.23±0.02 mmol mol^{-1}. With the exception of samples from the Gulf of Eilat, B/Ca and Mg/Ca are weakly correlated (R^2 = 0.23), although B/Ca appears to decrease with increasing Mg/Ca which is in agreement with the D_B-temperature relationship reported by *Foster* [2008] but not with that of *Yu et al.* [2007]. The lower (as expected) B/Ca ratio of the Eocene specimens suggests that more detailed modern calibration studies using LBF may produce useful boron-based pH/$[CO_3^{2-}]$ proxies.

Factors other than temperature clearly exert a significant control on B/Ca, Sr/Ca, Ba/Ca and Y-REE/Ca ratios, suggesting that these ratios may be useful as non-temperature proxies in these foraminifera. There is a good correlation between Sr/Ca and Ba/Ca for samples from the Celebes Sea, Great Barrier Reef and Spermonde Archipelago (figure S2A), implying a common control. Mean Ba/Ca is correlated with salinity, although Sr/Ca is not. Seawater Sr/Ca may exert a primary control on test Sr/Ca [e.g. *Lear et al.*, 2003] although it is not obvious why this should correlate with Ba/Ca as Sr/Ca cannot be modified by freshwater without a large (∼ 20‰) reduction in salinity, which foraminifera will not tolerate. Samples from the Gulf of Eilat are offset to high Ba/Ca ratios. This is likely to be a result of calcification during a period of intense upwelling, known to occur at this site [*Al-Rousan et al.*, 2003].

Al/Ca and Mn/Ca, typically used to assess diagenesis, show more than an order of magnitude of natural variation. Samples from the Great Barrier Reef are characterised by much lower Mn/Ca than any other sample site.

4.2 Geochemical preservation

4.2.1 Recent-Eocene X/Ca comparability

Figure S3 shows the relationship between X/Ca ratios frequently used to assess diagenesis in foraminifera (Al/Ca, Mn/Ca and Y/Ca) and Mg/Ca and U/Ca, which are present at a concentration of ∼2% and 50 ppb in well preserved large benthic foraminiferal calcite respectively. Each datapoint represents the mean value of all measurements from one individual specimen. For simplicity of comparison to Recent samples, fossil Mg/Ca ratios have been corrected for secular changes in the Mg/Ca ratio of seawater, based on the

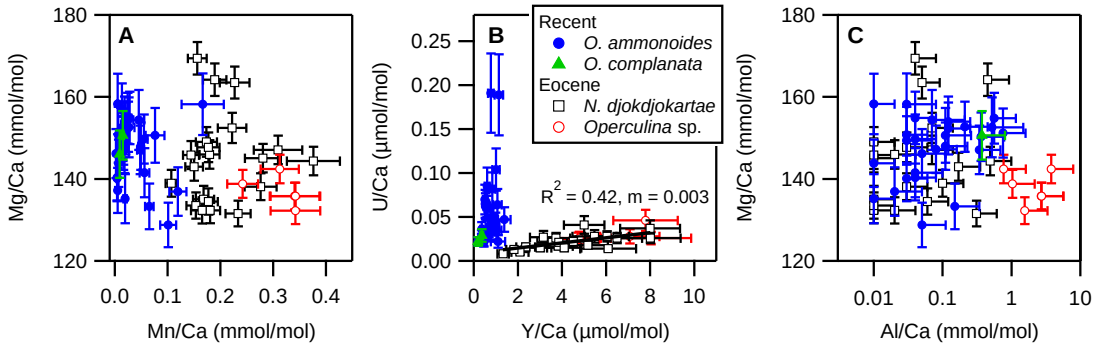

Figure S3: Mean Mg-Al-Mn-Y-U/Ca marginal cord crossplots demonstrating no covariation in contamination/diagenetic indicators and proxy element/Ca ratios. Error bars are the sum of 2SE of all measurements for that sample, accuracy and precision. Al/Ca errors are large because of the poor Al/Ca reproducibility.

Mg/Ca_{sw}-Mg/Ca_{test} relationship of *Raitzsch et al.* [2010] and assuming equivalent present day and Eocene Java coast SST. Mn/Ca is elevated in the fossil material although there is no relationship between Mg/Ca and Mn/Ca, implying that any minor diagenesis has not affected the Mg/Ca ratios of the fossil samples. However, U/Ca and Y/Ca show a weak correlation, suggesting that this data may be compromised. Mg/Ca does not correlate with Al/Ca, demonstrating that the cleaning procedure removed any remaining sedimentary clay particles and that no contamination was introduced during the polishing process. Fossil Al/Ca ratios are within the range of the Recent samples, with the exception of the fossil *Operculina* sp. which have higher Al/Ca. The fossil *Operculina* sp. have B-Mg-Sr/Ca ratios identical to the fossil *N. djokdjokartae* (see section 4.2.2), therefore the elevated Al/Ca of the fossil *Operculina* has not affected these proxy trace element ratios.

4.2.2 Fossil *Operculina-Nummulites* X/Ca comparability

A comparison of mean marginal chord element/Ca ratios for Eocene *N. djokdjokartae* and *Operculina* sp. is shown in figure S4. The most important proxy elements (B, Mg, Sr) lie on a 1:1 line demonstrating that the distribution coefficients of these elements are almost certainly the same in both species. 'Residual difference' provides an indication of the extent to which the difference in a given element/Ca ratio between the two species may be explained by the accuracy and precision of the measurement. This demonstrates that the Zn distribution coefficient is also the same, within error. Other deviations from a 1:1 are either elements that are very low in concentration and therefore highly susceptible to diagenetic alteration (e.g. U), or those which are used as alteration indicators (Al, Mn, Y). The Ba/Ca offset (~20 % higher in *Operculina* sp.) cannot be explained in this way and may be due to real differences between the species or a product of differential (e.g.) upwelling intensity which may have been variable on timescales that are not stratigraphically resolvable.

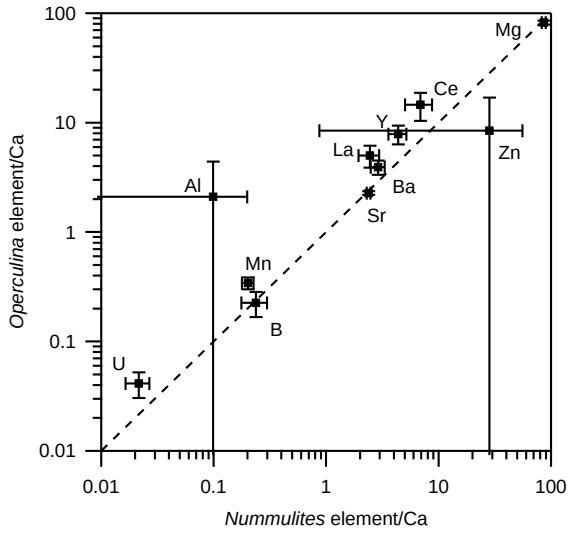

Figure S4: (A) A comparison of the mean of all measurements of Eocene *Numulites* and *Operculina*. (B) Percentage difference between the two species compared to the same difference with the total percentage error (accuracy + precision) removed.

4.3 Individual specimen-derived Mg/Ca-temperature

In order to assess the applicability of our field calibration to intratest Mg/Ca-derived seasonality reconstruction, Mg/Ca variability within the imaged specimens collected from the Gulf of Eilat was compared to the instrumental temperature record available from The Interuniversity Institute for Marine Sciences in Eilat (The Israel National Monitoring Program at the Gulf of Eilat; see http://www.iui-eilat.ac.il/NMP/database/database.aspx).

Mg/Ca-temperature relationships for individual specimens are compared to the calibration presented in the main text in figure S5. These trends were created by assuming a growth rate of 10 chambers per month (Evans, D., Erez, J., Oron, S. & Müller, W., unpublished data), in order to assign a date and hence an instrumental temperature to each chamber. Mean Mg/Ca was calculated for each chamber and plotted against recorded temperature. Temperature variation in the Gulf of Eilat is non-sinusoidal, being characterised by rapid (2 month) shifts between seasonal maximum and minimum values, where it remains constant within $\pm 0.5^{\circ}$ C for approximately four months. Therefore, the growth rate of *O. ammonoides* would have to be significantly faster than expected in order to bias these individual specimen calibrations. Very high growth rates would not be consistent with the total amount of chambers per specimen given that our own observations and the data shown in figure S5 imply essentially linear growth throughout the majority of the biomineralisation period.

The three slopes are in excellent agreement with each other and with the field calibration derived from the mean Mg/Ca measurements of samples from locations with different mean annual temperatures. These data therefore demonstrate that intratest Mg/Ca variability resulting from seasonal temperature variation has an equivalent sensitivity to mean test Mg/Ca resulting from differences in annual sample site temperature. Therefore, the

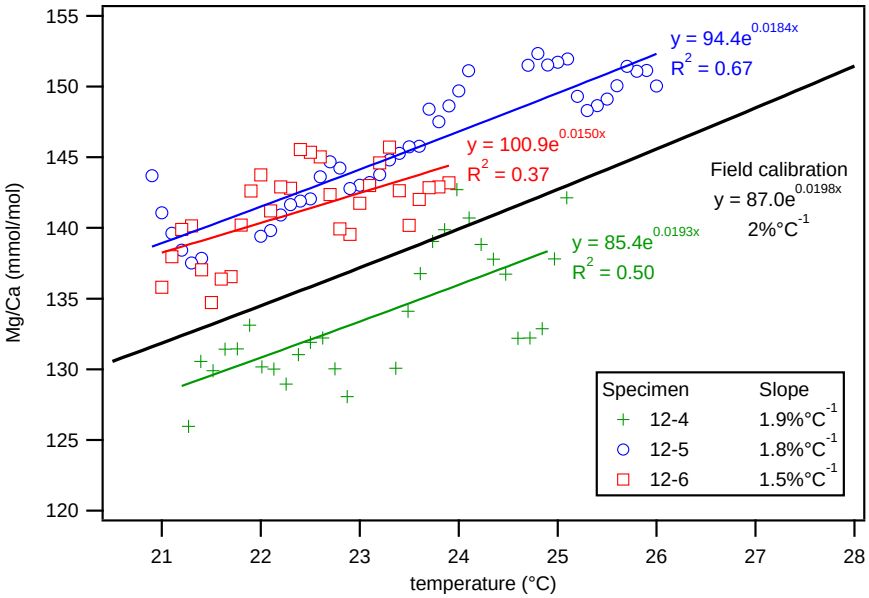

Figure S5: Mg/Ca-temperature slope calibration derived from individual imaged specimens. The consistency of the slopes between specimens and the comparability of these slopes to the Mg/Ca-temperature calibration presented in the main text demonstrates that this calibration is applicable to palaeoseasonality reconstruction.

calibration we report is applicable to palaeoseasonality reconstruction.

The scatter in these individual specimen calibrations is likely to be the result of the growth rate assumption which is unlikely to be completely linear over month timescales as the foraminifera respond to seasonally varying light and nutrient availability. The scatter in y-intercept between the three intratest Mg/Ca-temperature plots is unsurprising given the ~10 mmol mol^{-1} range in mean test Mg/Ca within a sample site (table S3) and does not represent a repeatability test of the calibration presented in the main text, which is derived from the mean of multiple individuals.

4.4 Nanggulan inter-stratigraphic level variation

There are no significant differences between any of the four sampled stratigraphic intervals in the Nanggulan Formation, when comparing the mean value for all samples of each interval, for any X/Ca ratio. Significance is defined as being achieved when the magnitude difference between two values exceeds the summation of their respective 2SE values.

5 Systematics of seasonality reconstruction

5.1 Dependency on calibration type

As stated in the main text, it is not possible to reconstruct seaosnality using a linear Mg/Ca-temperature relationship without prior knowledge of Mg/Ca_{sw}. This is shown

below.

5.1.1 Exponential Mg/Ca-temperature relationship

Re-arranging equation 6 of *Evans and Müller* [2012] gives:

$$T = ln\left(\frac{M}{5.2^H/s^H \times B}\right)/A \tag{5.1}$$

Where M is the measured Mg/Ca ratio, s is seawater Mg/Ca at some point in the past, and T, B and A have their usual meanings.
Seasonality is defined as being the difference between two measured Mg/Ca ratios:

$$\Delta T = ln\left(\frac{M_1}{5.2^H/s^H \times B}\right)/A - ln\left(\frac{M_2}{5.2^H/s^H \times B}\right)/A \tag{5.2}$$

Seasonality is not dependent on seawater Mg/Ca (s) if the right hand side of this equation does not change when s varies:

$$ln\left(\frac{M_1}{5.2^H/s_1^H \times B}\right)/A - ln\left(\frac{M_2}{5.2^H/s_1^H \times B}\right)/A = ln\left(\frac{M_1}{5.2^H/s_2^H \times B}\right)/A - ln\left(\frac{M_2}{5.2^H/s_2^H \times B}\right)/A \tag{5.3}$$

Which simplifies to:

$$ln\left(\frac{M_1 \times 5.2^H/s_1^H \times B}{M_2 \times 5.2^H/s_1^H \times B}\right) = ln\left(\frac{M_1 \times 5.2^H/s_2^H \times B}{M_2 \times 5.2^H/s_2^H \times B}\right) \tag{5.4}$$

The two sides of the equation are equivalent, proving non-dependence of seasonality reconstruction on seawater Mg/Ca.

5.1.2 Linear Mg/Ca-temperature relationship

Re-arranging a linear Mg/Ca-temperature relationship for T gives:

$$T = (M \times 5.2^H/s^H - A)/B \tag{5.5}$$

Analogously for equation 5.3, seasonality is not dependent on seawater Mg/Ca if:

$$(M_1 \times 5.2^H/s_1^H - A)/B - (M_2 \times 5.2^H/s_1^H - A)/B = (M_1 \times 5.2^H/s_2^H - A)/B - (M_2 \times 5.2^H/s_2^H - A)/B \tag{5.6}$$

Simplifying:

$$(M_1 - M_2) \times 5.2^H/s_1^H = (M_1 - M_2) \times 5.2^H/s_2^H \tag{5.7}$$

Implying:

$$\frac{s_2^H}{s_1^H} = 1 \tag{5.8}$$

Which is false. Therefore linear Mg/Ca-temperature calibrations cannot be used for palaeoseasonality reconstruction if the seawater Mg/Ca ratio is not known.

5.2 Mg/Ca smoothing

Both Recent and Eocene laser-ablation Mg/Ca profiles are characterised by significant fine-scale heterogeneity (see main text for details). Seasonality was reconstructed using the minimum and maximum Mg/Ca values from running-mean smoothed profiles. Therefore the degree of smoothing to some extent exerts a control on the seasonality reconstruction, tending towards lower magnitude reconstructions with a greater degree of smoothing. Figure S6 demonstrates this by applying a progressively coarser running mean to several specimens. There is a sharp initial decrease in reconstructed seasonality as the length of the running mean increases up to 20 points, which represents the removal of the effect of outliers and μm-scale Mg/Ca variability. This point is not specimen dependent as the magnitude of μm-scale Mg/Ca variability is consistent between all Recent and Eocene specimens. Running means of >50 points results in the dampening of longer-period Mg/Ca variability which is likely to be temperature controlled. We therefore use a 40 point running mean, in order to make the most conservative estimate of reconstructed seasonality without reducing the amplitude of long-period Mg/Ca shifts. There is a difference of $\pm$0.6°C in reconstructed seasonality over the range of 20 to 50 point running means, therefore this artefact of the necessary treatment of LBF Mg/Ca data in this way does not affect our reconstructed seasonality to a significant degree.

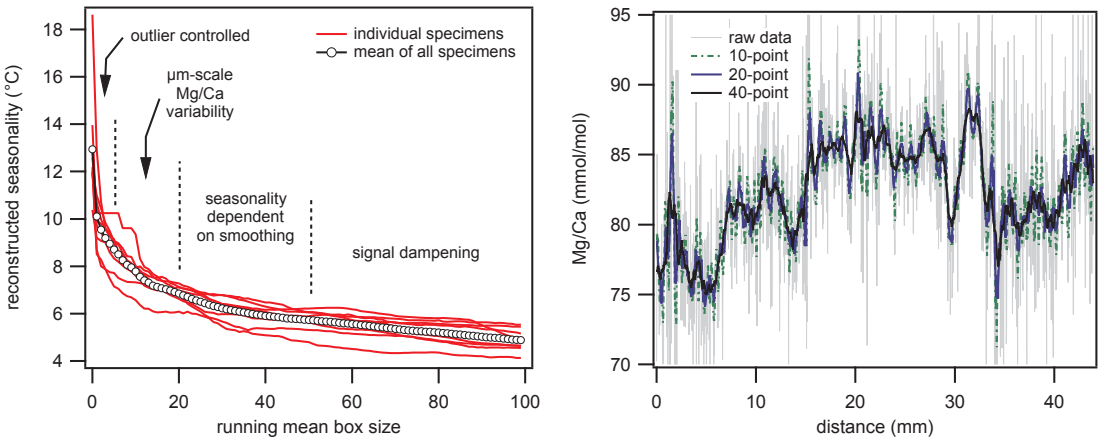

Figure S6: The control that the degree of smoothing applied to the fossil Mg/Ca laser-ablation profiles exerts on reconstructed seasonality.

6 Sample data

All mean marginal chord data with associated uncertainties are given in tables S3 and S4 for recent *Operculina* and Eocene samples respectively. Error bars are 2SE of the individual measurement, plus the sum of accuracy and precision given in table S2.

Table S3: All recent *Operculina* mean marginal chord analytical X/Ca data. Uncertainties reported separately for ease of re-plotting. B-Mg-Al-Mn-Sr/Ca data are given in mmol mol^{-1}; Zn-Y-Ba-La-Ce-U/Ca data are given in μmol mol^{-1}. Error estimates are individual specimen 2SE + accuracy + precision.

	value											uncertainty										
Sample ID	B	Mg	Al	Mn	Zn	Sr	Y	Ba	La	Ce	U	B	Mg	Al	Mn	Zn	Sr	Y	Ba	La	Ce	U
O. ammonoides																						
Spermonde Shelf, SW Sulawesi																						
BTE27-1	0.34	152.7	-	0.015	2.0	2.54	0.51	3.32	0.17	0.22	0.070	0.09	6.2	-	0.002	2.0	0.10	0.09	0.48	0.04	0.06	0.017
BTE27-2	0.37	148.7	-	0.016	2.6	2.58	0.61	3.67	0.14	0.25	0.085	0.10	6.5	-	0.002	2.7	0.12	0.11	0.58	0.03	0.07	0.021
BTE27-3	0.32	156.9	-	0.013	1.5	2.46	0.52	3.20	0.16	0.20	0.065	0.08	6.4	-	0.002	1.5	0.10	0.09	0.46	0.03	0.05	0.016
BTE27B-1	0.38	154.9	0.04	0.028	11.9	2.56	0.59	3.42	0.18	0.24	0.060	0.10	6.4	0.04	0.003	11.8	0.10	0.10	0.50	0.04	0.06	0.014
BTE27B-2	0.41	152.3	0.12	0.020	27.3	2.54	0.53	3.38	0.17	0.25	0.062	0.11	6.3	0.13	0.003	27.8	0.11	0.09	0.50	0.04	0.07	0.015
KKE30-1	0.30	154.8	0.56	0.024	3.8	2.50	1.14	3.32	0.25	0.42	0.189	0.08	6.2	0.60	0.003	3.9	0.10	0.19	0.50	0.05	0.11	0.046
KKE30-3	0.34	152.7	0.21	0.025	12.3	2.62	0.84	3.40	0.18	0.34	0.082	0.09	6.1	0.24	0.003	12.5	0.10	0.14	0.49	0.04	0.09	0.019
KKE30-2	0.35	154.0	0.12	0.018	3.8	2.46	1.01	3.03	0.23	0.42	0.104	0.09	6.1	0.13	0.002	4.0	0.10	0.17	0.44	0.05	0.11	0.024
KKE30-4	0.32	147.2	0.08	0.018	5.5	2.51	0.78	2.91	0.20	0.36	0.191	0.08	5.8	0.08	0.002	5.4	0.09	0.13	0.41	0.04	0.09	0.045
KKE30-5	0.31	149.7	0.04	0.055	9.0	2.43	0.35	3.15	0.17	0.22	0.028	0.08	6.0	0.04	0.007	9.2	0.09	0.06	0.45	0.03	0.06	0.007
Great Barrier Reef																						
SS07613	0.32	137.2	-	0.005	0.8	2.50	0.45	2.70	0.04	0.04	0.021	0.09	5.5	-	0.001	0.8	0.10	0.08	0.39	0.01	0.01	0.005
SS07613-3_1	0.44	146.2	0.05	0.002	2.0	2.32	0.40	2.58	0.03	0.04	0.027	0.11	6.0	0.06	0.000	2.1	0.09	0.08	0.37	0.01	0.01	0.007
SS07613-3_2	0.41	140.3	0.04	0.004	0.8	2.41	0.67	2.93	0.06	0.08	0.038	0.11	5.6	0.04	0.001	0.8	0.10	0.12	0.42	0.01	0.02	0.009
SS07613-3_3	0.43	140.1	0.03	0.004	1.5	2.51	0.38	3.00	0.04	0.05	0.023	0.11	5.6	0.03	0.001	1.6	0.10	0.07	0.43	0.01	0.01	0.005
SS07613-3_4	0.38	143.8	0.01	0.007	1.5	2.46	0.24	2.83	0.02	0.02	0.022	0.10	5.8	0.01	0.001	1.5	0.10	0.05	0.40	0.01	0.01	0.005
Celebes Sea, NE Kalimantan																						
BBx25C-1	0.39	149.4	0.03	0.016	2.6	2.22	0.35	2.26	0.11	0.16	0.025	0.10	5.9	0.04	0.002	2.5	0.08	0.06	0.32	0.02	0.05	0.006
BBx25C-2	0.41	151.2	0.75	0.015	2.4	2.23	0.44	2.64	0.14	0.22	0.022	0.10	6.0	0.85	0.002	2.3	0.08	0.08	0.42	0.03	0.07	0.005
BBx49A-a1	0.31	148.0	0.11	0.049	4.1	2.46	0.36	2.38	0.12	0.16	0.036	0.08	5.8	0.12	0.005	4.0	0.09	0.06	0.34	0.02	0.04	0.008
BBx49A-a3	0.26	147.1	0.34	0.048	12.4	2.35	0.59	2.51	0.22	0.36	0.065	0.07	5.9	0.35	0.006	12.1	0.09	0.10	0.37	0.05	0.10	0.015
BBx49A-a2	0.30	146.0	0.00	0.009	10.4	2.26	0.19	2.44	0.07	0.07	0.022	0.08	5.8	0.00	0.001	10.2	0.09	0.03	0.34	0.02	0.02	0.005
BBx49A-a4	0.30	150.3	0.36	0.015	3.8	2.15	0.36	1.98	0.15	0.22	0.024	0.08	5.9	0.42	0.002	3.9	0.08	0.06	0.28	0.03	0.06	0.006
Kepulauan Seribu, Jakarta																						
SER02-14_1	0.18	158.2	0.03	0.166	37.9	2.28	1.10	3.52	0.35	0.36	0.022	0.05	7.5	0.05	0.040	41.2	0.11	0.32	0.60	0.11	0.15	0.007
SER06-21_1	0.16	150.8	0.03	0.006	2.7	2.34	0.88	3.93	0.40	0.20	0.049	0.04	6.8	0.03	0.001	3.0	0.11	0.18	0.62	0.09	0.06	0.013
SER02-14_2	0.14	152.6	0.52	0.026	71.5	2.42	1.03	4.46	0.33	0.27	0.035	0.04	7.3	0.97	0.011	76.1	0.12	0.22	0.75	0.10	0.11	0.011
SER21-24_3	0.13	150.6	0.11	0.076	25.9	2.38	1.38	3.22	0.77	0.83	0.047	0.03	6.7	0.15	0.018	26.9	0.10	0.28	0.51	0.19	0.26	0.014
SER21-24_4	0.17	154.4	0.07	0.045	2.5	2.29	0.88	3.03	0.36	0.29	0.047	0.05	7.3	0.14	0.010	4.0	0.12	0.19	0.49	0.09	0.09	0.013
SER06-21_3	0.19	158.3	0.01	0.005	3.8	2.32	0.79	3.47	0.28	0.16	0.033	0.05	7.4	0.01	0.001	4.6	0.11	0.17	0.55	0.07	0.05	0.009
Gulf of Eilat, Red Sea																						
Eil12_1	0.31	128.8	0.05	0.101	17.7	2.55	0.77	9.33	-	-	0.048	0.08	5.4	0.06	0.015	17.4	0.11	0.14	1.72	-	-	0.013
Eil12_2	0.33	136.9	0.02	0.119	23.2	2.59	0.98	8.20	-	-	0.043	0.09	5.9	0.03	0.016	23.0	0.12	0.18	1.43	-	-	0.012
Eil12_3	0.34	133.3	0.15	0.065	47.8	2.62	1.08	13.60	-	-	0.064	0.09	5.6	0.19	0.008	48.4	0.12	0.20	2.53	-	-	0.018
Eil12_4	0.33	141.5	0.04	0.056	18.9	2.59	0.69	7.67	-	-	0.038	0.09	6.0	0.06	0.009	18.8	0.12	0.14	1.57	-	-	0.011
Eil12_6	0.32	135.2	0.01	0.019	17.0	2.72	0.70	6.36	-	-	0.034	0.09	6.0	0.01	0.003	17.4	0.14	0.17	1.22	-	-	0.012
O. complanata																						
Celebes Sea, NE Kalimantan																						
BBx49A-c1	0.30	146.0	0.00	0.009	10.3	2.26	0.19	2.44	0.07	0.07	0.022	0.08	5.8	0.00	0.001	10.2	0.09	0.03	0.34	0.02	0.02	0.005
BBx49A-c2	0.30	150.6	0.37	0.015	5.6	2.15	0.36	2.10	0.16	0.22	0.029	0.08	5.9	0.43	0.002	5.8	0.08	0.06	0.32	0.03	0.06	0.007

Table S4: All Eocene mean marginal chord analytical X/Ca data. Uncertainties reported separately for ease of re-plotting. B-Mg-Al-Mn-Sr/Ca data are given in mmol mol^{-1}; Zn-Y-Ba-La-Ce-U/Ca data are given in μmol mol^{-1}. Sample prefixes denote stratigraphic level, for example sample IDs beginning KW01 were collected from a different level to those beginning KW02. Error estimates are individual specimen 2SE + accuracy + precision.

	value											uncertainty										
Sample ID	B	Mg	Al	Mn	Zn	Sr	Y	Ba	La	Ce	U	B	Mg	Al	Mn	Zn	Sr	Y	Ba	La	Ce	U
N. djokdjokartae																						
KW01-1	0.18	88.9	0.01	0.173	18.76	2.20	2.36	2.88	1.46	3.36	0.016	0.05	3.6	0.01	0.020	0.02	0.11	0.43	0.40	0.30	0.91	0.004
KW01-2	0.19	91.0	0.07	0.222	36.43	2.29	3.56	2.96	2.35	6.27	0.021	0.05	3.7	0.07	0.027	0.04	0.12	0.67	0.42	0.52	1.78	0.005
KW01-21	0.23	79.0	0.01	0.180	2.16	2.54	3.73	2.80	1.84	4.90	0.026	0.06	3.1	0.01	0.019	0.00	0.12	0.65	0.39	0.38	1.31	0.006
KW01-22	0.27	86.6	0.01	0.280	4.24	2.28	5.01	2.91	2.58	6.73	0.041	0.07	3.5	0.01	0.034	0.00	0.12	0.92	0.42	0.56	1.87	0.010
KW01-23	0.25	80.6	0.01	0.168	4.45	2.63	3.16	2.99	1.41	3.78	0.027	0.07	3.3	0.01	0.020	0.00	0.13	0.61	0.42	0.31	1.08	0.007
KW01-24	0.26	82.4	0.03	0.276	6.49	2.33	8.00	3.09	5.22	15.11	0.037	0.07	3.3	0.03	0.030	0.01	0.12	1.36	0.44	1.06	3.98	0.009
KW01-25	0.26	87.1	0.02	0.179	7.58	2.33	3.83	2.80	1.92	4.97	0.017	0.07	3.5	0.02	0.019	0.01	0.12	0.66	0.39	0.39	1.31	0.004
KW02-11	0.24	87.0	0.01	0.144	12.00	2.32	3.02	2.79	1.73	4.34	0.015	0.06	3.4	0.01	0.015	0.01	0.11	0.50	0.38	0.34	1.12	0.004
KW02-12	0.26	82.9	0.10	0.107	17.62	2.27	3.86	2.77	2.22	6.13	0.021	0.07	3.3	0.10	0.011	0.02	0.11	0.65	0.40	0.45	1.60	0.005
KW02-13	0.24	79.7	0.01	0.153	0.52	2.63	2.09	2.86	1.06	2.80	0.010	0.06	3.2	0.01	0.018	0.00	0.13	0.39	0.40	0.23	0.78	0.003
KW02-14	0.22	88.2	0.03	0.177	25.02	2.31	1.83	2.63	1.08	2.67	0.013	0.06	3.6	0.03	0.021	0.02	0.12	0.35	0.37	0.24	0.75	0.003
KW02-15	0.20	87.8	0.07	0.309	83.20	2.30	6.10	2.74	1.78	8.26	0.014	0.05	3.5	0.07	0.046	0.08	0.12	1.27	0.39	0.37	2.50	0.003
KW03-11	0.26	79.0	0.02	0.165	14.37	2.77	4.51	3.03	2.10	5.65	0.022	0.07	3.2	0.02	0.021	0.01	0.14	0.84	0.43	0.45	1.56	0.005
KW03-12	0.29	86.2	0.49	0.376	16.96	2.46	6.50	3.24	2.71	9.98	0.026	0.07	3.5	0.50	0.050	0.02	0.12	1.14	0.47	0.56	2.67	0.006
KW03-13	0.27	80.3	0.06	0.177	4.12	2.57	6.04	3.31	3.36	9.66	0.028	0.07	3.2	0.06	0.018	0.00	0.13	1.00	0.48	0.67	2.50	0.006
KW03-14	0.22	101.1	0.04	0.156	11.50	2.33	1.33	2.80	0.75	2.64	0.008	0.06	4.0	0.04	0.018	0.01	0.12	0.26	0.39	0.15	0.76	0.002
KW03-15	0.19	97.6	0.05	0.227	65.60	2.22	4.10	2.73	2.43	6.17	0.015	0.05	3.9	0.04	0.028	0.06	0.11	0.77	0.39	0.53	1.71	0.004
KW05-11	0.26	78.5	0.31	0.233	2.16	2.58	8.01	3.07	5.70	15.18	0.026	0.07	3.1	0.30	0.024	0.00	0.13	1.37	0.44	1.16	3.97	0.006
KW05-12	0.26	85.3	0.17	0.150	12.28	2.22	5.17	2.62	3.87	9.72	0.018	0.07	3.4	0.18	0.017	0.01	0.11	0.91	0.37	0.82	2.61	0.004
KW05-13	0.22	98.0	0.45	0.189	222.46	2.22	5.48	2.97	3.42	9.81	0.028	0.06	4.0	0.47	0.022	0.21	0.11	1.00	0.44	0.74	2.71	0.007
***Operculina* spp.**																						
Op_KW01-2	0.21	85.0	3.79	0.312	3.85	2.21	7.79	4.00	6.02	17.08	0.046	0.05	3.5	4.11	0.036	0.00	0.11	1.46	0.60	1.31	4.79	0.012
Op_KW01-1	0.23	85.0	0.77	0.478	15.19	2.23	14.76	4.42	9.04	26.61	0.097	0.06	3.5	0.85	0.048	0.02	0.12	2.56	0.64	1.87	7.10	0.024
Op_KW01B-2	0.24	81.0	2.71	0.340	10.84	2.31	4.73	3.87	2.49	7.62	0.025	0.06	3.3	2.93	0.047	0.01	0.12	0.96	0.57	0.59	2.26	0.007
Op_KW01B-1	0.24	81.1	2.74	0.342	11.00	2.31	4.79	3.88	2.53	7.72	0.026	0.06	3.3	2.96	0.047	0.01	0.12	0.98	0.57	0.60	2.29	0.007
Op_KW02-1	0.22	82.9	1.03	0.242	6.58	2.26	7.08	3.36	4.72	12.83	0.028	0.06	3.4	1.13	0.029	0.01	0.12	1.35	0.50	1.06	3.64	0.008
Op_KW02-2	0.23	78.9	1.56	0.342	3.13	2.27	8.04	3.97	5.31	15.77	0.026	0.06	3.3	1.8	0.047	0.00	0.12	1.82	0.63	1.37	5.08	0.007

7 References

Al-Rousan, S., S. Al-Moghrabi, J. Pätzold, and G. Wefer (2003), Stable oxygen isotopes in porites corals monitor weekly temperature variations in the northern Gulf of Aqaba, Red Sea, *Coral Reefs*, *22*(4), 346–356.

Allen, K. A., B. Hönisch, S. M. Eggins, and Y. Rosenthal (2012), Environmental controls on B/Ca in calcite tests of the tropical planktic foraminifer species *Globigerinoides ruber* and *Globigerinoides sacculifer*, *Earth and Planetary Science Letters*, *351*, 270–280.

Evans, D., and W. Müller (2012), Deep time foraminifera Mg/Ca paleothermometry: Non-linear correction for secular change in seawater Mg/Ca, *Paleoceanography*, *PA4205*, doi:10.1029/2012PA002315.

Evans, D., and W. Müller (2013), LA-ICPMS elemental imaging of complex discontinuous carbonates: An example using large benthic foraminifera, *Journal of Analytical Atomic Spectrometry*, doi:10.1039/c3ja50053e.

Foster, G. (2008), Seawater pH, pCO_2 and $[CO_3^{2-}]$ variations in the Caribbean Sea over the last 130 kyr: A boron isotope and B/Ca study of planktic foraminifera, *Earth and Planetary Science Letters*, *271*(1), 254–266.

Heinrich, C., et al. (2003), Quantitative multi-element analysis of minerals, fluid and melt inclusions by laser-ablation inductively-coupled-plasma mass-spectrometry, *Geochimica et Cosmochimica Acta*, *67*(18), 3473–3497.

Jochum, K., et al. (2006), MPI-DING reference glasses for in situ microanalysis: New reference values for element concentrations and isotope ratios, *Geochemistry Geophysics Geosystems*, *7*(2), doi:10.1029/2005GC001060.

Jochum, K., et al. (2011), Determination of reference values for NIST SRM 610–617 glasses following ISO guidelines, *Geostandards and Geoanalytical Research*, doi:10.1111/j.1751-908X.2011.00120.x.

Lear, C., H. Elderfield, and P. Wilson (2003), A cenozoic seawater Sr/Ca record from benthic foraminiferal calcite and its application in determining global weathering fluxes, *Earth and Planetary Science Letters*, *208*(1), 69–84.

Lelono, E. B. (2000), Palynological study of the Eocene Nanggulan Formation Central Java, Indonesia, Ph.D. thesis, Royal Holloway, University of London, 453 p.

Locarnini, R., A. Mishonov, J. Antonov, T. Boyer, and H. Garcia (2010), *World Ocean Atlas 2009, Volume 1: Temperature*, 184 pp., U.S. Government Printing Office, Washington D. C.

Longerich, H., S. Jackson, and D. Günther (1996), Laser ablation inductively coupled plasma mass spectrometric transient signal data acquisition and analyte concentration calculation, *Journal of Analytical Atomic Spectrometry*, *11*(9), 899–904.

Müller, W., M. Shelley, P. Miller, and S. Broude (2009), Initial performance metrics of a new custom–designed ArF excimer LA–ICPMS system coupled to a two-volume laser–ablation cell, *Journal of Analytical Atomic Spectrometry*, *24*(2), 209–214.

Pearson, P. N., and M. R. Palmer (2000), Atmospheric carbon dioxide concentrations over the past 60 million years, *Nature*, *406*, 695–699.

Raitzsch, M., A. Dueñas-Bohórquez, G. Reichart, L. de Nooijer, and T. Bickert (2010), Incorporation of Mg and Sr in calcite of cultured benthic foraminifera: impact of calcium concentration and associated calcite saturation state, *Biogeosciences*, *7*(3), 869–881.

Reiss, Z., and L. Hottinger (1984), *The Gulf of Aqaba*, *Ecological Studies*, vol. 50, 354 pp., Springer-Verlag, Berlin.

Yu, J., H. Elderfield, and B. Hönisch (2007), B/Ca in planktonic foraminifera as a proxy for surface seawater pH, *Paleoceanography*, *22*(26), doi:10.1029/2006PA001347.

Chapter 6

Citation: Evans, D., Erez, J., Oron, S. & Müller, W. [2015]. Mg/Ca-temperature and seawater-test chemistry relationships in the shallow-dwelling large benthic foraminifera *Operculina ammonoides*. *Geochimica et Cosmochimica Acta* **148**:325. doi: 10.1016/j.gca.2014.09.039.

Includes 14 pages of supplementary data

Author contributions: DE designed the research in discussion with WM and JE, carried out the experimental and analytical work, interpreted the data and wrote the manuscript. JE directed the culturing-related experimental work, interpreted the data and edited the manuscript. SO collected the live foraminifera and helped carry out the experimental work. WM helped develop the analytical procedure and interpret the data, and edited the manuscript.

Corrigenda:

- Section 2.2.1 (page 327) incorrectly uses ultrasonication as a verb. Foraminifera were cleaned in deionised H_2O with ultrasonic agitation.
- On the third line of the left column of page 330, 'weekly' should read 'weakly'.
- Seawater with variable [Mg] was created by mixing natural seawater with artificial seawater with no added Mg. Whilst this is clearly stated in both this and the next chapter, it should also be noted that other parameters such as dissolved nutrient and organic carbon concentrations likely varied between cultures. Because the extent of this variation is not known, it is not possible to assess the potential impact on the results reported in these two chapters.
- The first two lines of the second paragraph of section 4.3 state that test Li/Ca is strongly controlled by seawater Li/Ca and temperature, which is not correct. Whilst there is a tight correlation between seawater-test Li/Ca, Li/Ca and temperature are in fact weakly correlated ($R^2 = 0.48$).

Available online at www.sciencedirect.com

ScienceDirect

Geochimica et Cosmochimica Acta 148 (2015) 325–342

Geochimica et Cosmochimica Acta

www.elsevier.com/locate/gca

Mg/Ca-temperature and seawater-test chemistry relationships in the shallow-dwelling large benthic foraminifera *Operculina ammonoides*

David Evans [a,*], Jonathan Erez [b], Shai Oron [c,d], Wolfgang Müller [a]

[a] *Department of Earth Sciences, Royal Holloway University of London, Egham TW20 0EX, UK*
[b] *Earth Science Institute, The Hebrew University of Jerusalem, Israel*
[c] *Department of Geological and Environmental Sciences, Ben-Gurion University of the Negev, Beer-Sheva, Israel*
[d] *The Interuniversity Institute for Marine Sciences (IUI), Eilat, Israel*

Received 14 February 2014; accepted in revised form 26 September 2014; available online 5 October 2014

Abstract

The foraminifera Mg/Ca palaeothermometer contributes significantly to our understanding of palaeoceanic temperature variation. However, since seawater Mg/Ca has undergone large secular variation and the relationship between seawater and test Mg/Ca has not been calibrated in detail for any species with a substantial fossil record, it is only possible to assess relative temperature changes in pre-Pleistocene fossil samples. In order to establish the basis of accurate quantitative Mg/Ca-derived deep-time temperature reconstructions, we have calibrated the relationship between test Mg/Ca, seawater chemistry and temperature in laboratory cultures of the shallow-dwelling large benthic species *Operculina ammonoides*. *Operculina* has a fossil range extending back to the early Paleogene and is the nearest living relative of the abundant genus *Nummulites*. We find a temperature sensitivity of 1.7% $°C^{-1}$ and a linear relationship between the Mg distribution coefficient and seawater Mg/Ca (Mg/Ca_{sw}) with $m = -1.9 \times 10^{-3}$, within error of the equivalent slope for inorganic calcite. The higher test Mg/Ca of *O. ammonoides* compared to inorganic calcite may be explained by an elevated pH of the calcifying fluid, implying that these foraminifera do not modify the Mg/Ca ratio of the seawater from which they calcify, differentiating them in this respect from most other perforate foraminifera. Applying these calibrations to previously published fossil data results in palaeo-Mg/Ca_{sw} reconstruction consistent with independent proxy evidence. Furthermore, our data enable accurate absolute palaeotemperature reconstructions if Mg/Ca_{sw} is constrained by another technique (e.g. ridge flank vein carbonate; fluid inclusions). Finally, we examine Li, Na, Sr and Ba incorporation into the test of *O. ammonoides* and discuss the control exerted by temperature, seawater chemistry, saturation state and growth rate on these emerging proxies.

1. INTRODUCTION

The Mg/Ca thermometer is an established palaeoclimatic tool and provides one of the most accurate quantitative techniques in Pleistocene-Holocene ocean temperature reconstruction. Notwithstanding the wealth of information on the climate system gained from the such studies, many of the most interesting intervals with respect to understanding the controls on Earth system sensitivity lie further back in time (Haywood et al., 2011). Since the initial development of the foraminifera Mg/Ca temperature proxy (Nürnberg et al., 1996; Rosenthal et al., 1997), many more species have been investigated and it is now well known that modern foraminifera exhibit a wide range of Mg/Ca ratios that are controlled by calcification physiology as well as temperature (summarised in Bentov and Erez, 2006).

* Corresponding author.
E-mail address: david.evans.2007@rhul.ac.uk (D. Evans).

http://dx.doi.org/10.1016/j.gca.2014.09.039
0016-7037/

The Mg/Ca palaeothermometer has been applied throughout the Cenozoic (e.g. Lear et al., 2000), although it is now clear that there are fundamental complications with the use of this proxy deeper in geological time, on top of the so-called 'vital effects' which introduce unknown error when applying calibrations to extinct foraminifera. This is principally because the dependence of test Mg/Ca (Mg/Ca_{test}) on seawater Mg/Ca (Mg/Ca_{sw}) is both non-linear and poorly known for all species abundant in the fossil record (see Evans and Müller, 2012, for an overview). Furthermore, the highest resolution Mg/Ca_{sw} data available (Fantle and DePaolo, 2006) suggest a significant rise (~2×) over the last 4 Ma, implying that even poorly-corrected or uncorrected Mg/Ca data from the Pliocene may result in inaccurate palaeotemperature estimates. In order for fossil foraminifera Mg/Ca data to yield accurate absolute temperature reconstructions, both a Mg/Ca-temperature and a Mg/Ca_{test}–Mg/Ca_{sw} calibration is required, along with knowledge of Mg/Ca_{sw} for the time of interest. As far as we are aware, this has not yet been achieved for any species. Here, we focus on *Operculina ammonoides* (Family: Nummulitidae), a species closely related to both *Heterostegina depressa*, for which a trace element study has been performed (Raitzsch et al., 2010), and the genus *Nummulites* (within the same sub-family) which were widespread throughout the Paleogene (sub)tropics to the extent that they are the principal component of some shallow water carbonates (e.g. Guido et al., 2011). Because of the abundance of the nummulitids in the fossil record they represent an under-utilised early-mid Cenozoic palaeoclimate archive.

Operculina are symbiont-bearing, shallow-dwelling benthic foraminifera with a peak abundance-depth range comparable to surface-dwelling planktic foraminifera (Evans et al., 2013, and references therein). The hyaline (glassy) appearance of the test is the result of the non-random orientation of the calcite crystals. Chambers are perforate and lamellar; calcite is mineralised each side of an organic matrix with the addition of a new layer to the entire outer test every time a new chamber is deposited (Reiss, 1958). Previous analyses of a number of fossil and recent non-cultured nummulitids have shown that the alkali earth metal distribution coefficients and their response to temperature and seawater chemistry variation are within error, therefore calibrations based on extant species can be applied to other species within this family in the fossil record (Evans et al., 2013). In order to facilitate comparison to previous work (Raitzsch et al., 2010; Evans and Müller, 2013; Evans et al., 2013) and because different parts of the test have subtly different X/Ca ratios, we focus our geochemical measurements on the marginal cord, the thickened test margin which plays an important reproductive and inter-chamber cytoplasm transport role.

In order to (1) investigate the controls on trace element incorporation in these LBF, (2) provide the basis of more accurate Mg/Ca-based deep-time (pre-Pleistocene) temperature reconstruction and (3) place constraints on the nummulitid biomineralisation mechanism, we present the first coupled temperature-seawater chemistry-test chemistry calibration for a foraminifera. Whilst we present spatially-resolved data for a suite of commonly analysed elements measured by laser-ablation ICPMS, we focus on the Mg/Ca ratio because of its potential for palaeoclimate reconstruction and the importance of understanding Mg incorporation for the assessment of biomineralisation models.

2. MATERIALS AND METHODS

2.1. Culture

All culturing work was carried out at the Institute of Earth Sciences, The Hebrew University of Jerusalem. *O. ammonoides* were collected from the sediment surface from the northernmost Gulf of Eilat (north beach, Eilat) in May 2012 at a depth of 10–15 m. Water temperature at the time of collection was 22 °C. *O. ammonoides* were by far the most abundant organism in the sediment and were sampled from the 1.0–1.3 mm size fraction. Live foraminifera were identified as being those which climbed container walls. Twelve groups of 50 foraminifera were isolated and placed into 130 ml glass-stoppered conical flasks. Seawater collected from the Gulf of Eilat was used as the basis for all culture reservoirs. Seawater was sampled upon preparation of every new reservoir and cumulative samples of water from the flasks were collected at a rate of 1 ml day^{-1} in order to assess potential water chemistry modification by the foraminifera. The water in each flask was completely replaced every second day, after which the cultures were sealed with Parafilm to prevent salinity modification through evaporation. The different cultures were distributed into water baths according to the requirements of each experiment. Water baths were simultaneously cooled and heated to maintain a temperature within ±0.3 °C of the desired value. Temperature and light measurements were performed twice per day for each water bath. Foraminifera were fed every 1–2 weeks with the diatom *Phaeodactylum tricornutum*. Occasional algal growth on some foraminifera, associated with a sharp decrease in calcification rate, was removed by cleaning individual specimens with a fine paint brush.

Growth rate was monitored by measuring the alkalinity of the individual flasks every second day using a Metrohm 716 DMS titrino. All measurements were duplicated and a third replicate sample was analysed if the difference between them was greater than 8 μEq l^{-1}. Accuracy was assessed by weekly analysis of the Scripps Institute of Oceanography reference seawater (batch 109). Long term reproducibility assessed over a two month period was ±11 μEq l^{-1}.

All reservoirs were spiked with ~0.15 μM $BaCl_2$ to provide a compositional marker of calcite grown in culture. Ba was chosen because foraminifera Ba/Ca relates linearly to seawater Ba/Ca in planktic species with minor secondary controls (e.g. Lea and Spero, 1992; Hönisch et al., 2011), enabling cultured material to be unambiguously identified via LA-ICPMS whilst simultaneously analysing proxy (trace) elements. The 0.15 μM spike used here results in seawater with a Ba/Ca ratio of 17.6 μmol mol^{-1}, ~3 times greater than Gulf of Eilat seawater at the time of foraminifera collection (6.0 μmol mol^{-1}). Cultures at 22.5 and 25.5 °C and all those in variable Mg/Ca_{sw} ratios were also

labelled with calcein at a concentration of 40 μM during the first 48 h of the experimental period.

All cultures were located in the same place and therefore had similar lighting conditions with the exception of those grown at 25.5 °C, which were located near a window and were exposed to light intensities ~10% lower than that provided by the artificial laboratory lights. Cultures grown at 27 °C were moved to this location (with a greater proportion of natural light) on day 40 of the experiment in order to make room for the 22.5 °C water bath.

2.1.1. Experiment DE1: variable temperature, constant seawater chemistry

To investigate the control of temperature on trace element incorporation, six water baths were prepared in the range 19–27 °C. Foraminifera cultured at 19, 21, 24 and 27 °C were grown for two months in duplicate cultures, those at 22.5 and 25.5 °C were started one month later. There were insufficient remaining foraminifera to duplicate these latter experiments. An attempt to culture *O. ammonoides* at 18 °C was unsuccessful, resulting in net dissolution. Reservoir water for all of these cultures was unmodified Gulf of Eilat seawater (Table 1).

2.1.2. Experiment DE2: variable seawater Mg/Ca, constant temperature

The effect of varying Mg/Ca_{sw} on Mg/Ca_{test} in *O. ammonoides* was investigated by culturing foraminifera at five different Mg/Ca_{sw} ratios in the range 2–7 mol mol^{-1} (present-day seawater has $Mg/Ca_{sw} = 5.2$ mol mol^{-1}). We found that this species ceases to calcify in response to sudden changes in seawater chemistry and therefore had to be gradually acclimatised in order to precipitate $CaCO_3$ in seawater with $Mg/Ca < 4$. A rate of Mg/Ca_{sw} decrease of 0.5 mol mol^{-1} day^{-1} ensured the survival and growth of most foraminifera at 2 mol mol^{-1}. Attempts to culture these foraminifera at both 1 and 1.5 mol mol^{-1} were not successful, resulting in growth cessation and the retraction of pseudopods. Modified seawater was prepared by mixing Gulf of Eilat seawater with artificial seawater prepared without Mg following the recipe of Millero (1996), with the exception of the seawater with $Mg/Ca = 7$ mol mol^{-1} which was made by spiking natural seawater with 20 mM $MgCl_2$. Seawater [Ca] was invariant between all experiments. Salinity was adjusted to 37‰ using a combination of distilled water and NaCl. Alkalinity was increased to that in the Gulf of Eilat at collection via addition of $NaHCO_3$. Individual reservoir characteristics are summarised in Table 1.

2.2. Analytical chemistry

2.2.1. Laser ablation

Prior to LA-ICPMS analysis, organic material was removed from the foraminifera by oxidisation in 10% NaOCl for eight hours. Following this, the foraminifera were ultrasonicated for two minutes, rinsed twice with deionised water, ultrasonicated for one minute in deionised water, rinsed and then left to dry in a class 100 laminar flow air hood overnight. All foraminifera were analysed using the RESOlution M-50 prototype 193 nm ArF laser-ablation system at Royal Holloway, coupled to an Agilent 7500ce ICPMS (Müller et al., 2009). In order to analyse the marginal cord without sectioning (which risks destroying the final chambers), foraminifera were mounted vertically in the ablation cell by pressing individual foraminifera into a pressure-sensitive adhesive such that the marginal cord of the final chambers was perpendicular to and coincides precisely with the laser focal plane, facilitating analysis by slow depth-profiling (drilling). Given the curved outer surface of the foraminifera we analysed only the final 3–5 chambers in order to remain within the laser focal plane. Because ^{55}Mn is an isotope of interest, but suffers from $^{40}Ar^{15}N$ interference, H_2 was used instead of N_2 as the additional diatomic gas, added downstream of the ablation cell. Depth-profiling analyses were carried out using a 44 μm spot and a repetition rate of 2 Hz at a fluence of ~3 J cm^{-1}. Because it is necessary to use a signal-smoothing device to avoid 'beating' at low repetition rates (Müller et al., 2009), 99% signal washout time was ~3 s, giving an effective spatial depth resolution of ~0.5 μm. ICPMS setup and data reduction was performed as previously described (Müller et al., 2009; Evans et al., 2013) with the exception of the Ar carrier gas flow rate, increased to ~600 ml min^{-1} as H_2 instead of N_2 was used as the additional diatomic gas. Isotopes analysed were ^{7}Li, ^{11}B, ^{24}Mg, ^{25}Mg, ^{27}Al, ^{43}Ca, ^{55}Mn, ^{66}Zn, ^{88}Sr, ^{89}Y, ^{137}Ba, ^{138}Ba, ^{146}Nd and ^{238}U. NIST612 was used as an external (calibration) standard, with the exception of B and Ba which

Table 1
Summary of experimental temperature and seawater characteristics for all foraminifera cultures. ESW and ASW denote natural Gulf of Eilat seawater and artificial seawater prepared with no Mg respectively. The increased alkalinity uncertainty for groups DE2-17(6) and 16(5) is the result of the preparation of new reservoirs with higher alkalinity midway through the experiment.

Sample prefix	Temp. (°C)	Mg/Ca_{sw} (mol mol^{-1})	[Ca] (mM)	Ratio ESW:ASW	Salinity (‰)	pH	Alkalinity (mEq l^{-1})
Experiment 1: variable temperature							
(DE1-) 1–8; 24; 25	19–27	5.42	12.3	1:0	40.7	8.05	2.487–2.503
Experiment 2: variable Mg/Ca_{sw}							
DE2-17(6)	24	6.82	10.7	1:0	38.0	8.09	2.175 ± 0.143
DE2-16(5)	24	5.33	10.6	1:0	37.0	8.05	2.243 ± 0.086
DE2-20(7)	24	4.28	11.3	4:1	37.0	7.98	2.318 ± 0.018
DE2-21(8)	24	3.34	11.7	3:2	37.0	8.04	2.505 ± 0.021
DE2-22(9)	24	2.27	11.4	2:3	37.0	8.14	2.502 ± 0.022

were calibrated to NIST610 and Mg which was calibrated to the MPI-DING komatiite glass GOR132 (Jochum et al., 2006). With the exception of Mg/Ca, the calibration standard was chosen by assessing GOR128 and GOR132 accuracy using both NIST glasses. GOR132 was used to calibrate Mg data as both NIST glasses exhibit Mg heterogeneity (both NIST glasses have Mg 2SD of ~7% compared to 0.9% for GOR132) which is large enough to enlarge errors and bias data if too few NIST analyses are performed to obtain a representative mean Mg intensity-concentration relationship.

Accuracy was assessed by calibrating 36 analyses of the MPI-DING glasses GOR132 and GOR128 to both NIST610 and NIST612. In all cases accuracy for X/Ca ratios discussed hereafter is better than 5%, with the exception of Li/Ca (12.4%) and Ba/Ca (7.4%). These values are based on the standard combination that resulted in the smallest accuracy (with the constraint that the calibration standard must be the same as that used for the foraminifera), as larger offsets were assumed to be the result of a combination of error in the reported value of the NIST or MPI glass, or heterogeneity in either the calibration standard or that treated as an unknown. A detailed assessment of the data quality is given in the Supplementary material. It was not possible to assess precision by repeat analysis of the foraminifera, as they are heterogeneous on a scale smaller than the diameter of the laser beam. Instead we report 2SD of the komatiite glasses GOR132 and GOR128. As before, the smallest precision value based on all possible NIST-MPI combinations was chosen as larger spreads likely indicate standard heterogeneity. Precision for all X/Ca ratios was better than 10% with the exception of Al/Ca and Sr/Ca (<5%) and Ba/Ca (13.7%); see the Supplementary material for a more comprehensive analysis. Whilst these precision data give an indication of the error that should be applied to an individual analysis, we do not propagate precision into error bars where the mean of a large number of analyses is under consideration.

2.2.2. Solution ICPMS

Seawater samples were analysed using an Agilent 7500cx ICPMS at the NERC Isotope Geosciences Laboratory (Keyworth, UK). Samples were acidified to 1% HNO_3 and 0.5% HCl and analysed at 25× dilution with the exception of Mg and Ca which were analysed at 50× dilution. Intensity/internal standard ratios were calibrated against three trace element (1, 10, 100 ppb) and three major element solutions. A pre-run calibration blank was used to define the y-intercept of the calibration lines. All samples were analysed twice, both with and without He (5.5 ml min^{-1}) in the collision/reaction cell; each reported m/z was monitored only in the most appropriate gas mode (see the Supplementary material).

Accuracy and precision were assessed either by triplicate analysis of the seawater standard NASS-4 and the riverine water standard SLRS-2, or using the analyses of the experiment seawater reservoirs in the case of Mg/Ca, Na/Ca and Sr/Ca (where these ratios were not modified through experimental design) as (1) these elements behave conservatively in the ocean and (2) there is no significant freshwater input to the Gulf of Eilat, therefore we expect to find ratios equivalent to the bulk ocean. It was not possible to assess accuracy for Li or B as no standards were analysed with certified values for these elements, in these cases errors are based only on NASS-4 precision. Similarly, accuracy derived from freshwater standards (Na, Ba, U) should be applied to seawater analyses with caution, although we nevertheless do so in the absence of a certified seawater standard and note that these data are likely to overestimate error because the ICPMS was configured to optimise data for high-Na samples with a very different matrix to riverine water. NASS-4 was diluted in the same way as the seawater samples, SLRS-2 was not diluted prior to analysis. All seawater Al, Mn, Zn, Y and REE data are below the LOD. Mg/Ca and Sr/Ca accuracy (%) ± precision (RSD) derived from all analyses of Gulf of Eilat seawater (reservoir and cumulative water samples, $n = 14$) compared to the Mg/Ca value of Lebel and Poisson (1976) and the mean Sr/Ca value of de Villiers (1999) are 3.5 ± 1.5 and $2.5 \pm 4.8\%$ respectively. Na/Ca, Ba/Ca and U/Ca accuracy ± precision are 3.6 ± 9.6, 10.2 ± 4.6 and $2.9 \pm 6.5\%$ respectively, based on triplicate SLRS-2 analyses (see the Supplementary material).

The major and trace element concentrations of the cumulative water samples are within error of the equivalent reservoir. Given that the reservoir samples have less potential for contamination (cumulative samples were opened every second day) we base our calculation of distribution coefficients on the reservoir seawater analyses.

2.3. Carbonate chemistry

Carbonate chemistry parameters not directly measured ($\Omega_{calcite}$, $[CO_3^{2-}]$) were calculated from alkalinity and pH using the co2sys Matlab function (Lewis and Wallace, 2006) and the same set of constants as Raitzsch et al. (2010). For the purpose of assessing the relationship between carbonate chemistry and trace element distribution coefficients we use the mean difference between the cumulative water samples (2 ml from the cultures was collected every second day when the water in the flasks was replenished) and the reservoir. It was necessary to replace the water every two days in this way as the foraminifera were cultured in a closed system and were present in sufficient number to modify the chemistry of seawater from which they calcified. For example, within the variable temperature experiment the pH of the cumulative water samples was 0.08 lower on average than that of the reservoir water, translating to a carbonate ion concentration reduction of ~40 μM.

3. RESULTS

Compositional data along with calculated physiological and carbonate chemistry parameters are shown in Tables 2 and 3.

3.1. Calcification

3.1.1. Calcification rate

Cumulative average growth curves derived from alkalinity measurements for each of the individual cultures are

Table 2
Reservoir and cumulative water sample carbonate chemistry and indicators of growth rate. Column n_1 gives the number of foraminifera that added at least one new chamber (the number of foraminifera analysed is shown in brackets) based on specimens with at least one analysis characterised by elevated Ba/Ca. Column n_2 gives the number of laser ablation depth-profiles positioned on calcite precipitated during the experimental period (the total number of analyses are shown in brackets). Normalised growth rate = growth rate × (total foraminifera analysed)/(foraminifera that precipitated at least one chamber in culture).

		Reservoir		Cumulative samples				Growth rate			
Culture	Temp. (°C)	Ω	$[CO_3^{2-}]$ (μM)	alkalinity (μEq l^{-1})	pH	Ω	$[CO_3^{2-}]$ (μM)	n_1	n_2	mean (μg $CaCO_3$	normalised ind.$^{-1}$ d^{-1})
DE1-1	18.9	5.11	224	2443	7.99	4.31	189	7(8)	23(37)	2.9	3.3
DE1-2	18.9	5.11	224	2474	7.97	4.25	187	2(8)	8(42)	1.2	4.8
DE1-3	20.9	5.42	238	2432	7.98	4.45	195	8(8)	27(35)	3.5	3.5
DE1-4	20.9	5.42	238	2482	8.01	4.88	214	3(4)	8(19)	0.8	1.0
DE1-24	22.5	5.67	249	2460	7.96	4.58	201	5(8)	14(37)	2.3	3.8
DE1-5	24.0	5.93	260	2411	7.97	4.77	209	8(8)	30(37)	4.8	4.8
DE1-6	24.0	5.93	260	2404	7.94	4.47	196	4(4)	14(16)	5.0	5.0
DE1-25	25.6	6.20	272	2436	7.98	5.16	226	9(14)	25(73)	3.4	5.3
DE1-7	27.0	6.48	284	2404	7.98	5.39	236	5(7)	23(36)	5.1	7.2
DE1-8	27.0	6.48	284	2443	8.02	5.74	251	6(8)	26(51)	2.9	3.8
DE2-17(6)	24.0	5.31	227	2067	7.84	3.10	132	4(7)	9(30)	1.5	2.7
DE2-16(5)	24.0	5.09	215	2317	7.67	2.49	105	7(8)	27(36)	2.3	2.6
DE2-20(7)	24.0	4.65	197	2517	7.56	2.14	91	7(8)	27(35)	2.3	2.6
DE2-21(8)	24.0	5.61	237	2451	7.71	2.86	121	7(8)	26(32)	2.1	2.3
DE2-22(9)	24.0	6.66	282	2456	7.67	2.64	112	6(8)	20(34)	1.5	1.9

shown in Fig. 1. Cultures kept at 24 °C grew consistently faster than all others, with the exception of culture DE1-7 (27 °C) which underwent an increase in growth rate after it was moved on day 40 to an area with ~10% lower mean light intensity and a greater proportion of natural light. No geochemical differences were observed between calcite precipitated prior to and after this time, including elements such as Sr which are known to be growth rate dependent in at least some planktic foraminifera (Kisakürek et al., 2008); see the Supplementary material. A probable explanation is that individual specimen growth rate did not change, but rather individuals that were not previously calcifying began to form new chambers when moved to an area of lower light intensity, given that calcification rates represent an average of 50 individuals. A change in the number of calcifying individuals rather than the overall calcification rate can also explain why no increase in growth rate was observed in the repeat culture at this temperature (Fig. 1). There is no evidence that moving this culture resulted in identifiable geochemical bias.

Light intensity for all cultures was virtually identical (aside from the previously mentioned exceptions), therefore this cannot explain the remainder of the inter-culture growth rate variation. For cultures of equivalent lighting conditions, those at 19 °C (DE1-1 and -2) and 27 °C (DE1-7 and -8) grew at 50% of the rate of those at 24 °C. It is unsurprising that the cultures characterised by the highest growth rates were those grown under conditions most similar to that of the mean annual Gulf of Eilat temperature at the foraminifera collection depth, although some of the observed variation may be a result of acclimatisation to the new conditions. Therefore, it is possible that culture growth rates do not translate in any meaningful way to natural changes in response to long-term environmental change. Duplicate cultures grown at the same temperature exhibit large differences in calcification rate despite all other conditions being equal. Repeat cultures show a difference in cumulative calcification of up to 360%, although those at 24 °C are within error of each other. Because each experiment consisted of 50 foraminifera, these substantial differences are unlikely to result from random variation in the initial population and may suggest that these foraminifera are capable of influencing overall group calcification rates. All cultures in the variable seawater chemistry experiment, including that with modern Mg/Ca_{sw}, grew at a rate ~50% of those at the same temperature (24 °C) in the Mg/Ca-temperature experiment. Given the variation in growth rate between repeat cultures in unmodified seawater, it is not possible to assess whether this was because of the modified seawater chemistry.

Fig. 1C shows the relationship between mean $\Omega_{calcite}$ (the average between the reservoir and cumulative water Ω for each culture) and growth rate, normalised by multiplying by the ratio of the number of foraminifera analysed to the number of foraminifera that precipitated at least one chamber during the culture period (see Table 2). Calcifying foraminifera were identified as those that precipitated at least one chamber with elevated Ba/Ca (see Section 3.1.2). Normalised growth rate is positively correlated with mean culture Ω for the variable temperature experiment, although cultures that calcified very slowly (DE1-4 and all DE2) do not fit this trend.

3.1.2. Identifying cultured calcite

Calcein labelling and modifying seawater [Ba] are both effective methods of identifying new chambers in cultured foraminifera. Newly formed chambers in specimens from cultures that were labelled with calcein (Table 1) are easily identifiable (Fig. 2). The majority of foraminifera precipitated at least one new chamber during the labelling period

Table 3
Seawater and foraminifera trace element data measured by solution and laser-ablation ICPMS respectively. Seawater analyses shown are of the reservoir water samples. Laser ablation data represent the mean of all analyses of newly precipitated calcite. Errors are precision (±2SD) for seawater analyses as the number of analyses was relatively small ($n = <10$), and ±2SE for laser-ablation data where n was typically greater than 30 (see Table 2).

Culture	value					error				
Seawater	Li/Ca mmol mol^{-1}	Na/Ca mol mol^{-1}	Mg/Ca mol mol^{-1}	Sr/Ca mmol mol^{-1}	Ba/Ca μmol mol^{-1}	Li/Ca mmol mol^{-1}	Na/Ca mol mol^{-1}	Mg/Ca mol mol^{-1}	Sr/Ca mmol mol^{-1}	Ba/Ca μmol mol^{-1}
(1) Gulf of Eilat at the time of collection										
	1.80	41.1	5.23	7.89	6.01	0.07	3.9	0.08	0.38	0.28
(2) Experiment reservoirs										
DE1-*x*	2.10	45.3	5.23	8.59	17.59	0.09	4.3	0.08	0.42	0.81
DE2-17(6)	2.01	42.6	6.82	8.66	18.98	0.08	4.1	0.10	0.42	0.87
DE2-16(5)	1.93	41.6	5.33	8.42	18.65	0.08	4.0	0.08	0.41	0.86
DE2-20(7)	1.60	42.3	4.28	9.27	19.13	0.07	4.0	0.06	0.45	0.88
DE2-21(8)	1.28	42.7	3.34	9.95	16.18	0.05	4.1	0.05	0.48	0.74
DE2-22(9)	0.79	47.1	2.27	10.87	15.63	0.03	4.5	0.03	0.53	0.72
Foraminifera	Li/Ca μmol mol^{-1}	Na/Ca mmol mol^{-1}	Mg/Ca mmol mol^{-1}	Sr/Ca mmol mol^{-1}	Ba/Ca μmol mol^{-1}	Li/Ca μmol mol^{-1}	Na/Ca mmol mol^{-1}	Mg/Ca mmol mol^{-1}	Sr/Ca mmol mol^{-1}	Ba/Ca μmol mol^{-1}
(1) Non-calcifying individuals										
	55.7	25.1	137.3	2.61	4.6	1.1	0.5	1.0	0.03	0.2
(2) Individual cultures										
DE1-1	58.2	23.0	129.9	2.65	13.0	2.4	0.4	1.6	0.04	0.7
DE1-2	61.8	23.3	131.2	2.63	12.2	2.4	0.4	1.6	0.04	0.7
DE1-3	58.0	23.2	135.5	2.60	12.9	1.8	0.7	2.0	0.05	0.6
DE1-4	60.1	23.2	131.4	2.56	11.5	2.6	0.3	1.7	0.04	0.6
DE1-24	61.4	25.0	140.0	2.60	12.3	1.4	0.9	2.4	0.07	0.5
DE1-5	55.1	24.9	143.4	2.58	11.8	2.2	0.9	1.7	0.05	0.6
DE1-6	54.1	26.2	144.2	2.54	11.2	3.6	1.3	2.0	0.04	0.4
DE1-25	55.6	26.3	149.1	2.58	11.4	4.6	1.8	2.2	0.04	0.3
DE1-7	53.0	25.4	151.0	2.53	11.4	2.3	0.7	1.0	0.02	0.4
DE1-8	57.5	25.0	152.5	2.63	11.8	1.5	0.8	2.5	0.04	0.5
DE2-17(6)	53.3	24.2	162.0	2.71	12.0	2.9	0.6	5.7	0.05	1.7
DE2-16(5)	49.9	24.1	141.4	2.56	12.4	2.6	1.0	2.0	0.03	0.4
DE2-20(7)	36.0	22.7	122.2	2.65	13.5	1.6	1.0	2.2	0.05	0.6
DE2-21(8)	30.7	22.1	106.7	2.72	10.2	2.7	0.7	4.0	0.04	0.4
DE2-22(9)	17.2	20.6	72.3	2.66	8.3	1.6	0.7	2.0	0.06	0.4
(3) Pooled duplicates										
19.0 °C	59.1	23.1	130.2	2.65	12.8	2.0	0.3	0.7	0.03	0.5
21.0 °C	58.5	24.1	134.6	2.59	12.6	1.6	1.5	1.7	0.04	0.6
22.5 °C	61.4	25.0	140.0	2.60	12.3	1.4	0.9	2.4	0.07	0.5
24.0 °C	54.8	25.5	143.6	2.56	11.6	1.9	0.8	1.3	0.03	0.4
25.5 °C	55.6	26.3	145.3	2.58	11.4	4.6	1.8	2.2	0.04	0.3
27.0 °C	55.4	25.2	151.8	2.58	11.6	1.5	0.6	1.4	0.03	0.3

from calcein-spiked vacuolised seawater (Fig. 2A, C and D), producing highly fluorescent calcite. Preceding chambers are weekly fluorescent because these foraminifera add a layer of calcite to their entire outer surface when a new chamber is formed (e.g. Erez, 2003), enabling newly formed calcite to be identified in foraminifera which did not calcify during the labelling period because new chambers are non-fluorescent (Fig. 2B).

Examples of laser-ablation profiles of calcifying and non-calcifying specimens are shown in Fig. 3C and D, respectively. These analyses demonstrate that *O. ammonoides* adds a new layer of calcite to the existing marginal cord during chamber formation, as some depth profiles show a decrease in both Mg/Ca and Ba/Ca representing the transition from calcite precipitated in culture to pre-existing calcite. The Ba/Ca–Mg/Ca pattern of the specimen shown in Fig. 3C is a result of the lower temperature of the Gulf of Eilat in which these foraminifera originally calcified (lower test Mg/Ca) compared to the culture temperature (27 °C), unambiguously identifiable using Ba/Ca. The specimen shown in Fig. 3D is characterised by lower Mg/Ca and Ba/Ca because it precipitated the analysed calcite prior to collection at ~22 °C, and in seawater that was not spiked with $BaCl_2$. Based on such profiles, all laser-ablation

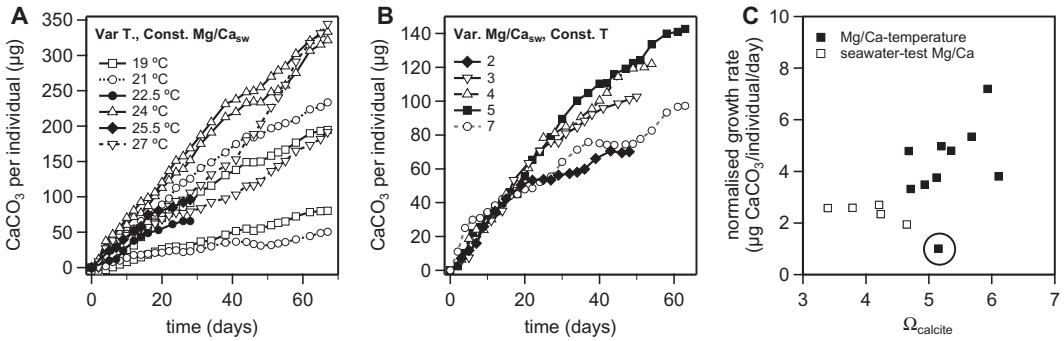

Fig. 1. Cumulative growth rates for each culture within (A) the variable temperature, constant seawater chemistry experiment (DE1) and (B) the variable seawater chemistry, constant temperature experiment (DE2). (C) The relationship between growth rate and mean calcite saturation state. With the exception of culture DE1-4 (highlighted), normalised growth rate is broadly positively correlated with $\Omega_{calcite}$ (see text for details).

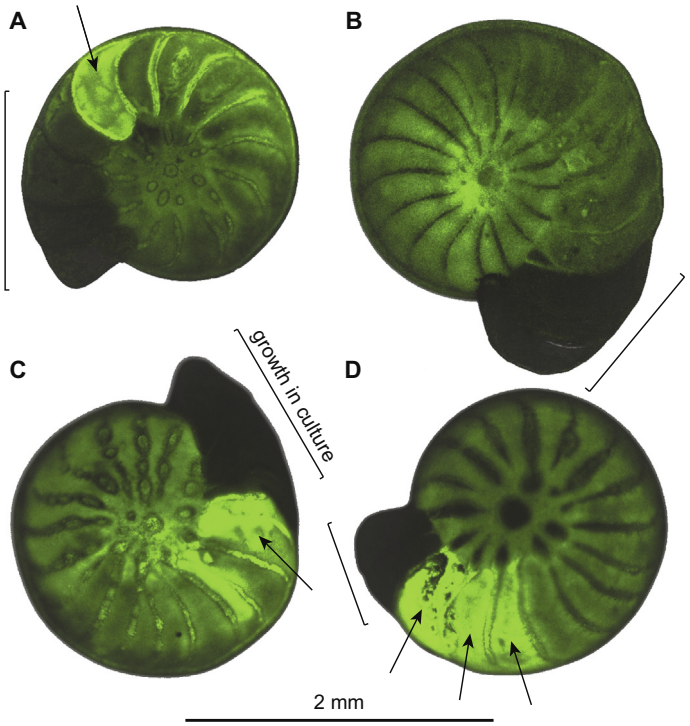

Fig. 2. Fluorescent confocal microscope images of calcein labelled *O. ammonoides*. Chambers that were grown during the calcein labelling period (48 h) are highlighted with arrows, marking the point from which calcite was first grown under controlled culture conditions (see text for details). Note that the specimen shown in B did not form any chambers during the labelling period but formed three chambers subsequently, brackets show chambers precipitated during the experimental period. In addition, all four specimens added secondary laminae to the existing chambers, which is the reason that the majority of the foraminifera are weakly fluorescent.

ICPMS data were categorised into representing new or existing calcite by setting a test Ba/Ca cut-off point at 9 µmol mol^{-1} below which it was judged that the analysed material was entirely or partially composed of calcite precipitated prior to culture. Furthermore, analyses characterised by Mg/Ca and Ba/Ca 2RSD >20% were also excluded on the basis that these were likely to partly consist of calcite grown at a temperature other than that of the culture (chamber f-4, Fig. 3C Mg/Ca RSD = 21.4% compared to 13.8% for the final chamber which also has consistently high Ba/Ca). These data therefore enable the non-qualitative exclusion of analyses which represent a mix of calcite precipitated before and after the start of the experiment.

All analyses from the two extremes of the variable temperature experiment are shown in Fig. 3E and F in order to further demonstrate the effectiveness of this technique. Each data point in these plots does not necessarily represent a single chamber, as it is possible to fit more than one ablation spot on the marginal cord within a single chamber (Fig. 3B). Analyses characterised by relatively low Ba/Ca

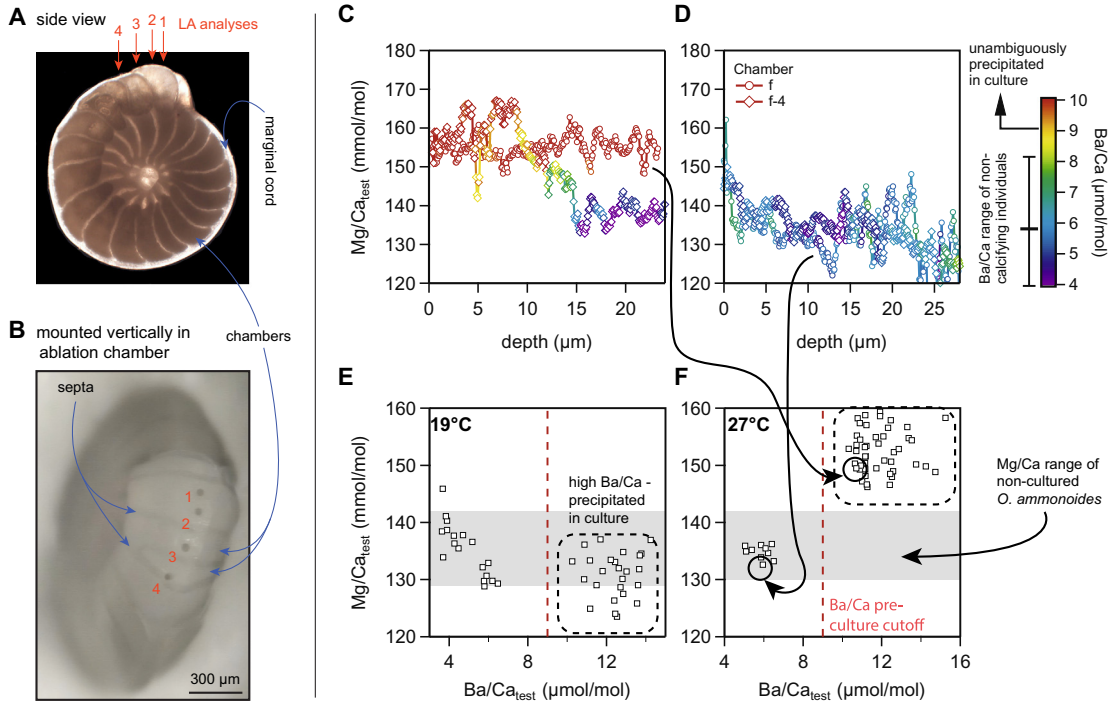

Fig. 3. (A) Live *O. ammonoides* under cross-polarised light. Arrows show orientation of laser-ablation depth profiles. (B) Post-analysis view of a specimen mounted sub-vertically in the ablation chamber. Laser craters are 44 μm in diameter. (C–F) Using a seawater Ba-spike (0.15 µM) in order to identify material precipitated during the culture period. (C) Two analyses of an individual specimen cultured at 27 °C that precipitated new chambers during the culture period (elevated test Ba/Ca) and (D) a specimen that stopped calcifying when placed in culture. Ba/Ca ratios are shown as a function of colour. 11-point Mg/Ca running means are plotted. Time was converted to depth assuming that each laser pulse removes 80 nm of calcite. (E and F) All analyses for the 19 °C and the 27 °C Mg/Ca-temperature calibration experiments respectively, demonstrating the effectiveness of this technique at discriminating newly formed and pre-existing calcite. Mg/Ca is relatively lower and higher in experiments conducted at 19 and 27 °C respectively, compared to pre-culture calcite, as expected given that these foraminifera were taken from seawater with a winter-spring average temperature of ~22 °C. (For interpretation of the references to colour in this figure legend, the reader is referred to the web version of this article.)

ratios (4–6 µmol mol^{-1}) have Mg/Ca ratios within the range of control specimens that were collected at the same time as cultured individuals but immediately washed and dried (Evans et al., 2013), implying that this calcite was formed prior to the start of the experiment. These data points are distinct in Mg–Ba space (i.e. there is no continuum) from those with high Ba/Ca ratios and Mg/Ca offset from that of non-cultured specimens. Within this subset, analyses derived from individuals cultured at 19 °C have lower Mg/Ca than the control group, whereas the opposite is the case for those cultured at 27 °C. This is consistent with the estimated growth temperature of these foraminifera prior to collection (early May), which remains at ~22 ± 1 °C from November to April. Therefore calcite precipitated prior to culture (with low Ba/Ca) should have an intermediate Mg/Ca ratio between the two extremes of the temperature experiment, as observed.

3.2. Trace element chemistry

3.2.1. Mg/Ca-temperature calibration

The results of our temperature calibration experiment define a Mg/Ca sensitivity within error of the gradient given by a comparative field calibration of the same species (Evans et al., 2013), see Fig. 4. Linear and exponential regressions describe the data equally well. We present both here to facilitate comparison to previous work and because the reconstruction of relative temperature shifts in fossil samples is more complex with linear Mg/Ca-temperature regressions (see Evans et al., 2013 and Supplementary material). Based on the culture data presented here, the relationship between Mg/Ca and temperature for *O. ammonoides* is:

$$ln(\mathrm{Mg/Ca}) = 0.0183 \pm 0.0025 \times T + 4.52 \pm 0.06 \quad (1)$$

Or in linear form:

$$\mathrm{Mg/Ca} = 2.57 \pm 0.37 \times T + 81.3 \pm 8.6 \quad (2)$$

Combining these laboratory culture data with the *O. ammonoides* field samples of Evans et al. (2013) results in the following exponential and linear relationships:

$$ln(\mathrm{Mg/Ca}) = 0.0169 \pm 0.0016 \times T + 4.55 \pm 0.04 \quad (3)$$

$$\mathrm{Mg/Ca} = 2.42 \pm 0.24 \times T + 84.2 \pm 6.1 \quad (4)$$

All regression errors are ±2SD. Mg/Ca error bars in Fig. 4 are ±2SE of the mean of all analyses for a given culture,

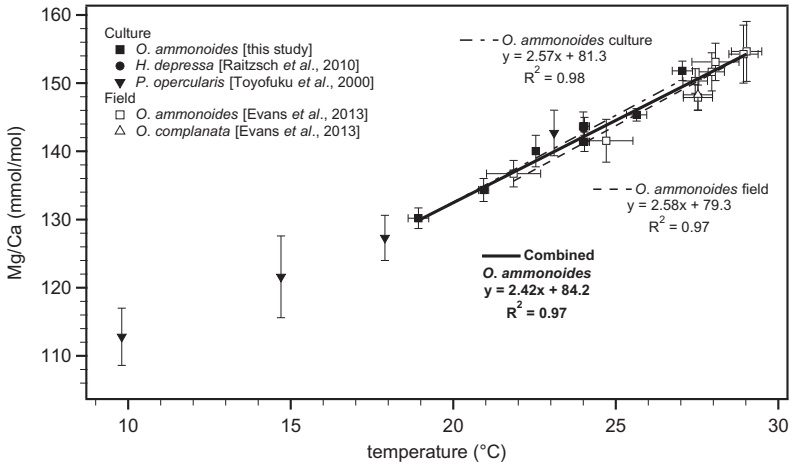

Fig. 4. The relationship between Mg/Ca_{test} and temperature in laboratory cultured *O. ammonoides* in the context of a comparative field-based calibration (Evans et al., 2013), data from other species within the family Nummulitidae and *P. opercularis* (Toyofuku et al., 2000), an unrelated shallow benthic foraminifera with a Mg/Ca-temperature sensitivity within error of that for *Operculina*. The datapoint of Raitzsch et al. (2010) is not visible as it lies almost precisely below the data presented here (24 °C, Mg/Ca = 143.3 mmol mol^{-1}). A linear regression through the *P. opercularis* data is within error of that for the nummulitids ($m = 2.23$, $c = 89.6$). We recommend using the 'combined' calibration for palaeoceanic reconstruction. Mg/Ca error bars are 2SE, temperature error bars are 2SD.

effectively comparable to calibrations based on analyses of multiple dissolved foraminifera analysed by solution ICP-MS/AES. Mg/Ca data from duplicate cultures were pooled as no significant offset was observed (Table 3). For comparison, data from the small, shallow-dwelling, hyaline benthic foraminifera *Planoglabratella opercularis* (Toyofuku et al., 2000) are also shown in Fig. 4. This species has a slope and intercept (2.23, 89.6) within error of our *O. ammonoides* calibration, although the species are not closely related.

The Gulf of Eilat seawater used for the culture calibration has a salinity of 40.65‰, up to 8‰ higher than the sample sites of Evans et al. (2013) which were predominantly within SE Asia and characterised by salinities of 33–36‰, yet the individual calibrations in Fig. 4 define Mg/Ca-temperature relationships that are virtually identical. Data from two other species within the Nummulitidae family, *O. complanata* (Evans et al., 2013) and *H. depressa* (Raitzsch et al., 2010), the latter cultured at a salinity of 36‰, fall on the same line. Therefore, there is no evidence that this large salinity difference between sample sites/cultures has any control on *O. ammonoides* Mg/Ca; the offset between foraminifera living at the same temperature but different salinity is always smaller than the error in the laser-ablation measurements.

3.2.2. Test-seawater Mg/Ca relationship

The relationship between Mg/Ca_{test}, D_{Mg} ($[Mg/Ca_{test}]/[Mg/Ca_{sw}]$) and Mg/Ca_{sw} is shown in Fig. 5. D_{Mg} varies linearly with Mg/Ca_{sw}:

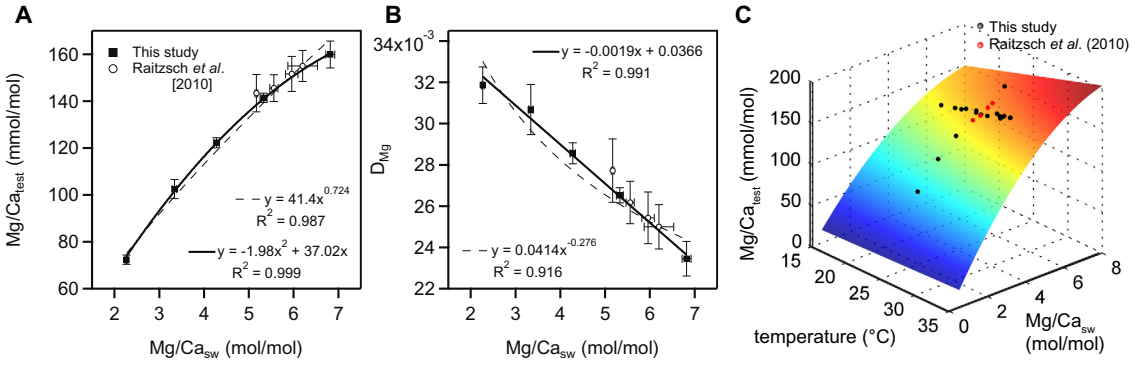

Fig. 5. The relationship between (A) test Mg/Ca and (B) the Mg/Ca distribution coefficient with seawater Mg/Ca. The linear relationship between D_{Mg} and Mg/Ca_{sw} implies a 2nd order polynomial relationship between Mg/Ca_{sw}–Mg/Ca_{test}, passing through the origin. Power-law regressions are shown for comparison. Error bars are ±2SE. (C) A coupled Mg/Ca_{test}–Mg/Ca_{sw}-temperature calibration showing the surface defined by Eq. 10 as well as the laboratory culture data of this study and Raitzsch et al. (2010). Colour is shown as a function of Mg/Ca_{test} (*z*-axis height). Regressions derived from *O. ammonoides* data only.

$$D_{Mg} = -0.00190 \pm 0.00034 \times Mg/Ca_{sw} + 0.0366 \pm 0.0016 \quad (5)$$

Manipulating this calibration by multiplying through by Mg/Ca_{sw} results in a 2nd order polynomial relationship between Mg/Ca_{sw} and Mg/Ca_{test} which passes through the origin, because $[D_{Mg} = a \times Mg/Ca_{sw} + b] \times Mg/Ca_{sw}$ is equivalent to $Mg/Ca_{test} = a \times (Mg/Ca_{sw})^2 + b \times Mg/Ca_{sw}$. Therefore, at 24 °C:

$$Mg/Ca_{test} = -1.98 \pm 0.39 \times (Mg/Ca_{sw})^2 + 37.02 \pm 2.16 \times Mg/Ca_{sw} \quad (6)$$

Where Mg/Ca_{test} is expressed in mmol mol^{-1}.

Previous studies that have examined the shape of the relationship between fluid and calcite Mg/Ca in both foraminiferal and inorganic calcite have argued that this relationship is best described by a power regression (Ries, 2004; De Choudens-Sánchez and González, 2009; Hasiuk and Lohmann, 2010; Evans and Müller, 2012). The linear relationship between D_{Mg} and Mg/Ca_{sw} reported here, which implies a polynomial relationship between Mg/Ca_{sw}–Mg/Ca_{test}, is comparable to that derived from inorganic precipitation experiments (Mucci and Morse, 1983) when only data over an equivalent range of Mg/Ca_{sw} values are considered. Whilst all inorganic data (including Mg/Ca_{sw} ratios >8 and <1) are best described by a power relationship between D_{Mg} and Mg/Ca_{sw} (De Choudens-Sánchez and González, 2009; Mucci and Morse, 1983), there is no evidence that Cenozoic seawater was characterised at any point by such ratios and we therefore limit our discussion to calcite precipitated from seawater with Mg/Ca between 1 and 8 mol mol^{-1}, for which a linear D_{Mg}–Mg/Ca_{sw} regression (and therefore a polynomial Mg/Ca_{sw}–Mg/Ca_{test} regression) best describes our data. The regressions defined in Eqs. 5 and 6 should not be extrapolated above $Mg/Ca_{sw} = 8$ mol mol^{-1}, as the vertex of the quadratic Mg/Ca_{sw}–Mg/Ca_{test} regression is approached.

To facilitate comparison to previous studies (e.g. Hasiuk and Lohmann, 2010) we also give the equivalent power regressions (these are shown in relation to previous foraminifera calibrations in the Supplementary material):

$$Mg/Ca_{test} = 41.4 \times Mg/Ca_{sw}^{0.72} \quad (7)$$

$$D_{Mg} = 0.041 \times Mg/Ca_{sw}^{-0.28} \quad (8)$$

Which have R^2 values of 0.99 and 0.92, the later of which is substantially lower than that for a linear D_{Mg}-Mg/Ca_{sw} regression (0.99, Fig. 5).

3.2.3. Controls on other proxy trace element incorporation in nummulitid calcite

Both calcite and seawater were also analysed for Li, Na, Sr and Ba, as these are either established or emerging proxy systems in other species and important for biomineralisation models. The cultures grown at different temperatures enable this potential control on other trace element distribution coefficients to be investigated, whilst the artificial-natural seawater mixes of the variable Mg/Ca_{sw} experiments are characterised by variable seawater Li–Na–Sr–Ba/Ca ratios. Specifically, the artificial seawater has ~3× lower Li/Ca and ~15% higher Sr/Ca than Gulf of Eilat seawater. The relationships described in this section should be viewed with caution given that some variables, namely growth rate and foraminifera-mediated saturation state changes, were beyond our control and may simultaneously affect proxy incorporation. This complication is not unique to our dataset, although our monitoring of growth rate and carbonate chemistry do enable preliminary interpretations to be drawn.

Test Li/Ca shows a weak negative correlation with temperature ($R^2 = 0.48$, Fig. 6A) with a gradient similar to *Cibicidoides pachyderma* corrected for saturation state (Lear et al. 2010; Bryan and Marchitto 2008). There is a strong positive relationship between seawater and test Li/Ca ($R^2 = 0.98$) with a slope ~30 times steeper than both the Li/Ca-temperature relationship observed here and the Li/Ca–ΔCO_3^{2-} relationship observed by Bryan and Marchitto (2008). Saturation state and Li/Ca are weakly negatively correlated in the variable seawater chemistry experiment ($R^2 = 0.22$) whereas the weak negative relationship between Li/Ca and Ω in the variable temperature experiment (Fig. 6C) is not significant because it is an artefact of the Li/Ca-temperature relationship, given that temperature exerts a control on Ω. Growth rate is strongly correlated with Li/Ca and Ω in experiment DE2 which is not supported by data from experiment DE1, this is likely to be an artefact of lower growth rates in the cultures with seawater chemistry most different from natural.

Na/Ca is weakly positively correlated with culture temperature ($R^2 = 0.72$) and uncorrelated with seawater Na/Ca in these experiments (Fig. 6E). The curved relationship with Na/Ca_{max} at ~25 °C is similar in appearance to the shape of the temperature-growth rate curve for these cultures suggesting that growth rate may be the principal reason for Na/Ca_{test} variation in our experiments. If the culture with the lowest growth rate is considered to be an outlier then growth rate and Na/Ca are moderately well correlated ($R^2 = 0.63$, Fig. 6H), based on the combination of both experiments. Moreover, the data from the variable seawater chemistry experiment show a very strong correlation with growth rate, despite constant temperature and broadly equivalent Na/Ca_{sw}. The salient point is that there are significant controls on Na/Ca incorporation in *O. ammonoides* other than salinity, which varies by only 1‰ between the cultures in experiment DE2 and yet these are characterised by a 4 mmol mol^{-1} (±10%) shift in Na/Ca. An extended discussion of our *O. ammonoides* Na/Ca data in the context of other foraminifera is given in Section 4.3 and the Supplementary material, with particular regard to our analytical and cleaning protocols. We demonstrate that the Na/Ca ratios of *O. ammonoides*, ~2× higher than some other foraminifera, are not artefacts of the sample preparation process.

There is no evidence for a relationship between Sr/Ca_{test} and temperature, Sr/Ca_{sw} (Fig. 6N) or growth rate based on our experiments in this foraminifera. See below and Section 4.3 for an explanation of the lack of a test-seawater Sr/Ca relationship. Similarly, there is no statistically significant correlation between Ω and Sr/Ca_{test} (Fig. 6O).

Ba/Ca is negatively correlated with temperature ($R^2 = 0.87$, Fig. 6Q), characterised by a shift of

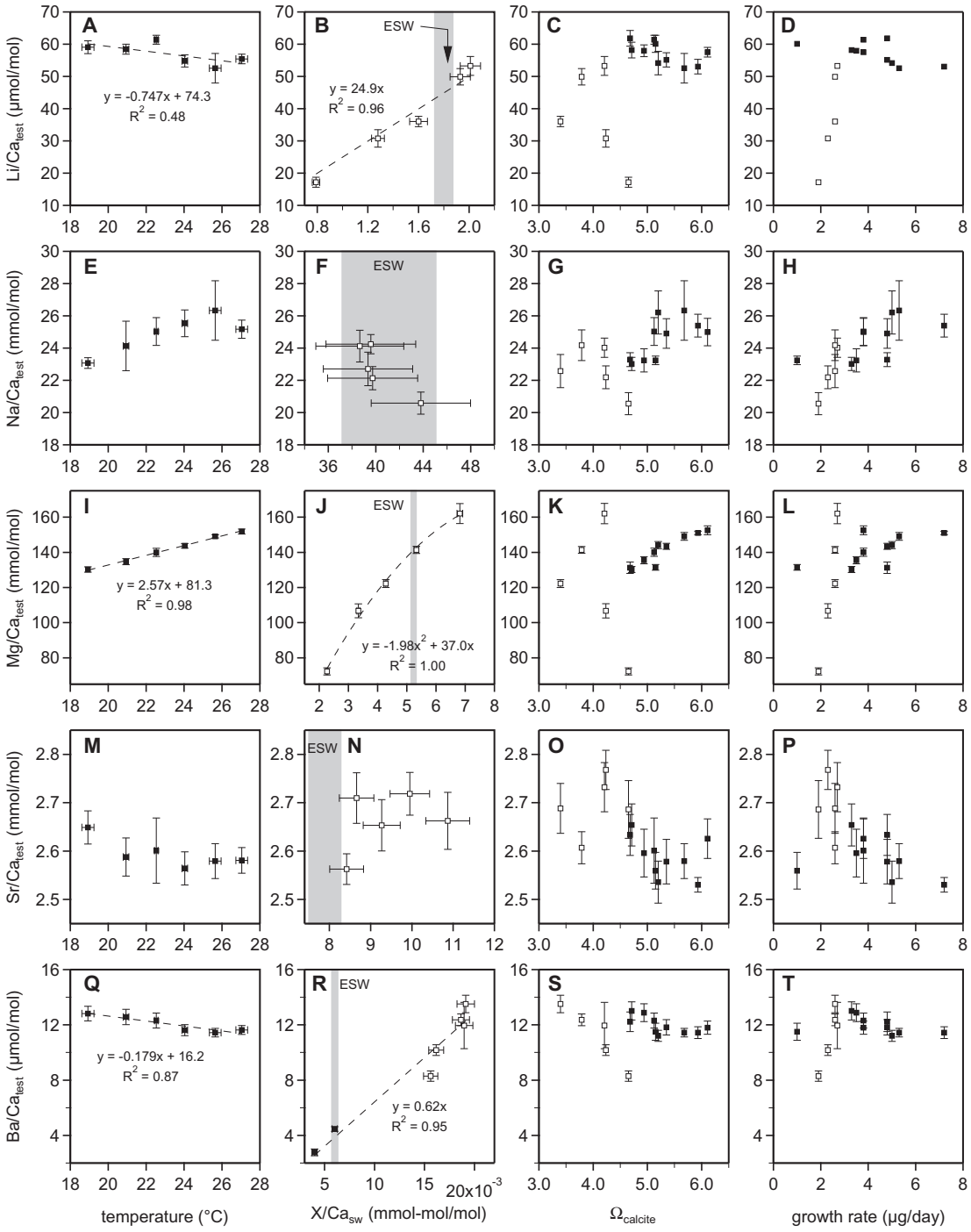

Fig. 6. Li–Na–Mg–Sr–Ba relationships with temperature, seawater chemistry, mean saturation state and growth rate. A normalisation factor was applied to the growth rate in order to correct for potential bias relating to foraminifera which did not calcify at all; growth rate is calculated from alkalinity, individual foraminifera were not monitored which may be a cause of significant inaccuracy in these estimates. Closed symbols represent data from the variable temperature experiment and open symbols represent data from the variable seawater chemistry experiment. Repeat experiments under equivalent conditions were not pooled for these plots because growth rate and calculated carbonate chemistry varied between these repeats. Error bars are 2SE for LA-ICPMS foraminifera data and 2SD precision for seawater data.

0.18 µmol mol^{-1} °C^{-1}. Similarly to the Na/Ca data, the cultures at 27 °C are offset from the trend defined by the rest of the experiments, although to a lesser extent. Our Ba/Ca_{test}-Ba/Ca_{sw} data confirm the linear relationship observed in planktic foraminifera (Hönisch et al., 2011) although the gradient for this species is more than four times steeper than that of *Orbulina universa*. The culture data presented here, along with Ba/Ca measurements of

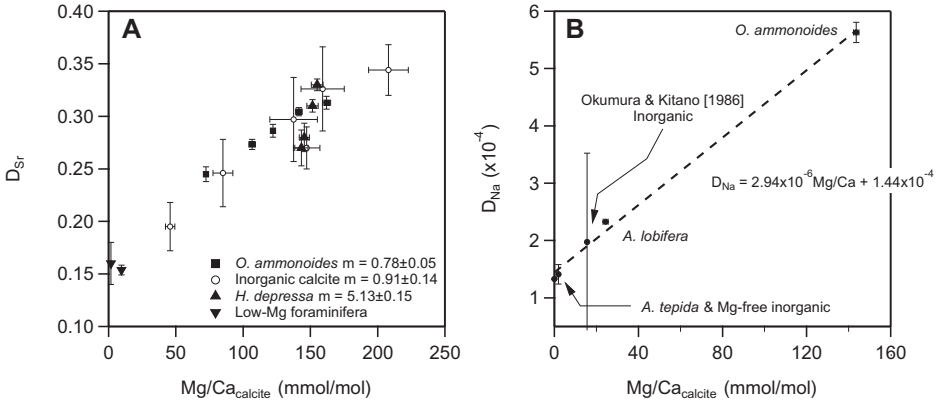

Fig. 7. (A) The relationship between $Mg/Ca_{calcite}$ and D_{Sr}. Our data for *O. ammonoides* fall on the same trend as that for inorganic calcite (Mucci and Morse, 1983). The analyses of Raitzsch et al. (2010) of the closely related foraminifera *H. depressa* are also broadly consistent with this trend, as are data from low-Mg planktic (*O. universa*; Russell et al. (2004)) and benthic (*A. tepida*; Raitzsch et al. (2010)) foraminifera. (B) D_{Na} variation is similarly related to $Mg/Ca_{calcite}$ when a wide range of calcites are considered, implying that lattice distortion from Mg incorporation may also allow more alkali metal ions into interstitial sites.

non-cultured *O. ammonoides* from both the Gulf of Eilat and several samples from southeast Asia (Evans et al., 2013), define the following test-seawater Ba/Ca relationship ($R^2 = 0.95$):

$$Ba/Ca_{test} = 0.62 \pm 0.003 \times Ba/Ca_{sw} \quad (9)$$

The Ba/Ca data from the variable seawater chemistry experiment alone define a steeper slope ($m = 1.16$) compared to Eq. 9. Furthermore, the cultures with the highest and lowest Ba/Ca_{sw} are offset from the line defined by Eq. 9 to an extent greater than that which may be reasonably expected based on the combined analytical errors for the seawater and calcite data. This implies that, in these foraminifera, Ba/Ca has a secondary control other than temperature, and/or that the test-seawater relationship is more appropriately described by an exponential relationship ($R^2 = 0.97$ based on all of the data shown in Fig. 6R). The data derived from experiment DE2 are very strongly correlated with Ω (Fig. 6S) although this is an artefact of the Ba/Ca_{sw} correlation with mean culture Ω. There is unlikely to be a causal relationship between these parameters, although it may not be coincidental that the extent to which the foraminifera modified the saturation state of the seawater is well correlated with the proportion of Eilat seawater in these artificial:natural seawater mixtures. The correlation between Ba/Ca_{test} and growth rate for experiment DE2 is likely an artefact for similar reasons, the variable temperature experiment does not support this relationship.

As well as the multiple dependent variables that complicate the interpretation of the X/Ca_{test}-growth rate-Ω relationships (Fig. 6), these data should also be viewed with the caveat that trace element distribution coefficients may influence each other. For example Sr/Ca incorporation in inorganic calcite is dependent to some extent on calcite Mg/Ca (Mucci and Morse, 1983). Fig. 6 implies that there is no significant temperature, growth rate or saturation state control on Sr-incorporation in *O. ammonoides*. In particular, the lack of correlation between seawater-test Sr/Ca is superficially surprising given that previous work on *H. depressa* have shown that these parameters are highly dependant. Following Mucci and Morse (1983), Fig. 7A shows the relationship between test Mg/Ca and D_{Sr}. The *O. ammonoides* D_{Sr}–Mg/Ca_{test} relationship is within error of that for inorganic calcite (see Fig. 7A for regression coefficients), demonstrating that Mg/Ca_{test} is the dominant control on D_{Sr} in our experiments. This is because the Mg/Ca_{test} ratio is far more variable between cultures than Sr/Ca_{sw}, which is why we observe no test-seawater Sr/Ca relationship. The data of Raitzsch et al. (2010) for *H. depressa* also broadly conform to both those presented here and to inorganic calcite, although the Mg/Ca_{test}-D_{Sr} slope is far steeper for *H. depressa* alone ($m = 5.13$ cf. 0.91 for inorganic calcite). A similar plot of D_{Na}–$Mg/Ca_{calcite}$ (Fig. 7B) shows that for a wide range of foraminiferal and inorganic calcites (Ishikawa and Ichikuni, 1984; Okumura and Kitano, 1986; Wit et al., 2013, this study and our unpublished laser-ablation data for *Amphistegina lobifera*), Na-incorporation is also controlled by the Mg/Ca ratio, with a gradient of 2.94×10^{-6} per 1 mmol mol^{-1} increase in Mg/Ca.

4. DISCUSSION

4.1. Mg/Ca-derived palaeoreconstruction

Accurate pre-Pleistocene Mg/Ca palaeothermometry requires a good understanding of the relationship between Mg/Ca_{sw}, Mg/Ca_{test} and temperature, as well as an independent estimate of seawater Mg/Ca for the time interval of interest (Evans and Müller, 2012). Given that the majority of proxy and model data show that seawater was characterised by lower Mg/Ca throughout almost all of the Cenozoic compared to the present day (e.g. Stanley and Hardie, 1998; Coggon et al., 2010), Mg/Ca data from fossil material older than a few million years may at best only be used to reconstruct relative changes in temperature. Although previous calibrations between seawater and test Mg/Ca have been carried out at lower than present-day

Mg/Ca_{sw} values for *Globigerinoides sacculifer* (Delaney et al., 1985) and two species of *Amphistegina* (Segev and Erez, 2006), these currently have limited applicability because Delaney et al. (1985) simultaneously varied several experimental parameters and there is no published Mg/Ca-temperature calibration for *Amphistegina*. Here, we show how our data may be used to accurately reconstruct absolute temperature derived from Mg/Ca measurements of pre-Pleistocene foraminifera, when seawater Mg/Ca cannot be assumed to be the same as present day.

The consistency of the Mg/Ca-temperature relationship between the field and laboratory, at different salinities, in seawater with different trace element chemistry, and between species in this family (Fig. 4) strongly suggests that secondary controls do not exert an influence on Mg/Ca_{test} greater than the magnitude of analytical error. Therefore, Eqs. (3)–(6) can be applied to fossil nummulitids with confidence, based on the combined data from field and laboratory cultured foraminifera. The data of Toyofuku et al. (2000) show that for a different shallow benthic foraminifera with a similar Mg/Ca-temperature sensitivity and Mg/Ca ratios to *O. ammonoides* (Fig. 4) salinity also does not significantly affect Mg incorporation, further demonstrating the robustness of Mg/Ca palaeothermometry based on these high-Mg foraminifera in the fossil record.

Following Evans and Müller (2012), coupling Eqs. 4 and 6 defines a surface in temperature-Mg/Ca_{test}–Mg/Ca_{sw} space that, given a fossil Mg/Ca measurement, can be used to reconstruct either temperature or Mg/Ca_{sw} if the other parameter is constrained independently (Fig. 5C):

$$Mg/Ca_{test} = \frac{-1.98 \times (Mg/Ca_{sw}^{t=t})^2 + 37.0 \times Mg/Ca_{sw}^{t=t}}{-1.98 \times (Mg/Ca_{sw}^{t=0})^2 + 37.0 \times Mg/Ca_{sw}^{t=0}} \times 94.8\exp^{0.0168T} \quad (10)$$

Where t=0 is the present and t=t is some point in the past. Coupling the calibrations in this way assumes that solution Mg/Ca does not alter the exponential constant of the Mg/Ca-temperature calibration. Whilst the mathematical form of this relationship differs slightly from the methodology described in Evans and Müller (2012) in that it is based on a polynomial rather than a power relationship between Mg/Ca_{sw} and Mg/Ca_{test}, using such a relationship does not alter the conclusions of Evans and Müller (2012) because both types of regression produce a convex-up curve that predicts a higher Mg/Ca_{test} at a given Mg/Ca_{sw} compared to the widely held assumption that there is a linear relationship between these two parameters. Therefore, the data we report here support the conclusions of Evans and Müller (2012), and it may be the case that planktic foraminifera and other marine organisms do mediate the calcification process such that a power relationship between test-seawater Mg/Ca most appropriately describes the data. We also stress that the calibrations presented here are consistent with those previously established for inorganic calcite, which indicate that over a very wide range of Mg/Ca_{sw} values (0.25–10 mol mol^{-1}) a power relationship best describes the change in D_{Mg} with Mg/Ca_{sw} (De Choudens-Sánchez and González, 2009). However, we fit a linear regression between these parameters as this most parsimoniously describes our data as well as the subset of inorganic calcite data over the range Mg/Ca_{sw} = 1–8 mol mol^{-1}.

Eq. 10 defines a surface in Mg/Ca_{sw}–Mg/Ca_{test}-temperature space (Fig. 5C). Given that it appears that secondary controls on Mg/Ca are within analytical error for this group of foraminifera, the point of intersection of this surface with any two of the three planes defined by a fossil Mg/Ca measurement and a palaeotemperature or Mg/Ca_{sw} reconstruction defines the position of the third. It is not possible to produce an absolute paleotemperature or Mg/Ca_{sw} reconstruction if the shape of this surface is not calibrated in these three dimensions. Applying this coupled calibration to the Eocene (Bartonian) fossil data reported in Evans et al. (2013) yields a reconstructed Mg/Ca_{sw} of 2.38 ± 0.23 mol mol^{-1}.

Whilst we provide the basis for the first accurate deep-time Mg/Ca-derived palaeotemperatures, considerable further work is required before this palaeothermometer can be accurately applied to samples older than ~1–2 Ma. Aside from complications resulting from secondary controls on Mg incorporation into foraminiferal calcite (with the exception of the nummulitids), three significant advances are required before this proxy can be widely applied with confidence: (1) the validity of assuming the constancy of the exponential component of a Mg/Ca-temperature calibration must be tested (see the Supplementary material for further discussion), (2) an accurate, Ma-resolution Cenozoic Mg/Ca_{sw} record is required and (3) coupled calibrations such as the one presented here are needed for planktic foraminifera widely utilised in ocean sediment cores.

4.2. Implications for biomineralisation

These foraminifera are characterised by test Mg/Ca ratios 10–100 times higher than planktic or deep-benthic foraminifera which typically have Mg/Ca <10 mmol mol^{-1} (e.g. Nürnberg et al., 1996; Lear et al., 2002). Furthermore, the gradient of the relationship between Mg/Ca and temperature for *O. ammonoides* (Eqs. (1)–(4); ~1.7% $°C^{-1}$) is much shallower than that for almost all other foraminifera species for which this relationship has been calibrated; planktic foraminifera are typically characterised by Mg/Ca-temperature calibration slopes which increase by more than 7% $°C^{-1}$ (e.g. Kisakürek et al., 2008). Several features of our laboratory culture data suggest that the biomineralisation mechanism of *O. ammonoides* resembles inorganic precipitation from seawater with unmodified elemental chemistry. The gradient of the D_{Mg}–Mg/Ca_{sw} calibration is within error of the respective slope for inorganic calcite precipitation (Mucci and Morse, 1983), and the relationship between D_{Mg} and temperature is much closer to that of inorganic calcite than to any other foraminifera (Oomori et al., 1987), see Fig. 8. This may suggest that, with the exception of the carbonate chemistry, these foraminifera do not significantly biologically mediate the major and trace element chemistry of the solution in the calcifying space from that of seawater.

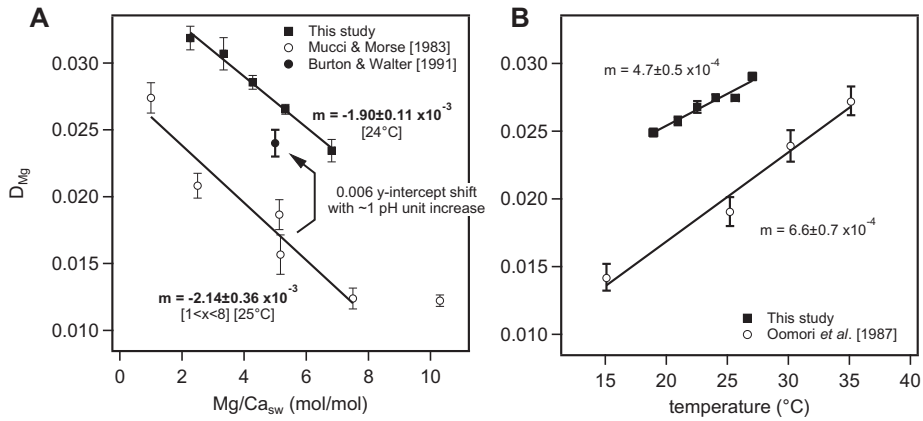

Fig. 8. A comparison of the relationship between (A) D_{Mg} and Mg/Ca_{sw} and (B) D_{Mg} and temperature in *O. ammonoides* and inorganic calcite (Mucci and Morse, 1983; Oomori et al., 1987). The D_{Mg}–Mg/Ca_{sw} slopes are within error of each other. The pH-D_{Mg} calibrations of Burton and Walter (1991) may provide an explanation for the offset in y-intercept of these foraminifera compared to inorganic calcite, as inorganic precipitation experiments at elevated pH are offset to higher D_{Mg} values, and foraminifera are known to elevate the pH of internal seawater vacuoles.

Given that foraminifera are known to elevate the pH of the internal seawater vacuoles that arrive to the site of calcification (Bentov et al., 2009), the D_{Mg} offset we observe between *O. ammonoides* and inorganic calcite for a given Mg/Ca_{sw} and temperature may be entirely explained by the biologically-mediated pH elevation during calcite precipitation (Fig. 8). This is because there is good evidence that pH exerts a control on the D_{Mg} of inorganic calcite (Burton and Walter, 1991) which likely accounts for the offset of our calibration to higher Mg/Ca_{test} ratios at a given seawater Mg/Ca ratio; these authors observed D_{Mg} ~0.006 higher at pH 8.9 compared to precipitates at normal seawater pH. If this hypothesis is correct, it provides further evidence that the calcification mechanism in *O. ammonoides* is not fundamentally different from inorganic precipitation from high-pH seawater. The y-intercept offset between our calibration and that for inorganic calcite provides a rudimentary way of calculating the pH of the calcification site, assuming that this relationship is indeed the case for this foraminifer, given that Burton and Walter (1991) demonstrate that D_{Mg} dependence on pH is linear, and that there is no significant temperature effect on the slope of this relationship. Inorganic calcite D_{Mg}-pH gradients vary inconsistently between 6.2 and 7.7×10^{-3} over the range 25–45 °C but are all within error of each other. Applying these slopes to the *O. ammonoides*-inorganic offset between D_{Mg} and Mg/Ca_{sw} or temperature shown in Fig. 8 would imply pH at the calcification site elevated 1.1–1.4 units above normal seawater, which is in broad agreement with Bentov et al. (2009) and de Nooijer et al. (2009).

The similarity between the Mg/Ca-temperature and seawater-test Mg/Ca relationships in this family and inorganic calcite may suggest a different biomineralisation mechanism to other foraminifera (with the exception of *P. opercularis* which has a similar or identical Mg/Ca-temperature slope to *O. ammonoides* (Toyofuku et al., 2000; Fig. 4), or at least a greatly reduced or absent role of calcite Mg/Ca manipulation by mitochondrial sequestration or binding with enzymes such as ATP, as suggested for other foraminifera (Bentov and Erez, 2006). It therefore seems possible that these foraminifera calcify by forcing inorganic precipitation from vacuolised seawater with an elevated pH but unmodified Mg–Sr/Ca. In order to precipitate 7 μg $CaCO_3$ day^{-1} (the maximum observed growth rate) these foraminifera would need to cycle ~14× their own volume in seawater which seems possible given the size and abundance of large vesicles observed in other large benthic species (e.g. Bentov et al., 2009). Elevating the pH of internal seawater vacuoles is consistent with a carbon concentrating mechanism such as that demonstrated by ter Kuile and Erez (1987) and ter Kuile et al. (1989) using the mechanism suggested by Bentov et al. (2009), whereby the foraminifer elevates the pH of the vacuole enabling diffusion of respiratory CO_2 from the surrounding cytoplasm and acidic seawater vesicles, which is necessary because modern seawater has $[Ca^{2+}] = 10.2$ mM but $[CO_3^{2-}] = \sim 200$ μM. In contrast, it is difficult to explain the high Mg/Ca ratio of the calcite produced by these foraminifera through modification of the concentration of the alkali earth metals in the seawater vacuoles as it would imply that Mg is being added rather than removed. Inorganic precipitation experiments investigating trace element distribution coefficients other than D_{Mg} conducted at elevated pH would test the validity of this model, as would Mg isotope measurements (Pogge von Strandmann, 2008).

The higher Na/Ca ratios of *O. ammonoides* compared to planktic foraminifera (Delaney et al., 1985), a low-Mg benthic foraminifera (Wit et al., 2013) and inorganic precipitates (Ishikawa and Ichikuni, 1984; Okumura and Kitano, 1986) is a direct result of the higher Mg/Ca ratios of this species (Fig. 7B). The inorganic precipitates described by Ishikawa and Ichikuni (1984) and Okumura and Kitano (1986) are characterised by D_{Na} similar to low-Mg foraminifera because they were precipitated from solutions with very low [Mg]. The relatively high Sr/Ca ratios of these foraminifera compared to other species is a consequence of lattice distortion as a result of their higher Mg concentration, as previously suggested for inorganic calcite (Mucci

and Morse, 1983), see Fig. 7. The data compilation shown in Fig. 7B suggests that D_{Na} may also be similarly controlled, even though Na occupies an interstitial site (Ishikawa and Ichikuni, 1984). This accounts for D_{Na} in *O. ammonoides* 2–3× that of previously studied foraminifera, as test Mg/Ca is two orders of magnitude higher than the species utilised by Wit et al. (2013). Whilst this explains the broad inter-species differences in Na/Ca, it does not negate our discussion of other controls on Na incorporation as a significant complication for this proxy (Section 4.3) because the D_{Na}–$Mg/Ca_{calcite}$ slope is low; other factors dominantly control Na incorporation within a narrower range of test Mg/Ca ratios.

The nummulitids originated in the late Cretaceous or early Paleocene (Hottinger, 1977) when seawater Mg/Ca was much lower than at present (e.g. Dickson, 2004). Early Cenozoic seawater [Ca] may have been ~2× present day (Horita et al., 2002) and Mg discrimination during calcification was less important because this biomineralisation mechanism would have produced calcite with an acceptably low Mg/Ca ratio (Fig. 5) without the requirement for energetically expensive biological processes to modify the chemistry of seawater vacuoles.

The consistency of our data with that of Raitzsch et al. (2010) provides further evidence that this biomineralisation mechanism is common to all nummulitid foraminifera (see also Evans et al., 2013 for data regarding proxy incorporation in *O. complanata* and *Nummulites*). Because Raitzsch et al. (2010) varied seawater [Ca] and [Mg], whereas we modified only seawater [Mg] in our variable chemistry experiment, these datasets furthermore demonstrate that it is the seawater Mg/Ca ratio that is the dominant control on test chemistry, as also shown by Segev and Erez (2006). This means that the application of these calibrations to fossil foraminifera do not suffer from uncertainty regarding the absolute secular variation in seawater Mg or Ca concentration.

4.3. Implications for other proxy systems

Since Cd/Ca was initially identified as a proxy in foraminiferal calcite (Hester and Boyle, 1982), many other trace element systems have been developed which relate to a number of environmental or physiological parameters (reviewed by Katz et al. (2010)). Here, we focus on Li, Na and Ba incorporation because these proxies are actively undergoing refinement and we find multiple controlling factors for each.

Li incorporation into *O. ammonoides* is strongly controlled by both Li/Ca_{sw} and temperature. Whilst we cannot eliminate further complicating factors in the application of foraminifera Li/Ca data based on our cultures, the inconsistent relationship between Li/Ca and Ω or growth rate between the two experiments strongly suggest that these variables exert at most a relatively minor control on test Li/Ca. The strong correlation observed between seawater and test Li/Ca (Fig. 6B) has significant implications for the use of Li/Ca or coupled Li–Mg/Ca data for simultaneous ΔCO_3^{2-}-temperature reconstructions (e.g. Bryan and Marchitto, 2008; Lear et al., 2010). Although it is likely that the slope of this relationship ($m = 29.0$) is steeper than that for planktic or deep benthic foraminifera (cf. Delaney et al., 1985) – our seawater-test Ba/Ca slope is much higher than that of planktic foraminifera – it is clear that relatively small shifts in Li/Ca_{sw} may result in Li/Ca_{test} variation equally as great as that resulting from temperature or ΔCO_3^{2-}. Whilst the relatively long residence time of Li and Ca in the ocean (2.5–4 Ma and 1–1.5 Ma respectively (Li, 1982)) eliminates secular variation in Li/Ca_{sw} as a complication on glacial-interglacial timescales, such changes may be significant in relation to records spanning several Ma, particularly across geological events such as the early Oligocene glaciation (Lear and Rosenthal, 2006) that might reasonably be expected to be associated with large changes in weathering rates.

Na/Ca in *O. ammonoides* is sensitive to temperature and growth rate across the range that these parameters varied in our experiments, which were at constant salinity within each experiment (variable temperature; variable seawater chemistry). Our data are consistent with that of Delaney et al. (1985), who also found a broad (inter-species) relationship between Na/Ca_{test} and temperature. Our data broadly support those of Wit et al. (2013) in that Na/Ca_{test} is higher in experiments conducted at a salinity of 41‰ compared to those at 37‰, although this may be a result of the higher growth rates in cultures at higher salinity. It is clear that the overprint from growth rate and/or temperature is significant to the point that it is difficult to see how this potential proxy would be applied in the fossil record without some independent constraint of these parameters. Utilising foraminiferal Na/Ca ratios as a palaeosalinity proxy may also be complicated by the location of Na^+ ions within the calcite lattice. Because it is likely that a predominant proportion of calcite and aragonite Na^+ is located in interstitial sites (Ishikawa and Ichikuni, 1984; Mitsuguchi et al., 2001), this may make fossil Na/Ca especially susceptible to diagenesis.

We find no significant relationship between foraminifera Sr/Ca and any of the investigated variables with the exception of the Mg/Ca ratio of calcite (Fig. 7). This is because Mg/Ca exerts a greater control on D_{Sr} in these experiments than other factors such as growth rate and Sr/Ca_{sw} (Fig. 6N), as these other factors varied to a less significant extent. Whilst this can explain the variation in measured Sr/Ca ratios in these foraminifera, it does not imply that these other factors do not play an important role within a more specific mineralogy (e.g. low-Mg calcite). The much steeper D_{Sr}–$Mg/Ca_{calcite}$ slope of *H. depressa* (Raitzsch et al., 2010) suggests that D_{Sr} may deviate from this trend when saturation state and/or seawater [Ca] and [Mg] is substantially different from modern. However, applying a correction to the data of (Raitzsch et al., 2010) for the variable test Mg/Ca in their experiments suggests that the slope of their Ω-D_{Sr} regression should be reduced from 8.7×10^{-3} to 7.1×10^{-3}. Finally, low-Mg planktic and benthic foraminifera such as *O. universa* (Russell et al., 2004) and *Ammonia tepida* (Raitzsch et al., 2010) fall broadly on the same D_{Sr}–$Mg/Ca_{calcite}$ line (Fig. 7), strongly suggesting that the lower Mg/Ca ratio of planktic and low-Mg benthic foraminifera directly results in the lower D_{Sr} of these foraminifera.

Evans et al. (2013) used the inorganic D_{Sr}-$Mg/Ca_{calcite}$ relationship to correct Eocene fossil Sr/Ca data before using the calculated D_{Sr} to reconstruct Eocene Sr/Ca_{sw}. At the time it was not certain that the data should be corrected in this way but these reconstructions can now be viewed with increased confidence.

The steep test-seawater Ba/Ca slope relative to planktic foraminifera potentially make the nummulitids a more sensitive archive of Ba/Ca_{sw}. The shallow depth-distribution of these foraminifera give them the potential to be good indicators of upwelling or freshwater flux to the surface ocean in the fossil record. Whilst there is no growth rate or saturation state control on Ba incorporation based on our data, we observe a significant temperature dependency, although a ~6 °C temperature shift is required to produce the same variation in Ba/Ca_{test} as a $1\ \mu mol\ mol^{-1}$ change in Ba/Ca_{sw}. Previous studies (e.g. Hönisch et al., 2011) investigating this relationship in planktic foraminifera find no significant temperature dependence on Ba/Ca_{test}, implying that it is observable in *O. ammonoides* because unlike planktic foraminifera, the Ba/Ca-temperature sensitivity is greater than analytical uncertainty.

5. CONCLUSION

We have performed laboratory calibrations on the shallow-dwelling large benthic foraminifera species *O. ammonoides*, principally in order to investigate the control exerted by temperature and seawater Mg/Ca on Mg incorporation in the calcite test. Based on laser-ablation ICPMS measurements at sub-chamber resolution facilitating unequivocal discrimination of calcite precipitated during culture, we find a Mg/Ca-temperature sensitivity of $\sim 1.7\%\ °C^{-1}$, in good agreement with the field calibration of Evans et al. (2013), and a D_{Mg}–Mg/Ca_{sw} gradient of -1.9×10^{-3}. To our knowledge, this is the first time that these relationships have been investigated in detail in three-dimensional Mg/Ca_{test}–Mg/Ca_{sw}-temperature space. This coupled calibration provides a way forward in the reconstruction of accurate Mg/Ca-derived palaeotemperatures from time periods with non-modern Mg/Ca_{sw} (pre-Pleistocene), or conversely a method of accurate Mg/Ca_{sw} reconstruction if palaeotemperature can be independently constrained. The similarity between these calibrations and those of inorganic calcite precipitation experiments imply that the biomineralisation mechanism of *O. ammonoides* is fundamentally different to other planktic and benthic species, in that this foraminifera appears to lack a mechanism capable of reducing the Mg/Ca ratio of the calcifying fluid. From a proxy development perspective this may be advantageous as the wealth of information regarding inorganic calcite precipitation is likely to be applicable to the nummulitid foraminifera.

Finally, we show data providing preliminary assessment of other proxy trace element systems (Li, Na, Sr, Ba) in *O. ammonoides*. We find significant multiple controls on Li, Na and Ba incorporation, highlighting the need for a good understanding of the control that all variables exert on such systems, particularly those such as growth rate which are challenging to constrain independently in the fossil record.

The abundance of fossil *Operculina* and closely related genera in climatically relevant periods of geological time such as the Eocene, and the longevity of these large benthic foraminifera, facilitating palaeo-seasonal proxy retrieval (Evans et al., 2013; Evans and Müller, 2013), make this species, and large benthic species in general, deserving of more detailed investigation.

ACKNOWLEDGEMENTS

DE acknowledges a NERC postgraduate studentship at Royal Holloway University of London. The authors acknowledge the Israel Science Foundation for funding the experimental part of this research (ISF grant 551/10 to J.E.). We are grateful to Simon Chenery and Tom Barlow (NERC Isotope Geosciences Laboratory) for performing the seawater analyses and for subsequent discussions of the data. We are indebted to the associate editor Yair Rosenthal and three anonymous reviewers for providing detailed and thoughtful comments which led to significant improvements in the presentation of this work.

APPENDIX A. SUPPLEMENTARY DATA

Supplementary data associated with this article can be found, in the online version, at http://dx.doi.org/10.1016/j.gca.2014.09.039.

REFERENCES

Bentov S., Brownlee C. and Erez J. (2009) The role of seawater endocytosis in the biomineralization process in calcareous foraminifera. *Proc. Natl. Acad. Sci.* **106**, 21500–21504.

Bentov S. and Erez J. (2006) Impact of biomineralization processes on the Mg content of foraminiferal shells: a biological perspective. *Geochem. Geophys. Geosyst.* **7**, Q01P08.

Bryan S. and Marchitto T. (2008) Mg/Ca–temperature proxy in benthic foraminifera: new calibrations from the Florida Straits and a hypothesis regarding Mg/Li. *Paleoceanography* **23**, PA2220.

Burton E. and Walter L. (1991) The effects of pCO_2 and temperature on magnesium incorporation in calcite in seawater and $MgCl_2$–$CaCl_2$ solutions. *Geochim. Cosmochim. Acta* **55**, 777–785.

Coggon R., Teagle D., Smith-Duque C., Alt J. and Cooper M. (2010) Reconstructing past seawater Mg/Ca and Sr/Ca from mid-ocean ridge flank calcium carbonate veins. *Science* **327**, 1114–1117.

De Choudens-Sánchez V. and González L. A. (2009) Calcite and aragonite precipitation under controlled instantaneous supersaturation: elucidating the role of $CaCO_3$ saturation state and Mg/Ca ratio on calcium carbonate polymorphism. *J. Sediment. Res.* **79**, 363–376.

Delaney M., Bé A. W. H. and Boyle E. A. (1985) Li, Sr, Mg, and Na in foraminiferal calcite shells from laboratory culture, sediment traps, and sediment cores. *Geochim. Cosmochim. Acta* **49**, 1327–1341.

Dickson J. (2004) Echinoderm skeletal preservation: calcite-aragonite seas and the Mg/Ca ratio of Phanerozoic oceans. *J. Sediment. Res.* **74**, 355–365.

Erez J. (2003) The source of ions for biomineralization in foraminifera and their implications for paleoceanographic proxies. *Rev. Mineral. Geochem.* **54**, 115–149.

Evans D. and Müller W. (2012) Deep time foraminifera Mg/Ca paleothermometry: nonlinear correction for secular change in seawater Mg/Ca. *Paleoceanography*, PA4205.

Evans D. and Müller W. (2013) LA-ICPMS elemental imaging of complex discontinuous carbonates: an example using large benthic foraminifera. *J. Anal. Atomic Spectrosc.* **28**, 1039–1044.

Evans D., Müller W., Oron S. and Renema W. (2013) Eocene seasonality and seawater alkaline earth reconstruction using shallow-dwelling large benthic foraminifera. *Earth Planet. Sci. Lett.* **381**, 104–115.

Fantle M. and DePaolo D. (2006) Sr isotopes and pore fluid chemistry in carbonate sediment of the Ontong Java Plateau: calcite recrystallization rates and evidence for a rapid rise in seawater Mg over the last 10 million years. *Geochim. Cosmochim. Acta* **70**, 3883–3904.

Guido A., Papazzoni C., Mastandrea A., Morsilli M., La Russa M., Tosti F. and Russo F. (2011) Automicrite in a 'nummulite bank' from the Monte Saraceno (Southern Italy): evidence for synsedimentary cementation. *Sedimentology* **58**, 878–889.

Hasiuk F. and Lohmann K. (2010) Application of calcite Mg partitioning functions to the reconstruction of paleocean Mg/Ca. *Geochim. Cosmochim. Acta* **74**, 6751–6763.

Haywood A., Ridgwell A., Lunt D., Hill D., Pound M., Dowsett H., Dolan A., Francis J., Williams M. and Haywood A., et al. (2011) Are there pre-quaternary geological analogues for a future greenhouse warming?. *Philos. Trans. R. Soc. A* **369** 933–956.

Hester K. and Boyle E. (1982) Water chemistry control of cadmium content in recent benthic foraminifera. *Nature* **298**, 260–262.

Hönisch B., Allen K., Russell A., Eggins S., Bijma J., Spero H., Lea D. and Yu J. (2011) Planktic foraminifers as recorders of seawater Ba/Ca. *Marine Micropaleontol.* **79**, 52–57.

Horita J., Zimmermann H. and Holland H. (2002) Chemical evolution of seawater during the Phanerozoic: implications from the record of marine evaporites. *Geochim. Cosmochim. Acta* **66**, 3733–3756.

Hottinger L. (1977) *Foraminifères Operculiniformes volume 40 of Série C, Sciences de la Terre*. Mémoires du Muséum National d'Histoire Naturelle.

Ishikawa M. and Ichikuni M. (1984) Uptake of sodium and potassium by calcite. *Chem. Geol.* **42**, 137–146.

Jochum K., Stoll B., Herwig K., Willbold M., Hofmann A., Amini M., Aarburg S., Abouchami W., Hellebrand E., Mocek B. et al. (2006) MPI-DING reference glasses for in situ microanalysis: New reference values for element concentrations and isotope ratios. *Geochem. Geophys. Geosyst.*, **7**.

Katz M., Cramer B., Franzese A., Hönisch B., Miller K., Rosenthal Y. and Wright J. (2010) Traditional and emerging geochemical proxies in foraminifera. *J. Foraminiferal Res.* **40**, 165–192.

Kisakürek B., Eisenhauer A., Bohm F., Garbe-Schönberg D. and Erez J. (2008) Controls on shell Mg/Ca and Sr/Ca in cultured planktonic foraminiferan, Globigerinoides ruber (white). *Earth Planet. Sci. Lett.* **273**, 260–269.

ter Kuile B. and Erez J. (1987) Uptake of inorganic carbon and internal carbon cycling in symbiont-bearing benthonic foraminifera. *Mar. Biol.* **94**, 499–509.

ter Kuile B., Erez J. and Padan E. (1989) Mechanisms for the uptake of inorganic carbon by two species of symbiont-bearing foraminifera. *Mar. Biol.* **103**, 241–251.

Lea D. W. and Spero H. J. (1992) Experimental determination of barium uptake in shells of the planktonic foraminifera *Orbulina universa* at 22 °C. *Geochim. Cosmochim. Acta* **56**, 2673–2680.

Lear C., Mawbey E. and Rosenthal Y. (2010) Cenozoic benthic foraminiferal Mg/Ca and Li/Ca records: toward unlocking temperatures and saturation states. *Paleoceanography* **25**, PA4215.

Lear C. H., Elderfield H. and Wilson P. A. (2000) Cenozoic deep-sea temperatures and global ice volumes from Mg/Ca in benthic foraminiferal calcite. *Science* **287**, 269–272.

Lear C. H. and Rosenthal Y. (2006) Benthic foraminiferal Li/Ca: insights into Cenozoic seawater carbonate saturation state. *Geology* **34**, 985–988.

Lear C. H., Rosenthal Y. and Slowey N. (2002) Benthic foraminiferal Mg/Ca-paleothermometry: a revised core-top calibration. *Geochim. Cosmochim. Acta* **66**, 3375–3387.

Lebel J. and Poisson A. (1976) Potentiometric determination of calcium and magnesium in seawater. *Mar. Chem.* **4**, 321–332.

Lewis E. and Wallace D. (2006) Program developed for CO_2 system calculations. *ORNL/CDIAC-105. Carbon Dioxide Information Analysis Center, Oak Ridge National Laboratory, US Department of Energy, Oak Ridge, Tennessee*, .

Li Y.-H. (1982) A brief discussion on the mean oceanic residence time of elements. *Geochim. Cosmochim. Acta* **46**, 2671–2675.

Millero F. J. (1996) *Chemical Oceanography*, second ed. CRC Press, Florida.

Mitsuguchi T., Uchida T., Matsumoto E., Isdale P. J. and Kawana T. (2001) Variations in Mg/Ca, Na/Ca, and Sr/Ca ratios of coral skeletons with chemical treatments: implications for carbonate geochemistry. *Geochim. Cosmochim. Acta* **65**, 2865–2874.

Mucci A. and Morse J. (1983) The incorporation of Mg^{2+} and Sr^{2+} into calcite overgrowths: influences of growth rate and solution composition. *Geochim. Cosmochim. Acta* **47**, 217–233.

Müller W., Shelley M., Miller P. and Broude S. (2009) Initial performance metrics of a new custom–designed ArF excimer LA–ICPMS system coupled to a two-volume laser–ablation cell. *J. Anal. Atomic Spectrom.* **24**, 209–214.

de Nooijer L. J., Toyofuku T. and Kitazato H. (2009) Foraminifera promote calcification by elevating their intracellular pH. *Proc. Natl. Acad. Sci.* **106**, 15374–15378.

Nürnberg D., Bijma J. and Hemleben C. (1996) Assessing the reliability of magnesium in foraminiferal calcite as a proxy for water mass temperatures. *Geochim. Cosmochim. Acta* **60**, 803–814.

Okumura M. and Kitano Y. (1986) Coprecipitation of alkali metal ions with calcium carbonate. *Geochim. Cosmochim. Acta* **50**, 49–58.

Oomori T., Kaneshima H., Maezato Y. and Kitano Y. (1987) Distribution coefficient of Mg^{2+} ions between calcite and solution at 10–50 °C. *Mar. Chem.* **20**, 327–336.

Raitzsch M., Dueñas-Bohórquez A., Reichart G.-J., de Nooijer L. and Bickert T. (2010) Incorporation of Mg and Sr in calcite of cultured benthic foraminifera: impact of calcium concentration and associated calcite saturation state. *Biogeosciences* **7**, 869–881.

Reiss Z. (1958) Classification of lamellar foraminifera. *Micropaleontology* **4**, 51–70.

Ries J. (2004) Effect of ambient Mg/Ca ratio on Mg fractionation in calcareous marine invertebrates: a record of the oceanic Mg/Ca ratio over the Phanerozoic. *Geology* **32**, 981–984.

Rosenthal Y., Boyle E. A. and Slowey N. (1997) Temperature control on the incorporation of magnesium, strontium, fluorine, and cadmium into benthic foraminiferal shells from Little Bahama Bank: prospects for thermocline paleoceanography. *Geochim. Cosmochim. Acta* **61**, 3633–3643.

Russell A., Hönisch B., Spero H. and Lea D. (2004) Effects of seawater carbonate ion concentration and temperature on shell U, Mg, and Sr in cultured planktonic foraminifera. *Geochim. Cosmochim. Acta* **68**, 4347–4361.

Segev E. and Erez J. (2006) Effect of Mg/Ca ratio in seawater on shell composition in shallow benthic foraminifera. *Geochem. Geophys. Geosyst.* **7**.

Stanley S. and Hardie L. (1998) Secular oscillations in the carbonate mineralogy of reef-building and sediment-producing organisms driven by tectonically forced shifts in seawater chemistry. *Palaeogeogr. Palaeoclimatol. Palaeoecol.* **144**, 3–19.

Pogge von Strandmann P. A. (2008) Precise magnesium isotope measurements in core top planktic and benthic foraminifera. *Geochem. Geophys. Geosyst.* **9**.

Toyofuku T., Kitazato H., Kawahata H., Tsuchiya M. and Nohara M. (2000) Evaluation of Mg/Ca thermometry in foraminifera: comparison of experimental results and measurements in nature. *Paleoceanography* **15**, 456–464.

de Villiers S. (1999) Seawater strontium and Sr/Ca variability in the Atlantic and Pacific oceans. *Earth Planet. Sci. Lett.* **171**, 623–634.

Wit J., Nooijer L. d., Wolthers M. and Reichart G. (2013) A novel salinity proxy based on Na incorporation into foraminiferal calcite. *Biogeosciences* **10**, 6375–6387.

Associate editor: Yair Rosenthal

1 Data quality

1.1 Laser ablation

Accuracy was assessed by treating the MPI-DING komatiite glasses as unknowns, calibrated using NIST610 and NIST612 under equivalent ablation conditions, given as a percentage offset between the reported value [*Jochum et al.*, 2006] and the mean measured value. In total 36 analyses of all four glasses was performed between December 2012 and April 2013. Precision is given as two standard deviations of these analyses and can be considered to be the result of combined heterogeneity in both glasses. Accuracy and precision were assessed four times by comparison of both GOR132 and GOR128 to NIST610 and NIST612. All data are shown in table S1. All NIST concentration values are the preferred value reported by *Jochum et al.* [2011]. Whilst these values result in worse NIST610 Mg accuracy compared to those that were previously given (i.e. using the *Jochum et al.* [2011] NIST610 value of 432 ppm instead of 465 ppm), it is not directly relevant to our Mg/Ca data which is standardised using GOR132 because it has a Mg concentration much closer to that of the samples and a much smaller Mg/Ca uncertainty.

It may be desirable to compare our Mg/Ca data to studies that use NIST610 for calibration, or to apply offsets to reported data as new NIST Mg concentration values become available. For such purposes, our GOR132-calibrated sample data can be converted to NIST610-calibrated data (based on a NIST610 Mg concentration value of 465 ppm) using the relationship:

$$\mathrm{Mg/Ca_{NIST610}} = 0.9817 \times \mathrm{Mg/Ca_{GOR132}} + 2.180 \tag{1.1}$$

Therefore, GOR132 and NIST610-calibrated analyses should be within 2 mmol mol^{-1} of each other over the range reported here, provided that the previously available NIST610 Mg concentration is used. In reality individual (i.e. single analysis) data-points cannot be easily converted between calibration standards because the relationship defined by equation 1.1 varies daily (figure S1A). This minor variation is likely to be the combined result of (1) the use of different slithers of NIST610 on different days in this study, (2) the daily ICPMS PA-factor calibration, as all Ca and NIST Mg intensities are measured in pulse mode, whereas GOR and sample Mg intensities are above the threshold at which the detector switches to analogue mode, and (3) minor shifts in the signal/background ratios for m/z 24, 25 and 43. Similar daily-specific offsets are also observed between NIST610 and NIST612 calibration (figure S1B), therefore these cannot purely be a function of PA factor calibration and must to a large extent be controlled by NIST heterogeneity. In any case a Mg/Ca uncertainty of ±4% should be added to any individual analysis (figure S1C) when comparing to Mg/Ca data standardised using NIST610. However, if the mean of many analyses is under consideration, such as the data reported here which are derived from many foraminifera and analysed over a period of several months, then a direct conversion may be made when comparing to NIST610-standardised data using equation 1.1. Finally, both the revised and previous NIST612 Mg concentration values [*Jochum et al.*, 2011] produce Mg/Ca data in poor agreement with any other standard (NIST610, GOR132, MACS-3, e.g. figure S1B); this glass should never be used for calibration when accurate Mg/Ca data are required.

Table S1: Laser-ablation accuracy and precision based on analyses of the MPI-DING komatiite glasses GOR132 and GOR128 standardised using intensity-concentration relationships derived from NIST610 and NIST612. All data were ratioed to Ca before accuracy and precision calculation.

Unknown	Standard Calibration	^{7}Li	^{11}B	^{23}Na	^{24}Mg	^{25}Mg	^{27}Al	^{55}Mn	^{66}Zn	^{88}Sr	^{89}Y	^{137}Ba	^{138}Ba	^{146}Nd	^{238}U
							Accuracy (%)								
GOR132	NIST610	16.8	8.5	4.3	-7.1	-6.8	4.6	1.6	-5.0	-1.2	-3.1	-5.7	7.4	-12.9	-33.4
GOR132	NIST612	16.6	6.2	4.3	10.7	14.9	3.7	2.4	-6.5	-2.2	-5.1	-6.4	6.3	-13.4	-33.9
GOR128	NIST610	12.5	-0.2	6.2	-6.1	-5.7	5.2	3.5	4.6	1.6	-2.2	-16.2	-4.9	-19.0	-90.6
GOR128	NIST612	12.4	-2.3	6.2	11.9	16.2	4.4	4.3	3.0	0.6	-4.3	-16.9	-5.9	-19.4	-90.7
							Precision (%)								
GOR132	NIST610	8.4	11.0	5.3	4.7	4.1	2.3	5.2	6.5	4.3	6.2	32.2	13.7	19.5	30.7
GOR132	NIST612	8.6	10.7	5.5	6.4	4.9	3.0	6.7	6.1	4.3	6.4	32.0	14.0	19.3	30.5
GOR128	NIST610	8.0	8.2	6.1	5.2	4.5	2.9	5.5	6.7	3.8	6.1	26.4	11.0	22.4	93.0
GOR128	NIST612	8.4	7.9	6.2	6.8	5.5	3.9	7.1	6.5	3.6	6.2	25.6	11.1	22.4	92.5

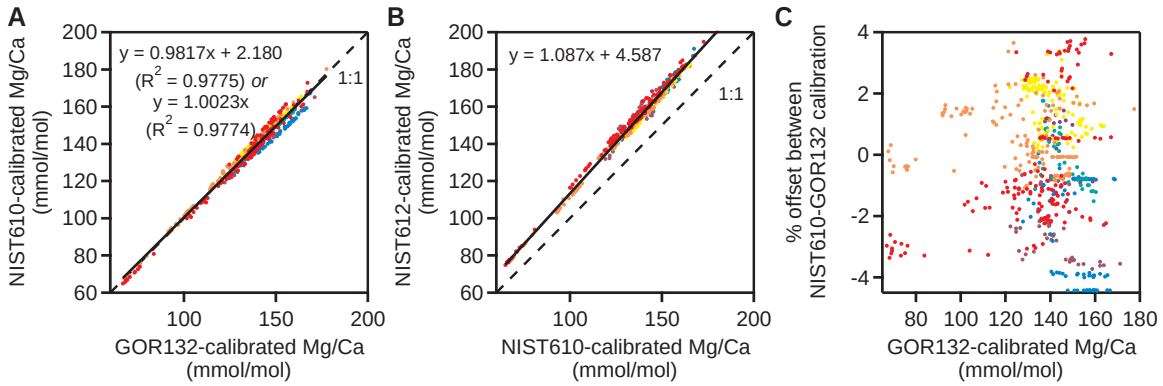

Figure S1: The relationship between all calcite Mg/Ca analyses used in this study (n=580) when calibrated using different standards. (A) All data calibrated using GOR132 compared to all data calibrated using NIST610 using a Mg concentration value of 465 ppm. (B) All data calibrated using NIST610 compared to all data calibrated using NIST612. Calibration using NIST612 results in offset to significantly higher Mg/Ca ratios. (C) The percentage difference for each analysis when using NIST610 compared to GOR132 as a calibration standard. If only one analysis is under consideration this scatter represents the uncertainty when comparing data calibrated using these two standards following a correction applied using the relationship shown in (A). Each colour represents all analyses carried out on the same day.

Because there is, to our knowledge, currently no homogeneous calcite standard suitable for laser-ablation use, it is not clear how our laser-ablation accuracy values relate to carbonate analyses. For this reason we do not use the accuracy values reported here for the purposes of laser-ablation data error propagation; errors are shown as ±2SE for individual analyses or ±2SD of all data where the mean of multiple analyses are shown. However, these values do allow our data to be corrected in future if it is shown that laser-ablation analyses of calcite are consistently offset from those of volcanic or synthetic glasses. *Evans et al.* [2013] report data in their supplementary material of the pressed powder carbonate standard MACS-3, also standardised using NIST610 and NIST612. These data demonstrate that it is likely that standardising calcite using synthetic glasses results in a bias of less than ∼10% for the isotopes (m/z) under consideration here [see also *Hathorne et al.*, 2008; *Strnad et al.*, 2009; *Jochum et al.*, 2012]. However, we do not use these data to assess accuracy because only information values for MACS-3 are available and our own analyses demonstrate that this standard is considerably more heterogeneous than the glass data presented here. Similarly, these precision values are not used for error propagation because they are largely considered to be a direct result of glass heterogeneity. For example, plotting ^{24}Mg/Ca accuracy for GOR128 against GOR132 calibrated using NIST610 (figure S2) results in a maximum difference between the two of 8%, identical to the combined uncertainty in the reported Mg concentration value for GOR132 and NIST610 (7.9%). Furthermore, the residual difference between the best fit line through GOR128-GOR132 accuracy is similar in magnitude to the combined percentage error of the Mg concentration in these komatiite glasses, suggesting that most of the scatter in the data can be explained in this way.

We observe no difference when calibrating sample Mg/Ca data using either m/z 24 or 25 (^{25}Mg = 1.0018 × ^{24}Mg - 0.3574 over the Mg/Ca range 60-170 mmol mol^{-1}), as the high Mg concentration of these samples means that the ^{48}Ca^{++} interference on ^{24}Mg is negligible [*Jochum*

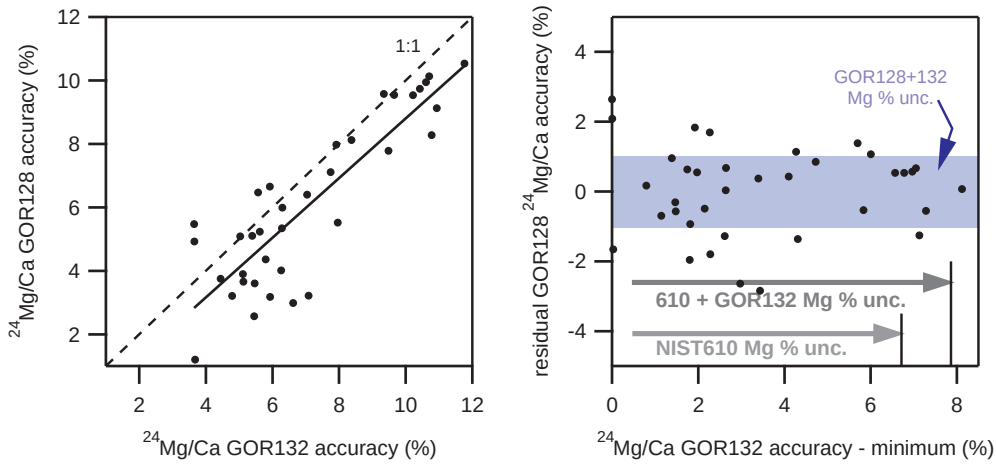

Figure S2: Mg/Ca GOR132-GOR128 accuracy for all standard analyses performed during the period during which sample data were collected. The range in the difference between these individual analysis accuracies is almost exactly equivalent to the combined percentage Mg concentration uncertainty for the calibration standard and GOR132. Similarly, the residual offset from the best fit line may be largely explained by the smaller Mg heterogeneity in the GOR glasses.

et al., 2012]. All Mg/Ca data reported in the main text are based on the average of values derived from both ^{24}Mg/Ca and ^{25}Mg/Ca.

1.2 Solution ICPMS

Seawater accuracy and precision data are shown in table S2, derived from analysis of the seawater and freshwater standards NASS-4 and SLRS-2 or, for conservative elements, all data derived from seawater which was not modified with respect to its chemistry. Li, B, Ba and U were analysed with no gas in the collision/reaction cell whereas Na, Mg, Ca, Mn and Sr were analysed with 5.5 ml min^{-1} He. Where accuracy data was available and derived from matrix matched analyses (i.e. Na, Mg and Sr/Ca), the sample data were corrected by multiplying each analysis by (100–accuracy)/100. An accuracy correction was not applied in this way to the Ba or U data because it is not clear how these values – derived from freshwater analyses – relate to

Table S2: Accuracy and precision of the solution ICPMS seawater analyses. Accuracy is the mean percentage deviation from the expected value. No accuracy data for Li or B is available as the concentration of these elements is naturally variable and no data are available for SLRS-2. A positive accuracy denotes a mean measured value positively offset from the known value.

X/Ca	Accuracy (%)	Method	Precision (1SD %)	Method	LOD μg l^{-1}
Li	–	-	4.1	triplicate NASS	59
B	–	-	5.9	triplicate NASS	156
Na	−3·6	all nat. sw	9.6	all nat. sw	24×10^3
Mg	3·5	all nat. sw	1.5	all nat. sw	1000
Sr	−2·5	all nat. sw	4.8	all nat. sw	7
Ba	−10·2	triplicate SLRS	4.6	triplicate NASS	3
U	−2·9	triplicate SLRS	6.5	triplicate NASS	0.04

seawater samples. Reported errors are ±precision and do not include accuracy as the data are corrected for this offset where possible.

2 Alkalinity-mass change growth rate estimation comparison

To alleviate concerns that our growth rate data may be biased by inorganic precipitation in the culture flasks, we compared the cumulative alkalinity-derived mass gain for each culture to that calculated by measuring the difference between the final dry sample weight of each culture and a control group (figure S3). The control group consisted of 50 specimens from the same size fraction and was killed at the onset of the experiments. Overall, the agreement between these techniques is very good; the slope of a linear fit between the two methods is within error of 1, and a large portion of the cultures lie within error when compared using the two techniques. A plot of the percentage difference between methods of assessing cumulative growth rate against the mass increase by comparison to a control group (figure S3B) shows that alkalinity is only an inaccurate method of assessing growth when cultured foraminifera consistently precipitate low amounts of $CaCO_3$. This is because alkalinity-derived calcium carbonate precipitation is calculated by measuring the difference between culture and reservoir alkalinity; this difference measurement becomes more inaccurate when the alkalinity difference between the two is smaller. These data suggest that for cultures characterised by low mean mass gain, alkalinity measurements overestimate growth and growth rates from experiments characterised by control-corrected mass gains of less than 50 μg ($\sim$25 μg month^{-1} individual^{-1}) should be treated with caution. However, there is also error in the estimates derived from comparison to a control group weight as there are small differences in the initial populations and therefore the comparison shown here may slightly underestimate the accuracy of alkalinity-derived growth. Overall there is no consistent offset between the two mass gain estimates, demonstrating that the majority of the alkalinity data must overall be reliable to within $\sim$ ±25% and that significant inorganic precipitation cannot have taken place within the culture flasks.

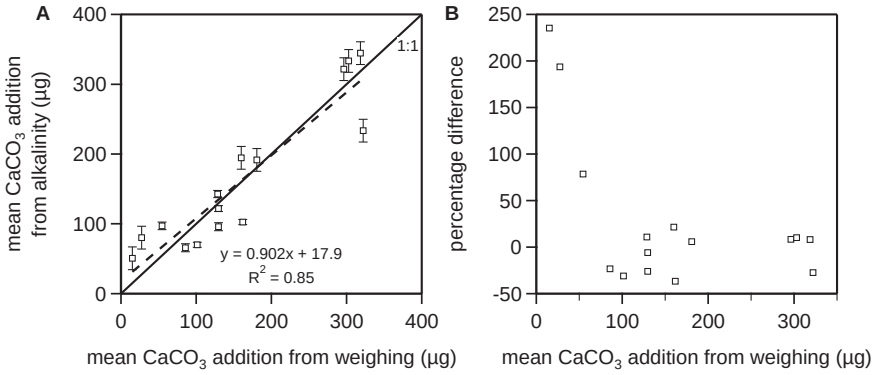

Figure S3: (A) Comparison of cumulative growth estimates (per specimen) using alkalinity depletion and by comparing final sample mass to a control group killed at the beginning of the experiments. (B) The percentage offset between the techniques. Only cultures characterised by consistently low growth rates and cumulative mass gain differ significantly.

3 27°C culture light-intensity shift

The two cultures at 27°C were moved to an area with a greater proportion of natural light and a slightly lower light intensity on day 40 of the experiment because of the addition of two cultures at 22.5°C and 25.5°C, given that cultures had to be arranged in increasing temperature order in order to maintain an efficient cooling system. Light intensity-time profiles for this new location are shown in figure S4. Although these data were collected subsequent to the experimental period during a different season, the photon fluxes are similar to measurements made during the experiment. For example, mean light intensity at 10 am for this location during the culture period (May-July 2012) was ~8 μmol photons m^{-2} s^{-1}. Mean growth rate increased in both cultures at 27°C following this change, and mean growth rate in culture DE1-7 doubled (see the main text).

Figure S5 shows trace element variation with distance around the marginal chord for both cultures at 27°C. 'Analysis position' refers to the relative location of laser-ablation analyses within one individual and does not necessarily indicate consistent spacing or consistent distance from the final chamber, therefore these data should be used as a guide only. A more accurate indication of how the changing spectrum and intensity of light may have affected calcite-seawater distribution coefficients is not possible given that there is no independent method of identifying calcite precipitated at a certain time during the experimental period. Nonetheless, assuming that calcifying foraminifera grew at an approximately constant rate, positions 1-3 are likely to broadly represent analyses of calcite precipitated after these cultures were moved. There is no significant trend between analysis position and any X/Ca ratio, demonstrating that shifts in light intensity of this magnitude are unlikely to affect the incorporation of any element into *O. ammonoides* calcite. The lack of any correlation between analysis position and Na/Ca or Sr/Ca, despite some evidence that these ratios are at least partially growth-rate dependent (see the main text), adds support to the hypothesis that the number of foraminifera actively calcifying within the culture increased, rather than an increase in individual specimen growth rate. Without individually monitoring foraminifera, which was not practically possible during this experiment, disentangling growth rate from the proportion of non-calcifying individuals is

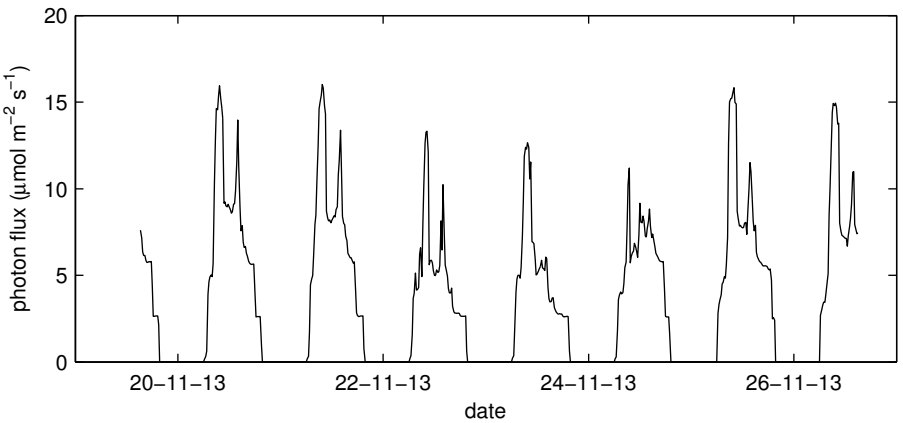

Figure S4: A representative light intensity-time curve for the location of cultures DE1-7/8. The 22nd-24th November 2013 were partially cloudy days in Jerusalem, whereas the 20th-21st and the 25th were sunny.

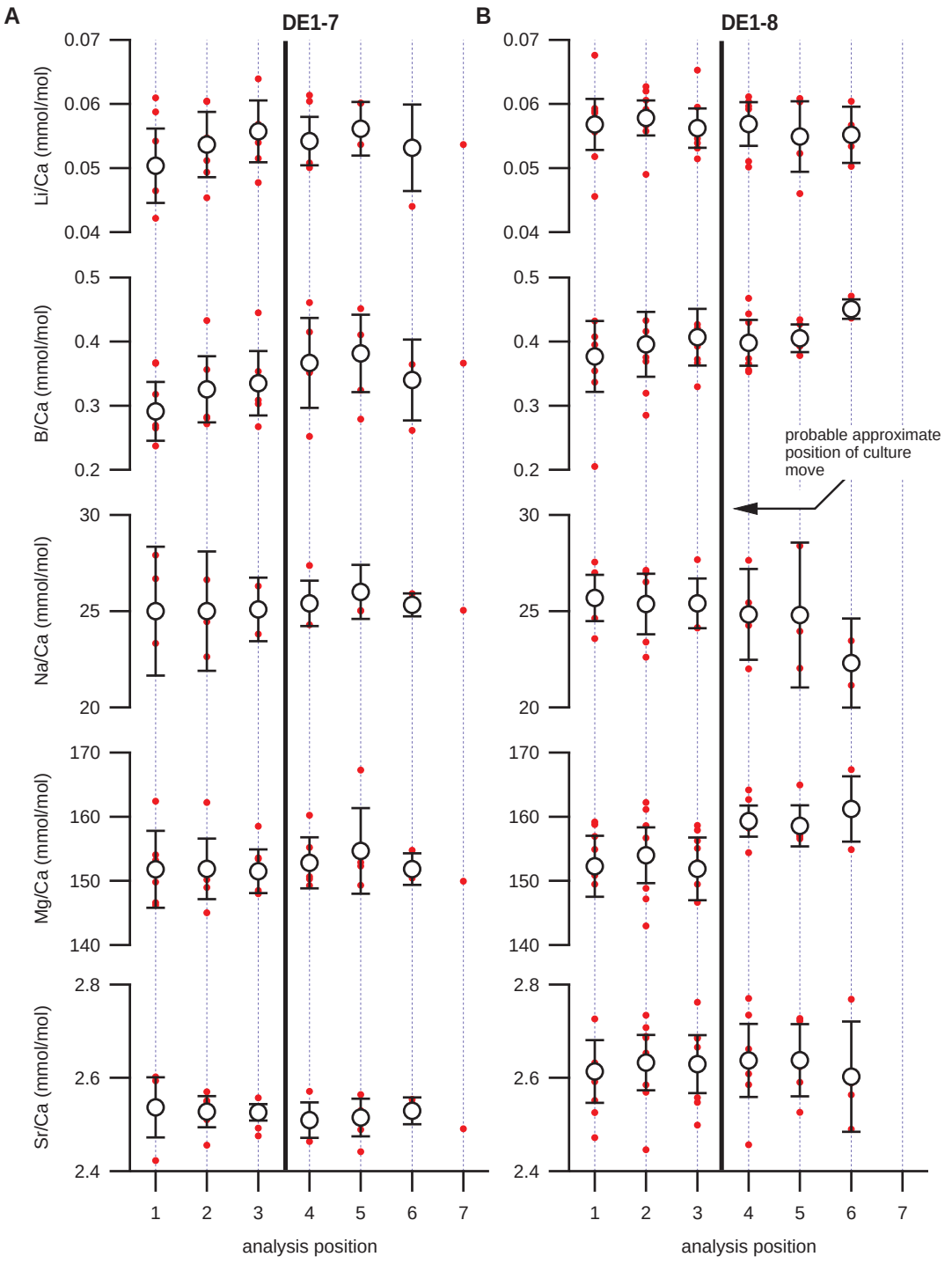

Figure S5: X/Ca variation with analysis position (an indication of distance from the final chamber, where 1 is on the final chamber and 7 is usually on f-3/f-4). (A) culture DE1-7, (B) culture DE1-8. Analysis position refers to the order of adjacent laser-ablation spots on the marginal chord on each individual foraminifera and does not represent consistent separation within or between specimens, although this was very broadly the case. All analyses with Ba/Ca<9 μmol mol^{-1} were excluded in order to avoid bias from pre-culture calcite.

not possible. The reason for the Mg/Ca shift in culture DE1-8 (figure S5B) is not clear, it is unlikely to be related to the shift in light intensity/spectrum that these cultures experienced as we do not observe it in DE1-7 (at the same temperature), which was characterised by a larger shift in net calcification rate (see the main text).

4 Na/Ca data quality

Our data show the *O. ammonoides* has Na/Ca ratios ∼2× higher than inorganic precipitates and other foraminifera [*Ishikawa and Ichikuni*, 1984; *Wit et al.*, 2013]. Before comparing this result to previous calcite Na data, we first demonstrate that the high Na/Ca ratios that we report are not an artefact of our cleaning procedure or remnant seawater inclusions or NaCl precipitates with the tube space of the marginal cord.

4.1 Oxidative cleaning procedure

Although the data we report are derived from specimens cleaned with reagent-grade NaOCl, we also initially tested H_2O_2 but found it to be less effective. However, this does mean that we have laser-ablation data from specimens that were never cleaned with NaOCl, and we can therefore demonstrate that the Na/Ca data we report are not biased by our cleaning procedure. Figure S6 shows a comparison of Na/Ca data of comparative specimens from three different cultures, cleaned in both H_2O_2 and NaOCl. All Na/Ca analyses fall within the range 25-35 mmol mol^{-1} which precludes contamination from NaOCl as a cause of these relatively high values. Moreover, those cleaned in H_2O_2 are offset to higher measured Na/Ca ratios than those cleaned in NaOCl indicating that in fact this reagent more thoroughly cleans the specimens; it is for this reason that we switched to NaOCl before conducting the majority of the analyses.

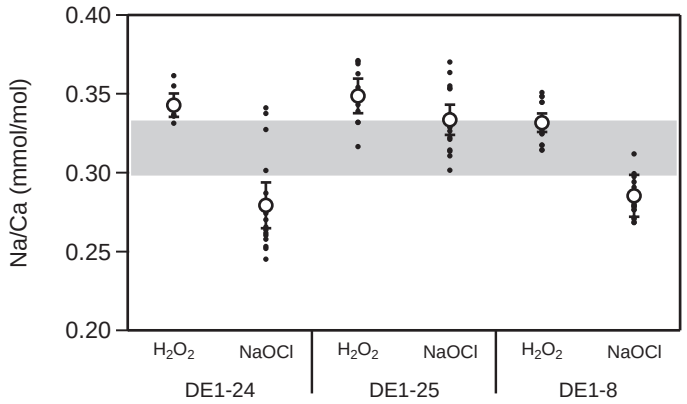

Figure S6: A comparison of measured test Na/Ca values using H_2O_2 and NaOCl as cleaning reagents for three cultures on which both were trialled. The grey shaded area shows the range of data that would be expected based on the Na/Ca precision reported in table S1.

4.2 Laser-ablation profiles of non-porous test areas

After eliminating our cleaning procedure as a potential cause of the relatively high Na/Ca ratios that we report, we also analysed a non-porous area of the foraminifera test (the knob area [*Segev and Erez*, 2006]) to demonstrate that these ratios cannot be the result of seawater micro-inclusions or NaCl precipitation from seawater that was not removed during ultrasonication in deionised water. We also compared a laser-ablation profile through this part of the test to the equivalent area on a different benthic foraminifera (*Amphistegina lobifera*), treated in exactly the same way (figure S7). There are three important points to note from these laser-ablation profiles:

- Non-porous test areas of *O. ammonoides* have Na/Ca ratios between 20-25 mmol mol^{-1}.
- If seawater micro-inclusions or NaCl precipitated were present, the profiles should show overall low values with a mean biased by occasional high Na/Ca values. This is not observed.
- A comparative profile of *A. lobifera* (another hyaline, perforate, shallow-dwelling large benthic foraminifera), prepared in exactly the same way has Na/Ca ratios around 10 mmol mol^{-1}. This demonstrates that the cleaning and analytical procedure that we utilise can reliably reproduce the lower Na/Ca ratios characteristic of inorganic calcite and other foraminifera [*Delaney et al.*, 1985; *Wit et al.*, 2013], and adds confidence to the higher Na/Ca ratios that we report for *O. ammonoides*, as it would seem highly unlikely that potential seawater inclusions or NaCl precipitation would affect only this specific species.

4.3 EPMA analysis

In order to conclusively demonstrate that our *O. ammonoides* Na/Ca data are not biased by NaCl precipitation we analysed the knob area of a single specimen by EPMA (Jeol JXA 8230 Electron Probe at the Hebrew University, Jerusalem). Four parts of three knobs were analysed in EDS mode (figure S8) with a beam diameter of 1-5 μm. The data are shown in table S3. Despite the large inter-analysis variability, showing the heterogeneity of *O. ammonoides* calcite,

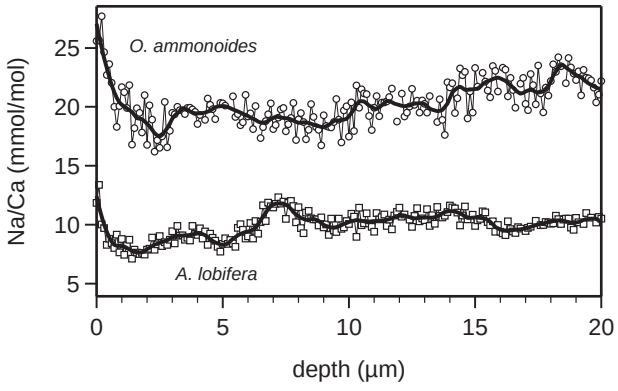

Figure S7: Example laser-ablation profiles through the knob area of two different benthic foraminifera, *O. ammonoides* and *Amphistegina lobifera*.

Table S3: EPMA analysis of the knob area of a single *O. ammonoides* specimen, acquired in EDS mode.

analysis	Na/Ca	Mg/Ca	Sr/Ca	Na/Cl
central knob	26.5	162.5	2.92	10.2
knob 2 line	34.9	165.4	2.10	7.0
knob 3 line	19.5	148.2	2.58	6.3
mean	27.0	158.7	2.53	7.9

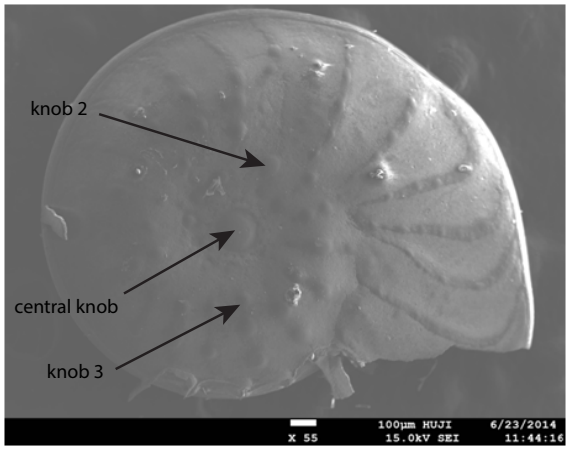

Figure S8: *O. ammonoides* specimen showing the location of the EPMA measurements listed in table S3.

the mean of these data are in excellent agreement with the laser-ablation analyses that we report in the main text. Furthermore, these Na/Cl ratios clearly show that the Na/Ca data are not biased by NaCl precipitation. Even if half of the Na was derived from contamination (assuming primary Na/Ca ratios ∼10 mmol mol^{-1}) this would imply the contaminant phase had Na/Cl = 4. Conversely, assuming all of the measured Cl is the result of contamination would only result in a Na/Ca bias of +2-3 mmol mol^{-1}. We stress that there is no evidence that either of these scenarios are the case (i.e. the EPMA Cl data represents Cl incorporated into calcite during biomineralisation – these analyses are from non-porous test portions), and together all of the data in this section conclusively demonstrate that *O. ammonoides* calcite is characterised by Na/Ca ratios of ∼25 mmol mol^{-1}.

4.4 *O. ammonoides* Na/Ca comparison to inorganic calcite

Although there are several studies examining alkali metal incorporation into inorganic calcite [*Kitano et al.*, 1975; *Ishikawa and Ichikuni*, 1984; *Okumura and Kitano*, 1986], unlike inorganic precipitation experiments such as that of *Mucci and Morse* [1983], none of these calcites were precipitated from seawater. The initial solutions were often very different in composition from seawater, for example the experiments of *Ishikawa and Ichikuni* [1984] contained no Mg, which is known to play an important role in Sr incorporation into calcite (for example). Furthermore, solution chemistry was not kept constant as precipitation progressed, with the implication that it is difficult to calculate distribution coefficients accurately from these data. In the experiments

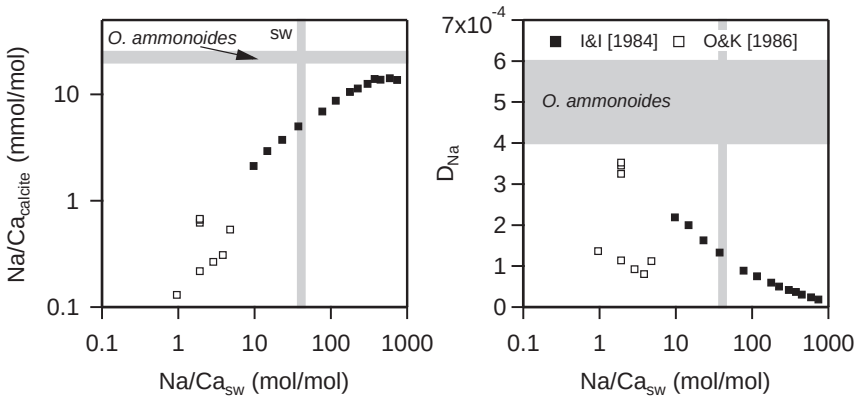

Figure S9: The variation of $Na/Ca_{calcite}$ and D_{Na} with $Na/Ca_{solution}$ for inorganic calcite precipitates from non-seawater solutions [*Ishikawa and Ichikuni*, 1984; *Okumura and Kitano*, 1986]. The grey shaded areas show the present day seawater Na/Ca ratio and the Na/Ca ratio and distribution coefficient of *O. ammonoides*.

of *Okumura and Kitano* [1986] the initial and final [Ca] differed by a factor of 8 and therefore the X/Ca ratio of the solution varied as precipitation occurred. With the caveat that these data may not be directly comparable to calcites precipitated from more complex solutions (i.e. seawater) or to experiments where solution composition was carefully maintained [e.g. *Mucci and Morse*, 1983], $Na/Ca_{calcite}$-Na/Ca_{sw}-D_{Na} relationships are shown in figure S9.

These data show that calcite Na/Ca ratios peak at 10-12 mmol mol^{-1}, with no increase in Na/Ca above $Na/Ca_{solution}$ ratios of ∼200 mol mol^{-1} (present-day seawater has Na/Ca = ∼40), implying that a mechanism other than (for example) modification of the Na/Ca ratio of the calcifying fluid is necessary to explain the higher Na concentration of *O. ammonoides* compared to planktic foraminifera [*Delaney et al.*, 1985] and the low-Mg benthic foraminifera *Ammonia tepida* [*Wit et al.*, 2013]. The inorganic precipitates of *Okumura and Kitano* [1986] show wide variation which appears to be dominantly controlled by whether or not $MgCl_2$ was added to the initial solutions; calcites precipitated from experiments with $MgCl_2$ are characterised by D_{Na} ∼2× that of those precipitated from Mg-free solutions. As we argue in the main text (figure 7), the higher Na/Ca ratios of *O. ammonoides* is a result of the high Mg concentration of the calcite which these foraminifera produce.

5 Seawater-test Mg/Ca calibration extrapolation in temperature space

The application of the surface defined by equation 10 (main text) in the fossil record requires that our Mg/Ca_{test}-Mg/Ca_{sw} calibration can be extrapolated to temperatures other than that at which this relationship was calibrated (24°C).

Füchtbauer and Hardie [1980] calibrated calcite-seawater Mg/Ca for inorganic calcite at three different temperatures, therefore providing an indication of how this relationship may be expected to shift in temperature space (figure S10A, curves given by slices through the surface defined by equation 10 at three different temperature are overlain). All regressions are quadratic equations forced through the origin. The higher $Mg/Ca_{calcite}$ ratios at a given Mg/Ca_{sw} of the

inorganic precipitates compared to our data is probably a result of the inorganic precipitation taking place in non-seawater solutions ($MgCl_2$-$CaCl_2$-Na_2CO_3 mixtures). Figure S10B and C show the shift in the regression coefficients with temperature with a comparison to that calculated based on our coupled calibration, demonstrating that the slope of the regression coefficients with temperature calculated by extrapolating our surface is in good agreement with the experimental data over the range 15-35°C. The effect of precipitation from a non-seawater solution is manifest in the first regression term (which is offset to higher values in the data of *Füchtbauer and Hardie* [1980]), but the slopes of the variation of the regression coefficients with temperature are very similar. Therefore, these data indicate that our coupled Mg/Ca_{sw}-Mg/Ca_{test}-temperature calibration can be extrapolated with confidence assuming that the data of *Füchtbauer and Hardie* [1980] can be robustly applied to inorganic calcites (or calcite very similar to inorganic calcite such as that produced by *O. ammonoides*). The error in the extrapolation of our calibrations over the range that we show in figure 5C (main text) is a maximum of ~3°C by comparison to these inorganic precipitates. The small difference in the slopes shown

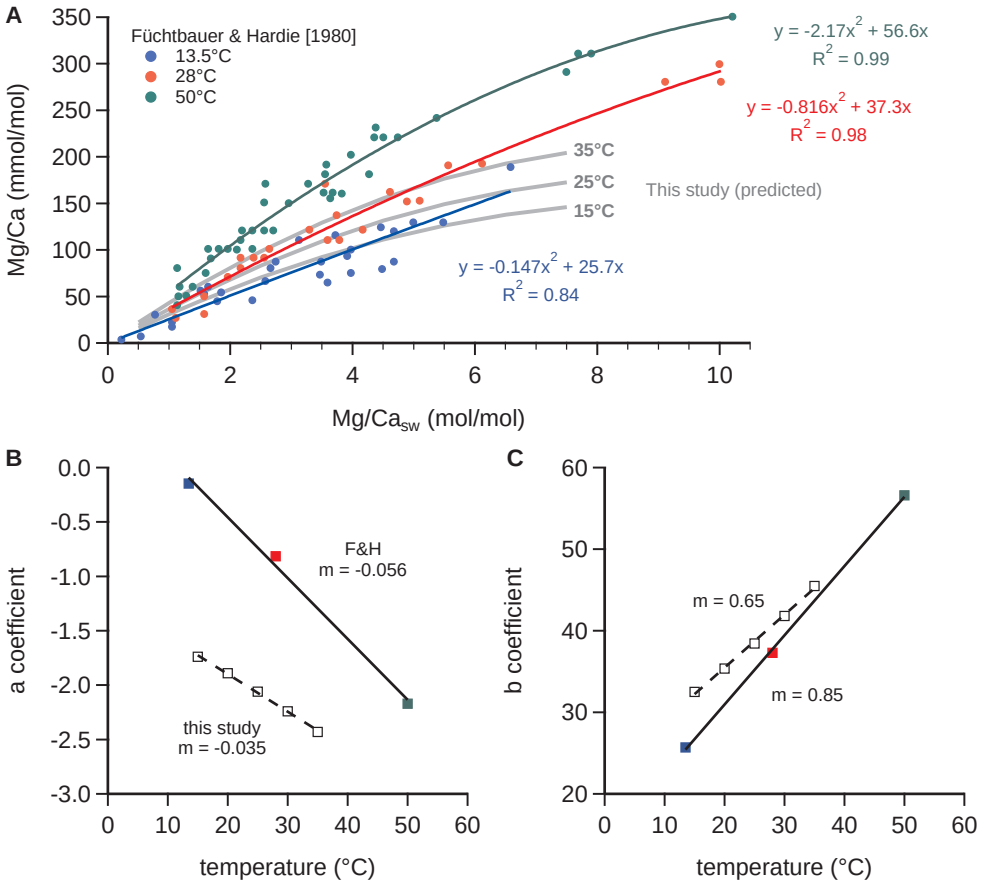

Figure S10: (A) Comparison of the inorganic seawater-calcite Mg/Ca calibrations of *Füchtbauer and Hardie* [1980] at three different temperatures to the predicted calibrations based on the extrapolation of our coupled Mg/Ca_{sw}-Mg/Ca_{test}-temperature calibration (main text equation 10). (B) and (C) Temperature response of the coefficients of a quadratic best fit ($y = ax^2 + bx$) through the Mg/Ca_{sw}-$Mg/Ca_{calcite}$ of *Füchtbauer and Hardie* [1980] and comparison to that predicted by our calibration. Extrapolating our Mg/Ca_{sw}-Mg/Ca_{test}-temperature surface between 15-35°C produces quadratic seawater-calcite Mg/Ca curves in excellent agreement with the experimental data.

in figure S10B and C implies that the slope of a calcite Mg/Ca-temperature calibration does not change exactly as predicted by coupling a $Mg/Ca_{calcite}$-temperature and Mg/Ca_{sw}-$Mg/Ca_{calcite}$ equation in the way that we show. However, for inorganic calcites and foraminifera that produce a test composed of something similar to or the same as inorganic calcite, these data indicate that this complication results in small inaccuracies.

6 Comparison to previous D_{Mg}-Mg/Ca_{sw} calibrations

Our Mg/Ca_{sw}-Mg/Ca_{test} calibration is shown in comparison to previous studies [after *Hasiuk and Lohmann*, 2010] in figure S11.

Although we recommend the application of a quadratic regression between test-seawater Mg/Ca (see the main text) we plot the power regression here (main text equations 7-8) because it is not as easily possible to normalise quadratic regressions to each other. All foraminifera studies so far are characterised by 0<H<1, and as previously demonstrated [*Evans and Müller*, 2012], no foraminifera have H close to 1; this relationship should never be assumed to be linear. The power regression for *O. ammonoides* falls closer to that for inorganic calcite than to any other foraminifera.

7 References

Delaney, M., A. W. H. Bé, and E. A. Boyle (1985), Li, Sr, Mg, and Na in foraminiferal calcite shells from laboratory culture, sediment traps, and sediment cores, *Geochimica et Cosmochimica Acta*, *49*(6), 1327–1341.

Evans, D., and W. Müller (2012), Deep time foraminifera Mg/Ca paleothermometry: Nonlinear correction for secular change in seawater Mg/Ca, *Paleoceanography*, *PA4205*, doi: 10.1029/2012PA002315.

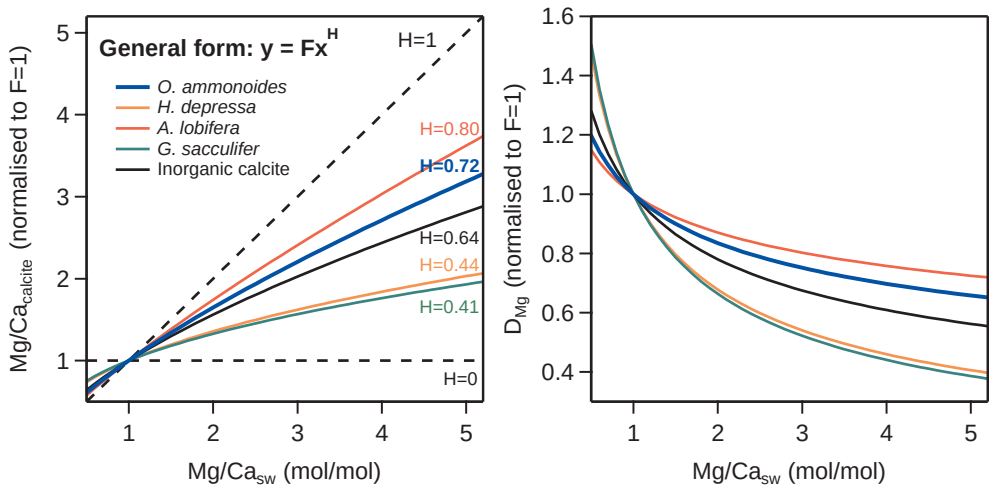

Figure S11: A comparison of the seawater-test Mg/Ca calibration reported here to previous work on foraminifera and inorganic calcite [modified from *Evans and Müller*, 2012].

Evans, D., W. Müller, S. Oron, and W. Renema (2013), Eocene seasonality and seawater alkaline earth reconstruction using shallow-dwelling large benthic foraminifera, *Earth and Planetary Science Letters*, *381*, 104–115, doi:10.1016/j.epsl.2013.08.035.

Füchtbauer, H., and L. Hardie (1980), Comparison of experimental and natural magnesian calcites, in *International Association of Sedimentologists Meeting, Bochum, Germany, Abstracts*, pp. 167–169.

Hasiuk, F., and K. Lohmann (2010), Application of calcite Mg partitioning functions to the reconstruction of paleocean Mg/Ca, *Geochimica et Cosmochimica Acta*, *74*(23), 6751–6763.

Hathorne, E., R. James, P. Savage, and O. Alard (2008), Physical and chemical characteristics of particles produced by laser ablation of biogenic calcium carbonate, *J. Anal. At. Spectrom.*, *23*(2), 240–243.

Ishikawa, M., and M. Ichikuni (1984), Uptake of sodium and potassium by calcite, *Chemical Geology*, *42*(1), 137–146.

Jochum, K., et al. (2006), MPI-DING reference glasses for in situ microanalysis: New reference values for element concentrations and isotope ratios, *Geochemistry Geophysics Geosystems*, *7*(2), doi:10.1029/2005GC001060.

Jochum, K., et al. (2011), Determination of reference values for NIST SRM 610–617 glasses following ISO guidelines, *Geostandards and Geoanalytical Research*, doi:10.1111/j.1751-908X.2011.00120.x.

Jochum, K. P., et al. (2012), Accurate trace element analysis of speleothems and biogenic calcium carbonates by LA-ICP-MS, *Chemical Geology*, *318*, 31–44.

Kitano, Y., M. Okumura, and M. Idogaki (1975), Incorporation of sodium, chloride and sulfate with calcium carbonate, *Geochem. J*, *9*(2), 75–84.

Mucci, A., and J. Morse (1983), The incorporation of Mg^{2+} and Sr^{2+} into calcite overgrowths: influences of growth rate and solution composition, *Geochimica et Cosmochimica Acta*, *47*(2), 217–233.

Okumura, M., and Y. Kitano (1986), Coprecipitation of alkali metal ions with calcium carbonate, *Geochimica et Cosmochimica Acta*, *50*(1), 49–58.

Segev, E., and J. Erez (2006), Effect of Mg/Ca ratio in seawater on shell composition in shallow benthic foraminifera, *Geochemistry, Geophysics, Geosystems*, *7*(2), doi:10.1029/2005GC000969.

Strnad, L., V. Ettler, M. Mihaljevic, J. Hladil, and V. Chrastny (2009), Determination of trace elements in calcite using solution and laser ablation ICP-MS: Calibration to NIST SRM glass and USGS MACS carbonate, and application to real landfill calcite, *Geostandards and Geoanalytical Research*, *33*(3), 347–355.

Wit, J. C., L. de Nooijer, M. Wolthers, and G.-J. Reichart (2013), A novel salinity proxy based on Na incorporation into foraminiferal calcite., *Biogeosciences*, *10*(10), 6375–6387.

Chapter 7

As of January 2015 this manuscript is under review for the journal *Geology*. It is cited in the critical evaluation as Evans *et al*. [Submitted]:

Citation: Evans, D., Brierley, C., Raymo, M. E., Erez, J. & Müller, W. Seawater Mg/Ca reconstruction over the past 5 million years: Implications for Pliocene ocean temperature and sea level. *In review*

Includes 16 pages of supplementary data

Author contributions: DE designed the research in discussion with WM, carried out the experimental and analytical work, interpreted the data and wrote the manuscript. CB designed the research and edited the manuscript. MER interpreted the data and edited the manuscript. JE directed the culturing-related experimental work and edited the manuscript. WM helped develop the analytical procedure and interpret the data, and edited the manuscript.

Corrigenda:

- Line 232 of this manuscript states that Pliocene seawater Mg/Ca reconstructed using this method was 4.0$\pm$0.9 mol mol^{-1}. The number of datapoints that formed this calculation was omitted, and should have been stated as n = 83.
- The caption to figure 1 uses the ambiguous phrase 'showing the location of the calibrations'. This should read 'showing the location of the calibrations in Mg/Ca_{sw} space', and does not refer to a physical location.

Seawater Mg/Ca reconstruction over the past 5 million years: Implications for Pliocene ocean temperature and sea level

David Evans[1*], Chris Brierley[2], Maureen E. Raymo[3], Jonathan Erez[4] & Wolfgang Müller[1]

[1] *Department of Earth Sciences, Royal Holloway University of London, UK*

[2] *Department of Geography, University College London, UK*

[3] *Lamont-Doherty Earth Observatory, Columbia University, USA*

[4] *Earth Science Institute, The Hebrew University of Jerusalem, Israel*

[*] david.evans.2007@rhul.ac.uk

ABSTRACT

Foraminifera Mg/Ca paleothermometery forms the basis of a substantial portion of ocean temperature reconstruction over the last 5 Ma. Furthermore, coupled Mg/Ca-oxygen isotope ($\delta^{18}O$) measurements of benthic foraminifera can constrain eustatic sea level (ESL) independent of paleo-shoreline derived approaches. However, these techniques suffer from uncertainty regarding the secular variation of the Mg/Ca seawater ratio (Mg/Ca_{sw}) on timescales of millions of years. Here we present coupled seawater-test Mg/Ca-temperature laboratory calibrations of *Globigerinoides ruber* in order to test the widely held assumptions that 1) seawater-test Mg/Ca co-vary linearly, and 2) the Mg/Ca-temperature sensitivity remains constant with changing Mg/Ca_{sw}. We find a nonlinear Mg/Ca_{test}-Mg/Ca_{sw} relationship and a substantial lowering of Mg/Ca-temperature sensitivity at lower than modern Mg/Ca_{sw} (from 9.0%°C^{-1} at Mg/Ca_{sw} = 5.2 mol mol^{-1} to 7.5%°C^{-1} at 3.4 mol mol^{-1}). Using our calibrations to more accurately calculate the offset between Mg/Ca and biomarker derived paleotemperatures for four sites, we derive a Pliocene Mg/Ca_{sw} ratio of 4.0±0.9 mol

mol^{-1}. This Mg/Ca$_{sw}$ implies Piacenzian deep ocean temperature estimates 1.4-2.4ºC higher than previously reported and, by extension, ESL >28 m lower compared to when one assumes that Pliocene Mg/Ca$_{sw}$ is the same as at present. However, Pliocene ESL estimates similar to present day are difficult to reconcile with inferred deep ocean temperatures >6°C, implying that additional factors may influence benthic foraminifera-derived ESL.

INTRODUCTION

The temperature-dependant incorporation of Mg/Ca into the calcite test of marine organisms, principally foraminifera, is widely used to reconstruct the Pliocene-Pleistocene temperature evolution of the oceans [e.g. Wara et al. 2005; Tian et al. 2006; O'Brien et al. 2014]. In benthic foraminifera, such reconstructions may be coupled with $\delta^{18}O$ data enabling ice volume and sea level to be estimated [e.g. Sosdian & Rosenthal 2009]. In the tropics, Pliocene Warm Period (PWP) Mg/Ca-derived sea surface temperature (SST) reconstruction suggests the West Pacific Warm Pool was slightly warmer [O'Brien et al. 2014] with a reduced or absent equatorial Pacific temperature gradient [Wara et al. 2005; Fedorov et al. 2010; Zhang et al. 2014]. These observations are only in partial agreement with climate models which do not exhibit a similar magnitude of change in these gradients [Haywood et al. 2013]. Potential mechanisms of reconciling this proxy-model discrepancy include enhanced tropical cyclones [Fedorov et al. 2010] and altered cloud radiative properties [Burls & Fedorov 2014]. Accurate knowledge of SST and temperature gradients is required to assess which mechanism, if any, is the most appropriate.

A confounding factor for Mg/Ca paleothermometry is the dependence of test Mg/Ca (Mg/Ca$_{test}$) on the Mg/Ca ratio of seawater (Mg/Ca$_{sw}$) [Evans & Müller 2012]. Most studies utilizing this proxy assume that Mg/Ca$_{sw}$ has remained constant since the Pliocene [e.g. Wara et al. 2005], although with a notable exception [Medina-Elizalde *et al*., 2008]. However, multiple lines of evidence suggest that this may not be the case [e.g. Horita *et al*., 2002;

Fantle & DePaolo 2006]. The data from these studies suggest a rise in Mg/Ca_{sw} from 3-4 mol mol^{-1} in the mid/late Pliocene to 5.2 mol mol^{-1} at present, with the direct implication that uncorrected Mg/Ca data would underestimate Pliocene warmth. O'Brien *et al*. [2014] found an offset between Mg/Ca and TEX_{86}^{H} temperature reconstructions during the Pliocene for ODP site 1143 (South China Sea) which they argued is most likely caused by secular change in Mg/Ca_{sw}. Whilst this multi-proxy record provides important evidence for a possible change in ocean chemistry since the Pliocene, Mg/Ca_{sw} reconstruction by this technique should be further evaluated for two reasons: (1) The relationship between Mg/Ca_{test}, Mg/Ca_{sw} and temperature has not been rigorously determined for any species of planktic foraminifera, leaving the widely-held assumption of invariant Mg/Ca-temperature sensitivity at below-modern Mg/Ca_{sw} untested. (2) Geochemical records may be biased by other factors, such as a shift in the seasonality of a given proxy or the intensity of carbonate dissolution through time. This is evidenced by the differential magnitude of biomarker and Mg/Ca SST discrepancies between the east and west Pacific [Dekens et al. 2008; O'Brien et al. 2014].

Here, we address both these issues. In order to more accurately reconstruct Mg/Ca_{sw} variation over the last 5 Ma, we have calibrated the relationship between Mg/Ca_{test}, Mg/Ca_{sw} and temperature for the planktic foraminifera, *Globigerinoides ruber* (white, *sensu stricto*). Using these relationships, we then calculate Mg/Ca_{sw} from coupled Mg/Ca-biomarker proxy data, for the four sites spanning the last ~5 Ma from which both proxies are available. Finally, we assess the implications of our results for coupled Mg/Ca-$\delta^{18}O$-derived ice volume and eustatic sea level (ESL) estimates for the Pliocene.

METHODS

Mg/Ca_{test}-Mg/Ca_{sw}-temperature calibration

Experimental setup

Foraminifera were collected from the northernmost Red Sea (Gulf of Eilat) by plankton drift tows at 20 m. Specimens were handpicked into individual sealed 120 ml culture jars and fed daily (*Artemia*). Two principal calibrations were carried out: (1) Mg/Ca_{test}-Mg/Ca_{sw} between Mg/Ca_{sw} = 2.2-6.2 mol mol^{-1} at 26°C and (2) Mg/Ca-temperature between 20-30°C at Mg/Ca_{sw} = 3.4 mol mol^{-1}. Each calibration consisted of five data points with 10-20 individual specimens cultured at each unique set of conditions. Seawater was isotopically labelled with 74 nM $^{135}BaCO_3$ in order to enable subsequent unambiguous identification of chambers precipitated in culture. The Mg/Ca ratio of seawater was modified by mixing natural Gulf of Eilat seawater with artificial Mg-free seawater (i.e seawater [Ca] was constant).

Laser-ablation ICPMS analysis

Specimens were ultrasonicated in ~10% NaOCl and rinsed in deionized water, mounted on carbon tape and analysed for X/Ca ratios using the 193 nm ArF laser-ablation ICPMS setup with two-volume cell at Royal Holloway [Müller et al. 2009]. The analytical procedures for foraminifera are described in Evans *et al*. [2014]. Only chambers characterized by elevated $^{135}Ba/^{138}Ba$ (within error of the culture seawater) were used to define calibration equations. See the data repository[1] for further details.

Dataset treatment

In order to examine secular variation in Mg/Ca_{sw} over the last 5 Ma, we utilize published Mg/Ca and TEX_{86} data from ODP site 806 [Wara et al. 2005; Zhang et al. 2014], Mg/Ca and $U^{K'}_{37}$ data from ODP847 [Liu & Herbert 2004; Lawrence et al. 2006; Wara et al. 2005], Mg/Ca, $U^{K'}_{37}$ and TEX_{86} data from ODP1143 [Li et al. 2011; Tian et al. 2006; O'Brien et al. 2014; Zhang et al. 2014] and Mg/Ca and $U^{K'}_{37}$ data from ODP999 [Seki et al. 2010; Schmidt et al. 2006; Badger et al. 2013; O'Brien et al. 2014]. Only $U^{K'}_{37}$ data below saturation was used; therefore no temperature record before 3.6 Ma is available from ODP999. *G. sacculifer* Mg/Ca was adjusted to *G. ruber* assuming that both species have the same Mg/Ca-

temperature sensitivity in the modern ocean [e.g. Anand 2003] and that a constant multiplicative offset is appropriate. Applying this adjustment to ODP999 for the interval 2.2-3.4 Ma (when high resolution records for both species are available) demonstrates that the *G. sacculifer-G. ruber* offset is likely to be constant through time (figure DR6). Therefore, our *G. ruber*-derived calibrations can be applied with confidence to *G. sacculifer* data. Mg/Ca dissolution was corrected by matching the Mg/Ca data to the biomarker temperatures for the last 400 ka. This approach is advantageous as no knowledge of the style of dissolution at the core site is required. See the data repository for a more detailed discussion of both these adjustments.

Mg/Ca and biomarker datasets for each site were LOESS-smoothed and re-sampled at 100 ka resolution with the exception of ODP999 (250 ka). These data were then used to iteratively back-calculate Mg/Ca_{sw} for each site based on our coupled calibration. Finally, calculated Mg/Ca_{sw} values from each site were combined and LOESS-smoothed to produce an average Mg/Ca_{sw} curve for the last 5 Ma.

RESULTS

Mg/Ca_{test} response to variable Mg/Ca_{sw} and temperature

Our calibrations are shown in figure 1 in comparison to a previous *G. ruber* Mg/Ca-temperature calibration at modern day Mg/Ca_{sw} (5.2 mol mol^{-1}) carried out in the same laboratory [Kisakürek et al. 2008]. The Mg/Ca-temperature relationship at Mg/Ca_{sw} = 3.4 mol mol^{-1} (figure 1C) is described by the exponential curve:

$$Mg/Ca_{test} = 0.48 \times \exp^{0.075T} \quad (1)$$

$R^2 = 0.99$, n = 44. Equation 1 defines a Mg/Ca-temperature sensitivity of 7.5%°C^{-1}. This is a significant reduction compared to calibrations in modern seawater for this species, where the exponential coefficient is routinely taken to be 0.09 [e.g. Anand et al. 2003], i.e. 9%°C^{-1}. Thus, the sensitivity of this thermometer is not constant at below-modern Mg/Ca_{sw} ratios.

Our Mg/Ca_{sw}-Mg/Ca_{test} calibration (figure 1B) confirms the nonlinear response to Mg/Ca_{sw} observed in other foraminifera [Segev & Erez 2006; Evans *et al*., 2014]:

$$Mg/Ca_{test} = -0.0591 \times Mg/Ca_{sw}^2 + 1.15 \times Mg/Ca_{sw} \quad (2)$$

$R^2 = 0.99$, n = 76.

The coupled calibration surface shown in figure 1A was produced by assuming that the shape of the Mg/Ca-temperature relationship is always of the form $Mg/Ca = B\exp^{AT}$, where the two coefficients vary as a function of Mg/Ca_{sw}. Five different assumptions were made regarding how these coefficients might be controlled by Mg/Ca_{sw}: invariant, linear, power, exponential or quadratic, producing a total of 25 different equations. These surfaces were then least-squares modeled to fit all the *G. ruber* laboratory cultures. The red and grey lines in figure 1B-E (mean model-data offset less and greater than 0.1 mmol mol^{-1} respectively) show the results of this modeling, including variation in the coefficients of a Mg/Ca-temperature calibration with changing Mg/Ca_{sw} (figure 1D,E). We find that it is only possible to produce a surface that matches all the observed features of the data (e.g. convex upwards Mg/Ca_{test}-Mg/Ca_{sw} relationship, reduced Mg/Ca-temperature sensitivity at lower Mg/Ca_{sw}) if both coefficients vary quadratically with Mg/Ca_{sw}. Although several of the models deviate from the data by less than 0.1 mmol mol^{-1} on average, only this one matches the observed Mg/Ca-temperature sensitivity reduction at below-modern Mg/Ca_{sw}. The equation of the coupled calibration surface (figure 1) is therefore modeled with the general form $Mg/Ca_{test} = B\exp^{AT}$, where:

$$B = 0.019 \times Mg/Ca_{sw}^2 + 0.16 \times Mg/Ca_{sw} + 0.804 \quad (3)$$

And:

$$A = -0.0029 \times Mg/Ca_{sw}^2 + 0.032 \times Mg/Ca_{sw} \quad (4)$$

The surface is well-constrained over the range that temperature and Mg/Ca_{sw} varied in the laboratory experiments (only quadratic regressions between these coefficients and Mg/Ca_{sw}

149 can reproduce the three calibrations, figure DR4). Therefore, variation in the sensitivity of the
150 Mg-temperature relationship (figure 1E) is well-defined by a limited number of Mg/Ca-
151 temperature calibrations at different Mg/Ca_{sw} (provided Mg/Ca_{test}-Mg/Ca_{sw} is also
152 calibrated), which means that our coupled calibration should also be applicable to earlier
153 Cenozoic reconstructions.

154 ***Pliocene-Recent Mg/Ca_{sw} reconstruction***

155 Foraminifera Mg/Ca data from all four sites are shown in figure 2A. At face value, these
156 records imply that the Pliocene tropics were the same temperature or cooler than present,
157 with the exception of ODP847. Mg/Ca-derived paleotemperatures are offset to values 5-15%
158 lower compared to those derived from biomarkers from the same site during the Pliocene
159 (figure 2B). Back-calculated Mg/Ca_{sw}, derived from these offsets and our calibration surface,
160 is shown in figure 2C in comparison to other proxy data. By averaging several records from
161 different depths spanning a large portion of the tropics (where potential seasonality bias is
162 limited), our Mg/Ca_{sw} record minimizes temporally variable proxy complications at any one
163 location. Nonetheless, we present two back-calculated Mg/Ca_{sw} records, both with and
164 without data from ODP847, a site that shows little biomarker-Mg/Ca temperature offset
165 through the last 5 Ma. Producing a back-calculated Mg/Ca_{sw} record that excludes data from
166 ODP847 may be justified as this site experiences the largest interannual SST variability of all
167 those utilized here and thus may be the most susceptible to changes in seasonal proxy bias
168 (see the data repository). Our preferred record (including all sites) suggests a Mg/Ca_{sw} value
169 of 4.0 mol mol^{-1} for the mid-Pliocene and, therefore, a minor reduction in the Mg/Ca-
170 temperature sensitivity for *G. ruber* to 8.2%$°C^{-1}$.

171 **DISCUSSION**

172 ***Mg/Ca_{sw} control on Mg/Ca-paleothermometry***

Our reconstructed Pliocene Mg/Ca_{sw} (23% lower than at present; figure 2C) is in line with what is known about the timescales of processes controlling the oceanic cycling of these elements. Our record is in agreement with the fluid inclusion data of Horita *et al*. [2002] and implies a broadly similar magnitude of Mg/Ca_{sw} change over the last 3 Ma compared to the pore fluid modeling of Fantle & DePaolo [2006]. In the mid Pliocene, the planktic foraminiferal Mg/Ca-derived palaeotemperature underestimation (i.e. the difference between assuming no seawater chemistry change and using our Mg/Ca_{sw} record) ranges from ~1°C when Mg/Ca_{test} values are ~1 mmol mol^{-1} (SST = ~9°C) to ~2.6°C when Mg/Ca_{test} values are >5 mmol mol^{-1} (SST >30°C). Thus, tropical temperatures during the PWP are likely underestimated by 2.3-2.7°C. Because the magnitude of this correction is dependent on Mg/Ca_{test}, one would also expect an impact on estimated Pliocene SST gradients, although this effect is minor (figure DR9).

Ultimately, if Mg/Ca_{sw} was lower as these data suggest, then foraminifera Mg/Ca-derived deep ocean temperatures have also been underestimated. Figure 3 shows the extent to which benthic foraminifera Mg/Ca-derived temperature may have been underestimated, based on our Mg/Ca_{sw} record and a calculated relationship between seawater-test Mg/Ca for benthic foraminifera [Evans & Müller 2012]. At DSDP607 [Sosdian & Rosenthal 2009], the implied underestimation of deep ocean temperatures is 1.2-2.1°C during the Pliocene, giving a mean PWP bottom water temperature of 6.1°C. The possibility remains that diagenesis or non-thermal Mg/Ca effects also exert an influence on these records, for instance as shown for Eocene planktic foraminifera [Kozdon et al. 2013]. Therefore, the exact degree to which benthic foraminfera Mg/Ca-derived temperatures have been underestimated at any site should be viewed with caution, although assuming no Pliocene-Recent change in Mg/Ca_{sw} would lead to a systematic inaccuracy in temperature irrespective of the importance of secondary and diagenetic Mg/Ca controls.

Implications for PWP sea level reconstruction

Ice volume and sea level estimates based on coupled benthic foraminifera Mg/Ca-$\delta^{18}O$ data are highly sensitive to the accuracy of the temperature reconstruction. Using a $\delta^{18}O$-sea level relationship of 0.01‰ m^{-1} [Adkins et al. 2002] and the *Cibicidoides* $\delta^{18}O$-temperature calibration of Marchitto *et al*. [2014], a 1°C systematic bias in bottom water temperature translates to ~23.5 m error in inferred eustatic sea level (ESL). Therefore, a direct implication of our Mg/Ca_{sw} reconstruction is that assuming no seawater chemistry change since the Pliocene would result in an overestimation of ESL during the PWP. Assuming no diagenetic or other source of temperature bias, applying this correction to the DSDP607 data [Sosdian & Rosenthal 2009] implies that ESL has been overestimated by 28-47 m during the PWP in that study. Taken at face value, this further implies that maximum reconstructed ESL would be about the same as present day, with a mean Pliocene ESL less than at present. Thus, the impact of secular variation in Mg/Ca_{sw} on benthic foraminifera Mg/Ca has important implications for the conclusions of any study that partly or entirely base ESL reconstructions on these data [e.g. Miller et al. 2012].

However, it is intuitively difficult to reconcile PWP deep ocean temperatures >6°C with a maximum ESL equivalent to present day, especially given that more direct evidence exists for East Antarctic Ice Sheet instability at this time [Cook et al. 2013; Patterson et al. 2014], and other factors may require more careful consideration when interpreting benthic foraminifer geochemistry. Given that benthic foraminifera $\delta^{18}O$ appears resistant to diagenesis [Edgar et al. 2013], resolutions to this discrepancy may lie in a combination of secular shifts in inter-basin $\delta^{18}O_w$ offsets and/or diagenetic and non-thermal (e.g. $[CO_3^{2-}]$) bias on Mg/Ca [Woodard et al. 2014]. For example, a 1°C bias resulting from Mg-rich overgrowths (equivalent to 0.11 mmol mol^{-1} Mg/Ca) equates to ~24 m of sea level,

highlighting the need for accurate determination of Mg/Ca ratios free from diagenetic contaminants.

CONCLUSION

Here, we present the first calibration of the response of planktic foraminifera Mg/Ca (*G. ruber*) to variation in both temperature and Mg/Ca_{sw}, a prerequisite for any paleoceanic study utilizing foraminifera Mg/Ca in sediments older than ~2 Ma, beyond which Mg/Ca_{sw} cannot be assumed to be the same as at present. We use these calibrations to more accurately estimate secular variation in Mg/Ca_{sw} over the last 5 Ma, assuming that the offset between Mg/Ca and biomarker proxies from tropical sites for this time period is best explained by a shift in this ratio [e.g. O'Brien *et al*., 2014]. We find that Mg/Ca_{sw} during the Pliocene was 4.0±0.9 mol mol^{-1} (2SD of all data), higher than previously proposed [O'Brien et al 2014] but 23% lower than at present. This implies both surface and deep ocean Mg/Ca-derived temperatures have been underestimated by 1.0-2.7°C. Coupled Mg/Ca-$\delta^{18}O$-derived ESL reconstructions are sensitive to an inaccuracy of this magnitude. The possibility that Pliocene benthic Mg/Ca data is biased by additional factors cannot be ruled out and indeed may even be suggested by our results.

Finally, our *G. ruber* calibrations in 3D temperature-Mg/Ca_{test}-Mg/Ca_{sw} space enables us to tightly constrain how the sensitivity of the Mg/Ca thermometer changes with Mg/Ca_{sw}. This change is significant: the Mg/Ca increase per °C is reduced to ~8% for the Pliocene and ~6% for the Eocene, assuming that seawater [Mg] and [Ca] exert an equal control on this sensitivity. Thus, our findings also have important implications for the use of this tool for relative temperature reconstruction over climatic events throughout the Cenozoic, such as the Paleocene-Eocene hyperthermals and the Eocene-Oligocene Transition.

ACKNOWLEDGMENTS

DE acknowledges a NERC postgraduate studentship at RHUL. We are grateful to Shai Oron (Interuniversity Institute for Marine Sciences, Eilat) for help with plankton tows and to Tom Barlow and Simon Chenery (BGS, UK) for ICPMS trace element analysis of seawater samples. An Israeli Science Foundation Grant #551/10 to JE supported the foraminifera culturing work. MER acknowledges support from NSF grant OCE-12-02632.

REFERENCES CITED

Adkins, J.F., Mcintyre, K. & Schrag, D.P., 2002. The Salinity, Temperature, and d18O of the Glacial Deep Ocean. *Science*, 298:1769–1773.

Anand, P., Elderfield, H. & Conte, M.H., 2003. Calibration of Mg/Ca thermometry in planktonic foraminifera from a sediment trap time series. *Paleoceanography*, 18(2).

Badger, M.P.S. et al., 2013. High-resolution alkenone palaeobarometry indicates relatively stable p CO2 during the Pliocene (3.3-2.8 Ma). *Philosophical transactions A*, 371.

Burls, N.J. & Fedorov, a. V., 2014. What Controls the Mean East–West Sea Surface Temperature Gradient in the Equatorial Pacific: The Role of Cloud Albedo. *Journal of Climate*, 27(7):2757–2778.

Cook, C.P. et al., 2013. Dynamic behaviour of the East Antarctic ice sheet during Pliocene warmth. *Nature Geoscience*, 6(9):765–769.

Dekens, P.S. et al., 2008. A 5 million year comparison of Mg/Ca and alkenone paleothermometers. *Geochemistry, Geophysics, Geosystems*, 9(10).

Edgar, K.M., Pälike, H. & Wilson, P. a., 2013. Testing the impact of diagenesis on the δ18O and δ13C of benthic foraminiferal calcite from a sediment burial depth transect in the equatorial Pacific. *Paleoceanography*, 28(3):468–480.

Evans, D. et al., 2014. Mg/Ca-temperature and seawater-test chemistry relationships in the shallow-dwelling large benthic foraminifera Operculina ammonoides. *Geochimica et Cosmochimica Acta*.

Evans, D. & Müller, W., 2012. Deep time foraminifera Mg/Ca paleothermometry: Nonlinear correction for secular change in seawater Mg/Ca. *Paleoceanography*, 27(4).

Fantle, M. & Depaolo, D., 2006. Sr isotopes and pore fluid chemistry in carbonate sediment of the Ontong Java Plateau: Calcite recrystallization rates and evidence for a rapid rise in seawater Mg over the last 10 million years. *Geochimica et Cosmochimica Acta*, 70(15):3883–3904.

Fedorov, A. V, Brierley, C.M. & Emanuel, K., 2010. Tropical cyclones and permanent El Niño in the early Pliocene epoch. *Nature*, 463(7284):1066–70.

Haywood, A. M. et al., 2013. Large-scale features of Pliocene climate: results from the Pliocene Model Intercomparison Project. *Climate of the Past*, 9(1):191–209.

Horita, J., Zimmermann, H. & Holland, H.D., 2002. Chemical evolution of seawater during the Phanerozoic : Implications from the record of marine evaporites. *Geochimica et Cosmochimica Acta*, 66(21):3733–3756.

284 Kisakürek, B. et al., 2008. Controls on shell Mg/Ca and Sr/Ca in cultured planktonic
285 foraminiferan, Globigerinoides ruber (white). *Earth and Planetary Science Letters*, 273(3-
286 4):260–269.

287 Kozdon, R. et al., 2013. In situ δ18O and Mg/Ca analyses of diagenetic and planktic
288 foraminiferal calcite preserved in a deep-sea record of the Paleocene-Eocene thermal
289 maximum. *Paleoceanography*, 28.

290 Lawrence, K.T., Liu, Z. & Herbert, T.D., 2006. Evolution of the eastern tropical Pacific
291 through Plio-Pleistocene glaciation. *Science*, 312(5770):79–83.

292 Li, L. et al., 2011. A 4-Ma record of thermal evolution in the tropical western Pacific and its
293 implications on climate change. *Earth and Planetary Science Letters*, 309(1-2):10–20.

294 Liu, Z. & Herbert, T.D., 2004. High-latitude influence on the eastern equatorial Pacific
295 climate in the early Pleistocene epoch. *Nature*, 427:720–723.

296 Marchitto, T.M. et al., 2014. Improved oxygen isotope temperature calibrations for
297 cosmopolitan benthic foraminifera. *Geochimica et Cosmochimica Acta*, 130:1–11.

298 Medina-Elizalde, M., Lea, D.W. & Fantle, M.S., 2008. Implications of seawater Mg/Ca
299 variability for Plio-Pleistocene tropical climate reconstruction. *Earth and Planetary*
300 *Science Letters*, 269(3-4):585–595.

301 Miller, K.G. et al., 2012. High tide of the warm Pliocene: Implications of global sea level for
302 Antarctic deglaciation. *Geology*, 40(5):407–410.

303 Müller, W. et al., 2009. Initial performance metrics of a new custom-designed ArF excimer
304 LA-ICPMS system coupled to a two-volume laser-ablation cell. *Journal of Analytical*
305 *Atomic Spectrometry*, 24(2):209.

306 O'Brien, C.L. et al., 2014. High sea surface temperatures in tropicalwarm pools during the
307 Pliocene. *Nature Geoscience*, 7:606.

308 Patterson, M. O. et al., 2014, Orbital forcing of the East Antarctic ice sheet during the
309 Pliocene and Early Pleistocene. *Nature Geoscience*, 7:841.

310 Schmidt, M.W., Vautravers, M.J. & Spero, H.J., 2006. Western Caribbean sea surface
311 temperatures during the late Quaternary. *Geochemistry, Geophysics, Geosystems*, 7(2).

312 Segev, E. & Erez, J., 2006. Effect of Mg/Ca ratio in seawater on shell composition in shallow
313 benthic foraminifera. *Geochemistry Geophysics Geosystems*, 7(2):1–8.

314 Seki, O. et al., 2010. Alkenone and boron-based Pliocene pCO2 records. *Earth and Planetary*
315 *Science Letters*, 292(1-2):201–211.

316 Sosdian, S. & Rosenthal, Y., 2009. Deep-sea temperature and ice volume changes across the
317 Pliocene-Pleistocene climate transitions. *Science*, 325(5938):306–10.

318 Tian, J. et al., 2006. Late Pliocene monsoon linkage in the tropical South China Sea. *Earth*
319 *and Planetary Science Letters*, 252(1-2):72–81.

320 Wara, M.W., Ravelo, A.C. & Delaney, M.L., 2005. Permanent El Niño-like conditions during
321 the Pliocene warm period. *Science*, 309(5735):758–61.

322 Woodard, S.C. et al., 2014. Antarctic role in Northern Hemisphere glaciation. *Science*,

323 Zhang, Y.G., Pagani, M. & Liu, Z., 2014. A 12-million-year temperature history of the
324 tropical Pacific Ocean. *Science*, 344(6179):84–7.

FIGURE CAPTIONS

Figure 1. Coupled Mg/Ca_{test}-Mg/Ca_{sw}-temperature calibration for *G. ruber*. (A) Calibration surface showing the location of the calibrations performed in this study and at modern Mg/Ca_{sw} [Kisakürek et al. 2008]. (B) Mg/Ca_{sw}-Mg/Ca_{test} calibration, (C) comparative Mg/Ca-temperature calibrations with varying Mg/Ca_{sw}. Error bars are 2SE. (D) Mg/Ca-sensitivity variation with Mg/Ca_{sw}, (E) pre-exponential coefficient variation with Mg/Ca_{sw}. Datapoints are taken from the calibrations shown in B and C. Red lines show modeled response by least-squares regression fitting the surface shown in A to the calibration datapoints, for a variety of initial assumptions regarding the form of the equation describing this surface (see data repository). Because the calibration surface is well defined by three planes, the modeled surface and therefore the coefficients of a Mg/Ca-temperature calibration are tightly constrained over this range of Mg/Ca_{sw}, despite the small number of datapoints in D, E. Red model lines are those that deviate from the three calibrations by no more than 0.1 mmol mol^{-1} on average. Note that only the bold red line (quadratic model) captures the Mg/Ca-sensitivity change with Mg/Ca_{sw}.

Figure 2. (A) Mg/Ca data from all sites for which at least one other palaeotemperature proxy (TEX_{86}, $U^{K'}_{37}$) is available for the last 5 Ma. With the exception of ODP847, at face value all records imply Pliocene tropical sea surface temperature equivalent or cooler than at present. (B) Fraction Mg/Ca-biomarker proxy offsets (smoothed, see methods); the majority of records indicate that Mg/Ca underestimates temperature by 5-15% in the Pliocene. (C) Back-calculated Mg/Ca_{sw} record, compared to previous reconstructions. Two scenarios are shown: our preferred reconstruction based on all sites (thick red line) and that excluding ODP847

(thin red line), see text. Other proxy data is shown for comparison [Fantle & DePaolo 2006; Horita et al. 2002].

Figure 3. Underestimate in benthic foraminifera Mg/Ca-derived temperatures resulting from the assumption that Mg/Ca_{sw} has remained constant over the past 5 Ma, shown as a function of color. Contour line units are temperature underestimate in °C. DSDP607 data [Sosdian & Rosenthal 2009] overlain for comparison.

[1]GSA Data Repository item 2009xxx, [detailed analytical methodology, foraminifera Mg/Ca calibration modeling, calculations] is available online at www.geosociety.org/pubs/ft2009.htm, or on request from editing@geosociety.org or Documents Secretary, GSA, P.O. Box 9140, Boulder, CO 80301, USA.

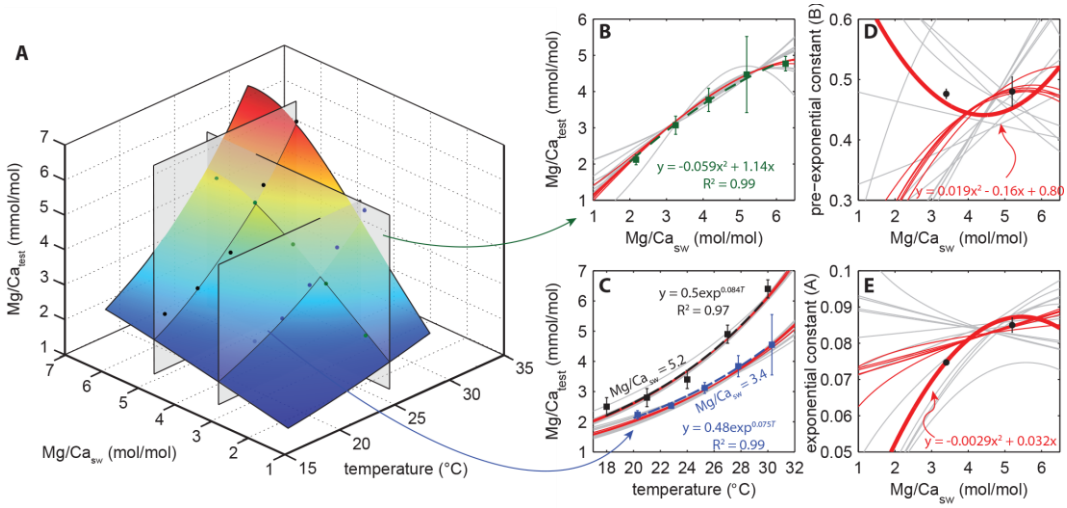

362

363 Figure 1

364 6.7×14 cm = 0.23 pages

365

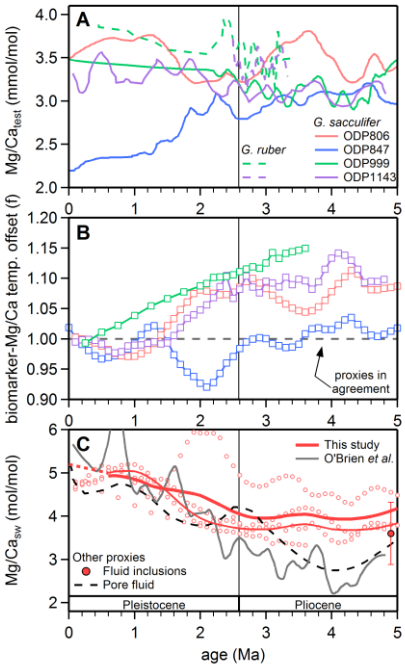

366

367 Figure 2

368 9.2×6.3 cm = 0.14 pages

369

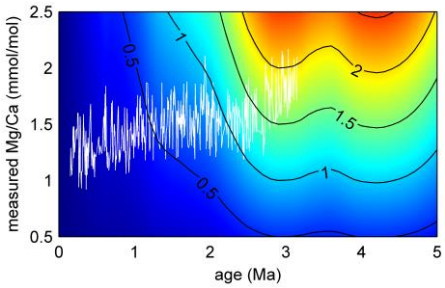

370

371 Figure 3

372 3.9×5.9 cm = 0.06 pages

1 Further experiment details

Plankton drift tows (using only the wind to drag the net) were always carried out at a location with a bathymetry of >300 m. Foraminifera were immediately picked from plankton concentrates to recovery dishes, whereupon they were measured, photographed and transferred to individual culture jars if they accepted a juvenile *Artemia* (brine shrimp). The culture jars were sealed with parafilm and placed into water baths that were simultaneously cooled and heated to maintain a long-term temperature variability of less than ±0.3°C. Individual foraminifera were measured and fed daily, although feeding was never forced by killing the *Artemia*. All individual foraminifera were cultured until they underwent gametogenesis (usually no more than 7 days, see also *Kisakürek et al.* [2008]) and were transferred to new jars if algal growth was detected.

All culture seawater was isotopically labelled to facilitate unambiguous identification of chambers precipitated exclusively in culture. ^{135}Ba was chosen as a seawater spike because highly enriched (93.5%) $^{135}BaCO_3$ is relatively inexpensive and the low seawater [Ba] (<10 ppb) means little spike is required to greatly modify the isotopic composition of large volumes of seawater. Furthermore, planktic foraminifera Ba/Ca is known to respond linearly to seawater Ba/Ca [e.g. *Hönisch et al.*, 2011]. Culture seawater $^{135}Ba/^{138}Ba$ was dependent on the seawater [Ba] before the spike was added, which was in turn dependent on the proportion of Mg-free artificial seawater used to create seawater with variable Mg/Ca ratios from artificial-natural seawater mixes. Artificial seawater was characterised by a higher [Ba] than Gulf of Eilat seawater at the time the experiment was carried out; therefore culture seawater $^{135}Ba/^{138}Ba$ ratios varied between 0.52 at Mg/Ca_{sw} = 2.2 to 1.82 at Mg/Ca_{sw} = 5.2. These ratios are easily distinguishable from natural by LA-ICPMS.

2 Data quality and processing

2.1 Laser ablation

Foraminifera trace element data quality and procedures are discussed in detail in the supplementary material of *Evans et al.* [2014] and we focus here only on the isotope ratio data used to discriminate chambers precipitated in culture from those present at the time of collection.

Briefly, we utilise the slow depth profiling procedure previously outlined [*Evans et al.*, 2014] in order to maximise vertical spatial resolution through the chamber walls. Ablation parameters were: 44-57 μm spot size, 2 Hz laser repetition rate, and a 'squid' inline gas smoothing device was used to avoid beating (spectral skew) at low repetition rates. Ba isotope data quality was optimised by increasing the m/z = 135 dwell time to 100 ms (∼1/3 total dwell time), the maximum practically possible given the simultaneous requirements to monitor 10 other m/z and to keep the total ICPMS sweep time below 0.35 s. Whilst unnecessary for samples grown in cultured seawater with $^{135}Ba/^{138}Ba$ >0.5, the relatively low natural abundance of ^{135}Ba ($^{135}Ba/^{138}Ba$ = 0.09194) means that this is necessary to optimise data at lower $^{135}Ba/^{138}Ba$ ratios, given the low (1-2 ppm) Ba concentration in foraminiferal calcite.

$^{135}Ba/^{138}Ba$ data of *Globigerinoides ruber* chambers of plankton tow specimens that were

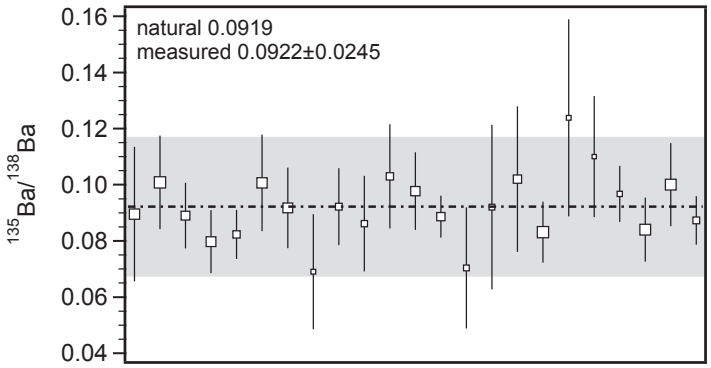

Figure DR1: $^{135}Ba/^{138}Ba$ ratio measurements of non-cultured *G. ruber*. Marker size is shown as a function of analysis length (number of ICPMS sweep times) which is proportional to chamber wall thickness.

not cultured (and never exposed to seawater with isotopically modified $^{135}Ba/^{138}Ba$) are shown in figure DR1. These analyses have mean measured $^{135}Ba/^{138}Ba = 0.0922 \pm 0.0245$, equivalent to an accuracy of 0.26% and precision of 26.5%. The mean 2SE of an individual measurement is 18.1%. Better accuracy and precision are not necessary when identifying very large shifts in isotopic composition, such as the 5-20× increase here. Therefore, we do not apply a mass bias correction and the low accuracy is simply fortuitous. Precision derived from these data may slightly overestimate the uncertainty in analyses of material with elevated $^{135}Ba/^{138}Ba$, as the m/z = 135 counting statistics improve, although this is difficult to assess, as the error on individual analyses is also governed by other factors such as intra-chamber compositional variability and shell thickness (i.e. analysis length).

An example of the use of this technique to identify in-culture growth is shown in figure DR2. These analyses represent chambers from foraminifera cultured in seawater at 26°C and Mg/Ca_{sw} = 2.17 mol mol^{-1} and are therefore expected to have lower Mg/Ca_{test} values than those grown in natural Gulf of Eilat seawater. Aside from some outliers this is the case. Only analyses characterised by $^{135}Ba/^{138}Ba$ within error of that of the relevant seawater analysis were used to define the calibrations that we present here. In order to avoid potential bias by integrating data from partial chamber wall profiles with variable $^{135}Ba/^{138}Ba$ (as gametogenic calcite was more likely to be precipitated in culture), only chambers with consistently elevated Ba-isotope ratios were used to define the calibrations. Mean values were integrated from the entire chamber wall in order that our laser-ablation measurements are directly comparable to solution analysis of dissolved tests. Unlike calibrations based on bulk (solution) analysis of multiple individuals, this method eliminates the need for mass-balance corrections. These may add uncertainty into calibrations if the proportion of calcite precipitated prior to foraminifera collection is poorly/unconstrained.

^{135}Ba isotope spikes are therefore an effective tool capable of unambiguously identifying foraminifera calcite precipitated in culture, given the ease with which seawater $^{135}Ba/^{138}Ba$ may be modified; a ∼74 nM spike was used here, equivalent to ∼2 ml 174.5 μM $^{135}BaCO_3$ solution in 5 l of seawater.

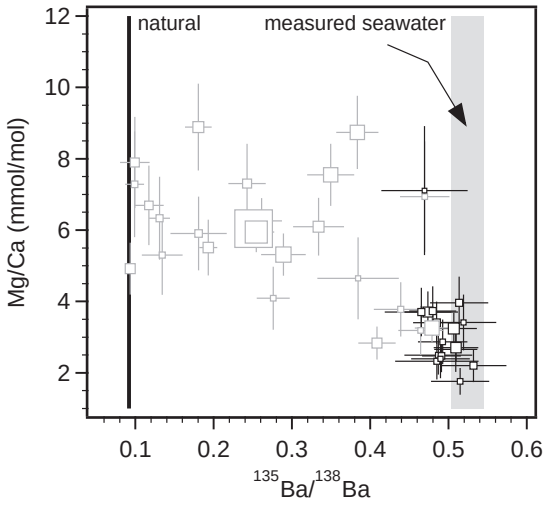

Figure DR2: Ba isotope data from experiment DE3-2-26 (temperature = 26°C, Mg/Ca_{sw} = 2.17 mol mol^{-1}). Cultured foraminifera Mg/Ca is lower than pre-culture calcite because these foraminifera were grown in seawater with a lower Mg/Ca ratio. Marker size is shown as a function of analysis length. Black symbols are those which lie within error of the measured seawater $^{135}Ba/^{138}Ba$. These analyses were used to define the calibrations we present. Other analyses represent a mixture of culture and pre-culture growth and were discarded. Note one high-Mg outlier from a very short analysis that is within error of the seawater ratio.

2.2 Seawater ICPMS analysis

Trace element data quality as measured by ICPMS at the NERC Isotope Geosciences Laboratory (British Geological Survey, UK) is described in the supporting material of *Evans et al.* [2014]. The procedure was not modified except to include ^{135}Ba. Measured $^{135}Ba/^{138}Ba$ was normalised to a BGS QC seawater with natural $^{135}Ba/^{138}Ba$ ([Ba] = ∼300 ppm). The magnitude of this accuracy correction is 2.8%, following which data quality (accuracy ± precision) based on triplicate analysis of the seawater standard NASS-4 ([Ba] = ∼7 ppm) was 2.0±3.9 %.

3 Detailed results

Pertinent trace element chemistry, $^{135}Ba/^{138}Ba$ ratios, carbonate chemistry details and culture conditions for all experiments are given in table DR1. Seawater Mg/Ca was modified by mixing natural Gulf of Eilat seawater (ESW) with artificial seawater prepared with no Mg, as previously described [*Evans et al.*, 2014; *Segev and Erez*, 2006]. Salinity was modified to 37‰ (Gulf of Eilat = 40.65‰) for all experiments using NaCl and distilled water. Experiment DE3 (variable Mg/Ca_{sw}) was carried out a lower pH (mean 8.0) than experiment DE4 (mean pH = 8.2).

4 Mg/Ca data and calibration form

4.1 pH adjustment

Foraminifera Mg/Ca is known to be controlled by pH and/or $[CO_3^{2-}]$, which is also evident in these cultures. The point at which the two calibrations approximately intersect (Mg/Ca_{sw} =

Table DR1: Culture details. n is the number of chamber analyses that went into producing the mean foraminifera Mg/Ca values shown in the final two columns. Saturation state and $[CO_3^{2-}]$ were calculated from alkalinity and pH using co2sys [*Lewis and Wallace*, 2006] using the same parameters as *Evans et al.* [2014]. Both measured and adjusted Mg/Ca used for the coupled-calibration (see text) are shown.

				seawater					foraminifera	
Experiment	n	Temp.	Mg/Ca	alkalinity	$[CO_3^{2-}]$	Ω	pH	$^{135}Ba/^{138}Ba$	Mg/Ca	Mg/Ca adj.
Variable Mg/Ca_{sw}, constant temperature										
DE3-6-26	12	26.3	6.25	2211.0	240.5	5.70	8.0	1.60±0.02	6.80±0.20	4.77
DE3-5-26	8	26.3	5.19	2263.6	207.5	4.92	8.0	1.83±0.02	6.37±1.05	4.47
DE3-4-26	22	26.3	4.15	2298.6	210.9	5.00	8.0	0.98±0.04	5.38±0.32	3.77
DE3-3-26	15	26.3	3.25	2352.3	216.0	5.12	8.0	0.63±0.07	4.38±0.25	3.07
DE3-2-26	19	26.3	2.17	2477.0	228.0	5.41	8.0	0.52±0.06	3.03±0.14	2.12
Variable temperature, constant Mg/Ca_{sw}										
DE4-3-30	2	30.3	3.40	2532.4	307.0	7.33	8.2	1.72±0.07	4.55±1.00	-
DE4-3-27.5	4	27.8	3.40	2532.4	288.5	6.86	8.2	1.72±0.07	3.84±0.35	-
DE4-3-25	27	25.3	3.40	2412.7	352.6	8.35	8.2	1.71±0.07	3.12±0.18	-
DE4-3-22.5	6	22.8	3.40	2412.7	332.5	7.85	8.2	1.71± 0.06	2.53±0.08	-
DE4-3-20	5	20.3	3.40	2412.7	312.6	7.36	8.2	1.71±0.06	2.23±0.14	-

3.4, temperature = 26°C) is offset; experiment DE3-3-26 has mean Mg/Ca = 4.45±0.25 mmol mol^{-1}, whereas the Mg/Ca-temperature calibration at Mg/Ca_{sw} = 3.4 has predicted Mg/Ca at 26°C of 3.35 mmol mol^{-1}. This offset is most easily explained by the 0.2 pH unit difference between the cultures, given that all other conditions were equal and both experiments were made up of a large number of foraminifera. This offset (32.6%) is remarkably similar to the pH-Mg/Ca variation observed by [*Kisakürek et al.*, 2008]. The linear best fit of their pH-Mg/Ca calibration has m = -7.62 which is equivalent to Mg/Ca 33.4% higher at pH = 8 compared to 8.2. Furthermore, our Mg/Ca datapoint from the experiment with modern Mg/Ca_{sw} (DE3-5-26) is offset by approximately the same magnitude (42.6% per 0.2 pH) compared to the datapoint of *Kisakürek et al.* [2008] at pH = 8.3. The consistency of this offset between these experiments, conducted in seawater with different chemistry, means that we can apply this as a constant offset to our data with a high degree of confidence. Therefore, in order to produce a coupled calibration at modern pH, we multiply all data from experiment DE3 by 1/1.426, shown in the final column of table DR1.

4.2 Mg/Ca_{test}-Mg/Ca_{sw} regression form

Previous studies have argued that a power regression most appropriately describes the variation of Mg/Ca_{test} with Mg/Ca_{sw} [*Ries*, 2004; *Hasiuk and Lohmann*, 2010; *Evans and Müller*, 2012]. However, we present this relationship as a quadratic regression forced through the origin, because the linear D_{Mg}-Mg/Ca_{sw} relationship (main text figure 1B) implies this [see also *Evans et al.*, 2014]. This does not affect the conclusions of [*Evans and Müller*, 2012], as the shape of this relationship is similar to a power curve (with 0>H>1) in that it is offset to higher Mg/Ca_{test} at a given Mg/Ca_{sw} over the range 0-5.2 mol mol^{-1}.

4.3 Defining the calibration surface

Defining the surface that describes how Mg/Ca_{test}, Mg/Ca_{sw} and temperature covary in 3D requires some assumption about the form that this relationship should take. Traditionally it has been assumed that the sensitivity of the Mg/Ca-temperature relationship does not change with Mg/Ca_{sw}. However, our calibrations demonstrate that this is not the case (see the main text), and we immediately discount the possibility that only the pre-exponential constant of a Mg/Ca-temperature calibration varies with Mg/Ca_{sw}. Before further discussion of the most appropriate general form for a coupled calibration, we first discount the other most obvious possibility; that the pre-exponential constant remains invariant and the exponential constant varies in some way with changing Mg/Ca_{sw}.

The modelled variation of Mg/Ca_{test}-Mg/Ca_{sw} and Mg/Ca_{test}-temperature at two different Mg/Ca_{sw} ratios (the three calibrations for *G. ruber* now available) are shown in figure DR3 in comparison to the respective empirical calibrations, for a range of possible regression forms between the exponential coefficient and Mg/Ca_{sw} (linear, power, exponential, quadratic). For example, the constant pre-exponential coefficient, linearly variable exponential coefficient model was constructed as such:

$$Mg/Ca_{test} = B \times exp^{(a_1 \times Mg/Ca_{sw} + b_1) \times T} \tag{4.1}$$

Where $A = a_1 \times Mg/Ca_{sw} + b_1$.

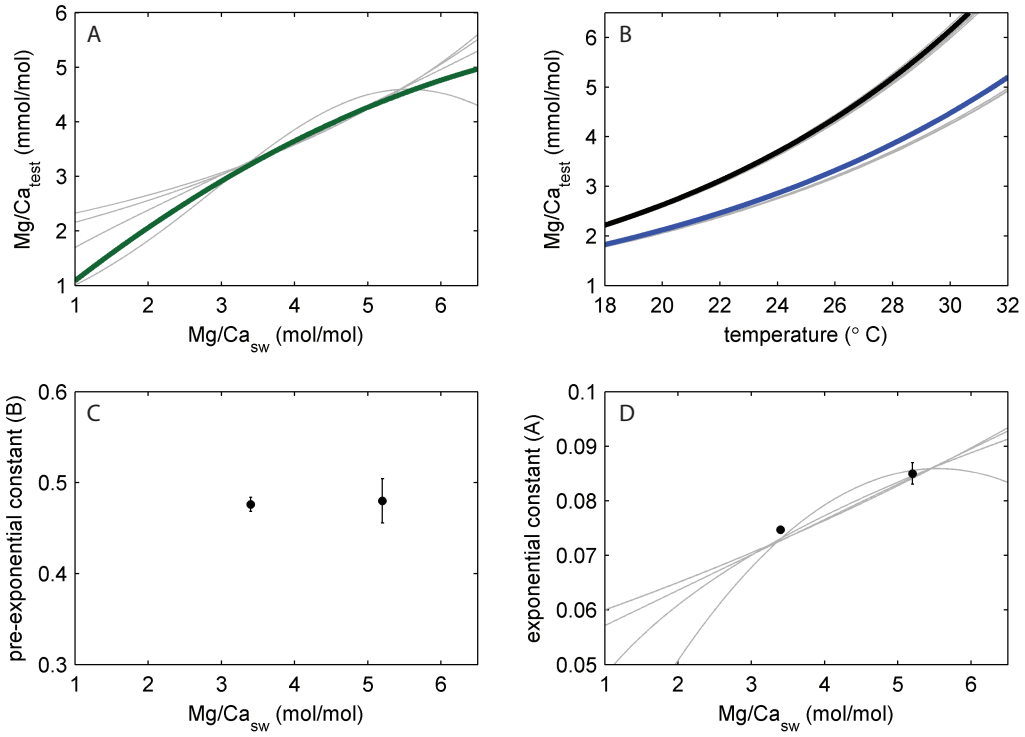

Figure DR3: Modelled Mg/Ca_{test}-Mg/Ca_{sw}-temperature relationships (grey lines) compared to those empirically determined (coloured lines represent the empirical calibration regressions from the main text). The pre-exponential coefficient was held constant with Mg/Ca_{sw}.

No relationship between the exponential coefficient (A) and Mg/Ca_{sw} is capable of accurately reproducing all of the empirical calibration features. In particular, it is not possible to reproduce the nonlinear Mg/Ca_{sw}-Mg/Ca_{test} relationship (figure DR3) with a linear, power, exponential or quadratic regression between A and Mg/Ca_{sw} if the pre-exponential constant is held constant. A model of this form generally produces convex-downwards Mg/Ca_{sw}-Mg/Ca_{test} relationships.

Although more complex functions may be written that would allow better calibration-model matching with a constant pre-exponential coefficient, it is more parsimonious to assume some variation in both coefficients. Figure DR4 shows 25 different models encompassing all possible combinations of linear, power, exponential and quadratic relationship for both coefficients. Red lines designate models which do not deviate from the empirical calibrations by more than 0.1 mmol mol^{-1} on average, whereas grey lines are those that do. In order to produce a 3D relationship between Mg/Ca_{test}-Mg/Ca_{sw}-temperature (main text figure 1), we chose the only model that most accurately fits all three calibrations, as well maintaining the observed Mg/Ca-temperature sensitivity decrease and the minimal variation in the pre-exponential coefficient that we observe (figure DR4C). This model assumes quadratic variation in both coefficients with Mg/Ca_{sw} such that:

$$B = 0.019 \times Mg/Ca_{sw}{}^{2} - 0.16 \times Mg/Ca_{sw} + 0.804 \tag{4.2}$$

And:

$$A = -0.0029 \times Mg/Ca_{sw}{}^{2} + 0.032 \times Mg/Ca_{sw} \tag{4.3}$$

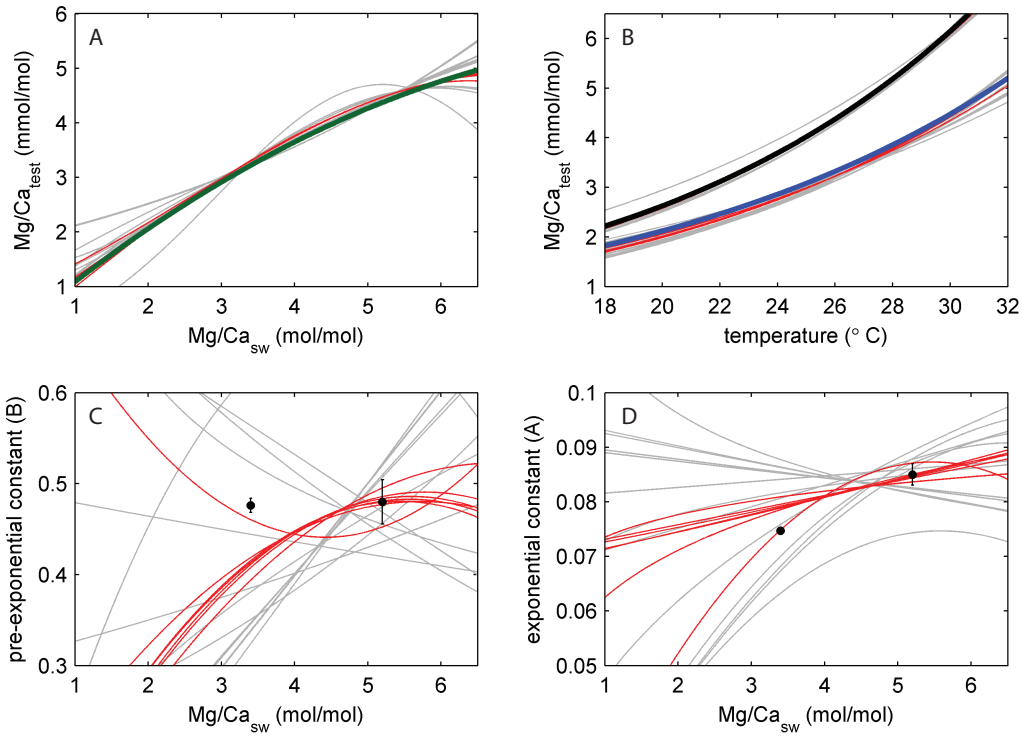

Figure DR4: Modelled Mg/Ca_{test}-Mg/Ca_{sw}-temperature relationships (red and grey lines) compared to those empirically determined (coloured lines represent the empirical calibration regressions from the main text). Both coefficients were allowed to vary with Mg/Ca_{sw}.

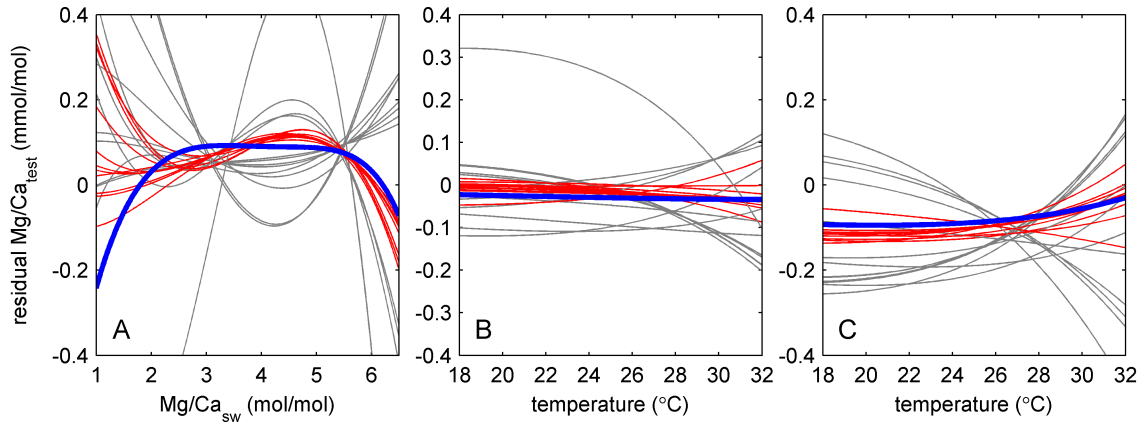

Figure DR5: Residuals between the modelled relationship between Mg/Ca_{test}-Mg/Ca_{sw}-temperature and the empirical calibrations. Residual model-calibration offset for (A) the Mg/Ca_{sw}-Mg/Ca_{test} calibration, (B) the Mg/Ca_{test}-temperature calibration in modern seawater [*Kisakürek et al.*, 2008], and (C) the Mg/Ca_{test}-temperature calibration at Mg/Ca_{sw} = 3.4. Red and grey lines are defined as in figure DR4, blue lines show the chosen 'double-quadratic' model.

As before, more complex models could be used that would describe that data equally well over the range that the dependent variables were investigated. However, our chosen 'double quadratic' model is the simplest way of producing a good model-data fit. It exactly matches the observed Mg/Ca-temperature sensitivity decrease at lower Mg/Ca_{sw}, and maintains the pre-exponential constant between 0.45-0.5 over the range Mg/Ca_{sw} = 2-6 mol mol^{-1}, as observed.

The residuals between our double quadratic model (equations 4.2 and 4.3) and the empirical calibrations are shown in figure DR5. The model chosen to represent the calibration surface presented in the main text (blue line) is that which shows the least trend in residuals from the temperature calibration, and the only model to show no significant trend in residuals from our Mg/Ca_{sw}-Mg/Ca_{test} calibration. Outside of the range that this latter relationship was calibrated the model becomes substantially worse (as do all others). However, over the range that Mg/Ca_{sw} is thought to have varied over the Cenozoic [e.g. *Coggon et al.*, 2010; *Horita et al.*, 2002] the model is accurate to within ±0.2 mmol mol^{-1}, smaller than the error in our Mg/Ca measurements.

5 Fossil data treatment

The following dissolution and foraminifera Mg/Ca species-offset corrections were applied prior to dataset smoothing and Mg/Ca_{sw} calculation.

5.1 Species offset correction

In order to apply our coupled calibration based on *G. ruber* laboratory cultures to fossil *G. sacculifer* data, we used the offset between a laboratory Mg/Ca-temperature calibration of the two species; *Nürnberg et al.* [1996] and *Kisakürek et al.* [2008]. We use laboratory cultures to calculate this offset because unlike sediment trap or core top calibrations, these studies are unambiguously unbiased by dissolution or diagenesis. In line with previous studies [e.g. *Anand*

et al., 2003], we use an exponential coefficient of 0.09 for both species in modern seawater. Based on this assumption *G. ruber* and *G. sacculifer* have pre-exponential constants of 0.43 and 0.39 respectively which equates to a temperature-independent offset of 10.3%, in line with that suggested by previous work [*Dekens et al.*, 2002].

Data from both species exists for ODP site 999 (Caribbean Sea) at high resolution between ~3.4-2.2 Ma, enabling the accuracy of this correction through time and for foraminifera growing in seawater with potentially variable Mg/Ca to be assessed (figure DR6). LOESS-smoothed curves of this portion of the dataset show high coherence, demonstrating that this correction appropriately deals with secular Mg/Ca trends through time. Because our Mg/Ca_{sw} record indicates that this ratio was lower than present over this time interval, this also demonstrates that this correction is independent of both temperature and Mg/Ca_{sw}.

5.2 Dissolution correction

A dissolution correction is necessary to counter the effects of the preferential loss of relatively high-Mg portions of the foraminifera test when exposed to seawater with $\Delta[CO_3^{2-}]$ <21 μmol kg^{-1}. See *Dekens et al.* [2002]; *Regenberg et al.* [2014]; *Fehrenbacher and Martin* [2014] for further details.

We considered two options for dissolution correction of the Mg/Ca data. Correcting the data in these different ways before back-calculating Mg/Ca_{sw} as we describe produces subtly different reconstructions, although the specific correction applied does not signficantly affect the reconstructed magnitude or timing of Pliocene-Recent Mg/Ca_{sw} shifts.

Method 1: Proxy matching over the last 400 ka. The Mg/Ca_{sw} reconstruction we present in the main text is produced by matching the Mg/Ca data to the biomarker temperatures

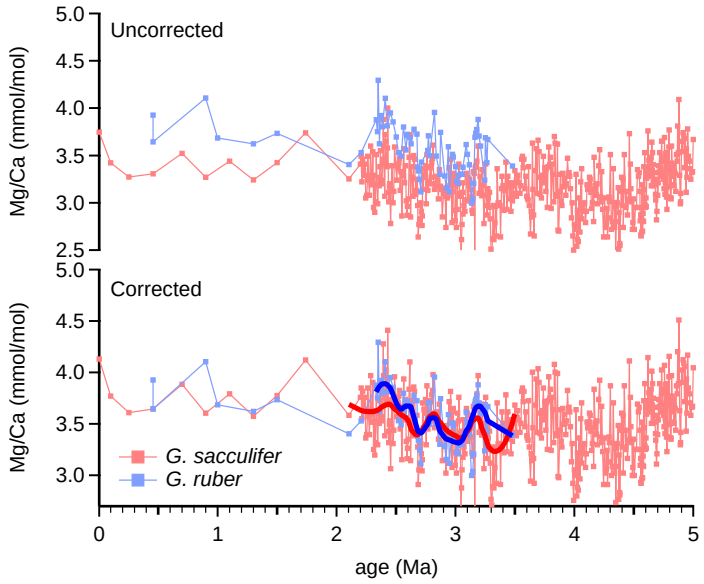

Figure DR6: Comparison of Mg/Ca data from ODP site 999 following species offset correction. Both uncorrected (top) and corrected (bottom) data are shown. The highly coherent LOESS-smoothed Mg/Ca trends strongly imply that the magnitude of this correction is constant through time and at non-modern seawater chemistry.

over the past 400 ka (i.e. without a dissolution correction *per se*). This method implicitly assumes that the offset between Mg/Ca and biomarker derived temperatures over the last four glacial cycles (when invariant Mg/Ca_{sw} can be assumed) is the combined result of seasonal differences in the proxies and Mg/Ca dissolution, where the latter is likely to exert a far larger effect given minimal seasonality at most of the sites included in this study. The advantage of this approach is that it requires no assumption regarding the relationship between core depth or core site carbonate chemistry and dissolution, as opposed to previously suggested dissolution corrections [*Dekens et al.*, 2002; *Regenberg et al.*, 2006] which may be inaccurate outside of the region in which they were defined. The global dissolution assessment of *Regenberg et al.* [2014] provides an alternate method of addressing this issue. However we do not apply this correction here because it is not clear how fossil Mg/Ca is most appropriately transformed using a Mg/Ca-$\Delta[CO_3^{2-}]$ slope and a $\Delta[CO_3^{2-}]$ value for the core site depth in the region of interest.

Method 2: Depth-specific Mg/Ca-temperature calibrations. Here, a dissolution correction was applied using the ocean and depth-specific equations of *Dekens et al.* [2002]. These take the form:

$$Mg/Ca = B \exp^{0.09(T - a_1 d - a_2)} \tag{5.1}$$

Where B is species specific, a_1 and a_2 are constants and d is core depth in km. In order to apply a dissolution correction to the raw fossil Mg/Ca data from these equations we separate out a correction factor by multiplying out the exponential component:

$$Mg/Ca = B \exp^{0.09T} \exp^{-0.09(a_1 d + a_2)} \tag{5.2}$$

So that:

$$Mg/Ca_{corr.} = \frac{Mg/Ca_{meas.}}{\exp^{-0.09(a_1 d + a_2)}} \tag{5.3}$$

Fehrenbacher and Martin [2014] show preferential loss of Mg from high-Mg bands in *G. ruber* which implies that any dissolution correction should be multiplicative and not additive. Both of the two corrections we tested conform to this. A comparison of the two correction techniques is shown in figure DR7, demonstrating that our Mg/Ca_{sw} is insensitive to the exact correction applied. The similarity of the two methods essentially demonstrates that correcting the raw Mg/Ca data to the mean biomarker temperature for the last 400 ka (method 1) is a good site-specific approximation method for the degree of Mg/Ca dissolution. We prefer the first method because it does not require us to apply the Pacific calibrations of *Dekens et al.* [2002] to the South China Sea, given that *Regenberg et al.* [2014] show that dissolution is controlled by regional variation in bottom water $\Delta[CO_3^{2-}]$. *Rosenthal and Lohmann* [2002] describe an alternative approach to Mg/Ca dissolution correction using shell weight. However, we do not utilise this method because shell weight data are not available for all published Mg/Ca records, and *Marshall et al.* [2013] show that shell density is also controlled by surface water $[CO_3^{2-}]$.

We cannot rule out a systematic error that may result from a bias in all records. For example, a globally lower deep ocean $\Delta[CO_3^{2-}]$ during the Pliocene would impact the robustness of the dissolution correction that we apply. This correction is essentially based on the assumption that bottom water $\Delta[CO_3^{2-}]$ has not changed significantly at any individual site over the last 5 Ma. All other studies reporting dissolution-corrected Mg/Ca data also make this assumption.

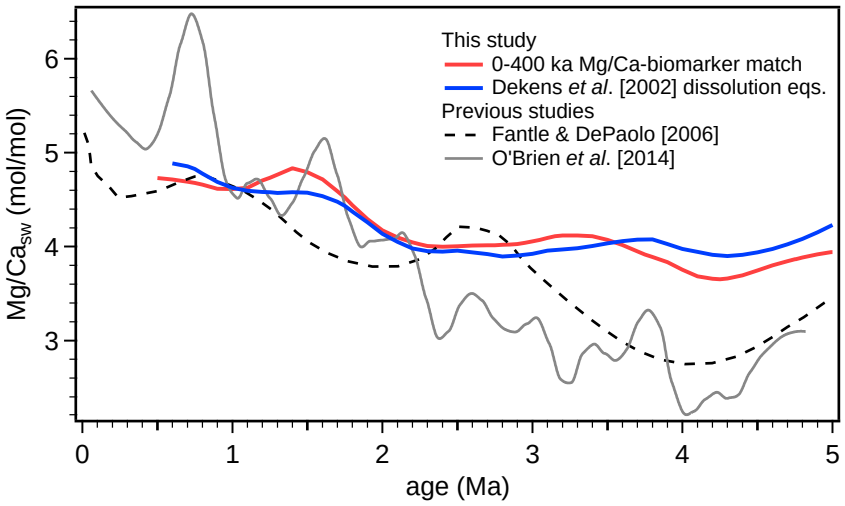

Figure DR7: The sensitivity of our Mg/Ca_{sw} reconstruction to the Mg/Ca-dissolution correction applied. Red line (method one) is based on correcting the Mg/Ca data at each site so that the mean Mg/Ca and biomarker temperatures are equivalent over the past 400 ka. Blue line (method two) is derived from Mg/Ca data corrected according to the basin-specific equations of *Dekens et al.* [2002].

However, on a global scale, variable Pliocene-Recent deep ocean $[CO_3^{2-}]$ may not be a significant complication, as the principal control on dissolution ($\Delta[CO_3^{2-}]$; *Regenberg et al.* [2014]) could have remained broadly constant over this time. A lower Pliocene Mg/Ca_{sw} essentially implies a higher [Ca], given the long (∼14 Ma) residence time of Mg in the ocean [*Li*, 1982]. Therefore, a given saturation state is associated with a lower $[CO_3^{2-}]$, so that $\Delta[CO_3^{2-}]$ may be approximately maintained despite potentially lower Pliocene deep ocean DIC.

6 Site-specific Mg/Ca_{sw} calculation

The Mg/Ca_{sw} curves presented in the main text are derived by combining reconstructions from the individual sites. Site-specific reconstructions, i.e. Mg/Ca_{sw} calculated by comparing Mg/Ca and biomarker temperatures at any given site, are shown in figure DR8.

Those derived from ODP1143 and ODP806 are in excellent agreement throughout the last 5 Ma, both in terms of the finer detail in these records as well as the absolute magnitude of Pliocene-Recent Mg/Ca_{sw} rise. The ODP999 record is broadly in good agreement with these. The most likely explanation for the apparent offset between this and the other records between ∼0.5-1.5 Ma is the poor temporal resolution of both the alkenone and Mg/Ca datasets at ODP999 between 0-2 Ma. The agreement between the Mg/Ca_{sw} record from these three sites in distinct basins strongly supports the hypothesis that the offset between the biomarker and Mg/Ca proxies over this interval is primarily the result of seawater chemistry change.

In contrast to these three sites, the biomarker and Mg/Ca data from ODP847 show little proxy disagreement over the past 5 Ma [*Dekens et al.*, 2008, see the main text], and consequently the Mg/Ca_{sw} record calculated from these datasets is in poor agreement with that from other sites (figure DR8), although there is still an overall trend to lower Mg/Ca_{sw} ratios in the Pliocene. Our preferred Mg/Ca_{sw} reconstruction does not exclude this dataset because there is

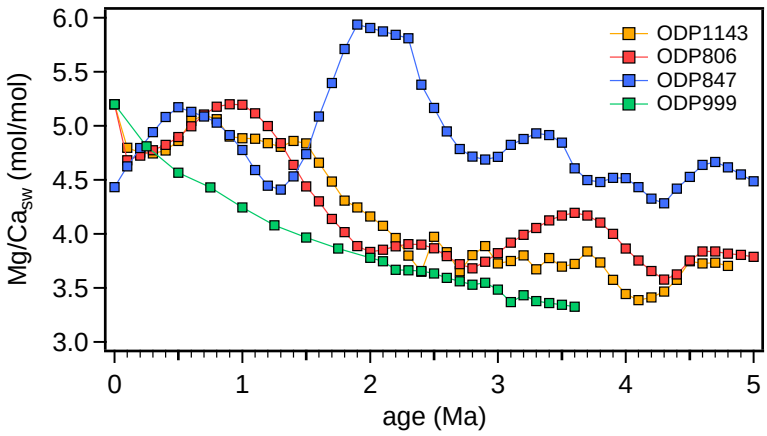

Figure DR8: Site-specific back-calculated Mg/Ca$_{sw}$.

no clear reason for doing so. However, we also present a Mg/Ca$_{sw}$ record that excludes ODP847 as reconstructions derived from the other sites are in agreement to within ±0.5 mol mol^{-1}, and because it may be the case that other factors in the Eastern Equatorial Pacific bias this reconstruction. Specifically, it is this site which exhibits the highest present-day inter-annual SST variability and it may therefore be the case that this Mg/Ca$_{sw}$ reconstruction is affected by changes in the seasonal and inter-annual bias of these proxies through time.

7 Variable Mg/Ca-temperature sensitivity implications

Our finding that the sensitivity of the Mg/Ca-temperature relationship varies with Mg/Ca$_{sw}$ has implications for the reconstruction of the magnitude of relative temperature changes though time, as well as latitudinal and zonal gradients within a given timeslice. We specifically examine the implications that this has for the equatorial Pacific zonal gradient, which has been the subject of much recent debate [e.g. *Zhang et al.*, 2014; *O'Brien et al.*, 2014; *Wara et al.*, 2005].

Based on our coupled calibration, a Pliocene Mg/Ca$_{sw}$ ratio of 4.1 mol mol^{-1} would result in a minor reduction of the exponential constant of the Mg/Ca-temperature calibration to 0.0825 (see main text). The generic implications of this for temperature gradient reconstruction during the Pliocene is shown in figure DR9.

Because the reduction in Mg/Ca-sensitivity compared to present day is small during the Pliocene, this complication is only moderately important when comparing tropical Mg/Ca data with that from mid-high latitudes. Specifically, the inter-site temperature gradient error that would result from assuming modern day Mg/Ca-temperature sensitivity in the Pliocene is only greater than 0.3°C if there is a >1 mmol mol^{-1} difference in measured Mg/Ca$_{test}$ between the two sites. Therefore this factor cannot resolve discrepancies in model-data zonal temperature gradients.

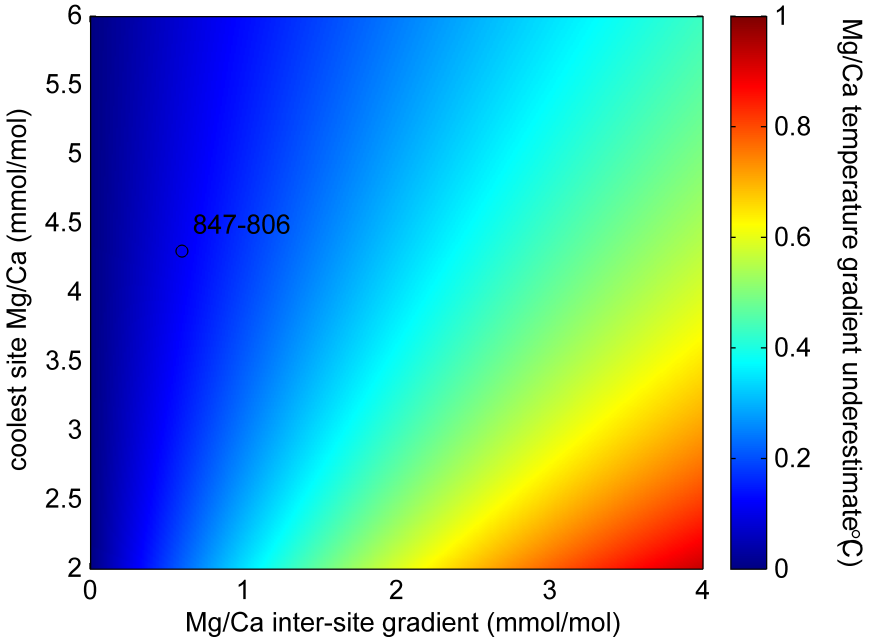

Figure DR9: Error in Pliocene Mg/Ca-derived zonal and latitudinal temperature gradients resulting from the assumption that the sensitivity of this thermometer is invariant with Mg/Ca_{sw}. There is only a minor reduction in sensitivity in the Pliocene with the implication that this potential complication cannot resolve model-data discrepancies in the tropics. However, not accounting for this may lead to a minor to moderate underestimate in latitudinal gradients (0.2-0.6°C) when comparing the tropics and high latitudes.

8 Further considerations

8.1 pH

There is evidence that pH exerts a control on Mg/Ca [*Russell et al.*, 2004; *Kisakürek et al.*, 2008], which we also observe in our cultures (section 4.1). Because there is evidence that pCO_2 during the Pliocene Warm Period was higher than pre-industrial [e.g. *Pagani et al.*, 2009], resulting in a lower surface ocean pH, Mg/Ca derived temperatures may be systematically biased. Specifically, a lower late-Pliocene pH would result in higher Mg/Ca ratios and therefore the Mg/Ca-biomarker discrepancy would be underestimated. *Seki et al.* [2010] report late-Pliocene *G. ruber* δ^{11}B-derived pH estimates 0.05-0.1 units lower than today. Assuming that the Mg/Ca-pH relationship is essentially linear over this range, then a pH change of this magnitude would bias Mg/Ca ratios by 11-21%. Using the Mg/Ca-pH sensitivity derived in section 4.1, this equates to a potential 1.4-2.7°C temperature underestimate. We do not apply a correction here because a *G. ruber*-derived pH record is lacking before 3.5 Ma. However, our Mg/Ca_{sw} record should be viewed with the caveat that the Mg/Ca data are not corrected for potential pH changes. It is therefore possible that we overestimate Pliocene Mg/Ca_{sw}, although this overestimate would be on the order of ~0.5 mol mol^{-1}.

8.2 Mg/Ca bias from high-Mg overgrowths

It has been shown that Mn-Mg-rich overgrowths such as kutnahorite may bias fossil Mg/Ca measurements [*Pena et al.*, 2005]. Whilst this is an important consideration for some samples, it is demonstrably not the case that foraminifera Mg/Ca is substantially biased by such overgrowths at any of the sites that we utilise. Potential diagenesis of this nature at ODP site 847 and 806 is discussed in detail by *Wara et al.* [2005], and sites 1143 and 999 are discussed in a similar fashion by *O'Brien et al.* [2014]. As alluded to by *Wara et al.* [2005], the fact that dissolution corrected Mg/Ca-derived temperatures (i.e. using the calibrations of *Dekens et al.* [2002]) agree well with TEX_{86} and alkenones during the Pleistocene at these sites indicates that significant bias resulting from Mn-Mg-carbonate overgrowths is unlikely.

8.3 Mg/Ca_{test}-Mg/Ca_{sw} relationship calculation in benthic foraminifera

Evans and Müller [2012] describe in detail how the relationship between Mg/Ca_{test} and Mg/Ca_{sw} may be indirectly calculated in deep benthic foraminifera that are difficult to culture. We update this calculation to reflect new information regarding Eocene Mg/Ca_{sw} [*Evans et al.*, 2013], and without the 'CCD-correction' suggested by *Cramer et al.* [2011]. We assume a power relationship between Mg/Ca_{test}-Mg/Ca_{sw} which gives H = 0.51, where $Mg/Ca_{test} = F \times Mg/Ca_{sw}{}^{H}$.

The error in previously reported Pliocene-Recent benthic Mg/Ca-derived temperatures (main text figure 3) is based on coupling this *O. umbonatus* Mg/Ca_{sw}-Mg/Ca_{test} relationship to the temperature calibration of *Sosdian and Rosenthal* [2009]. We use the Mg/Ca-temperature sensitivity of this study (0.15 mmol mol^{-1} $°C^{-1}$) despite criticism that it is a two-point calibration [*Yu and Broecker*, 2010]. This is because the site to which this calibration was originally applied (DSDP607), and to which the authors argue that it is applicable [*Sosdian and Rosenthal*, 2010], is the only location for which a continuous deep ocean coupled Mg/Ca-$\delta^{18}O$ record is available as far back as the PWP. The magnitude of this systematic temperature bias for a given measured Mg/Ca_{test} ratio is similar if other benthic foraminifera Mg/Ca-temperature calibrations were to be used [*Bryan and Marchitto*, 2008; *Curry and Marchitto*, 2008]. We implicitly make the assumption that all deep benthic foraminifera are characterised by the same Mg/Ca_{test}-Mg/Ca_{sw} relationship.

9 References

Anand, P., H. Elderfield, and M. Conte (2003), Calibration of Mg/Ca thermometry in planktonic foraminifera from a sediment trap time series, *Paleoceanography*, *18*(2), 28–31.

Bryan, S., and T. Marchitto (2008), Mg/Ca–temperature proxy in benthic foraminifera: New calibrations from the Florida Straits and a hypothesis regarding Mg/Li, *Paleoceanography*, *23*(2), PA2220, doi:10.1029/2007PA001553.

Coggon, R., D. Teagle, C. Smith-Duque, J. Alt, and M. Cooper (2010), Reconstructing past seawater Mg/Ca and Sr/Ca from mid-ocean ridge flank calcium carbonate veins, *Science*, *327*, 1114–1117.

Cramer, B., K. Miller, P. Barrett, and J. Wright (2011), Late Cretaceous–Neogene trends in deep ocean temperature and continental ice volume: Reconciling records of benthic foraminiferal geochemistry (δ^{18}O and Mg/Ca) with sea level history, *Journal of Geophysical Research*, *116*(C12), doi:doi:10.1029/2011JC007255, 2.

Curry, W. B., and T. M. Marchitto (2008), A secondary ionization mass spectrometry calibration of *Cibicidoides pachyderma* Mg/Ca with temperature, *Geochemistry, Geophysics, Geosystems*, *9*(4).

Dekens, P. S., D. W. Lea, D. K. Pak, and H. J. Spero (2002), Core top calibration of Mg/Ca in tropical foraminifera: Refining paleotemperature estimation, *Geochemistry, Geophysics, Geosystems*, *3*(4), 1–29.

Dekens, P. S., A. C. Ravelo, M. D. McCarthy, and C. A. Edwards (2008), A 5 million year comparison of Mg/Ca and alkenone paleothermometers, *Geochemistry, Geophysics, Geosystems*, *9*(10).

Evans, D., and W. Müller (2012), Deep time foraminifera Mg/Ca paleothermometry: Nonlinear correction for secular change in seawater Mg/Ca, *Paleoceanography*, *PA4205*, doi: 10.1029/2012PA002315.

Evans, D., W. Müller, S. Oron, and W. Renema (2013), Eocene seasonality and seawater alkaline earth reconstruction using shallow-dwelling large benthic foraminifera, *Earth and Planetary Science Letters*, *381*, 104–115, doi:10.1016/j.epsl.2013.08.035.

Evans, D., J. Erez, S. Oron, and W. Müller (2014), Mg/Ca-temperature and seawater-test chemistry relationships in the shallow-dwelling large benthic foraminifer *Operculina ammonoides*, *Geochimica et Cosmochimica Acta*, in press.

Fehrenbacher, J. S., and P. A. Martin (2014), Exploring the dissolution effect on the intrashell Mg/Ca variability of the planktic foraminifer *Globigerinoides ruber*, *Paleoceanography*.

Hasiuk, F., and K. Lohmann (2010), Application of calcite Mg partitioning functions to the reconstruction of paleocean Mg/Ca, *Geochimica et Cosmochimica Acta*, *74*(23), 6751–6763.

Hönisch, B., K. Allen, A. Russell, S. Eggins, J. Bijma, H. Spero, D. Lea, and J. Yu (2011), Planktic foraminifers as recorders of seawater Ba/Ca, *Marine Micropaleontology*, *79*(1), 52–57.

Horita, J., H. Zimmermann, and H. Holland (2002), Chemical evolution of seawater during the Phanerozoic: Implications from the record of marine evaporites, *Geochimica et Cosmochimica Acta*, *66*(21), 3733–3756.

Kisakürek, B., A. Eisenhauer, F. Bohm, D. Garbe-Schönberg, and J. Erez (2008), Controls on shell Mg/Ca and Sr/Ca in cultured planktonic foraminiferan, *Globigerinoides ruber* (white), *Earth and Planetary Science Letters*, *273*(3-4), 260–269.

Lewis, E., and D. Wallace (2006), Program developed for CO_2 system calculations, *ORNL/CDIAC-105. Carbon Dioxide Information Analysis Center, Oak Ridge National Laboratory, US Department of Energy, Oak Ridge, Tennessee.*

Li, Y.-H. (1982), A brief discussion on the mean oceanic residence time of elements, *Geochimica et Cosmochimica Acta*, *46*(12), 2671–2675.

Marshall, B. J., R. C. Thunell, M. J. Henehan, Y. Astor, and K. E. Wejnert (2013), Planktonic foraminiferal area density as a proxy for carbonate ion concentration: A calibration study

using the Cariaco Basin ocean time series, *Paleoceanography*, *28*(2), 363–376.

Nürnberg, D., J. Bijma, and C. Hemleben (1996), Assessing the reliability of magnesium in foraminiferal calcite as a proxy for water mass temperatures, *Geochimica et Cosmochimica Acta*, *60*(5), 803–814.

O'Brien, C. L., G. L. Foster, M. A. Martínez-Botí, R. Abell, J. W. Rae, and R. D. Pancost (2014), High sea surface temperatures in tropical warm pools during the Pliocene, *Nature Geoscience*, *7*(8), 606–611.

Pagani, M., Z. Liu, J. LaRiviere, and A. C. Ravelo (2009), High Earth-system climate sensitivity determined from Pliocene carbon dioxide concentrations, *Nature Geoscience*, *3*(1), 27–30.

Pena, L. D., E. Calvo, I. Cacho, S. Eggins, and C. Pelejero (2005), Identification and removal of Mn-Mg-rich contaminant phases on foraminiferal tests: Implications for Mg/Ca past temperature reconstructions, *Geochem. Geophys. Geosyst*, *6*, doi:10.1029/2005GC000930.

Regenberg, M., D. Nürnberg, S. Steph, J. Groeneveld, D. Garbe-Schönberg, R. Tiedemann, and W.-C. Dullo (2006), Assessing the effect of dissolution on planktonic foraminiferal Mg/Ca ratios: Evidence from Caribbean core tops, *Geochemistry, Geophysics, Geosystems*, *7*(7).

Regenberg, M., A. Regenberg, D. Garbe-Schönberg, and D. W. Lea (2014), Global dissolution effects on planktonic foraminiferal Mg/Ca ratios controlled by the calcite-saturation state of bottom waters, *Paleoceanography*, *29*(3), 127–142.

Ries, J. (2004), Effect of ambient Mg/Ca ratio on Mg fractionation in calcareous marine invertebrates: A record of the oceanic Mg/Ca ratio over the Phanerozoic, *Geology*, *32*(11), 981–984.

Rosenthal, Y., and G. P. Lohmann (2002), Accurate estimation of sea surface temperatures using dissolution-corrected calibrations for Mg/Ca paleothermometry, *Paleoceanography*, *17*(3).

Russell, A., B. Hönisch, H. Spero, and D. Lea (2004), Effects of seawater carbonate ion concentration and temperature on shell U, Mg, and Sr in cultured planktonic foraminifera, *Geochimica et cosmochimica acta*, *68*(21), 4347–4361.

Segev, E., and J. Erez (2006), Effect of Mg/Ca ratio in seawater on shell composition in shallow benthic foraminifera, *Geochemistry, Geophysics, Geosystems*, *7*(2), doi: 10.1029/2005GC000969.

Seki, O., G. L. Foster, D. N. Schmidt, A. Mackensen, K. Kawamura, and R. D. Pancost (2010), Alkenone and boron-based Pliocene pCO_2 records, *Earth and Planetary Science Letters*, *292*(1), 201–211.

Sosdian, S., and Y. Rosenthal (2009), Deep-sea temperature and ice volume changes across the Pliocene-Pleistocene climate transitions, *Science*, *325*(5938), 306–310.

Sosdian, S., and Y. Rosenthal (2010), Response to comment on "Deep-sea temperature and ice volume changes across the Pliocene-Pleistocene climate transitions", *Science*, *328*(5985), 1480–1480.

Wara, M. W., A. C. Ravelo, and M. L. Delaney (2005), Permanent El Niño-like conditions during the Pliocene warm period, *Science*, *309*(5735), 758–761.

Yu, J., and W. Broecker (2010), Comment on deep-sea temperature and ice volume changes across the pliocene-pleistocene climate transitions, *Science*, *328*(5985), 1480.

Zhang, Y. G., M. Pagani, and Z. Liu (2014), A 12-million-year temperature history of the

tropical Pacific Ocean, *science*, *344*(6179), 84–87.

Critical evaluation

8.1 Research synthesis

Along with chapter 2 which examines the broad state of 193 nm laser ablation data quality, *Evans and Müller* [2013] and the methodology sections of *Evans et al.* [2013, 2015, Submitted] develop this technique for foraminiera. Whilst the benefits of performing LA-ICPMS analysis of these organisms have been realised for more than a decade [*Reichart et al.*, 2003; *Eggins et al.*, 2003; *Creech et al.*, 2010], these new contributions represent an advance in (1) trace element mapping of complex, discontinuous samples, and (2) unambiguous identification of calcite precipitated in culture using both Ba concentration and isotopic labelling. This issue has previously been overcome using mass-balance corrections for the existing material, when samples were analysed by solution ICPMS [e.g. *Kisakürek et al.*, 2008; *Henehan et al.*, 2013], or by assuming that the calcite of the last few chambers was precipitated in culture [e.g. *Wit et al.*, 2013]. As demonstrated in *Evans et al.* [Submitted], a ^{135}Ba spike is a relatively inexpensive way of labelling large volumes of seawater. This technique may have particular utility for planktic foraminifera cultures which are typically short term due to the longevity of most planktic species. The linear test-seawater Ba/Ca relationship for planktic species [*Hönisch et al.*, 2011] means that both seawater [Ba] and ^{135}Ba/^{138}Ba are easily implemented.

At the time of publication, the (mainly) theoretical assertions of *Evans and Müller* [2012] were based on the likelihood that foraminifera were characterised by strongly nonlinear test-seawater Mg/Ca relationships by analogy to other marine calcifiers [*Ries*, 2004] and the limited data that was available at the time [*Delaney et al.*, 1985; *Segev and Erez*, 2006; *Raitzsch et al.*, 2010]. The papers and manuscripts presented here confirm that this is the case for both planktic and shallow-dwelling large benthic foraminifera, immediately lending confidence to the implications laid out in *Evans and Müller* [2012] for Paleogene Mg/Ca_{sw}. By extension, the indirectly calculated seawater-test Mg/Ca relationship for the deep benthic foraminifera *Oridorsalis umbonatus* can be viewed with increased confidence, which has implications for the accuracy of deep ocean Mg/Ca-derived temperature reconstruction and coupled Mg/Ca-δ^{18}O derived sea level reconstruction [*Evans et al.*, Submitted].

Taking an independent approach, *Evans et al.* [2013, 2015] provide new evidence that Paleogene Mg/Ca_{sw} was indeed in the region of 2.0-2.5 mol mol^{-1}. Although previously indicated by other proxies [*Horita et al.*, 2002; *Dickson*, 2004; *Coggon et al.*, 2010], this finding was disputed by some workers on grounds of feasibility [*Broecker and Yu*, 2011], or the impossibility of producing

realistic Paleogene foraminifera Mg/Ca-derived SST using Mg/Ca_{sw} ratios this low [*Dutton et al.*, 2005]. As argued, this is now known to be a result of an incorrect assumption regarding test-seawater Mg/Ca [*Evans and Müller*, 2012]. Furthermore, the *G. ruber* cultures of *Evans et al.* [Submitted] provide additional evidence for a large recent change in Mg/Ca_{sw}, adding to previous records implying or arguing for a rapid Miocene-Recent rise in this ratio [*Fantle and DePaolo*, 2006; *Rausch et al.*, 2013]. Analogously to the Paleogene, this accurate new record has implications for both surface and deep ocean Mg/Ca-derived Pliocene palaeotemperatures.

The remaining detailed implications of the fossil and cultured LBF trace element data for Paleogene palaeoceanography and the biomineralisation mechanism of the nummulitid foraminifera are discussed in detail in *Evans et al.* [2013, 2015] and do not directly relate to, or have implication for, the data presented in the remainder of the thesis with the exception of the discussion below, although both studies serve to highlight how LBF are an underutilised source of palaeoceanic information.

Given that a sufficiently accurate and precise Mg/Ca_{sw} record does not exist, precluding direct palaeocean temperature reconstruction using the nummulitids at present, the following discussion is based on the requirement for an independent temperature proxy. In order to overcome this a preliminary clumped isotope dataset and trace element analysis of several exceptionally preserved *Nummulites* samples was produced, in collaboration with Dr. Martin Ziegler (ETH, Zürich). This dataset enables a more confident discussion of tropical SST in a high-CO_2 world. Moreover, it facilitates more accurate Mg/Ca_{sw} reconstruction using LBF, as it removes the need to assume a range of palaeotemperatures [cf. *Evans et al.*, 2013].

8.2 Extending the *Nummulites* trace element record

The papers and chapters presented here confirm that trace elements in large benthic foraminifera are valuable palaeoceanic tools, with utility as seasonal and mean annual temperature archives and recorders of seawater chemistry [*Evans et al.*, 2013, 2015]. In order to extend the reconstructions of *Evans et al.* [2013], a low-resolution record of seawater chemistry and tropical sea surface temperatures (SST) for the Paleogene was produced using exceptionally preserved specimens from a number of fossil sites. Fossil localities not already mentioned in *Evans et al.* [2013] are shown in figure 8.1. These localities span the early Eocene to the early Oligocene and are globally distributed:

- Two samples were collected from the UK Hampshire Basin. *N. prestwichianus* from the Bartonian Barton Beds at Alum Bay on the Isle of Wight, and *N. laevigatus* from the Lutetian

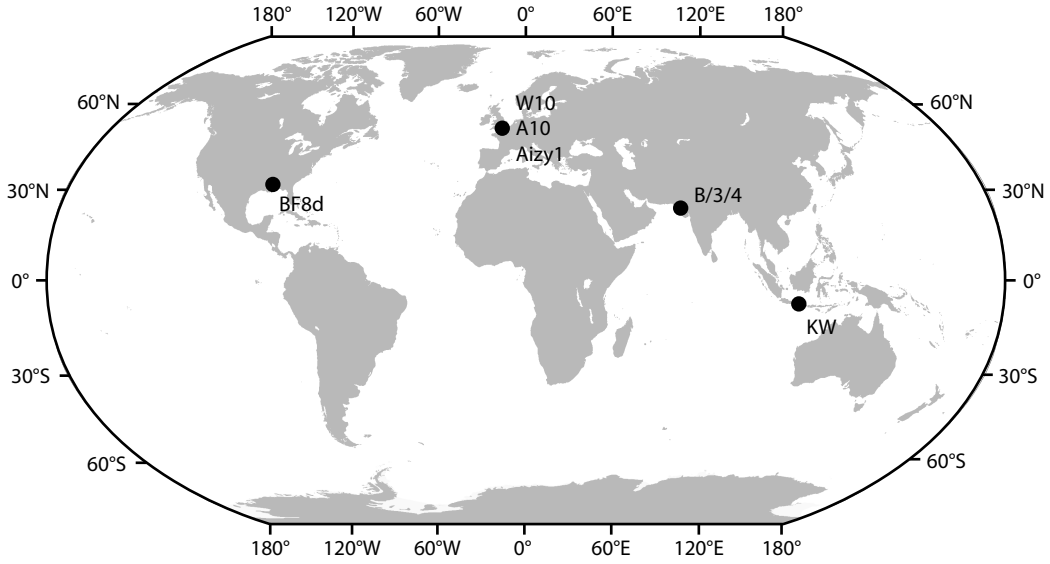

Figure 8.1: Location of the additional fossil sites. See table 1 for details. Samples with prefix KW (Nanggulan) are discussed in *Evans et al.* [2013].

Bracklesham Formation exposed at Whitecliff Bay, Isle of Wight, UK.

- One sample (*Nummulites* sp.) from the Ypresian of the Paris Basin (collected by Dr. Jonathan Todd, Natural History Museum, UK).
- One sample (*Nummulites* sp.) from Kutch, India. Biostratigraphically dated to ∼56 Ma and may be of PETM age (collected by Dr. Pratul Saraswati, Indian Institue of Technology, Bombay).
- One sample (*Nummulites* sp.) from the early Oligocene strata of Mississippi (collected by Dr. Willem Renema, Naturalis, The Netherlands).

Table 1: Sample details and selected laser-ablation trace element data of further exceptionally preserved *Nummulites*. See *Evans et al.* [2013, 2015] for details of analytical methodology.

Sample details					Geochemistry (mmol/mol)			
Sample location	Stratigraphic unit	Sample prefix	Age (Ma)	n	Mg/Ca	Al/Ca	Mn/Ca	Sr/Ca
Whitecliff Bay, Isle of Wight, UK	Bracklesham Group	W10	43.5	3	78.5±6.4	0.02±NaN	0.39±0.16	2.14±0.11
Alum Bay, Isle of Wight, UK	Barton Clay Fm.	A10	40	1	61.5	-	0.13	1.85
Paris Basin, France	-	Aizy1	52.5	3	74.2±9.0	0.10±0.12	0.17±0.12	1.95±0.01
Kutch, India	-	B/3/4	56	6	99.2±3.9	0.15±0.31	1.68±0.63	1.96±0.18
Mississippi, US	-	BF8d	30.3	7	74.2±7.5	0.09±0.50	0.32±0.31	2.01±0.12

All specimens were analysed by LA-ICPMS for trace elements as previously described [*Evans et al.*, 2013], geochemistry and sample ages are given in table 1. All samples are characterised by low Al/Ca, demonstrating that cleaning (ultrasonication in acetone, methanol and deionised water) removed any significant clay mineral contamination; these ratios are within the range observed in live-collected *Operculina* [*Evans et al.*, 2013]. Mn/Ca ratios are comparable to specimens from Nanggulan, and whilst elevated above that of modern specimens, these values do not suggest Mn-Mg overgrowths pervasive enough to significantly bias Mg/Ca data. Of all the samples, those from Kutch are the least well preserved, although these do appear glassy under optical microscopy. It is difficult to assess to what extent such overgrowths may bias Mg-derived palaeoceanic recontruction without knowing the Mg/Mn ratio of the contaminant phase. Assuming a worst case scenario (Mg/Mn = 1, far higher than observed by *Pena et al.* [2005]), even the Mn/Ca ratios of the Kutch specimens would result in a $<$5% Mg/Ca bias.

Similarly to *N. djokdjokartae* from Nanggulan, all samples are characterised by Mg/Ca $\sim$50% of Recent-collected *Operculina*. To a first-order approximation, this indicates lower Mg/Ca_{sw} throughout the Paleogene, given that tropical temperatures are unlikely to have been substantially lower than present during this epoch. Sr/Ca ratios of *Nummulites* from the sites listed in table 1 are slightly lower but similar to those from Nanggulan. Using a D_{Sr}-Mg/Ca_{test} slope for *O. ammonoides* of 7.8×10^{-4} [*Evans et al.*, 2015], 0.07-0.20 mmol mol^{-1} of this offset can be explained by the broadly lower Mg/Ca ratios of these specimens.

Because trace element incorporation in this family of LBF is far more sensitive to seawater chemistry than temperature, these simple observations indicate that both the Mg/Ca and Sr/Ca ratio of seawater was relatively invariant throughout the Paleogene. It follows that the concentration of these alkali earth metals was also approximately invariant, given that they have widely different residence times and concentrations [*Li*, 1982]. The implications of this are discussed further in section 8.4, following the introduction and presentation of the clumped isotope dataset.

8.3 Clumped isotope analysis of fossil *Nummulites*

8.3.1 Introduction to clumped isotopes

The clumped isotope thermometer is based on the propensity for heavy isotopes to preferentially bond to each other, in order to form multiply-substituted isotopologues (molecules containing more than one heavy isotope, such as $^{13}C^{18}O^{16}O$) [*Eiler*, 2007; *Ghosh et al.*, 2006; *Eiler*, 2011]. A substitution of heavy isotopes into molecules containing one other heavy isotope occurs because the

bonding energy is reduced, i.e. there is a lower zero point (vibrational) energy for bonds between two heavy isotopes than between a heavy and light isotope or two light isotopes [*Eiler*, 2007]. Because there is an enthalpy change associated with the substitution of one or more heavy isotopes, there is a temperature-dependent distribution coefficient associated with exchange reactions such as $^{13}C^{16}O^{16}O \rightleftharpoons {}^{13}C^{18}O^{16}O$ [*Tripati et al.*, 2010; *Eiler*, 2007].

The fundamental advance offered by this technique is that it is the deviation of the distribution of doubly-substituted heavy isotopes from random, and not the absolute abundance of any isotopologue that relates to the distribution coefficient of this substitution. Therefore, clumped isotope palaeothermometry offers the possibility of temperature reconstruction from (e.g.) carbonate geochemistry *independent* of the isotopic composition of the solution from which precipitation took place [e.g. *Ghosh et al.*, 2006]. Furthermore, there is little or no biological control on the degree of clumping [*Tripati et al.*, 2010], which means that for many organisms species or group-specific calibrations are unnecessary (figure 8.2). Furthermore, inorganic calibrations, or those derived from broadly similar organisms may be applicable to extinct fossil groups (for example, in the case of belemnites [*Bernasconi et al.*, 2011]). However, not all carbonate precipitates lie on the same calibration line, therefore the style of calcite precipitation must be considered when interpreting clumped isotope data of carbonates for which a calibration is not available or cannot be produced. Specifically, Δ_{47} data of calcite precipitated under disequilibrium conditions – such as many speleothems – whereby precipitation may be associated with rapid CO_2 degassing from drip

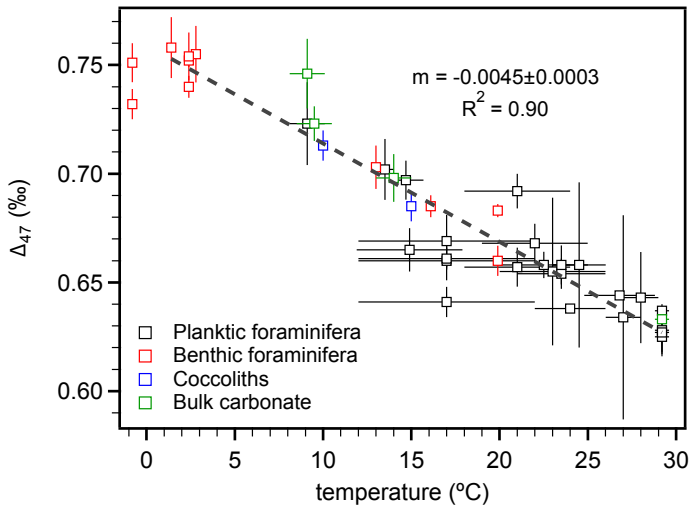

Figure 8.2: Calibration of the clumped isotope thermometer in marine calcifiers. Data from *Tripati et al.* [2010]. Eight species of planktic foraminifera, five species of benthic foraminifera and two coccolithophores lie on the same calibration line. The relatively large scatter in the planktic foraminifera data is most easily explained by the uncertainty in the calcification temperature of these samples. See *Eiler* [2007] for the definition of Δ_{47}.

water, cannot be easily interpreted in terms of temperature [*Daëron et al.*, 2011; *Affek and Zaarur*, 2014]. Similarly, bivalves may modify the chemistry of their internal seawater pool too quickly for equilibrium to be established between dissolved carbonate species, and are offset from the calibration line defined by other marine calcifiers and inorganic calcite [*Henkes et al.*, 2013]. Irrespective of this, foraminifera do not deviate significantly from the line defined by inorganic calcite [*Tripati et al.*, 2010; *Eiler*, 2011], implying that they precipitate calcite in equilibrium with the vacuolised seawater. Growth rates for planktic foraminifera are not significantly different from that of the LBF *O. ammonoides*. This large benthic species is characterised by a rate of $\sim$2-6 μg day^{-1} in laboratory cultures [*Evans et al.*, 2015], whereas planktic foraminifera growth rate calculated from the cultures of *Evans et al.* [Submitted], assuming the cross sectional area can be related to shell weight [following *Henehan et al.*, 2013], is 0.3-3.2 μg day^{-1}. Therefore, there is no reason to suspect that large benthic foraminifera precipitate calcite in disequilibrium with the calcifying fluid, and data derived from these organisms should not deviate from the calibration line defined by planktic foraminifera and inorganic calcite, although this currently remains untested.

8.3.2 Eocene tropical palaeotemperatures

Clumped isotope temperatures of the majority of the samples listed in table 1 are shown in table 2. With the exception of the sample from Kutch, India, which is possibly of Paleocene-Eocene Thermal Maximum (PETM) age, the (sub)tropical localities are characterised by temperatures similar to present day. The extent to which these palaeotemperatures are representative of SST depends on the habitat and mixed layer depth during the life of the foraminifera. *Evans et al.* [2013] showed that *O. ammonoides* mineralise throughout winter in the Red Sea, with a seasonal minimum temperature of 20-21°C. Therefore by analogy, it seems unlikely that the Paleogene low-mid latitudes were seasonally cool enough for discontinuous calcification of these *Nummulites*. If this assumption is correct, data are likely not substantially biased away from being representative of mean annual

Table 2: Preliminary clumped isotope temperatures of Paleogene *Nummulites*. Analysis performed by Dr. Martin Ziegler, ETH Zürich [see *Meckler et al.*, 2014].

Sample location	Sample prefix	Age (Ma)	Δ_{47} temp. (°C)	1SE	replicates
Nanggulan, Java	KW	39	26.0	1.6	24
Whitecliff Bay, Isle of Wight, UK	W10	43.5	21.6	2.3	12
Paris Basin, France	Aizy1	53.5	21.5	1.5	29
Kutch, India	B/3/4	56	38.5	2.2	13
Mississippi, US	BF8d	30.3	26.0	2.6	9

averages, even if low-latitude seasonality was greater in a high-CO_2 world compared to present [*Evans et al.*, 2013]. Nontheless, Recent *Operculina* have a peak abundance at 20-40 m and may live at depths of up to $\sim$100 m [*Renema*, 2008; *Reiss and Hottinger*, 1984]. Shallow benthic temperatures may be 1-2°C lower than surface temperatures over this depth range, although it should be considered that a similar offset may also apply to 'surface-dwelling' planktic foraminifera which are also found at depths of up to 50 m (in the case of *G. ruber*). Conversely, deriving sea surface temperatures from the planktic foraminifera test with the most negative δ^{18}O [*Pearson et al.*, 2001, 2007; *Aze et al.*, 2014], results in SST that relate to transient seasonal maxima (i.e. the warmest season in the $\sim 10^2$-10^4 years presumably covered by a single core interval).

Because the relationship between test-seawater Mg/Ca and temperature is now known in detail for the one group of LBF [*Evans et al.*, 2015], nummulitid Mg/Ca data may be used as a temperature proxy if an independent Mg/Ca_{sw} reconstruction is available from a different technique [*Evans and Müller*, 2012]. However, there is no proxy dataset spanning the Paleogene at sufficient resolution; geochemical models are the only source of continuous Mg/Ca_{sw} data. Palaeotemperatures derived from the Mg/Ca data shown in table 1 using the geochemical model of [*Stanley and Hardie*, 1998] are in the range of 32-52°C, with the exception of samples from Kutch, which are unrealistically high ($>$70°C). Because the nummulitids suffer from little secondary bias on Mg/Ca (e.g. from salinity [*Evans et al.*, 2013]), unlike planktic foraminifera [*Kisakürek et al.*, 2008], this result implicitly suggests that Paleogene Mg/Ca_{sw} was higher than this model indicates. However, the data also show that the model of *Stanley and Hardie* [1998] is substantially more accurate than that of *Wilkinson and Algeo* [1989] over this time period, which would imply temperatures $<5°$, as previously argued based on deep benthic foraminifera data [*Evans and Müller*, 2012]. A more detailed analysis of the implications of this dataset for seawater chemistry are given in section 8.4.

Given that inaccuracies or gaps in current Mg/Ca_{sw} records currently preclude the use of Mg/Ca in the nummulitids for palaeotemperature reconstruction, the following discussion of Eocene (sub) tropical SSTs are based only on the clumped isotope temperatures from table 2 and previously published datasets (see figure 8.3 caption for references). This compilation of Paleogene SST is given in figure 8.3, in the context of both modern mean annual temperature (MAT) and seasonal range, and data from two GCM models of Eocene climate. The models suggest latitudinal temperature gradients similar to present day, and are essentially characterised by a global warming of the oceans of the order of 5-10°C. In contrast, the majority of the proxy data indicate tropical SST within the range of present, albeit with a mean shift to values 1-2°C above present day (figure 8.3) potentially im-

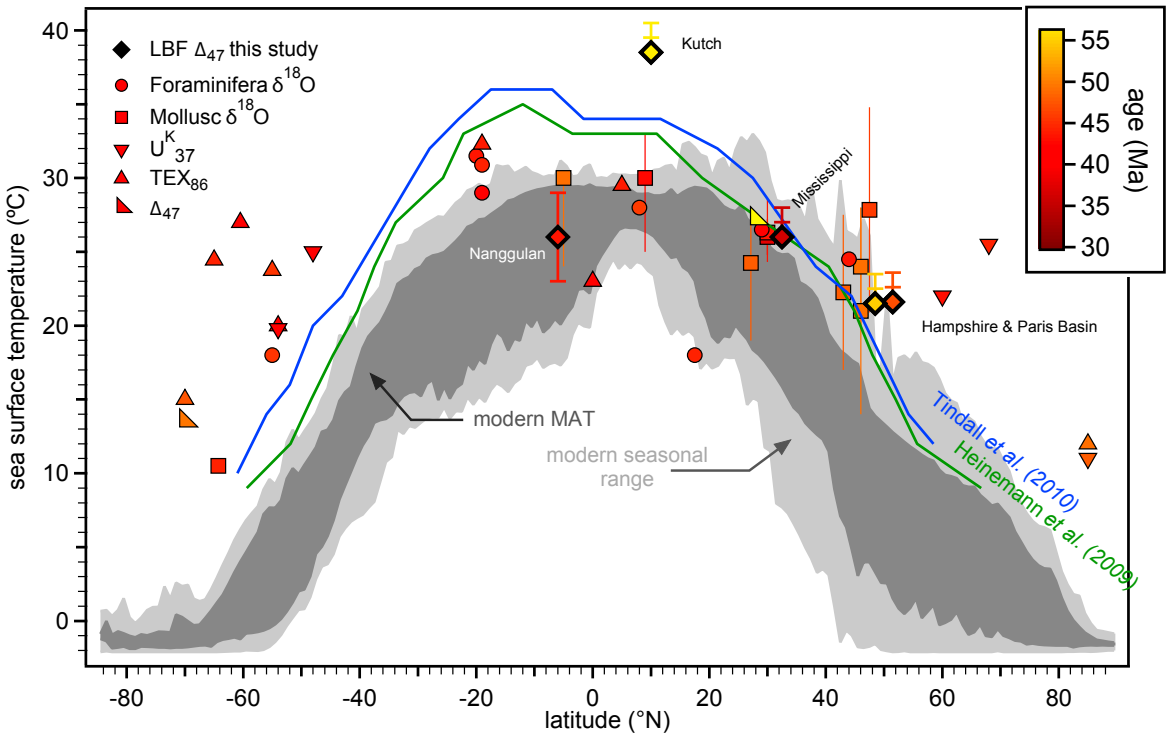

Figure 8.3: Compilation of Paleogene SST reconstruction, grouped by proxy and shown with colour as a function of age. The output from two GCMs [*Tindall et al.*, 2010; *Heinemann et al.*, 2009] are shown for comparison. LBF clumped isotope data (this study) are labelled. LBF error bars show 1 and 2°C above the datapoint to illustrate possible temperature underestimate due to calcification at 20-100 m water depth, with the exception of that from Nanggulan, which shows the seasonality estimate of *Evans et al.* [2013]. All mollusc δ^{18}O data are shown with estimates of seasonality. All δ^{18}O data are associated with large and variable errors resulting from assumptions regarding $\delta^{18}O_{sw}$. TEX_{86} data have not been updated according to the Bayesian calibration of *Tierney and Tingley* [2014]. Data from multiple sources [*Andreasson and Schmitz*, 1996, 1998, 2000; *Bijl et al.*, 2009; *Burgess et al.*, 2008; *Creech et al.*, 2010; *Douglas et al.*, 2014; *Dutton et al.*, 2002; *Ivany et al.*, 2004; *Keating-Bitonti et al.*, 2011; *Kobashi et al.*, 2004; *Liu et al.*, 2009; *Pearson et al.*, 2001, 2007; *Purton and Brasier*, 1997; *Sangiorgi et al.*, 2008; *Tripati and Zachos*, 2002; *Weller and Stein*, 2008, and references therein].

plying the warmest part of the Paleogene oceans have not been sampled. It has been argued that this broad model-data mismatch is a result of inaccurate proxy data [*Huber*, 2008], given that there is possible evidence that Eocene continental interiors were far higher than modern [*Head et al.*, 2009]. Exceptionally preserved planktic foraminifera δ^{18}O data and tropical TEX_{86} measurements of bulk sediment have been invoked as examples of more robust SST reconstruction [*Huber and Caballero*, 2011; *Huber*, 2008]. However, accurate calibration of GDGT-derived indices to temperature is non-trivial [*Kim et al.*, 2008, 2010; *Liu et al.*, 2009], for example the extent to which it makes sense to apply a spatially-varying calibration model [*Tierney and Tingley*, 2014] to a world substantially different from that in which the calibration is defined may be questioned. The relationship between single specimen foraminifera δ^{18}O and MAT has already been discussed. Considering the

Tanzania data to be seasonal maxima brings these SST into agreement with the rest of the tropical data and moreover, the tropical and sub-tropical clumped isotope data presented here and of *Keating-Bitonti et al.* [2011] support the hypothesis that the Eocene tropics were no more than a few degrees warmer than present.

At least some of the apparent data-model discrepancy shown in figure 8.3 may result from the comparison of globally-distributed proxy datasets with central Pacific model output. Nonetheless, the difference in model-data latitudinal temperature gradient is clear, and although the models and data agree that the mid-high latitudes were substantially warmer than at present, there is also a large discrepancy in the reconstructed magnitude of this warming, particularly in the southern hemisphere. Improved Eocene boundary conditions, such as more precise atmospheric CO_2 reconstructions, will undoubtedly produce more comparable model output [*Lunt et al.*, 2012], although (e.g) increased pCO_2 broadly acts in the models to raise SST globally [e.g. *Huber and Caballero*, 2011]. The reason for this fundamental disagreement continues to evade explanation, although proxy data showing cooler tropics and warmer high latitudes in comparison to model output immediately points to the efficiency of surface heat transfer away from the tropics as a source of model inaccuracy. Given that changes in ocean circulation are not thought to be able to transfer this heat to the high latitudes fast enough, other processes such as the quantity and intensity of tropical storms, both of which are thought to increase at higher pCO_2, may provide an explanation [*Korty et al.*, 2008]. Both model and independent sedimentological evidence indicates that this was the case [*Schmitz and Pujalte*, 2007], and the increasing evidence for higher SST seasonality in the Eocene [*Brassell*, 2014] has also been suggested to result from tropical storms [*Evans et al.*, 2013]. However, it may be that tropical hurricane parameterisation in models underestimates either of these two factors, or that the models do not capture the efficiency with which parameterised storms transfer heat to the mid-high latitude surface ocean.

The clumped isotope data point from Kutch, which may be of PETM age, indicates that tropical ocean temperatures at this time may have been substantially warmer than at any other point during the early-mid Eocene. Whilst it is conceivable that this sample suffers from diagenesis, given the elevated Al/Ca and Mn/Ca ratios (see table 1), the higher clumped isotope temperature is in good agreement with the higher Mg/Ca ratio. This further suggests that significant diagenetic recrystallisation is unlikely, whereby the clumped isotope data could represent burial temperature, as in the diagenetic cements analysed by *Douglas et al.* [2014], as high-Mg calcite undergoes rapid Mg loss during recrystallisation [e.g. *Budd and Hiatt*, 1993]. Assuming no significant seawater chemistry

change between 56-54 Ma, i.e. that the samples from Kutch and the Paris Basin mineralised in seawater with the same [Mg] and [Ca], the 25 mmol mol^{-1} difference in Mg/Ca_{test} equates to a 17.3°C temperature offset between the two samples. This is identical to the difference in clumped isotope temperature (table 2), suggesting that both datasets are robust. Sub-tropical PETM temperatures of this magnitude have also been reported based on planktic foraminifera $\delta^{18}O$ [*Aze et al.*, 2014]. Whilst tropical temperatures may remain within a few degrees of present at substantially elevated pCO_2 (figure 8.3), the clumped isotope data presented here may add to the growing evidence for significant warming of tropical SST associated with rapid, transient carbon release [*Zachos et al.*, 2003; *Aze et al.*, 2014]. Such warming appears to occur even in the context of a background climate state characterised by mean global temperatures far higher than at present.

8.3.3 Sensitivity of tropical SST to pCO_2

The asymmetrical distribution of tropical SST at present (peak cumulative frequency at $\sim$29°C and no MAT $>$31°C) has been used as evidence for the existence of a tropical thermostat, defined as one or more mechanisms that limit tropical SST below a certain threshold [*Pierrehumbert*, 1995; *Ramanathan and Collins*, 1991]. It was originally suggested that such a mechanism may be a negative feedback between incoming radiation and evaporation/cloud feedbacks [*Ramanathan and Collins*, 1991]. However, it is now thought that the entire asymmetric curve shifts to higher temperatures with increased pCO_2 [*Williams et al.*, 2009]; it appears that a thermostat mechanism of this nature cannot explain the 'warm, not hot' [*Keating-Bitonti et al.*, 2011] proxy Paleogene tropical SST reconstructions (figure 8.3). The extent of the rise of modelled tropical SST with increasing pCO_2 is shown in figure 8.4, with both Pliocene and Eocene data overlain. Pliocene data are taken from the four tropical sites for which both a biomarker and Mg/Ca dataset are available [see *Evans et al.*, Submitted, and references therein], Eocene data are those from figure 8.3. The warmest Pliocene data are within error of the model SST-pCO_2 line; there is fairly good agreement that during the warmest part of the Pliocene, the tropical oceans were up to 1-2°C warmer than at present. As discussed above, there is a larger discrepancy in the Eocene which may be interpreted in two ways: (1) The model SST-pCO_2 slope is too high, particularly given that some models are characterised by even higher slopes (for example, at 6$\times$ pre-industrial CO_2, *Tindall et al.* [2010] reconstruct western Pacific warm pool tropical SST of 36-38°C). (2) Alternatively, pCO_2 reconstructions are broad overestimates in the Paleogene. If actual values were towards the lower end of the reconstructions, the data would imply an equally high tropical SST-CO_2 slope as the models. It should also be

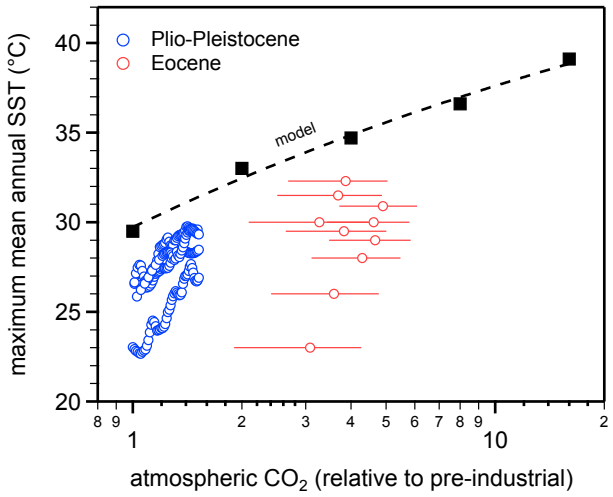

Figure 8.4: A comparison of model and proxy data examining the relationship between tropical SST and pCO_2. Pliocene error bars are not plotted for clarity, however these data are associated with pCO_2 errors of $\sim \pm 100$ ppm. Model tropical SST from *Williams et al.* [2009]. pCO_2 data are from *Pagani et al.* [2005] and *Pagani et al.* [2009]. No alkenone CO_2 record is available before 43 Ma, therefore mid-Eocene values are assumed for samples older than 43 Ma. PETM data were excluded as there are a large range of pCO_2 reconstructions for this brief interval.

considered that discontinuous spatial coverage of the proxy data means that the warmest part of the Eocene oceans have not necessarily been sampled. Conversely, the majority of the proxy data indicate tropical SST 1-2°C lower than the warmest reconstructions, especially for the Paleogene (figure 8.4). The mid-Eocene clumped isotope data point presented here (table 2) – including the first robust estimate of Eocene west Pacific Warm Pool (wPWP) temperature from Nanggulan, Java – indicates that unlike today, this region may not have been the warmest region of the Paleogene tropics.

In conclusion, both proxy and model data agree that increased atmospheric CO_2 results in tropical SST warming, as well as the widely accepted rise in mid-high latitude surface ocean temperatures [see also *Zhang et al.*, 2014]. A rise in tropical SST can therefore be expected through the next century as anthropogenic activity continues to raise atmospheric CO_2. Proxy data likely indicate tropical SST-pCO_2 slopes lower than models, although the two are within error of each other if the lower bounds of pCO_2 reconstructions are thought to be most representative of the Paleogene atmosphere. More precise pCO_2 reconstructions are clearly a prerequisite of solving this incongruity.

8.4 Cenozoic seawater chemistry: Synthesis

8.4.1 Mg/Ca

Precise and accurate reconstruction of seawater Mg/Ca is critical for quantitative trace element palaeothermometry and to constrain the processes controlling the cycling of these elements on geological timescales. Based on detailed calibrations of the relationship between temperature, Mg/Ca_{test} and Mg/Ca_{sw}, *Evans et al.* [Submitted] present a new high-resolution record for the last 5 Ma, whilst *Evans et al.* [2013] show how LBF may be used to reconstruct seawater chemistry deeper in geological time. The accuracy of this latter reconstruction can be improved using clumped isotope temperature data, because the previously assumed calcification temperature covered a broad range. Using the trace element and clumped isotope data presented here (tables 1, 2), this technique can be extended to samples spanning much of the Paleogene (figure 8.5). These new data are in excellent agreement with those derived from fluid inclusions [*Coggon et al.*, 2010; *Rausch et al.*, 2013] for the Paleogene, suggesting that Mg/Ca_{sw} remained between 2.0-2.5 mol mol^{-1} from the mid-Paleocene to at least the latest Oligocene.

The implications for the planktic foraminifera-derived Mg/Ca_{sw} record for Pliocene-Recent palaeothermometry and ice volume reconstruction are discussed in detail in *Evans et al.* [Submitted]. However, given these new Mg/Ca_{sw} reconstructions, the coupled Mg/Ca_{test}-Mg/Ca_{sw}-temperature

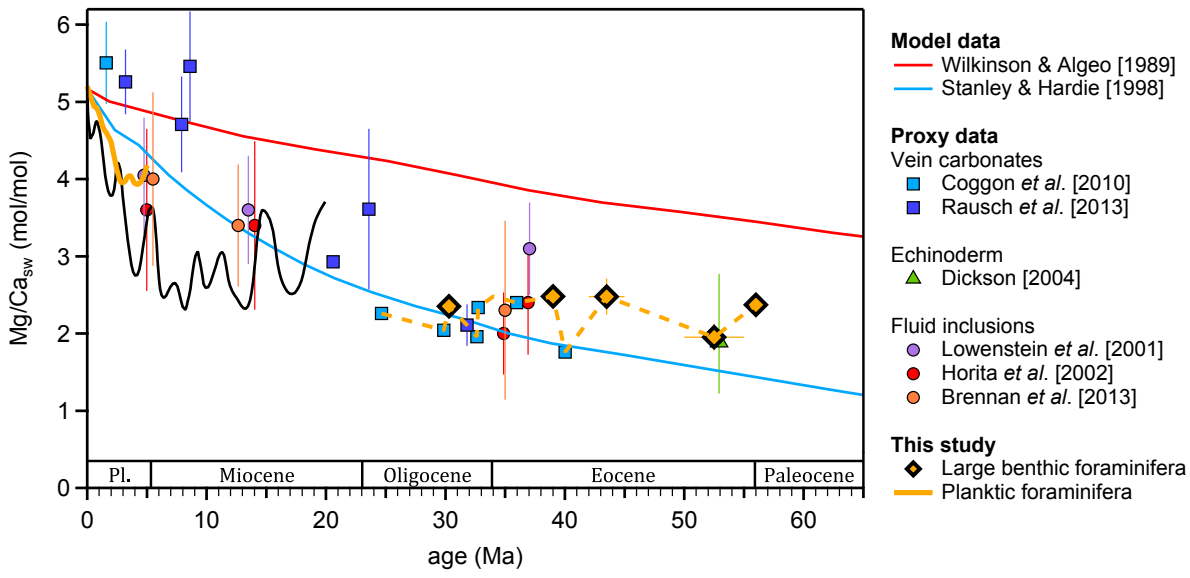

Figure 8.5: Compiled Cenozoic seawater Mg/Ca data, including data from this study [*Evans et al.*, 2013, Submitted]. Modified from *Evans and Müller* [2012]. The dashed yellow line is the combined record from LBF and ridge flank vein carbonates, which are characterised by similarly small errors for this period.

calibration for *G. ruber* from the same study may now be used to define a Mg/Ca_{test}-temperature sensitivity for the Paleogene for the first time. Equations 3 and 4 of *Evans et al.* [Submitted] define the calibration:

$$Mg/Ca_{test} = 0.54 \exp^{0.057T}$$

For an average Paleogene Mg/Ca_{sw} of 2.25 mol mol^{-1}. This implies a significant reduction in the sensitivity of this palaeothermometer during this period, and directly suggests that the magnitude of relative temperature shifts may have been underestimated. Assuming that planktic foraminifera Mg/Ca_{test} is equally sensitive to ocean [Mg] and [Ca], i.e. that it is only the Mg/Ca_{sw} ratio and not the absolute concentration of these elements that exerts a control on test chemistry [*Segev and Erez*, 2006], the reconstructed temperature difference between two samples is 54% smaller using a exponential coefficient of 0.09 compared to 0.057. If planktic foraminifera Mg/Ca is unaffected by secularly-differential secondary controls on Mg incorporation (e.g. salinity, $[CO_3^{2-}]$ [*Kisakürek et al.*, 2008]) over such events, this would indicate that surface ocean warming during the PETM hyperthermal [e.g. *Zachos et al.*, 2003] has been previously underestimated.

Whilst large gaps remain in the record (figure 8.5), the small secular variation in Mg/Ca_{sw} during the Paleogene means that a ratio of 2.0-2.5 mol mol^{-1} appears applicable throughout, i.e. that large Mg/Ca_{sw} excursions are unlikely in the 3-4 Ma gaps that exist. Finally, the fact that LBF are far more sensitive to Mg/Ca_{sw} than temperature [*Evans et al.*, 2015] means that the clumped isotope temperature-derived error associated with these reconstructions translates into small errors when utilising planktic foraminifera. This is because planktic foraminifera are approximately equally sensitive to both Mg/Ca_{sw} and temperature [*Evans et al.*, Submitted], so that a 0.25 mol mol^{-1} Mg/Ca_{sw} error (from a 3°C LBF Δ_{47} error), translates to a planktic foraminifera temperature of just 1.3°C at an absolute calcification temperature of ∼26°C (Mg/Ca_{test} = ∼2.5 mmol mol^{-1}), and 0.7°C at ∼18°C.

It has been recently argued that the ridge flank vein carbonate Mg/Ca_{sw} reconstructions of *Coggon et al.* [2010] require revision [*Broecker and Yu*, 2011]. The revised reconstructions were suggested to be at odds with the timescales of the processes that control the cycling of these elements, i.e. *Broecker and Yu* [2011] argued that it is difficult to imagine the mechanism(s) that could result in a 3-5× rise in Mg/Ca_{sw} over the Cenozoic. A Mg/Ca_{sw} rise is likely to be the combined result of a rise in [Mg] and a fall in [Ca] [*Horita et al.*, 2002; *Brennan et al.*, 2013]. Calcium input sources are weathering, hydrothermal activity and dolomitisation, whilst the dominant sink is $CaCO_3$ precipitation. The predominant Mg source is from weathering, whilst hydrothermal activity and dolomitisation

are sinks. More recently it has been argued that the most significant part of this rise occurred over the last 30 Ma [*Rausch et al.*, 2013], which is in agreement with the reconstructions presented here (figure 8.5). The planktic foraminifera-derived reconstructions of *Evans et al.* [Submitted] and the pore fluid modelling of *Fantle and DePaolo* [2006] both suggest that a significant portion of this rise took place as recently as the last 5 Ma. Together, these data indicate that secular Mg/Ca_{sw} variation may be dominated by relatively rapid shifts on $<$10 Ma timescales, as well as the well-known long-period Phanerozoic oscillations [*Stanley and Hardie*, 1998]. Over the last 5 Ma, the long residence time of Mg ($\sim$14 Ma [*Li*, 1982]) means that most of this change must have been accommodated by a 20-25% lowering of ocean [Ca].

8.4.2 Sr/Ca

LBF-derived Sr/Ca_{sw} reconstructions, derived from the data in table 1 using the technique outlined in *Evans et al.* [2013] are given in figure 8.6. These new reconstructions are in broad agreement with those previously derived from deep benthic foraminifera [*Lear et al.*, 2003] and fall within the error estimates of the gastropod data of *Sosdian et al.* [2012]. Whilst the LBF data also suggest that Sr/Ca_{sw} was slightly higher in the Eocene [*Tripati et al.*, 2009], the data indicate that this was no more than $\sim$10% above modern, with late Paleocene values identical to present day. The data presented here, as well as published values based on well-preserved foraminifera and molluscs, provide strong evidence for Paleogene Sr/Ca_{sw} 0-20% higher than at present. Given that these

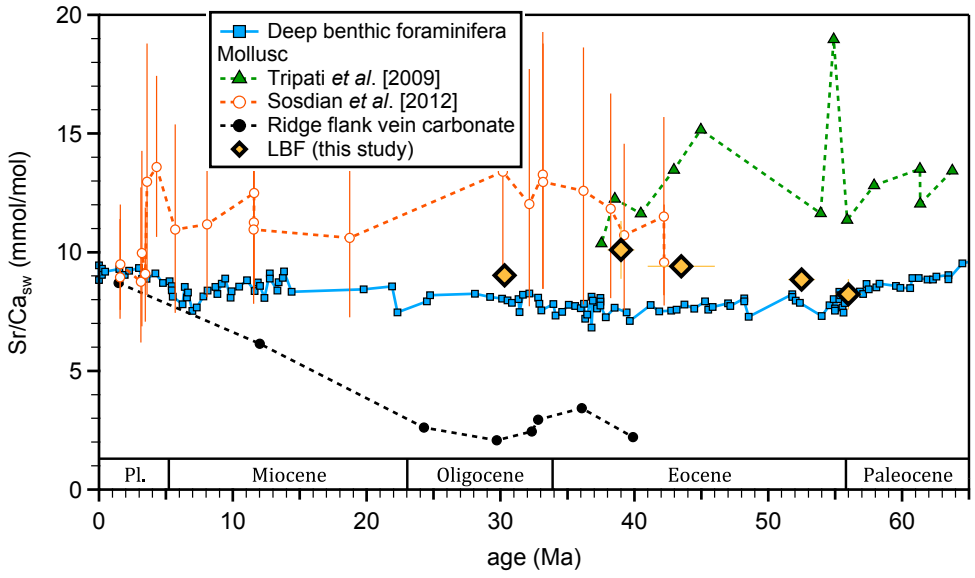

Figure 8.6: Compiled Cenozoic seawater Sr/Ca data, including data from this study. Previously published data from [*Coggon et al.*, 2010; *Lear et al.*, 2003; *Tripati et al.*, 2009; *Sosdian et al.*, 2012].

come from multiple, globally-distributed independent proxies, this indicates a problem with the ridge flank vein carbonate data of *Coggon et al.* [2010]. It is likely that these data are inaccurate as a result of uncertainties derived from the way in which the [Sr]-temperature slope should be extrapolated back to deep ocean values [see *Coggon et al.*, 2010, supplementary figure 2]. Leaving this reconstruction aside, all the datasets indicate that the Paleogene was a period of approximately constant Sr/Ca_{sw}, which is also the case for Mg/Ca.

The large difference between the residence times of Mg, Ca and Sr in the ocean means that this directly implies little change in the concentration of any of these elements between the early Paleocene and the latest Oligocene. For example, a hypothetical $2\times$ shift in [Mg] would necessarily have to be associated with an identical change in ocean [Ca] (in order to maintain a constant ratio as observed), and therefore [Sr] would also have to change by the same amount. This is implausible given the large differences in concentration and residence times of these elements. The broadly constant Paleocene-Eocene $^{87}Sr/^{86}Sr$ composition of marine carbonates supports this [*McArthur et al.*, 2001], implying no significant shift in global weathering over this interval.

Conclusion

- Foraminifera, like other marine organisms, are characterised by nonlinear seawater-test Mg/Ca relationships. The laboratory cultures presented here demonstrate that this is the case for both high-Mg benthic (*O. ammonoides*) and low-Mg planktic (*G. ruber*) species.
- Previous constraints on Paleogene Mg/Ca_{sw} derived from foraminifera are inaccurate as a result of the previously held assumption that this relationship is linear.
- Shallow-dwelling large benthic foraminifera are an under-utilised source of palaeoceanic proxy information. Sea surface temperature, seasonality and seawater chemistry may be derived from coupled clumped isotope-trace element measurements of these organisms.
- Mid-Eocene seasonality was likely greater than present day, which may be most easily explained by an increase in the frequency and/or intensity of tropical hurricanes.
- Paleogene Mg/Ca_{sw} was around 50% of modern. Both Mg/Ca_{sw} and Sr/Ca_{sw} are likely to have been relatively invariant throughout the first half of the Cenozoic.
- Clumped isotope measurements of Eocene *Nummulites* indicate only a small increase in (sub) tropical sea surface temperatures with increased atmospheric CO_2. Based on a compilation of Paleogene surface ocean palaeotemperature reconstructions, climate models appear to overestimate tropical warming.
- Coupled Mg/Ca_{test}-Mg/Ca_{sw}-temperature calibrations such as those presented here are a prerequisite of pre-Pleistocene trace element palaeothermometry.
- Seawater Mg/Ca was $\sim$20% lower during the Pliocene. As a direct consequence, Mg/Ca-derived ocean temperatures probably underestimate Pliocene warmth by 1-2°C.

References

Affek, H. P., and S. Zaarur (2014), Kinetic isotope effect in co_2 degassing: Insight from clumped and oxygen isotopes in laboratory precipitation experiments, *Geochimica et Cosmochimica Acta*, *143*, 319–330.

Allison, N., H. Austin, W. Austin, and D. Paterson (2011), Effects of seawater pH and calcification rate on test Mg/Ca and Sr/Ca in cultured individuals of the benthic, calcitic foraminifera *Elphidium williamsoni*, *Chemical Geology*, *289*(1), 171–178.

Anand, P., H. Elderfield, and M. Conte (2003), Calibration of Mg/Ca thermometry in planktonic foraminifera from a sediment trap time series, *Paleoceanography*, *18*(2), 28–31.

Andreasson, F., and B. Schmitz (1996), Winter and summer temperatures of the early middle Eocene of France from Turritella δ^{18}O profiles, *Geology*, *24*(12), 1067–1070.

Andreasson, F., and B. Schmitz (1998), Tropical Atlantic seasonal dynamics in the early middle Eocene from stable oxygen and carbon isotope profiles of mollusk shells, *Paleoceanography*, *13*(2), 183–192.

Andreasson, F. P., and B. Schmitz (2000), Temperature seasonality in the early middle Eocene North Atlantic region: Evidence from stable isotope profiles of marine gastropod shells, *GSA Bulletin*, *112*, 628–640.

Arbuszewski, J., P. Demenocal, A. Kaplan, and E. Farmer (2010), On the fidelity of shell-derived $\delta^{18}O_{seawater}$ estimates, *Earth and Planetary Science Letters*, *300*, 185–196.

Aze, T., et al. (2014), Extreme warming of tropical waters during the Paleocene–Eocene Thermal Maximum, *Geology*, *42*(9), 739–742.

Bé, A. W., and W. H. Hutson (1977), Ecology of planktonic foraminifera and biogeographic patterns of life and fossil assemblages in the Indian Ocean, *Micropaleontology*, pp. 369–414.

Beavington-Penney, S., and A. Racey (2004), Ecology of extant nummulitids and other larger benthic foraminifera: applications in palaeoenvironmental analysis, *Earth-Science Reviews*, *67*(3-4), 219–265.

Bentov, S., and J. Erez (2006), Impact of biomineralization processes on the Mg content of foraminiferal shells: A biological perspective, *Geochemistry Geophysics Geosystems*, *7*(1), Q01P08.

Bernasconi, S. M., T. W. Schmid, A.-L. Grauel, and J. Mutterlose (2011), Clumped-isotope geochemistry of carbonates: a new tool for the reconstruction of temperature and oxygen isotope composition of seawater, *Applied Geochemistry*, *26*, S279–S280.

Bijl, P., S. Schouten, A. Sluijs, G. Reichart, J. Zachos, and H. Brinkhuis (2009), Early Palaeogene temperature evolution of the southwest Pacific Ocean, *Nature*, *461*(7265), 776–779.

Bijma, J., J. Erez, and C. Hemleben (1990), Lunar and semi-lunar reproductive cycles in some spinose planktonic foraminifers, *Journal of Foraminiferal Research*, *20*(2), 117–127.

Bots, P., L. Benning, R. Rickaby, and S. Shaw (2011), The role of SO_4 in the switch from calcite to aragonite seas, *Geology*, *39*(4), 331–334.

Bowen, G. J., B. J. Maibauer, M. J. Kraus, U. Röhl, T. Westerhold, A. Steimke, P. D. Gingerich, S. L. Wing, and W. C. Clyde (2014), Two massive, rapid releases of carbon during the onset of the Palaeocene-Eocene thermal maximum, *Nature Geoscience*.

Brassell, S. C. (2014), Climatic influences on the Paleogene evolution of alkenones, *Paleoceanography*, *29*(3), 255–272.

Brennan, S. T., T. K. Lowenstein, and D. I. Cendón (2013), The major-ion composition of Cenozoic seawater: The past 36 million years from fluid inclusions in marine halite, *American Journal of Science*, *313*(8), 713–775.

Brierley, C. M., A. V. Fedorov, Z. Liu, T. D. Herbert, K. T. Lawrence, and J. P. LaRiviere (2009), Greatly expanded tropical warm pool and weakened Hadley circulation in the early Pliocene, *Science*, *323*(5922), 1714–1718.

Briguglio, A., and J. Hohenegger (2014), Growth oscillation in larger foraminifera, *Paleobiology*,

40(3), 494–509.
Broecker, W. (2013), How to think about the evolution of the ratio of Mg to Ca in seawater, *American Journal of Science*, *313*(8), 776–789.
Broecker, W., and J. Yu (2011), What do we know about the evolution of Mg to Ca ratios in seawater?, *Paleoceanography*, *26*, doi:10.1029/2011PA002120.
Budd, D. A., and E. E. Hiatt (1993), Mineralogical stabilization of high-magnesium calcite: geochemical evidence for intracrystal recrystallization within Holocene porcellaneous foraminifera, *Journal of Sedimentary Research*, *63*(2).
Burgess, C., P. Pearson, C. Lear, H. Morgans, L. Handley, R. Pancost, and S. Schouten (2008), Middle Eocene climate cyclicity in the southern Pacific: Implications for global ice volume, *Geology*, *36*(8), 651–654.
Burls, N., and A. Fedorov (2014), What controls the mean east–west sea surface temperature gradient in the equatorial pacific: The role of cloud albedo, *Journal of Climate*, *27*(7), 2757–2778.
Coggon, R., D. Teagle, C. Smith-Duque, J. Alt, and M. Cooper (2010), Reconstructing past seawater Mg/Ca and Sr/Ca from mid-ocean ridge flank calcium carbonate veins, *Science*, *327*, 1114–1117.
Coggon, R., D. Teagle, and T. Jones (2011), Comment on "what do we know about the evolution of Mg to Ca ratios in seawater?" by Wally Broecker and Jimin Yu, *Paleoceanography*, *26*(3), PA3224.
Creech, J., J. Baker, C. Hollis, H. Morgans, and E. Smith (2010), Eocene sea temperatures for the mid-latitude southwest Pacific from Mg/Ca ratios in planktonic and benthic foraminifera, *Earth and Planetary Science Letters*, *299*, 483–495.
Daëron, M., et al. (2011), $^{13}C^{18}O$ clumping in speleothems: Observations from natural caves and precipitation experiments, *Geochimica et Cosmochimica Acta*, *75*(12), 3303–3317.
Dawber, C., and A. Tripati (2012), Relationships between bottom water carbonate saturation and element/Ca ratios in coretop samples of the benthic foraminifera *Oridorsalis umbonatus*, *Biogeosciences*, *9*(8), 3029–3045.
De Choudens-Sánchez, V., and L. A. González (2009), Calcite and aragonite precipitation under controlled instantaneous supersaturation: Elucidating the role of $CaCO_3$ saturation state and Mg/Ca ratio on calcium carbonate polymorphism, *Journal of Sedimentary Research*, *79*(6), 363–376.
De Villiers, S., J. Dickson, and R. Ellam (2005), The composition of the continental river weathering flux deduced from seawater Mg isotopes, *Chemical Geology*, *216*(1), 133–142.
Dekens, P. S., D. W. Lea, D. K. Pak, and H. J. Spero (2002), Core top calibration of Mg/Ca in tropical foraminifera: Refining paleotemperature estimation, *Geochemistry, Geophysics, Geosystems*, *3*(4), 1–29.
Delaney, M., A. W. H. Bé, and E. A. Boyle (1985), Li, Sr, Mg, and Na in foraminiferal calcite shells from laboratory culture, sediment traps, and sediment cores, *Geochimica et Cosmochimica Acta*, *49*(6), 1327–1341.
Dettmering, C., J. Hohenegger, and R. Schmaljohann (1998), The trimorphic life cycle in foraminifera: observations from cultures allow new evaluation, *European Journal of Protistology*, *34*(4), 363–367.
Dickson, J. (2004), Echinoderm skeletal preservation: calcite-aragonite seas and the Mg/Ca ratio of Phanerozoic oceans, *Journal of Sedimentary Research*, *74*(3), 355–365.
Douglas, P. M., H. P. Affek, L. C. Ivany, A. J. Houben, W. P. Sijp, A. Sluijs, S. Schouten, and M. Pagani (2014), Pronounced zonal heterogeneity in Eocene southern high-latitude sea surface temperatures, *Proceedings of the National Academy of Sciences*, *111*(18), 6582–6587.
Dowsett, H. J., et al. (2012), Assessing confidence in pliocene sea surface temperatures to evaluate predictive models, *Nature Climate Change*, *2*(5), 365–371.
Durrant, S. F. (1994), Feasibility of improvement in analytical performance in laser ablation inductively coupled plasma-mass spectrometry (LA-ICP-MS) by addition of nitrogen to the argon plasma, *Fresenius' journal of analytical chemistry*, *349*(10-11), 768–771.
Dutton, A., K. Lohmann, and W. Zinsmeister (2002), Stable isotope and minor element proxies for Eocene climate of Seymour Island, Antarctica, *Paleoceanography*, *17*(2), doi:

10.1029/2000PA000593.

Dutton, A., K. Lohmann, and R. Leckie (2005), Insights from the Paleogene tropical Pacific: Foraminiferal stable isotope and elemental results from Site 1209, Shatsky Rise, *Paleoceanography*, *20*(26), doi:10.1029/2004PA001098.

Eggins, S., L. Kinsley, and J. Shelley (1998), Deposition and element fractionation processes during atmospheric pressure laser sampling for analysis by ICP-MS, *Applied Surface Science*, *127*, 278–286.

Eggins, S., P. De Deckker, and J. Marshall (2003), Mg/Ca variation in planktonic foraminifera tests: implications for reconstructing palaeo-seawater temperature and habitat migration, *Earth and Planetary Science Letters*, *212*(3-4), 291–306.

Eggins, S., A. Sadekov, and P. De Deckker (2004), Modulation and daily banding of Mg/Ca in *Orbulina universa* tests by symbiont photosynthesis and respiration: a complication for seawater thermometry?, *Earth and Planetary Science Letters*, *225*, 411–419.

Eggins, S. M., and J. M. G. Shelley (2002), Compositional heterogeneity in NIST SRM 610-617 glasses, *Geostandards Newsletter*, *26*(3), 269–286.

Eiler, J. M. (2007), "clumped-isotope" geochemistry–the study of naturally-occurring, multiply-substituted isotopologues, *Earth and Planetary Science Letters*, *262*(3), 309–327.

Eiler, J. M. (2011), Paleoclimate reconstruction using carbonate clumped isotope thermometry, *Quaternary Science Reviews*, *30*(25), 3575–3588.

Elderfield, H., M. Vautravers, and M. Cooper (2002), The relationship between shell size and Mg/Ca, Sr/Ca, δ^{18}O, and δ13C of species of planktonic foraminifera, *Geochemistry, Geophysics, Geosystems*, *3*(8), 1–13.

Emiliani, C. (1954), Depth habitats of some species of pelagic foraminifera as indicated by oxygen isotope ratios, *American Journal of Science*, *252*(3), 149–158.

Emiliani, C. (1966), Isotopic paleotemperatures., *Science*, *154*(3751), 851.

Erez, J. (2003), The source of ions for biomineralization in foraminifera and their implications for paleoceanographic proxies, *Reviews in mineralogy and geochemistry*, *54*(1), 115–149.

Erez, J., and B. Luz (1983), Experimental paleotemperature equation for planktonic foraminifera, *Geochimica et Cosmochimica Acta*, *47*(6), 1025–1031.

Evans, D. (2011), Seasonally-resolved Eocene tropical surface ocean temperatures from large benthic foraminifera, Master's thesis.

Evans, D., and W. Müller (2012), Deep time foraminifera Mg/Ca paleothermometry: Nonlinear correction for secular change in seawater Mg/Ca, *Paleoceanography*, *PA4205*, doi: 10.1029/2012PA002315.

Evans, D., and W. Müller (2013), LA-ICPMS elemental imaging of complex discontinuous carbonates: An example using large benthic foraminifera, *Journal of Analytical Atomic Spectroscopy*, *28*, 1039–1044, doi:10.1039/c3ja50053e.

Evans, D., W. Müller, S. Oron, and W. Renema (2013), Eocene seasonality and seawater alkaline earth reconstruction using shallow-dwelling large benthic foraminifera, *Earth and Planetary Science Letters*, *381*, 104–115, doi:10.1016/j.epsl.2013.08.035.

Evans, D., J. Erez, S. Oron, and W. Müller (2015), Mg/Ca-temperature and seawater-test chemistry relationships in the shallow-dwelling large benthic foraminifer *Operculina ammonoides*, *Geochimica et Cosmochimica Acta*, *148*, 325–342.

Evans, D., C. Brierley, M. E. Raymo, J. Erez, and W. Müller (Submitted), Seawater Mg/Ca reconstruction over the past 5 million years: Implications for Pliocene ocean temperature and sea level, *In. rev.*

Fantle, M., and D. DePaolo (2006), Sr isotopes and pore fluid chemistry in carbonate sediment of the Ontong Java Plateau: Calcite recrystallization rates and evidence for a rapid rise in seawater Mg over the last 10 million years, *Geochimica et Cosmochimica Acta*, *70*(15), 3883–3904.

Fedorov, A., C. Brierley, K. Lawrence, Z. Liu, P. Dekens, and A. Ravelo (2013), Patterns and mechanisms of early Pliocene warmth, *Nature*, *496*(7443), 43–49.

Fedorov, A. V., C. M. Brierley, and K. Emanuel (2010), Tropical cyclones and permanent El Niño in the early Pliocene epoch, *Nature*, *463*(7284), 1066–1070.

Fernández, B., F. Claverie, C. Pécheyran, O. F. Donard, and F. Claverie (2007), Direct analysis of solid samples by fs-LA-ICP-MS, *TrAC Trends in Analytical Chemistry*, *26*(10), 951–966.

Foster, G. L., and E. J. Rohling (2013), Relationship between sea level and climate forcing by CO_2 on geological timescales, *Proceedings of the National Academy of Sciences*, *110*(4), 1209–1214.

Fraile, I., M. Schulz, S. Mulitza, M. Kucera, et al. (2008), Predicting the global distribution of planktonic foraminifera using a dynamic ecosystem model, *Biogeosciences*, *5*(3), 891–911.

Ghosh, P., J. Adkins, H. Affek, B. Balta, W. Guo, E. A. Schauble, D. Schrag, and J. M. Eiler (2006), ^{13}C–^{18}O bonds in carbonate minerals: A new kind of paleothermometer, *Geochimica et Cosmochimica Acta*, *70*(6), 1439–1456.

Goudeau, M.-L. S., G.-J. Reichart, J. Wit, L. de Nooijer, A.-L. Grauel, S. Bernasconi, and G. de Lange (2014), Seasonality variations in the Central Mediterranean during climate change events in the Late Holocene, *Palaeogeography, Palaeoclimatology, Palaeoecology*.

Greenwood, D. R., and S. L. Wing (1995), Eocene continental climates and latitudinal temperature gradients, *Geology*, *23*(11), 1044–1048.

Guillong, M., and D. Günther (2002), Effect of particle size distribution on ICP-induced elemental fractionation in laser ablation-inductively coupled plasma-mass spectrometry, *Journal of Analytical Atomic Spectrometry*, *17*(8), 831–837.

Hallock, P. (1985), Why are larger foraminifera large?, *Paleobiology*, *11*(2), 195–208.

Hathorne, E., R. James, P. Savage, and O. Alard (2008), Physical and chemical characteristics of particles produced by laser ablation of biogenic calcium carbonate, *J. Anal. At. Spectrom.*, *23*(2), 240–243.

Haynes, J. (1981), *Foraminifera*, 433 pp., MacMilan, London.

Haywood, A., et al. (2011), Are there pre-quaternary geological analogues for a future greenhouse warming?, *Philosophical Transactions of the Royal Society A: Mathematical, Physical and Engineering Sciences*, *369*(1938), 933–956.

Haywood, A., et al. (2013), Large-scale features of Pliocene climate: results from the Pliocene Model Intercomparison Project, *Clim. Past*, *9*, 191–209.

Head, J., J. Bloch, A. Hastings, J. Bourque, E. Cadena, F. Herrera, P. Polly, and C. Jaramillo (2009), Giant boid snake from the Palaeocene neotropics reveals hotter past equatorial temperatures, *Nature*, *457*(7230), 715–717.

Hegerl, G. C., T. J. Crowley, W. T. Hyde, and D. J. Frame (2006), Climate sensitivity constrained by temperature reconstructions over the past seven centuries, *Nature*, *440*(7087), 1029–1032.

Heinemann, M., J. Jungclaus, and J. Marotzke (2009), Warm Paleocene/Eocene climate as simulated in ECHAM5/MPI-OM, *Climate of the Past*, *5*, 785–802.

Henehan, M. J., et al. (2013), Calibration of the boron isotope proxy in the planktonic foraminifera *Globigerinoides ruber* for use in palaeo-co_2 reconstruction, *Earth and Planetary Science Letters*, *364*, 111–122.

Henkes, G. A., B. H. Passey, A. D. Wanamaker Jr, E. L. Grossman, W. G. Ambrose Jr, and M. L. Carroll (2013), Carbonate clumped isotope compositions of modern marine mollusk and brachiopod shells, *Geochimica et Cosmochimica Acta*, *106*, 307–325.

Hollis, C. J., et al. (2012), Early Paleogene temperature history of the Southwest Pacific Ocean: Reconciling proxies and models, *Earth and Planetary Science Letters*, *349*, 53–66.

Hönisch, B., K. Allen, A. Russell, S. Eggins, J. Bijma, H. Spero, D. Lea, and J. Yu (2011), Planktic foraminifers as recorders of seawater Ba/Ca, *Marine Micropaleontology*, *79*(1), 52–57.

Horita, J., H. Zimmermann, and H. Holland (2002), Chemical evolution of seawater during the Phanerozoic: Implications from the record of marine evaporites, *Geochimica et Cosmochimica Acta*, *66*(21), 3733–3756.

Huber, M. (2008), A hotter greenhouse?, *Science*, *321*, 353–354.

Huber, M., and R. Caballero (2011), The early Eocene equable climate problem revisited, *Climate of*

the Past Discussions, *7*(1), 241–304.

Huber, M., and L. Sloan (2001), Heat transport, deep waters, and thermal gradients: Coupled simulation of an Eocene greenhouse climate, *Geophysical Research Letters*, *28*(18), 3481–3484.

IPCC (2013), *Climate Change 2013: The Physical Science Basis. Contribution of Working Group I to the Fifth Assessment Report of the Intergovernmental Panel on Climate Change*, 1535 pp., Cambridge University Press, Cambridge, United Kingdom and New York, NY, USA.

Ivany, L., B. Wilkinson, K. Lohmann, E. Johnson, B. McElroy, and G. Cohen (2004), Intra-annual isotopic variation in *Venericardia* bivalves: implications for early Eocene temperature, seasonality, and salinity on the US Gulf Coast, *Journal of Sedimentary Research*, *74*(1), 7–19.

Ivany, L. C., W. P. Patterson, and K. C. Lohmann (2000), Cooler winters as a possible cause of mass extinctions at the Eocene/Oligocene boundary, *Nature*, *407*(6806), 887–890.

Jochum, K., et al. (2011), Determination of reference values for NIST SRM 610–617 glasses following ISO guidelines, *Geostandards and Geoanalytical Research*, doi:10.1111/j.1751-908X.2011.00120.x.

Jochum, K. P., et al. (2012), Accurate trace element analysis of speleothems and biogenic calcium carbonates by LA-ICP-MS, *Chemical Geology*, *318*, 31–44.

Jochum, K. P., B. Stoll, U. Weis, D. E. Jacob, R. Mertz-Kraus, and M. O. Andreae (2014), Non-matrix-matched calibration for the multi-element analysis of geological and environmental samples using 200 nm femtosecond LA-ICP-MS: A comparison with nanosecond lasers, *Geostandards and Geoanalytical Research*.

Keating-Bitonti, C. R., L. C. Ivany, H. P. Affek, P. Douglas, and S. D. Samson (2011), Warm, not superhot, temperatures in the early Eocene subtropics, *Geology*, *39*(8), 771–774.

Keeling, C. D. (1960), The concentration and isotopic abundances of carbon dioxide in the atmosphere, *Tellus*, *12*(2), 200–203.

Kim, J., S. Schouten, E. Hopmans, B. Donner, and J. Sinninghe Damsté (2008), Global sediment core-top calibration of the TEX_{86} paleothermometer in the ocean, *Geochimica et Cosmochimica Acta*, *72*(4), 1154–1173.

Kim, J., J. Van der Meer, S. Schouten, P. Helmke, V. Willmott, F. Sangiorgi, N. Koc, E. Hopmans, and J. Damsté (2010), New indices and calibrations derived from the distribution of crenarchaeal isoprenoid tetraether lipids: Implications for past sea surface temperature reconstructions, *Geochimica et Cosmochimica Acta*, *74*(16), 4639–4654.

Kisakürek, B., A. Eisenhauer, F. Bohm, D. Garbe-Schönberg, and J. Erez (2008), Controls on shell Mg/Ca and Sr/Ca in cultured planktonic foraminiferan, *Globigerinoides ruber* (white), *Earth and Planetary Science Letters*, *273*(3-4), 260–269.

Klein, R., K. Lohmann, and C. Thayer (1996), Bivalve skeletons record sea-surface temperature and $\delta^{18}O$ via Mg/Ca and $^{18}O/^{16}O$ ratios, *Geology*, *24*(5), 415.

Kobashi, T., E. Grossman, D. Dockery, and L. Ivany (2004), Water mass stability reconstructions from greenhouse (Eocene) to icehouse (Oligocene) for the northern Gulf Coast continental shelf (USA), *Paleoceanography*, *19*(1), PA1022, doi:10.1029/2003PA000934.

Koch, J., and D. Günther (2011), Review of the state-of-the-art of laser ablation inductively coupled plasma mass spectrometry, *Applied spectroscopy*, *65*(5), 155–162.

Korty, R. L., K. A. Emanuel, and J. R. Scott (2008), Tropical cyclone-induced upper-ocean mixing and climate: Application to equable climates, *Journal of Climate*, *21*(4), 638–654.

LaRiviere, J. P., A. C. Ravelo, A. Crimmins, P. S. Dekens, H. L. Ford, M. Lyle, and M. W. Wara (2012), Late Miocene decoupling of oceanic warmth and atmospheric carbon dioxide forcing, *Nature*, *486*(7401), 97–100.

Lear, C., H. Elderfield, and P. Wilson (2003), A cenozoic seawater Sr/Ca record from benthic foraminiferal calcite and its application in determining global weathering fluxes, *Earth and Planetary Science Letters*, *208*(1), 69–84.

Lear, C. H., H. Elderfield, and P. A. Wilson (2000), Cenozoic deep-sea temperatures and global ice volumes from Mg/Ca in benthic foraminiferal calcite, *Science*, *287*, 269–272.

Lear, C. H., Y. Rosenthal, and N. Slowey (2002), Benthic foraminiferal Mg/Ca-paleothermometry: A

revised core-top calibration, *Geochimica et Cosmochimica Acta*, *66*(19), 3375–3387.
Li, Y.-H. (1982), A brief discussion on the mean oceanic residence time of elements, *Geochimica et Cosmochimica Acta*, *46*(12), 2671–2675.
Liu, Z., M. Pagani, D. Zinniker, R. DeConto, M. Huber, H. Brinkhuis, S. Shah, R. Leckie, and A. Pearson (2009), Global cooling during the Eocene-Oligocene climate transition, *Science*, *323*, 1187–1190.
Locarnini, R., A. Mishonov, J. Antonov, T. Boyer, and H. Garcia (2010), *World Ocean Atlas 2009, Volume 1: Temperature*, vol. NOAA Atlas NESDIS, 184 pp., U.S. Government Printing Office, Washington D. C.
Lowenstein, T., M. Timofeeff, S. Brennan, L. Hardie, and R. Demicco (2001), Oscillations in Phanerozoic seawater chemistry: Evidence from fluid inclusions, *Science*, *294*, 1086–1088.
Lunt, D. J., et al. (2012), A model–data comparison for a multi-model ensemble of early Eocene atmosphere–ocean simulations: EoMIP, *Climate of the Past*, *8*(5), 1717–1736.
Lüthi, D., et al. (2008), High-resolution carbon dioxide concentration record 650,000–800,000 years before present, *Nature*, *453*(7193), 379–382.
Luz, B., and Z. Reiss (1983), Stable carbon isotopes in Quaternary foraminifera from the Gulf of Aqaba (Eilat), Red Sea, *Utrecht Micropaleontol. Bull*, *30*, 129–140.
McArthur, J., R. Howarth, and T. Bailey (2001), Strontium isotope stratigraphy: LOWESS version 3: Best fit to the marine Sr-isotope curve for 0–509 Ma and accompanying look-up table for deriving numerical age, *The Journal of Geology*, *109*(2), 155–170.
Meckler, A. N., M. Ziegler, M. I. Millán, S. F. Breitenbach, and S. M. Bernasconi (2014), Long-term performance of the Kiel carbonate device with a new correction scheme for clumped isotope measurements, *Rapid Communications in Mass Spectrometry*, *28*(15), 1705–1715.
Medina-Elizalde, M., D. Lea, and M. Fantle (2008), Implications of seawater Mg/Ca variability for Plio-Pleistocene tropical climate reconstruction, *Earth and Planetary Science Letters*, *269*(3-4), 585–595.
Mucci, A., and J. Morse (1983), The incorporation of Mg^{2+} and Sr^{2+} into calcite overgrowths: influences of growth rate and solution composition, *Geochimica et Cosmochimica Acta*, *47*(2), 217–233.
Müller, W., M. Shelley, P. Miller, and S. Broude (2009), Initial performance metrics of a new custom–designed ArF excimer LA–ICPMS system coupled to a two-volume laser–ablation cell, *Journal of Analytical Atomic Spectrometry*, *24*(2), 209–214.
Nürnberg, D., J. Bijma, and C. Hemleben (1996), Assessing the reliability of magnesium in foraminiferal calcite as a proxy for water mass temperatures, *Geochimica et Cosmochimica Acta*, *60*(5), 803–814.
Pagani, M., J. C. Zachos, K. H. Freeman, B. Tipple, and S. Bohaty (2005), Marked decline in atmospheric carbon dioxide concentrations during the Paleogene, *Science*, *309*(5734), 600–603.
Pagani, M., Z. Liu, J. LaRiviere, and A. C. Ravelo (2009), High Earth-system climate sensitivity determined from Pliocene carbon dioxide concentrations, *Nature Geoscience*, *3*(1), 27–30.
Pearson, P., B. Van Dongen, C. Nicholas, R. Pancost, S. Schouten, J. Singano, and B. Wade (2007), Stable warm tropical climate through the Eocene Epoch, *Geology*, *35*(3), 211–214.
Pearson, P. N., P. W. Ditchfield, J. Singano, K. G. Harcourt-Brown, C. J. Nicholas, R. K. Olsson, N. J. Shackleton, and M. A. Hall (2001), Warm tropical sea surface temperatures in the Late Cretaceous and Eocene epochs, *Nature*, *413*, 481–487.
Pena, L. D., E. Calvo, I. Cacho, S. Eggins, and C. Pelejero (2005), Identification and removal of Mn-Mg-rich contaminant phases on foraminiferal tests: Implications for Mg/Ca past temperature reconstructions, *Geochem. Geophys. Geosyst*, *6*, doi:10.1029/2005GC000930.
Piechota, T. C., and J. A. Dracup (1996), Drought and regional hydrologic variation in the united states: Associations with the El Niño-Southern Oscillation, *Water Resources Research*, *32*(5), 1359–1373.
Pierrehumbert, R. T. (1995), Thermostats, radiator fins, and the local runaway greenhouse, *Journal of the atmospheric sciences*, *52*(10), 1784–1806.

Pisonero, J., and D. Günther (2008), Femtosecond laser ablation inductively coupled plasma mass spectrometry: fundamentals and capabilities for depth profiling analysis, *Mass spectrometry reviews*, *27*(6), 609–623.

Prescott, C. L., A. M. Haywood, A. M. Dolan, S. J. Hunter, J. O. Pope, and S. J. Pickering (2014), Assessing orbitally-forced interglacial climate variability during the mid-Pliocene Warm Period, *Earth and Planetary Science Letters*, *400*, 261–271.

Purton, L., and M. Brasier (1997), Gastropod carbonate δ^{18}O-water and δ^{13}C values record strong seasonal productivity and stratification shifts during the late Eocene in England, *Geology*, *25*(10), 871–874.

Purton, L., and M. Brasier (1999), Giant protist *Nummulites* and its Eocene environment: Life span and habitat insights from δ^{18}O and δ^{13}C data from *Nummulites* and *Venericardia*, Hampshire basin, UK, *Geology*, *27*(8), 711–714.

Raitzsch, M., A. Dueñas-Bohórquez, G.-J. Reichart, L. de Nooijer, and T. Bickert (2010), Incorporation of Mg and Sr in calcite of cultured benthic foraminifera: impact of calcium concentration and associated calcite saturation state, *Biogeosciences*, *7*(3), 869–881.

Raja, R., P. Saraswati, K. Rogers, and K. Iwao (2005), Magnesium and strontium compositions of recent symbiont-bearing benthic foraminifera, *Marine Micropaleontology*, *58*(1), 31–44.

Raja, R., P. Saraswati, and K. Iwao (2007), A field-based study on variation in Mg/Ca and Sr/Ca in larger benthic foraminifera, *Geochemistry Geophysics Geosystems*, *8*(10), doi: 10.1029/2006GC001478.

Ramanathan, V., and W. Collins (1991), Thermodynamic regulation of ocean warming by cirrus clouds deduced from observations of the 1987 El Niño, *Nature*, *351*(6321), 27–32.

Randall, D., M. Khairoutdinov, A. Arakawa, and W. Grabowski (2003), Breaking the cloud parameterization deadlock, *Bulletin of the American Meteorological Society*, *84*(11), 1547–1564.

Rausch, S., F. Böhm, W. Bach, A. Klügel, and A. Eisenhauer (2013), Calcium carbonate veins in ocean crust record a threefold increase of seawater Mg/Ca in the past 30 million years, *Earth and Planetary Science Letters*, *362*, 215–224.

Ravelo, A., and R. Fairbanks (1992), Oxygen isotopic composition of multiple species of planktonic foraminifera: Recorders of the modern photic zone temperature gradient, *Paleoceanography*, *7*(6), 815–831.

Regenberg, M., A. Regenberg, D. Garbe-Schönberg, and D. W. Lea (2014), Global dissolution effects on planktonic foraminiferal Mg/Ca ratios controlled by the calcite-saturation state of bottom waters, *Paleoceanography*, *29*(3), 127–142.

Reichart, G.-J., F. Jorissen, P. Anschutz, and P. R. Mason (2003), Single foraminiferal test chemistry records the marine environment, *Geology*, *31*(4), 355–358.

Reiss, Z., and L. Hottinger (1984), *The Gulf of Aqaba Ecological Micropaleontology*, Spriner-Verlag, Berlin.

Renema, W. (2006), Large benthic foraminifera from the deep photic zone of a mixed siliciclastic-carbonate shelf off East Kalimantan, Indonesia, *Marine Micropaleontology*, *58*(2), 73–82.

Renema, W. (2008), Habitat selective factors influencing the distribution of larger benthic foraminiferal assemblages over the Kepulauan Seribu, *Marine Micropaleontology*, *68*(3), 286–298.

Renema, W., B. Hoeksema, J. Van Hinte, and J. van Hinte (2001), Larger benthic foraminifera and their distribution patterns on the Spermonde shelf, South Sulawesi, *Zoologische Verhandelingen*, pp. 115–150.

Ries, J. (2004), Effect of ambient Mg/Ca ratio on Mg fractionation in calcareous marine invertebrates: A record of the oceanic Mg/Ca ratio over the Phanerozoic, *Geology*, *32*(11), 981–984.

Röttger, R., M. Spindler, R. Schmaljohann, M. Richwien, and M. Fladung (1984), Functions of the canal system in the rotaliid foraminifer, *Heterostegina depressa*, *Nature*, *309*, 789–791.

Russell, A., B. Hönisch, H. Spero, and D. Lea (2004), Effects of seawater carbonate ion concentration and temperature on shell U, Mg, and Sr in cultured planktonic foraminifera, *Geochimica et cosmochimica acta*, *68*(21), 4347–4361.

Russo, R. E., X. Mao, H. Liu, J. Gonzalez, and S. S. Mao (2002), Laser ablation in analytical chemistry–a review, *Talanta*, *57*(3), 425–451.

Sadekov, A., S. Eggins, P. De Deckker, and D. Kroon (2008), Uncertainties in seawater thermometry deriving from intratest and intertest Mg/Ca variability in Globigerinoides ruber, *Paleoceanography*, *23*(1), doi:10.1029/2007PA001452.

Sadekov, A., S. M. Eggins, P. De Deckker, U. Ninnemann, W. Kuhnt, and F. Bassinot (2009), Surface and subsurface seawater temperature reconstruction using Mg/Ca microanalysis of planktonic foraminifera *Globigerinoides ruber*, *Globigerinoides sacculifer*, and *Pulleniatina obliquiloculata*, *Paleoceanography*, *24*(3).

Sandberg, P. (1983), An oscillating trend in Phanerozoic non-skeletal carbonate mineralogy, *Nature*, *305*, 19–22.

Sangiorgi, F., et al. (2008), Cyclicity in the middle Eocene central Arctic Ocean sediment record: Orbital forcing and environmental response, *Paleoceanography*, *23*, doi:10.1029/2007PA001487.

Schmitz, B., and V. Pujalte (2007), Abrupt increase in seasonal extreme precipitation at the Paleocene-Eocene boundary, *Geology*, *35*(3), 215–218.

Segev, E., and J. Erez (2006), Effect of Mg/Ca ratio in seawater on shell composition in shallow benthic foraminifera, *Geochemistry, Geophysics, Geosystems*, *7*(2), doi:10.1029/2005GC000969.

Seki, O., G. L. Foster, D. N. Schmidt, A. Mackensen, K. Kawamura, and R. D. Pancost (2010), Alkenone and boron-based Pliocene pCO_2 records, *Earth and Planetary Science Letters*, *292*(1), 201–211.

Seton, M., C. Gaina, R. Müller, and C. Heine (2009), Mid-Cretaceous seafloor spreading pulse: Fact or fiction?, *Geology*, *37*(8), 687–690.

Shackleton, N. J., and N. D. Opdyke (1973), Oxygen isotope and palaeomagnetic stratigraphy of Equatorial Pacific core V28-238: Oxygen isotope temperatures and ice volumes on a 10^5 year and 10^6 year scale, *Quaternary research*, *3*(1), 39–55.

Sosdian, S. M., C. H. Lear, K. Tao, E. L. Grossman, A. O'Dea, and Y. Rosenthal (2012), Cenozoic seawater Sr/Ca evolution, *Geochemistry, Geophysics, Geosystems*, *13*(10).

Stanley, S., and L. Hardie (1998), Secular oscillations in the carbonate mineralogy of reef-building and sediment-producing organisms driven by tectonically forced shifts in seawater chemistry, *Palaeogeography, Palaeoclimatology, Palaeoecology*, *144*(1-2), 3–19.

Tierney, J. E., and M. P. Tingley (2014), A bayesian, spatially-varying calibration model for the TEX_{86} proxy, *Geochimica et Cosmochimica Acta*, *127*, 83–106.

Tindall, J., R. Flecker, P. Valdes, D. Schmidt, P. Markwick, and J. Harris (2010), Modelling the oxygen isotope distribution of ancient seawater using a coupled ocean-atmosphere GCM: implications for reconstructing early Eocene climate, *Earth and Planetary Science Letters*, *292*(3-4), 265–273.

Toyofuku, T., H. Kitazato, H. Kawahata, M. Tsuchiya, and M. Nohara (2000), Evaluation of Mg/Ca thermometry in foraminifera: Comparison of experimental results and measurements in nature, *Paleoceanography*, *15*, 456–464.

Tripati, A., and J. Zachos (2002), Late Eocene tropical sea surface temperatures: A perspective from Panama, *Paleoceanography*, *17*(3), doi:10.1029/2000PA000605.

Tripati, A., W. Allmon, and D. Sampson (2009), Possible evidence for a large decrease in seawater strontium/calcium ratios and strontium concentrations during the Cenozoic, *Earth and Planetary Science Letters*, *282*(1-4), 122–130.

Tripati, A. K., R. A. Eagle, N. Thiagarajan, A. C. Gagnon, H. Bauch, P. R. Halloran, and J. M. Eiler (2010), ^{13}C–^{18}O isotope signatures and □clumped isotope□thermometry in foraminifera and coccoliths, *Geochimica et Cosmochimica Acta*, *74*(20), 5697–5717.

Tripati, A. K., S. Sahany, D. Pittman, R. A. Eagle, J. D. Neelin, J. L. Mitchell, and L. Beaufort (2014), Modern and glacial tropical snowlines controlled by sea surface temperature and atmospheric mixing, *Nature Geoscience*, *7*(3), 205–209.

Wara, M. W., A. C. Ravelo, and M. L. Delaney (2005), Permanent El Niño-like conditions during the Pliocene warm period, *Science*, *309*(5735), 758–761.

Wefer, G., and W. Berger (1980), Stable isotopes in benthic foraminifera: seasonal variation in large

tropical species, *Science*, *209*(4458), 803–805.

Weller, P., and R. Stein (2008), Paleogene biomarker records from the central Arctic Ocean (Integrated Ocean Drilling Program Expedition 302): Organic carbon sources, anoxia, and sea surface temperature, *Paleoceanography*, *23*(1), doi:10.1029/2007PA001472.

Wilkinson, B., and T. Algeo (1989), Sedimentary carbonate record of calcium-magnesium cycling, *American Journal of Science*, *289*(10), 1158–1194.

Williams, I. N., R. T. Pierrehumbert, and M. Huber (2009), Global warming, convective threshold and false thermostats, *Geophysical Research Letters*, *36*(21).

Wit, J., G.-J. Reichart, S. Jung, and D. Kroon (2010), Approaches to unravel seasonality in sea surface temperatures using paired single-specimen foraminiferal δ^{18}O and Mg/Ca analyses, *Paleoceanography*, *25*(4), PA4220.

Wit, J. C., L. de Nooijer, M. Wolthers, and G.-J. Reichart (2013), A novel salinity proxy based on Na incorporation into foraminiferal calcite., *Biogeosciences*, *10*(10), 6375–6387.

Zachos, J., G. Dickens, and R. Zeebe (2008), An early Cenozoic perspective on greenhouse warming and carbon-cycle dynamics, *Nature*, *451*, 279–283.

Zachos, J. C., M. W. Wara, S. Bohaty, M. L. Delaney, M. R. Petrizzo, A. Brill, T. J. Bralower, and I. Premoli-Silva (2003), A transient rise in tropical sea surface temperature during the Paleocene-Eocene thermal maximum, *Science*, *302*(5650), 1551–1554.

Zhang, Y. G., M. Pagani, and Z. Liu (2014), A 12-million-year temperature history of the tropical Pacific Ocean, *science*, *344*(6179), 84–87.

Appendix

All LA-ICPMS standard data

The following graphs detail analyses of 20-21 of the most commonly monitored masses on 10 standards using the LA-ICPMS system at Royal Holloway University of London. Primary standardisation using both NIST612 (the first 20) and NIST610 are shown. See the caption of figure 4, chapter 2 for an explanation of the formatting of these figures.

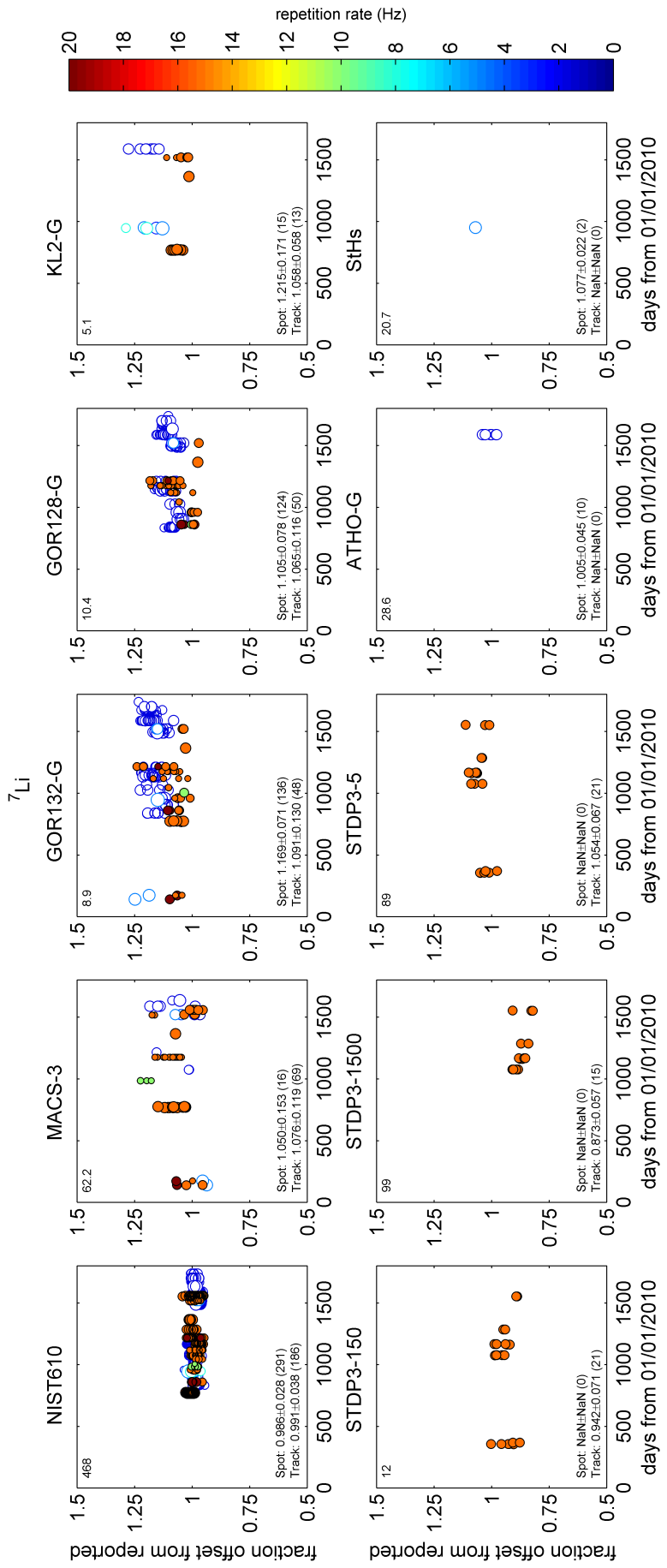
repetition rate (Hz)
0
2
4
6
8
10
12
14
16
18
20
^{7}Li
NIST610
MACS-3
GOR132-G
STDP3-5
GOR128-G
KL2-G
STDP3-150
STDP3-1500
ATHO-G
StHs
fraction offset from reported
days from 01/01/2010
0.5
0.75
1
1.25
1.5
0
500
1000
1500
468
62.2
8.9
89
10.4
5.1
12
99
28.6
20.7
Spot: 0.986±0.028 (291)
Track: 0.991±0.038 (186)
Spot: 1.050±0.153 (16)
Track: 1.076±0.119 (69)
Spot: 1.169±0.071 (136)
Track: 1.091±0.130 (48)
Spot: NaN±NaN (0)
Track: 1.054±0.067 (21)
Spot: 1.105±0.078 (124)
Track: 1.065±0.116 (50)
Spot: 1.215±0.171 (15)
Track: 1.058±0.058 (13)
Spot: NaN±NaN (0)
Track: 0.942±0.071 (21)
Spot: NaN±NaN (0)
Track: 0.873±0.057 (15)
Spot: NaN±NaN (0)
Track: NaN±NaN (0)
Spot: 1.005±0.045 (10)
Track: NaN±NaN (0)
Spot: 1.077±0.022 (2)
Track: NaN±NaN (0)

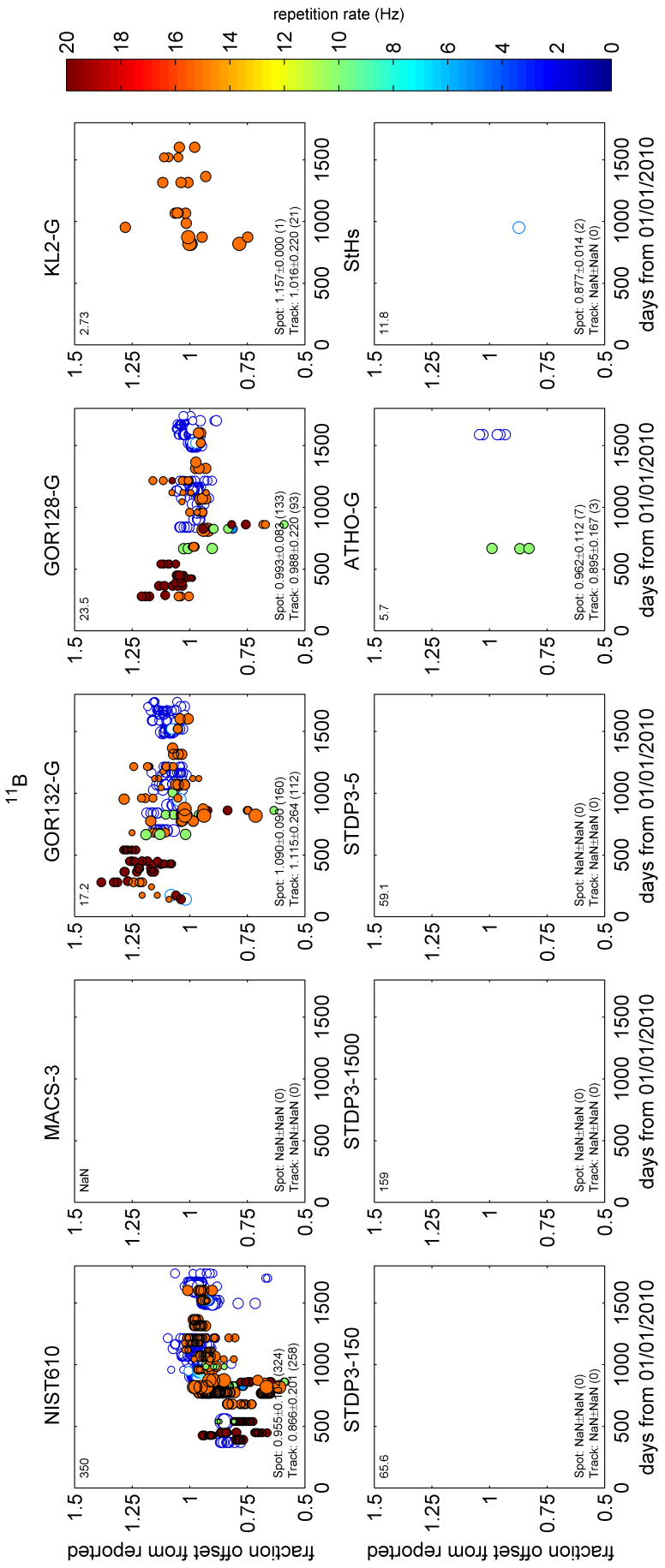
repetition rate (Hz)
20
18
16
14
12
10
8
6
4
2
0
^{11}B
NIST610
MACS-3
GOR132-G
STDP3-5
GOR128-G
ATHO-G
KL2-G
StHs
STDP3-150
STDP3-1500
STDP3-5
STDP3-1500
ATHO-G
StHs
fraction offset from reported
days from 01/01/2010
Spot: 0.955±0.(324)
Track: 0.866±0.201 (258)
Spot: NaN±NaN (0)
Track: NaN±NaN (0)
Spot: 1.090±0.090 (160)
Track: 1.115±0.264 (112)
Spot: 0.993±0.083 (133)
Track: 0.988±0.220 (93)
Spot: 1.157±0.000 (1)
Track: 1.016±0.220 (21)
Spot: 0.962±0.112 (7)
Track: 0.895±0.167 (3)
Spot: 0.877±0.014 (2)
Track: NaN±NaN (0)

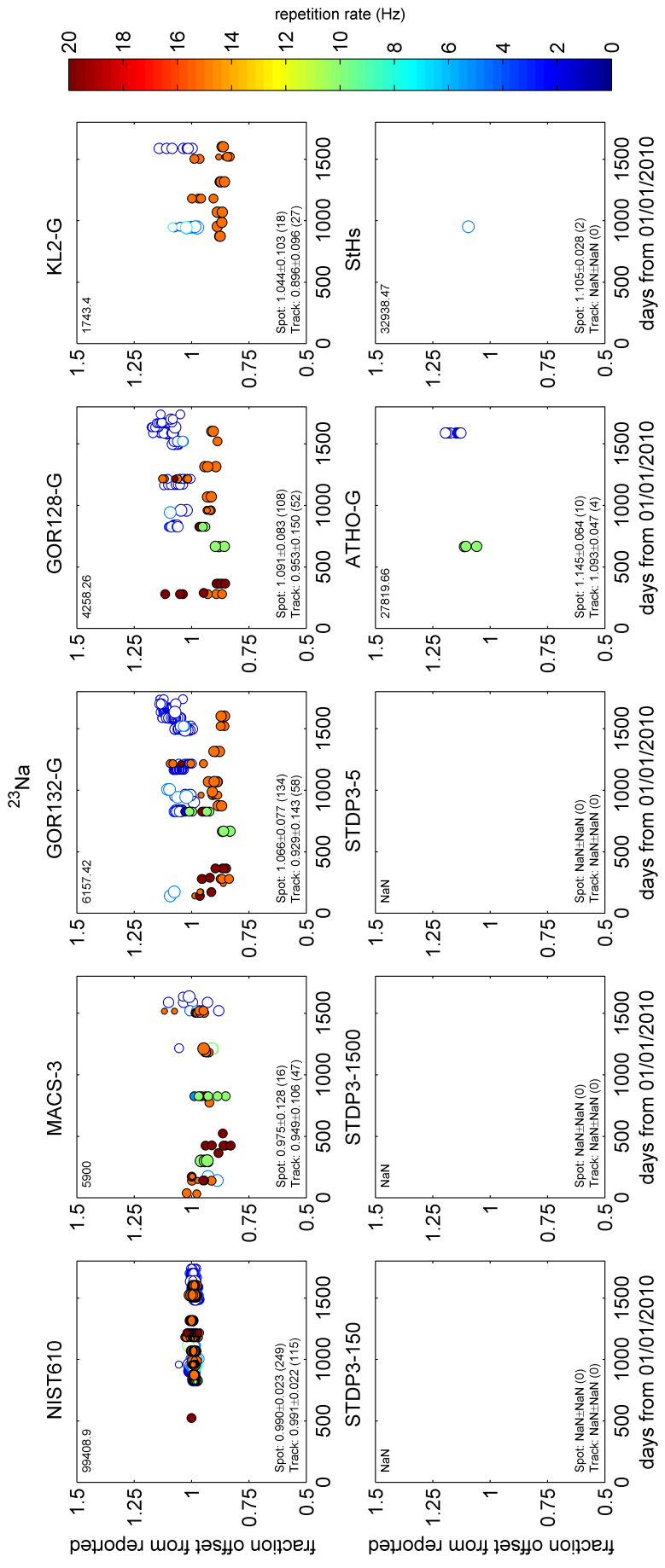
repetition rate (Hz)
20
18
16
14
12
10
8
6
4
2
0
^{23}Na
NIST610
MACS-3
GOR132-G
STDP3-5
KL2-G
GOR128-G
ATHO-G
StHs
STDP3-150
STDP3-1500
fraction offset from reported
days from 01/01/2010
99408.9
5900
6157.42
NaN
1743.4
4258.26
27819.66
32938.47
Spot: 0.990±0.023 (249)
Track: 0.991±0.022 (115)
Spot: 0.975±0.128 (16)
Track: 0.949±0.106 (47)
Spot: 1.066±0.077 (134)
Track: 0.929±0.143 (58)
Spot: NaN±NaN (0)
Track: NaN±NaN (0)
Spot: 1.044±0.103 (18)
Track: 0.896±0.096 (27)
Spot: 1.091±0.083 (108)
Track: 0.953±0.150 (52)
Spot: 1.145±0.064 (10)
Track: 1.093±0.047 (4)
Spot: 1.105±0.028 (2)
Track: NaN±NaN (0)

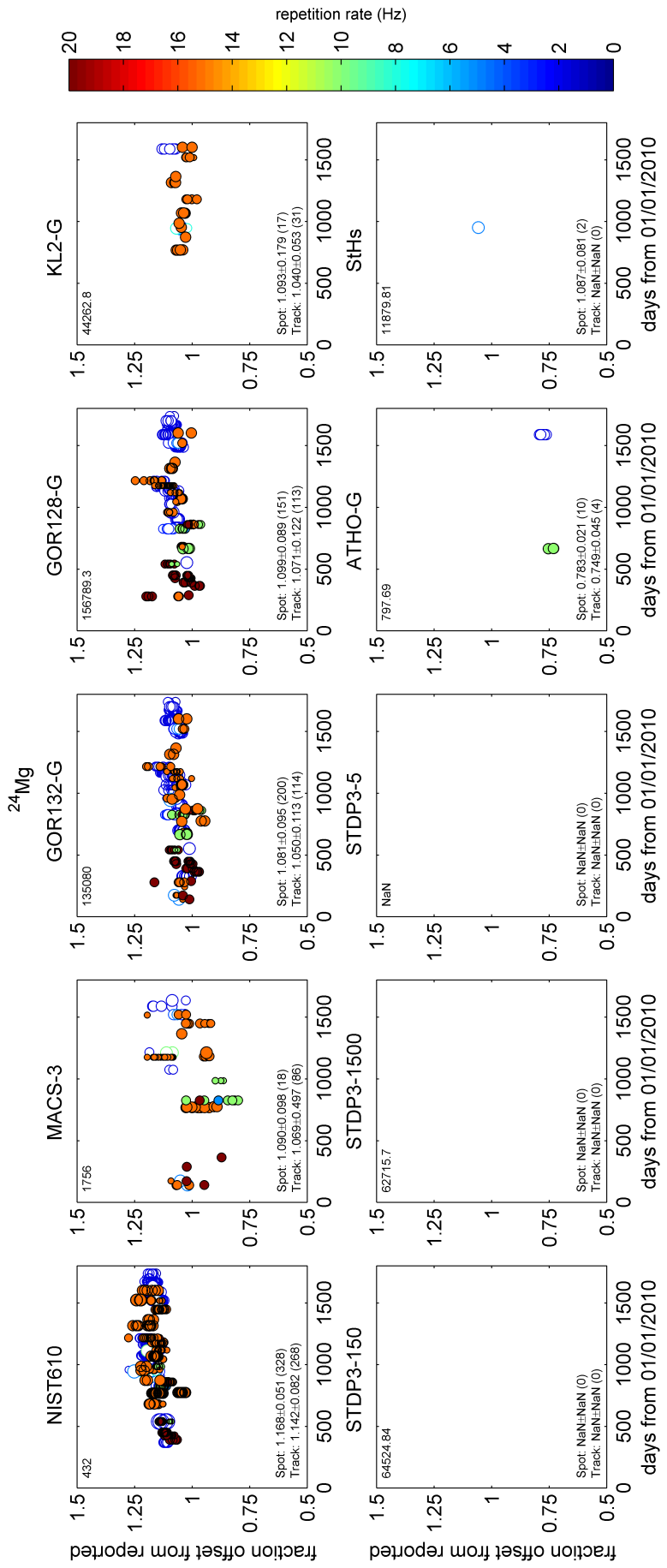
repetition rate (Hz)
20
18
16
14
12
10
8
6
4
2
0
^{24}Mg
NIST610
MACS-3
GOR132-G
STDP3-5
GOR128-G
ATHO-G
KL2-G
StHs
STDP3-150
STDP3-1500
fraction offset from reported
days from 01/01/2010
Spot: 1.168±0.051 (328)
Track: 1.142±0.082 (268)
Spot: 1.090±0.098 (18)
Track: 1.069±0.497 (86)
Spot: 1.081±0.095 (200)
Track: 1.050±0.113 (114)
Spot: NaN±NaN (0)
Track: NaN±NaN (0)
Spot: 1.099±0.089 (151)
Track: 1.071±0.122 (113)
Spot: 0.783±0.021 (10)
Track: 0.749±0.045 (4)
Spot: 1.093±0.179 (17)
Track: 1.040±0.053 (31)
Spot: 1.087±0.081 (2)
Track: NaN±NaN (0)

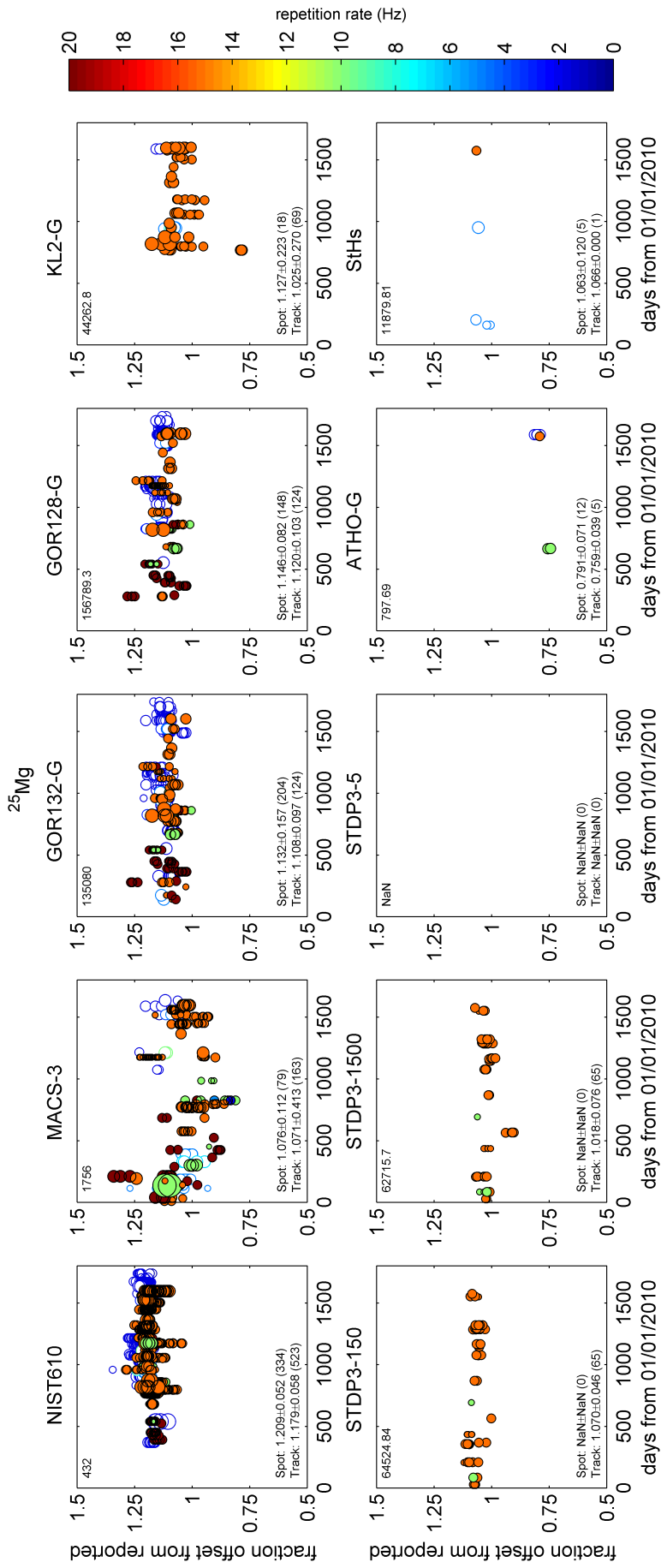
repetition rate (Hz)
20
18
16
14
12
10
8
6
4
2
0
^{25}Mg
NIST610
MACS-3
GOR132-G
STDP3-5
GOR128-G
ATHO-G
KL2-G
STHs
STDP3-150
STDP3-1500
GOR132-G
STDP3-5
GOR128-G
ATHO-G
STHs
fraction offset from reported
days from 01/01/2010
Spot: 1.209±0.052 (334)
Track: 1.179±0.058 (523)
Spot: 1.076±0.112 (79)
Track: 1.071±0.413 (163)
Spot: 1.132±0.157 (204)
Track: 1.108±0.097 (124)
Spot: NaN±NaN (0)
Track: NaN±NaN (0)
Spot: 1.146±0.082 (148)
Track: 1.120±0.103 (124)
Spot: 0.791±0.071 (12)
Track: 0.759±0.039 (5)
Spot: 1.127±0.223 (18)
Track: 1.025±0.270 (69)
Spot: 1.063±0.120 (5)
Track: 1.066±0.000 (1)
Spot: NaN±NaN (0)
Track: 1.070±0.046 (65)
Spot: NaN±NaN (0)
Track: 1.018±0.076 (65)
Spot: NaN±NaN (0)
Track: NaN±NaN (0)
Spot: NaN±NaN (0)
Track: NaN±NaN (0)
Spot: NaN±NaN (0)
Track: NaN±NaN (0)
Spot: NaN±NaN (0)
Track: NaN±NaN (0)
Spot: NaN±NaN (0)
Track: NaN±NaN (0)

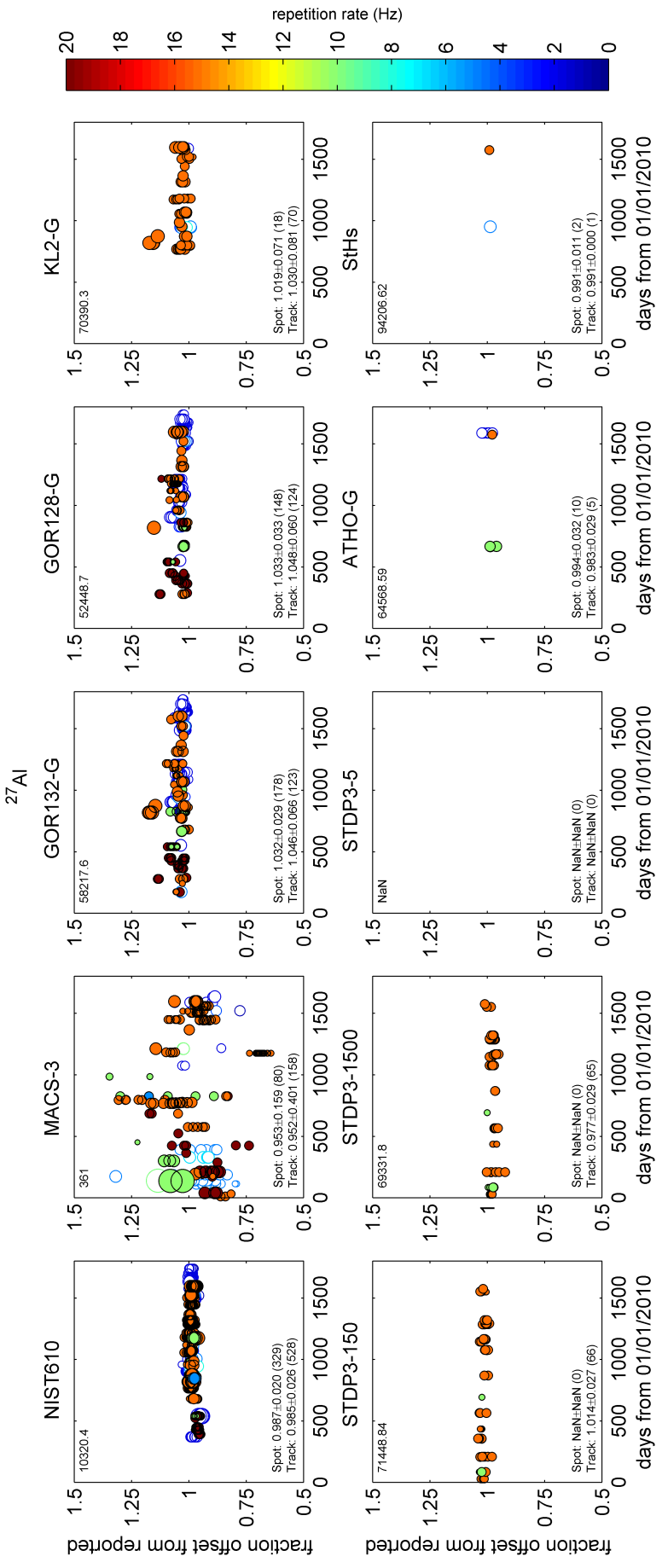
repetition rate (Hz)
20
18
16
14
12
10
8
6
4
2
0
^{27}Al
NIST610
MACS-3
GOR132-G
STDP3-5
GOR128-G
ATHO-G
KL2-G
StHs
STDP3-150
STDP3-1500
GOR132-G
STDP3-5
GOR128-G
ATHO-G
KL2-G
StHs
fraction offset from reported
days from 01/01/2010
10320.4
361
58217.6
NaN
52448.7
64568.59
70390.3
94206.62
71448.84
69331.8
58217.6
NaN
52448.7
64568.59
70390.3
94206.62
Spot: 0.987±0.020 (329)
Track: 0.985±0.026 (528)
Spot: 0.953±0.159 (80)
Track: 0.952±0.401 (158)
Spot: 1.032±0.029 (178)
Track: 1.046±0.066 (123)
Spot: NaN±NaN (0)
Track: NaN±NaN (0)
Spot: 1.033±0.033 (148)
Track: 1.048±0.060 (124)
Spot: 0.994±0.032 (10)
Track: 0.983±0.029 (5)
Spot: 1.019±0.071 (18)
Track: 1.030±0.081 (70)
Spot: 0.991±0.011 (2)
Track: 0.991±0.000 (1)
Spot: NaN±NaN (0)
Track: 1.014±0.027 (66)
Spot: NaN±NaN (0)
Track: 0.977±0.029 (65)

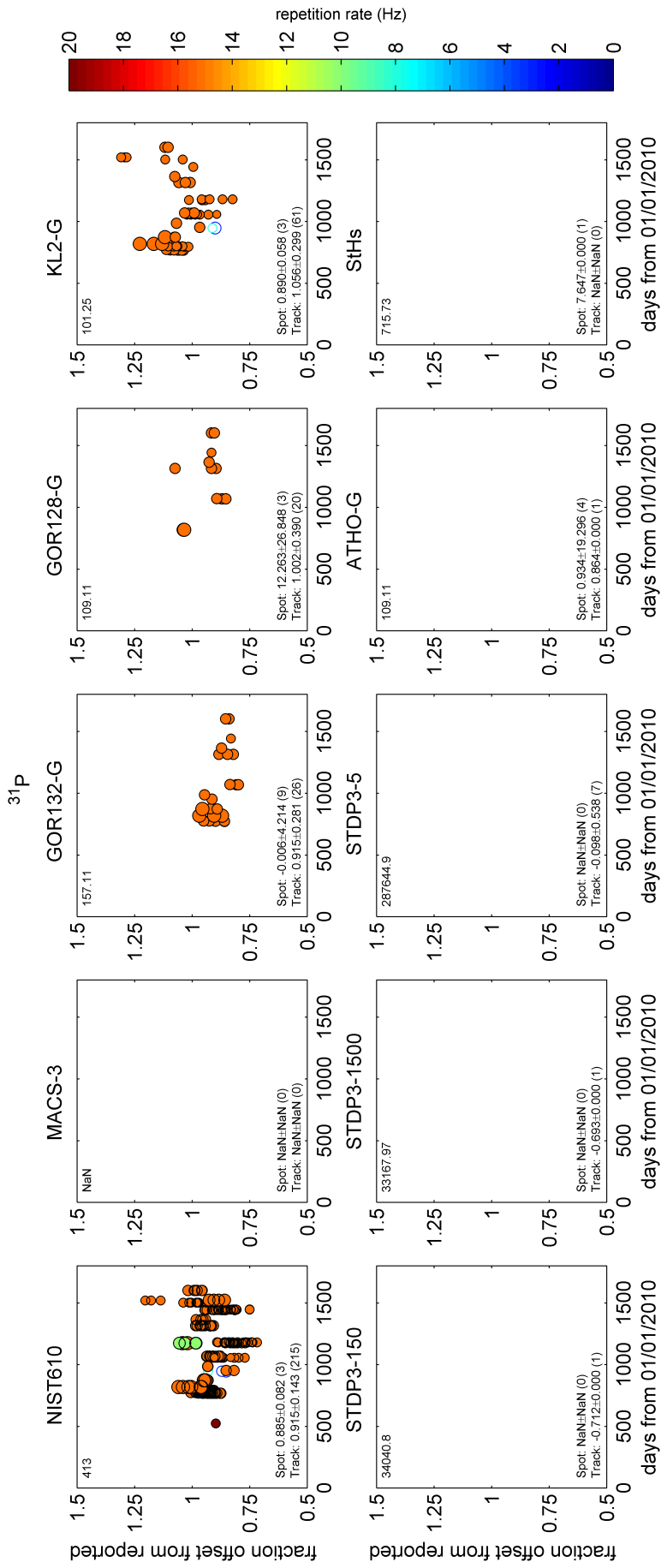
^{31}P
repetition rate (Hz)
0
2
4
6
8
10
12
14
16
18
20
NIST610
MACS-3
GOR132-G
GOR128-G
KL2-G
STDP3-150
STDP3-1500
STDP3-5
ATHO-G
StHs
fraction offset from reported
days from 01/01/2010
413
NaN
157.11
109.11
101.25
34040.8
33167.97
287644.9
109.11
715.73
Spot: 0.885±0.082 (3)
Track: 0.915±0.143 (215)
Spot: NaN±NaN (0)
Track: NaN±NaN (0)
Spot: -0.006±4.214 (9)
Track: 0.915±0.281 (26)
Spot: 12.263±26.848 (3)
Track: 1.002±0.390 (20)
Spot: 0.890±0.058 (3)
Track: 1.056±0.299 (61)
Spot: NaN±NaN (0)
Track: -0.712±0.000 (1)
Spot: NaN±NaN (0)
Track: -0.693±0.000 (1)
Spot: NaN±NaN (0)
Track: -0.098±0.538 (7)
Spot: 0.934±19.296 (4)
Track: 0.864±0.000 (1)
Spot: 7.647±0.000 (1)
Track: NaN±NaN (0)

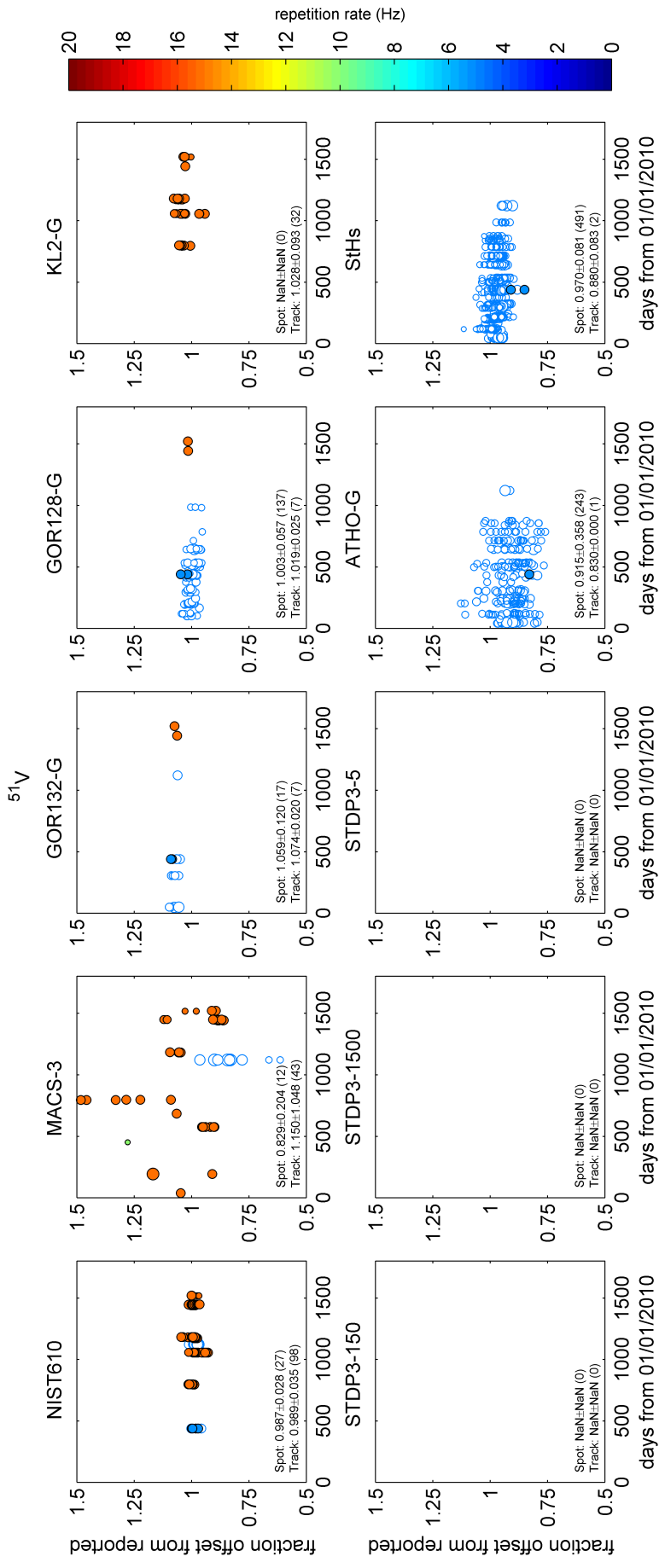
repetition rate (Hz)
20
18
16
14
12
10
8
6
4
2
0
^{51}V
NIST610
MACS-3
GOR132-G
STDP3-5
GOR128-G
ATHO-G
KL2-G
STHs
STDP3-150
STDP3-1500
fraction offset from reported
days from 01/01/2010
Spot: 0.987±0.028 (27)
Track: 0.989±0.035 (98)
Spot: 0.829±0.204 (12)
Track: 1.150±1.048 (43)
Spot: 1.059±0.120 (17)
Track: 1.074±0.020 (7)
Spot: NaN±NaN (0)
Track: NaN±NaN (0)
Spot: 1.003±0.057 (137)
Track: 1.019±0.025 (7)
Spot: 0.915±0.358 (243)
Track: 0.830±0.000 (1)
Spot: NaN±NaN (0)
Track: 1.028±0.093 (32)
Spot: 0.970±0.081 (491)
Track: 0.880±0.083 (2)

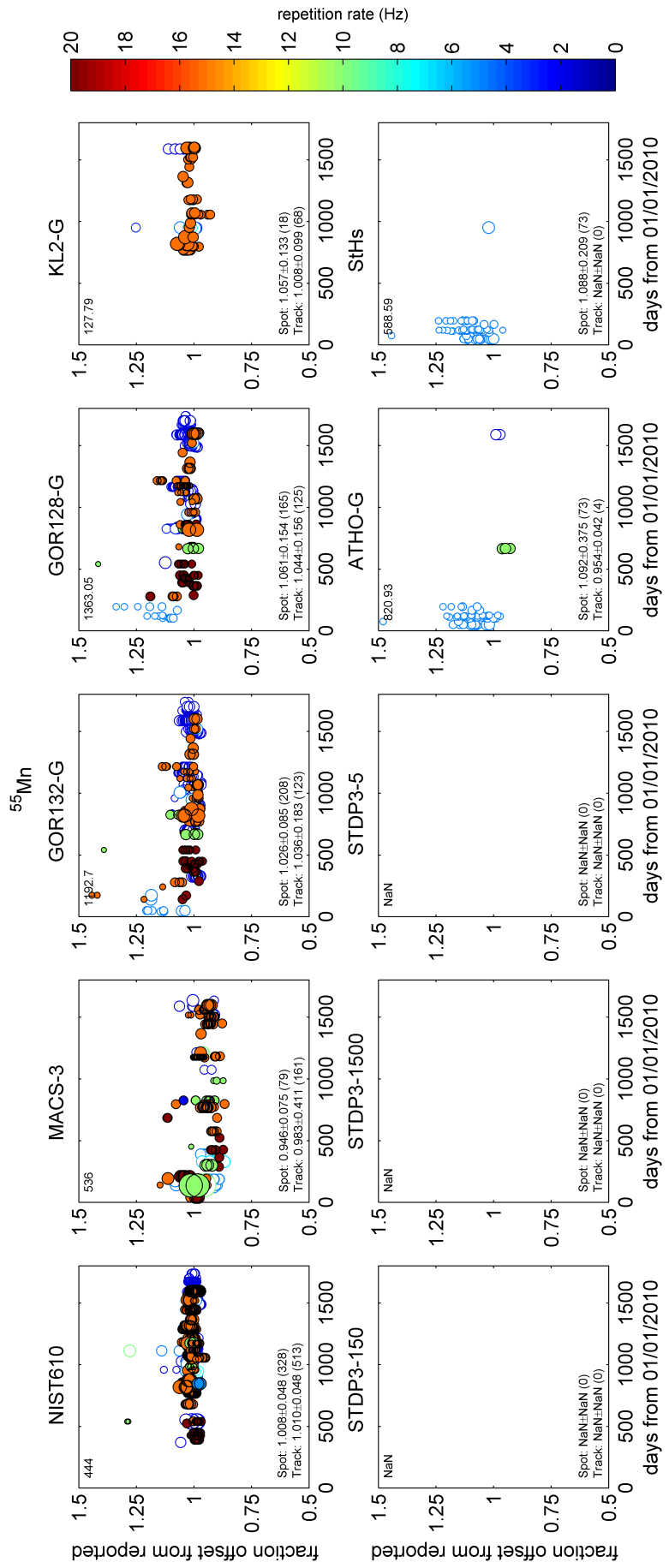
repetition rate (Hz)
20
18
16
14
12
10
8
6
4
2
0
^{55}Mn
NIST610
MACS-3
GOR132-G
STDP3-5
GOR128-G
ATHO-G
KL2-G
STHs
STDP3-150
STDP3-1500
fraction offset from reported
days from 01/01/2010
444
536
1392.7
NaN
1363.05
820.93
127.79
588.59
Spot: 1.008±0.048 (328)
Track: 1.010±0.048 (513)
Spot: 0.946±0.075 (79)
Track: 0.983±0.411 (161)
Spot: 1.026±0.085 (208)
Track: 1.036±0.183 (123)
Spot: NaN±NaN (0)
Track: NaN±NaN (0)
Spot: 1.061±0.154 (165)
Track: 1.044±0.156 (125)
Spot: 1.092±0.375 (73)
Track: 0.954±0.042 (4)
Spot: 1.057±0.133 (18)
Track: 1.008±0.099 (68)
Spot: 1.088±0.209 (73)
Track: NaN±NaN (0)

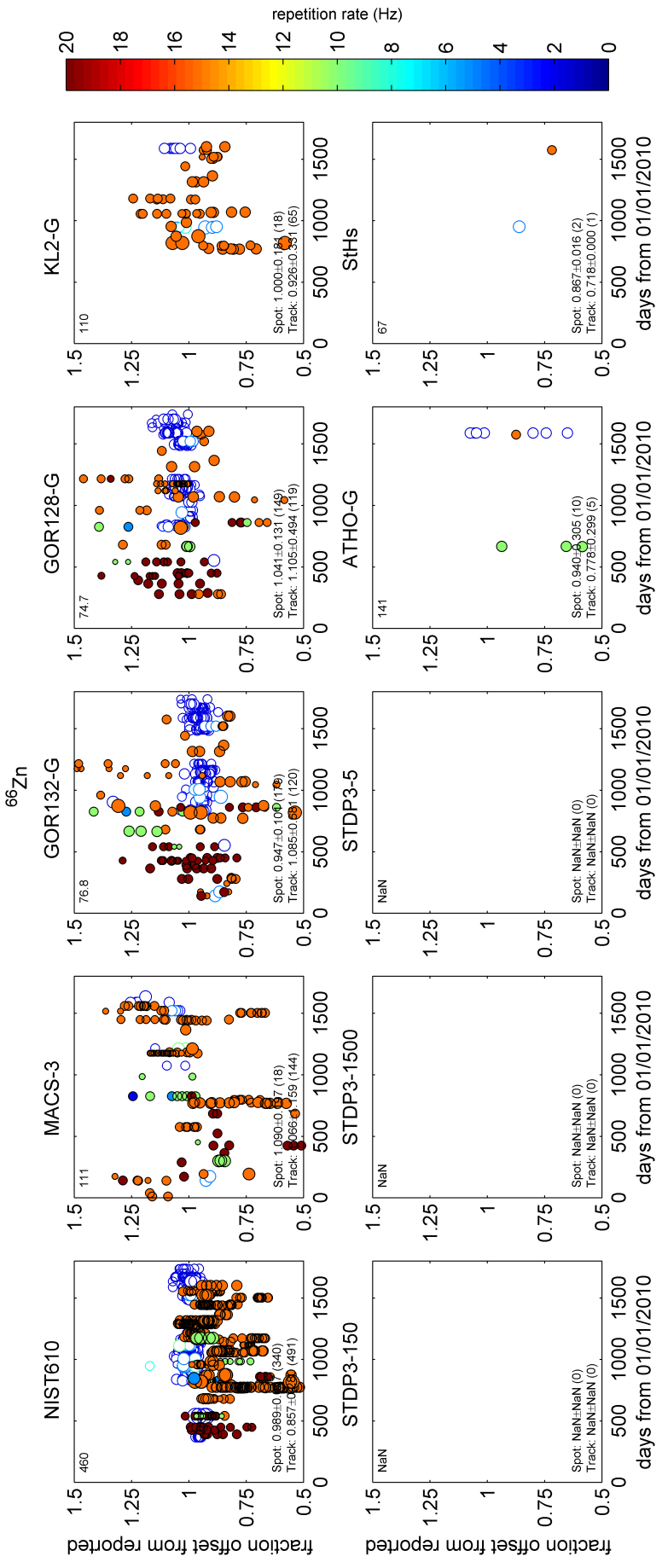
repetition rate (Hz)
20
18
16
14
12
10
8
6
4
2
0
^{66}Zn
NIST610
MACS-3
GOR132-G
STDP3-5
GOR128-G
ATHO-G
KL2-G
StHs
STDP3-150
STDP3-1500
fraction offset from reported
days from 01/01/2010
460
111
76.8
NaN
74.7
141
110
67
Spot: 0.989±0.(340) (491)
Track: 0.857±0.(491)
Spot: 1.090±0.17 (18)
Track: 1.066±0.159 (144)
Spot: 0.947±0.106 (178)
Track: 1.085±0.091 (120)
Spot: NaN±NaN (0)
Track: NaN±NaN (0)
Spot: 1.041±0.131 (149)
Track: 1.105±0.494 (119)
Spot: 0.940±0.305 (10)
Track: 0.778±0.299 (5)
Spot: 1.000±0.184 (18)
Track: 0.926±0.351 (65)
Spot: 0.867±0.016 (2)
Track: 0.718±0.000 (1)

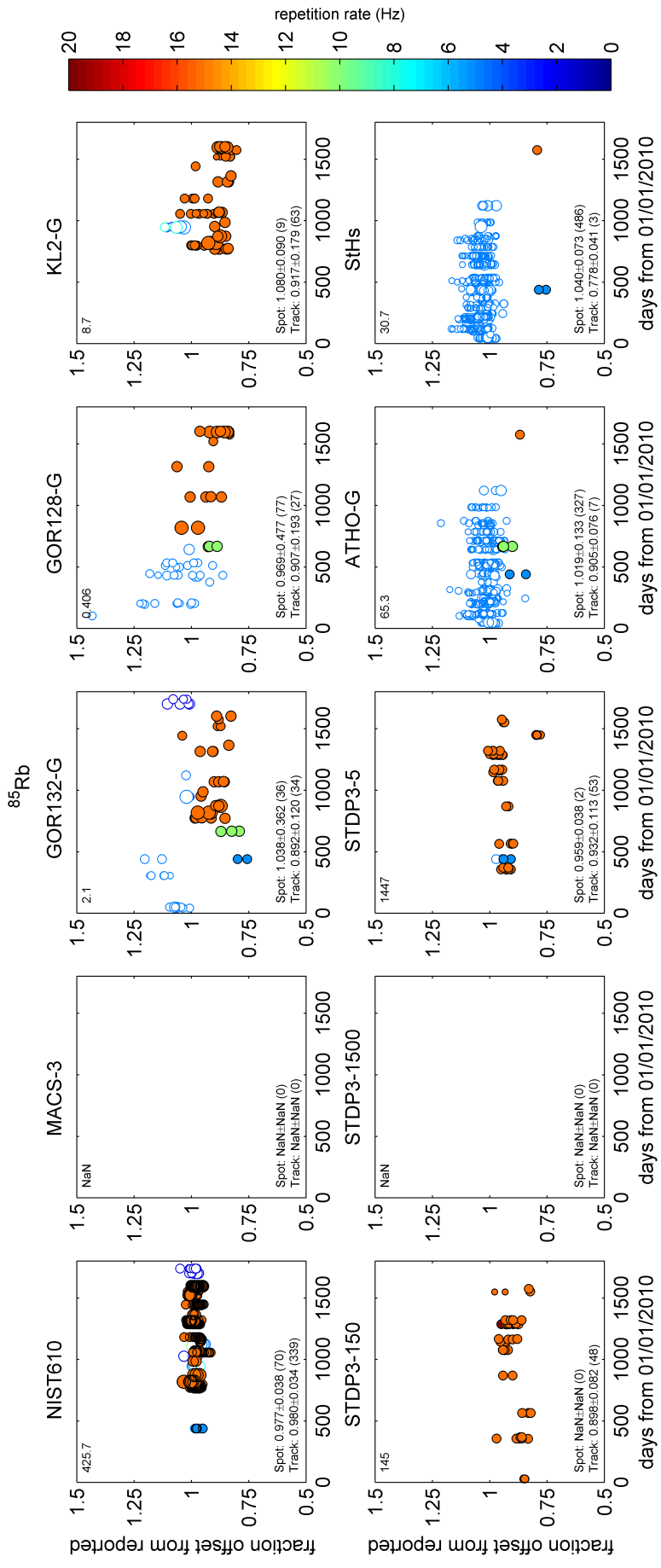
repetition rate (Hz)
20
18
16
14
12
10
8
6
4
2
0
^{85}Rb
NIST610
MACS-3
GOR132-G
GOR128-G
KL2-G
STDP3-150
STDP3-1500
STDP3-5
ATHO-G
StHs
fraction offset from reported
days from 01/01/2010
425.7
NaN
2.1
9.406
8.7
145
NaN
1447
65.3
30.7
Spot: 0.977±0.038 (70)
Track: 0.980±0.034 (339)
Spot: NaN±NaN (0)
Track: NaN±NaN (0)
Spot: 1.038±0.362 (36)
Track: 0.892±0.120 (34)
Spot: 0.969±0.477 (77)
Track: 0.907±0.193 (27)
Spot: 1.080±0.090 (9)
Track: 0.917±0.179 (63)
Spot: NaN±NaN (0)
Track: 0.898±0.082 (48)
Spot: NaN±NaN (0)
Track: NaN±NaN (0)
Spot: 0.959±0.038 (2)
Track: 0.932±0.113 (53)
Spot: 1.019±0.133 (327)
Track: 0.905±0.076 (7)
Spot: 1.040±0.073 (486)
Track: 0.778±0.041 (3)

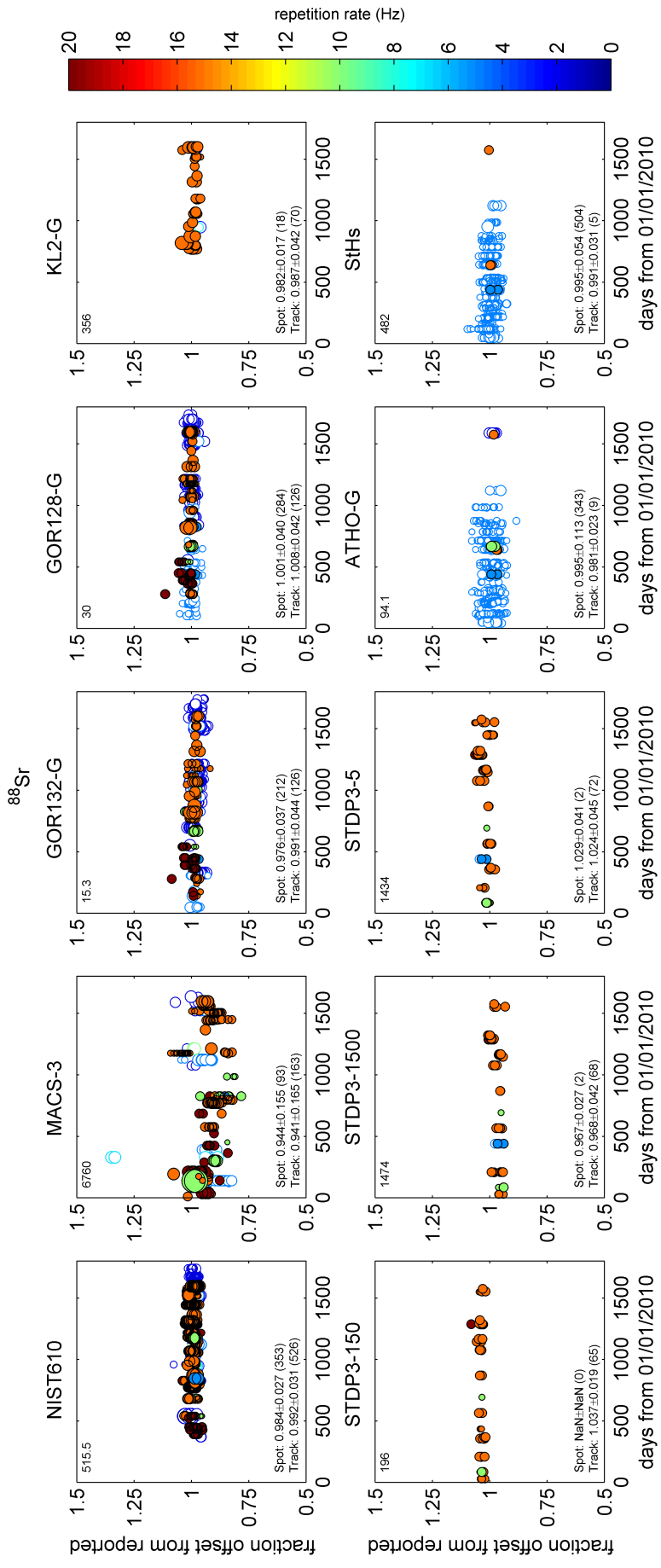
repetition rate (Hz)
20
18
16
14
12
10
8
6
4
2
0
^{88}Sr
NIST610
MACS-3
GOR132-G
STDP3-5
GOR128-G
ATHO-G
KL2-G
StHs
STDP3-150
STDP3-1500
GOR132-G
STDP3-5
GOR128-G
ATHO-G
KL2-G
StHs
515.5
6760
15.3
1434
30
94.1
356
482
196
1474
15.3
1434
30
94.1
356
482
Spot: 0.984±0.027 (353)
Track: 0.992±0.031 (526)
Spot: 0.944±0.155 (93)
Track: 0.941±0.165 (163)
Spot: 0.976±0.037 (212)
Track: 0.991±0.044 (126)
Spot: 1.029±0.041 (2)
Track: 1.024±0.045 (72)
Spot: 1.001±0.040 (284)
Track: 1.008±0.042 (126)
Spot: 0.995±0.113 (343)
Track: 0.981±0.023 (9)
Spot: 0.982±0.017 (18)
Track: 0.987±0.042 (70)
Spot: 0.995±0.054 (504)
Track: 0.991±0.031 (5)
Spot: NaN±NaN (0)
Track: 1.037±0.019 (65)
Spot: 0.967±0.027 (2)
Track: 0.968±0.042 (68)
fraction offset from reported
1.5
1.25
1
0.75
0.5
0
500
1000
1500
days from 01/01/2010

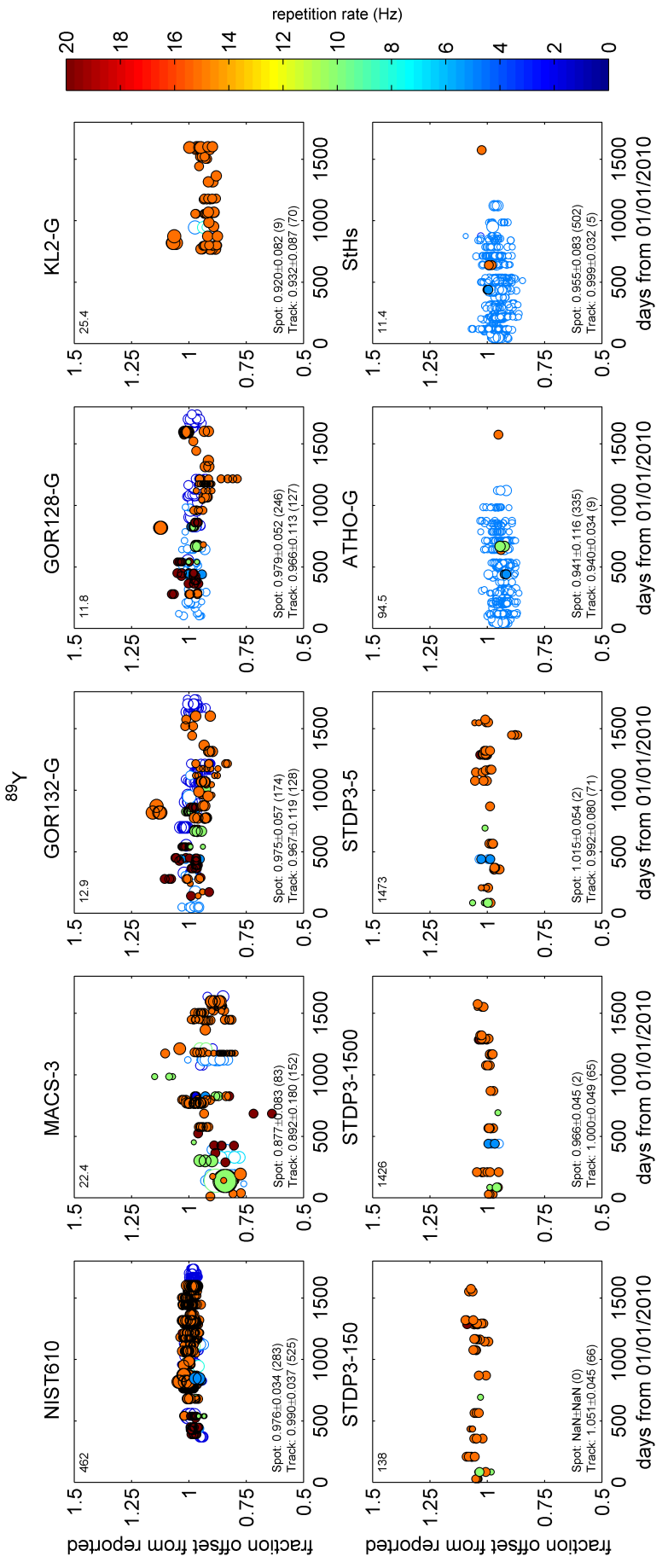
repetition rate (Hz)
20
18
16
14
12
10
8
6
4
2
0
89Y
NIST610
MACS-3
GOR132-G
STDP3-5
GOR128-G
ATHO-G
KL2-G
StHs
STDP3-150
STDP3-1500
GOR132-G
STDP3-5
GOR128-G
ATHO-G
KL2-G
StHs
fraction offset from reported
days from 01/01/2010
462
Spot: 0.976±0.034 (283)
Track: 0.990±0.037 (525)
22.4
Spot: 0.877±0.083 (83)
Track: 0.892±0.180 (152)
12.9
Spot: 0.975±0.057 (174)
Track: 0.967±0.119 (128)
1473
Spot: 1.015±0.054 (2)
Track: 0.992±0.080 (71)
11.8
Spot: 0.979±0.052 (246)
Track: 0.966±0.113 (127)
94.5
Spot: 0.941±0.116 (335)
Track: 0.940±0.034 (9)
25.4
Spot: 0.920±0.082 (9)
Track: 0.932±0.087 (70)
11.4
Spot: 0.955±0.083 (502)
Track: 0.999±0.032 (5)
138
Spot: NaN±NaN (0)
Track: 1.051±0.045 (66)
1426
Spot: 0.966±0.045 (2)
Track: 1.000±0.049 (65)

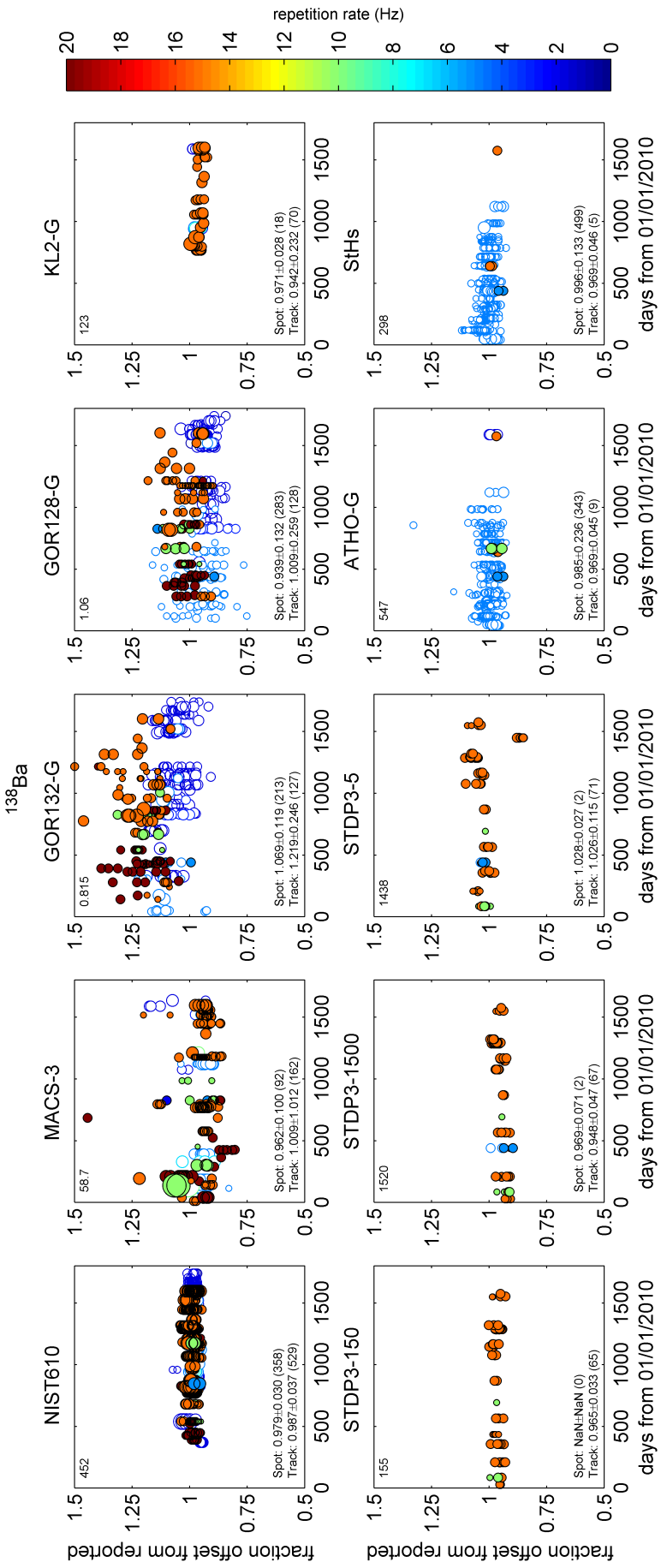
repetition rate (Hz)
20
18
16
14
12
10
8
6
4
2
0
^{138}Ba
NIST610
MACS-3
GOR132-G
GOR128-G
KL2-G
STDP3-150
STDP3-1500
STDP3-5
ATHO-G
StHs
fraction offset from reported
days from 01/01/2010
452
58.7
0.815
1.06
123
155
1520
1438
547
298
Spot: 0.979±0.030 (358)
Track: 0.987±0.037 (529)
Spot: 0.962±0.100 (92)
Track: 1.009±1.012 (162)
Spot: 1.069±0.119 (213)
Track: 1.219±0.246 (127)
Spot: 0.939±0.132 (283)
Track: 1.009±0.259 (128)
Spot: 0.971±0.028 (18)
Track: 0.942±0.232 (70)
Spot: NaN±NaN (0)
Track: 0.965±0.033 (65)
Spot: 0.969±0.071 (2)
Track: 0.948±0.047 (67)
Spot: 1.028±0.027 (2)
Track: 1.026±0.115 (71)
Spot: 0.985±0.236 (343)
Track: 0.969±0.045 (9)
Spot: 0.996±0.133 (499)
Track: 0.969±0.046 (5)

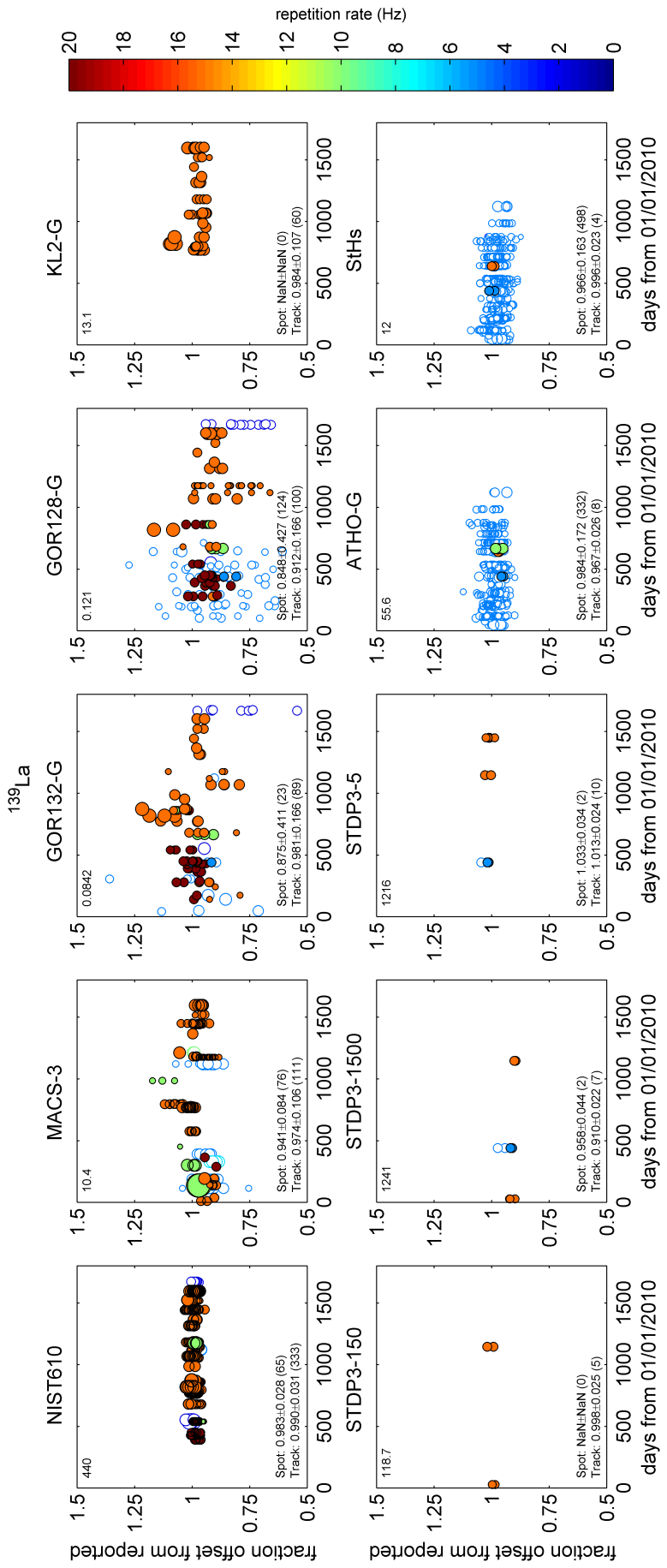
repetition rate (Hz)
20
18
16
14
12
10
8
6
4
2
0
^{139}La
NIST610
MACS-3
GOR132-G
GOR128-G
KL2-G
STDP3-150
STDP3-1500
STDP3-5
ATHO-G
StHs
fraction offset from reported
days from 01/01/2010
0
500
1000
1500
0.5
0.75
1
1.25
1.5
440
Spot: 0.983±0.028 (65)
Track: 0.990±0.031 (333)
10.4
Spot: 0.941±0.084 (76)
Track: 0.974±0.106 (111)
0.0842
Spot: 0.875±0.411 (23)
Track: 0.981±0.166 (89)
0.121
Spot: 0.848±0.427 (124)
Track: 0.912±0.166 (100)
13.1
Spot: NaN±NaN (0)
Track: 0.984±0.107 (60)
118.7
Spot: NaN±NaN (0)
Track: 0.998±0.025 (5)
1241
Spot: 0.958±0.044 (2)
Track: 0.910±0.022 (7)
1216
Spot: 1.033±0.034 (2)
Track: 1.013±0.024 (10)
55.6
Spot: 0.984±0.172 (332)
Track: 0.967±0.026 (8)
12
Spot: 0.966±0.163 (498)
Track: 0.996±0.023 (4)

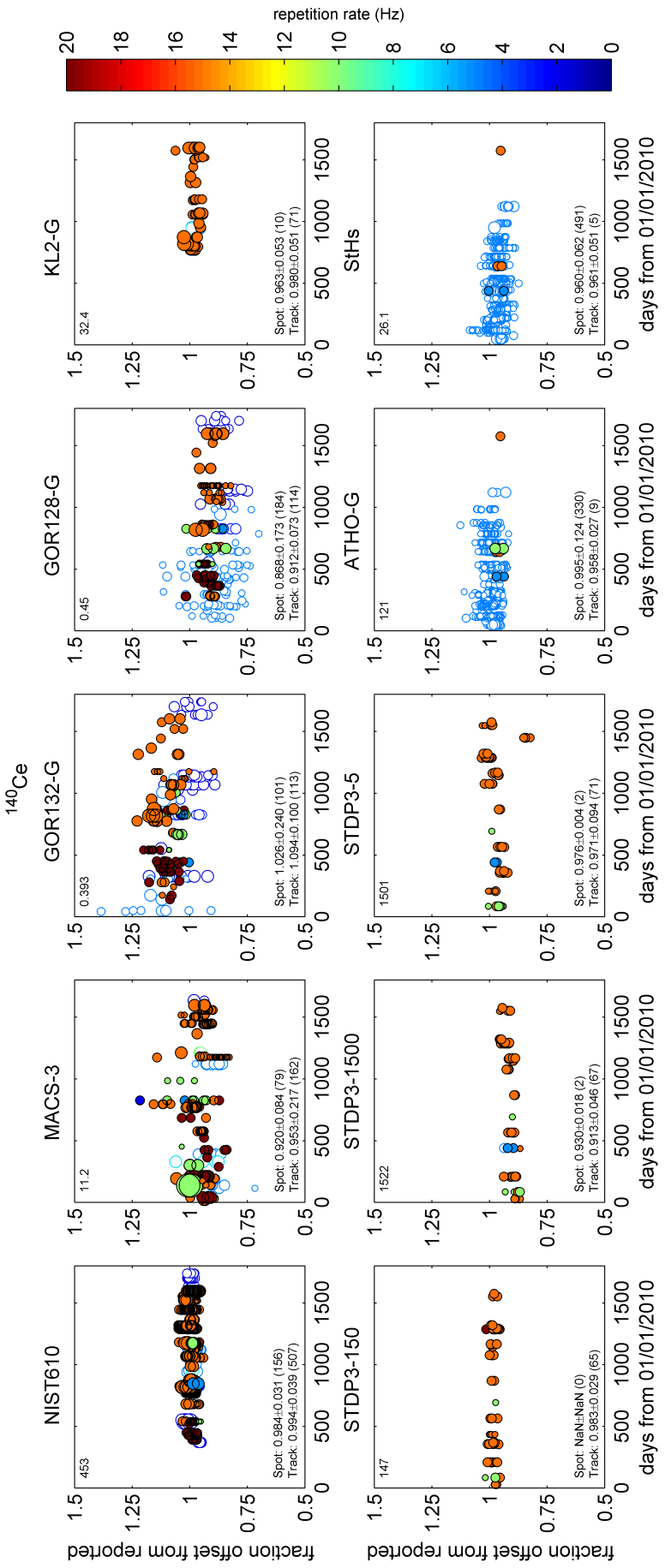
repetition rate (Hz)
20
18
16
14
12
10
8
6
4
2
0
^{140}Ce
NIST610
MACS-3
GOR132-G
GOR128-G
KL2-G
STDP3-150
STDP3-1500
STDP3-5
ATHO-G
StHs
fraction offset from reported
days from 01/01/2010
453
Spot: 0.984±0.031 (156)
Track: 0.994±0.039 (507)
11.2
Spot: 0.920±0.084 (79)
Track: 0.953±0.217 (162)
0.393
Spot: 1.026±0.240 (101)
Track: 1.094±0.100 (113)
0.45
Spot: 0.868±0.173 (184)
Track: 0.912±0.073 (114)
32.4
Spot: 0.963±0.053 (10)
Track: 0.980±0.051 (71)
147
Spot: NaN±NaN (0)
Track: 0.983±0.029 (65)
1522
Spot: 0.930±0.018 (2)
Track: 0.913±0.046 (67)
1501
Spot: 0.976±0.004 (2)
Track: 0.971±0.094 (71)
121
Spot: 0.995±0.124 (330)
Track: 0.958±0.027 (9)
26.1
Spot: 0.960±0.062 (491)
Track: 0.961±0.051 (5)

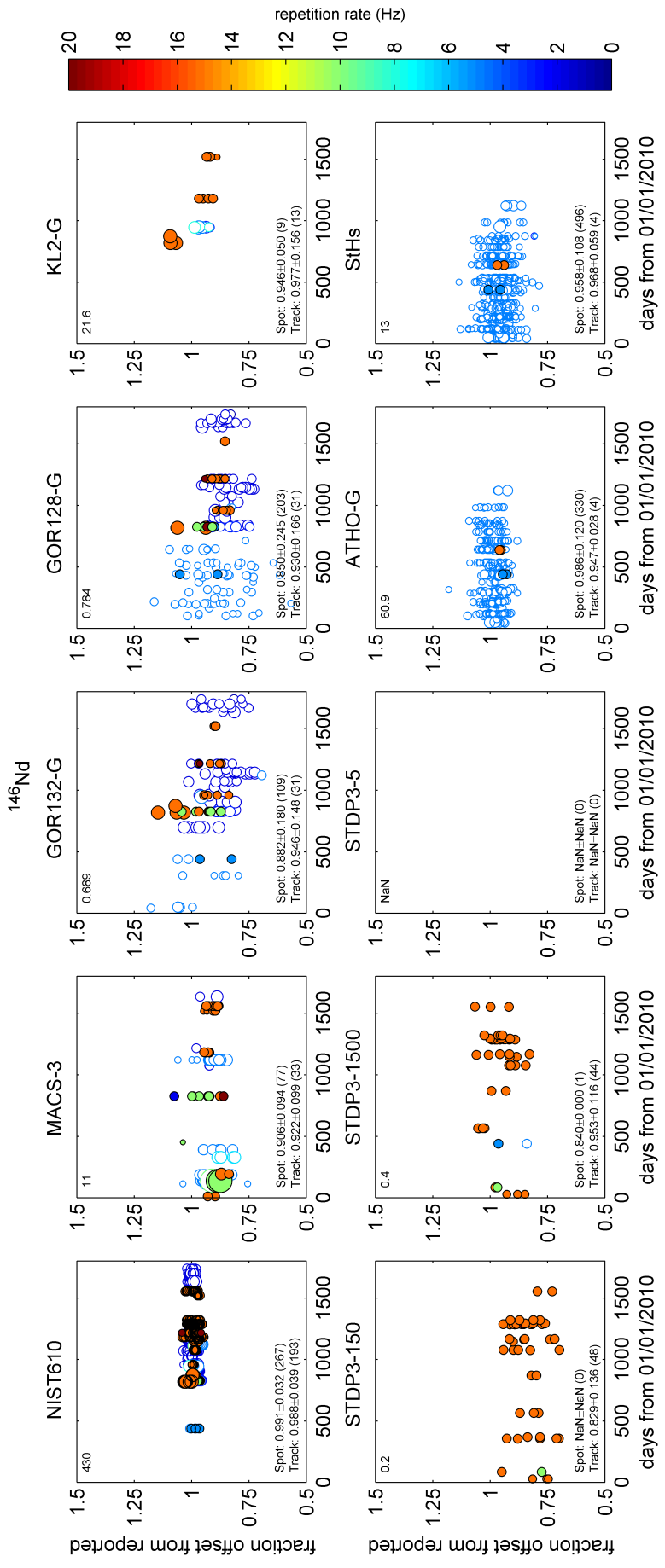
repetition rate (Hz)
20
18
16
14
12
10
8
6
4
2
0
^{146}Nd
NIST610
MACS-3
GOR132-G
STDP3-5
GOR128-G
ATHO-G
KL2-G
StHs
STDP3-150
STDP3-1500
STDP3-5
ATHO-G
StHs
fraction offset from reported
days from 01/01/2010
Spot: 0.991±0.032 (267)
Track: 0.988±0.039 (193)
Spot: 0.906±0.094 (77)
Track: 0.922±0.099 (33)
Spot: 0.882±0.180 (109)
Track: 0.946±0.148 (31)
Spot: NaN±NaN (0)
Track: NaN±NaN (0)
Spot: 0.850±0.245 (203)
Track: 0.930±0.166 (31)
Spot: 0.986±0.120 (330)
Track: 0.947±0.028 (4)
Spot: 0.946±0.050 (9)
Track: 0.977±0.156 (13)
Spot: 0.958±0.108 (496)
Track: 0.968±0.059 (4)
Spot: NaN±NaN (0)
Track: 0.829±0.136 (48)
Spot: 0.840±0.000 (1)
Track: 0.953±0.116 (44)

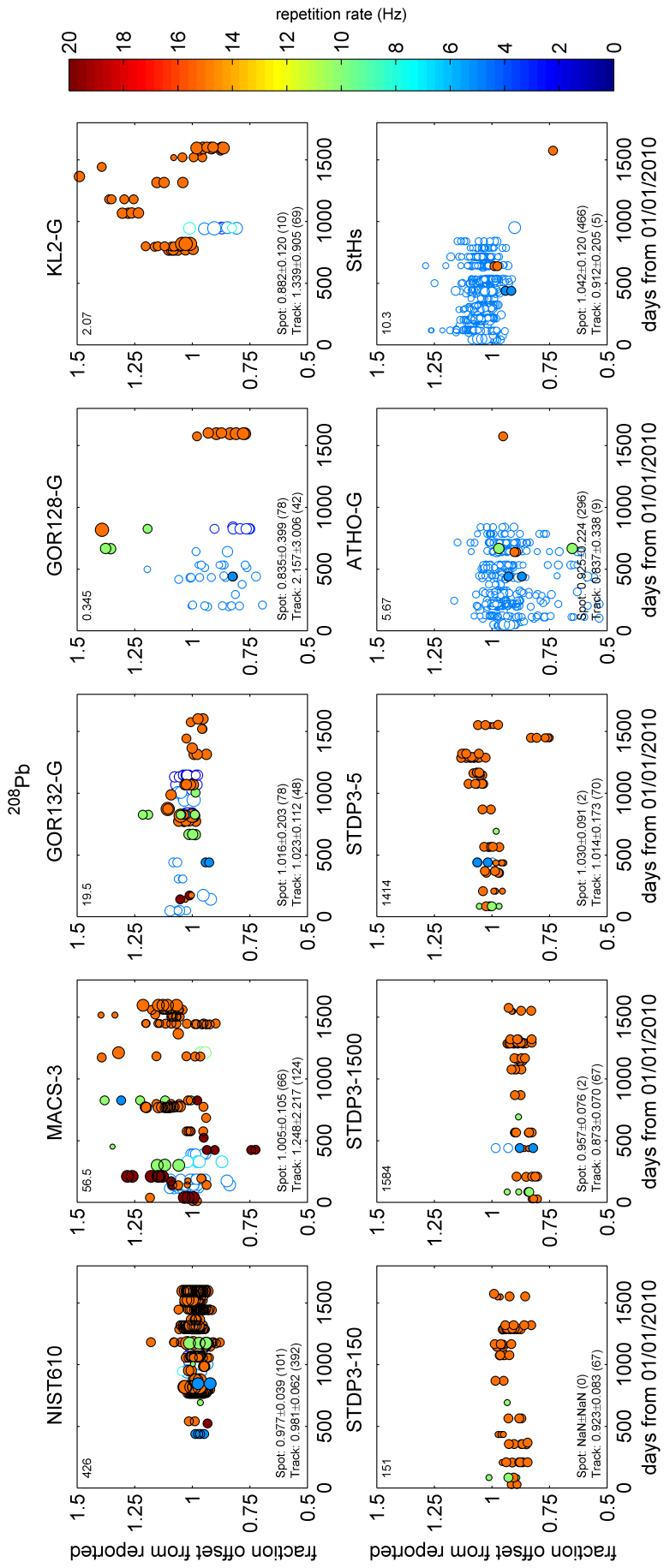
repetition rate (Hz)
20
18
16
14
12
10
8
6
4
2
0
^{208}Pb
NIST610
MACS-3
GOR132-G
GOR128-G
KL2-G
STDP3-150
STDP3-1500
STDP3-5
ATHO-G
StHs
fraction offset from reported
days from 01/01/2010
426
56.5
19.5
0.345
2.07
151
1584
1414
5.67
10.3
Spot: 0.977±0.039 (101)
Track: 0.981±0.062 (392)
Spot: 1.005±0.105 (66)
Track: 1.248±2.217 (124)
Spot: 1.016±0.203 (78)
Track: 1.023±0.112 (48)
Spot: 0.835±0.399 (78)
Track: 2.157±3.006 (42)
Spot: 0.882±0.120 (10)
Track: 1.339±0.905 (69)
Spot: NaN±NaN (0)
Track: 0.923±0.083 (67)
Spot: 0.957±0.076 (2)
Track: 0.873±0.070 (67)
Spot: 1.030±0.091 (2)
Track: 1.014±0.173 (70)
Spot: 0.925±0.224 (296)
Track: 0.837±0.338 (9)
Spot: 1.042±0.120 (466)
Track: 0.912±0.205 (5)

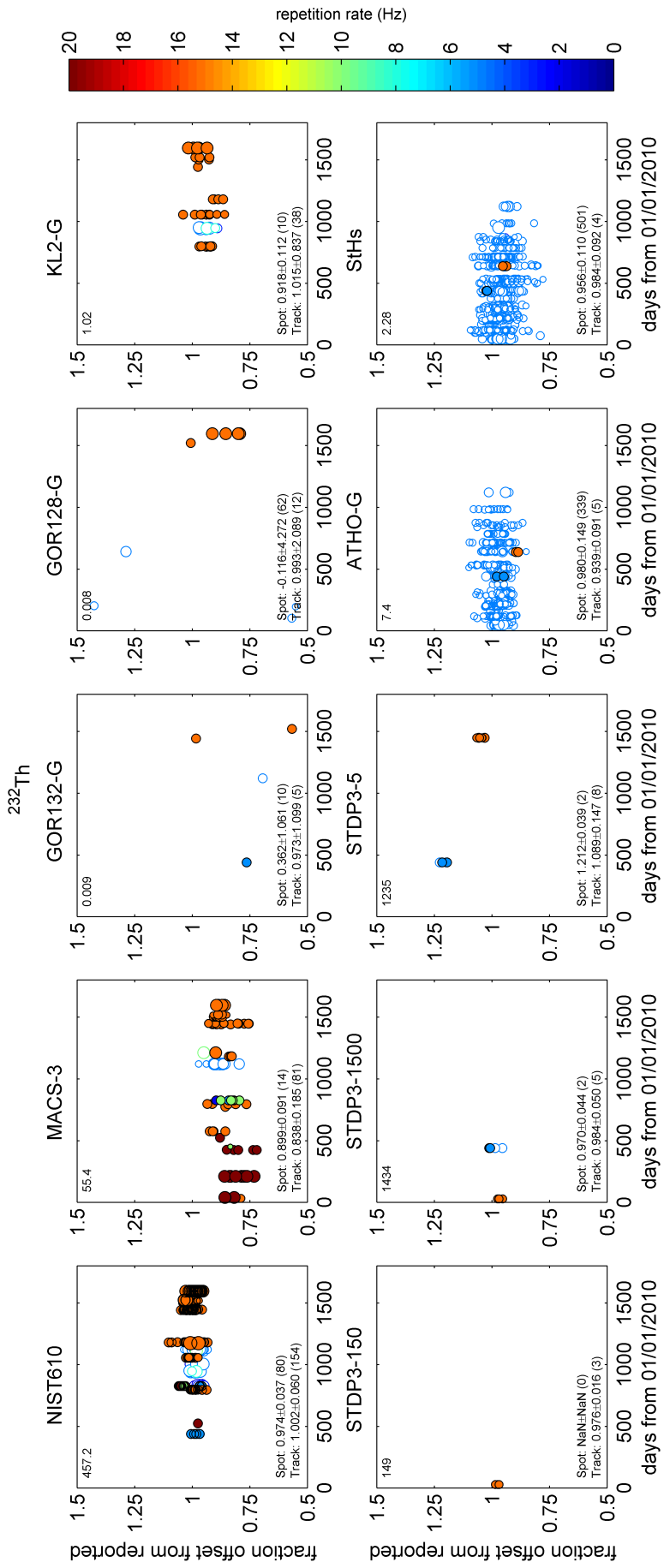
repetition rate (Hz)
20
18
16
14
12
10
8
6
4
2
0
^{232}Th
NIST610
MACS-3
GOR132-G
STDP3-5
GOR128-G
ATHO-G
KL2-G
StHs
STDP3-150
STDP3-1500
GOR132-G
STDP3-5
GOR128-G
ATHO-G
StHs
fraction offset from reported
days from 01/01/2010
457.2
Spot: 0.974±0.037 (80)
Track: 1.002±0.060 (154)
55.4
Spot: 0.899±0.091 (14)
Track: 0.838±0.185 (81)
0.009
Spot: 0.362±1.061 (10)
Track: 0.973±1.099 (5)
1235
Spot: 1.212±0.039 (2)
Track: 1.089±0.147 (8)
0.008
Spot: -0.116±4.272 (62)
Track: 0.993±2.089 (12)
7.4
Spot: 0.980±0.149 (339)
Track: 0.939±0.091 (5)
1.02
Spot: 0.918±0.112 (10)
Track: 1.015±0.837 (38)
2.28
Spot: 0.956±0.110 (501)
Track: 0.984±0.092 (4)
149
Spot: NaN±NaN (0)
Track: 0.976±0.016 (3)
1434
Spot: 0.970±0.044 (2)
Track: 0.984±0.050 (5)

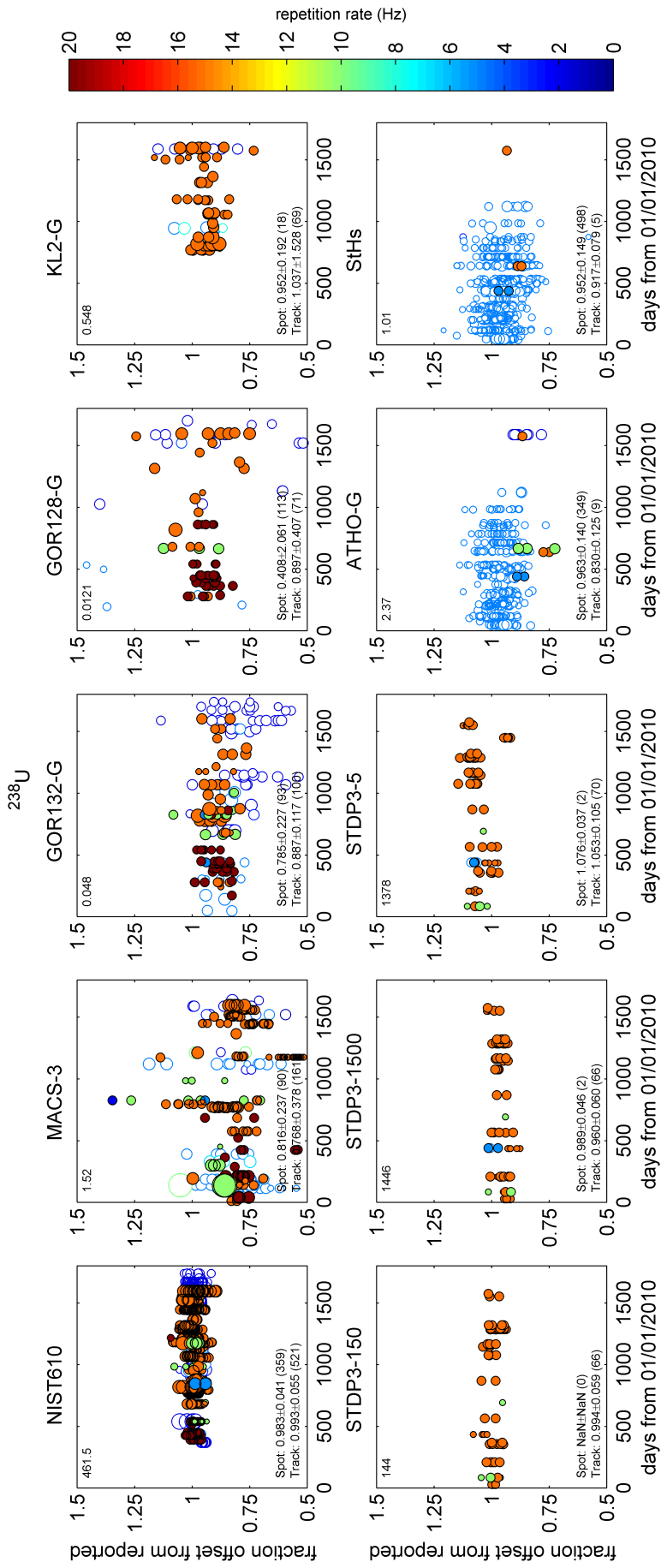
repetition rate (Hz)
20
18
16
14
12
10
8
6
4
2
0
^{238}U
NIST610
MACS-3
GOR132-G
STDP3-5
GOR128-G
ATHO-G
KL2-G
StHs
STDP3-150
STDP3-1500
fraction offset from reported
days from 01/01/2010
461.5
Spot: 0.983±0.041 (359)
Track: 0.993±0.055 (521)
1.52
Spot: 0.816±0.237 (90)
Track: 0.768±0.378 (161)
0.048
Spot: 0.785±0.227 (93)
Track: 0.887±0.117 (106)
1378
Spot: 1.076±0.037 (2)
Track: 1.053±0.105 (70)
0.0121
Spot: 0.408±2.061 (113)
Track: 0.897±0.407 (71)
2.37
Spot: 0.963±0.140 (349)
Track: 0.830±0.125 (9)
0.548
Spot: 0.952±0.192 (18)
Track: 1.037±1.528 (69)
1.01
Spot: 0.952±0.149 (498)
Track: 0.917±0.079 (5)
144
Spot: NaN±NaN (0)
Track: 0.994±0.059 (66)
1446
Spot: 0.989±0.046 (2)
Track: 0.960±0.060 (66)

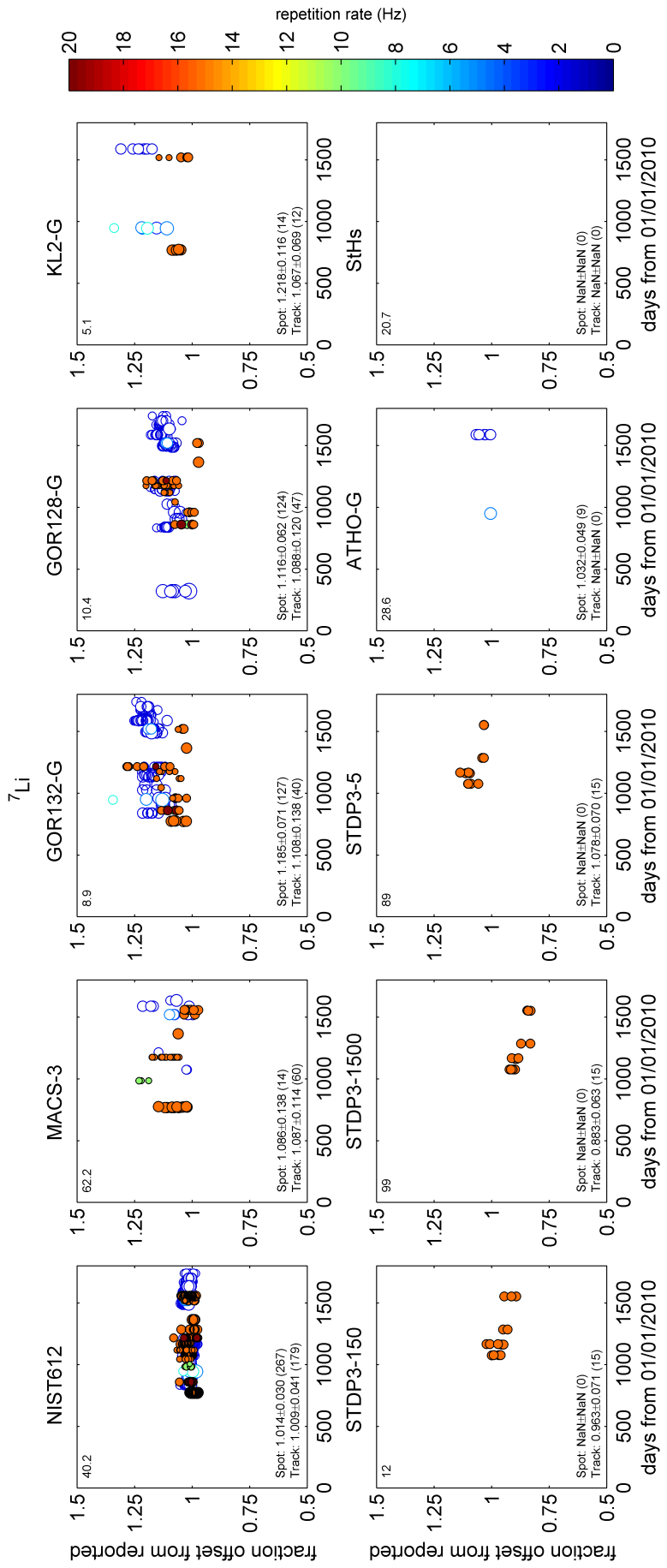
repetition rate (Hz)
0
2
4
6
8
10
12
14
16
18
20
^{7}Li
NIST612
MACS-3
GOR132-G
STDP3-5
GOR128-G
ATHO-G
KL2-G
StHs
STDP3-150
STDP3-1500
fraction offset from reported
days from 01/01/2010
Spot: 1.014±0.030 (267)
Track: 1.009±0.041 (179)
Spot: 1.086±0.138 (14)
Track: 1.087±0.114 (60)
Spot: 1.185±0.071 (127)
Track: 1.108±0.138 (40)
Spot: NaN±NaN (0)
Track: 1.078±0.070 (15)
Spot: 1.116±0.062 (124)
Track: 1.088±0.120 (47)
Spot: NaN±NaN (0)
Track: NaN±NaN (0)
Spot: 1.218±0.116 (14)
Track: 1.067±0.069 (12)
Spot: NaN±NaN (0)
Track: 0.963±0.071 (15)
Spot: NaN±NaN (0)
Track: 0.883±0.063 (15)
Spot: 1.032±0.049 (9)
Track: NaN±NaN (0)
Spot: NaN±NaN (0)
Track: NaN±NaN (0)

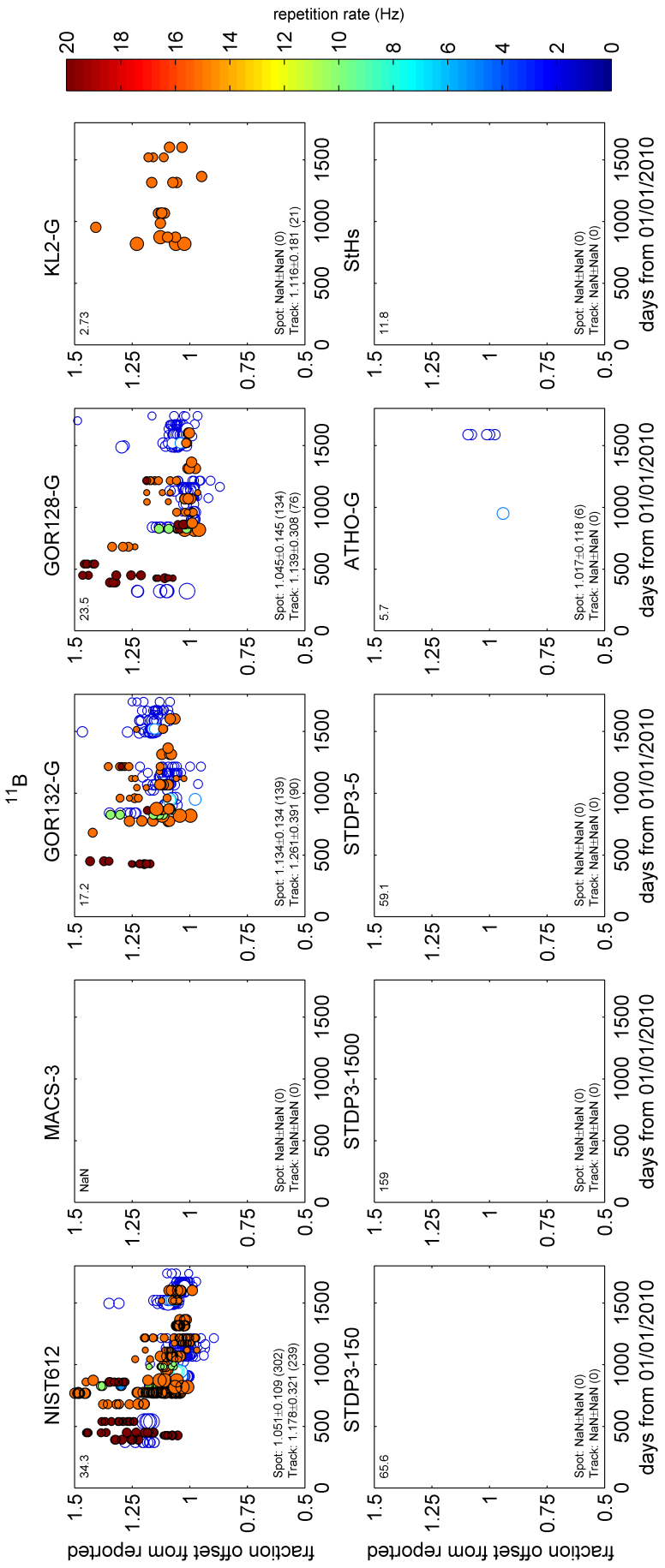
repetition rate (Hz)
20
18
16
14
12
10
8
6
4
2
0
^{11}B
NIST612
MACS-3
GOR132-G
GOR128-G
KL2-G
STDP3-150
STDP3-1500
STDP3-5
ATHO-G
StHs
fraction offset from reported
days from 01/01/2010
34.3
NaN
17.2
23.5
2.73
65.6
159
59.1
5.7
11.8
Spot: 1.051±0.109 (302)
Track: 1.178±0.321 (239)
Spot: NaN±NaN (0)
Track: NaN±NaN (0)
Spot: 1.134±0.134 (139)
Track: 1.261±0.391 (90)
Spot: 1.045±0.145 (134)
Track: 1.139±0.308 (76)
Spot: 1.116±0.181 (21)
Spot: 1.017±0.118 (6)

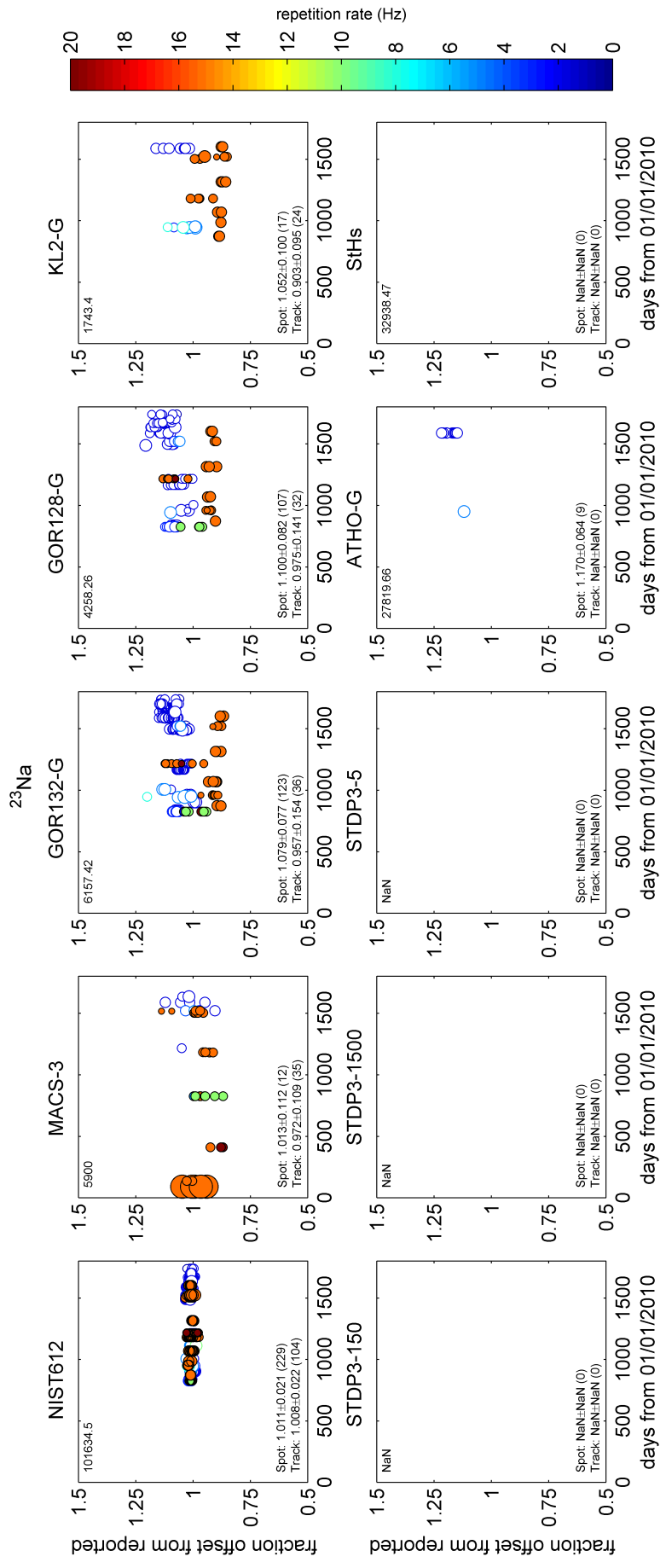
repetition rate (Hz)
20
18
16
14
12
10
8
6
4
2
0
^{23}Na
NIST612
MACS-3
GOR132-G
STDP3-5
GOR128-G
ATHO-G
KL2-G
StHs
STDP3-150
STDP3-1500
fraction offset from reported
days from 01/01/2010
101634.5
5900
6157.42
NaN
4258.26
27819.66
1743.4
32938.47
Spot: 1.011±0.021 (229)
Track: 1.008±0.022 (104)
Spot: 1.013±0.112 (12)
Track: 0.972±0.109 (35)
Spot: 1.079±0.077 (123)
Track: 0.957±0.154 (36)
Spot: NaN±NaN (0)
Track: NaN±NaN (0)
Spot: 1.100±0.082 (107)
Track: 0.975±0.141 (32)
Spot: 1.170±0.064 (9)
Track: NaN±NaN (0)
Spot: 1.052±0.100 (17)
Track: 0.903±0.095 (24)
Spot: NaN±NaN (0)
Track: NaN±NaN (0)

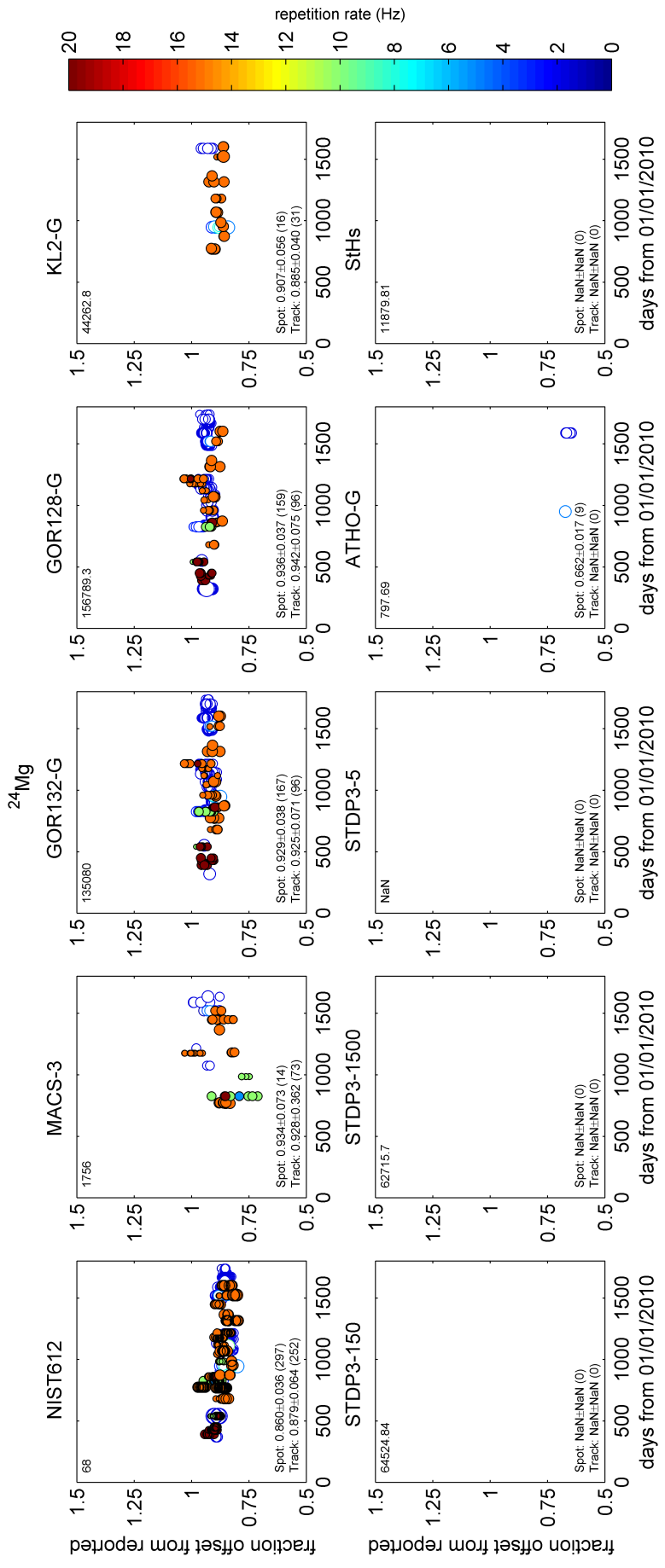
repetition rate (Hz)
0
2
4
6
8
10
12
14
16
18
20
^{24}Mg
NIST612
MACS-3
GOR132-G
STDP3-5
GOR128-G
ATHO-G
KL2-G
StHs
STDP3-150
STDP3-1500
STDP3-5
ATHO-G
StHs
fraction offset from reported
days from 01/01/2010
0.5
0.75
1
1.25
1.5
0
500
1000
1500
68
1756
135080
NaN
156789.3
797.69
44262.8
11879.81
64524.84
62715.7
Spot: 0.860±0.036 (297)
Track: 0.879±0.064 (252)
Spot: 0.934±0.073 (14)
Track: 0.928±0.362 (73)
Spot: 0.929±0.038 (167)
Track: 0.925±0.071 (96)
Spot: NaN±NaN (0)
Track: NaN±NaN (0)
Spot: 0.936±0.037 (159)
Track: 0.942±0.075 (96)
Spot: 0.662±0.017 (9)
Track: NaN±NaN (0)
Spot: 0.907±0.056 (16)
Track: 0.885±0.040 (31)
Spot: NaN±NaN (0)
Track: NaN±NaN (0)

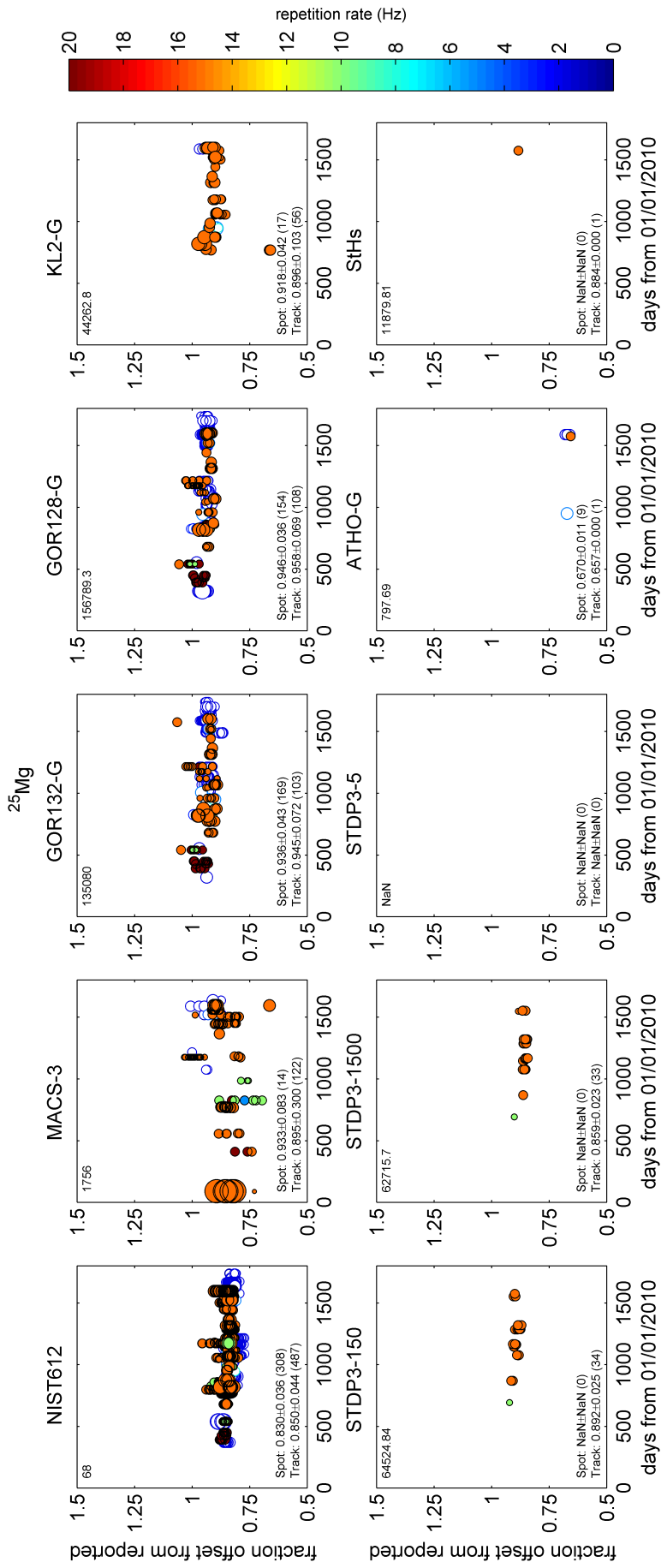
repetition rate (Hz)
20
18
16
14
12
10
8
6
4
2
0
^{25}Mg
NIST612
MACS-3
GOR132-G
STDP3-5
ATHO-G
StHs
GOR128-G
KL2-G
STDP3-150
STDP3-1500
STDP3-5
ATHO-G
StHs
GOR128-G
KL2-G
fraction offset from reported
days from 01/01/2010
68
1756
135080
NaN
797.69
11879.81
156789.3
44262.8
64524.84
62715.7
Spot: 0.830±0.036 (308)
Track: 0.850±0.044 (487)
Spot: 0.933±0.083 (14)
Track: 0.895±0.300 (122)
Spot: 0.936±0.043 (169)
Track: 0.945±0.072 (103)
Spot: NaN±NaN (0)
Track: NaN±NaN (0)
Spot: 0.670±0.011 (9)
Track: 0.657±0.000 (1)
Spot: NaN±NaN (0)
Track: 0.884±0.000 (1)
Spot: 0.946±0.036 (154)
Track: 0.958±0.069 (108)
Spot: 0.918±0.042 (17)
Track: 0.896±0.103 (56)
Spot: NaN±NaN (0)
Track: 0.892±0.025 (34)
Spot: NaN±NaN (0)
Track: 0.859±0.023 (33)

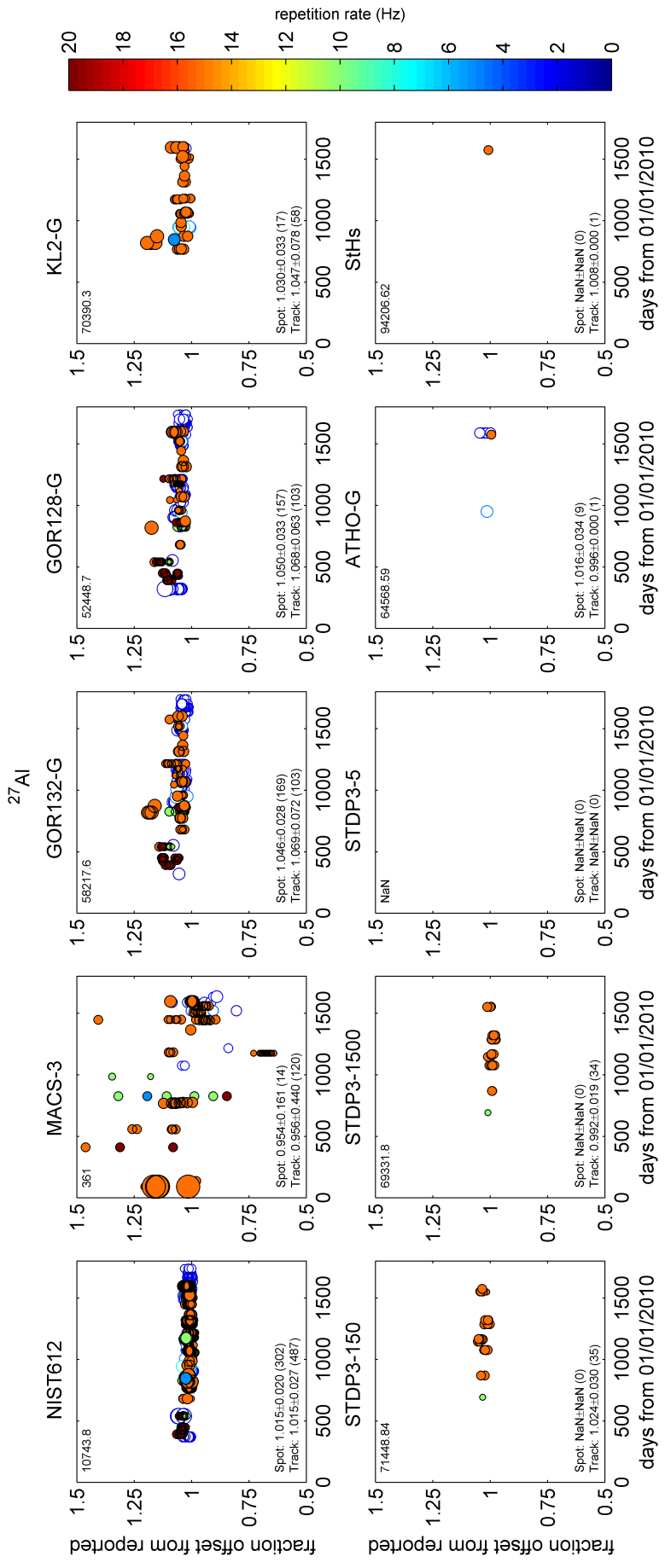
repetition rate (Hz)
20
18
16
14
12
10
8
6
4
2
0
^{27}Al
NIST612
MACS-3
GOR132-G
STDP3-5
GOR128-G
ATHO-G
KL2-G
StHs
STDP3-150
STDP3-1500
fraction offset from reported
days from 01/01/2010
10743.8
Spot: 1.015±0.020 (302)
Track: 1.015±0.027 (487)
361
Spot: 0.954±0.161 (14)
Track: 0.956±0.440 (120)
58217.6
Spot: 1.046±0.028 (169)
Track: 1.069±0.072 (103)
NaN
Spot: NaN±NaN (0)
Track: NaN±NaN (0)
52448.7
Spot: 1.050±0.033 (157)
Track: 1.068±0.063 (103)
64568.59
Spot: 1.016±0.034 (9)
Track: 0.996±0.000 (1)
70390.3
Spot: 1.030±0.033 (17)
Track: 1.047±0.078 (58)
94206.62
Spot: NaN±NaN (0)
Track: 1.008±0.000 (1)
71448.84
Spot: NaN±NaN (0)
Track: 1.024±0.030 (35)
69331.8
Spot: NaN±NaN (0)
Track: 0.992±0.019 (34)

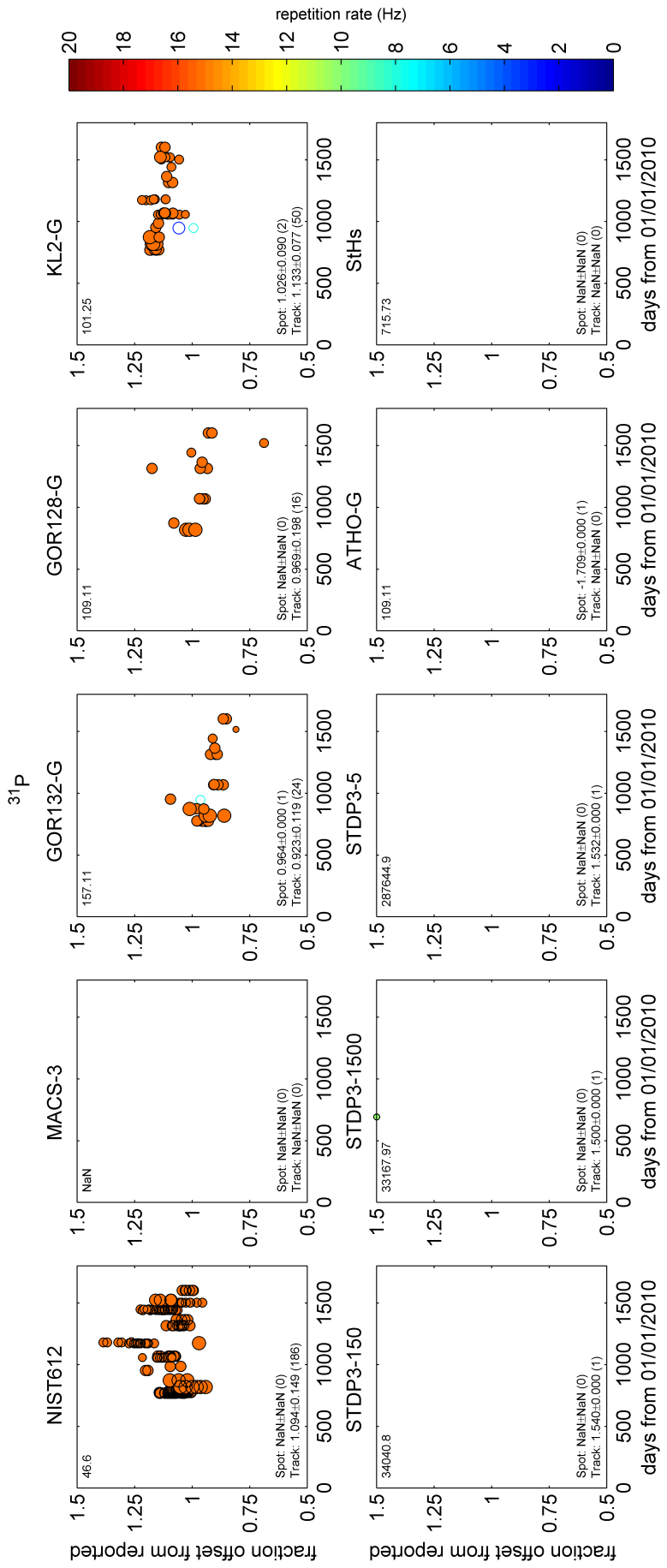
repetition rate (Hz)
20
18
16
14
12
10
8
6
4
2
0
^{31}P
NIST612
MACS-3
GOR132-G
GOR128-G
KL2-G
STDP3-150
STDP3-1500
STDP3-5
ATHO-G
StHs
fraction offset from reported
days from 01/01/2010
46.6
NaN
157.11
109.11
101.25
34040.8
33167.97
287644.9
109.11
715.73
Spot: NaN±NaN (0)
Track: 1.094±0.149 (186)
Spot: NaN±NaN (0)
Track: NaN±NaN (0)
Spot: 0.964±0.000 (1)
Track: 0.923±0.119 (24)
Spot: NaN±NaN (0)
Track: 0.969±0.198 (16)
Spot: 1.026±0.090 (2)
Track: 1.133±0.077 (50)
Spot: NaN±NaN (0)
Track: 1.540±0.000 (1)
Spot: NaN±NaN (0)
Track: 1.500±0.000 (1)
Spot: NaN±NaN (0)
Track: 1.532±0.000 (1)
Spot: -1.709±0.000 (1)
Track: NaN±NaN (0)
Spot: NaN±NaN (0)
Track: NaN±NaN (0)

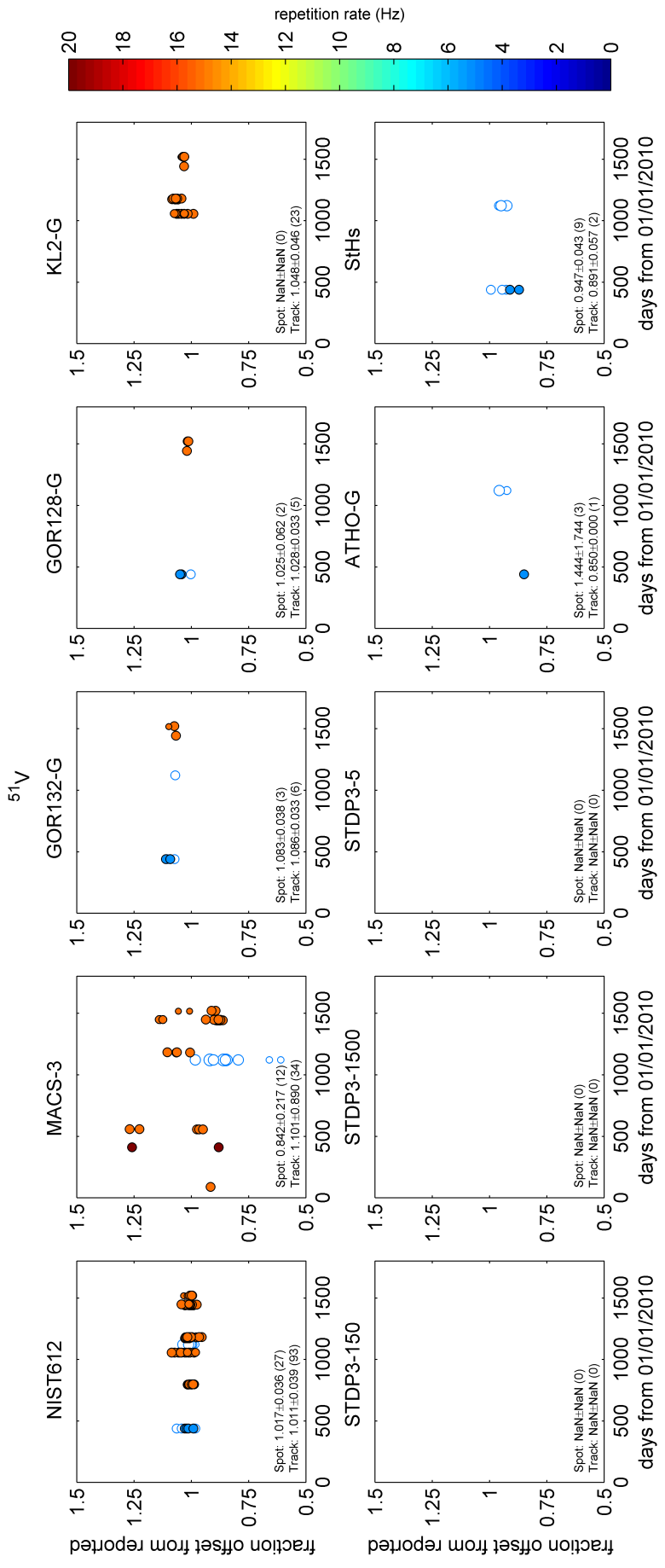
^{51}V
repetition rate (Hz)
20
18
16
14
12
10
8
6
4
2
0
NIST612
MACS-3
GOR132-G
GOR128-G
KL2-G
STDP3-150
STDP3-1500
STDP3-5
ATHO-G
StHs
Spot: 1.017±0.036 (27)
Track: 1.011±0.039 (93)
Spot: 0.842±0.217 (12)
Track: 1.101±0.890 (34)
Spot: 1.083±0.038 (3)
Track: 1.086±0.033 (6)
Spot: 1.025±0.062 (2)
Track: 1.028±0.033 (5)
Spot: NaN±NaN (0)
Track: 1.048±0.046 (23)
Spot: NaN±NaN (0)
Track: NaN±NaN (0)
Spot: NaN±NaN (0)
Track: NaN±NaN (0)
Spot: NaN±NaN (0)
Track: NaN±NaN (0)
Spot: 1.444±1.744 (3)
Track: 0.850±0.000 (1)
Spot: 0.947±0.043 (9)
Track: 0.891±0.057 (2)
fraction offset from reported
days from 01/01/2010
0.5
0.75
1
1.25
1.5
0
500
1000
1500

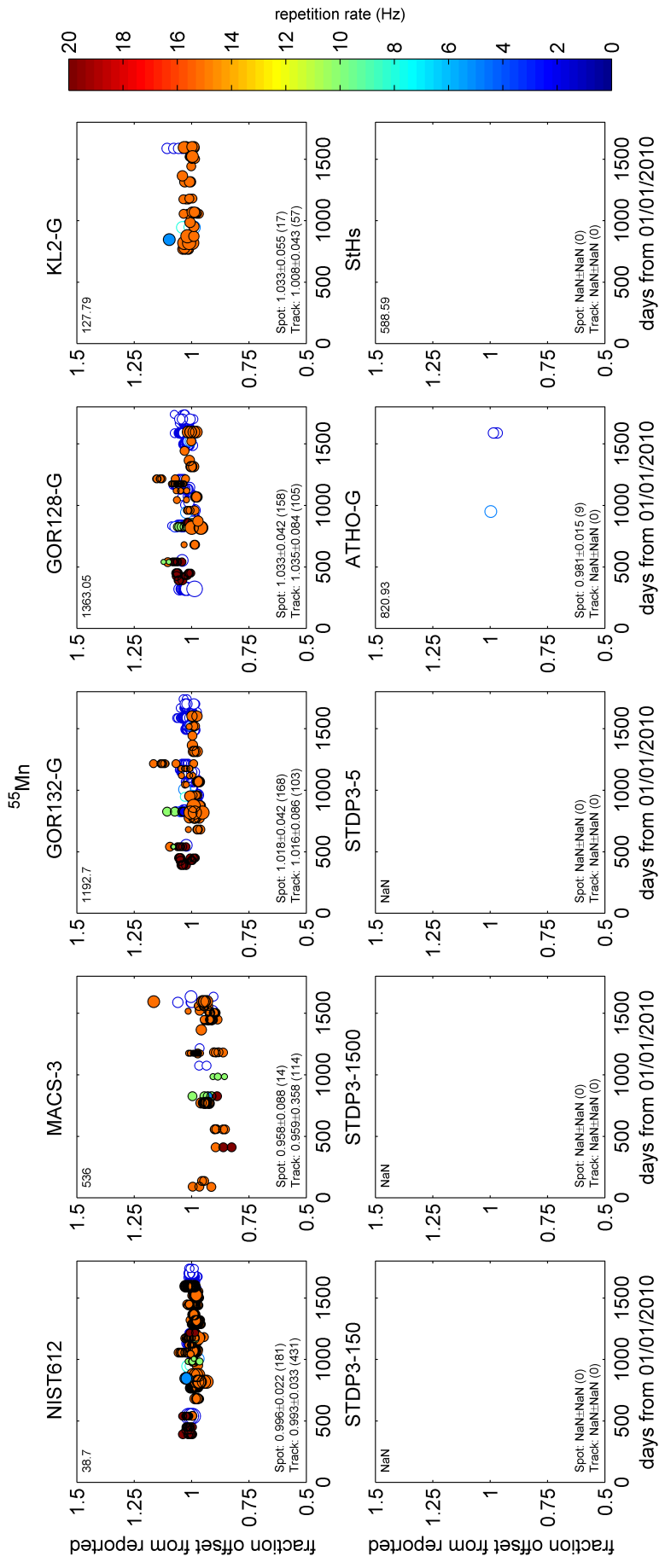
repetition rate (Hz)
20
18
16
14
12
10
8
6
4
2
0
^{55}Mn
NIST612
MACS-3
GOR132-G
GOR128-G
KL2-G
STDP3-150
STDP3-1500
STDP3-5
ATHO-G
StHs
fraction offset from reported
days from 01/01/2010
38.7
536
1192.7
1363.05
127.79
588.59
820.93
NaN
Spot: 0.996±0.022 (181)
Track: 0.993±0.033 (431)
Spot: 0.958±0.088 (14)
Track: 0.959±0.358 (114)
Spot: 1.018±0.042 (168)
Track: 1.016±0.086 (103)
Spot: 1.033±0.042 (158)
Track: 1.035±0.084 (105)
Spot: 1.033±0.055 (17)
Track: 1.008±0.043 (57)
Spot: 0.981±0.015 (9)
Spot: NaN±NaN (0)
Track: NaN±NaN (0)

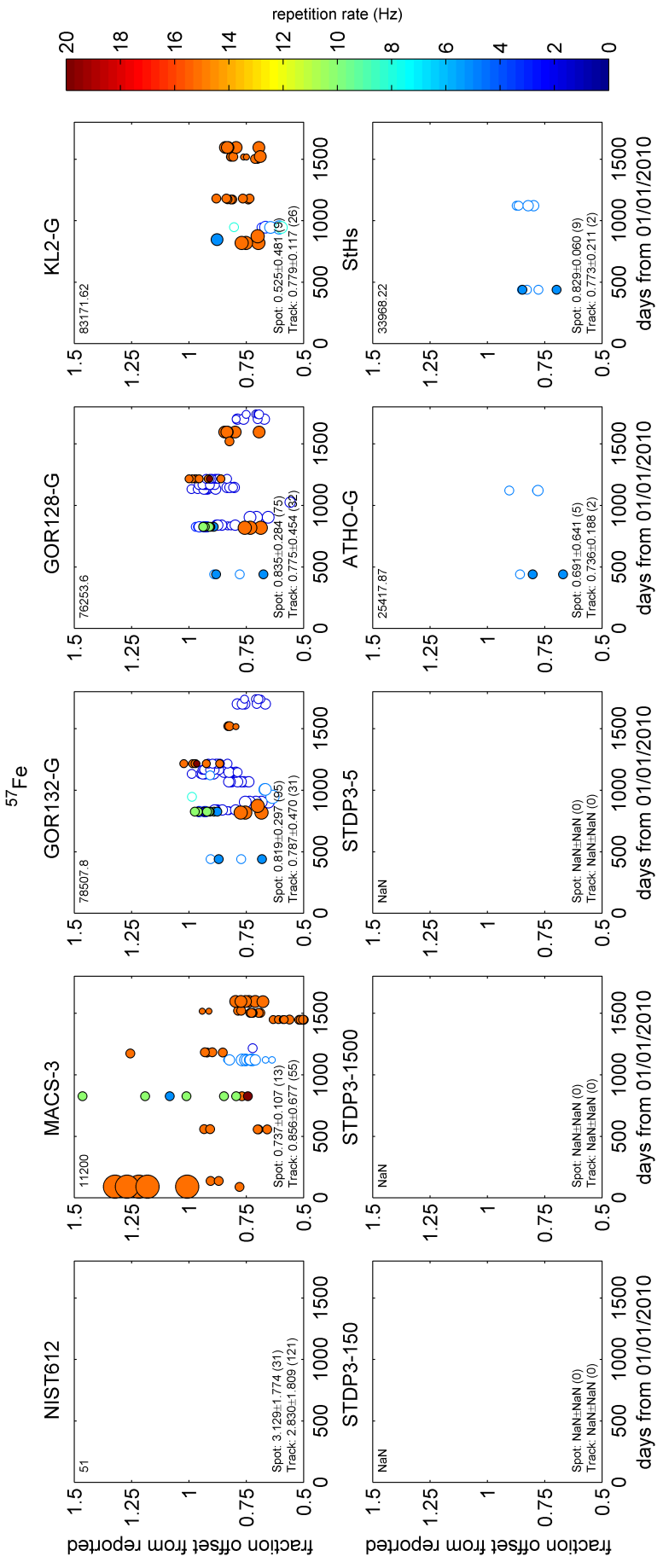
repetition rate (Hz)
20
18
16
14
12
10
8
6
4
2
0
^{57}Fe
NIST612
MACS-3
GOR132-G
STDP3-5
GOR128-G
ATHO-G
KL2-G
STHs
STDP3-150
STDP3-1500
fraction offset from reported
days from 01/01/2010
51
11200
78507.8
NaN
76253.6
25417.87
83171.62
33968.22
Spot: 3.129±1.774 (31)
Track: 2.830±1.809 (121)
Spot: 0.737±0.107 (13)
Track: 0.856±0.677 (55)
Spot: 0.819±0.297 (65)
Track: 0.787±0.470 (31)
Spot: NaN±NaN (0)
Track: NaN±NaN (0)
Spot: 0.835±0.284 (75)
Track: 0.775±0.454 (62)
Spot: 0.691±0.641 (5)
Track: 0.736±0.188 (2)
Spot: 0.525±0.481 (9)
Track: 0.779±0.117 (26)
Spot: 0.829±0.060 (9)
Track: 0.773±0.211 (2)

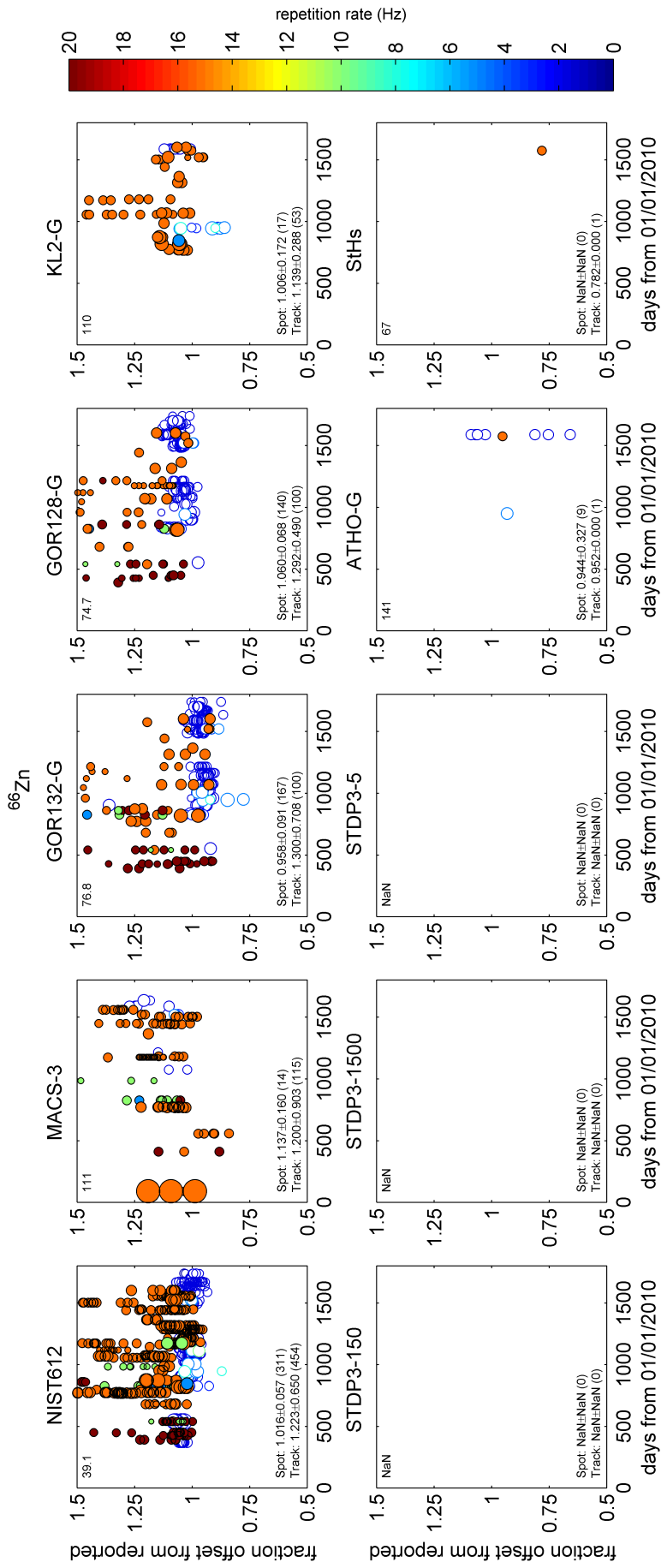
repetition rate (Hz)
20
18
16
14
12
10
8
6
4
2
0
^{66}Zn
NIST612
MACS-3
GOR132-G
STDP3-5
STDP3-1500
STDP3-150
GOR128-G
ATHO-G
KL2-G
StHs
fraction offset from reported
days from 01/01/2010
Spot: 1.016±0.057 (311)
Track: 1.223±0.650 (454)
Spot: 1.137±0.160 (14)
Track: 1.200±0.903 (115)
Spot: 0.958±0.091 (167)
Track: 1.300±0.708 (100)
Spot: NaN±NaN (0)
Track: NaN±NaN (0)
Spot: 1.060±0.068 (140)
Track: 1.292±0.490 (100)
Spot: 0.944±0.327 (9)
Track: 0.952±0.000 (1)
Spot: 1.006±0.172 (17)
Track: 1.139±0.288 (53)
Spot: NaN±NaN (0)
Track: 0.782±0.000 (1)

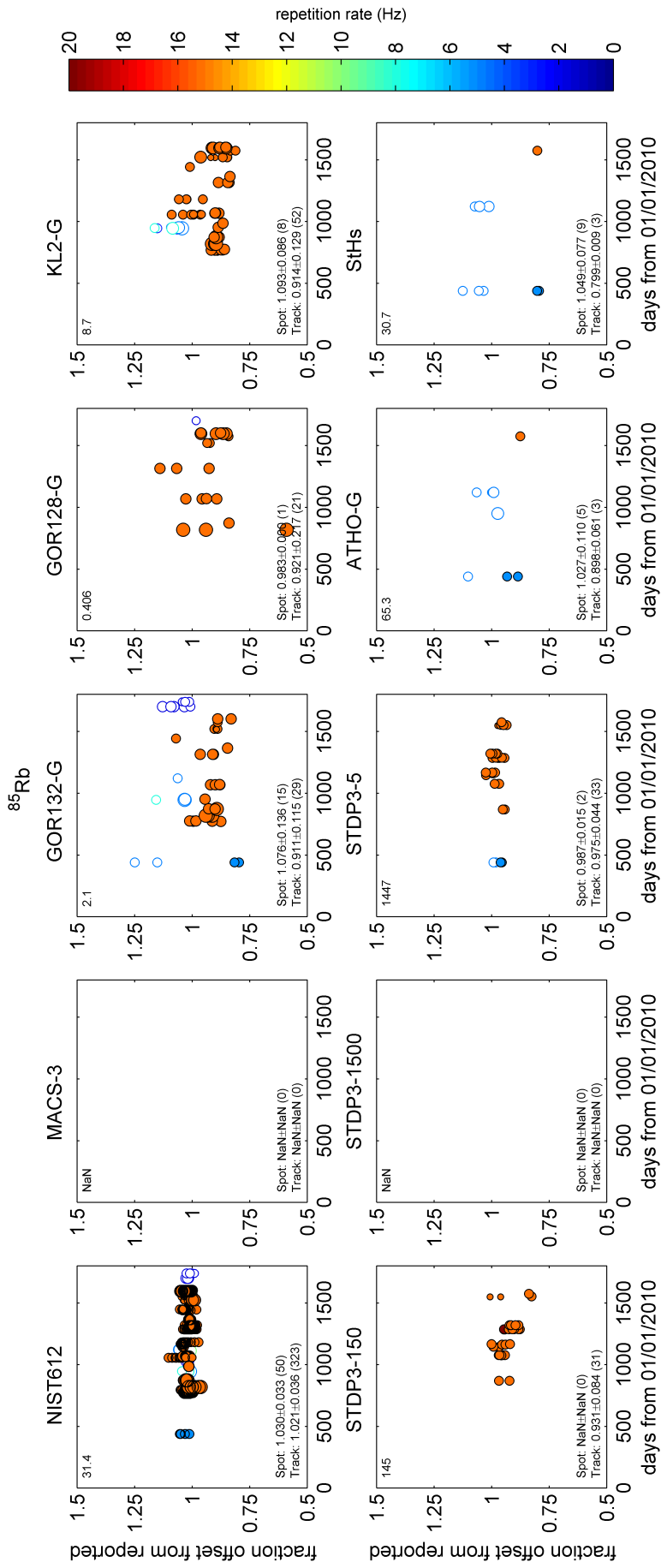
repetition rate (Hz)
20
18
16
14
12
10
8
6
4
2
0
^{85}Rb
NIST612
MACS-3
GOR132-G
GOR128-G
KL2-G
STDP3-150
STDP3-1500
STDP3-5
ATHO-G
StHs
fraction offset from reported
days from 01/01/2010
31.4
NaN
2.1
0.406
8.7
145
NaN
1447
65.3
30.7
Spot: 1.030±0.033 (50)
Track: 1.021±0.036 (323)
Spot: NaN±NaN (0)
Track: NaN±NaN (0)
Spot: 1.076±0.136 (15)
Track: 0.911±0.115 (29)
Spot: 0.983±0.000 (1)
Track: 0.921±0.217 (21)
Spot: 1.093±0.086 (8)
Track: 0.914±0.129 (52)
Spot: NaN±NaN (0)
Track: NaN±NaN (0)
Spot: 0.987±0.015 (2)
Track: 0.975±0.044 (33)
Spot: 1.027±0.110 (5)
Track: 0.898±0.061 (3)
Spot: 1.049±0.077 (9)
Track: 0.799±0.009 (3)
Spot: NaN±NaN (0)
Track: 0.931±0.084 (31)

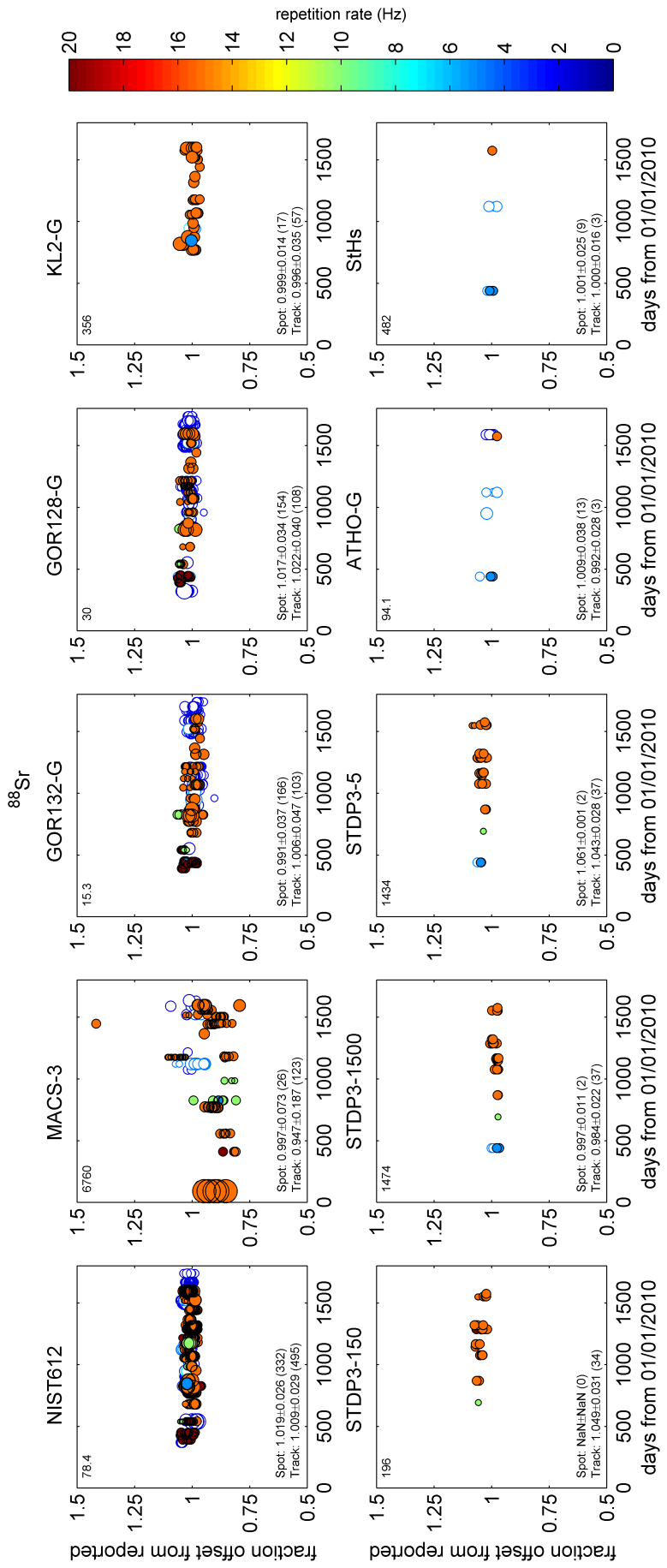
repetition rate (Hz)
20
18
16
14
12
10
8
6
4
2
0
^{88}Sr
NIST612
MACS-3
GOR132-G
GOR128-G
KL2-G
STDP3-150
STDP3-1500
STDP3-5
ATHO-G
StHs
fraction offset from reported
days from 01/01/2010
78.4
6760
15.3
30
356
196
1474
1434
94.1
482
Spot: 1.019±0.026 (332)
Track: 1.009±0.029 (495)
Spot: 0.997±0.073 (26)
Track: 0.947±0.187 (123)
Spot: 0.991±0.037 (166)
Track: 1.006±0.047 (103)
Spot: 1.017±0.034 (154)
Track: 1.022±0.040 (108)
Spot: 0.999±0.014 (17)
Track: 0.996±0.035 (57)
Spot: NaN±NaN (0)
Track: 1.049±0.031 (34)
Spot: 0.997±0.011 (2)
Track: 0.984±0.022 (37)
Spot: 1.061±0.001 (2)
Track: 1.043±0.028 (37)
Spot: 1.009±0.038 (13)
Track: 0.992±0.028 (3)
Spot: 1.001±0.025 (9)
Track: 1.000±0.016 (3)

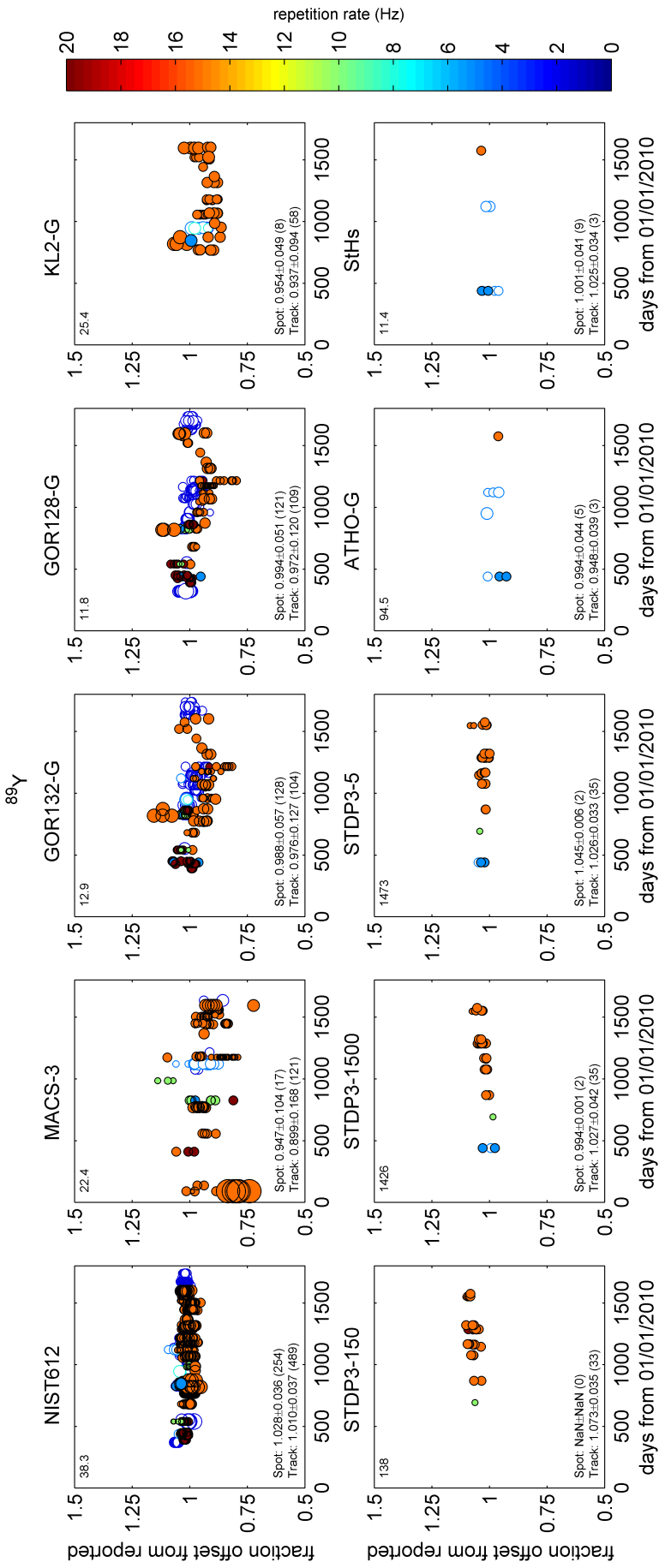
repetition rate (Hz)
89Y
NIST612
MACS-3
GOR132-G
GOR128-G
KL2-G
STDP3-150
STDP3-1500
STDP3-5
ATHO-G
StHs
fraction offset from reported
days from 01/01/2010

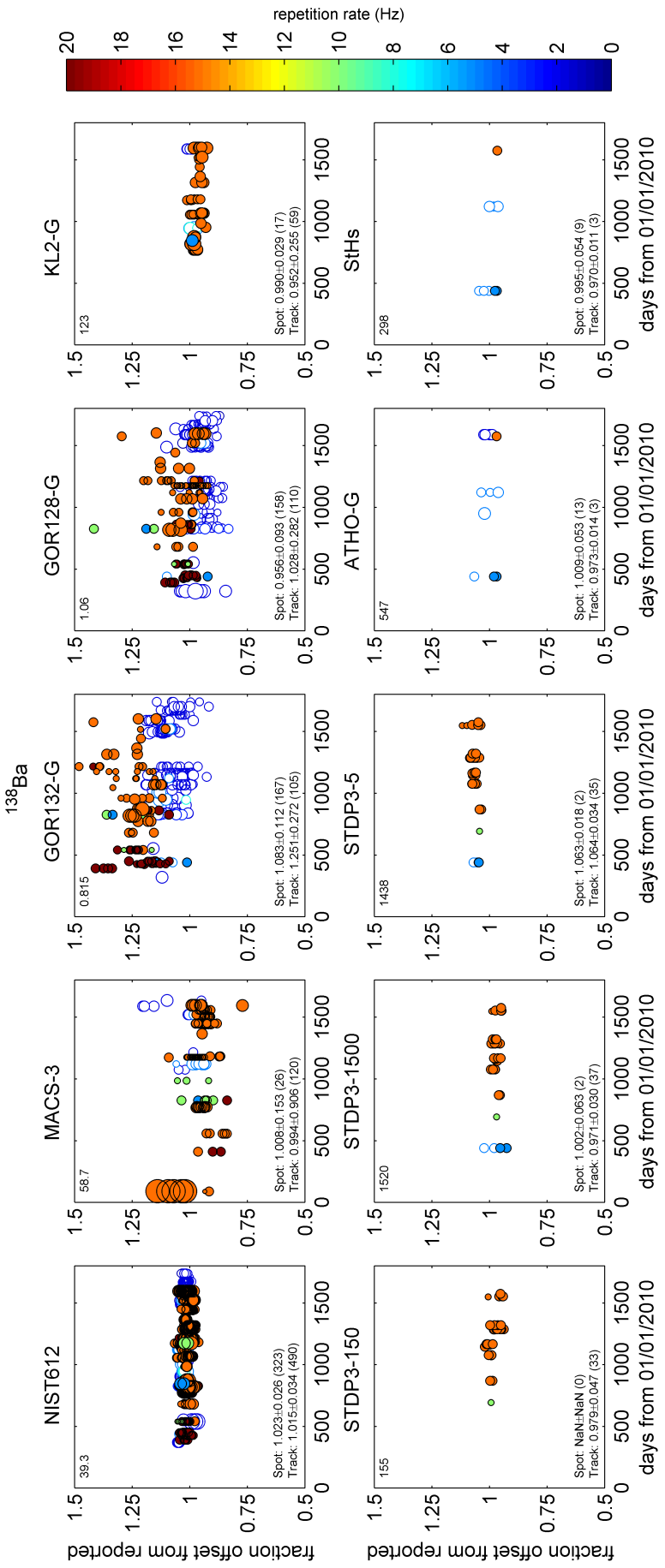
repetition rate (Hz)
20
18
16
14
12
10
8
6
4
2
0
^{138}Ba
NIST612
MACS-3
GOR132-G
GOR128-G
KL2-G
STDP3-150
STDP3-1500
STDP3-5
ATHO-G
StHs
fraction offset from reported
days from 01/01/2010
39.3
58.7
0.815
1.06
123
155
1520
1438
547
298
Spot: 1.023±0.026 (323)
Track: 1.015±0.034 (490)
Spot: 1.008±0.153 (26)
Track: 0.994±0.906 (120)
Spot: 1.083±0.112 (167)
Track: 1.251±0.272 (105)
Spot: 0.956±0.093 (158)
Track: 1.028±0.282 (110)
Spot: 0.990±0.029 (17)
Track: 0.952±0.255 (59)
Spot: NaN±NaN (0)
Track: 0.979±0.047 (33)
Spot: 1.002±0.063 (2)
Track: 0.971±0.030 (37)
Spot: 1.063±0.018 (2)
Track: 1.064±0.034 (35)
Spot: 1.009±0.053 (13)
Track: 0.973±0.014 (3)
Spot: 0.995±0.054 (9)
Track: 0.970±0.011 (3)

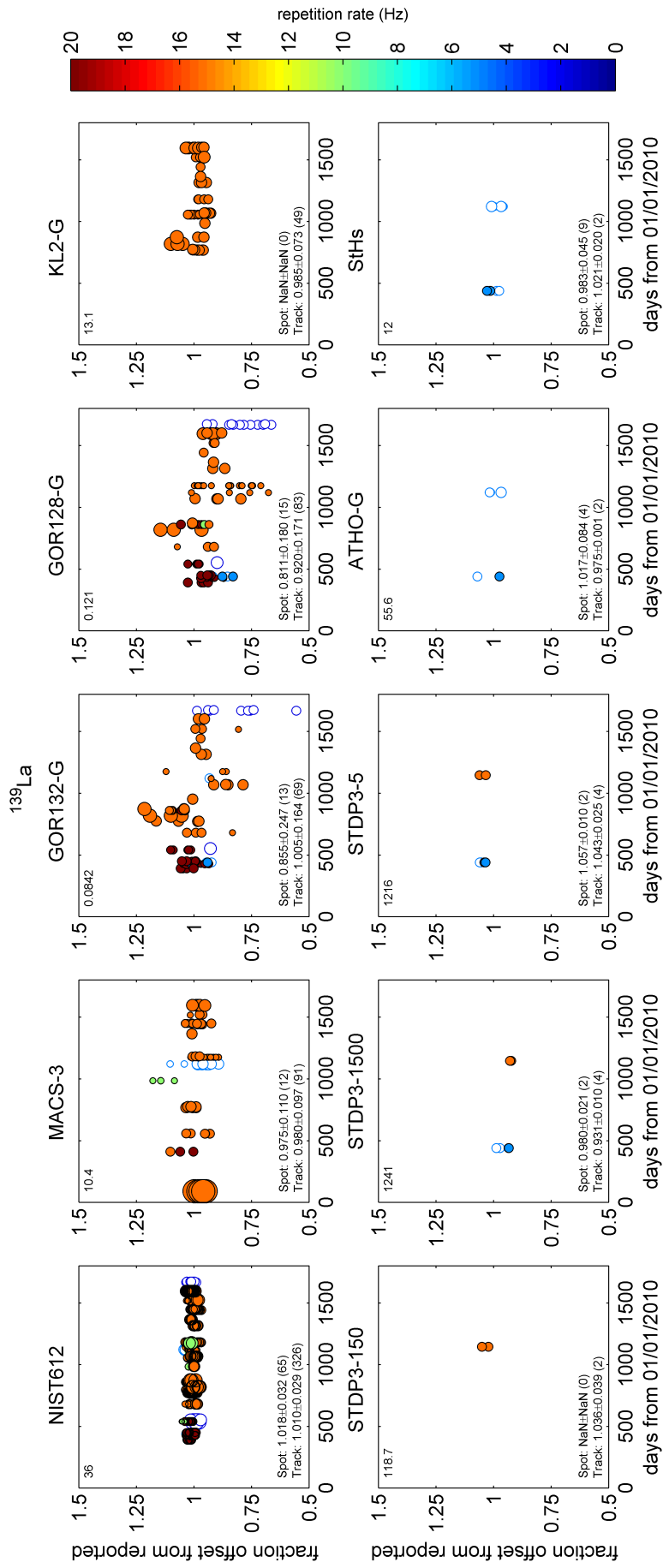
repetition rate (Hz)
20
18
16
14
12
10
8
6
4
2
0
^{139}La
NIST612
MACS-3
GOR132-G
GOR128-G
KL2-G
STDP3-150
STDP3-1500
STDP3-5
ATHO-G
StHs
fraction offset from reported
days from 01/01/2010
36
10.4
0.0842
0.121
13.1
118.7
1241
1216
55.6
12
Spot: 1.018±0.032 (65)
Track: 1.010±0.029 (326)
Spot: 0.975±0.110 (12)
Track: 0.980±0.097 (91)
Spot: 0.855±0.247 (13)
Track: 1.005±0.164 (69)
Spot: 0.811±0.180 (15)
Track: 0.920±0.171 (83)
Spot: NaN±NaN (0)
Track: 0.985±0.073 (49)
Spot: NaN±NaN (0)
Track: 1.036±0.039 (2)
Spot: 0.980±0.021 (2)
Track: 0.931±0.010 (4)
Spot: 1.057±0.010 (2)
Track: 1.043±0.025 (4)
Spot: 1.017±0.084 (4)
Track: 0.975±0.001 (2)
Spot: 0.983±0.045 (9)
Track: 1.021±0.020 (2)

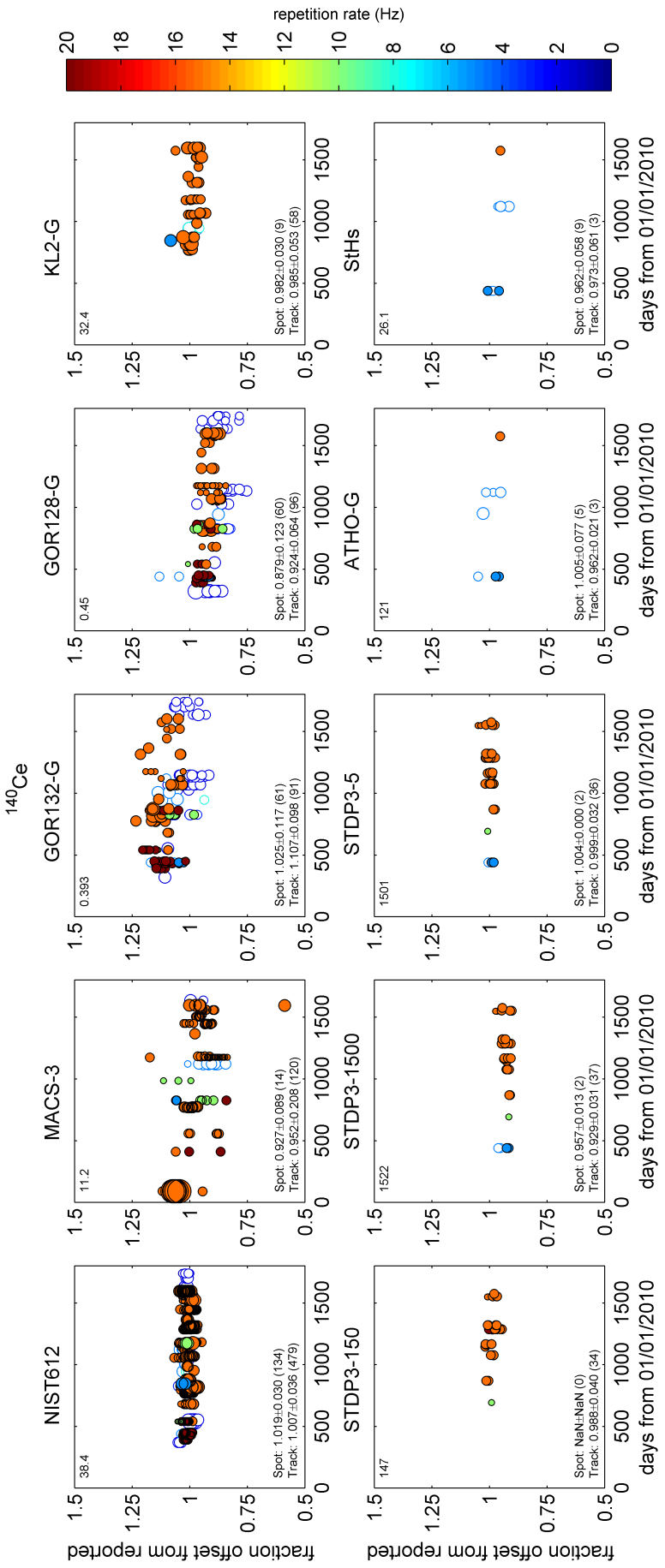
repetition rate (Hz)
20
18
16
14
12
10
8
6
4
2
0
^{140}Ce
NIST612
MACS-3
GOR132-G
GOR128-G
KL2-G
STDP3-150
STDP3-1500
STDP3-5
ATHO-G
StHs
fraction offset from reported
days from 01/01/2010
38.4
11.2
0.393
0.45
32.4
147
1522
1501
121
26.1
Spot: 1.019±0.030 (134)
Track: 1.007±0.036 (479)
Spot: 0.927±0.089 (14)
Track: 0.952±0.208 (120)
Spot: 1.025±0.117 (61)
Track: 1.107±0.098 (91)
Spot: 0.879±0.123 (60)
Track: 0.924±0.064 (96)
Spot: 0.982±0.030 (9)
Track: 0.985±0.053 (58)
Spot: NaN±NaN (0)
Track: 0.988±0.040 (34)
Spot: 0.957±0.013 (2)
Track: 0.929±0.031 (37)
Spot: 1.004±0.000 (2)
Track: 0.999±0.032 (36)
Spot: 1.005±0.077 (5)
Track: 0.962±0.021 (3)
Spot: 0.962±0.058 (9)
Track: 0.973±0.061 (3)

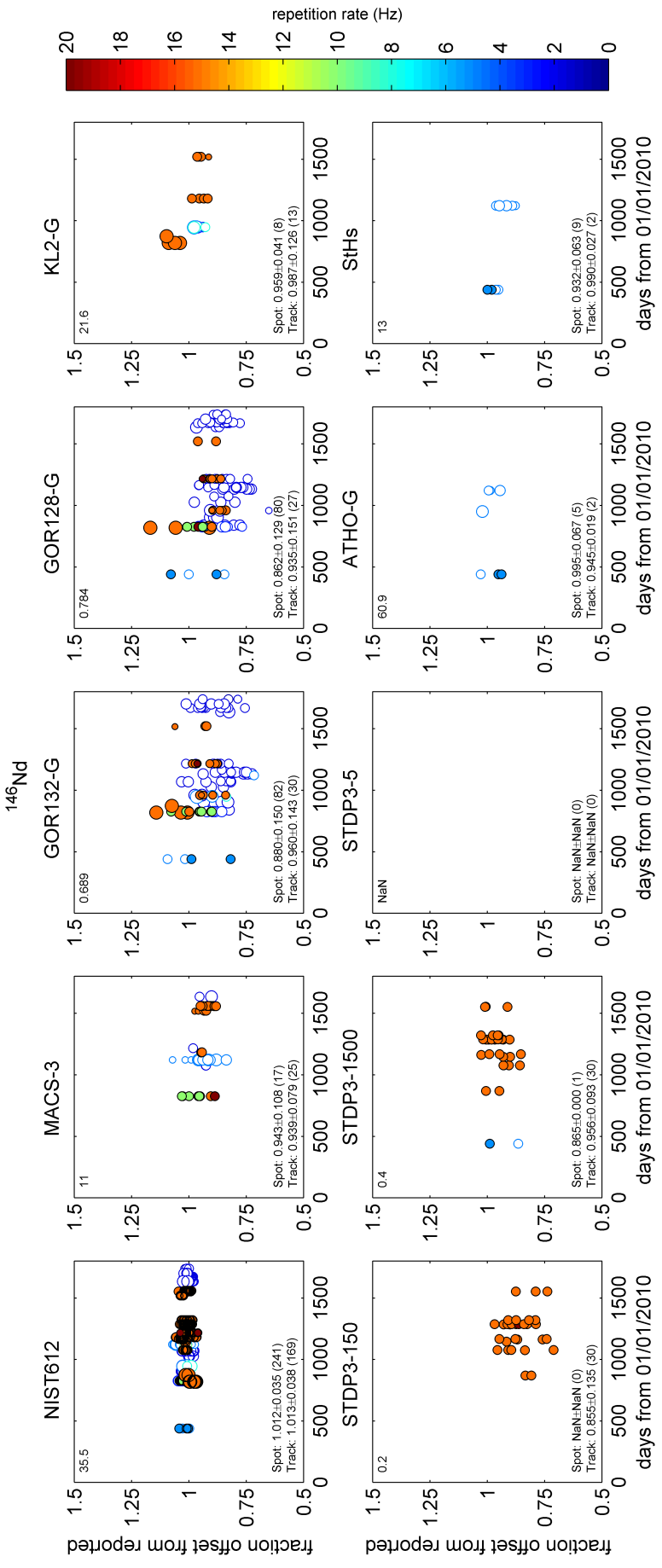
repetition rate (Hz)
20
18
16
14
12
10
8
6
4
2
0
146Nd
NIST612
MACS-3
GOR132-G
STDP3-5
GOR128-G
ATHO-G
KL2-G
StHs
STDP3-150
STDP3-1500
fraction offset from reported
days from 01/01/2010
35.5
Spot: 1.012±0.035 (241)
Track: 1.013±0.038 (169)
11
Spot: 0.943±0.108 (17)
Track: 0.939±0.079 (25)
0.689
Spot: 0.880±0.150 (82)
Track: 0.960±0.143 (30)
NaN
Spot: NaN±NaN (0)
Track: NaN±NaN (0)
0.784
Spot: 0.862±0.129 (80)
Track: 0.935±0.151 (27)
60.9
Spot: 0.995±0.067 (5)
Track: 0.945±0.019 (2)
21.6
Spot: 0.959±0.041 (8)
Track: 0.987±0.126 (13)
13
Spot: 0.932±0.063 (9)
Track: 0.990±0.027 (2)
0.2
Spot: NaN±NaN (0)
Track: 0.855±0.135 (30)
0.4
Spot: 0.865±0.000 (1)
Track: 0.956±0.093 (30)

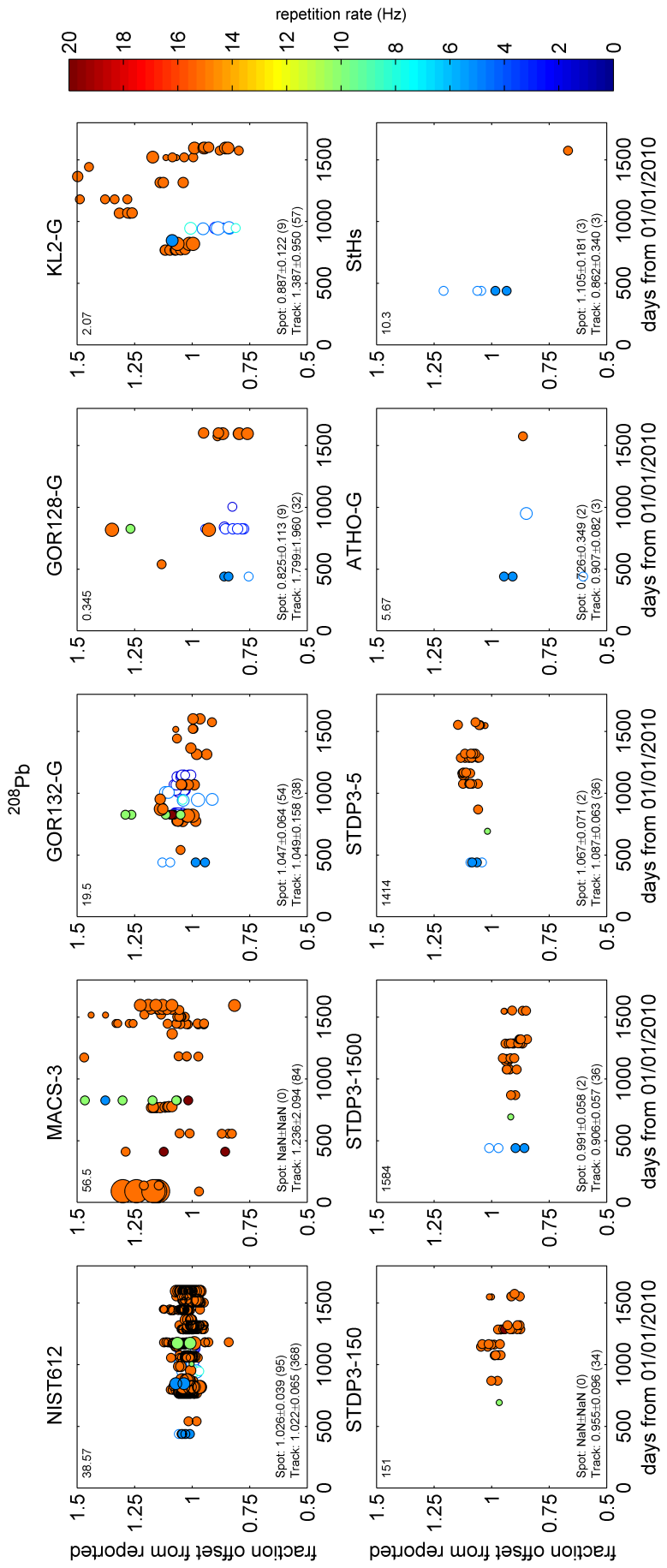
repetition rate (Hz)
20
18
16
14
12
10
8
6
4
2
0
^{208}Pb
NIST612
MACS-3
GOR132-G
GOR128-G
KL2-G
STDP3-150
STDP3-1500
STDP3-5
ATHO-G
StHs
fraction offset from reported
days from 01/01/2010
38.57
56.5
19.5
0.345
2.07
151
1584
1414
5.67
10.3
Spot: 1.026±0.039 (95)
Track: 1.022±0.065 (368)
Spot: NaN±NaN (0)
Track: 1.236±2.094 (84)
Spot: 1.047±0.064 (54)
Track: 1.049±0.158 (38)
Spot: 0.825±0.113 (9)
Track: 1.799±1.960 (32)
Spot: 0.887±0.122 (9)
Track: 1.387±0.950 (57)
Spot: NaN±NaN (0)
Track: 0.955±0.096 (34)
Spot: 0.991±0.058 (2)
Track: 0.906±0.057 (36)
Spot: 1.067±0.071 (2)
Track: 1.087±0.063 (36)
Spot: 0.726±0.349 (2)
Track: 0.907±0.082 (3)
Spot: 1.105±0.181 (3)
Track: 0.862±0.340 (3)

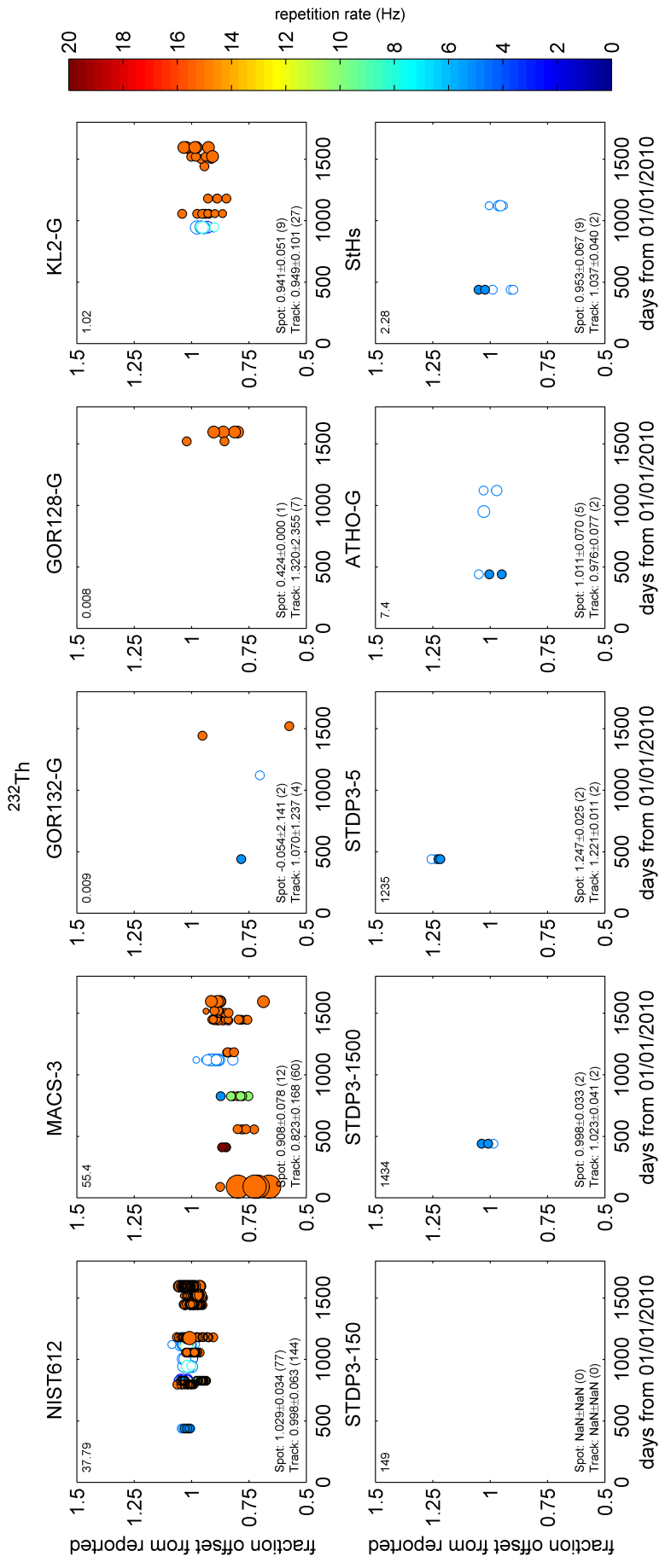
repetition rate (Hz)
20
18
16
14
12
10
8
6
4
2
0
^{232}Th
NIST612
MACS-3
GOR132-G
GOR128-G
KL2-G
STDP3-150
STDP3-1500
STDP3-5
ATHO-G
StHs
fraction offset from reported
days from 01/01/2010
37.79
55.4
0.009
0.008
1.02
149
1434
1235
7.4
2.28
Spot: 1.029±0.034 (77)
Track: 0.998±0.063 (144)
Spot: 0.908±0.078 (12)
Track: 0.823±0.168 (60)
Spot: -0.054±2.141 (2)
Track: 1.070±1.237 (4)
Spot: 0.424±0.000 (1)
Track: 1.320±2.355 (7)
Spot: 0.941±0.051 (9)
Track: 0.949±0.101 (27)
Spot: NaN±NaN (0)
Track: NaN±NaN (0)
Spot: 0.998±0.033 (2)
Track: 1.023±0.041 (2)
Spot: 1.247±0.025 (2)
Track: 1.221±0.011 (2)
Spot: 1.011±0.070 (5)
Track: 0.976±0.077 (2)
Spot: 0.953±0.067 (9)
Track: 1.037±0.040 (2)

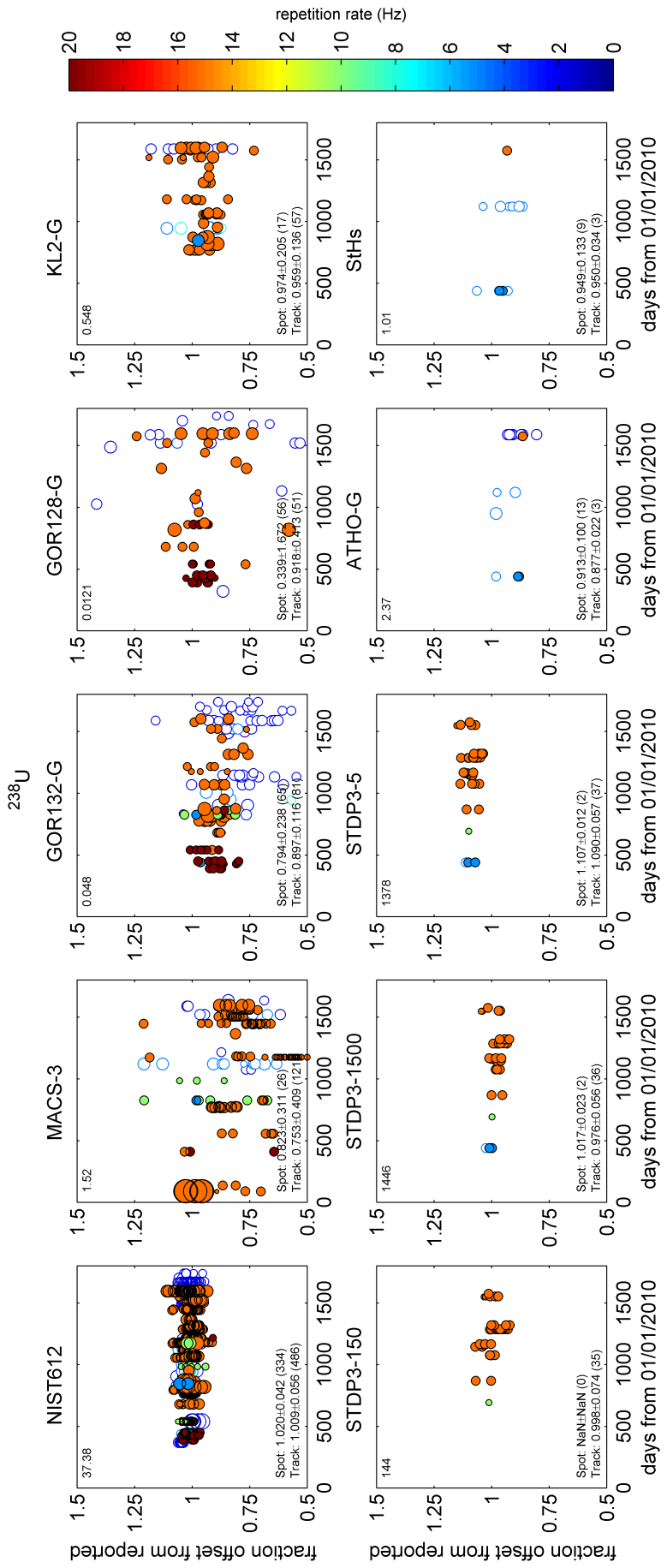
repetition rate (Hz)
20
18
16
14
12
10
8
6
4
2
0
^{238}U
NIST612
MACS-3
GOR132-G
STDP3-5
GOR128-G
ATHO-G
KL2-G
StHs
STDP3-150
STDP3-1500
fraction offset from reported
days from 01/01/2010
37.38
1.52
0.048
1378
0.0121
2.37
0.548
1.01
144
1446
Spot: 1.020±0.042 (334)
Track: 1.009±0.056 (486)
Spot: 0.823±0.311 (26)
Track: 0.753±0.409 (121)
Spot: 0.794±0.238 (65)
Track: 0.897±0.116 (81)
Spot: 1.107±0.012 (2)
Track: 1.090±0.057 (37)
Spot: 0.339±1.672 (56)
Track: 0.918±0.473 (51)
Spot: 0.913±0.100 (13)
Track: 0.877±0.022 (3)
Spot: 0.974±0.205 (17)
Track: 0.959±0.136 (57)
Spot: 0.949±0.133 (9)
Track: 0.950±0.034 (3)
Spot: 1.017±0.023 (2)
Track: 0.976±0.056 (36)
Spot: NaN±NaN (0)
Track: 0.998±0.074 (35)